Determination of Quantum States and the Quantum Measure using Interferometry

RRI

Sanchari Chakraborti

Supervisor: Prof. Urbasi Sinha

Light and Matter Physics

Raman Research Institute

Bengaluru, Karnataka 560080, India

A Thesis Submitted for the Degree of

Doctor of Philosophy

to

Jawaharlal Nehru University

New Delhi 110067, India

ज.ने.वि.
JNU

Declaration

The scientific work reported in this thesis, titled "**Determination of Quantum States and the Quantum Measure using Interferometry**" is based on the experimental research carried out at the **Quantum Information and Computing (QuIC) Lab**, Light and Matter Physics Group, **Raman Research Institute**, Bangalore, India, unless otherwise specified. The work involved various collaborations both within India and abroad. No part of the thesis has been submitted elsewhere for any other degree or qualification. The content of this thesis has been run through the **DrillBit** software to check for plagiarism.

Sanchari Chakraborti
Student
Light and Matter Physics,
Raman Research Institute,
Bangalore, India.

Prof. Urbasi Sinha
Supervisor
Light and Matter Physics,
Raman Research Institute,
Bangalore, India.

Certificate

This is to certify that the thesis entitled "**Determination of Quantum States and the Quantum Measure using Interferometry**" submitted by **Sanchari Chakraborti** for the award of the degree of **Doctor of Philosophy** at **Jawaharlal Nehru University** in New Delhi, India, is an authentic record of the original research work carried out by the candidate at the **Raman Research Institute** in Bangalore, India. This work has not been submitted to any other University or Institute for the attainment of any other degree or diploma.

Prof. Tarun Sauradeep
Director
Raman Research Institute,
Bangalore, India.

Prof. Urbasi Sinha
Supervisor
Light and Matter Physics,
Raman Research Institute,
Bangalore, India.

Synopsis

Determination of Quantum States and the Quantum Measure using Interferometry

Introduction:

The wave nature of light manifests itself, giving rise to an interference pattern which has found numerous applications in science and technology ranging from sensing rotations in laser gyroscopes to the recent detection of gravitational waves. Even in the quantum domain, where the particle nature of light cannot be avoided while describing the detection of individual photons, the interference pattern emerges as a collective statistical consequence of the wavefunction description. Attempts to describe the kinematics of a quantum particle as having classical-like histories would require a new description of a probability-like quantity in order to explain the interference phenomena. From the perspective of a foundational description of quantum mechanics suitable for accommodating a theory of space-time, the notion of considering quantum mechanics as a theory involving a generalization of probability, called the "quantum measure" was proposed [1]. Mapping of theoretical elements to the experimental scenario would aid towards a concrete description of non-classical behavior along with presenting opportunities for future tests of fundamental aspects of quantum theory. On the application side, interferometeric techniques can be useful in quantum information processing, where characterization of prepared quantum states is vital to gauge the eventual fidelity of quantum computation or communication protocols.

In this thesis, interferometric techniques have been used (i) as a tool to present a method to determine unknown quantum states using the information processed from interference patterns, and (ii) to exemplify the non-classical value of "quantum measure" associated with a system. Although the experiments described in the thesis were performed with classical laser light, the results are applicable in the analysis of the behavior of an ensemble of single photons. This is because an interference pattern generated from a coherent source (wave nature) of light is equivalent to the average pattern produced by an ensemble of single photons (corpuscular nature). The first few chapters of the thesis discuss the theoretical descriptions of the quantum state determination scheme and give an experimental demonstration of the technique for the characterization of two-dimensional quantum states, called qubits. The scheme is extended in theory for pure qudit ($d-$dimensional system with $d > 2$) and pure bipartite qubits as well. The last part of the thesis presents a demonstration for determining the value of quantum measure for a particular event in an experimental scenario, which according to the original proposal [2] could demonstrate an experimental scenario that can give a non-classical measure.

Quantum State Estimation:

In quantum mechanics, the knowledge of the quantum state is essential while dealing with quantum systems in quantum information and communication protocols, the tests on quantum foundations, or even for predicting the probabilistic behavior of the system subject to any measurement. The standard and widely used method for characterizing an unknown quantum state is Quantum State Tomography (QST) which requires multiple distinct projective measurements to be performed on many identical copies of the same system and additional post-processing to ensure the physicality of the reconstructed density matrix [3]. One of the alternatives to standard QST is the direct state estimation technique employing weak measurement [4] where an unknown quantum state is inferred from the complex weak values of the projectors obtained for different post-selections. Direct measurement of quantum states in a strong interaction regime can also be performed, one such possible method is to obtain the quantum state by measuring the expectation values of non-Hermitian column operators [5].

In this thesis, a new technique has been presented which utilizes the phenomena of interference in order to infer an unknown quantum state of an ensemble of identically prepared particles. We name the technique Quantum State Interferography (QSI), using which any unknown qubit state can be reconstructed by post-processing a single interference pattern

[6]. The general density matrix of a mixed qubit state can be parameterized by three quantities, say (θ, ϕ, μ). For a qubit state (say, represented in $\{|0\rangle, |1\rangle\}$ basis or for instance, $\{|H\rangle, |V\rangle\}$ basis in polarization d.o.f.) the three parameters can be uniquely determined from the expectation values of two operators: $\hat{\Pi}_0 = |0\rangle\langle 0|$, the projection operator along $|0\rangle$ and $\hat{\sigma}_- = \hat{\sigma}_x - i\hat{\sigma}_y$, the spin ladder operator. Further, the complex expectation value of the non-Hermitian $\hat{\sigma}_-$ operator can be experimentally obtained by polar decomposing $\hat{\sigma}_-$ into a unitary $\hat{\sigma}_x$ and a Hermitian $\hat{\Pi}_0$, i.e., $\hat{\sigma}_- = \hat{\sigma}_x\hat{\Pi}_0$ and finding the expectation values of the two [7, 8].

The three quantities (θ, ϕ, μ) specifying an unknown density matrix $\rho(\theta, \phi, \mu)$ form an one to one map with the set of the following three quantities: average intensity $(\bar{I})$, phase shift (Φ) and visibility (V) of an interference pattern obtained at the end of a two-path interferometer with $\hat{\sigma}_x$ operator in one path and $\hat{\Pi}_0$ in the other. Thus, QSI enables one to experimentally determine an unknown qubit state from a single experimental setup by observing $(\bar{I}, \Phi, V)$ obtained from a single interference pattern without the need to change any internal settings within the setup (single-shot) in between the incidence of the unknown state and the extraction of the state information.

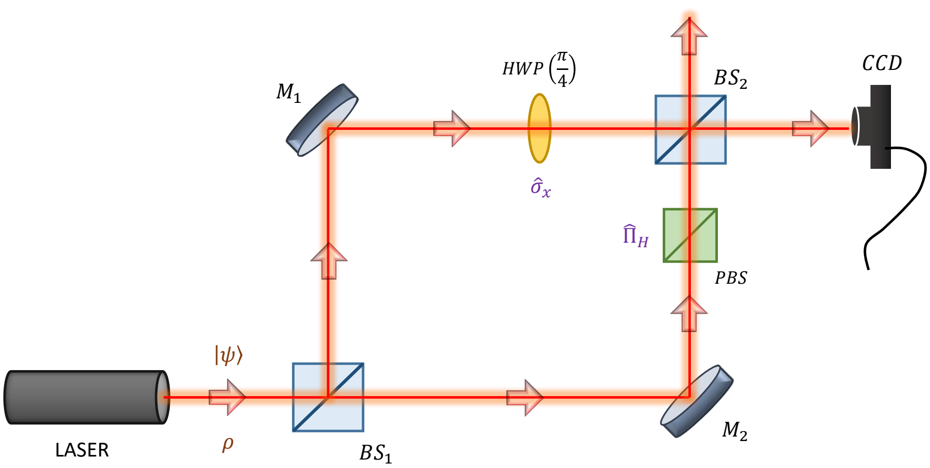

Figure 1: The schematic for the polarization state interferography using a two-path Interferometer formed with two beam splitters BS_1, BS_2 and two mirrors M_1, M_2. We use the non-unitary Hermitian operator $\hat{\Pi}_H$ in one of the paths and unitary $\hat{\sigma}_x$ Pauli operator in the other path. The resultant interference pattern (intensity as a function of phase shift) can be analyzed to obtain the unknown polarization state of the incident light.

In this thesis, we have presented the experimental implementation of the QSI scheme in an optical setup for characterizing the polarization state of light. The experimental attempt to perform QSI with Mach-Zehnder Interferometer (MZI) is discussed. Several experimental challenges that affect the state determination in MZI are mentioned. Some of them were overcome by using a Dispaced Sagnac Interferometer (DSI). A comparative study of both the techniques along with the analysis of the data obtained from the two different interferometers has also been presented in the thesis.

Theoretically, the protocol of QSI is extended for the reconstruction of pure state in $d-$dimensional Hilbert space (qudits) $|\psi\rangle^{(d)}$, where $d > 2$. A $d-$dimensional pure qudit state reconstruction using QSI requires the processing of $(d-1)$ interference patterns, each of which is obtained by performing single qubit QSI on the two-dimensional subspaces of the pure qudit arranged in a particular sequence. Thus, with the dimensionality of the Hilbert space the required number of measurements scales linearly in QSI.

QSI can also be employed to infer an unknown bipartite qubit $|\Psi\rangle_{AB}$, if known to be pure, by post-processing interference patterns obtained from two measurement settings. QSI provides an efficient way to quantify the entanglement of a pure bipartite qubit by performing single qubit QSI on any one of the subsystems.

Determination of Non-classical Measure:

A history based framework of quantum mechanics, namely the Quantum Measure Theory (QMT) is considered as a generalized probability theory inspired by the path-integral approach. Unlike classical measure theory, quantum measure theory allows for interference and assigns a non-negative real number $\mu(E)$ to every set of histories E (called an event) associated with the system. $\mu(E)$ is called the "quantum measure" for the event E, which in general, can not be interpreted as an ordinary probability measure since $\mu(E)$ neither follows the probability sum rule nor does it have an upper bound of one. Thus, any value of measure obtained to be greater than one makes it non-classical.

We present an experimental setup allowing interference, the analysis of which gives us a non-classical quantum measure. An experimental demonstration in an optical setup is presented where a particular event associated with a photonic system is filtered out and the value of the quantum measure corresponding to that event is analyzed. We experimentally characterized the setup and measured the probability of occurrence of the event associated with a photonic system. If the probability of occurrence of each event were ideally non-destructively measured using ancillas and analyzing the ancilla states, we could have experimentally obtained the non-classical quantum measure. The comparison of the above two approaches has been discussed.

Outlook:

In this thesis, we present the use of interferometric technique in two experimental scenarios; Quantum State Interferography (QSI) potentially is useful in any quantum information processing applications while the determination of non-classical quantum measure can direct foundational studies in quantum mechanics and has the potential to provide an experimental footing to the largely theoretical construct so far. Quantum state interferography, the state determination technique employing interferometry, provides a "black-box approach" to quantum state determination. The slit version of it will be useful in miniaturizing (only a few *cm* long) the state estimating device and making it robust against external phase noise. Determination of quantum states is an important resource for all quantum technology-based applications, for instance, quantum computation and quantum communication, and also for experiments in quantum foundations where QSI can serve as an efficient tool for state characterization. Interferometry is also used to determine the value of quantum measure which forms one of the basis of theoretical studies towards quantum gravity and generalized probability theories.

References

[1] Rafael D. Sorkin. "Quantum Mechanics as Quantum Measure Theory". In: *Modern Physics Letters A* 09.33 (1994), pp. 3119–3127. DOI: 10.1142/s021773239400294x.

[2] Álvaro Mozota Frauca and Rafael Dolnick Sorkin. "How to Measure the Quantum Measure". In: *International Journal of Theoretical Physics* 56.1 (2017), pp. 232–258. DOI: 10.1007/s10773-016-3181-x.

[3] Daniel F. V. James et al. “Measurement of qubits”. In: *Physical Review A* 64.5 (2001), p. 052312. DOI: 10.1103/PhysRevA.64.052312.

[4] Jeff S. Lundeen et al. “Direct measurement of the quantum wavefunction”. In: *Nature* 474.7350 (2011), pp. 188–191. DOI: 10.1038/nature10120.

[5] Eliot Bolduc, Genevieve Gariepy, and Jonathan Leach. “Direct measurement of large-scale quantum states via expectation values of non-Hermitian matrices”. In: *Nature Communications* 7.1 (2016), p. 10439. DOI: 10.1038/ncomms10439.

[6] Surya Narayan Sahoo et al. “Quantum State Interferography”. In: *Physical Review Letters* 125.12 (2020). DOI: 10.1103/physrevlett.125.123601.

[7] Arun Kumar Pati, Uttam Singh, and Urbasi Sinha. “Measuring non-Hermitian operators via weak values”. In: *Phys. Rev. A* 92 (5 2015), p. 052120. DOI: 10.1103/PhysRevA.92.052120.

[8] Gaurav Nirala et al. “Measuring average of non-Hermitian operator with weak value in a Mach-Zehnder interferometer”. In: *Phys. Rev. A* 99 (2 2019), p. 022111. DOI: 10.1103/PhysRevA.99.022111.

Sanchari Chakraborti
Student
Light and Matter Physics,
Raman Research Institute,
Bangalore, India.

Prof. Urbasi Sinha
Supervisor
Light and Matter Physics,
Raman Research Institute,
Bangalore, India.

List of Publications

Published Articles in Academic Journal

[1] Surya Narayan Sahoo, Sanchari Chakraborti, Arun Kumar Pati, and Urbasi Sinha. Quantum State Interferography. Phys. Rev. Lett. **125**, 123601 (2020).

DOI: 10.1103/PhysRevLett.125.123601 **arXiv:** quant-ph, 2002.07446v2

(This work forms Chapter-2, Chapter-3 and Chapter-4 of the thesis.)

[2] Surya Narayan Sahoo, Sanchari Chakraborti, Som Kanjilal, Saumya Ranjan Behera, Dipankar Home, Alex Matzkin, and Urbasi Sinha. Unambiguous joint detection of spatially separated properties of a single photon in the two arms of an interferometer. Commun. Phys. **6**, 203 (2023).

DOI: 10.1038/s42005-023-01317-7 **arXiv:** quant-ph, 2201.11425

(This work is not included in the thesis. It has formed a part of the thesis of Surya Narayan Sahoo submitted in May, 2022.)

Article in Preparation

[1] Sanchari Chakraborti, Rafael D. Sorkin, and Urbasi Sinha. Measuring a "Probability" > 1, To be submitted by Dec, 2023 (Title subject to modification).

(This work forms Chapter-5 and Chapter-6 of the thesis.)

Published Article in Scientific Magazine

[1] Urbasi Sinha, Surya Narayan Sahoo, Ashutosh Singh, Kaushik Joarder, Rishab Chatterjee, and Sanchari Chakraborti. Single-photon Sources. Opt. Photon. News, 30(9):32–39, Sep 2019.

DOI: 10.1364/OPN.30.9.000032

Sanchari Chakraborti
Student
Light and Matter Physics,
Raman Research Institute,
Bangalore, India.

Prof. Urbasi Sinha
Supervisor
Light and Matter Physics,
Raman Research Institute,
Bangalore, India.

Acknowledgements

In this long journey, which started with travelling to different cities within India for Ph.D. interviews to finally writing the thesis with the hope of getting the degree, life has presented a variety of experiences that have fostered personal growth. It has been a ride with its share of peaks and troughs, moments of exhilaration and despair, a treasure trove of memories, and of course, the thrill of scientific discoveries through discussions, observations, learning and performing experiments. This journey has been shaped by the contributions of many individuals, whose combined efforts are the manifestation of this thesis.

First, I would like to extend my gratitude to the RRI Ph.D. student selection committee of 2016, who found me capable and granted me the opportunity to pursue a Ph.D. at this prestigious institution. Next, I thank my supervisor, Prof. Urbasi Sinha, for letting me conduct the research in the QuIC Lab and for her guidance throughout these years. I also express my sincere thanks to my external collaborators Prof. Rafael Sorkin (Perimeter Institute, Canada), Prof. Arun K. Pati (HRI, India), Prof. Alex Matzkin (CNRS, France) and Prof. Dipankar Home (Bose Institute, India) for the scientific discussions, insights and ideas that helped in addressing some of the challenges encountered during this journey. I am profoundly thankful to Meena Ma'am, Mugundhan, Rakshita, and Nagalakshmi for their assistance in the design and characterization of various electronic circuits and equipment, required for setting up the experiments. Further, I wish to acknowledge my thesis advisory committee for their time and feedback during the annual assessments.

I would like to convey my appreciation to the individuals from various departments at RRI, including the Administration, Library, IT and Computer section, Accounts, Workshop, E and B, Civil, Clinic, Store, Canteen and Guest house, for their support in different instances. I wholeheartedly thank Savitha Ma'am from Light and Matter Physics Group (the department secretary); Harini Ma'am and Radha Ma'am from Administration; Manjunath KP and Nagraj sir from Library; Jacob sir from the Computer section for their understanding, assistance, and prompt co-operation in various moments of need. I am grateful for the respective contributions of the cleaning staff, shuttle drivers, security guards, and RMV hostel cooks, who have played a part in making this journey smooth and lively.

I want to express my heartfelt gratitude towards my lab mate and collaborator, Surya Narayan Sahoo, for his indispensable contributions to this academic journey (and beyond). His guidance in various aspects – from teaching me the basics like optics handling to tools like LabView for device interfacing; from explaining different scientific concepts to various techniques for troubleshooting – has been instrumental in my learning process. The stimulating discussions that we've had on various topics, including nature, science, technology, society, animal behavior, music etc., during the work breaks have helped to keep the lab environment vibrant and engaging. Whether offering clear solutions or providing motivation during times of confusion or disappointment – his presence and companionship have greatly enriched my experience, for which I am eternally thankful.

I will forever be indebted to the members of SAAC (Students Academic Affairs Committee) of the academic year 2021-2022, especially the chairperson Prof. Sadiq Ali Rangwala. His inspiring words, encouragement, empathy and immense support have been a significant force propelling my journey forward during the most challenging phase of my life thus far. Furthermore, I owe a deep sense of gratitude to Arun Bahuleyan and Vardhan R. Thakar, who took the initiative and put in proactive efforts to ensure that I get the necessary permissions from the administration to continue the final phase of this journey from home, which allowed me to be with my family at the time of dare need.

Last but certainly not least, the people who need special mentions for their substantial support during various instances throughout the Ph.D. tenure are Sourav da, Ankita di, Bapan, Ranita, Abhishek, Shampa aunty, Subham and Deyashree. Others who made this journey a memorable one are Rishab, Saikat, Anand, Shovan, Swarnadeep, Ingita, Akhil, Jyotirmoy, Avik, Animesh da, Shilpa, Dipak, Subhajit da, Kaushik da, Maheswar da, Arup da, Sagar da, Saumya, Sayari, Gourab, Shreya, Anirban, Shreshtha and many more. How could I ever forget the cats on the RRI campus? I am immensely grateful to these adorable creatures for their comforting presence and the lively interactions that invariably enhanced my mood. They have always brought a smile to my face, infusing each encounter with a sense of delight and satisfaction.

Table of Contents

1 Introduction **1**

1.1 Role of Interference and Interferometric Experiments in Science and Technology: An Overview . . . 1

1.2 Diving into the Thesis: Background, Motivation and the Outline . . . 3

1.3 The Interferometric State Determination Scheme: Quantum State Interferography . . . 7

1.4 Inferring the Generalized Probability of an Event: The non-Classical Measure 10

2 Quantum State Interferography for Qubits **23**

2.1 Qubits and Its Different Representations . . . 25

2.1.1 Parameterization of Qubits: (μ, θ, ϕ) Representation . . . 26

2.1.2 Bloch Sphere Representation of Qubits . . . 29

2.2 Quantum State Interferography for Pure Qubits . . . 32

2.2.1 Theory . . . 32

2.2.2 Polar Decomposition and Determination of Complex Expectation Value of a non-Hermitian Operator . . . 34

2.2.3 Experimental Protocol for Inferring an Unknown Pure Qubit . . . 37

2.2.4 Inferring State Parameters (θ, ϕ) from the Interferogram . . . 44

2.2.5 Inferring the State Parameters (θ, ϕ): An Alternate Derivation . . . 48

2.3 Experimental Implementation of Polar Decomposed Components of Non-Hermitian Ladder Operator $\hat{\sigma}_-$ . . . 49

2.3.1 Physical Implementation of $\hat{R}$ . . . 50

2.3.2 Physical Implementation of $\hat{U}$ . . . 51

2.4 Quantum State Interferography for Qubits: The Operator Description . . . 52

2.5 Quantum State Interferography for Mixed Qubits 55
2.5.1 Theory 56
2.5.2 Experimental Protocol for Inferring an Unknown Mixed Qubit . . . 58
2.5.3 Inferring the State Parameters (μ, θ, ϕ) from the Interferogram . . . 62
2.6 Inferring Expectation Value of the non-Hermitian Operator $\hat{\sigma}_{-}$ from Interferometric Information 65
2.7 Quantum State Interferography for Qubits: The Unitary Description 68
2.8 Uniqueness of State Parameters with Phase Shift, Average Intensity and Visibility of an Interferogram 81
2.9 Quantum State Interferography for Qubits: Inferring the Bloch Parameters 82
2.10 Conclusion 86
2.A Geometric Interpretation of Qubits in the (μ, θ, ϕ) and Bloch Representation: A comparative Analysis 87

3 Experimental Reconstruction of Polarization Qubit using Quantum State Interferography 99

3.1 Comparison of Quantum State Interferography Technique in Various Interferometric Setups 101
3.2 Quantum State Interferography for Characterizing Polarization Qubits . . . 105
3.2.1 Effect of Linear Retarders in Polarization State Interferography: . . 106
3.3 Experimental Implementation of Polarization State Interferography With Mach-Zehnder Interferometer 108
3.3.1 The Experimental Setup 109
3.3.2 Phase Stabilization of Mach-Zehnder Interferometer 116
3.3.3 Effect of the Use of Wave Plates meant for Different Wavelength . . 120
3.3.4 Experimental Method 125
3.3.5 Experimental Results and Discussions 130
3.4 Experimental Implementation of Polarization State Interferography With Sagnac Interferometer 135
3.4.1 The Experimental Setup 135
3.4.2 Experimental Method 138
3.4.3 Choice of Statistics for Data Acquisition and Data Analysis 142
3.4.4 Experimental Results 143

3.4.5 Inferring the State Parameters from Interferometric Information . . . 148
3.4.6 Purity and Fidelity of the States Reconstructed Using QSI 151
3.5 Ensuring Physicality of the Reconstructed Density Matrix in Quantum State Interferography 155
3.6 Conclusion 158
3.A Circular Mean and Circular Standard Deviation 159
3.B Individual Plots for Phase Shift, Average Intensity and Visibility obtained from Sagnac Interferometer 160
3.C Variation of Fidelity of Qubits with the Mixedness 164

4 Quantum State Interferography for Higher Dimensional and Bipartite Quantum Systems 169

4.1 Parametric Representation of Higher Dimensional Quantum States – The Qudits 171
4.1.1 Majorana Representation 172
4.1.2 Episphere Representation 178
4.1.3 Episphere Representation of Qutrits 179
4.1.4 Episphere Representation of Qudits 184
4.1.5 Implication from the Normalization Condition for Qudit 189
4.2 Quantum State Interferography for Qutrit 191
4.2.1 Theory 192
4.2.2 Experimental Protocol 194
4.2.3 Inferring the State Parameters to Reconstruct a Pure Qutrit 197
4.3 Quantum State Interferography for Qudit: The General Scheme 202
4.3.1 Theory 204
4.3.2 Experimental Protocol 207
4.3.3 Inferring the State Parameters to Reconstruct the Pure Qudit 211
4.3.4 Quantum State Interferography for Mixed Qudit 217
4.4 Quantum State Interferography for Qudit: The Scheme Employing Two Interferometers 219
4.4.1 Experimental Protocol for Single-Shot Characterization of Pure Qudit: $2D$ Imaging with Two Interferometers 220
4.4.2 Operator Descriptions for d-dimensions: 224

4.4.3 Quantum State Interferography for Pure Qudit: An Alternate Approach with Two Interferometers . . . 228
4.5 Quantum State Interferography for Bipartite Qubits . . . 231
4.5.1 Parameterization of Pure Bipartite Qubit . . . 232
4.5.2 Experimental Protocol . . . 235
4.5.3 Method and Inferring the State Parameters . . . 238
4.6 Quantification of Entanglement using QSI Scheme . . . 250
4.7 Conclusion . . . 252
4.A Quantum State Interferography for Pure Qudits: Discussion With Normalization . . . 253
4.A.1 Theory Considering Normalization . . . 254
4.A.2 Experimental protocol and Inferring the State Parameters Considering Normalization . . . 256
4.B QSI for Qudit: Estimating Losses in Schemes with (d-1) Interferometers vs Two Interferometers . . . 260

5 Quantum Measure Theory and Measuring the Quantum Measure 265
5.1 Introduction: Conventional Quantum Theory to Quantum Measure Theory 267
5.1.1 Quantum Measure Theory: An Alternate Formulation . . . 269
5.2 Quantum Measure Space: A Brief Overview . . . 269
5.2.1 Quantum Measure as Generalized Probability . . . 271
5.2.2 Different Types of Events and the Quantum Measure . . . 275
5.3 Generalized Experimental Scheme for Measuring the Quantum Measure . . 278
5.3.1 Finding the Amplitude of a History . . . 280
5.3.2 Marking Outcomes via Ancilla Coupling . . . 282
5.3.3 Joint State of System-Ancilla After Coupling . . . 283
5.3.4 Determining the Quantum Measure via Projective Measurements on Suitable Ancilla Basis . . . 285
5.4 Determination of Quantum Measure in Photonic Systems . . . 291
5.4.1 Overview of the Scheme for Photonic System . . . 292
5.4.2 Measuring the Quantum Measure for Photonic Systems: Design of an Event filter, Choice of Ancilla and Measurements . . . 295

5.4.3 Comparing the Original Scheme and the Proposed Experiment: Addressing Potential Challenges and Limitations . . . 301

5.5 Inferring the Quantum Measure of a Photonic Event: An Experimental Demonstration . . . 307

5.5.1 The Experimental Setup: . . . 308

5.6 Conclusion . . . 313

5.A Histories Approach to Quantum Theory: State Based Formalism to History Based Formalism . . . 314

5.A.1 Defining Histories in Standard Formalism . . . 314

6 Experimental Determination of Quantum Measure in Photonic Systems 321

6.1 The Quantum Measure . . . 323

6.2 Experimental Implementation of an Event Filter for Determining the Quantum Measure . . . 324

6.2.1 Aim of the Experiment: . . . 325

6.2.2 The Experimental Setup . . . 325

6.2.3 Method and Data Acquisition . . . 332

6.3 Experimental Data Analysis: Dealing with Errors . . . 333

6.3.1 Types of Experimental Error . . . 333

6.3.2 Data Analysis Considering Experimental Non-idealness . . . 335

6.4 Determination of the Experimental Distribution of Quantum Measure . . . 337

6.4.1 Understanding the Nature of Power Data . . . 338

6.4.2 Fast Fourier Transformation of the Recorded Data . . . 341

6.4.3 Determination of Probability Distribution . . . 342

6.4.4 Quantum Measure Inferred from the Experiment . . . 345

6.5 Determination of the Theoretical Distribution of Quantum Measure . . . 346

6.5.1 The Quantum Measure: Theoretical Expression Considering Various Experimental Parameters . . . 347

6.5.2 Computing the Measure from Modified Amplitudes: Accounting for Real Optical Components . . . 349

6.5.3 Computing the Measure from the Intensities: Accounting for Power Fluctuations and Real Optical Components . . . 353

6.5.4 Computing the Measure with Experimental Uncertainties: Accounting for Real Optical Components, Power Variation and Interferometric Phase Fluctuation 355
6.6 Quantum Measure of a Photonic Event: A Comparison of Experimental and Theoretical Distributions 363
6.7 Statistical Significance Analysis and Hypothesis Testing 364
6.7.1 Null Hypothesis Testing 367
6.7.2 Alternate Hypothesis Testing 370
6.8 Conclusion 371

7 Summary and Outlook **375**

Chapter 1

Introduction

1.1 Role of Interference and Interferometric Experiments in Science and Technology: An Overview

The phenomena of interference and interferometric experiments are fundamental to quantum physics [1], providing critical insights into the wave-particle duality of quantum objects [2]. Interference allows us to observe the superposition principle in action [3], according to which a quantum system can exist in multiple states simultaneously until measured. The interferometric experiments are pivotal in the observation and analysis of quantum interference in different systems under various conditions [4]. These experiments employing interferometry have enabled precise measurements of physical quantities, provided a platform for testing theories of quantum foundations and quantum gravity, and serve as a tool for holographic imaging [5] and for the verification of quantum entanglement [6, 7] – a key resource in quantum computing and quantum cryptography. Therefore, interferometric experiments are not only central to understanding the quantum world but also instrumental in harnessing its potential for technological advancements.

The information obtained from an interference pattern and the interferometric experiment under a specific condition can be incredibly insightful [8]. Hence, they have found numerous applications in science and technology ranging from simply finding the optical path length difference [9] and the refractive index of materials [10] to finding the gravity gradients [11, 12, 13] and the fundamental constants such as the fine structure constant

[14]; from analyzing the spectral properties of light [15, 16] to examining the surface quality of the optical components up to nanometer precision [17]; from sensing the rotation of laser gyroscopes [18, 19] to the detection of gravitational waves [20, 21], etc.. The interferometric techniques have been of profound importance in classical physics as well, allowing for measurements with sub-micrometer precision and thus paving the way for the development of the field of precision metrology. In the field of astronomy and in experiments based on weak measurement within the quantum theory, interference is employed for the amplification of extremely small signals [22, 23, 24]. Furthermore, interferometric methodologies have been used for the verification of geometric phases [25, 26] and observation of the scalar Aharonov-Bohm effect [27, 28].

Interferometry contributes to quantum computing by providing effective and efficient algorithms in order to address intricate problems, as well as enables manipulation of the probability amplitudes of the potential results. By implementing the quantum gates that generate a superposition of the input states and adjusting their relative phases, interference can be strategically employed in quantum circuits to produce specific outcomes while suppressing the others. Interferometers are the devices that allow quantum systems to exist in a state of superposition and thereby, producing interference patterns [29]. These devices utilize the principle of interference to extract the valuable information in an experiment. Interferometers come in a variety of forms, including slit-based interferometers like double-slit or triple-slit interferometers, as well as Michelson, Fabry-Perot, Fizeau, Mach-Zehnder, and Sagnac interferometers. Each of them possess its own unique configuration and application, rendering them as adaptable tools for different experimental setups and for designing various practical instruments.

Hence, interferometry based experiments and the use of interferometers have played a pivotal role in enhancing our knowledge and understanding of the universe and in paving the way for the development of innovative technologies that could potentially lead to new scientific discoveries. In this thesis, we will explore two potential applications of interferometric techniques: *firstly*, as a tool to introduce a method for characterizing the unknown states of a quantum system utilizing the information processed from interference patterns, and *secondly*, as a model to demonstrate the determination of the non-classical nature of "generalized probabilities" described within the framework of path-integral approach to quantum theory, in contrast to the standard Kolmogorov probabilities. The research documented in this thesis will showcase the practical implementation of Mach-Zehnder and Sagnac interferometers while providing a comparative theoretical study of the techniques with the double-slit interferometer.

1.2 Diving into the Thesis: Background, Motivation and the Outline

Quantum interference, a fundamental and intriguing concept in quantum mechanics (QM), continues to remain a subject of intense research and interpretational debate due to its paradoxical nature that challenges our classical intuition about the physical world [30]. Despite of its success in explaining different natural phenomena related to the dynamics of a quantum system and its widespread use in developing advanced quantum technologies such as quantum computing and quantum information protocols etc., a full comprehension of the underlying mechanics of quantum interference remains elusive [31]. The crux of the conundrum is the wave-particle duality [32] − the observation that the quantum systems evolving through an interferometer collectively exhibit the wave-like interference and form an interference pattern after the interferometer, yet show a particle-like characteristics upon detection. This counter-intuitive behavior of a quantum object can be demonstrated in the most simple scenario using two path interferometers, such as a double-slit or a Mach-Zehnder Interferometer. As we delve deeper into the quantum realm, the mystery of quantum interference continues to inspire new questions, driving the quest for a profound understanding of the universe.

The principle of superposition in quantum theory allows a quantum system to evolve through all the indistinguishable paths within an interferometer at once, which when recombined forms an interference pattern at the end. This phenomenon does not invoke any extraordinary feature other than the mere overlap of the waves when we describe this evolution (of the quantum system) as the propagation of waves according to wave mechanics. For instance, the formation of interference patterns can be observed through the overlap of the water waves as well (in the classical domain). However, the surprising feature emerges when we attempt to detect the quantum system, where only one detector, among those placed along various paths of an interferometer, is observed to be triggered at any given moment. This leads to the question, how a quantum system that is presumed to evolve as a wave through all the paths of an interferometer simultaneously, is found in only one of the paths upon detection? In other words, how does a quantum system considered to have an extended spatial distribution, collapse as a localized object in space at the individual events of detection? When exactly does this transformation occur? When and how does the quantum system even decide whether to exhibit the particle-like or the wave-like characteristics? All these questions form the core of the quantum measurement problem [33], which seeks to answer a broader question "*What exactly happens during a measurement?*"

Despite years of extensive research and numerous proposed interpretations of quantum theory [34] aimed at elucidating the physical process during a measurement and deepening our understanding of whether quantum mechanics provides a complete theory, an universally acceptable answer is still absent. No consensus has been reached concerning which interpretation most accurately reflects the reality [35]. This essentially highlights the difficulties arriving in our attempts to reconcile the deterministic perception of reality with the inherently probabilistic nature of quantum mechanics, which pertains to the random outcomes obtained in different instances of a quantum measurement. On the other hand, the "shut up and calculate" approach [36, 37] encourages focusing on the results of the measurements rather than making an explicit effort to unravel the fundamental procedures leading to these results. In the conventional theory of quantum mechanics, the experimental observations are explained with two dynamical laws: (i) the Schrödinger wave equation [38] allowing the *deterministic Unitary time evolution* of the wave-function, associated with a system, under a given Hamiltonian and (ii) the *probabilistic non-Unitary reduction* of the wave-function upon measurement. Therefore, the knowledge of the wave-function at an instant (t_0), enables one to accurately compute the probabilities of different possible outcomes of a measurement at a time $t > t_0$. Here, the wave-function is considered as a mathematical construct that embodies our knowledge about the quantum system.

The description of the reality of a quantum system and its evolution, inherently demands the physical interpretation of the wave-function of the system, which has always been a subject of debate [39, 40]. To be able to assign an ontological meaning to the wave-function [41, 42], would be a significant stride towards addressing the question posed by the quantum measurement problem. However, amidst all the foundational debates, attempts are made to provide a different perspective on the observed probabilistic nature of quantum mechanics, without going into the complexity of wave-function collapse or the consistent macro- vs micro-world division [43, 44] to define the observer and the observed in a measurement and avoiding many of the unresolved issues like finding the true meaning of the wave-function etc.. This is achieved by introducing more realistic theories for the description of quantum mechanics, in which the kinematics of the quantum systems are considered to be similar to the classical systems. Quantum Measure Theory (QMT) [45] is one such formulation that offers a realist space-time approach to quantum theory based on the sum over histories [46] or the path integral [47] formalism. This approach characterizes the reality of a micro-system in terms of the space-time histories and interprets its dynamics through the lens of generalized stochastic theory [48].

Within the framework of Quantum Measure Theory (QMT), the efforts to describe the ontology of a quantum system in a manner akin to classical realism, without involving concepts like wave-function, superposition principle and the Born rule [49] as the integral parts of the formalism, demands a new description of the probability-like measure in order to explain the interference phenomena and to predict the evolution of the quantum system. Quantum Measure Theory assigns a non-negative real number − termed as the *quantum measure* to a set of histories, called an 'event', as the generalization of the concept of probability. This, in essence, goes beyond the limitations of standard probability theory while still maintaining consistency with the predictions made by the conventional quantum formalism. The fact that *the quantum measure, also known as the 'generalized probability', differs from the standard Kolmogorov probabilities in the presence of interference*, would form the basis of a part of the work presented in the thesis.

Here, we aim to capture the non-classical nature of the quantum measure by devising an experimental setup allowing interference. The thesis, in one part, presents an experimental implementation of a model of the general scheme proposed for determining the quantum measure of an event associated with a quantum system [50]. To be able to infer the quantum measure from an experiment, not only provides an experimental grounding to what has predominantly been a theoretical construct so far, but also enables us to make predictions about the behavior of the quantum system, much like how the computation of the Born rule probability does with the knowledge of the quantum state of the system. Another part of this thesis addresses the second, which is characterizing the quantum system by determining the state it belongs to. This knowledge about the quantum state would enable us to make predictions about the possible distribution of the outcomes of a quantum measurement performed on the system. The thesis presents an introduction of a new technique that utilizes the phenomena of interference to infer the unknown quantum state of an ensemble of identically prepared quantum systems, with an experimental demonstration of the protocol showing the reconstruction of the qubits. The technique we name as 'Quantum State Interferography', processes a set of interferometric quantities such as the phase shift, average intensity, and visibility derived from interference patterns, which is shown to establish a unique one-to-one map with the set of parameters that completely characterize the density matrix [51], when the unknown state evolves through an interferometric setup with certain operators in the individual paths of the interferometer.

In conclusion, interferometry has been one of the ubiquitous tools utilized in the majority of experiments studying the fundamentals of quantum physics because of its versatility and ability to provide information with high precision. The thesis presents the use of interferometric techniques in two distinct scenarios − one involving the characterization of the unknown states of a quantum system, useful for effective and efficient manipulations of the quantum systems for quantum information processing applications; while the other for inferring of the non-classical quantum measure of an event associated with a quantum system, that offers future possibilities towards further studies on the fundamental aspects of quantum theory. The practical implementation and demonstration of both these techniques are presented in an experimental scenario for photonic systems within optical setups. The experiments reported in this thesis use laser light as the source. According to the optical equivalence theorem, *the average statistical properties of light are equivalent whether observed with an ensemble of discrete photons or with a coherent beam* [52]. Therefore, the interference and the formation of interference patterns with a coherent laser light (wave nature) would be identical to the average pattern produced by an ensemble of identical single photons (corpuscular nature). Since the experiments in this thesis employ interferometry as a tool for analyzing the results, the results obtained from the laser source would apply consistently for the analysis of the behavior of a stream of single photons as well.

1.3 The Interferometric State Determination Scheme: Quantum State Interferography

A thorough understanding and characterization of the states of quantum systems is essential for harnessing the full potential of emerging quantum technologies. However, an unknown quantum state of a single particle cannot be directly determined from any experiment [53]. Nevertheless, if we have an ensemble of identically prepared particles, we can reconstruct the quantum state by measuring the distribution of outcomes or simply the expectation values of different observables. Quantum State Tomography (QST) has been the traditional and one of the widely used methods for characterizing an unknown quantum state, where the elements of the density matrix of a quantum state [54] are estimated by analyzing the results of several distinct projective measurements performed on many identical copies of the same system [55, 56]. The state reconstruction using QST often requires additional post-processing to ensure the physicality of the reconstructed density matrix [57, 58]. To reconstruct an arbitrary state of a d-dimensional quantum system using QST, typically one requires to perform (d^2-1) number of distinct measurements. However, with the prior knowledge about the system state being pure, measurement of $(5d-7)$ observables suffices to give the unique state information [59, 60]. Hence, owing to this quadratic scaling ($\mathcal{O}(d^2)$) of the required number of measurements with the dimensionality (d) of the Hilbert space and the increasing complexity of the state reconstruction algorithms from the measurement results, the higher dimensional state reconstruction using QST becomes a cumbersome process.

Over the last decade, several schemes towards improving the scaling of Quantum State Tomography (QST) with the dimension of the Hilbert space have been suggested [61, 62, 63, 64]. Some other alternatives to the standard QST technique using projective measurements have also been explored with the aim of reducing the required number of experimental settings [65, 66]. The alternate state characterization techniques, ranging from those involving strong interactions [67] to those involving weak interaction [68, 69, 70] have been investigated. Since weak measurements [71, 72] can give us the complex weak values of observables, they have paved the way for the *direct measurement* of quantum states [73, 74, 75]. The term "direct" in this approach implies that the real and imaginary components of a quantum state can be inferred (up to a proportionality constant) from the observations of the shift in the pointer variable and the shift in the momentum conjugate to the pointer variable respectively [1] [73], without the need to have any complicated set of measurement settings or post-processing algorithms.

Direct measurements have been employed for the state reconstruction of not only qubits [77] but also extended for systems with higher dimensions [78, 79], even as high as a million [80]. When compared with the standard QST protocol, reconstruction of the quantum state involving weak measurements demands a simpler experimental implementation but appears to be less efficient and less precise than QST [81] owing to the fundamental nature of weak measurements. Weak measurement involves post-selection that discards a significant number of particles undergoing the experiment, leading to inefficiency and involves an inherent error introduced due to the first-order approximation (which is accurate only when the coupling strength tends to zero) made even in the presence of finite non-zero interaction strengths, resulting in impreciseness in the outcomes [82]. However, the concept of direct measurement has been generalized to arbitrary measurement strengths and it has been shown that strong direct measurement can sometimes outperform weak direct measurements in terms of precise and accurate state estimation [83, 84, 85].

Further, it has been demonstrated that complex weak values can be obtained without performing a weak measurement [86, 87], which can lead to the efficient direct measurement of quantum states [88]. Knowing the weak value of a Hermitian operator subject to a particular pre-selection and a post-selection can give us the expectation value of a related non-Hermitian operator [89]. The expectation value of non-Hermitian column operators has been used for the direct measurement of the quantum state [90]. Recently, the focus has been towards the *single-shot state estimation*, i.e., obtaining the state of a quantum system from a single setup without any required change in the experimental settings [91, 92, 93]. Our work in this thesis focuses on the use of interferometric method as opposed to direct measurement techniques to characterize an unknown quantum state. We present a novel method, named *Quantum State Interferography*, that uses the phenomena of interference to infer the state parameters from the quantities processed from interference patterns.

[1] These observations correspond to measuring the real and imaginary parts of the complex weak value when the given system is weakly coupled to the pointer [76].

Quantum State Interferography is a *single-shot* technique for quantum state characterization, where an unknown state of a quantum system is determined by measuring the expectation value of non-Hermitian spin ladder operator $\hat{\sigma}_{\pm}$ in an interferometric setup. Once aligned, this setup does not require any changes in the measurement settings during the course of data acquisition. This thesis will present how the interferometric scheme − Quantum State Interferography (QSI) can be employed for the reconstruction of quantum states of a qubit along with its experimental implementation in a two path interferometer and how this scheme can be extended to infer the state of d-dimensional qudits and pure bipartite qubits as well, which serve as the viable alternatives to QST. The parameters that describe a quantum state are shown to have unique relationships with the quantities such as the phase shift, phase averaged intensity, and visibility of the interference pattern generated when the state evolves through the QSI setup. These relations can be used to reconstruct the state incident on the setup by analyzing the produced interference patterns. Compared to the direct state estimation techniques, which aim to minimize the post-processing at the expense of changing the experimental settings, quantum state interferography (QSI) focuses on minimizing the number of data acquisitions as all parameters describing the state are obtained at once by post-processing the interference patterns.

In **Chapter. 2** of the thesis, a comprehensive theoretical discussion on the principle of operation of the Quantum State Interfrography (QSI) scheme for the *single-shot* characterization of any arbitrary qubit, be it pure or mixed, is presented. The chapter effectively shows how a *single* interference pattern generated in a *single setting* of an interferometric setup can be analyzed to infer the elements of a 2×2 density matrix, as compared to *two* or *three* settings (for pure or mixed qubit state reconstruction) required in QST. An experimental demonstration of the method for the reconstruction of polarization qubits using a beam from 778 *nm* diode laser in a Mach-Zehnder interferometer setup and using a beam from 632.8 *nm* Helium-Neon laser in a displaced Sagnac interferometer setup is presented in **Chapter. 3**. The fidelity of the reconstructed states compared to the states prepared in the lab is reported as the quantification of the efficiency of this interferometric state determination technique. **Chapter. 4** proposes an extension of the interferometric scheme for the characterization of pure states in higher dimensional ($d > 2$) Hilbert space, utilizing the information processed from $(d - 1)$ interference patterns in a *single-shot* method. Additionally, the chapter discusses a protocol for pure bipartite qubit state reconstruction using a dual interferometer setup, requiring only *three* measurements in QSI as compared to *nine* measurements needed in standard QST.

1.4 Inferring the Generalized Probability of an Event: The non-Classical Measure

According to the standard formalism of quantum theory, a measurement performed on a quantum system involves three distinct stages $-$ *preparation*: the system is prepared to be in a definite initial state at time $t = t_i$; next *interaction*: the system interacts with an apparatus and undergoes an *unitary evolution* through the interaction Hamiltonian $\mathcal{H}_{int}$ that couples the system observable under investigation to a pointer variable within the time $t_m - \dfrac{\Delta t}{2} < t < t_m + \dfrac{\Delta t}{2}$, where Δt is the duration of interaction [2] about $t = t_m$; finally *detection*: the quantum system undergoes a *non-unitary evolution* upon observation at time $t = t_f$ and is found to be in any one of the eigen states of the observable being measured [94]. In this mathematical model for quantum measurement, in general, we ignore all the events occurring at instances $t < t_i$ and $t > t_f$ for the sake of simplicity and consider that the 'in-between events' i.e., the events that have happened at times $t_i < t < t_f$ are inaccessible to observation. Therefore, at the end of an experiment, we are left only with a particular outcome without having any information about the physical processes or the reality of the micro-system between the *preparation* and *detection.* The knowledge about such 'in-between' events, however, would provide exact physical interpretations of abstract mathematical notions such as wavefunctions, complex transition amplitudes, and state reduction in the microscopic realm. This understanding would subsequently aid in addressing the core foundational puzzles posed by quantum theory.

In order to bridge the existing explanatory gaps i.e., to unravel the reality of a micro-system as it evolves from an initial state (at t_i) to a final state (at t_f), we need measurement techniques that would focus on temporally extended events associated with the physical world rather than just momentary states. A specific kind of measurement procedure, known as *weak measurements* [71, 72], is designed to illuminate the intermediate physi-

[2] Δt in some cases determines the strength of interaction as well.

cal processes (i.e., the 'in-between' events) through weak interactions between the system and the pointer. This method probes the system information at an intermediate time (say, t_w) between *pre-selection* – the initial state and *post-selection* – the final state, in terms of the *weak values* of the operators at $t_w \in [t_i, t_f]$ [95]. The weak value, typically a complex number, can be directly interpreted as the *in-out transition amplitude* [3] associated with Feynman propagators in the path-integral formulation of quantum mechanics [96]. This perspective incorporating *path integrals* offers an intuitive understanding of the micro-world within a history-based framework that considers the entire physical processes from the start to represent the histories in space-time, instead of merely providing system information through wave functions evolving over time.

Inspired by the path integral approach [97] or the related sum over histories approach [98], Quantum Measure Theory (QMT) is introduced as a reformulation of quantum mechanics, which regards the 'histories' of a physical system as the fundamental elements of reality [45]. This history-based formalism to quantum mechanics, at its core, does not include concepts like wave functions, superposition, state reduction, operators as observables, etc., and visualizes the behavior of a quantum system from the perspective of generalized stochastic theory [48]. QMT describes the kinematics (or the "ontology") of a physical system in terms of its *histories*; such as the trajectories of a particle or the space-time configurations of a field, and so on. It encodes the dynamics of a quantum system in terms of *quantum measure* – a function that assigns a generalized probability, which is real and non-negative, to every *event*. An 'event' in Quantum Measure Theory is defined as a set of histories associated with a system [4].

This history-based framework provides meaning to the intermediate events that occur between t_i and t_f, in the context of assigning the *quantum measure* for a set of histories, subject to the knowledge of their 'start' and 'end'. Consider a situation where a particle traverses through an experimental setup consisting of a series of devices, each with multiple outputs. One might wonder if the particle has followed one of the paths belonging to a specific set (realizing a specific 'event') while moving from the source to the detector. However, due to the inherent uncertainty associated with the stochastic behavior of the

[3] Commonly known to quantum field theorists as the *in-out expectation value*.

[4] Similar to the definition in probability theory, according to which an 'event' is a subset of the sample space to which a probability can be assigned.

system, a definitive answer to this question is not possible, but a probabilistic response could be provided. In this thesis, we will address this question with an aim of finding whether a specific event has happened, in an experimental scenario, by determining the 'generalized probability' or the 'quantum measure' related to the event of interest.

The quantum measure $\mu(E)$ for an event E signifies the probabilistic behavior of a micro-system, but in general, it can not be treated as the standard probability in the Kolmogorov sense. This is because Quantum Measure Theory (QMT) allows for interference, which sets the *quantum measure* apart from the *conventional probability measure* as it does not follow the probability sum rule and can accommodate the non-classical values exceeding the classical upper limit of one. Therefore, in addition to the theoretical developments in the fields of quantum gravity and quantum cosmology based on QMT, being able to attribute an experimental significance to the quantum measure would be a step forward toward providing a comprehensive depiction of the reality of a quantum system. Moreover, aligning abstract theoretical concepts with practical (or experimental) situations or physical processes would enhance our understanding of the non-classical behavior of a micro-system along with opening avenues for future investigations on the fundamental aspects of quantum theory.

The thesis presents a study of the two-site hopper model [99] within the framework of Quantum Measure Theory (QMT) and reports an experiment that determines the 'quantum measure' of a hopper event using an ancilla-based event-filtering scheme. It shows the implementation of an 'event filter' in an optical setup involving interference, inspired by the proposal in [50], that selects a desired set of trajectories for a photonic system and enables one to analyze the non-classical 'quantum measure'. In **Chapter. 5**, the introductory ideas to QMT are provided emphasizing the importance of measuring the 'quantum measure', along with a description of the generalized protocol to infer its value from the probability of a specific outcome of a projective measurement. **Chapter. 6** provides a table-top experimental demonstration of this scheme for determining the value of 'quantum measure' of a particular photonic event, by devising a toy model of the proposed event filter setup. The chapter also presents the statistical significance analysis, establishing the non-classical nature of the experimentally derived quantity, with respect to the *classical-quantum boundary*, i.e., the maximum limit for *classical probability measure*.

References

[1] B. Bransden and C. Joachain. *Quantum Mechanics*. 2nd Edition. Pearson, 2000.

[2] Richard P. Feynman; Robert B. Leighton; Matthew Sands. *The Feynman Lectures on Physics: Vol. 3*. Addison-Wesley, 1971.

[3] P. A. M. Dirac. *The Principles of Quantum Mecanics*. Oxford, Clarendon Press, 1981.

[4] W.H. Steel. *Interferometry*. Cambridge Studies in Modern Optics. Cambridge: Cambridge University Press, 1985.

[5] Guillaume Thekkadath et al. "Intensity interferometry for holography with quantum and classical light". In: *Science Advances* 9.27 (2023), eadh1439. DOI: 10.1126/sciadv.adh1439.

[6] Jian-Wei Pan et al. "Multiphoton entanglement and interferometry". In: *Rev. Mod. Phys.* 84 (2 2012), pp. 777–838. DOI: 10.1103/RevModPhys.84.777.

[7] Christopher K. Zeitler et al. "Entanglement Verification of Hyperentangled Photon Pairs". In: *Phys. Rev. Appl.* 18 (5 2022), p. 054025. DOI: 10.1103/PhysRevApplied.18.054025.

[8] Ajoy Ghatak. *Optics*. Tata McGraw-Hill Publishing Company Limited, 2009.

[9] Max Born et al. *Principles of Optics: Electromagnetic Theory of Propagation, Interference and Diffraction of Light*. 7th ed. Cambridge University Press, 1999.

[10] J J Fendley. "Measurement of refractive index using a Michelson interferometer". In: *Physics Education* 17.5 (1982), p. 209. DOI: 10.1088/0031-9120/17/5/001.

[11] M. J. Snadden et al. "Measurement of the Earth's Gravity Gradient with an Atom Interferometer-Based Gravity Gradiometer". In: *Phys. Rev. Lett.* 81 (5 1998), pp. 971–974. DOI: 10.1103/PhysRevLett.81.971.

[12] J. M. McGuirk et al. "Sensitive absolute-gravity gradiometry using atom interferometry". In: *Phys. Rev. A* 65 (3 2002), p. 033608. DOI: 10.1103/PhysRevA.65.033608.

[13] G. D'Amico et al. "Bragg interferometer for gravity gradient measurements". In: *Phys. Rev. A* 93 (6 2016), p. 063628. DOI: 10.1103/PhysRevA.93.063628.

[14] Chenghui Yu et al. "Atom-Interferometry Measurement of the Fine Structure Constant". In: *Annalen der Physik* 531.5 (2019), p. 1800346. DOI: https://doi.org/10.1002/andp.201800346.

[15] Anne P. Thorne and Malcolm R. Howells. "4. Interferometric Spectrometers". In: *Vacuum Ultraviolet Spectroscopy II*. Ed. by J.A.R. Samson and D.L. Ederer. Vol. 32. Experimental Methods in the Physical Sciences. Academic Press, 1998, pp. 73–106. DOI: https://doi.org/10.1016/S0076-695X(08)60277-X.

[16] Robert john Bell. *Introductory Fourier Transform Spectroscopy*. Academic Press, 1972. DOI: 10.1016/B978-0-12-085150-8.50006-1.

[17] Dahi Ghareab Abdelsalam and Baoli Yao. "Interferometry and its Applications in Surface Metrology". In: *Optical Interferometry*. Ed. by Alexander A. Banishev, Mithun Bhowmick, and Jue Wang. Rijeka: IntechOpen, 2017. Chap. 5. DOI: 10.5772/66275.

[18] V. Vali and R. W. Shorthill. "Fiber ring interferometer". In: *Appl. Opt.* 15.5 (1976), pp. 1099–1100. DOI: 10.1364/AO.15.001099.

[19] R A Bergh, H C Lefevre, and H J Shaw. "All-single-mode fiber-optic gyroscope". In: *Opt. Lett.* 6.4 (1981), pp. 198–200.

[20] B. P. Abbott et al. "Observation of Gravitational Waves from a Binary Black Hole Merger". In: *Phys. Rev. Lett.* 116 (6 2016), p. 061102. DOI: 10.1103/PhysRevLett.116.061102.

[21] Charlotte Bond et al. "Interferometer techniques for gravitational-wave detection". In: *Living Reviews in Relativity* 19.1 (2017), p. 3.

[22] Onur Hosten and Paul Kwiat. "Observation of the spin hall effect of light via weak measurements". en. In: *Science* 319.5864 (2008), pp. 787–790. DOI: 10.1126/science.1152697.

[23] P. Ben Dixon et al. "Ultrasensitive Beam Deflection Measurement via Interferometric Weak Value Amplification". In: *Phys. Rev. Lett.* 102 (17 2009), p. 173601. DOI: 10.1103/PhysRevLett.102.173601.

[24] John D Monnier. "Optical interferometry in astronomy". In: *Reports on Progress in Physics* 66.5 (2003), p. 789. DOI: 10.1088/0034-4885/66/5/203.

[25] Marie Ericsson et al. "Measurement of Geometric Phase for Mixed States Using Single Photon Interferometry". In: *Phys. Rev. Lett.* 94 (5 2005), p. 050401. DOI: 10.1103/PhysRevLett.94.050401.

[26] Paul G. Kwiat and Raymond Y. Chiao. "Observation of a nonclassical Berry's phase for the photon". In: *Phys. Rev. Lett.* 66 (5 1991), pp. 588–591. DOI: 10.1103/PhysRevLett.66.588.

[27] B. E. Allman et al. "Observation of the scalar Aharonov-Bohm effect by neutron interferometry". In: *Phys. Rev. A* 48 (3 1993), pp. 1799–1807. DOI: 10.1103/PhysRevA.48.1799.

[28] G. Badurek. "Neutron Interferometric Experiments on Quantum Mechanics". In: *The Present Status of the Quantum Theory of Light*. Ed. by Stanley Jeffers et al. Dordrecht: Springer Netherlands, 1997, pp. 281–292. DOI: 10.1007/978-94-011-5682-0_28.

[29] P. Hariharan. *Basics of Interferometry*. Second Edition. Burlington: Elsevier Academic Press, 2007. DOI: 10.1016/B978-0-12-373589-8.X5000-7.

[30] Wayne Myrvold. "Philosophical Issues in Quantum Theory". In: *The Stanford Encyclopedia of Philosophy*. Ed. by Edward N. Zalta and Uri Nodelman. Fall 2022. Metaphysics Research Lab, Stanford University, 2022.

[31] J. S. Bell and Alain Aspect. *Speakable and Unspeakable in Quantum Mechanics: Collected Papers on Quantum Philosophy*. 2nd ed. Cambridge University Press, 2004.

[32] Louis-Victor de Broglie. "Recherches sur la théorie des quanta". English Translation: Researches On the Theory of Quanta. 1925.

[33] Maximilian Schlosshauer. "Decoherence, the measurement problem, and interpretations of quantum mechanics". In: *Rev. Mod. Phys.* 76 (4 2005), pp. 1267–1305. DOI: 10.1103/RevModPhys.76.1267.

[34] Graham P. Collins. "The Many Interpretations of Quantum Meachanics". In: *Scientific American* (2007).

[35] Maximilian Schlosshauer, Johannes Kofler, and Anton Zeilinger. "A snapshot of foundational attitudes toward quantum mechanics". In: *Studies in History and Philosophy of Science Part B: Studies in History and Philosophy of Modern Physics* 44.3 (2013), pp. 222–230. DOI: https://doi.org/10.1016/j.shpsb.2013.04.004.

[36] N. David Mermin. “Could Feynman Have Said This?” In: *Physics Today* 57.5 (2004), pp. 10–11. DOI: 10.1063/1.1768652.

[37] Anders Johansson et al. ““Shut up and calculate”: the available discursive positions in quantum physics courses”. In: *Cultural Studies of Science Education* 13.1 (2018), pp. 205–226. DOI: 10.1007/s11422-016-9742-8.

[38] E. Schrödinger. “An Undulatory Theory of the Mechanics of Atoms and Molecules”. In: *Phys. Rev.* 28 (6 1926), pp. 1049–1070. DOI: 10.1103/PhysRev.28.1049.

[39] Y. Aharonov, J. Anandan, and L. Vaidman. “Meaning of the wave function”. In: *Phys. Rev. A* 47 (6 1993), pp. 4616–4626. DOI: 10.1103/PhysRevA.47.4616.

[40] M. Ringbauer et al. “Measurements on the reality of the wavefunction”. In: *Nature Physics* 11.3 (2015), pp. 249–254. DOI: 10.1038/nphys3233.

[41] Matthew Leifer. “Is the Quantum State Real? An Extended Review of Ψ-ontology Theorems”. In: *Quanta* 3.1 (2014), pp. 67–155. DOI: 10.12743/quanta.v3i1.22.

[42] Lucien Hardy. “ARE QUANTUM STATES REAL?” In: *International Journal of Modern Physics B* 27.01n03 (2013), p. 1345012. DOI: 10.1142/S0217979213450124.

[43] Wojciech H. Zurek. “Decoherence and the Transition from Quantum to Classical”. In: *Physics Today* 44.10 (1991), pp. 36–44. DOI: 10.1063/1.881293.

[44] George F.R. Ellis. “On the limits of quantum theory: Contextuality and the quantum–classical cut”. In: *Annals of Physics* 327.7 (2012). July 2012 Special Issue, pp. 1890–1932. DOI: https://doi.org/10.1016/j.aop.2012.05.002.

[45] Rafael D. Sorkin. “QUANTUM MECHANICS AS QUANTUM MEASURE THEORY”. In: *Modern Physics Letters A* 09.33 (1994), pp. 3119–3127. DOI: 10.1142/S021773239400294X.

[46] Paul A. M. Dirac. “The Lagrangian in quantum mechanics”. In: *Phys. Z. Sowjetunion* 3 (1933), pp. 64–72.

[47] R. P. Feynman. “Space-Time Approach to Non-Relativistic Quantum Mechanics”. In: *Rev. Mod. Phys.* 20 (2 1948), pp. 367–387. DOI: 10.1103/RevModPhys.20.367.

[48] Rafael D. Sorkin. *Quantum Measure Theory and its Interpretation*. 1997.

[49] Nicolaas P. Landsman. "Born Rule and its Interpretation". In: *Compendium of Quantum Physics*. Ed. by Daniel Greenberger, Klaus Hentschel, and Friedel Weinert. Berlin, Heidelberg: Springer Berlin Heidelberg, 2009, pp. 64–70. DOI: 10.1007/978-3-540-70626-7_20.

[50] Álvaro Mozota Frauca and Rafael Dolnick Sorkin. "How to Measure the Quantum Measure". In: *International Journal of Theoretical Physics* 56.1 (2017), pp. 232–258. DOI: 10.1007/s10773-016-3181-x.

[51] Lucien Hardy. *Quantum Theory From Five Reasonable Axioms*. 2001.

[52] E. C. G. Sudarshan. "Equivalence of Semiclassical and Quantum Mechanical Descriptions of Statistical Light Beams". In: *Phys. Rev. Lett.* 10 (7 1963), pp. 277–279. DOI: 10.1103/PhysRevLett.10.277.

[53] Stephen M. Barnett and Sarah Croke. "Quantum state discrimination". In: *Advances in Optics and Photonics* 1.2 (2009), pp. 238–278. DOI: 10.1364/AOP.1.000238.

[54] Michael A. Nielsen and Isaac L. Chuang. *Quantum Computation and Quantum Information: 10th Anniversary Edition*. Cambridge University Press, 2010. DOI: 10.1017/CBO9780511976667.

[55] Ermes Toninelli et al. "Concepts in quantum state tomography and classical implementation with intense light: a tutorial". In: *Advances in Optics and Photonics* 11.1 (2019), pp. 67–134. DOI: 10.1364/AOP.11.000067.

[56] K. Banaszek, M. Cramer, and D. Gross. "Focus on quantum tomography". In: *New Journal of Physics* 15.12 (2013), p. 125020. DOI: 10.1088/1367-2630/15/12/125020.

[57] Daniel F. V. James et al. "Measurement of qubits". In: *Physical Review A* 64.5 (2001), p. 052312. DOI: 10.1103/PhysRevA.64.052312.

[58] K. Banaszek et al. "Maximum-likelihood estimation of the density matrix". In: *Physical Review A* 61.1 (1999), p. 010304. DOI: 10.1103/PhysRevA.61.010304.

[59] Jianxin Chen et al. "Uniqueness of quantum states compatible with given measurement results". In: *Phys. Rev. A* 88 (1 2013), p. 012109. DOI: 10.1103/PhysRevA.88.012109.

[60] Xian Ma et al. "Pure-state tomography with the expectation value of Pauli operators". In: *Phys. Rev. A* 93 (3 2016), p. 032140. DOI: 10.1103/PhysRevA.93.032140.

[61] William K Wootters and Brian D Fields. "Optimal state-determination by mutually unbiased measurements". In: *Annals of Physics* 191.2 (1989), pp. 363–381. DOI: https://doi.org/10.1016/0003-4916(89)90322-9.

[62] Marcus Cramer et al. "Efficient quantum state tomography". In: *Nature Communications* 1.1 (2010), pp. 1–7. DOI: 10.1038/ncomms1147.

[63] Bo Qi et al. "Quantum State Tomography via Linear Regression Estimation". In: *Scientific Reports* 3.1 (2013), p. 3496. DOI: 10.1038/srep03496.

[64] J. J. Díaz, I. Sainz, and A. B. Klimov. "Quantum tomography via nonorthogonal basis and weak values". In: *Physical Review A* 91.6 (2015), p. 062127. DOI: 10.1103/PhysRevA.91.062127.

[65] Shengjun Wu. "State tomography via weak measurements". In: *Scientific Reports* 3.1 (2013), p. 1193. DOI: 10.1038/srep01193.

[66] Antonio Di Lorenzo. "Sequential Measurement of Conjugate Variables as an Alternative Quantum State Tomography". In: *Phys. Rev. Lett.* 110 (1 2013), p. 010404. DOI: 10.1103/PhysRevLett.110.010404.

[67] Antonio Di Lorenzo. "Quantum state tomography from a sequential measurement of two variables in a single setup". In: *Phys. Rev. A* 88 (4 2013), p. 042114. DOI: 10.1103/PhysRevA.88.042114.

[68] Xi Chen et al. "Alternative method of quantum state tomography toward a typical target via a weak-value measurement". In: *Phys. Rev. A* 97 (3 2018), p. 032120. DOI: 10.1103/PhysRevA.97.032120.

[69] Ezad Shojaee et al. "Optimal Pure-State Qubit Tomography via Sequential Weak Measurements". In: *Phys. Rev. Lett.* 121 (13 2018), p. 130404. DOI: 10.1103/PhysRevLett.121.130404.

[70] Joachim Fischbach and Matthias Freyberger. "Quantum optical reconstruction scheme using weak values". In: *Phys. Rev. A* 86 (5 2012), p. 052110. DOI: 10.1103/PhysRevA.86.052110.

[71] Yakir Aharonov, David Z. Albert, and Lev Vaidman. "How the result of a measurement of a component of the spin of a spin-1/2 particle can turn out to be 100". In: *Phys. Rev. Lett.* 60 (14 1988), pp. 1351–1354. DOI: 10.1103/PhysRevLett.60.1351.

[72] I. M. Duck, P. M. Stevenson, and E. C. G. Sudarshan. "The sense in which a "weak measurement" of a spin-1/2 particle's spin component yields a value 100". In: *Phys. Rev. D* 40 (6 1989), pp. 2112–2117. DOI: 10.1103/PhysRevD.40.2112.

[73] Jeff S. Lundeen et al. "Direct measurement of the quantum wavefunction". In: *Nature* 474.7350 (2011), pp. 188–191. DOI: 10.1038/nature10120.

[74] Jeff S. Lundeen and Charles Bamber. "Procedure for Direct Measurement of General Quantum States Using Weak Measurement". In: *Physical Review Letters* 108.7 (2012), p. 070402. DOI: 10.1103/PhysRevLett.108.070402.

[75] G. S. Thekkadath et al. "Direct Measurement of the Density Matrix of a Quantum System". In: *Phys. Rev. Lett.* 117 (12 2016), p. 120401. DOI: 10.1103/PhysRevLett.117.120401.

[76] Richard Jozsa. "Complex weak values in quantum measurement". In: *Phys. Rev. A* 76 (4 2007), p. 044103. DOI: 10.1103/PhysRevA.76.044103.

[77] Jeff Z. Salvail et al. "Full characterization of polarization states of light via direct measurement". In: *Nature Photonics* 7.4 (2013), pp. 316–321. DOI: 10.1038/nphoton.2013.24.

[78] Mehul Malik et al. "Direct measurement of a 27-dimensional orbital-angular-momentum state vector". In: *Nature Communications* 5.1 (2014), p. 3115. DOI: 10.1038/ncomms4115.

[79] Mohammad Mirhosseini et al. "Compressive Direct Measurement of the Quantum Wave Function". In: *Physical Review Letters* 113.9 (2014), p. 090402. DOI: 10.1103/PhysRevLett.113.090402.

[80] Zhimin Shi et al. "Direct measurement of an one-million-dimensional photonic state". In: *2016 Progress in Electromagnetic Research Symposium (PIERS)*. 2016, pp. 187–187. DOI: 10.1109/PIERS.2016.7734289.

[81] Lorenzo Maccone and Cosimo C. Rusconi. "State estimation: A comparison between direct state measurement and tomography". In: *Physical Review A* 89.2 (2014), p. 022122. DOI: 10.1103/PhysRevA.89.022122.

[82] Debmalya Das and Arvind. "Estimation of quantum states by weak and projective measurements". In: *Phys. Rev. A* 89 (6 2014), p. 062121. DOI: 10.1103/PhysRevA.89.062121.

[83] Ping Zou, Zhi-Ming Zhang, and Wei Song. "Direct measurement of general quantum states using strong measurement". In: *Physical Review A* 91.5 (2015), p. 052109. DOI: 10.1103/PhysRevA.91.052109.

[84] Giuseppe Vallone and Daniele Dequal. "Strong Measurements Give a Better Direct Measurement of the Quantum Wave Function". In: *Physical Review Letters* 116.4 (2016), p. 040502. DOI: 10.1103/PhysRevLett.116.040502.

[85] Luca Calderaro et al. "Direct Reconstruction of the Quantum Density Matrix by Strong Measurements". In: *Physical Review Letters* 121.23 (2018), p. 230501. DOI: 10.1103/PhysRevLett.121.230501.

[86] Gaurav Nirala et al. "Measuring average of non-Hermitian operator with weak value in a Mach-Zehnder interferometer". In: *Phys. Rev. A* 99 (2 2019), p. 022111. DOI: 10.1103/PhysRevA.99.022111.

[87] Alastair A. Abbott et al. "Anomalous Weak Values Without Post-Selection". In: *Quantum* 3 (2019), p. 194. DOI: 10.22331/q-2019-10-14-194.

[88] Kazuhisa Ogawa et al. "A framework for measuring weak values without weak interactions and its diagrammatic representation". In: *New Journal of Physics* 21.4 (2019), p. 043013. DOI: 10.1088/1367-2630/ab0773.

[89] Arun Kumar Pati, Uttam Singh, and Urbasi Sinha. "Measuring non-Hermitian operators via weak values". In: *Phys. Rev. A* 92 (5 2015), p. 052120. DOI: 10.1103/PhysRevA.92.052120.

[90] Eliot Bolduc, Genevieve Gariepy, and Jonathan Leach. "Direct measurement of large-scale quantum states via expectation values of non-Hermitian matrices". In: *Nature Communications* 7.1 (2016), p. 10439. DOI: 10.1038/ncomms10439.

[91] Ming-Wei Lin and Igor Jovanovic. "Single-Shot Measurement of Temporally-Dependent Polarization State of Femtosecond Pulses by Angle-Multiplexed Spectral-Spatial Interferometry". In: *Scientific Reports* 6.1 (2016), p. 32839. DOI: 10.1038/srep32839.

[92] Ziyi Zhu et al. "Single-Shot Direct Tomography of the Complete Transverse Amplitude, Phase, and Polarization Structure of a Light Field". In: *Physical Review Applied* 12.3 (2019), p. 034036. DOI: 10.1103/PhysRevApplied.12.034036.

[93] Athira B S et al. "Single-shot measurement of the space-varying polarization state of light through interferometric quantification of the geometric phase". In: *Phys. Rev. A* 101 (1 2020), p. 013836. DOI: 10.1103/PhysRevA.101.013836.

[94] Robert T. Beyer John von Neumann and Nicholas A. Wheeler. *Mathematical Foundations of Quantum Mechanics: New Edition*. Princeton Landmarks in Mathematics and Physics, Princeton University Press, 2018.

[95] Justin Dressel et al. "Colloquium: Understanding quantum weak values: Basics and applications". In: *Rev. Mod. Phys.* 86 (1 2014), pp. 307–316. DOI: 10.1103/RevModPhys.86.307.

[96] A. Matzkin. "Weak values from path integrals". In: *Phys. Rev. Res.* 2 (3 2020), p. 032048. DOI: 10.1103/PhysRevResearch.2.032048.

[97] R.P. Feynman, A.R. Hibbs, and D.F. Styer. *Quantum Mechanics and Path Integrals*. Dover Books on Physics. Dover Publications, 2010.

[98] Sukanya Sinha and Rafael D. Sorkin. "A sum-over-histories account of an EPR(B) experiment". In: *Foundations of Physics Letters* 4.4 (1991), pp. 303–335. DOI: 10.1007/BF00665892.

[99] Stanley P. Gudder and Rafael D. Sorkin. "Two-site quantum random walk". In: *General Relativity and Gravitation* 43.12 (2011), pp. 3451–3475. DOI: 10.1007/s10714-011-1245-z.

Chapter 2

Quantum State Interferography for Qubits

Contents

2.1 Qubits and Its Different Representations

2.2 Quantum State Interferography for Pure Qubits

2.3 Experimental Implementation of Polar Decomposed Components of Non-Hermitian Ladder Operator $\hat{\sigma}_-$

2.4 Quantum State Interferography for Qubits: The Operator Description

2.5 Quantum State Interferography for Mixed Qubits

2.6 Inferring Expectation Value of the non-Hermitian Operator $\hat{\sigma}_-$ from Interferometric Information

2.7 Quantum State Interferography for Qubits: The Unitary Description

2.8 Uniqueness of State Parameters with Phase Shift, Average Intensity and Visibility of an Interferogram

2.9 Quantum State Interferography for Qubits: Inferring the Bloch Parameters

2.10 Conclusion

2.A Geometric Interpretation of Qubits in the (μ, θ, ϕ) and Bloch Representation: A comparative Analysis

The inherent probabilistic features of quantum measurement play a central role in quantum mechanics. The probability distribution of different outcomes of any measurement performed on a quantum system can be predicted if its state is known. The state of a quantum system is a complex mathematical construct that encapsulates the complete information about the system at a given point of time. Hence, characterization of the state of a quantum system is essential in understanding the behavior of the system subject to evolution and for effective and efficient manipulations of the quantum systems in practical applications of quantum mechanics such as quantum information processing, or quantum metrology based experiments etc. [1, 2]. Here, we introduce a unique approach for identifying an unknown quantum state, using interferometry as the tool, which we refer to as "Quantum State Interferography".

Quantum State Interferography (*QSI*) is a novel state characterization technique, where an unknown quantum state can be determined by analyzing the information processed from one or more interference patterns, also known as *interferograms*. The visibility, phase shift, average intensity, the centroid position, fringe widths, average fringe shift etc. are, in general, the information that can be extracted from an interference pattern, generated when an ensemble of identical particles is evolved through an interferometric setup. This chapter delves into the theory behind how the interferometry based scheme QSI, can be utilized to infer any arbitrary qubit, whether pure or mixed, from an interference pattern obtained in a single setup without the need to change any experimental settings − a process referred to as *single shot state estimation*. In this chapter, the representation of the qubits using different sets of parameters would be presented with the discussion on the physical significance of each of them. Next, the functional relationships to evaluate the state parameters in order to reconstruct an unknown qubit from the interferometric information would be established. Both the non-unitary and unitary approaches of characterizing the two-dimensional quantum states in a two path interferometer setup with the physical implementation of the necessary operators will be discussed. Whether, this interferometric method can, in principle, be generalized to higher dimensional systems or multi-particle systems will be explored in **Chapter. 4**.

2.1 Qubits and Its Different Representations

The state of any two-dimensional quantum system is called a qubit, an abbreviated form of *quantum bit*, which is considered as the fundamental unit of quantum information. Unlike the classical bit[1] that is characterized to be in any one of the two distinct states 0 or 1, a quantum bit can be in a linear superposition of the two orthonormal states that spans the two dimensional Hilbert space [3]. In Fock state basis $\{|0\rangle, |1\rangle\}$, a qubit is given as

$$|\psi\rangle = \alpha|0\rangle + \beta|1\rangle \tag{2.1}$$

where α and β respectively represent the complex probability amplitudes associated with the states $|0\rangle$ and $|1\rangle$[2], provided the *normalization condition* $|\alpha|^2 + |\beta|^2 = 1$. The qubits, in general, can be represented in any choice of basis in any given degree of freedom of a two-level system; for example, $|\psi\rangle_p = \alpha|H\rangle + \beta|V\rangle$ represents a polarization qubit of a photon in $\{|H\rangle, |V\rangle\}$ basis, $|\psi\rangle_s = \alpha|\uparrow\rangle + \beta|\downarrow\rangle$ represents a spin qubit of a spin-$\frac{1}{2}$ particle in $\hat{\sigma}_z$ eigen basis etc.

A state vector $|\psi\rangle$ expressed as the coherent superposition of the two basis states in Eqn. 2.1, represents a pure qubit. However, a mixed qubit, which is an incoherent statistical mixture of different pure qubits $\{|\psi_i\rangle\}$ with the associated statistical weights $\{p_i\}$, is expressed as a density operator $\hat{\rho}_{mixed} = \sum_i p_i |\psi_i\rangle\langle\psi_i|$, where $0 \leq p_i \leq 1$ and $\sum_i p_i = 1$. Therefore, the most general description of a two-dimensional quantum state is given using the density matrix formalism [4] and is represented by a 2×2 density matrix $\hat{\rho}$, with $\mathrm{Tr}(\hat{\rho}^2) = 1$ representing pure qubits and $\mathrm{Tr}(\hat{\rho}^2) < 1$ representing mixed qubits.

$$\hat{\rho} = \sum_{i,j=0}^{1} p_{ij} |i\rangle\langle j| \tag{2.2}$$

[1] A classical bit can assume either of the two values 0 or 1, representing the physical conditions like "on", "off" states of a device, or "up", "down" positions of a mechanical lever or "high", "low" levels of DC voltage etc..

[2] The states $|0\rangle = \begin{pmatrix} 1 \\ 0 \end{pmatrix}$ and $|1\rangle = \begin{pmatrix} 0 \\ 1 \end{pmatrix}$, are also known as the computational basis states.

provided (i) the diagonal elements of the density matrix p_{00}, p_{11} are real, and the off-diagonal elements p_{01}, p_{10} are complex with $p_{01} = p_{10}^*$, corresponding to the *Hermiticity* condition $\hat{\rho}^\dagger = \hat{\rho}$ and (ii) $p_{00} + p_{11} = 1$, corresponding to the *Normalization* condition $\mathrm{Tr}(\hat{\rho}) = 1$ and (iii) $p_{00}p_{11} - p_{01}p_{10} \geq 0$, corresponding to the *Positive semi-definiteness* condition $\hat{\rho} \succcurlyeq 0$ of the density matrix. Hence, only three parameters[3], say (a, b, c), can completely describe a general qubit as the following,

$$\hat{\rho} = \begin{pmatrix} a & b+ic \\ b-ic & 1-a \end{pmatrix} \qquad \text{provided,} \quad a(1-a) - b^2 - c^2 \geq 0 \tag{2.3}$$

The condition $a(1-a) - b^2 - c^2 \geq 0$ represents the Sylvester's criteria [5] for the Hermitian matrix $\hat{\rho}$ to be positive semi-definite. The purity of the state $\hat{\rho}$ is determined from the value of $\mathrm{Tr}\big(\hat{\rho}^2\big)$. Here, the purity is obtained to be $\mathrm{Tr}\big(\hat{\rho}^2\big) = 1 + 2(a(a-1) + b^2 + c^2) \leq 1$.

2.1.1 Parameterization of Qubits: (μ, θ, ϕ) Representation

A pure state in a two-dimensional Hilbert space, is a complex-valued vector with unit norm. In the computational basis $\{|0\rangle, |1\rangle\}$ a pure state is given as,

$$|\psi\rangle = \alpha|0\rangle + \beta|1\rangle = \begin{pmatrix} \alpha \\ \beta \end{pmatrix} = \begin{pmatrix} |\alpha|e^{i\phi_\alpha} \\ |\beta|e^{i\phi_\beta} \end{pmatrix} = e^{i\phi_\alpha} \begin{pmatrix} |\alpha| \\ |\beta|e^{i(\phi_\beta - \phi_\alpha)} \end{pmatrix} \tag{2.4}$$

$$\text{Normalization Condition:} \qquad |\alpha|^2 + |\beta|^2 = 1 \tag{2.5}$$

In the above, representing each complex number (z) in terms of its magnitude $(|z|)$ and argument $(\arg(z) = \phi_z)$, we get the pure state $|\psi\rangle$ expressed using four parameters $(|\alpha|, |\beta|, \phi_\alpha, \phi_\beta)$. However, given the normalization constraint in Eqn. 2.5 the number of parameters required to specify $|\psi\rangle$ reduces to three (as $|\beta| = \sqrt{1 - |\alpha|^2}$). Again, the global phase ϕ_α in the description of a single qubit $|\psi\rangle$ in Eqn. 2.4 can be ignored as it does not have any physically observable consequences upon measurement[4]. Hence, for a pure

[3] Considering $p_{00} = a$ and $p_{01} = b + ic$

[4] It is only the relative phase between the basis vectors that has observable effects on the experimental outcomes.

qubit α appears to be a real positive number. Therefore, only two parameters $(|\alpha|, \phi_{\beta\alpha})$ suffices to give a complete description of a pure qubit, where $\phi_{\beta\alpha} = \phi_\beta - \phi_\alpha$ represents the relative phase between $|0\rangle$ and $|1\rangle$.

$$|\psi\rangle = \begin{pmatrix} |\alpha| \\ \sqrt{1-|\alpha|^2}\; e^{i\phi_{\beta\alpha}} \end{pmatrix} \tag{2.6}$$

$$\text{where,} \quad |\alpha| \in [0,1] \quad \text{and} \quad \phi_{\beta\alpha} \in [-\pi, \pi)$$

Now, the normalization condition in Eqn. 2.5 constraints the value of α to be $|\alpha| \leq 1$. Hence, it can be parameterized as $|\alpha| = \cos\left(\frac{\theta}{2}\right)$, where θ varies from 0 to π giving $0 \leq \cos\left(\frac{\theta}{2}\right) \leq 1$. Therefore, assuming $\phi_{\beta\alpha} = \phi$, the pure state $|\psi\rangle$ can be parameterized using the two (θ, ϕ), where $\theta \in [0, \pi]$ and $\phi \in [-\pi, \pi)$.

$$|\psi\rangle = \begin{pmatrix} \cos\left(\frac{\theta}{2}\right) \\ e^{i\phi}\sin\left(\frac{\theta}{2}\right) \end{pmatrix} = \cos\left(\frac{\theta}{2}\right)|0\rangle + e^{i\phi}\sin\left(\frac{\theta}{2}\right)|1\rangle \tag{2.7}$$

The density matrix representation of the pure qubit $|\psi\rangle$ is given as,

$$\hat{\rho}_{pure} = |\psi\rangle\langle\psi| = \begin{pmatrix} \cos^2\left(\frac{\theta}{2}\right) & \frac{1}{2}e^{-i\phi}\sin(\theta) \\ \frac{1}{2}e^{i\phi}\sin(\theta) & \sin^2\left(\frac{\theta}{2}\right) \end{pmatrix} \tag{2.8}$$

Here, $\mathrm{Tr}\big(\hat{\rho}^2_{pure}\big) = \cos^4\left(\frac{\theta}{2}\right) + \frac{1}{2}\sin^2(\theta) + \sin^4\left(\frac{\theta}{2}\right) = \left(\cos^2\left(\frac{\theta}{2}\right) + \sin^2\left(\frac{\theta}{2}\right)\right)^2 = 1$, represents the purity of the state.

A mixed state can be obtained from decoherence-imposed decay of the off-diagonal terms in the pure state density matrix [6] given in Eqn. 2.8. Therefore, we introduce a factor μ that varies from 0 to 1, which when multiplied with the off-diagonal terms of the above density matrix gives the generic mixed state $\hat{\rho}$, as the following:

$$\hat{\rho} = |\psi\rangle\langle\psi| = \begin{pmatrix} \cos^2\left(\frac{\theta}{2}\right) & \frac{\mu}{2}e^{-i\phi}\sin(\theta) \\ \frac{\mu}{2}e^{i\phi}\sin(\theta) & \sin^2\left(\frac{\theta}{2}\right) \end{pmatrix} \tag{2.9}$$

So, the density matrix associated with a generic mixed state can be uniquely described with three parameters, i.e., $\hat{\rho} \equiv \hat{\rho}(\mu, \theta, \phi)$. The purity of the state $\hat{\rho}$ is given as,

$$\textbf{Purity:} \qquad \mathrm{Tr}\big(\hat{\rho}^2\big) = 1 - \left(\frac{1-\mu^2}{2}\right)\sin^2(\theta) = \frac{1}{4}[3 + \mu^2 + (1-\mu^2)\cos(2\theta)] \tag{2.10}$$

Hence, purity of the density matrix $\hat{\rho}$ appears to be a function of μ and θ. When $\mu = 1$, we get the purity $\mathrm{Tr}\big(\hat{\rho}^2\big) = 1$. Therefore $\mu = 1$ corresponds to pure qubits, for all $\theta \in [0, \pi]$ and $\phi \in [-\pi, \pi)$. Next, when $\theta = 0$ or $\theta = \pi$, we get $\mathrm{Tr}\big(\hat{\rho}^2\big) = 1$ representing the pure states. From Eqn. 2.9, we can see $\theta = 0$ corresponds to $\hat{\rho}(\mu, \theta = 0, \phi) = |0\rangle\langle 0|$ and $\theta = \pi$ corresponds to $\hat{\rho}(\mu, \theta = \pi, \phi) = |1\rangle\langle 1|$. Hence, $\theta = 0$ and $\theta = \pi$ represent the basis states $|0\rangle$ and $|1\rangle$ of the two-dimensional Hilbert space. Now, when $\mu = 0$ we have $\mathrm{Tr}\big(\hat{\rho}^2\big) = \frac{1}{4}[3 + \cos(2\theta)]$ and the corresponding state is given by,

$$\hat{\rho}(\mu = 0, \theta, \phi) = \cos^2\left(\frac{\theta}{2}\right)|0\rangle\langle 0| + \sin^2\left(\frac{\theta}{2}\right)|1\rangle\langle 1| \tag{2.11}$$

which in general is a mixed state. Therefore, $\mu = 0$ with $\theta = \frac{\pi}{2}$ gives $\hat{\rho}(\mu = 0, \theta = \frac{\pi}{2}, \phi) = \frac{1}{2}(|0\rangle\langle 0| + |1\rangle\langle 1|) = \frac{\hat{\mathbb{1}}}{2}$, which is the maximally mixed state.

Therefore, a general qubit can be uniquely represented using three parameters (μ, θ, ϕ) as shown in Eqn. 2.9, with $\mu \in [0, 1]$, $\theta \in [0, \pi]$, and $\phi \in [-\pi, \pi)$. The parameter μ introduces the mixedness in the state through decoherence of the off-diagonal terms in a pure state density matrix and hence, is related to the purity of the state. $\hat{\rho}(\mu = 1, \theta, \phi)$ represents the pure states and $\hat{\rho}(\mu = 0, \theta = \frac{\pi}{2}, \phi)$ represents the maximally mixed state in the two dimensional Hilbert space. What this representation implies physically and geometrically for a two-level quantum system, will be discussed in Appendix. 2.A.

2.1.2 Bloch Sphere Representation of Qubits

In quantum mechanics, the standard geometric representation of a two-dimensional state space is provided using the Bloch sphere – a sphere of unit radius in $\mathbb{R}^3$. In the Bloch sphere representation, any state of a single two-level quantum system, i.e., any single qubit can be visualized as a point in the sphere, parameterized using spherical polar co-ordinates. The pure qubits ($|\psi\rangle$) are represented by the points on the surface of the Bloch sphere, with the two diametrically opposite points on the surface denoting the pair of orthogonal states ($|\psi\rangle$ and $|\psi\rangle^T$). Therefore, $\theta_b \in [0, \pi]$ and $\phi_b \in [-\pi, \pi)$ can completely and uniquely describe a pure state in the two dimensions[5]. A pure qubit represented in terms of Bloch parameters (θ_b, ϕ_b) is given as,

$$|\psi\rangle = \cos\left(\frac{\theta_b}{2}\right)|0\rangle + e^{i\phi_b}\sin\left(\frac{\theta_b}{2}\right)|1\rangle \tag{2.12}$$

However, the mixed qubits are represented by the points within the Bloch sphere, with the center of the sphere denoting the maximally mixed state $\hat{\rho} = \frac{\hat{\mathbb{1}}}{2}$. Therefore, apart from the angles θ_b and ϕ_b, the description of a mixed qubit requires an additional parameter (say, r_b) that would control the mixedness.

In Bloch sphere representation, any arbitrary density matrix associated with a qubit can be written as a linear combination of the identity operator $\hat{\mathbb{1}}$ and the Pauli matrices $(\hat{\sigma}_x, \hat{\sigma}_y, \hat{\sigma}_z)$ [7], as the following

$$\hat{\rho} = \frac{1}{2}\left(\hat{\mathbb{1}} + \vec{r}\cdot\vec{\sigma}\right) \tag{2.13}$$

$$\text{where,}\quad \vec{\sigma} = (\hat{\sigma}_x, \hat{\sigma}_y, \hat{\sigma}_z) \quad \text{and} \quad \vec{r} = (r_x, r_y, r_z) \quad \text{with} \quad \|\vec{r}\| \leq 1$$

Here, $\vec{r}$ is the three-dimensional vector, known as the Bloch vector, corresponding to the state $\hat{\rho}$. The vector $\vec{r}$ associated with a mixed state spans the entire volume of the Bloch sphere, with $|\vec{r}|$ scaling uniformly with the mixedness of the state. $|\vec{r}| = 1$ for pure states

[5]Here, the subscript 'b' is used to distinguish the Bloch parameters, θ_b and ϕ_b from θ and ϕ of (μ, θ, ϕ) representation, introduced earlier.

and $0 \leq |\vec{r}| < 1$ for mixed states, with $|\vec{r}| = 0$ representing the maximally mixed state.

Therefore, visualizing in terms of spherical polar co-ordinates, any arbitrary qubit can be geometrically represented by a point located at the tip of a vector $\vec{r} \in \mathbb{R}^3$ – the Bloch vector, which can be uniquely characterized with three parameters (r_b, θ_b, ϕ_b) – known as the Bloch parameters. The polar angle $\theta_b \in [0, \pi]$ and the azimuthal angle $\phi_b \in [-\pi, \pi)$ together give the direction of the vector $\vec{r}$ and $r_b = |\vec{r}| \in [0, 1]$ gives its length which governs the purity of the state. Therefore,

$$\vec{r} = (r_x, r_y, r_z) = (\ |\vec{r}| \sin(\theta_b) \cos(\phi_b),\ |\vec{r}| \sin(\theta_b) \sin(\phi_b),\ |\vec{r}| \cos(\theta_b)\ ) \tag{2.14}$$

Hence, using the components of Bloch vector $\vec{r}$ as shown above and the operators

$$\hat{\mathbb{1}} = \begin{pmatrix} 1 & 0 \\ 0 & 1 \end{pmatrix}, \quad \hat{\sigma}_x = \begin{pmatrix} 0 & 1 \\ 1 & 0 \end{pmatrix}, \quad \hat{\sigma}_y = \begin{pmatrix} 0 & -i \\ i & 0 \end{pmatrix}, \quad \hat{\sigma}_z = \begin{pmatrix} 1 & 0 \\ 0 & -1 \end{pmatrix} \tag{2.15}$$

we get the generic density matrix in Eqn. 2.13 corresponding to any arbitrary qubit, represented in terms of the Bloch parameters as the following:

$$\hat{\rho} = \frac{1}{2} \begin{pmatrix} 1 + r_z & r_x - i r_y \\ r_x + i r_y & 1 - r_z \end{pmatrix} = \frac{1}{2} \begin{pmatrix} 1 + |\vec{r}| \cos(\theta_b) & |\vec{r}| \sin(\theta_b)\ e^{-i\phi_b} \\ |\vec{r}| \sin(\theta_b)\ e^{i\phi_b} & 1 - |\vec{r}| \cos(\theta_b) \end{pmatrix} \tag{2.16}$$

The purity of the state is represented by the length of the Bloch vector $|\vec{r}|$ and is given as,

$$\textbf{Purity:} \qquad \mathrm{Tr}\big(\hat{\rho}^2\big) = \frac{1}{2}(1 + |\vec{r}|^2) \tag{2.17}$$

In quantum theory, one of the popularly used representations of a qubit is the Bloch sphere representation, in which a state in the two-dimensional complex vector space can be visualized using a unit 2-sphere ($\mathbb{S}^{(2)}$). The pure states given by $\hat{\rho}(r_b = 1, \theta_b, \phi_b)$ lie on the surface of the sphere and the mixed states given by $\hat{\rho}(r_b < 1, \theta_b, \phi_b)$ lie within the volume of the sphere, where $r_b = |\vec{r}|$ is the magnitude of the Bloch vector $\vec{r}$ corresponding to a given state. Bloch sphere representation of a general density matrix of a qubit is shown in Eqn. 2.16, where $|\vec{r}| = r_b \in [0, 1],\ \theta_b \in [0, \pi],\ \phi \in [-\pi, \pi)$. This representation of the two-dimensional state space is useful in characterizing and manipulating a qubit in the applications of quantum computing and quantum information processing, as it provides a simple and intuitive way to visualize any one qubit operation (unitary or non-unitary) as the rotation of the Bloch sphere [3].

In summary, any arbitrary state in a two-dimensional Hilbert space can be characterized with three real parameters. This section presents two of the many representations of a general qubit − one with the (μ, θ, ϕ) parameters, where $\mu \in [0, 1]$, $\theta \in [0, \pi]$, $\phi \in [-\pi, \pi)$, in the *Decoherence Representation* and another with the (r_b, θ_b, ϕ_b) parameters, where $r_b \in [0, 1]$, $\theta_b \in [0, \pi]$, $\phi_b \in [-\pi, \pi)$ in the *Bloch Sphere Representation*, each having their individual significance. A connection between the two representations from the perspective of visualizing the geometry of the Hilbert space can be seen in the Appendix. 2.A. The Bloch sphere representation is more useful in quantum computing and quantum information as visualization of any (unitary or non-unitary) operations in the two-dimensional Hilbert space is simple in terms of rotations of the Bloch sphere, while the decoherence representation is useful in quantum dynamics, where a system evolves through environment interactions. One representation of qubit over the other appears to be more appropriate, depending on the applications and the type of experiments they are involved in.

In the interferometric technique of state characterization − *Quantum State Interferography* (*QSI*), where an unknown qubit can be identified from a single interference pattern, we prefer the (μ, θ, ϕ) representation as shown in Sec. 2.5. However, *QSI* as a technique is consistent in characterizing any arbitrary qubit given in the standard Bloch sphere representation as well. The only difference would be in the post-processing of the collected data from the experiment, as the interferometric quantities (such as the phase shift, average intensity, and visibility) obtained from an interference pattern would have different functional relationships with the state parameters in the two different representations. The details for identifying the Bloch parameters (r_b, θ_b, ϕ_b) of an unknown qubit using the quantum state interferography technique will be discussed in Sec. 2.9.

2.2 Quantum State Interferography for Pure Qubits

The pure states of a two-dimensional quantum system are in general reconstructed using the standard quantum state determination technique, i.e., Quantum State Tomography (QST) which requires two distinct projective measurements to be performed on the system. In this section, we will present an interferometric scheme – *Quantum State Interferography*, where a pure qubit can be inferred from the phase shift and the average intensity of a single interference pattern.

Any pure state for a 2-dimensional quantum system i.e., a pure qubit can be written in terms of Bloch sphere co-ordinates[6] as,

$$|\psi\rangle = \begin{pmatrix} \cos\left(\dfrac{\theta}{2}\right) \\ \exp(i\phi)\sin\left(\dfrac{\theta}{2}\right) \end{pmatrix} \tag{2.18}$$

where $\theta \in [0, \pi]$ and $\phi \in [-\pi, \pi)$. The co-ordinates (θ, ϕ) represent the direction of the state vector in the Bloch sphere. By knowing these two parameters from an experiment, we can infer any unknown pure state in two dimensions. Here in this section, we will describe how the two unknown parameters (θ, ϕ) can be obtained at once from an experiment employing interferometry.

2.2.1 Theory

The spin-ladder operators $\hat{\sigma}_{\pm}$ for the two-dimensional Hilbert space (say, spanned by the basis $\{|0\rangle, |1\rangle\}$) are given by,

$$\hat{\sigma}_{\pm} = \frac{1}{2}\left(\hat{\sigma}_x \pm i\hat{\sigma}_y\right) \tag{2.19}$$

[6]Here, we have dropped the subscript ‘b’ while addressing Bloch parameters as both the representations give the same descriptions for pure states.

where, $\hat{\sigma}_x$ and $\hat{\sigma}_y$ are the respective Pauli matrices[7]. The operations of the lowering ($\hat{\sigma}_-$) and raising operators ($\hat{\sigma}_+$) are given as, $\hat{\sigma}_- |0\rangle = |1\rangle$, $\hat{\sigma}_- |1\rangle = 0$ and $\hat{\sigma}_+ |0\rangle = 0$, $\hat{\sigma}_+ |1\rangle = |0\rangle$. The expectation value of $\hat{\sigma}_\pm$ in the state $|\psi\rangle$ can be computed to be,

$$\langle \hat{\sigma}_\pm \rangle = \frac{\langle \psi | \hat{\sigma}_\pm | \psi \rangle}{\langle \psi | \psi \rangle} = \frac{1}{2} \exp(\pm i\phi) \sin(\theta) \tag{2.20}$$

Hence, when computing the expectation value of any one of the spin ladder operators $\hat{\sigma}_\pm = \frac{1}{2}(\hat{\sigma}_x \pm i\hat{\sigma}_y)$ in the state $|\psi\rangle$, we have the polar co-ordinate θ appearing only in the magnitude of $\langle \hat{\sigma}_\pm \rangle$ and the azimuthal co-ordinate ϕ appearing only as a phase in the Argand plane, i.e.,

$$|\langle \hat{\sigma}_\pm \rangle| = \frac{1}{2} \sin(\theta) \tag{2.21}$$

$$\arg\left(\langle \hat{\sigma}_\pm \rangle\right) = \pm\, \phi \tag{2.22}$$

So, for a pure qubit $|\psi\rangle$, the state parameters θ and ϕ can be obtained directly from the complex expectation value $\langle \hat{\sigma}_\pm \rangle$ as the following,

$$\theta = \sin^{-1}\left(2|\langle \hat{\sigma}_\pm \rangle|\right) \tag{2.23}$$

$$\phi = \pm \arg\left(\langle \hat{\sigma}_\pm \rangle\right) \tag{2.24}$$

However, the solution to θ is not unique in $[0, \pi]$ and $(\pi - \theta)$ is a solution as well, since $\sin(\pi - \theta) = \sin(\theta)$. Thus, in order to uniquely determine the polar angle θ, we need to measure the expectation value of another column operator, which in this case is the projector to the state $|0\rangle$, i.e., $\hat{\Pi}_0 = |0\rangle\langle 0|$. The expectation value of $\hat{\Pi}_0$ in the state $|\psi\rangle$ is given by,

$$\left\langle \hat{\Pi}_0 \right\rangle = \frac{\langle \psi | \hat{\Pi}_0 | \psi \rangle}{\langle \psi | \psi \rangle} = \cos^2\left(\frac{\theta}{2}\right) \tag{2.25}$$

[7]Here, $\hat{\sigma}_x = \begin{pmatrix} 0 & 1 \\ 1 & 0 \end{pmatrix}$, $\hat{\sigma}_y = \begin{pmatrix} 0 & -i \\ i & 0 \end{pmatrix}$, which makes $\hat{\sigma}_+ = \begin{pmatrix} 0 & 1 \\ 0 & 0 \end{pmatrix}$ and $\hat{\sigma}_- = \begin{pmatrix} 0 & 0 \\ 1 & 0 \end{pmatrix}$.

Once $\left\langle \hat{\Pi}_0 \right\rangle$ is known, θ is uniquely determined in $[0, \pi]$ as,

$$\theta = 2\cos^{-1}\left(\sqrt{\left\langle \hat{\Pi}_0 \right\rangle}\right) \tag{2.26}$$

Hence, the unknown qubit $|\psi\rangle$ can be characterized by measuring the expectation values of the two operators $-$ any one of the ladder operators i.e., $\hat{\sigma}_+$ or $\hat{\sigma}_-$ and the projector $\hat{\Pi}_0$. For further discussion we will choose the spin ladder operator $\hat{\sigma}_-$ and show the detail derivation of how we achieve the state parameters from the expectation value of $\hat{\sigma}_-$ obtained experimentally employing interferometry. So we get,

$$\phi = -\arg\left(\langle \hat{\sigma}_- \rangle\right) \tag{2.27}$$

$$\text{where,} \qquad \hat{\sigma}_- = \frac{1}{2}\left(\hat{\sigma}_x - i\hat{\sigma}_y\right) = \begin{pmatrix} 0 & 0 \\ 1 & 0 \end{pmatrix} \tag{2.28}$$

Now, the operator $\hat{\sigma}_-$ is non-Hermitian, the expectation value of which, is in general complex. Experimentally, the complex expectation value of the non-Hermitian spin ladder operator $\hat{\sigma}_-$ cannot be obtained from the statistical distribution of the measurement outcomes. However, polar decomposition can be used to determine the expectation value of the non-Hermitian operator $(\hat{\sigma}_-)$ in the form of the complex weak value [8] of a Hermitian operator $\hat{R}$ in the pre-selected state $|\psi\rangle$ and the post-selected state $|\phi\rangle = \hat{U}^\dagger |\psi\rangle$, where $\hat{U}$ is a Unitary operator and $\hat{R} = \sqrt{\hat{\sigma}_-^\dagger \hat{\sigma}_-}$ satisfying $\hat{\sigma}_- = \hat{U}\hat{R}$ [9], the details of which has been shown in SubSec. 2.2.2.

2.2.2 Polar Decomposition and Determination of Complex Expectation Value of a non-Hermitian Operator

Let, $\hat{A}$ be a non-Hermitian operator whose expectation value in the state $|\psi\rangle$ needs to be determined experimentally. In quantum mechanics, the observables are often represented by the Hermitian operators [10] since they have real eigen spectrum and the non-degenerate eigen values are associated with the eigen states that form a complete set. The eigen spectrum of the non-Hermitian operators is, in general complex, and therefore we can not obtain the complex expectation value of the non-Hermitian operator by evaluating the average of the distribution of the measurement outcomes of the operator. However, the non-Hermitian operator $\hat{A}$ can be polar decomposed as $\hat{A} = \hat{U}\hat{R}$, where $\hat{U}$ is an Unitary operator and $\hat{R}$ is a positive semi-definite Hermitian operator given by $\hat{R} = \sqrt{\hat{A}^\dagger \hat{A}}$ [11]. So, the expectation value of the operator $\hat{A}$ in the state $|\psi\rangle$ can be expressed as,

$$\left\langle \hat{A} \right\rangle = \frac{\langle\psi|\hat{A}|\psi\rangle}{\langle\psi|\psi\rangle} = \frac{\langle\psi|\hat{U}\hat{R}|\psi\rangle}{\langle\psi|\psi\rangle} \tag{2.29}$$

$$\implies \quad \left\langle \hat{A} \right\rangle = \frac{\langle\psi|\hat{U}|\psi\rangle}{\langle\psi|\psi\rangle}\frac{\langle\psi|\hat{U}\hat{R}|\psi\rangle}{\langle\psi|\hat{U}|\psi\rangle} = \frac{\langle\phi|\psi\rangle}{\langle\psi|\psi\rangle}\frac{\langle\phi|\hat{R}|\psi\rangle}{\langle\phi|\psi\rangle} = \frac{\langle\phi|\psi\rangle}{\langle\psi|\psi\rangle}\left\langle \hat{R} \right\rangle^{(w)} \tag{2.30}$$

$$\text{where,} \quad \left\langle \hat{R} \right\rangle^{(w)} = \frac{\langle\phi|\hat{R}|\psi\rangle}{\langle\phi|\psi\rangle} \tag{2.31}$$

$$\text{and} \qquad |\phi\rangle = \hat{U}^\dagger |\psi\rangle \tag{2.32}$$

Hence from Eqn. 2.30 it can be seen that the expectation value of the non-Hermitian operator $\hat{A}$ can be expressed in terms of the weak value $\left\langle \hat{R} \right\rangle^{(w)}$ of the Hermitian part of the polar decomposed operator in the pre-selected state $|\psi\rangle$ and post-selected state $|\phi\rangle = \hat{U}^\dagger |\psi\rangle$. The quantity $\frac{\langle\phi|\psi\rangle}{\langle\psi|\psi\rangle} = \frac{\langle\psi|\hat{U}|\psi\rangle}{\langle\psi|\psi\rangle}$ is the expectation value of the operator $\hat{U}$ in the state $|\psi\rangle$ and can, in general, be complex. Thus, the complex expectation value $\left\langle \hat{A} \right\rangle$ can be inferred experimentally by directly measuring the weak value of the Hermitian component $\hat{R}$ and knowing the expectation value of the Unitary component $\hat{U}$ corresponding to the operator $\hat{A}$, where $\hat{A} = \hat{U}\hat{R}$. Experimentally, the complex weak value of $\hat{R}$ can be determined by measuring the shift in the pointer variable which gives the real part of the weak value and the shift in the momentum conjugate to the pointer variable which gives the imaginary part of the weak value [12].

Now, as discussed in 2.2.1, to infer an unknown pure qubit from an experiment, the expectation value of the non-Hermitian spin ladder operator $\hat{\sigma}_-$ in that state needs to be determined. According to Dirac, in quantum theory "observables" are the only quantities that can be measured, where an observable would be defined as a real dynamical variable whose eigen states form a complete set [13]. For the two-dimensional state space spanned by the basis $\{|0\rangle, |1\rangle\}$, the operator $\hat{\sigma}_- = \frac{1}{2}(\hat{\sigma}_x - i\hat{\sigma}_y)$ transforms $|0\rangle$ to $|1\rangle$ and annihilates $|1\rangle$. The operator $\hat{\sigma}_-$ has real eigenvalues[8] but does not have sufficient eigen states that can form a complete set. Hence, $\hat{\sigma}_-$ can not be considered as an *observable* and the operator can not be realized physically in an experiment. Therefore, the expectation value of $\hat{\sigma}_-$ can not be measured experimentally.

However, the complex expectation value of the non-Hermitian $\hat{\sigma}_-$ operator can be determined experimentally employing polar decomposition and obtaining weak value of the Hermitian component, as discussed earlier. Consider $\hat{\sigma}_-$ is polar decomposed into the Unitary $\hat{U}$ and positive semi-definite Hermitian $\hat{R}$ as $\hat{\sigma}_- = \hat{U}\hat{R}$. Here, the operator $\hat{R}$ can determined as the following,

$$\hat{R} = \sqrt{\hat{\sigma}_-^\dagger \hat{\sigma}_-} \tag{2.33}$$

$$\hat{R} = \sqrt{\begin{pmatrix} 0 & 1 \\ 0 & 0 \end{pmatrix}\begin{pmatrix} 0 & 0 \\ 1 & 0 \end{pmatrix}} = \sqrt{\begin{pmatrix} 1 & 0 \\ 0 & 0 \end{pmatrix}} = \begin{pmatrix} 1 & 0 \\ 0 & 0 \end{pmatrix} \tag{2.34}$$

Knowing the Hermitian operator $\hat{R}$, the Unitary operator $\hat{U}$ related to the non-Hermitian operator $\hat{\sigma}_-$ can be computed to be,

$$\hat{U} = \begin{pmatrix} 0 & 1 \\ 1 & 0 \end{pmatrix} \tag{2.35}$$

From the matrix representation of the operators $\hat{R}$ and $\hat{U}$ given in Eqn. 2.34 and Eqn. 2.35, we can conclude that $\hat{U}$ is the Pauli-X operator, i.e., $\hat{\sigma}_x = |0\rangle\langle 1| + |1\rangle\langle 0|$ (or the NOT operator) and $\hat{R}$ is the projection operator associated with the state $|0\rangle$ i.e., $\hat{\Pi}_0 = |0\rangle\langle 0|$ in the two dimensional Hilbert space spanned by the basis $\{|0\rangle, |1\rangle\}$. Therefore,

[8] Eigen values fo $\hat{\sigma}_-$ are $(0, 0)$ which are real, as determined by solving the characteristic equation $\det(\hat{\sigma}_- - \lambda\hat{\mathbb{1}}) = 0$ for the eigen value λ.

$$\hat{\sigma}_- = \begin{pmatrix} 0 & 0 \\ 1 & 0 \end{pmatrix} = \begin{pmatrix} 0 & 1 \\ 1 & 0 \end{pmatrix} \begin{pmatrix} 1 & 0 \\ 0 & 0 \end{pmatrix} = \hat{U}\hat{R} \tag{2.36}$$

$$\text{where,} \qquad \hat{U} = \hat{\sigma}_x = |0\rangle\langle 1| + |1\rangle\langle 0| \qquad \text{and} \qquad \hat{R} = \hat{\Pi}_0 = |0\rangle\langle 0| \tag{2.37}$$

Thus, as shown in Eqn. 2.30, the expectation value of the non-Hermitian ladder operator $\hat{\sigma}_-$ can be inferred experimentally from the weak value of the Hermitian component $\hat{R}$, where $\hat{R} = \sqrt{\hat{\sigma}_-^\dagger \hat{\sigma}_-} = \hat{\Pi}_0$, in the pre-selected state $|\psi\rangle$ and the post-selected state $|\phi\rangle = \hat{U}^\dagger |\psi\rangle = \hat{\sigma}_x^\dagger |\psi\rangle$, where $\hat{\sigma}_x = \hat{U}$ is a Unitary matrix satisfying $\hat{\sigma}_- = \hat{\sigma}_x \hat{\Pi}_0 = \hat{U}\hat{R}$. It has been experimentally shown that the weak value of a Hermitian operator can be obtained directly from the visibility and phase shift of an interference pattern without requiring any post-selection and without performing the conventional weak measurement [14]. Thus, using an interferometric technique we can determine the expectation value of the non-Hermitian operator $\hat{\sigma}_-$ from which the state parameters can be inferred, as discussed in the following.

2.2.3 Experimental Protocol for Inferring an Unknown Pure Qubit

As discussed in SubSec. 2.2.1, the unique determination of any pure qubit $|\psi(\theta, \phi)\rangle$, would require one to measure the expectation values of the projector $\hat{\Pi}_0$ and the spin ladder operator $\hat{\sigma}_-$ in the state $|\psi\rangle$. Experimentally the expectation values can be determined using the quantities obtained from an interference pattern formed in a two path interferometer. Here, we discuss the experimental protocol in an optical setup using a Mach-Zehnder Interferometer (MZI) [15, 16], with the aim to reconstruct the polarization qubits associated with an ensemble of identically prepared photons.

Let, a stream of identically prepared photons in the polarization state $|\psi\rangle$ be incident on a Mach-Zehnder Interferometer (MZI) as shown in Fig. 2.1. The MZI consists of two $50 : 50$ beam splitters BS_1 and BS_2 and two mirrors M_A and M_B in the two respective paths of the interferometer labeled as A and B. The two output ends of the MZI are labeled as C and D respectively and a photo detector is placed at the output port D.

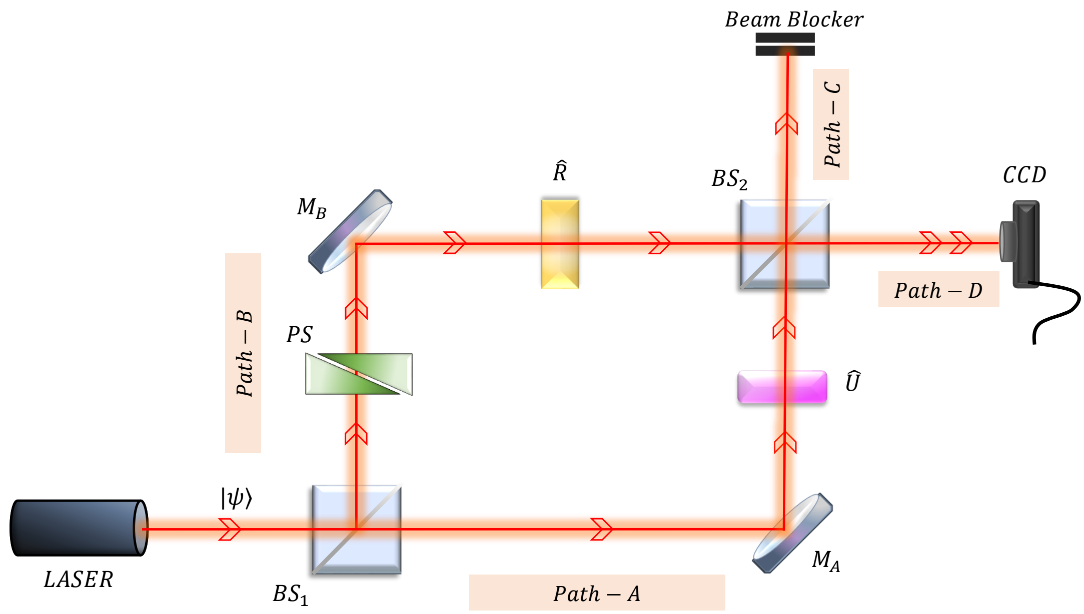

Figure 2.1: Schematic of the Quantum State Interferography setup consisting of a Mach-Zehnder Interferometer having Unitary $\hat{U}$ in path-A and Hermitian $\hat{R}$ in path-B, with the phase shifter (PS) controlling the relative phase (ϵ) between the two paths.

In polarization degree of freedom, an unknown quantum state (known to be pure) in the two-dimensional Hilbert space is denoted by,

$$|\psi\rangle = \alpha\,|H\rangle + \beta\,|V\rangle = \begin{pmatrix}\alpha\\ \beta\end{pmatrix} = \begin{pmatrix}\cos\left(\dfrac{\theta}{2}\right)\\ \exp(i\phi)\sin\left(\dfrac{\theta}{2}\right)\end{pmatrix} \tag{2.38}$$

with α and β being the complex coefficients associated with the basis states $|H\rangle$ and $|V\rangle$ corresponding to the horizontal polarization and vertical polarization respectively, constrained by the normalization condition $|\alpha|^2 + |\beta|^2 = 1$. Here, we need not worry about the global phase as it does not have any direct physical consequence upon measurement, hence, we can ignore it. We are only interested in the relative phase ϕ between the $|H\rangle$ and $|V\rangle$ components. Thus, to infer the polarization qubit $|\psi\rangle$ we need to find the state parameters θ and ϕ from the experiment.

A $50:50$ beam splitter BS splits the incident beam into two spatial modes with equal intensities, i.e., a part of the beam is transmitted through the BS with amplitude A_T and another part is reflected from the BS with amplitude A_R, given $|A_T|^2 + |A_R|^2 = 1$ for an ideal lossless beam splitter [17]. Now, $|A_T| = |A_R|$ for $50:50$ beam splitter. In general, it is considered that the beam reflected from the BS undergoes a phase shift φ relative to the transmitted beam, making $A_R = e^{i\varphi}A_T$. Now, $\varphi = \frac{\pi}{2}$ for a symmetric beam splitter (BS_{sym}) [18, 19] for which the beams acquires the same phase shift $\frac{\pi}{2}$ upon reflection, irrespective of the input port of the BS (i.e., irrespective of the port from which the beam is incident on the BS) and $\varphi = 0$ or π for an asymmetric beam splitter (BS_{asym}) [20] for which the beams acquire different phase shifts upon reflection, depending on the input port from which the beam is incident onto the BS [9]. Thus, the unitary transformation matrices associated with the $50:50$ beam splitters are given by,

$$BS_{sym} = \frac{1}{\sqrt{2}}\begin{pmatrix} 1 & i \\ i & 1 \end{pmatrix}, \qquad BS_{asym} = \frac{1}{\sqrt{2}}\begin{pmatrix} 1 & 1 \\ -1 & 1 \end{pmatrix} \tag{2.39}$$

For establishing the idea of Quantum State Interferography for qubits we will consider BS_1 and BS_2 to be lossless symmetric beam splitters that do not affect the polarization degree of freedom of the stream of particles or the beam. The beam splitter BS_1 splits the incident beam with the polarization state $|\psi\rangle$ into two spatial modes $|A\rangle$ and $|B\rangle$ corresponding to the two paths, A and B of the interferometer respectively. So, after BS_1 the state would be,

$$|\Psi_1\rangle = \frac{1}{\sqrt{2}}|\psi\rangle\left(|A\rangle + i\,|B\rangle\right) \tag{2.40}$$

where $|\Psi_1\rangle$ represents the joint state of the photons in polarization and path degrees of freedom after BS_1. $|A\rangle$ and $|B\rangle$ are the states in spatial d.o.f.[10] associated with the beams transmitted and reflected from BS_1 respectively.

[9] In practice, the relative phase between A_T and A_R is arbitrary which depends on the boundary conditions i.e., the uncertainty in the size of the beam splitter cube, quality of the surface at the locations where the beam is hitting while entering into and emerging out of the beam splitter etc..

[10] Throughout the thesis the terms “spatial d.o.f.” and “path d.o.f.” have been used alternatively.

Now, to find the state parameters we need to find the expectation value of the non-Hermitian spin ladder operator $\hat{\sigma}_-$ in the state $|\psi\rangle$ [11]. For this, we apply the operator $\hat{U}$ in arm A and the operator $\hat{R}$ in arm B of the interferometer, where $\hat{U}$ and $\hat{R}$ acts on the polarization d.o.f. only and is related to the non-Hermitian operator of interest $\hat{\sigma}_-$ as $\hat{\sigma}_- = \hat{U}\hat{R}$. Therefore, after evolving through the two operators the joint state of the photons just before BS_2 is given by,

$$|\Psi_2\rangle = \frac{1}{\sqrt{2}}\left(\hat{U}\,|\psi\rangle\,|A\rangle + i\hat{R}\,|\psi\rangle\,|B\rangle\right) \tag{2.41}$$

Now, the two beams from the two paths of the interferometer are recombined at the second beam splitter BS_2 and the combined beam propagates towards the two output ports C and D corresponding to the spatial modes $|C\rangle$ and $|D\rangle$ respectively. For BS_2, the output mode $|C\rangle$ consists of the beams transmitted from path-A and reflected from path-B. Similarly, the output mode $|D\rangle$ consists of the beams reflected from path-A and transmitted from path-B. Thus, the transformations are given by,

$$|A\rangle \xrightarrow{BS_2} \frac{1}{\sqrt{2}}(|C\rangle + i\,|D\rangle) \tag{2.42}$$

$$|B\rangle \xrightarrow{BS_2} \frac{1}{\sqrt{2}}(i\,|C\rangle + |D\rangle) \tag{2.43}$$

After the recombination of the two beams coming from path-A and path-B at the final beam splitter BS_2, we get the final state as the superposition of states in port C and port D respectively. The final state is given by,

$$|\Psi_3\rangle = \frac{1}{\sqrt{2}}\left(\hat{U}\,|\psi\rangle\,\frac{|C\rangle + i\,|D\rangle}{\sqrt{2}} + ie^{i\epsilon}\hat{R}\,|\psi\rangle\,\frac{i\,|C\rangle + |D\rangle}{\sqrt{2}}\right) \tag{2.44}$$

$$|\Psi_3\rangle = \frac{1}{2}\left(\hat{U}\,|\psi\rangle + i^2e^{i\epsilon}\hat{R}\,|\psi\rangle\right)|C\rangle + \frac{1}{2}\left(i\hat{U}\,|\psi\rangle + ie^{i\epsilon}\hat{R}\,|\psi\rangle\right)|D\rangle$$

$$|\Psi_3\rangle = \frac{1}{2}\left(\hat{U}\,|\psi\rangle - e^{i\epsilon}\hat{R}\,|\psi\rangle\right)|C\rangle + \frac{i}{2}\left(\hat{U}\,|\psi\rangle + e^{i\epsilon}\hat{R}\,|\psi\rangle\right)|D\rangle \tag{2.45}$$

[11] The operator $\hat{\sigma}_-$ when acts on polarization d.o.f. converts $|H\rangle$ to $|V\rangle$ and annihilates $|V\rangle$.

where ϵ is the relative phase between the two paths A and B of the interferometer. ϵ is associated with the path length difference ($\Delta l = l_A - l_B$) between the two paths of the interferometer. The quantity ϵ also captures the phase differences introduced due to the reflection of the beams from different optical components, propagation through optical elements of different thicknesses and refractive indices, and the phase difference introduced due to any alignment inconsistency. This phase difference ϵ can be controlled using a phase shifter (PS) in the setup as shown in Fig 2.1. The phase shifter adds a phase to the beam in the path-B which in turn changes the overall relative phase ϵ of the interferometer. In general, a phase shifter can be a glass plate with variable thickness across the transverse plane of the beam or a glass plate with adjustable tilt, so that the optical path length of the beam propagating through the glass plate can be adjusted.

A detector is placed at the output port D and the port C remains undetected. The detector records the intensity I_d of the beam that emerged in the port D as a function of the phase difference ϵ. This detector can be a photo detector (PD) which records the intensity associated with a particular phase at a time and generates the intensity profile when the phase is scanned from $-\pi$ to π (mostly useful for collinear geometry of the interferometer) using the phase shifter (PS). Alternatively, it can be a CCD camera that records a $2D$ image of the intensity distribution $I_d(\epsilon)$ as a function of phase ϵ at once (for non-collinear geometry of the interferometer). This intensity profile (i.e., I_d vs ϵ) recorded by the photo detector or camera is the interference pattern formed at the end of the Mach-Zehnder interferometer with operator $\hat{U}$ in arm A and operator $\hat{R}$ in arm B.

The component of the final state after evolving through the interferometer in the output port D (where the detector is placed) is obtained by projecting the state after BS_2 i.e., the state $|\Psi_3\rangle$ given by Eqn. 2.45 onto the spatial mode $|D\rangle$ as shown below,

$$|\Psi_D\rangle = \hat{\Pi}_D |\Psi_3\rangle \qquad \text{where,} \quad \hat{\Pi}_D = |D\rangle\langle D| \tag{2.46}$$

$$|\Psi_D\rangle = \frac{i}{2}\left(\hat{U}|\psi\rangle + e^{i\epsilon}\hat{R}|\psi\rangle\right)|D\rangle = \frac{i}{2}\left(\hat{U} + e^{i\epsilon}\hat{R}\right)|\psi\rangle|D\rangle \tag{2.47}$$

Thus, the intensity distribution as recorded by the detector in port D is obtained to be,

$$I_d(\epsilon) = \||\Psi_D\rangle\|^2 = \left\|\hat{\Pi}_D |\Psi_3\rangle\right\|^2 = \left|\frac{i}{2}\left(\hat{U}|\psi\rangle + e^{i\epsilon}\hat{R}|\psi\rangle\right)|D\rangle\right|^2 \tag{2.48}$$

$$I_d(\epsilon) = \frac{1}{4}\left(\langle\psi|\hat{U}^\dagger + e^{-i\epsilon}\langle\psi|\hat{R}^\dagger\right)\left(\hat{U}|\psi\rangle + e^{i\epsilon}\hat{R}|\psi\rangle\right)\langle D|D\rangle$$

$$I_d(\epsilon) = \frac{1}{4}\left[\langle\psi|\hat{U}^\dagger\hat{U}|\psi\rangle + \langle\psi|\hat{R}^\dagger\hat{R}|\psi\rangle + e^{i\epsilon}\langle\psi|\hat{U}^\dagger\hat{R}|\psi\rangle + e^{-i\epsilon}\langle\psi|\hat{R}^\dagger\hat{U}|\psi\rangle\right] \tag{2.49}$$

Since the operators $\hat{U}$ and $\hat{R}$ are the polar decomposed components of $\hat{\sigma}_-$, we know that $\hat{U}$ is Unitary and $\hat{R}$ is Hermitian. So, we get $\hat{U}^\dagger\hat{U} = \hat{\mathbb{1}}$ and $\hat{R}^\dagger = \hat{R}$ i.e., $\hat{R}^\dagger\hat{R} = \hat{R}^2$. Thus, the expectation values of the first two terms of the expression in Eqn. 2.49 become,

$$\langle\psi|\hat{U}^\dagger\hat{U}|\psi\rangle = \langle\psi|\hat{\mathbb{1}}|\psi\rangle = \langle\psi|\psi\rangle = 1 \tag{2.50}$$

$$\langle\psi|\hat{R}^\dagger\hat{R}|\psi\rangle = \langle\psi|\hat{R}^2|\psi\rangle = \left\langle\hat{R}^2\right\rangle \tag{2.51}$$

Both the above quantities have real values. The last two terms of expression shown in Eqn. 2.49 are in general complex and they are complex conjugate to each other. These two terms give rise to the interference. We can denote $\langle\psi|\hat{U}^\dagger\hat{R}|\psi\rangle = z$, thus we have $\langle\psi|\hat{R}^\dagger\hat{U}|\psi\rangle = \langle\psi|\hat{U}^\dagger\hat{R}|\psi\rangle^* = z^*$, where z is a complex quantity given by $z = |z|e^{i\chi}$ with $\chi = \arg(z)$. Hence, the last two terms of the expression in Eqn. 2.49 that gives rise to the interference can be written in terms of z as the following,

$$\begin{aligned} t_{int} &= e^{i\epsilon}\langle\psi|\hat{U}^\dagger\hat{R}|\psi\rangle + e^{-i\epsilon}\langle\psi|\hat{R}^\dagger\hat{U}|\psi\rangle \\ &= ze^{i\epsilon} + z^*e^{-i\epsilon} \\ &= |z|e^{i\chi}e^{i\epsilon} + |z|e^{-i\chi}e^{-i\epsilon} \end{aligned} \tag{2.52}$$

$$\implies \quad t_{int} = 2|z|\cos(\chi+\epsilon) = 2|z|\cos(\epsilon+\chi) \tag{2.53}$$

Therefore, the intensity pattern recorded by the detector in port D as a function of relative phase ϵ is then given by,

$$I_d(\epsilon) = \frac{1}{4}\left[1 + \left\langle \hat{R}^2 \right\rangle + 2|z|\cos(\epsilon + \chi)\right] \tag{2.54}$$

$$\text{where,} \qquad |z|e^{i\chi} = z = \left\langle \hat{U}^\dagger \hat{R} \right\rangle \tag{2.55}$$

The polar decomposed components $\hat{U}$ and $\hat{R}$ of the non-Hermitian operator $\hat{\sigma}_-$ are given as $\hat{U} = \hat{\sigma}_x$ and $\hat{R} = \hat{\Pi}_0 = |0\rangle\langle 0|$ as shown in SubSec. 2.2.2. In polarization degree of freedom with the basis $\{|H\rangle, |V\rangle\}$ the projector $\hat{\Pi}_0$ is the projector to the horizontal state $|H\rangle$ i.e., $\hat{\Pi}_0 \equiv \hat{\Pi}_H = |H\rangle\langle H|$. Thus, we have $\hat{R}^2 = \hat{R}\hat{R} = \hat{\Pi}_H\hat{\Pi}_H = |H\rangle\langle H|H\rangle\langle H| = |H\rangle\langle H| = \hat{R}$.

$$\hat{U} = \hat{\sigma}_x = |V\rangle\langle H| + |H\rangle\langle V| = \begin{pmatrix} 0 & 1 \\ 1 & 0 \end{pmatrix} \tag{2.56}$$

$$\text{and} \qquad \hat{R} = \hat{\Pi}_H = |H\rangle\langle H| = \begin{pmatrix} 1 & 0 \\ 0 & 0 \end{pmatrix} \tag{2.57}$$

Evaluating the quantities in the expression of intensity $I_d(\epsilon)$ given in Eqn. 2.54 for the state $|\psi\rangle$ represented in polar form as shown in Eqn. 2.38, we can write the intensity $I_d(\epsilon)$ in terms of the state parameters θ and ϕ. The expectation value of $\hat{R}^2$ in the state $|\psi\rangle$ is obtained to be,

$$\left\langle \hat{R}^2 \right\rangle = \left\langle \hat{R} \right\rangle = \langle\psi|\hat{R}|\psi\rangle = \langle\psi|\hat{\Pi}_H|\psi\rangle = \cos^2\left(\frac{\theta}{2}\right) \tag{2.58}$$

The complex quantity z can be evaluated as the following,

$$z = \langle\psi|\hat{U}^\dagger\hat{R}|\psi\rangle = \langle\psi|\begin{pmatrix} 0 & 1 \\ 1 & 0 \end{pmatrix}\begin{pmatrix} 1 & 0 \\ 0 & 0 \end{pmatrix}|\psi\rangle = \langle\psi|\begin{pmatrix} 0 & 0 \\ 1 & 0 \end{pmatrix}|\psi\rangle = \langle\psi|\hat{\sigma}_-|\psi\rangle \tag{2.59}$$

Threfore, using the expression of $|\psi\rangle$ in terms of θ and ϕ as given in Eqn. 2.38, we get

$$z = \langle \hat{\sigma}_- \rangle = \frac{1}{2}\exp(-i\phi)\sin(\theta) \tag{2.60}$$

$$\text{Hence,} \qquad |z| = \frac{1}{2}\sin(\theta) \qquad \text{and} \qquad \arg(z) = \chi = -\phi \tag{2.61}$$

Putting the values of different quantities from Eqn. 2.58 and Eqn. 2.61 in the expression in Eqn. 2.54, we get the intensity $I_d(\epsilon)$ in port D expressed in terms of θ and ϕ as,

$$I_d(\epsilon) = \frac{1}{4}\left[1 + \cos^2\left(\frac{\theta}{2}\right) + \sin(\theta)\cos(\epsilon - \phi)\right] \tag{2.62}$$

$$I_d(\epsilon) = \frac{1}{8}\left[3 + \cos(\theta) + 2\sin(\theta)\cos(\epsilon - \phi)\right] \tag{2.63}$$

$I_d(\epsilon)$ is the interference pattern (also known as "interferogram") formed at the end of the QSI setup consisting of a Mach-Zehnder Interferometer with operators $\hat{U}$ and $\hat{R}$ in the two respective paths, when a pure polarization qubit is made incident onto it.

2.2.4 Inferring State Parameters (θ, ϕ) from the Interferogram

In the Quantum State Interferography technique for reconstructing a qubit, the generated interference pattern, the mathematical form of which is given in the Eqn. 2.63, is post-processed to infer the quantum state being evolved through the interferometer. From the experimentally obtained interference pattern, we can find different quantities like the phase shift, average intensity, visibility etc. which can be used to determine the state parameters. For the characterization of the pure polarization qubit $|\psi\rangle$, we need to infer the two parameters θ and ϕ, from the interferometric quantities extracted from the interferogram.

The ***phase shift*** (Φ) of the interference pattern is obtained at the value of phase ϵ at which the intensity $I_d(\epsilon)$ is maximum. This value can be obtained by solving the equation $\dfrac{\partial I_d(\epsilon)}{\partial \epsilon} = 0$ for the ϵ that maximizes $I_d(\epsilon)$ (as shown in Eqn. 2.64) and ensuring that the criteria mentioned in Eqn. 2.65 is satisfied. Therefore, for $\epsilon = \Phi$ we have the following:

$$\left.\frac{\partial I_d(\epsilon)}{\partial \epsilon}\right|_{\epsilon=\Phi} = 0 \tag{2.64}$$

$$\left.\frac{\partial^2 I_d(\epsilon)}{\partial \epsilon^2}\right|_{\epsilon=\Phi} < 0 \tag{2.65}$$

For the pure state $|\psi(\theta,\phi)\rangle$ incident on the QSI setup, we have

$$\left.\frac{\partial I_d(\epsilon)}{\partial \epsilon}\right|_{\epsilon=\Phi} = -\frac{1}{4}\sin(\theta)\sin(\Phi-\phi) = 0 \tag{2.66}$$

$$\left.\frac{\partial^2 I_d(\epsilon)}{\partial \epsilon^2}\right|_{\epsilon=\Phi} = -\frac{1}{4}\sin(\theta)\cos(\Phi-\phi) \tag{2.67}$$

Since $0 \leq \theta \leq \pi$, we have $\sin(\theta) > 0$, giving $(\Phi - \phi)$ to be 0 or π. However, satisfying the condition in Eqn. **2.65**, we get $\Phi = \phi$. Thus, the state parameter ϕ can be directly obtained from the phase shift of the experimentally obtained interference pattern.

The ***phase averaged intensity*** $(\bar{I})$ of the interference pattern is obtained by integrating $I_d(\epsilon)$ over all possible phases $\epsilon \in [-\pi, \pi]$.

$$\bar{I} = \int_{\epsilon} I_d(\epsilon) d\epsilon = \frac{1}{8}\int_{-\pi}^{\pi} \left[3 + \cos(\theta) + 2\sin(\theta)\cos(\epsilon - \phi)\right] d\epsilon \tag{2.68}$$

$$\bar{I} = \frac{3 + \cos(\theta)}{8} \tag{2.69}$$

So, the average intensity $\bar{I}$ is obtained to be a unique function of the state parameter θ. Therefore, θ can be determined from the phase averaged intensity of the interferogram. Hence, the interferometric state determination technique QSI enables us to infer the state parameters (θ, ϕ) corresponding to the pure qubit $|\psi\rangle$ from the experimentally obtained phase shift (Φ) and the phase averaged intensity $(\bar{I})$ as the following,

$$\phi = \Phi, \qquad \theta = \cos^{-1}(8\bar{I} - 3) \tag{2.70}$$

Additionally, from the interference pattern $I_d(\epsilon)$ formed at the end of the QSI setup, the ***visibility*** (V) of the interferogram can be computed as the following,

$$V = \frac{I_{max} - I_{min}}{I_{max} + I_{min}} \tag{2.71}$$

where I_{max} and I_{min} respectively represent the maximum and minimum values of the intensities associated with the interference pattern. Both the values can be obtained by, solving the equation $\frac{\partial I_d(\epsilon)}{\partial \epsilon} = 0$ for ϵ and finding the values $\epsilon^{(max)}$, $\epsilon^{(min)}$ which satisfy the criteria $\left.\frac{\partial^2 I_d(\epsilon)}{\partial \epsilon^2}\right|_{\epsilon=\epsilon^{(max)}} < 0$ and $\left.\frac{\partial^2 I_d(\epsilon)}{\partial \epsilon^2}\right|_{\epsilon=\epsilon^{(min)}} > 0$ respectively.

Here, for the pure state $|\psi(\theta, \phi)\rangle$ evolved through the QSI setup, we have

$$I_{max} = I_d(\epsilon^{(max)}) = \frac{1}{8}\left[3 + \cos(\theta) + 2\sin(\theta)\right] \tag{2.72}$$

$$I_{min} = I_d(\epsilon^{(min)}) = \frac{1}{8}\left[3 + \cos(\theta) - 2\sin(\theta)\right] \tag{2.73}$$

giving the visibility (V) of the interference pattern to be,

$$V = \frac{2\sin(\theta)}{3 + \cos(\theta)} \tag{2.74}$$

Thus, the visibility of the interference pattern formed for a pure state is also a function of θ.

Therefore, the parameter θ can be determined from the visibility of the interference pattern as well. From the Eqn: 2.74 we have,

$$2\sin(\theta) = 3V + \cos(\theta)V \tag{2.75}$$

$$\implies \quad 2\sin(\theta) - 3V = \cos(\theta)V = \left(\sqrt{1 - \sin^2(\theta)}\right)V$$

$$\implies \quad 4\sin^2(\theta) - 12V\sin(\theta) + 9V^2 = (1 - \sin^2(\theta))V^2$$

$$\implies \quad (4 + V^2)\sin^2(\theta) - 12V\sin(\theta) + 8V^2 = 0 \tag{2.76}$$

Since we have $\theta \in [0, \pi]$ we can convert everything in terms of $\sin(\theta)$ and while solving the above equation we can use the fact that within the range of θ, $0 \leq \sin(\theta) \leq 1$. From the expression given in Eqn. 2.76 we get,

$$\sin(\theta) = \frac{12V \pm \sqrt{144V^2 - 32V^2(4+V^2)}}{2(4+V^2)} = \frac{6V \pm 2V\sqrt{1-2V^2}}{4+V^2} \tag{2.77}$$

Thus, a particular value of Visibility may correspond to two different values of θ representing two individual states. For example, the state $|H\rangle$ corresponding to $\theta = 0$ and the state $|V\rangle$ corresponding to $\theta = \pi$ both give visibility to be 0. Hence, θ can not be uniquely determined from the visibility.

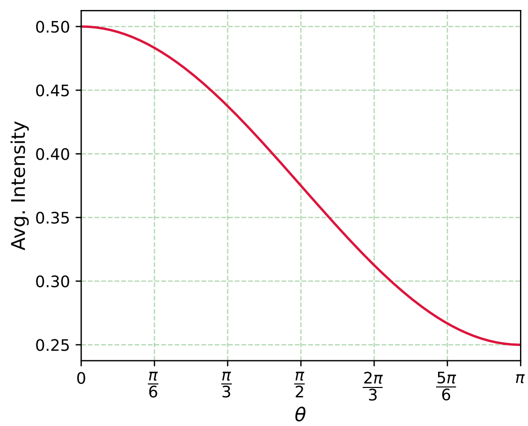

(a) Average intensity ($\bar{I}$) as a function of θ

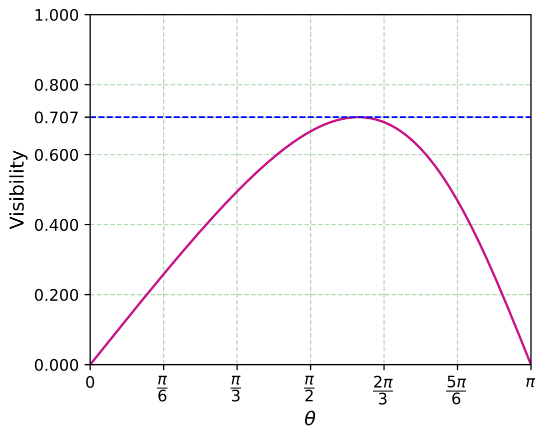

(b) Visibility (V) as a function of θ

Figure 2.2: Average intensity ($\bar{I}$) and Visibility (V) obtained from an interference pattern formed when a pure qubit $|\psi(\theta, \phi)\rangle$ evolves through the QSI setup. Visibility is found to be a bi-valued function of θ, therefore it can not uniquely identify the state parameter θ. On the other hand, average intensity is found to be a unique function of θ and therefore, is sufficient to uniquely determine the state parameter (θ). However, it has less sensitivity in the region where θ approaches 0 or π.

In summary, the characterization of an unknown pure qubit $|\psi\rangle$ requires two parameters $\theta \in [0, \pi]$ and $\phi \in [-\pi, \pi)$ to be determined from an experiment. In the Quantum State Interferography (QSI) technique, obtaining the phase averaged intensity ($\bar{I}$) and the phase shift (Φ) from the interference pattern formed at the end of the experimental setup, enables one to uniquely reconstruct the polarization state (given in Eqn. 2.38) being incident on the setup. This is because the map between the interferometric quantities $(\bar{I}, \Phi)$ and the state parameters (θ, ϕ) is bijective, as can be seen in Eqn. 2.70. Therefore, for pure qubit state reconstruction, QSI provides a single-shot state estimation scheme based on interferometry, which does not require any change in the experimental setting during the course of data acquisition.

2.2.5 Inferring the State Parameters (θ, ϕ): An Alternate Derivation

Any pure state in the two-dimensional Hilbert space in polarization d.o.f. (say) can be represented as $|\psi\rangle = \alpha\,|H\rangle + \beta\,|V\rangle$, where α and β are the probability amplitudes associated the basis states $|H\rangle$ and $|V\rangle$ respectively, with the constraint that $|\alpha|^2 + |\beta|^2 = 1$. In the polar form, i.e., in terms of the state parameters, $\theta \in [0, \pi]$ and $\phi \in [-\pi, \pi)$ the complex amplitudes can be written as,

$$\alpha = \cos\left(\frac{\theta}{2}\right), \qquad \beta = e^{i\phi} \sin\left(\frac{\theta}{2}\right) \tag{2.78}$$

The mathematical expression for the intensity distribution as a function of the relative phase ϵ, formed when the state $|\psi\rangle$ is incident on a Mach-Zehnder Interferometer (MZI) having a Unitary operator $\hat{U} = \hat{\sigma}_x$ in one arm and a Hermitian operator $\hat{R} = \hat{\Pi}_H$ in the other arm, is given in Eqn. 2.54.

$$I_d(\epsilon) = \frac{1}{4}\left[1 + \left\langle \hat{R}^2 \right\rangle + 2|z|\cos(\epsilon + \chi)\right] \quad \text{where,} \quad |z|e^{i\chi} = z = \left\langle \hat{U}^\dagger \hat{R} \right\rangle$$

From the above intensity distribution, the phase shift (Φ), i.e., the phase corresponding to the maximum intensity I_d and the phase averaged intensity $(\bar{I})$ can be computed as,

$$\Phi = -\chi = -\arg(z) = -\arg\left(\left\langle \hat{U}^\dagger \hat{R} \right\rangle\right) \tag{2.79}$$

$$\bar{I} = \frac{1}{4}\left(1 + \left\langle \hat{R}^2 \right\rangle\right) \tag{2.80}$$

where the expectation values in the state $|\psi\rangle$ are obtained to be,

$$z = \langle\psi|\hat{U}^{\dagger}\hat{R}|\psi\rangle = \begin{pmatrix}\alpha^* & \beta^*\end{pmatrix}\begin{pmatrix}0 & 1\\ 1 & 0\end{pmatrix}\begin{pmatrix}1 & 0\\ 0 & 0\end{pmatrix}\begin{pmatrix}\alpha\\ \beta\end{pmatrix} = \alpha\beta^* \tag{2.81}$$

$$\left\langle\hat{R}^2\right\rangle = \langle\psi|\hat{R}^2|\psi\rangle = \begin{pmatrix}\alpha^* & \beta^*\end{pmatrix}\begin{pmatrix}1 & 0\\ 0 & 0\end{pmatrix}\begin{pmatrix}1 & 0\\ 0 & 0\end{pmatrix}\begin{pmatrix}\alpha\\ \beta\end{pmatrix} = |\alpha|^2 \tag{2.82}$$

Thus, we have

$$\Phi = -\arg(z) = -\arg(\alpha\beta^*) = -(\arg(\alpha) - \arg(\beta)) = \phi_{\beta\alpha} = \phi \tag{2.83}$$

$$\bar{I} = \frac{1}{4}\left(1 + \left\langle\hat{R}^2\right\rangle\right) = \frac{1}{4}\left(1 + |\alpha|^2\right) = \frac{1}{4}\left(1 + \cos^2\left(\frac{\theta}{2}\right)\right) = \frac{1}{8}(3 + \cos(\theta)) \tag{2.84}$$

Therefore, the state parameters θ and ϕ characterizing a pure qubit can be directly obtained from the average intensity $\bar{I}$ and the phase shift Φ of the interferogram, respectively.

2.3 Experimental Implementation of Polar Decomposed Components of Non-Hermitian Ladder Operator $\hat{\sigma}_-$

In the last section, we have seen that employing Quantum State Interferography (QSI), an unknown polarization qubit $|\psi(\theta,\phi)\rangle$ can be reconstructed by measuring the complex expectation value of the non-Hermitian ladder operator $\hat{\sigma}_-$ and the expectation value of the projection operator $\hat{\Pi}_H$ from an experiment, which is designed with a Mach-Zehnder Interferometer having the operators $\hat{U}$ and $\hat{R}$ in the individual arms of the interferometer. These two operators $\hat{U}$ and $\hat{R}$ are respectively the polar decomposed Unitary and positive semi-definite Hermitian components of the non-Hermitian ladder operator $\hat{\sigma}_-$, i.e., $\hat{\sigma}_- = \hat{U}\hat{R}$, where $\hat{R} = \sqrt{\hat{\sigma}_-^{\dagger}\hat{\sigma}_-} = \hat{\Pi}_H$ giving $\hat{U} = \hat{\sigma}_x$ as shown in Eqn. 2.56. and Eqn. 2.57. These two operators ($\hat{U}$ and $\hat{R}$) need to be physically realized using optical components in order to use them in the experiment for inferring the qubit represented in the polarization degree of freedom of light.

2.3.1 Physical Implementation of $\hat{R}$

The operator $\hat{R} = \hat{\Pi}_H$ is the projector to the Horizontal polarization state $|H\rangle$, i.e., $\hat{\Pi}_H = |H\rangle\langle H|$. A projector to a polarization state (say, $\hat{\Pi}_\zeta = |\zeta\rangle\langle\zeta|$) can be realized using a polarizer, that transmits only the component of the incident polarization which is parallel to its transmission axis (also called the pass axis) and absorbs the component orthogonal to it. Therefore, the projector $\hat{\Pi}_\zeta = |\zeta\rangle\langle\zeta|$ would be realized using a polarizer whose transmission axis is oriented such that $|\zeta\rangle$ component of the incident polarization passes through it while the orthogonal component $|\zeta\rangle^T$ gets absorbed [12]. So, when a polarization state $|\psi\rangle$ is incident on a linear polarizer with the transmission axis oriented at an angle ϑ from the Horizontal, the state after transmission would be linearly polarized with the polarization angle being at ϑ w. r. to Horizontal. *Malus law* gives the transmission probability of any state $|\psi\rangle$ incident on the polarizer oriented to pass component $|\zeta\rangle$ as, $T = |\langle\zeta|\psi\rangle|^2$. The Jones matrix representation of a linear polarizer with the transmission axis along ϑ with respect to horizontal is given by,

$$\hat{LP}(\vartheta) = \begin{pmatrix} \cos^2(\vartheta) & \sin(\vartheta)\cos(\vartheta) \\ \sin(\vartheta)\cos(\vartheta) & \sin^2(\vartheta) \end{pmatrix} \tag{2.85}$$

Thus, the projector to Horizontal polarization state $|H\rangle$ can be realized with a linear polarizer (LP) with the transmission axis oriented at angle $\vartheta = 0$, i.e.,

$$\hat{LP}(\vartheta = 0) = \begin{pmatrix} 1 & 0 \\ 0 & 0 \end{pmatrix} = \begin{pmatrix} 1 \\ 0 \end{pmatrix} \begin{pmatrix} 1 & 0 \end{pmatrix} = |H\rangle\langle H| = \hat{\Pi}_H = \hat{R} \tag{2.86}$$

Alternatively, the operator $\hat{R} = \hat{\Pi}_H$ can also be effectively realized using a polarizing beam splitter (PBS) when we only consider its transmitting port. An ideal Polarizing Beam Splitter transmits only the horizontal component and reflects the vertical component

[12]Some polarizers like Glan-Thompson Polarizer, Glan-Taylor polarizer transmits the polarization state $|\zeta\rangle$ and directs the orthogonal component $|\zeta\rangle^T$ along a different path.

of the polarization state incident on it [13]. Let, the state $|\psi\rangle = \alpha|H\rangle + \beta|V\rangle$ is incident on a PBS from one of the input ports (say, port i) of the PBS. The action of PBS (considering the PBS to be ideal and lossless) on the state can be written as,

$$|i\rangle|\psi\rangle = |i\rangle(\alpha|H\rangle + \beta|V\rangle) \xrightarrow{PBS_{i\to(t,r)}} \alpha|t\rangle|H\rangle + \beta|r\rangle|V\rangle \tag{2.87}$$

where, $|t\rangle$ and $|r\rangle$ represent the spatial modes associated with the transmitting and reflecting ports of the PBS, when the incident beam is in the spatial mode $|i\rangle$. Therefore, a PBS creates an entanglement between spatial and polarization degrees of freedom of light, known as *intra-particle entanglement* [21, 22]. Only considering the transformation of the photon state from the spatial mode $|i\rangle$ to $|t\rangle$ through an ideal PBS we get,

$$\begin{pmatrix}\alpha\\ \beta\end{pmatrix}_{|i\rangle} \xrightarrow{PBS_{i\to t}} \begin{pmatrix}\alpha\\ 0\end{pmatrix}_{|t\rangle} \implies PBS_{i\to t} = \begin{pmatrix}1 & 0\\ 0 & 0\end{pmatrix} = \hat{\Pi}_H = \hat{R} \tag{2.88}$$

Hence, the transmission through PBS can be considered as projection to $|H\rangle$ with the effective operator associated with transmission being $\hat{\Pi}_H$.

2.3.2 Physical Implementation of $\hat{U}$

Any 2×2 Unitary operator in polarization degree of freedom of light can be realized using a combination of half-wave plate (HWP) and quater-wave plates (QWP) [23, 24, 25], both of which are birefringent crystals [14] of appropriate thickness that introduces a phase shift of δ between the ordinary and extraordinary components of the beam propagating through it [15], where $\delta_h = \pi$ for HWP and $\delta_q = \dfrac{\pi}{2}$ for QWP. The Unitary polar component $\hat{U} = \hat{\sigma}_x$

[13]In practice, few vertical [horizontal] photons can be found in the transmitting [reflecting] port of the PBS depending on the extinction ratio of that port. Generally, the extinction ratio in the reflecting port is relatively poor compared to that in the transmitting port.

[14]Birefringent materials are optically anisotropic materials, in which the refractive index varies depending on the direction of oscillation of the electric field of light propagating through it, i.e., depending on the polarization of light.

[15]Light at wavelength λ when propagates through a birefringent crystal of thickness d, the relative phase introduced between the o-ray and e-ray (corresponding to the refractive indices n_o and n_e) is given by, $\delta = \dfrac{2\pi}{\lambda}(n_o - n_e)d$.

can be realized using a half-wave plate (HWP) that transforms a linear polarization to another, depending on the orientation of its fast (or slow) axis in the plane normal to the propagation vector of the beam. Jones matrix representation of a half-wave plate (HWP) whose fast axis is aligned at an angle ϑ with respect to the horizontal is given by,

$$\hat{S}_h(\vartheta) = \begin{pmatrix} \cos(2\vartheta) & \sin(2\vartheta) \\ \sin(2\vartheta) & -\cos(2\vartheta) \end{pmatrix} \tag{2.89}$$

Thus, we can physically realize $\hat{\sigma}_x$ by orienting the fast axis of a half-wave plate (HWP) at an angle $\vartheta = \frac{\pi}{4}$, as shown below

$$\hat{S}_h\left(\frac{\pi}{4}\right) = \begin{pmatrix} 0 & 1 \\ 1 & 0 \end{pmatrix} = \hat{\sigma}_x \tag{2.90}$$

In summary, the Unitary component $\hat{U} = \hat{\sigma}_x$ can be realized using a half-wave plate (HWP) with its fast axis oriented at $\frac{\pi}{4}$ with respect to the Horizontal and the Hermitian component $\hat{R} = \hat{\Pi}_H = |H\rangle\langle H|$ can be realized using a linear polarizer with its transmission axis aligned along the Horizontal or using a polarizing beam splitter (PBS) considering only its transmitting port while ignoring the reflecting port. The operator $\hat{R} = \hat{\Pi}_H$ reduces any polarization state to $|H\rangle$, making the evolution through the corresponding optical component inside the QSI setup to be non-Unitary.

2.4 Quantum State Interferography for Qubits: The Operator Description

An unknown quantum state $|\psi\rangle$ in two-dimensions corresponding to a stream of identical particles when evolves through the Quantum State Interferography (QSI) setup i.e., through a MZI with $\hat{U}$ in one arm and $\hat{R}$ in the other arm (where, $\hat{U} = \hat{\sigma}_x$ and $\hat{R} = \hat{\Pi}_H$), we get the final state at the end of the setup as $|\Psi_3\rangle$ shown in Eqn. 2.45. The state $|\Psi_3\rangle$ is a joint state of the particles in path and polarization d.o.f. and is represented as a superposition of the two states in the output ports C and D of the interferometer respectively, as shown in Fig. 2.1. Let, $\hat{\mathcal{E}}$ be the effective operator that evolves the particles in the polarization state $|\psi\rangle$ incident on the QSI setup (i.e., on BS_1) towards the output port D. Therefore, the evolution of the polarization qubit through QSI setup can be expressed as,

$$\hat{\mathcal{E}}\,|\psi\rangle = \frac{i}{2}\left(\hat{U} + e^{i\epsilon}\hat{R}\right)|\psi\rangle \tag{2.91}$$

Here, the factor $\dfrac{1}{2}$ arises due to the fact that the particles propagate through two $50:50$ beam splitters, BS_1 and BS_2, towards the ports C and D, whereas we are only selecting one of the output ports (D) of BS_2 for the detection. $\hat{U}$ and $\hat{R}$ are the polar decomposed components of $\hat{\sigma}_-$ as discussed in SubSec. 2.2.2 and ϵ is the relative phase between the two paths (path-A and path-B) of MZI which can be controlled using the phase shifter (PS) in one of the paths in collinear configuration or directly through the non-collinear configuration of the interferometer. Since, a path length difference of the order of a fraction of the wavelength ($\approx$ few hundreds of nm) affects the relative phase, the factors like the surface flatness, scratch-digs, different refractive indices of the optical components present in the two paths of the setup would affect the optical path lengths and thus, will change intensity distribution across the detector plane.

The factor $i = e^{i(\pi/2)}$ only adds a global phase to the final state at the detector port D. The global phase can be ignored since it has no effect on the measurement outcome as we are only interested in recording the intensity distribution as a function of relative phase ϵ. Thus, the overall evolution operator through the QSI setup can be expressed as,

$$\hat{\mathcal{E}} = \frac{1}{2}\left(\hat{U} + e^{i\epsilon}\hat{R}\right) \tag{2.92}$$

$$\hat{\mathcal{E}} = \frac{1}{2}\left[\begin{pmatrix} 0 & 1 \\ 1 & 0 \end{pmatrix} + e^{i\epsilon}\begin{pmatrix} 1 & 0 \\ 0 & 0 \end{pmatrix}\right] = \frac{1}{2}\begin{pmatrix} e^{i\epsilon} & 1 \\ 1 & 0 \end{pmatrix} \tag{2.93}$$

The description of $\hat{\mathcal{E}}$ involves the operator $\hat{R}$, which is the polar decomposed Hermitian component of $\hat{\sigma}_-$ and is obtained as $\hat{R} = \sqrt{\hat{\sigma}_-^{\dagger}\hat{\sigma}_-} = \hat{\Pi}_H = |H\rangle\langle H|$. Therefore, $\hat{R}$ being the projector to polarization $|H\rangle$, introduces losses in the setup, since its action to the polarization state orthogonal to $|H\rangle$ gives $\hat{\Pi}_H |V\rangle = 0$. This makes the overall evolution operator $\hat{\mathcal{E}}$ non-Unitary, i.e., $\hat{\mathcal{E}}^\dagger \hat{\mathcal{E}} \neq \hat{\mathbb{1}} \neq \hat{\mathcal{E}}\hat{\mathcal{E}}^\dagger$. Using the matrix form of $\hat{\mathcal{E}}$ given in Eqn. **2.93** we get,

$$\hat{\mathcal{E}}^\dagger \hat{\mathcal{E}} = \frac{1}{4}\begin{pmatrix} 2 & e^{-i\epsilon} \\ e^{i\epsilon} & 1 \end{pmatrix} \quad \text{and} \quad \hat{\mathcal{E}}\hat{\mathcal{E}}^\dagger = \frac{1}{4}\begin{pmatrix} 2 & e^{i\epsilon} \\ e^{-i\epsilon} & 1 \end{pmatrix} \tag{2.94}$$

Since, the evolution operator $\hat{\mathcal{E}}$ associated with the quantum state interferography (QSI) setup is obtained to be non-Unitary, any state that undergoes evolution through this setup, does not preserve its norm, or in other words, the *probability is not conserved*.

Using the operator $\hat{\mathcal{E}}$, the intensity at the detector in the port D of the experimental setup when an unknown qubit $|\psi\rangle$ is incident on it can be directly obtained as,

$$I_d(\epsilon) = \left\| \hat{\mathcal{E}} \, |\psi\rangle \right\|^2 = \left| \langle \psi | \hat{\mathcal{E}}^\dagger \hat{\mathcal{E}} | \psi \rangle \right|^2 \tag{2.95}$$

$$\text{where,} \quad \hat{\mathcal{E}} \, |\psi\rangle = |\psi\rangle_d = \frac{1}{2}\begin{pmatrix} e^{i\epsilon}\cos\left(\frac{\theta}{2}\right) + e^{i\phi}\sin\left(\frac{\theta}{2}\right) \\ \cos\left(\frac{\theta}{2}\right) \end{pmatrix} \tag{2.96}$$

where $|\psi\rangle_d$ is the polarization state at the output port D, obtained when the input state $|\psi\rangle$ evolves to the output D through the operator $\hat{\mathcal{E}}$. Thus, using the operator description of QSI, the intensity profile at the detector plane can be obtained as,

$$I_d(\epsilon) = \frac{1}{8}\left[3 + \cos(\theta) + 2\sin(\theta)\cos(\epsilon - \phi)\right] \tag{2.97}$$

Next, state parameters (θ, ϕ) associated with a pure qubit can be computed by determining the phase averaged intensity $(\bar{I})$ and phase shift (Φ) of the interference pattern $I_d(\epsilon)$, in the same manner discussed in Sec. 2.2. Once (θ, ϕ) are uniquely determined from the interferogram, we know the polarization state $|\psi\rangle$ incident on the setup.

2.5 Quantum State Interferography for Mixed Qubits

Quantum State Tomography (QST) is the traditional method to characterize an arbitrary state in two-dimensional Hilbert space. In general, the process of Tomography for single qubit reconstruction requires three projective measurements. Two measurement suffices with the prior knowledge about the system state being pure. However, in the Sec. 2.2 we have seen how a pure state of a two dimensional quantum system can be characterized using the interferometric state determination scheme *Quantum State Interferography* (QSI). With QSI, the direction of the unit state vector $|\psi(\theta, \phi)\rangle$ in the Bloch sphere ($\mathbb{S}^{(2)}$) can be uniquely inferred from the phase shift and the average intensity of a single interference pattern. For any generic state $\hat{\rho}$ (not necessarily pure) in the two dimensions, another parameter needs to be added in the description of the state in order to comment on the degree of mixedness (given by the purity $\mathrm{Tr}(\hat{\rho}^2)$).

As shown in Sec. 2.1, the mixedness in the system can be introduced by the parameter μ that represents the decay of the off-diagonal terms of a pure state density matrix in the presence of decoherence, where μ would be related to the length of the Bloch vector ($|\vec{r}|$) corresponding to a state described in a Bloch sphere. Thus, the complete description of a mixed state for a two-dimensional quantum system (say, a spin $\frac{1}{2}$ particle) requires the knowledge of three parameters θ, ϕ and μ (when given in decoherence representation). Here, we aim to infer any arbitrary qubit $\hat{\rho}(\mu, \theta, \phi)$ from the quantities obtained from an interference pattern, without the need to change any internal settings during the process of measurement – in other words, we aim to establish a 'single shot' measurement of any arbitrary state in two dimensions.

The density matrix $\hat{\rho}$ associated with a mixed qubit can be represented in terms of the parameters (μ, θ, ϕ) as,

$$\hat{\rho} = \begin{pmatrix} \cos^2\left(\frac{\theta}{2}\right) & \frac{1}{2}\mu e^{-i\phi}\sin(\theta) \\ \frac{1}{2}\mu e^{i\phi}\sin(\theta) & \sin^2\left(\frac{\theta}{2}\right) \end{pmatrix} \tag{2.98}$$

where the coordinates $\theta \in [0, \pi]$ and $\phi \in [-\pi, \pi)$ describe the direction of the vector in the Bloch sphere representation and $\mu \in [0, 1]$ is related to the length of the Bloch vector and governs the purity of the density matrix $\hat{\rho}$. The purity of the state $\hat{\rho}$ is given as,

$$\mathrm{Tr}(\hat{\rho}^2) = 1 - \frac{1 - \mu^2}{2} \sin^2(\theta) = \frac{1}{4} \left[3 + \mu^2 + \left(1 - \mu^2\right) \cos(2\theta)\right] \tag{2.99}$$

Therefore, $\mu = 1$ gives $\mathrm{Tr}(\hat{\rho}^2) = 1$, i.e., represents the pure states.

Any unknown mixed qubit or more precisely saying, any unknown qubit, whether mixed or pure, can be reconstructed by knowing the three parameters (θ, ϕ, μ) from an experiment. In this section, we will describe how the interferometric scheme $-$ Quantum State Interferography enables us to infer a mixed qubit from a single interference pattern as opposed to three distinct projective measurements required in standard Quantum State Tomography (QST) technique.

2.5.1 Theory

The expectation values of the two-dimensional spin-ladder operators $\hat{\sigma}_{\pm} = \frac{1}{2}(\hat{\sigma}_x \pm i\hat{\sigma}_y)$ in the state $\hat{\rho}$ given in Eqn. 2.98 are obtained to be,

$$\langle \hat{\sigma}_{\pm} \rangle = \mathrm{Tr}(\hat{\rho}\hat{\sigma}_{\pm}) = \frac{1}{2} \exp(\pm i\phi)\ \mu \sin(\theta) \tag{2.100}$$

So, the argument of the complex expectation value $\langle \hat{\sigma}_{\pm} \rangle$ directly gives the azimuthal coordinate ϕ and the magnitude $|\langle \hat{\sigma}_{\pm} \rangle|$ is a function θ and μ. For a general qubit $\hat{\rho}$ the magnitude and the argument of the expectation values of the non-Hermitian spin ladder operators can be obtained to be,

$$|\langle \hat{\sigma}_{\pm} \rangle| = \frac{1}{2} \mu \sin(\theta) \tag{2.101}$$

$$\arg\left(\langle \hat{\sigma}_{\pm} \rangle\right) = \pm\ \phi \tag{2.102}$$

For a pure qubit, $\mu = 1$ and hence, the polar coordinate θ can be obtained from the magnitude of the expectation value $\langle\hat{\sigma}_{\pm}\rangle$ as $\sin^{-1}(2|\langle\sigma_{\pm}\rangle|)$. However, as we have discussed in Sec. 2.2, this solution to θ is not unique for $\theta \in [0, \pi]$, since $\sin(\pi - \theta) = \sin(\theta)$. Hence, $(\pi - \theta)$ is a solution as well. For the unique determination of θ, the expectation value of another column operator $\hat{\Pi}_0 = |0\rangle\langle 0|$ [16] needs to be computed. For the mixed state $\hat{\rho}(\theta, \phi, \mu)$, we get the expectation value of $\hat{\Pi}_0$ as the following,

$$\left\langle \hat{\Pi}_0 \right\rangle = \mathrm{Tr}\left(\hat{\rho}\hat{\Pi}_0\right) = \cos^2\left(\frac{\theta}{2}\right) \tag{2.103}$$

So, from $\left\langle \hat{\Pi}_0 \right\rangle$ the value of θ can be uniquely determined in $[0, \pi]$ as,

$$\theta = 2\cos^{-1}\left(\sqrt{\left\langle \hat{\Pi}_0 \right\rangle}\right) \tag{2.104}$$

Therefore, once θ is known, μ can be determined as

$$\mu = \frac{2|\langle\hat{\sigma}_{\pm}\rangle|}{\sin(\theta)} \tag{2.105}$$

Hence, all the three state parameters (θ, ϕ, μ) corresponding to an arbitrary qubit $\hat{\rho}$ can be determined from the expectation values of the two operators $-$ projector to $|0\rangle$ i.e., $\hat{\Pi}_0$ and any one of the spin ladder operators $\hat{\sigma}_+$ or $\hat{\sigma}_-$. Here, we will choose $\hat{\sigma}_- = \frac{1}{2}(\hat{\sigma}_x - i\hat{\sigma}_y)$ for further discussion. Therefore, evaluating the expectation values $\left\langle \hat{\Pi}_0 \right\rangle$ and $\langle\hat{\sigma}_-\rangle$, the state parameters (θ, ϕ, μ) can be determined as the following,

$$\theta = 2\cos^{-1}\left(\sqrt{\left\langle \hat{\Pi}_0 \right\rangle}\right), \qquad \phi = -\arg\left(\langle\hat{\sigma}_-\rangle\right), \qquad \mu = \frac{2|\langle\hat{\sigma}_-\rangle|}{\sin(\theta)} \tag{2.106}$$

Once all the state parameters are known, $\hat{\rho}$ can be inferred from the Eqn. 2.98. In the next section, we will show how the expectation values $\left\langle \hat{\Pi}_0 \right\rangle$ and $\langle\hat{\sigma}_-\rangle$ are obtained in an experiment in order to infer an unknown one-qubit mixed state.

[16] which is the projector to the state $|0\rangle$ when the two-dimensional Hilbert space is spanned in the Fock basis, i.e., $\{|0\rangle, |1\rangle\}$.

2.5.2 Experimental Protocol for Inferring an Unknown Mixed Qubit

As shown in SubSec. 2.5.1, an unknown state ($\hat{\rho}$) of a two-dimensional quantum system can be inferred experimentally by determining the state parameters (θ, ϕ, μ) from the measured expectation values of the operators $\hat{\Pi}_0$ and $\hat{\sigma}_-$. Now, expectation value of $\hat{\sigma}_-$ can not be determined from the statistical distribution of the measurement outcomes in an experiment as $\hat{\sigma}_-$ is a non-Hermitian operator and is not in general physically realizable. However, as discussed in SubSec. 2.2.2, $\hat{\sigma}_-$ can be polar decomposed into a Unitary operator $\hat{U}$ and a positive semi-definite Hermitian operator $\hat{R}$ that satisfies $\hat{\sigma}_- = \hat{U}\hat{R}$, where $\hat{R} = \sqrt{\hat{\sigma}_-^\dagger \hat{\sigma}_-} = \hat{\Pi}_0$, giving $\hat{U} = \hat{\sigma}_x$. Then evolving the qubit state $\hat{\rho}$ through the operators $\hat{U}$ and $\hat{R}$ in the individual arms of a two-path interferometer in an interferometric setup, the expectation value of the non-Hermitian operator ($\hat{\sigma}_-$) can be obtained.

$$\hat{\sigma}_- = \hat{U}\hat{R} = \hat{\sigma}_x\hat{\Pi}_0 \tag{2.107}$$

Here, the experimental protocol for determining $\left\langle \hat{\Pi}_0 \right\rangle$ and $\langle \hat{\sigma}_- \rangle$ using the Quantum State Interferography (QSI) technique will be presented with the aim to characterize an unknown qubit in the polarization degree of freedom of light utilizing those values.

A generic mixed state in two-dimensional Hilbert space spanned by the polarization basis $\{|H\rangle, |V\rangle\}$ can be expressed as,

$$\hat{\rho} = \cos^2\left(\frac{\theta}{2}\right)|H\rangle\langle H| + \frac{\mu}{2}e^{-i\phi}\sin(\theta)\,|H\rangle\langle V| + \frac{\mu}{2}e^{i\phi}\sin(\theta)\,|V\rangle\langle H| + \sin^2\left(\frac{\theta}{2}\right)|V\rangle\langle V| \tag{2.108}$$

the matrix form of which is given in Eqn. 2.98, provided the parameters $\theta \in [0, \pi]$, $\phi \in [-\pi, \pi)$ and $\mu = [0, 1]$. These three quantities that uniquely specify the polarization state of light ($\hat{\rho}$) can be determined experimentally from a single interference pattern obtained in a single setting of a two path interferometer setup as shown in Fig. 2.3.

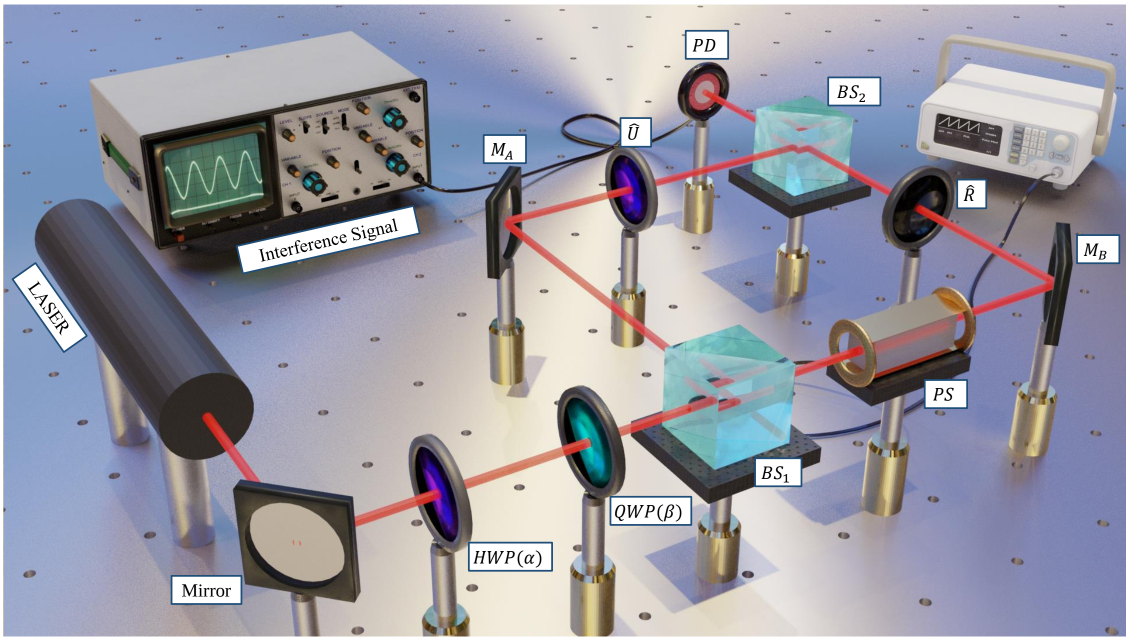

Figure 2.3: Experimentally the polarization state is prepared by using a half-wave plate (HWP) and a quarter-wave plate (QWP) which can be at arbitrary orientations. The setup for the polarization state characterization is formed using a Mach-Zehnder interferometer MZI, with one arm having a HWP, whose fast axis is oriented at $\frac{\pi}{4}$ w.r.to the horizontal, that effectively realizes the $\hat{U} = \hat{\sigma}_x$ operator and the other arm, having a polarizer with the transmission axis oriented along horizontal, or alternatively, considering the transmitting port of a polarizing beam splitter (PBS) to effectively realize the operator $\hat{R} = \hat{\Pi}_H$. The phase shifter (PS) introduces a relative phase ϵ between the two arms of the interferometer and the intensity as a function of ϵ is measured at the photo detector (PD), which results in an interference signal. Experimentally, the phase shifter can be avoided by making the interferometer non-collinear.

The optical setup for polarization state characterization of light using Quantum State Interferography is shown in Fig. 2.3. The QSI setup consists of a Mach Zehnder Interferometer (MZI), formed with the 50 : 50 beam splitters (BS_1, BS_2) and mirrors (M_A, M_B), consisting of the optical components corresponding to operators $\hat{U}$ and $\hat{R}$ in arm-A and arm-B respectively, with a photo detector (PD) or a CCD camera placed at one of the output ports of BS_2. The operator $\hat{U}$ and $\hat{R}$ are the polar decomposed components of the non-Hermitian spin ladder operator $\hat{\sigma}_-$, which when acts on the polarization basis $\{|H\rangle, |V\rangle\}$, transforms $|H\rangle$ to $|V\rangle$ and annihilates $|V\rangle$. Therefore, $\hat{\sigma}_- |H\rangle = |V\rangle$, $\hat{\sigma}_- |V\rangle = 0$. Operators $\hat{U}$ and $\hat{R}$ only affect the polarization d.o.f. of light leaving the path d.o.f. unaffected.

The operators $\hat{U}$ and $\hat{R}$ are given as,

$$\hat{U} = \hat{\sigma}_x = |V\rangle\langle H| + |H\rangle\langle V| \qquad \text{and} \qquad \hat{R} = \hat{\Pi}_H = |H\rangle\langle H| \tag{2.109}$$

Experimentally, the operator $\hat{U}$ can be realized using a half-wave plate (HWP) with its fast axis oriented at an angle $\frac{\pi}{4}$ from the horizontal and the operator $\hat{R}$ can be realized using a linear polarizer with its transmission axis oriented along the horizontal. Alternatively, the operator $\hat{R} = \hat{\Pi}_H$ can be effectively realized considering only the transmission through a polarizing beam splitter (PBS), as discussed in Sec. 2.3. At the detector position, the overall evolution operator $\hat{\mathcal{E}}$ corresponding to the MZI along with the optical components present in the two paths in the QSI setup, can be expressed as

$$\hat{\mathcal{E}} = \frac{1}{2}\left(\hat{U} + e^{i\epsilon}\hat{R}\right) = \frac{1}{2}\left(\hat{\sigma}_x + e^{i\epsilon}\hat{\Pi}_H\right) = \frac{1}{2}\begin{pmatrix} e^{i\epsilon} & 1 \\ 1 & 0 \end{pmatrix} \tag{2.110}$$

Here, ϵ is the relative phase between the two paths of the interferometer that effectively manifests any path length difference between path-A and path-B of the interferometer which includes the misalignment, the effect due to surface quality of the optical components, different refractive indices of the components, etc.

Consider a stream of photons in the unknown polarization state $\hat{\rho}$ is incident on the setup shown in Fig. **2.3**. The intensity distribution as a function of the relative phase at the detector position would be,

$$I_d(\epsilon) = \text{Tr}\left(\hat{\mathcal{E}}\ \hat{\rho}\ \hat{\mathcal{E}}^\dagger\right) \tag{2.111}$$

$$= \frac{1}{4}\,\text{Tr}\left((\hat{U} + e^{i\epsilon}\hat{R})\ \hat{\rho}\ (\hat{U}^\dagger + e^{-i\epsilon}\hat{R}^\dagger)\right)$$

$$= \frac{1}{4}\left[\text{Tr}\left(\hat{U}\hat{\rho}\hat{U}^\dagger\right) + \text{Tr}\left(\hat{R}\hat{\rho}\hat{R}^\dagger\right) + e^{i\epsilon}\,\text{Tr}\left(\hat{R}\hat{\rho}\hat{U}^\dagger\right) + e^{-i\epsilon}\,\text{Tr}\left(\hat{U}\hat{\rho}\hat{R}^\dagger\right)\right]$$

$$= \frac{1}{4}\left[\left\langle\hat{U}^\dagger\hat{U}\right\rangle + \left\langle\hat{R}^\dagger\hat{R}\right\rangle + e^{i\epsilon}\left\langle\hat{U}^\dagger\hat{R}\right\rangle + e^{-i\epsilon}\left\langle\hat{R}^\dagger\hat{U}\right\rangle\right] \tag{2.112}$$

The above expression for the intensity $I_d(\epsilon)$ is obtained using the characterization properties of trace [26], which are (i) $\mathrm{Tr}(A+B) = \mathrm{Tr}(A) + \mathrm{Tr}(B)$, (ii) $\mathrm{Tr}(cA) = c\,\mathrm{Tr}(A)$, (iii) $\mathrm{Tr}(ABC) = \mathrm{Tr}(BCA) = \mathrm{Tr}(CAB)$, where A, B, C are the square matrices and c is a scalar constant. Also, the formula $\mathrm{Tr}\left(\hat{\rho}\hat{O}\right) = \left\langle \hat{O} \right\rangle$, that represents the expectation value of the operator $\hat{O}$ in the state $\hat{\rho}$, has been used in the above.

Since, the operators $\hat{U}$ and $\hat{R}$ are respectively the polar decomposed Unitary and Hermitian components of the non-Hermitian operator $\hat{\sigma}_-$, we get $\hat{U}^\dagger \hat{U} = \hat{\mathbb{1}}$ and $\hat{R}^\dagger = \hat{R}$. Therefore, $\left\langle \hat{U}^\dagger \hat{U} \right\rangle = \langle \hat{\mathbb{1}} \rangle = 1$ and $\left\langle \hat{R}^\dagger \hat{R} \right\rangle = \left\langle \hat{R}^2 \right\rangle$. Also, Eqn. 2.109 shows that $\hat{U} = \hat{\sigma}_x$ and $\hat{R} = \hat{\Pi}_H$, satisfying $\hat{\sigma}_- = \hat{\sigma}_x \hat{\Pi}_H$. Thus, here $\hat{U}^\dagger = \hat{\sigma}_x^\dagger = \hat{\sigma}_x$ and $\hat{R}^2 = \hat{\Pi}_H^2 = |H\rangle \langle H|H\rangle \langle H| = |H\rangle \langle H| = \hat{\Pi}_H = \hat{R}$. Now, consider a complex quantity z with magnitude $|z|$ and argument χ, as the following

$$z = |z|e^{i\chi} = \left\langle \hat{U}^\dagger \hat{R} \right\rangle = \left\langle \hat{\sigma}_x^\dagger\, \hat{\Pi}_H \right\rangle = \left\langle \hat{\sigma}_x\, \hat{\Pi}_H \right\rangle = \langle \hat{\sigma}_- \rangle \tag{2.113}$$

$$\text{giving,} \quad z^* = |z|e^{-i\chi} = \left\langle \hat{U}^\dagger \hat{R} \right\rangle^* = \left\langle \hat{R}^\dagger \hat{U} \right\rangle = \langle \hat{\sigma}_- \rangle^* \tag{2.114}$$

$$\text{where,} \quad |z| = |\langle \hat{\sigma}_- \rangle| \quad \text{and} \quad \chi = \arg\left(\langle \hat{\sigma}_- \rangle\right) \tag{2.115}$$

Hence, the expression for intensity at the detector position given in Eqn. 2.112 can be written as,

$$I_d(\epsilon) = \frac{1}{4}\left[\langle \hat{\mathbb{1}} \rangle + \left\langle \hat{R}^2 \right\rangle + \langle \hat{\sigma}_- \rangle e^{i\epsilon} + \langle \hat{\sigma}_- \rangle^* e^{-i\epsilon}\right] \tag{2.116}$$

$$I_d(\epsilon) = \frac{1}{4}\left[1 + \left\langle \hat{R} \right\rangle + |z|e^{i\chi}e^{i\epsilon} + |z|e^{-i\chi}e^{-i\epsilon}\right]$$

$$I_d(\epsilon) = \frac{1}{4}\left[1 + \left\langle \hat{R} \right\rangle + 2|z|\cos(\epsilon + \chi)\right]$$

$$I_d(\epsilon) = \frac{1}{4}\left[1 + \left\langle \hat{\Pi}_H \right\rangle + 2|\langle \hat{\sigma}_- \rangle| \cos\left(\epsilon + \arg\left(\langle \hat{\sigma}_- \rangle\right)\right)\right] \tag{2.117}$$

Therefore, an unknown quantum state $\hat{\rho}$ incident on the QSI setup, when evolves through the effective evolution operator $\hat{\mathcal{E}}$, we get the intensity distribution $I_d(\epsilon)$ at one of the output ports of the setup. Hence, using the QSI technique from a single interference pattern (intensity distribution I_d as a function of relative phase ϵ) we can experimentally determine the expectation values of the desired operators ($\hat{\Pi}_H$ and $\hat{\sigma}_-$) in the state $\hat{\rho}$. The state parameters (θ, ϕ, μ) corresponding to the unknown state $\hat{\rho}$ can then be obtained using the expressions presented in Eqn. 2.106.

Now, the expression for the intensity at the detector, when we put the values of $\left\langle \hat{\Pi}_H \right\rangle$, $|\langle\hat{\sigma}_-\rangle|$, $\arg\left(\langle\hat{\sigma}_-\rangle\right)$ computed for the state $\hat{\rho}$ as shown in Eqn. 2.103, Eqn. 2.101 and Eqn. 2.102, can be seen in the following,

$$I_d(\epsilon) = \frac{1}{4}\left[1 + \cos^2\left(\frac{\theta}{2}\right) + 2\,\frac{\mu}{2}\,\sin(\theta)\cos\left(\epsilon - \phi\right)\right] \tag{2.118}$$

$$I_d(\epsilon) = \frac{1}{8}\left[3 + \cos(\theta) + 2\mu\sin(\theta)\cos(\epsilon - \phi)\right] \tag{2.119}$$

This expression for intensity, obtained when a mixed state $\hat{\rho}$ evolves through the QSI setup, is similar to the expression of intensity for pure state given in Eqn. 2.63, except that the factor μ that controls the purity of the state appears in the interference term. Note that, the operator $\hat{\mathcal{E}}$ given in Eqn. 2.92 is not Unitary. Hence, while computing $I_d = \mathrm{Tr}\left(\hat{\mathcal{E}}\ \hat{\rho}\ \hat{\mathcal{E}}^\dagger\right)$, the evolution $\hat{\mathcal{E}}\ \hat{\rho}\ \hat{\mathcal{E}}^\dagger$ does not preserve the properties of the density matrices. This interference pattern obtained from the experiment is post-processed to infer the state parameters for the characterization of the unknown polarization qubit $\hat{\rho}$.

2.5.3 Inferring the State Parameters (μ, θ, ϕ) from the Interferogram

Here we will show how the state parameters (μ, θ, ϕ) associated with the unknown polarization qubit $\hat{\rho}$ can be obtained from the phase shift (Φ), average intensity $(\bar{I})$ and visibility (V) of the interference pattern $I_d(\epsilon)$.

❑ **Phase Shift:** The phase shift (Φ) of the interference pattern is obtained at the value of phase ϵ that maximizes the experimentally obtained intensity $I_d(\epsilon)$. Therefore at $\epsilon = \Phi$, the conditions $\left.\dfrac{\partial I_d(\epsilon)}{\partial\epsilon}\right|_{\epsilon=\Phi} = 0$ and $\left.\dfrac{\partial^2 I_d(\epsilon)}{\partial\epsilon^2}\right|_{\epsilon=\Phi} < 0$ satisfy simultaneously. From the interference pattern $I_d(\epsilon)$ obtained when a mixed state $\hat{\rho}(\mu,\theta,\phi)$ is evolved through the setup, we get

$$\left.\frac{\partial I_d(\epsilon)}{\partial \epsilon}\right|_{\epsilon=\Phi} = -\frac{1}{4}\mu\sin(\theta)\sin(\Phi-\phi) = 0 \tag{2.120}$$

$$\left.\frac{\partial^2 I_d(\epsilon)}{\partial \epsilon^2}\right|_{\epsilon=\Phi} = -\frac{1}{4}\mu\sin(\theta)\cos(\Phi-\phi) \tag{2.121}$$

Expression in Eqn. 2.120 gives two solutions as $\Phi=\phi$ or $\Phi=\pi+\phi$. In the expression in Eqn. 2.121 we have $0\leq\mu\leq 1$ and $\sin(\theta)>0$ since $0\leq\theta\leq\pi$. Thus, satisfying the criteria $\left.\frac{\partial^2 I_d(\epsilon)}{\partial \epsilon^2}\right|_{\epsilon=\Phi} < 0$ implies $\Phi=\phi$. Thus, the phase shift (Φ) of the interference pattern directly gives the state parameter ϕ.

❑ **Average Intensity:** The phase averaged intensity of the interference pattern is obtained by integrating $I_d(\epsilon)$ over all possible phases ϵ, i.e.,

$$\bar{I} = \int_\epsilon I_d(\epsilon)d\epsilon = \frac{1}{8}(3+\cos(\theta)) \tag{2.122}$$

Thus, the average intensity of the interference pattern for mixed state is the same as the average intensity obtained for a pure state shown in Eqn. 2.69. Average intensity $\bar{I}$ is a unique function of state parameter θ. Hence, $\theta\in[0,\pi]$ can be uniquely determined from $\bar{I}$, which is experimentally always normalized with the incident intensity.

❑ **Visibility:** Next, the visibility (V) of the interference pattern is obtained by varying the optical path length difference between the two paths of the interferometer and finding the maximum (I_{max}) and minimum (I_{min}) values of the intensity distribution $I_d(\epsilon)$ at the detector position and the putting them in the following expression,

$$V = \frac{I_{max}-I_{min}}{I_{max}+I_{min}} \tag{2.123}$$

For a mixed state $\hat{\rho}$ incident on the QSI setup, we get

$$I_{max} = \frac{1}{8}\left[3 + \cos(\theta) + 2\mu\sin(\theta)\right] \tag{2.124}$$

$$I_{min} = \frac{1}{8}\left[3 + \cos(\theta) - 2\mu\sin(\theta)\right] \tag{2.125}$$

$$\text{giving,} \qquad V = \frac{2\mu\sin(\theta)}{3 + \cos(\theta)} \tag{2.126}$$

So, visibility V for the mixed state is a function of two state parameters θ and μ. Once θ is uniquely known from $\bar{I}$, the parameter μ can be computed from the experimentally obtained value of visibility (V) using the known value of θ.

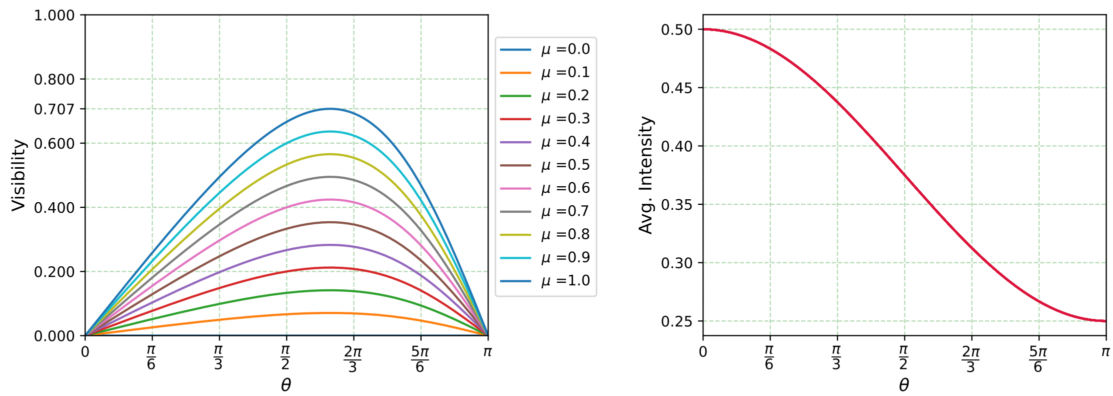

(a) Visibility (V) as a function of μ and θ (b) Avg. intensity $(\bar{I})$ as a function of θ

Figure 2.4: Visibility (V) and Average intensity $(\bar{I})$ obtained from an interferogram formed when an arbitrary qubit evolves through the QSI setup. Visibility for different μ values, where $\mu \in [0, 1]$ is found to be a bi-valued function of θ. However, the average intensity is found to be a unique function of θ and is independent of μ.

Hence, we can conclude that by employing the QSI technique, all the three state parameters θ, ϕ and μ specifying an unknown polarization qubit $\hat{\rho}(\mu, \theta, \phi)$ given in Eqn. 2.98 can be reconstructed from the experimentally determined interferometric quantities $(\bar{I}, \Phi, V)$, as given in the following,

$$\theta = \cos^{-1}(8\bar{I} - 3), \qquad \phi = \Phi, \qquad \mu = \frac{3 + \cos(\theta)}{2\sin(\theta)} V \tag{2.127}$$

In summary, this section presents how a one qubit mixed state $\hat{\rho}(\mu, \theta, \phi)$ in the polarization degree of freedom of light can be reconstructed from a single interference pattern formed at the end of a MZI with the operators $\hat{\sigma}_x$ and $\hat{\Pi}_H$ in the respective arms, as shown in Fig. 2.3. The parameters θ and ϕ can be directly inferred from the phase averaged intensity $\bar{I}$ and the phase shift Φ obtained from the interferogram. The expressions for the quantities $\bar{I}(\theta)$ and $\Phi(\phi)$ remain the same irrespective of the incident state being pure or mixed. The parameter μ, controlling the purity of the two-dimensional state $\hat{\rho}$, can be computed from the visibility V of the interference pattern, from the already known value of θ. Thus, knowing the quantities $\bar{I}$, Φ and V experimentally from a single interference pattern, any one-qubit mixed state can be characterized.

2.6 Inferring Expectation Value of the non-Hermitian Operator $\hat{\sigma}_-$ from Interferometric Information

In quantum mechanics, the observables are often considered to be Hermitian for which the eigen values are real and the associated non-degenerate eigenstates are orthogonal to each other that forms a complete set [13]. Now, according to the measurement postulate in quantum theory, the act of measuring an observable which is a real dynamical variable of the system, would always result in one of the eigenvalues of the operator associated with the observable. The eigenvalues of the observables are considered to be real numbers as the measuring apparatus, from which the measurement outcomes are inferred, can only produce real numbers [10]. The eigen values of the non-Hermitian operators are in general complex and therefore, can not be obtained directly from the measurement outcomes. However, Eqn. 2.30 shows that the complex expectation value of a non-Hermitian operator $\hat{A}$ in the state $|\psi\rangle$ can be inferred from the complex weak value of a Hermitian operator $\hat{R}$, in the pre-selected state $|\psi\rangle$ and post-selected state $|\phi\rangle = \hat{U}^\dagger |\psi\rangle$ [9]. Here, $\hat{R} = \sqrt{\hat{A}^\dagger \hat{A}}$ is the polar decomposed positive semi-definite Hermitian component of $\hat{A}$, with the associated Unitary component $\hat{U}$ giving $\hat{A} = \hat{U}\hat{R}$ [11], discussed in SubSec, 2.2.2. It has been shown that the weak value $\left\langle \hat{R} \right\rangle^{(w)}$ of the Hermitian operator can be obtained directly even without performing a proper weak measurement i.e., without weak coupling and post-selection, using an interferometric technique [14]. Here, we will show how the setup used for determining an unknown quantum state in the Quantum State Interferography (QSI) technique, can be employed to find the expectation value of the non-Hermitian spin ladder operator $\hat{\sigma}_-$ [17]. Note that, the QSI scheme for identifying the state parameters (μ, θ, ϕ) of an unknown qubit relies on calculating the complex expectation value of $\hat{\sigma}_-$ operator described for two-dimensions.

In SubSec. 2.5.2, we have presented that $\langle \hat{\sigma}_- \rangle$ can be obtained by post-processing the interferogram obtained from the setup shown in Fig. 2.3. The intensity distribution as a function of relative phase ϵ, expressed in terms of $\langle \hat{\sigma}_- \rangle$ and $\left\langle \hat{\Pi}_H \right\rangle$ is shown in Eqn. 2.117,

$$I_d(\epsilon) = \frac{1}{4}\left[1 + \left\langle \hat{\Pi}_H \right\rangle + 2|\langle \hat{\sigma}_- \rangle| \cos\left(\epsilon + \arg\left(\langle \hat{\sigma}_- \rangle\right)\right)\right]$$

From the above expression, we can compute the phase shift (Φ) and the visibility of the interference pattern as,

$$\Phi = -\arg(\langle \hat{\sigma}_- \rangle) \tag{2.128}$$

$$V = \frac{2|\langle \hat{\sigma}_- \rangle|}{1 + \left\langle \hat{\Pi}_H \right\rangle} \tag{2.129}$$

So, the argument of the complex expectation value of $\hat{\sigma}_-$ can be obtained from the phase shift (Φ) of the interference pattern. Phase shift is experimentally determined by finding that value of relative phase ϵ which corresponds to the maximum intensity in the detector, i.e., $I_d(\epsilon = \Phi) = I_d^{(max)}$. The magnitude of the expectation value of $\hat{\sigma}_-$ can be determined from the visibility of the interference pattern that is computed using Eqn. 2.123, provided $\left\langle \hat{\Pi}_H \right\rangle$ is known. Now, experimentally finding the average intensity $\bar{I}$ of the interference pattern, the expectation value of the projector $\hat{\Pi}_H = |H\rangle\langle H|$ can be computed as,

[17] Though $\hat{\sigma}_-$ has real eigen values, it does not qualify as an observable since it fails to provide a complete set of eigen vectors.

$$\bar{I} = \frac{1}{4}\left(1 + \left\langle \hat{\Pi}_H \right\rangle\right) \quad \Longrightarrow \quad \left\langle \hat{\Pi}_H \right\rangle = 4\bar{I} - 1 \tag{2.130}$$

Hence, we get the complex expectation value of the non-Hermitian spin ladder operator $\hat{\sigma}_- = \frac{1}{2}(\hat{\sigma}_x - i\hat{\sigma}_y)$ in two dimensions as,

$$\langle \hat{\sigma}_- \rangle = |\langle \hat{\sigma}_- \rangle| \exp\left(i \arg\left(\langle \hat{\sigma}_- \rangle\right)\right) \tag{2.131}$$

where,

$$\arg\left(\langle \hat{\sigma}_- \rangle\right) = -\Phi \tag{2.132}$$

$$|\langle \hat{\sigma}_- \rangle| = \frac{1}{2}\left(1 + \left\langle \hat{\Pi}_H \right\rangle\right) V = \frac{1}{2}\left(1 + 4\bar{I} - 1\right) V = 2\bar{I}V \tag{2.133}$$

giving,

$$\langle \hat{\sigma}_- \rangle = 2\bar{I}V \; e^{-i\Phi} \tag{2.134}$$

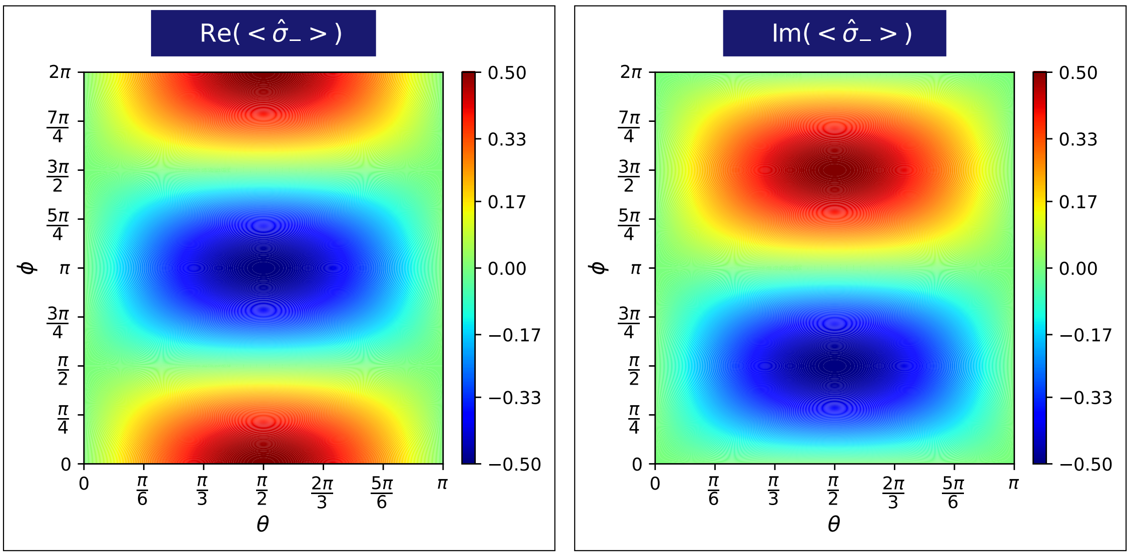

Figure 2.5: Real and Imaginary parts of the complex expectation value of non-Hermitian operator $\hat{\sigma}_-$ in different states $|\psi(\theta, \phi)\rangle$, obtained from the visibility (V), average intensity $(\bar{I})$ and phase shift (Φ) of an interferogram generated using the QSI setup.

Thus, the setup designed for Quantum State Interferography (QSI) technique can be employed to infer the expectation values of 2×2 non-Hermitian operators $\hat{A}$ from a single interference pattern generated in a Mach-Zehnder Interferometer (MZI) with the operators $\hat{U}$ and $\hat{R}$ in the respective arms, where $\hat{R} = \sqrt{\hat{A}^\dagger \hat{A}}$, satisfying $\hat{A} = \hat{U}\hat{R}$. The interferometric quantities obtained from the interference pattern generated at the end of the interferometric setup would vary depending on the parameters of the state incident on the setup, processing which the expectation value $\left\langle \hat{A} \right\rangle$ could be determined.

2.7 Quantum State Interferography for Qubits: The Unitary Description

In standard quantum mechanics, the dynamics of a quantum system is described according to the Schrödinger Wave equation, in which the state associated with the quantum system undergoes a Unitary evolution under a given Hamiltonian. All the evolution operators, in general, manifest Unitary transformations of the system state until a measurement is performed, which is considered to be the non-unitary state reduction [27]. Therefore, in quantum mechanics, we deal with two kinds of evolutions $-$ reversible norm-preserving *Unitary evolution* and irreversible non-norm preserving *non-Unitary evolution*. The operator $\hat{\mathcal{E}} = \frac{1}{2}\left(\hat{U} + e^{i\epsilon}\hat{R}\right)$ as described in Sec. 2.4, which evolves an incident unknown qubit ($\hat{\rho}$ or $|\psi\rangle$) through the Quantum State Interferography (QSI) setup to the output where the interference pattern is recorded, appears to be non-Unitary. As shown in Eqn. 2.94, $\hat{\mathcal{E}}\hat{\mathcal{E}}^\dagger \neq \hat{\mathbb{1}}$ and $\hat{\mathcal{E}}^\dagger\hat{\mathcal{E}} \neq \hat{\mathbb{1}}$. An evolution operator being non-Unitary is considered to be impractical as it fails to conserve the probability, unlike a Unitary operator. In order to ensure that the quantum state is physical after evolving through the QSI setup, the overall evolution operator needs to be Unitary.

The apparent non-unitarity of the evolution operator $\mathcal{E}$ for the setup shown in Fig. 2.1 and Fig. 2.3 arises due to the losses in the setup which corresponds to the light that does not make its way to the detector. In the Quantum State Interferography (QSI) setup for inferring an unknown polarization qubit, one of the paths in the two path interferometer includes a Polarizing Beam Splitter (PBS) or alternatively, a linear polarizer that effectively realizes the operator $\hat{R} = \hat{\Pi}_H$ i.e., the projector to the polarization state $|H\rangle$, which introduces loss in the setup and makes the operator non-Unitary.

$$\hat{\Pi}_H^\dagger \hat{\Pi}_H = \hat{\Pi}_H \hat{\Pi}_H^\dagger = \hat{\Pi}_H \neq \hat{\mathbb{1}} \tag{2.135}$$

In the polarization subspace, the Jones representation for a linear polarizer with transmission axis oriented along the horizontal (Eqn. 2.86) or the matrix representation for a Polarizing Beam Splitter (PBS) considering only its transmitting port (Eqn. 2.88) becomes a non-Unitary matrix. The two are almost identical in their usage when we are only interested in the transmission, as both of them transmit only the horizontal component of polarization of the incident beam; with the difference being that the linear polarizer (as $\hat{\Pi}_H$) absorbs the light with the polarization component orthogonal to $|H\rangle$, i.e., with the polarization component $|V\rangle$ and the PBS reflects the light with the polarization component $|V\rangle$ to a path that does not reach the detector. Hence, either of them introduces a loss in the QSI setup owing to a part of the beam either being absorbed or being in a spatial mode that is ignored. This makes the overall evolution operator $\hat{\mathcal{E}}$, which describes the Mach-Zehnder interferometer along with the optical components realizing the operators $\hat{R}$ and $\hat{U}$ shown in Fig. 2.3, non-trace preserving.

The schematic of the Quantum State Interferography setup for inferring an unknown polarization state of a two-dimensional quantum system, is shown in Fig 2.6. The setup consists of a Mach-Zehnder Interferometer (MZI) formed with two beam splitters BS_1, BS_2 and two mirrors M_A, M_B having operators $\hat{U} = \hat{\sigma}_x$ and $\hat{R} = \hat{\Pi}_H$ in the respective arms of the interferometer. The beam splitter BS_1 has two input ports a and b and two output ports c and d respectively. The beam in port c corresponds to path-A of the interferometer and is redirected by the mirror M_A towards BS_2. Similarly, the beam in port d corresponds to path-B of the interferometer and is redirected towards BS_2 by the mirror M_B. Here, for the Unitary description of the evolution of the beam through the QSI setup, the mirrors M_A and M_B are considered to be lossless with reflectivity for both the polarization components being one, i.e., $R_p = R_s = 1$. Further, all other optical components are considered to be ideal as well.

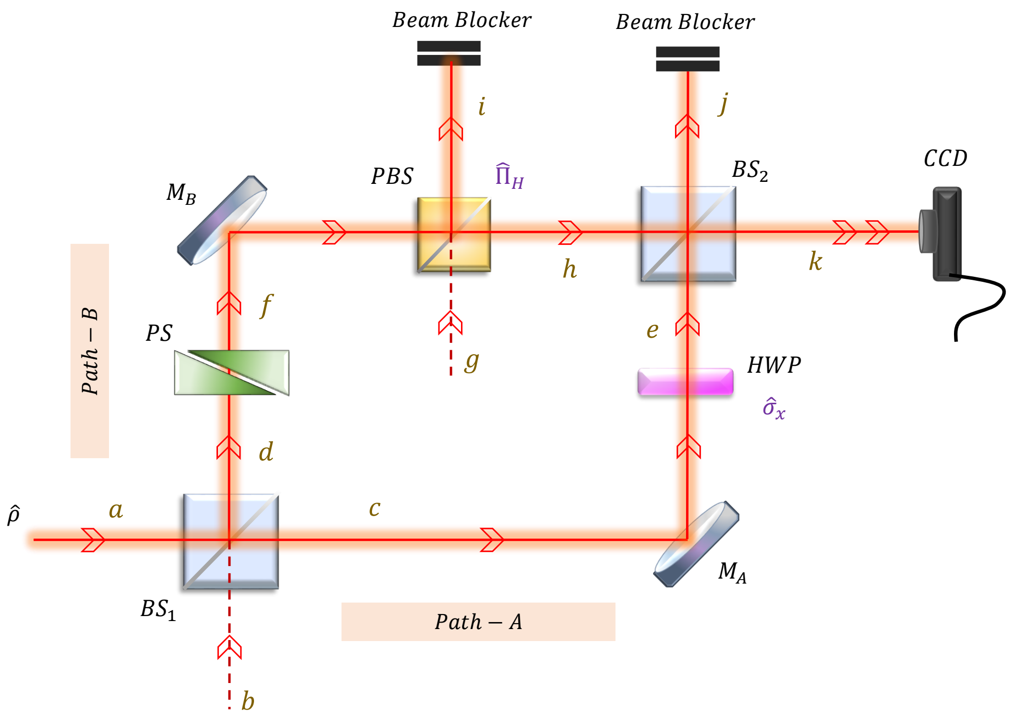

Figure 2.6: Mach Zehnder Interferometer set-up with the optical components realizing the operators $\hat{U}$ and $\hat{R}$ for Polarization State Interferography.

The operator $\hat{U} = \hat{\sigma}_x$ can be realized using a half-wave plate (HWP) with its fast axis oriented at $\frac{\pi}{4}$ w.r.to horizontal. $\hat{\sigma}_x$ is Unitary, thus it is trace preserving. The operator $\hat{R} = \hat{\Pi}_H$, which is the projector to $|H\rangle$, can be realized using a linear polarizer with the transmission axis oriented along Horizontal. This configuration of the polarizer allows only the horizontal component of polarization of the beam incident on it to pass through and absorbs the vertical component of polarization of the beam. Thus, there are losses associated with the polarizer operation when the incident beam has the polarization something other than horizontal ($|H\rangle$). Equivalently, a polarizing beam splitter (PBS) can be used to realize $\hat{\Pi}_H$, where we only consider the beam in the transmitting port of it. A PBS transmits the Horizontal polarization component and reflects the Vertical polarization component of the beam incident on it.

When the operator $\hat{\Pi}_H$ in the QSI setup is physically implemented using a PBS, which is placed in path-B of the interferometer, the two input ports can be labeled as f and g and the two output ports as h and i as shown in the figure Fig 2.6. The ports f and h

lie on path-B of the interferometer. Thus, the light emerging in the output port i is going away from the interferometer and is not detected by the detector placed at the end of the interferometer, introducing loss in the setup. The part of the beam that is getting lost and is not able to reach the detector, either due to absorption in the polarizer or due to the reflection away from the setup, is one of the reasons for the apparent non-Unitarity of the overall evolution operator $\hat{\mathcal{E}}$. The operator $\hat{\sigma}_x$ placed in path-A, can be considered to have c and e as the input and output, respectively.

Next, the beam splitter BS_2 has two input ports e and h and two output ports j and k respectively. The beam in port k is detected using a detector placed in this port and the beam in port j remains undetected which again is associated with the loss in the setup and is responsible for the non-unitary nature of the evolution operator $\hat{\mathcal{E}}$. Therefore, there are three input paths (a, b, g) and three output paths (i, j, k) to the entire QSI setup or we can say, to the Mach-Zehnder interferometer. Only the beam in one, (say k) out of the three output paths is detected while the beams in the other paths (i.e., in ports i, j) are ignored. To have a Unitary description of the evolution of a qubit through the QSI setup, the states in the path d.o.f. associated with all the ports in the setup need to be included and therefore, the description of the operators in a higher dimensional Hilbert space, i.e., a joint Hilbert space of path and polarization degrees of freedom, would be required.

❑ Input State Density Matrix in the Joint Hilbert Space:

Consider, $\{|a\rangle, |b\rangle, |g\rangle\}$ are the spatial modes corresponding to the input paths a, b and g respectively, as can be seen from Fig 2.6. The stream of particles or the beam with the unknown polarization state $\hat{\rho}_p$ [18] is made incident only in port a, where $\hat{\rho}_p$ is any arbitrary density matrix in the two-dimensional polarization subspace spanned by the basis $\{|H\rangle, |V\rangle\}$. In terms of the parameters (μ, θ, ϕ) the state is represented as the following,

$$\hat{\rho}_p = \begin{pmatrix} \cos^2\left(\dfrac{\theta}{2}\right) & \dfrac{1}{2}\mu e^{-i\phi}\sin(\theta) \\ \dfrac{1}{2}\mu e^{i\phi}\sin(\theta) & \sin^2\left(\dfrac{\theta}{2}\right) \end{pmatrix}_{\{|H\rangle,|V\rangle\}} \tag{2.136}$$

[18] The subscript 'p' in $\hat{\rho}_p$ represents that the corresponding density matrix is in polarization d.o.f..

where $\mu \in [0,1]$, $\theta \in [0,\pi]$ and $\phi \in [-\pi,\pi)$. These state parameters need to be determined in order to infer the unknown state. The combined Hilbert space of path and polarization degrees of freedom is $3 \times 2 = 6$ dimensional, i.e., $\mathcal{H}^{(6)} = \mathcal{H}_s^{(3)} \otimes \mathcal{H}_p^{(2)}$, where the subscripts '$s$' and '$p$' respectively represent the spatial (path) degree of freedom and polarization (or spin) degree of freedom of the system.

Since the beam is incident on input port a only, the density matrix associated with the incident beam, represented in the path d.o.f. in the basis $\{|a\rangle, |b\rangle, |g\rangle\}$ is given as follows:

$$\hat{\rho}_s = \begin{pmatrix} 1 & 0 & 0 \\ 0 & 0 & 0 \\ 0 & 0 & 0 \end{pmatrix}_{\{|a\rangle,|b\rangle,|g\rangle\}} \tag{2.137}$$

The subscript 's' in $\hat{\rho}_s$ represents that the corresponding density matrix $\hat{\rho}$ is defined in the spatial (path) d.o.f.. The combined state of the incident beam may then be represented as an outer product of the path (spatial) and polarization (spin) density matrices, i.e., $\hat{\rho}_s \otimes \hat{\rho}_p$.

$$\hat{\rho}_i = \hat{\rho}_s \otimes \hat{\rho}_p = \begin{pmatrix} 1 & 0 & 0 \\ 0 & 0 & 0 \\ 0 & 0 & 0 \end{pmatrix} \otimes \begin{pmatrix} \cos^2\left(\frac{\theta}{2}\right) & \frac{1}{2}\mu e^{-i\phi}\sin(\theta) \\ \frac{1}{2}\mu e^{i\phi}\sin(\theta) & \sin^2\left(\frac{\theta}{2}\right) \end{pmatrix} \tag{2.138}$$

$$\hat{\rho}_i = \begin{pmatrix} \cos^2\left(\frac{\theta}{2}\right) & \frac{1}{2}\mu e^{-i\phi}\sin(\theta) & 0 & 0 & 0 & 0 \\ \frac{1}{2}\mu e^{i\phi}\sin(\theta) & \sin^2\left(\frac{\theta}{2}\right) & 0 & 0 & 0 & 0 \\ 0 & 0 & 0 & 0 & 0 & 0 \\ 0 & 0 & 0 & 0 & 0 & 0 \\ 0 & 0 & 0 & 0 & 0 & 0 \\ 0 & 0 & 0 & 0 & 0 & 0 \end{pmatrix}_{\{|a\rangle,|b\rangle,|g\rangle\}\otimes\{|H\rangle,|V\rangle\}} \tag{2.139}$$

Note that the above representation of the density matrix associated with the incident beam is in the basis $\{|a\rangle, |b\rangle, |g\rangle\} \otimes \{|H\rangle, |V\rangle\}$ as indicated in the subscript of Eqn. 2.139.

❑ The Unitary Evolution Operators of the Beam Splitters:

The beam splitters BS_1 and BS_2 are considered to be symmetric, lossless, and ideal that only affect the spatial degree of freedom of the beam and leave the polarization degree of freedom unaffected. The first beam-splitter BS_1 transforms the input modes $\{|a\rangle, |b\rangle\}$ to the modes $\{|c\rangle, |d\rangle\}$ and leaves the mode $|g\rangle$ in the input port g unaffected. Therefore, the matrix representation of the beam splitter action in the path subspace is given as,

$$\hat{B}_{1s} = \frac{1}{\sqrt{2}} \begin{pmatrix} 1 & i & 0 \\ i & 1 & 0 \\ 0 & 0 & \sqrt{2} \end{pmatrix}_{\{|a\rangle,|b\rangle,|g\rangle\} \to \{|c\rangle,|d\rangle,|g\rangle\}} \tag{2.140}$$

The complete beam splitter operator for BS_1 considering the action on the combined path and polarization degrees of freedom is given as $\hat{B}_1 = \hat{B}_{1s} \otimes \hat{\mathbb{1}}_p^{(2)}$. Here $\hat{\mathbb{1}}_p^{(2)}$ is the 2×2 identity operator in the polarization degree of freedom which indicates that the polarization of the beam does not get affected as it propagates through the beam splitter. Thus, the Unitary operator associated with evolution through the beam splitter in the joint Hilbert space of path and polarization degrees of freedom can be expressed as,

$$\hat{B}_1 = \hat{B}_{1s} \otimes \hat{\mathbb{1}}_p^{(2)} = \frac{1}{\sqrt{2}} \begin{pmatrix} 1 & 0 & i & 0 & 0 & 0 \\ 0 & 1 & 0 & i & 0 & 0 \\ i & 0 & 1 & 0 & 0 & 0 \\ 0 & i & 0 & 1 & 0 & 0 \\ 0 & 0 & 0 & 0 & \sqrt{2} & 0 \\ 0 & 0 & 0 & 0 & 0 & \sqrt{2} \end{pmatrix}_{\{|a\rangle,|b\rangle,|g\rangle\}\otimes\{|H\rangle,|V\rangle\} \to \{|c\rangle,|d\rangle,|g\rangle\}\otimes\{|H\rangle,|V\rangle\}} \tag{2.141}$$

Therefore, BS_1 transforms the spacial modes, $\{|a\rangle, |b\rangle, |g\rangle\}$ to $\{|c\rangle, |d\rangle, |g\rangle\}$, without affecting the polarization of the beam.

Similarly, the second beam-splitter BS_2 transforms $\{|e\rangle, |h\rangle\}$ to the modes $\{|j\rangle, |k\rangle\}$ which are the spatial modes associated with the output ports j and k of the interferometer and leaves the output mode $|i\rangle$ in the port i unaffected. Hence, the matrix representation of BS_2 in the path subspace is as follows:

$$\hat{B}_{2s} = \frac{1}{\sqrt{2}} \begin{pmatrix} 1 & i & 0 \\ i & 1 & 0 \\ 0 & 0 & \sqrt{2} \end{pmatrix}_{\{|e\rangle,|h\rangle,|i\rangle\} \rightarrow \{|j\rangle,|k\rangle,|i\rangle\}} \tag{2.142}$$

The complete unitary operator for the beam splitter BS_2 in the combined path and polarization degrees of freedom is given by $\hat{B}_2 = \hat{B}_{2s} \otimes \hat{\mathbb{1}}_p^{(2)}$, i.e.,

$$\hat{B}_2 = \hat{B}_{2s} \otimes \hat{\mathbb{1}}_p^{(2)} = \frac{1}{\sqrt{2}} \begin{pmatrix} 1 & 0 & i & 0 & 0 & 0 \\ 0 & 1 & 0 & i & 0 & 0 \\ i & 0 & 1 & 0 & 0 & 0 \\ 0 & i & 0 & 1 & 0 & 0 \\ 0 & 0 & 0 & 0 & \sqrt{2} & 0 \\ 0 & 0 & 0 & 0 & 0 & \sqrt{2} \end{pmatrix}_{\{|e\rangle,|h\rangle,|i\rangle\} \otimes \{|H\rangle,|V\rangle\} \rightarrow \{|j\rangle,|k\rangle,|i\rangle\} \otimes \{|H\rangle,|V\rangle\}} \tag{2.143}$$

❑ Evolution Through Operators in Path-A of the Interferometer:

The state after the action of the first beam splitter can be computed by transforming $\hat{\rho}_i$ with $\hat{B}_1$, as the following

$$\hat{\rho}^{(\hat{B}_1 \rightarrow)} = \hat{B}_1 \cdot \hat{\rho}_i \cdot \hat{B}_1^{\dagger} \tag{2.144}$$

The superscript $(\hat{B}_1 \rightarrow)$ in the above expression indicates the state after the evolution through BS_1. The beam transmitted from the beam-splitter BS_1 i.e., the beam in the path-A encounters the HWP whose fast axis is oriented at $\frac{\pi}{4}$ with respect to the horizontal. The action of this half-wave plate (HWP) present in arm A of the interferometer can be viewed as the $\hat{U} = \hat{\sigma}_x$ operation on input mode $|c\rangle$ and identity on the modes $\{|d\rangle, |g\rangle\}$. The operator $\hat{U}$ only acts on the polarization degree of freedom and does not in general effect the spatial degree of freedom [19]. Thus, the spatial mode in the output of the HWP

[19] The beam can have slight deviation from its original path due to refraction through the material of the HWP when the normal to the surface of the HWP is not aligned along the incident beam.

remains the same as the spatial mode in the input of the HWP, i.e., $|e\rangle = |c\rangle$, where e is shown as the output port of the HWP in Fig 2.6. The Unitary transformation associated with this operator $\hat{U}$ is given by,

$$\hat{H} = \hat{\Pi}_c \otimes \hat{\sigma}_x + (\hat{\mathbb{1}}_s^{(3)} - \hat{\Pi}_c) \otimes \hat{\mathbb{1}}_p^{(2)} \tag{2.145}$$

Here, $\hat{\mathbb{1}}_s^{(3)}$ is the 3×3 identity operator in the path subspace spanned by the basis states $\{|c\rangle, |d\rangle, |g\rangle\}$, i.e., $\hat{\mathbb{1}}_s^{(3)} = |c\rangle\langle c| + |d\rangle\langle d| + |g\rangle\langle g| = \hat{\Pi}_c + \hat{\Pi}_d + \hat{\Pi}_g$ and $\hat{\mathbb{1}}_p^{(2)}$ is the 2×2 identity operator in the polarization subspace spanned by the basis states $\{|H\rangle, |V\rangle\}$, i.e., $\hat{\mathbb{1}}_p^{(2)} = \hat{\Pi}_H + \hat{\Pi}_V$. Overall operator $\hat{H}$ is given by,

$$\hat{H} = \left[\begin{pmatrix} 1 & 0 & 0 \\ 0 & 0 & 0 \\ 0 & 0 & 0 \end{pmatrix} \otimes \begin{pmatrix} 0 & 1 \\ 1 & 0 \end{pmatrix} + \begin{pmatrix} 0 & 0 & 0 \\ 0 & 1 & 0 \\ 0 & 0 & 1 \end{pmatrix} \otimes \begin{pmatrix} 1 & 0 \\ 0 & 1 \end{pmatrix}\right]_{\{|c\rangle,|d\rangle,|g\rangle\}\otimes\{|H\rangle,|V\rangle\}} \tag{2.146}$$

$$\Longrightarrow \quad \hat{H} = \begin{pmatrix} 0 & 1 & 0 & 0 & 0 & 0 \\ 1 & 0 & 0 & 0 & 0 & 0 \\ 0 & 0 & 1 & 0 & 0 & 0 \\ 0 & 0 & 0 & 1 & 0 & 0 \\ 0 & 0 & 0 & 0 & 1 & 0 \\ 0 & 0 & 0 & 0 & 0 & 1 \end{pmatrix}_{\{|e\rangle=|c\rangle,|d\rangle,|g\rangle\}\otimes\{|H\rangle,|V\rangle\}} \tag{2.147}$$

❑ Evolution Through Operators in Path-B of the Interferometer:

The phase-shifter (PS) acts only on path-B which controls the relative phase between the two paths of the interferometer. The phase shifter adds a phase φ to the beam in the spatial mode $|d\rangle$ only and leaves the modes $|c\rangle$ and $|g\rangle$ unaffected. The operation of the phase shifter can be expressed as, $|f\rangle = e^{i\varphi}|d\rangle$, where $|f\rangle$ is the spatial mode at the output port of the phase shifter. Hence the operator for the phase shifter can be written as,

$$\hat{\Phi}(\varphi) = \left(\hat{\Pi}_c + \exp(i\varphi)\hat{\Pi}_d + \hat{\Pi}_g\right) \otimes \hat{\mathbb{1}}_p^{(2)} \tag{2.148}$$

$\hat{\mathbb{1}}_p^{(2)}$ in the above expression implies that the phase shifter does not affect the polarization of the beam, at all. The complete description of the phase shifter is given by,

$$\hat{\Phi}(\varphi) = \begin{pmatrix} 1 & 0 & 0 & 0 & 0 & 0 \\ 0 & 1 & 0 & 0 & 0 & 0 \\ 0 & 0 & e^{i\varphi} & 0 & 0 & 0 \\ 0 & 0 & 0 & e^{i\varphi} & 0 & 0 \\ 0 & 0 & 0 & 0 & 1 & 0 \\ 0 & 0 & 0 & 0 & 0 & 1 \end{pmatrix}_{\{|c\rangle,|d\rangle,|g\rangle\}\otimes\{|H\rangle,|V\rangle\}\to\{|c\rangle,|f\rangle,|g\rangle\}\otimes\{|H\rangle,|V\rangle\}} \tag{2.149}$$

After passing through the phase shifter, the beam in path-B of the interferometer encounters the operator $\hat{R} = \hat{\Pi}_H$ which is the projector to the horizontal polarization. This operator can be realized either by a linear polarizer with the transmission axis along the horizontal or by using a polarizing beam splitter (PBS) and selecting only the transmitting port of it. Jones matrix representation of a linear polarizer [28] with its axis of transmission aligned at an angle ϑ is given by,

$$\hat{LP}(\vartheta) = \begin{pmatrix} \cos^2(\vartheta) & \sin(\vartheta)\cos(\vartheta) \\ \sin(\vartheta)\cos(\vartheta) & \sin^2(\vartheta) \end{pmatrix}_{\{|H\rangle,|V\rangle\}} \tag{2.150}$$

The matrix $\hat{LP}$ is non-Unitary, thus the projection operation violates the conservation of probability. When the transmission axis remained aligned along the Horizontal, we get the projector to $|H\rangle$ in the polarization subspace,

$$\hat{LP}(\vartheta = 0^\circ) = \begin{pmatrix} 1 & 0 \\ 0 & 0 \end{pmatrix}_{\{|H\rangle,|V\rangle\}} = |H\rangle\langle H| = \hat{\Pi}_H \tag{2.151}$$

Alternatively, a polarizing beam splitter can be used to physically realize the operator $\hat{R} = \hat{\Pi}_H$. A polarizing beam splitter (PBS) transmits only the horizontally polarized component and reflects the vertically polarized component of the beam incident on it. A polarizer and PBS are equivalent in their operation as long as we are only interested in the beam transmitted from the PBS. The transformation of the input modes $\{|f\rangle, |g\rangle\}$ to the output modes $\{|h\rangle, |i\rangle\}$ through the PBS are given as follows,

$$(\alpha_1 |H\rangle + \beta_1 |V\rangle) |f\rangle \xrightarrow{PBS} \alpha_1 |H\rangle |h\rangle + \beta_1 |V\rangle |i\rangle \tag{2.152}$$

$$(\alpha_2 |H\rangle + \beta_2 |V\rangle) |g\rangle \xrightarrow{PBS} \beta_2 |V\rangle |h\rangle + \alpha_2 |H\rangle |i\rangle \tag{2.153}$$

Here, $(\alpha_m |H\rangle + \beta_m |V\rangle)$ with $m = 1, 2$ are the polarization states incident onto the PBS from the input ports f and g respectively. Therefore, the transformation matrix of a PBS in 2×2 dimensional Hilbert space can be given by,

$$P\hat{B}S = \begin{pmatrix} 1 & 0 & 0 & 0 \\ 0 & 0 & 0 & 1 \\ 0 & 0 & 1 & 0 \\ 0 & 1 & 0 & 0 \end{pmatrix}_{\{|f\rangle,|g\rangle\}\otimes\{|H\rangle,|V\rangle\}\rightarrow\{|h\rangle,|i\rangle\}\otimes\{|H\rangle,|V\rangle\}} \tag{2.154}$$

So far the operator $P\hat{B}S$ is Unitary. Since we are only concerned with the transmission of the beam for effectively realizing the operator $\hat{R} = \hat{\Pi}_H$, we have to consider the beam in the output port h when the beam is incident from the input port f of the PBS. It implies a projection operation $\hat{\Pi}_h = \hat{\mathbb{1}}_p^{(2)} \otimes |h\rangle\langle h|$ on the state after the transformation from PBS. From Eqn. 2.152 we get,

$$(\alpha_1 |H\rangle + \beta_1 |V\rangle) |f\rangle \xrightarrow[Transmission]{PBS} \hat{\Pi}_h \cdot (\alpha_1 |H\rangle |h\rangle + \beta_1 |V\rangle |i\rangle) = \alpha_1 |H\rangle |h\rangle \tag{2.155}$$

This transformation, where we select only the transmitted beam in the h port, is non-Unitary though the overall transformation of the PBS is Unitary. So, the matrix representation corresponding to the Unitary transformation of the PBS from $\{|f\rangle, |g\rangle\}$ to $\{|h\rangle, |i\rangle\}$ with the mode $|c\rangle$ remaining unaffected can be expressed as,

$$\hat{P} = \begin{pmatrix} 1 & 0 & 0 & 0 & 0 & 0 \\ 0 & 1 & 0 & 0 & 0 & 0 \\ 0 & 0 & 1 & 0 & 0 & 0 \\ 0 & 0 & 0 & 0 & 0 & 1 \\ 0 & 0 & 0 & 0 & 1 & 0 \\ 0 & 0 & 0 & 1 & 0 & 0 \end{pmatrix}_{\{|c\rangle,|f\rangle,|g\rangle\}\otimes\{|H\rangle,|V\rangle\}\rightarrow\{|c\rangle,|h\rangle,|i\rangle\}\otimes\{|H\rangle,|V\rangle\}} \tag{2.156}$$

❑ Final State after the Unitary Evolution Through the QSI Setup:

The state just before the second beam splitter i.e., the state after the beam propagates through the operator $\hat{U}$ in path-A and the operators $\hat{\Phi}$ and $\hat{R}$ in path-B is given by,

$$\hat{\rho}^{(\hat{B}_1\rightarrow\hat{H}\rightarrow\hat{\Phi}\rightarrow\hat{P}\rightarrow)} = \hat{\rho}^{(\leftarrow\hat{B}_2)} = \hat{P}\cdot(\hat{\Phi}\cdot(\hat{H}\cdot(\hat{B}_1\cdot\hat{\rho}_i\cdot\hat{B}_1^{\dagger})\cdot\hat{H}^{\dagger})\cdot\hat{\Phi}^{\dagger})\cdot\hat{P}^{\dagger} \tag{2.157}$$

The superscript $(\leftarrow \hat{B}_2)$ represents the state before BS_2. The density matrix associated with the system after the action of half-wave plate (HWP) in path-A and polarizing beam splitter (PBS) in path-B are represented in the basis $\{|c\rangle, |h\rangle, |i\rangle\} \otimes \{|H\rangle, |V\rangle\}$. The spatial mode $|e\rangle$ which is one of the input modes to the BS_2 is identical to mode $|c\rangle$ since the HWP does not act on the path d.o.f., i.e., $|e\rangle = |c\rangle$. Thus, the subscript in BS_2 transformation matrix, shown in Eqn. 2.143, can be expressed by $\{|c\rangle, |h\rangle, |i\rangle\} \otimes \{|H\rangle, |V\rangle\} \rightarrow \{|j\rangle, |k\rangle, |i\rangle\} \otimes \{|H\rangle, |V\rangle\}$. The overall evolution of the quantum system through the QSI setup with different operators, in terms of spatial modes, can be seen as:

$$\hat{\rho}_i = \hat{\rho}_s \otimes \hat{\rho}_p$$

$$\Downarrow$$

$$\{|a\rangle, |b\rangle, |g\rangle\} \xrightarrow{\hat{B}_1} \{|c\rangle, |d\rangle, |g\rangle\} \xrightarrow{\hat{H}} \{|e\rangle = |c\rangle, |d\rangle, |g\rangle\} \xrightarrow{\hat{\Phi}} \ldots$$

$$\ldots \xrightarrow{\hat{\Phi}} \{|e\rangle = |c\rangle, |f\rangle, |g\rangle\} \xrightarrow{\hat{P}} \{|e\rangle = |c\rangle, |h\rangle, |i\rangle\} \xrightarrow{\hat{B}_2} \{|j\rangle, |k\rangle, |i\rangle\}$$

$$\Downarrow$$

$$\hat{\rho}_f$$

The three output ports of the QSI setup are i, j, k with the corresponding spatial modes $\{|i\rangle, |j\rangle, |k\rangle\}$. The final density matrix after the Mach-Zehnder interferometer is represented in the basis $\{|j\rangle, |k\rangle, |i\rangle\} \otimes \{|H\rangle, |V\rangle\}$. The final state of the system after evolving through the entire setup can be computed as follows,

$$\hat{\rho}_f^{(\hat{B}_1 \to \hat{H} \to \hat{\Phi} \to \hat{P} \to \hat{B}_2 \to)} = \hat{B}_2 \cdot (\hat{P} \cdot (\hat{\Phi} \cdot (\hat{H} \cdot (\hat{B}_1 \cdot \hat{\rho}_i \cdot \hat{B}_1^\dagger) \cdot \hat{H}^\dagger) \cdot \hat{\Phi}^\dagger) \cdot \hat{P}^\dagger) \cdot \hat{B}_2^\dagger \tag{2.158}$$

Till now, all the evolution has been Unitary and the above density matrix has a unit trace. Now, the non-unitarity would be introduced when we select the beam only in one of the output ports of the setup.

❑ The Non-Unitary Evolution of the Final State Through Projection in One of the Output Ports of the QSI Setup:

We now place the detector (PD) or the beam profiler (CCD) only in port k of the setup. It can be considered as a projective measurement of the state $\hat{\rho}_f$ on the spatial mode $|k\rangle$. In the 3×2 dimensional Hilbert space $\mathcal{H} = \mathcal{H}_s \otimes \mathcal{H}_p$ the projector $\hat{\Pi}_k$ is represented as,

$$\hat{\Pi}_k = |k\rangle\langle k| \otimes \hat{\mathbb{1}}_p^{(2)} = \begin{pmatrix} 0 & 0 & 0 \\ 0 & 1 & 0 \\ 0 & 0 & 0 \end{pmatrix}_{\{|j\rangle,|k\rangle,|i\rangle\}} \otimes \begin{pmatrix} 1 & 0 \\ 0 & 1 \end{pmatrix}_{\{|H\rangle,|V\rangle\}} \tag{2.159}$$

$$\hat{\Pi}_k = \begin{pmatrix} 0 & 0 & 0 & 0 & 0 & 0 \\ 0 & 0 & 0 & 0 & 0 & 0 \\ 0 & 0 & 1 & 0 & 0 & 0 \\ 0 & 0 & 0 & 1 & 0 & 0 \\ 0 & 0 & 0 & 0 & 0 & 0 \\ 0 & 0 & 0 & 0 & 0 & 0 \end{pmatrix}_{\{|j\rangle,|k\rangle,|i\rangle\}\otimes\{|H\rangle,|V\rangle\}} \tag{2.160}$$

The resultant state in the combined Hilbert space of path and polarization subspaces, in the port k of the QSI setup is obtained to be $\hat{\rho}_k = \hat{\Pi}_k \cdot \hat{\rho}_f \cdot \hat{\Pi}_k^\dagger$.

$$\hat{\rho}_k = \hat{\Pi}_k \cdot \hat{\rho}_f \cdot \hat{\Pi}_k^{\dagger} \tag{2.161}$$

$$\hat{\rho}_k = \frac{1}{4}\begin{pmatrix} 0 & 0 & 0 & 0 & 0 & 0 \\ 0 & 0 & 0 & 0 & 0 & 0 \\ 0 & 0 & 1+\mu\sin(\theta)\cos(\varphi-\phi) & \cos^2\left(\frac{\theta}{2}\right)e^{i\varphi}+\frac{\mu}{2}e^{i\phi}\sin(\theta) & 0 & 0 \\ 0 & 0 & \cos^2\left(\frac{\theta}{2}\right)e^{-i\varphi}+\frac{\mu}{2}e^{-i\phi}\sin\theta & \cos^2\left(\frac{\theta}{2}\right) & 0 & 0 \\ 0 & 0 & 0 & 0 & 0 & 0 \\ 0 & 0 & 0 & 0 & 0 & 0 \end{pmatrix} \tag{2.162}$$

Here, we can see that the density matrix ($\hat{\rho}_k$) obtained after evolving through $\hat{\Pi}_k$ does not preserve the norm, i.e., $\mathrm{Tr}(\hat{\rho}_k) \neq 1$.

The component of the final density matrix $\hat{\rho}_f$ in the spatial mode $|k\rangle$ that is going to be detected is obtained as the reduced density matrix in the basis $|k\rangle \otimes \{|H\rangle, |V\rangle\} \equiv \{|k\rangle|H\rangle, |k\rangle|V\rangle\}$. The reduced density matrix (say, $\hat{\rho}_d$) in port k is given as follows,

$$\hat{\rho}_d = \frac{1}{8}\begin{pmatrix} 2\left(1+\mu\sin(\theta)\cos(\varphi-\phi)\right) & e^{i\varphi}(1+\cos(\theta))+\mu e^{i\phi}\sin(\theta) \\ e^{-i\varphi}(1+\cos(\theta))+\mu e^{-i\phi}\sin(\theta) & 1+\cos(\theta) \end{pmatrix}_{\{|H\rangle,|V\rangle\}} \tag{2.163}$$

The trace of the density matrix $\mathrm{Tr}(\hat{\rho}_d) = \frac{1}{8}\left(3+\cos(\theta)+2\mu\sin(\theta)\cos(\varphi-\phi)\right) \neq 1$, which is a result of the non-Unitary evolution through the projection $\hat{\Pi}_k$. This expression of $\mathrm{Tr}(\hat{\rho}_d)$ gives the intensity distribution in the port k as a function of relative phase φ.

❑ Inferring the State Parameters from the Interferogram:

Total intensity recorded at the detector or the beam profiler, placed in the port k, can be obtained by computing the trace of the density matrix $\hat{\rho}_d$, i.e.,

$$I_d(\varphi) = \mathrm{Tr}(\hat{\rho}_d) = \frac{1}{8}\left(3 + \cos(\theta) + 2\mu \sin(\theta)\cos(\varphi - \phi)\right) \tag{2.164}$$

The phase shift (Φ) of the above interference pattern is obtained at the value of φ that maximizes the intensity I_d. Since, $0 \le \theta \le \pi$, $\sin(\theta)$ in the last term (i.e., the interference term) is always positive and $\mu > 0$, hence the phase shift is given by $\Phi = \phi$. The phase averaged intensity $\bar{I}$ is obtained by integrating the intensity $I_d(\varphi)$ over all possible phases $\varphi \in [-\pi, \pi)$ and is given by $\bar{I} = \frac{1}{8}(3 + \cos(\theta))$, which is a unique function of θ. Thus, the state parameters θ and ϕ can be uniquely determined from the average intensity ($\bar{I}$) and the phase shift (Φ) of the interference pattern obtained in an interferometer port. Now, the visibility of the interference pattern is computed as, $V = \frac{I_d^{(max)} - I_d^{(min)}}{I_d^{(max)} + I_d^{(min)}} = \frac{2\mu \sin(\theta)}{3 + \cos(\theta)}$. Therefore, once θ is known, μ can be obtained from the visibility V.

Therefore, the phase shift, average intensity and visibility obtained from an interference pattern generated at one of the output ports of the QSI setup can be processed to get the state parameters from which the unknown polarization state, given in Eqn. 2.136, that is incident on the setup can be reconstructed. So once the setup is aligned, data collection in QSI does not demand any change in the experimental settings − making it a true 'single-shot' technique for state estimation.

2.8 Uniqueness of State Parameters with Phase Shift, Average Intensity and Visibility of an Interferogram

Quantum State Interferography is an interferometric state characterization scheme, using which any arbitrary qubit can be uniquely determined from the phase shift, average intensity and visibility obtained from a single interference pattern that is generated in a two path interferometer with the individual paths respectively having the Unitary ($\hat{U} = \hat{\sigma}_x$) and Hermitian ($\hat{R} = \hat{\Pi}_0 \equiv \hat{\Pi}_H$) operators. Below, we have presented the density plots to show the uniqueness of the state parameters with the interferometric quantities. The functional relationship between $(\Phi, \bar{I}, V)$ obtained from an interferogram and the state parameters (μ, θ, ϕ) is established in Sec. 2.5, which are given as the following:

$$\Phi = \phi, \qquad \bar{I} = \frac{1}{8}(3 + \cos(\theta)), \qquad V = \frac{2\mu \sin(\theta)}{3 + \cos(\theta)} \tag{2.165}$$

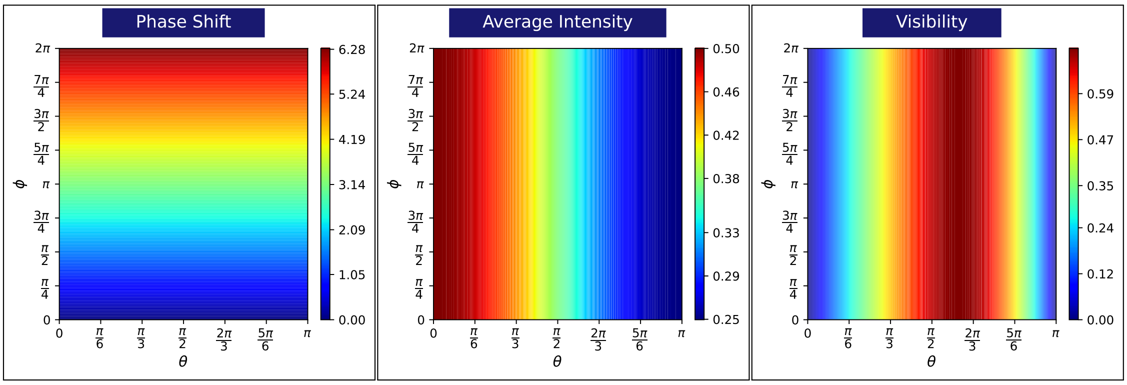

Figure 2.7: Phase Shift (Φ), Average Intensity ($\bar{I}$) and Visibility (V) as function of Bloch Sphere parameters θ and ϕ. The quantities ($\Phi, \bar{I}, V$) are obtained from an interferogram when a qubit (with $\mu = 1$) evolves through the QSI setup.

From the above plots, it can be seen that the phase shift (Φ) of the interferogram is independent of θ and is a unique function of ϕ. The phase averaged intensity ($\bar{I}$) of the interference pattern is independent of ϕ and is a unique function of θ. Visibility (V), however, although independent of ϕ, is many (two) to one function of θ. Therefore, we choose the average intensity, which forms a one-to-one map with θ, for uniquely identifying the state parameter θ. Visibility, nevertheless, helps in distinguishing μ, the parameter that governs the purity of a two-dimensional state.

2.9 Quantum State Interferography for Qubits: Inferring the Bloch Parameters

In this Chapter, we have shown, how any arbitrary qubit, whether mixed or pure, can be characterized using an interferometric state determination scheme – Quantum State Interferography. So far we have presented the procedure and the post-processing algorithms to identify the state parameters (μ, θ, ϕ) representing the qubits (Eqn. 2.9), from the interferometric quantities such as visibility (V), average intensity ($\bar{I}$) and phase shift (Φ) of a single interference pattern. Note that, the parameters (μ, θ, ϕ) correspond to the decoherence representation of qubits, which is chosen for the state characterization in QSI as the set (μ, θ, ϕ) bears a simple functional relationship with the set of interferometric quantities ($V, \bar{I}, \Phi$). However, the intuitive and most commonly used representation for qubits (Eqn. 2.16) is the Bloch sphere representation, where any arbitrary qubit is considered to be in a Bloch sphere which is a unit 2-sphere ($\mathbb{S}^{(2)}$). A state in this representation is parameterized in terms of the Bloch co-ordinates (r_b, θ_b, ϕ_b), where $r_b = |\vec{r}| \in [0, 1]$ is the length of the Bloch vector, $\theta_b \in [0, \pi]$ is the polar angle and $\phi_b \in [-\pi, \pi)$ is the azimuthal angle corresponding to the qubit in the Bloch sphere. Here, in this section, we will show that Quantum State Interferography consistently provides a 'single-shot' qubit determination scheme even when the qubits are represented in terms of Bloch parameters.

Any arbitrary state in the two-dimensional Hilbert space visualized in the Bloch sphere representation is given as,

$$\hat{\rho}(|\vec{r}|, \theta_b, \phi_b) = \frac{1}{2} \begin{pmatrix} 1 + |\vec{r}| \cos(\theta_b) & |\vec{r}| \sin(\theta_b)\ e^{-i\phi_b} \\ |\vec{r}| \sin(\theta_b)\ e^{i\phi_b} & 1 - |\vec{r}| \cos(\theta_b) \end{pmatrix} \tag{2.166}$$

Consider, a stream of particles in the state $\hat{\rho}(|\vec{r}|, \theta_b, \phi_b)$ is incident on the QSI setup, which consists of a two path interferometer, say, a Mach-Zehnder Interferometer (MZI) with $\hat{U} = \hat{\sigma}_x$ in one path and $\hat{R} = \hat{\Pi}_0$ in the other path (as shown in the Fig. 2.3). The state $\hat{\rho}(|\vec{r}|, \theta_b, \phi_b)$ evolves through the operator $\hat{\mathcal{E}} = \frac{1}{2}\left(\hat{U} + e^{i\epsilon}\hat{R}\right) = \frac{1}{2}\left(\hat{\sigma}_x + e^{i\epsilon}\hat{\Pi}_0\right)$ (matrix representation of which is shown in Eqn. 2.93), where ϵ is the relative phase between the two paths of the interferometer. The intensity distribution as a function of relative phase (ϵ), obtained in one of the output ports of the setup, is given as

$$I_d(\epsilon) = \mathrm{Tr}\left(\hat{\mathcal{E}}\ \hat{\rho}\ \hat{\mathcal{E}}^\dagger\right) = \frac{1}{8}\left[3 + |\vec{r}| \cos(\theta_b) + 2|\vec{r}| \sin(\theta_b) \cos(\epsilon - \phi_b)\right] \tag{2.167}$$

The generated interferogram ($I_d(\epsilon)$), needs to be processed to determine the interferometric quantities Φ, $\bar{I}$ and V from which the Bloch parameters $|\vec{r}|$, θ_b and ϕ_b would be inferred.

❑ **Phase Shift:** The phase shift (Φ) of the interference pattern $I_d(\epsilon)$ is obtained at that value of ϵ which gives maximum value of I_d and is obtained from the following conditions.

$$\left.\frac{\partial I_d(\epsilon)}{\partial \epsilon}\right|_{\epsilon=\Phi} = -\frac{1}{4}|\vec{r}|\sin(\theta_b)\sin(\Phi-\phi_b) = 0 \tag{2.168}$$

$$\left.\frac{\partial^2 I_d(\epsilon)}{\partial \epsilon^2}\right|_{\epsilon=\Phi} = -\frac{1}{4}|\vec{r}|\sin(\theta_b)\cos(\Phi-\phi_b) < 0 \tag{2.169}$$

Since $\theta_b \in [0,\pi]$, we get $0 \leq \sin(\theta_b) \leq 1$ and $|\vec{r}| > 0$. Therefore, Eqn. 2.168 gives $\Phi - \phi_b = 0$ or $\Phi - \phi_b = \pi$. However, the condition in Eqn. 2.169 would satisfy when $\Phi - \phi_b = 0$. Hence, we get the phase shift of the interferogram as $\Phi = \phi_b$.

❑ **Average Intensity:** The Average intensity of the interference pattern is obtained as follows,

$$\bar{I} = \int_{\epsilon} I_d(\epsilon)d\epsilon = \frac{1}{8}(3 + |\vec{r}|\cos(\theta_b)) \tag{2.170}$$

Hence the average intensity in Bloch sphere representation is not a unique function of θ_b or $|\vec{r}|$. Therefore, to uniquely determine the state parameters $|\vec{r}|$ and θ_b, one would require another quantity obtained from the interferogram.

❑ **Visibility:** The visibility of the interference pattern is computed using the maximum ($I_d^{(max)}$) and minimum ($I_d^{(min)}$) values of intensity as the following,

$$V = \frac{I_d^{(max)} - I_d^{(min)}}{I_d^{(max)} + I_d^{(min)}} = \frac{2|\vec{r}|\sin(\theta_b)}{3 + |\vec{r}|\cos(\theta_b)} \tag{2.171}$$

Therefore, the visibility is again a function of $|\vec{r}|$ and θ_b.

❑ **Determining the State Parameters:** Therefore, the state parameter ϕ_b can be directly obtained from the phase shift Φ of the interferogram, similar to determining ϕ in (μ,θ,ϕ) representation. However, the other two Bloch parameters i.e., $|\vec{r}|$ and θ_b can be obtained by simultaneously solving the expressions $\bar{I}(|\vec{r}|, \theta_b)$ and $V(|\vec{r}|, \theta_b)$ given in Eqn. 2.170 and Eqn. 2.171. Now, from Eqn. 2.170 we can write,

$$|\vec{r}| = \frac{8\bar{I} - 3}{\cos(\theta_b)} \tag{2.172}$$

Using this value of $|\vec{r}|$ in Eqn. 2.171, we get the state parameter θ_b in terms of interferometric quantities $\bar{I}$ and V.

$$V = \frac{2(8\bar{I} - 3)\tan(\theta_b)}{3 + (8\bar{I} - 3)} = \frac{8\bar{I} - 3}{4\bar{I}} \tan(\theta_b) \tag{2.173}$$

$$\implies \qquad \theta_b = \arctan\left(\frac{4\bar{I}V}{8\bar{I} - 3}\right) \tag{2.174}$$

Once, θ_b is obtained from $\bar{I}$ and V, the length of the Bloch vector $|\vec{r}|$ can be determined from Eqn. 2.172. Therefore, Quantum State Interferography (QSI) can interpret the set of Bloch parameters from a single interference pattern, as well.

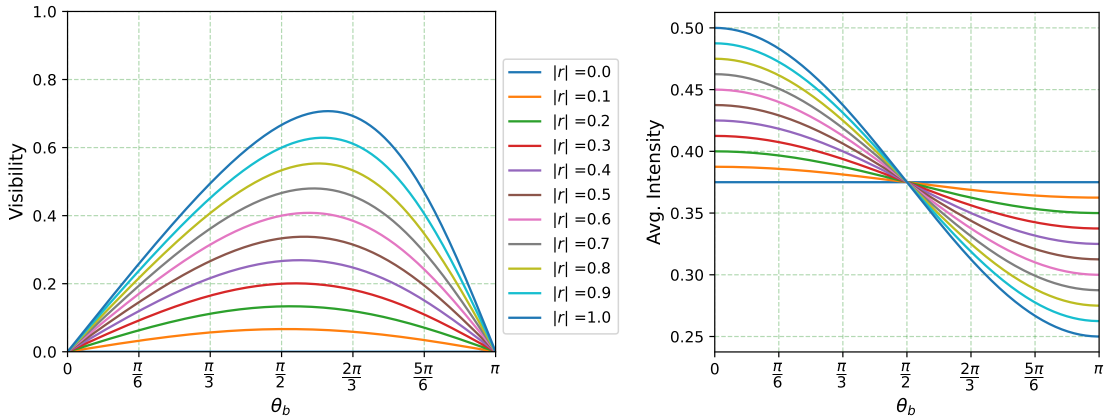

(a) Visibility (V) as a function of $|\vec{r}|$ and θ_b

(b) Avg. intensity ($\bar{I}$) as a function of $|\vec{r}|$ and θ_b

Figure 2.8: Visibility (V) and Average intensity ($\bar{I}$) obtained from an interferogram formed when an arbitrary qubit $\hat{\rho}(|\vec{r}|, \theta_b, \phi_b)$ evolves through the QSI setup. As $|\vec{r}|$ varies from 0 to 1, visibility for different $|\vec{r}|$ values is found to be a bi-valued function of θ_b, whereas, average intensity for different $|\vec{r}|$ values is obtained to be a unique function of θ_b.

In summary, we can conclude that the interferometric state determination technique, Quantum state interferography (QSI), enables one to infer the Bloch parameters corresponding to an arbitrary qubit using the information processed from an interference pattern produced at the end of a two-path interferometer, in the same manner how the (μ, θ, ϕ) parameters of the qubit are inferred. Therefore, QSI can be used to reconstruct any arbitrary qubit independent of its representation in a single-shot state estimation procedure. When the determination of $(|\vec{r}|, \theta_b, \phi_b)$ parameters is compared with the determination of (μ, θ, ϕ) parameters, QSI as the technique i.e., the experimental setup, the evolution of the unknown state through the operator $\hat{\mathcal{E}}$, recording the interference pattern at the end and processing it to get the quantities $(\Phi, \bar{I}, V)$, appears to be the same. The only difference arises in the algorithm to get the state parameters from the interferometric quantities. However, the determination of θ_b involves an arctan function, which is not bounded, unlike arccos function that is used to determine θ. Therefore, in the regions where θ_b approaches $\frac{\pi}{2}$, any small experimental error would get amplified while determining θ_b from $\bar{I}$ and V.

2.10 Conclusion

This chapter introduces a novel method for state characterization $-$ *Quantum State Interferography* $-$ that uses interferometry as a tool to infer the unknown states of a quantum system. Quantum State Interferography (QSI) provides a true 'single-shot' state determination scheme for qubits, using which any unknown qubit, whether mixed or pure, can be inferred from the phase shift (Φ), phase-averaged intensity $(\bar{I})$, and visibility (V) of a single interference pattern generated in a Mach-Zehnder Interferometer (MZI), with the operator $\hat{\sigma}_x$ present in one arm and the operator $\hat{\Pi}_0$ (when the Hilbert space is spanned by the Fock basis $\{|0\rangle, |1\rangle\}$) or equivalently the operator $\hat{\Pi}_H$ (for the polarization basis $\{|H\rangle, |V\rangle\}$) in the other arm. The three quantities processed from the interferogram i.e., $(\bar{I}, \Phi, V)$ forms a unique map with the set of parameters (θ, ϕ, μ) or (θ_b, ϕ_b, r_b) that describes any arbitrary state $\hat{\rho}$ in the two-dimensional Hilbert space. If the state is known to be pure, the determination of the phase shift and the phase averaged intensity from the interference pattern are enough to reconstruct the unknown state. Since the procedure of state characterization using QSI does not demand any modifications in the experimental settings during data acquisition, it shows the potential to develop an enclosed state estimating device, which when fed with an input beam in an unknown state would generate the corresponding state information in the output.

Here, we have discussed the QSI scheme by describing the experimental setup taking an example of a MZI. However, it can be realized with any two-path interferometer including double-slit interferometer which can be factory designed and can serve as a robust miniaturization in the state estimating device. The scheme can also be realized using a displaced Sagnac Interferometer (DSI), details of which will be discussed in **Chapter. 3**.

Appendix

2.A Geometric Interpretation of Qubits in the (μ, θ, ϕ) and Bloch Representation: A comparative Analysis

In Sec. 2.1, we have shown the representation of a general qubit with two sets of parameters, (μ, θ, ϕ) and (r_b, θ_b, ϕ_b). Though both the sets represent a unique state, they are not the same and have different physical meanings. The density matrix in **2.16** is one of the most commonly used forms of representing an arbitrary single qubit, visualized using a vector $\vec{r}$ within a sphere of unit radius in $\mathbb{R}^3$. Here, the length of the vector $|\vec{r}|$ scales uniformly with the mixedness of the state. On the other hand, the density matrix in Eqn. **2.9** gives another standard form of a general qubit, representing the emergence of mixed states from the pure states under decoherence. Here, μ is the parameter that controls the mixedness. μ is not the same as the length of the Bloch vector, but is related to it. Since, the density matrices in two different representations correspond to the same state (say, $\hat{\rho}$) in a given two-dimensional Hilbert space, we can write the purity of the state as the following:

$$\mathrm{Tr}\left(\hat{\rho}^2\right) = \frac{1}{2}\left(1 + |\vec{r}|^2\right) = 1 - \left(\frac{1-\mu^2}{2}\right)\sin^2(\theta) \tag{2.175}$$

Therefore, using the fact that $\mathrm{Tr}\left(\hat{\rho}^2\right)$ would represent the purity of the given state $\hat{\rho}$ irrespective of the parametric representations, we get the functional relationship between the length of the Bloch vector $|\vec{r}|$ and mixedness parameter μ.

$$|\vec{r}| = \sqrt{\cos^2(\theta) + \mu^2\sin^2(\theta)} \tag{2.176}$$

From the above expression, it can be seen that the length of the Bloch vector $|\vec{r}|$ is a function of μ and θ. $\mu = 1$ corresponds to $|\vec{r}| = \sqrt{\cos^2(\theta) + \sin^2(\theta)} = 1$. Therefore, $\mu = 1$ represents the states on the surface of the Bloch sphere, i.e., the pure qubits. Further, $\mu = 0$ corresponds to $|\vec{r}| = \sqrt{\cos^2(\theta)}$. Therefore, $\mu = 0$ simply does not represent the maximally mixed state; $\mu = 0$ with $\theta = \frac{\pi}{2}$ represents $\frac{\hat{\mathbb{1}}}{2}$.

❑ Functional Relationship Between the Two Sets of Parameters:

Now, let us consider a point P within a sphere of unit radius in $\mathbb{R}^3$ as shown in Fig. 2.9, that represents an arbitrary mixed state given by the density matrix $\hat{\rho}$. This point P lies on the tip of the vector $\vec{OP} = \vec{r} = r_x\hat{x} + r_y\hat{y} + r_z\hat{z}$, known as the Bloch vector associated with the given state. Relating the Bloch parameters (r_b, θ_b, ϕ_b) for the given state to the Cartesian co-ordinates we can see $r_b = |\vec{r}| = \left|\vec{OP}\right| = \sqrt{r_x^2 + r_y^2 + r_z^2} \in [0, 1]$ is the length of the Bloch vector, $\theta_b \in [0, \pi]$ is the angle between $\vec{r}$ and $\hat{z}$ and $\phi_b \in [-\pi, \pi)$ is the angle between the projection of $\vec{r}$ on the $x - y$ plane (i.e., $\vec{OM}$) and $\hat{x}$. Therefore, from the expression of the density matrix $\hat{\rho} = \frac{1}{2}\left(\hat{\mathbb{1}} + r_x\hat{\sigma}_x + r_y\hat{\sigma}_y + r_z\hat{\sigma}_z\right)$, we get

$$\langle\hat{\sigma}_x\rangle = \mathrm{Tr}(\hat{\rho}\hat{\sigma}_x) = r_x = |\vec{r}|\sin(\theta_b)\cos(\phi_b) \tag{2.177}$$

$$\langle\hat{\sigma}_y\rangle = \mathrm{Tr}(\hat{\rho}\hat{\sigma}_y) = r_y = |\vec{r}|\sin(\theta_b)\sin(\phi_b) \tag{2.178}$$

$$\langle\hat{\sigma}_z\rangle = \mathrm{Tr}(\hat{\rho}\hat{\sigma}_z) = r_z = |\vec{r}|\cos(\theta_b) \tag{2.179}$$

Here, (r_x, r_y, r_z) are the co-ordinates of the point P representing the mixed state $\hat{\rho}$.

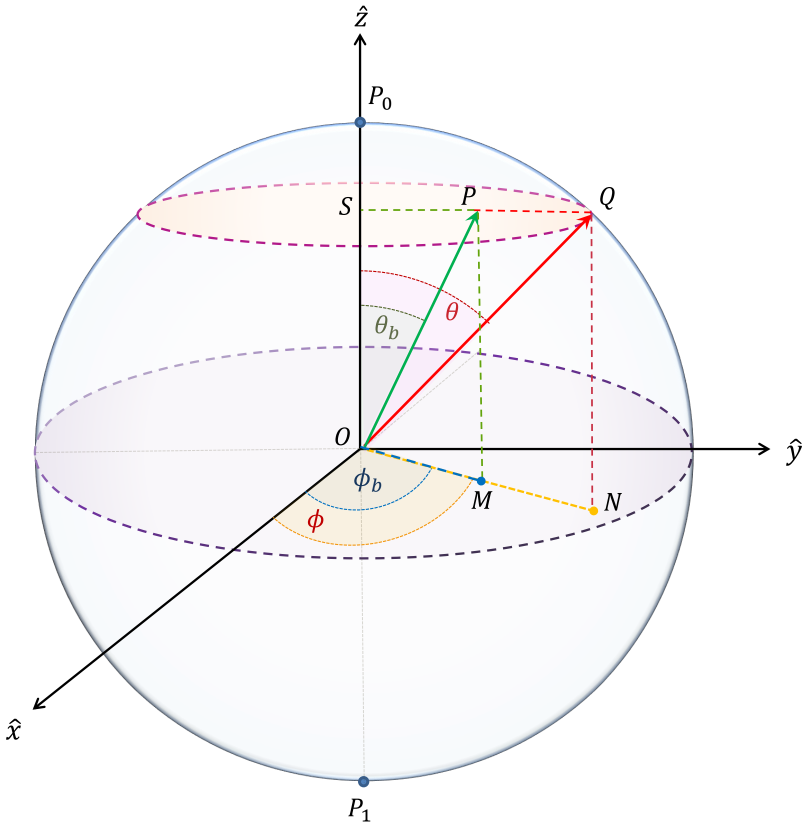

Figure 2.9: Geometric representation of an arbitrary qubit, given by the point P at the tip of the 'green' vector $\vec{OP}$ within a sphere of unit radius centered at O, in different parametric representations – (x, y, z), (r_b, θ_b, ϕ_b) and (μ, θ, ϕ).

Now, when we attempt to visualize the same state $\hat{\rho}$ parameterized by (μ, θ, ϕ) with $\mu \in [0, 1]$, $\theta \in [0, \pi]$ and $\phi \in (-\pi, \pi]$ in the Cartesian co-ordinates, the functional relationship between the two sets of parameters can be established. The expectation value of the Pauli matrices computed for the density matrix $\hat{\rho}$ in (μ, θ, ϕ) representation given in Eqn. 2.9, are expressed as:

$$\langle \hat{\sigma}_x \rangle = \mathrm{Tr}(\hat{\rho}\hat{\sigma}_x) = \mu \sin(\theta) \cos(\phi) \tag{2.180}$$

$$\langle \hat{\sigma}_y \rangle = \mathrm{Tr}(\hat{\rho}\hat{\sigma}_y) = \mu \sin(\theta) \sin(\phi) \tag{2.181}$$

$$\langle \hat{\sigma}_z \rangle = \mathrm{Tr}(\hat{\rho}\hat{\sigma}_z) = \cos(\theta) \tag{2.182}$$

Therefore, comparing $\langle\hat{\sigma}_i\rangle$ (where $i = x, y, z$) for the two representations of the same state $\hat{\rho}$, we see that the parameters (μ, θ, ϕ) relate to the Cartesian parameters (r_x, r_y, r_z) in a manner which is different from how the Bloch parameters $(|\vec{r}|, \theta_b, \phi_b)$ would relate. The physical significance of the parameters μ, θ, and ϕ will be clear when we form a one-to-one map between the two sets of parameters.

Now, comparing the quantities $\langle\hat{\sigma}_z\rangle$ and $(\langle\hat{\sigma}_x\rangle^2 - \langle\hat{\sigma}_y\rangle^2)$ obtained from the two representations, we get

$$\langle\hat{\sigma}_z\rangle = |\vec{r}|\cos(\theta_b) = \cos(\theta) \tag{2.183}$$

$$\langle\hat{\sigma}_x\rangle^2 - \langle\hat{\sigma}_y\rangle^2 = |\vec{r}|^2\sin^2(\theta_b)\cos(2\phi_b) = \mu^2\sin^2(\theta)\cos(2\phi) \tag{2.184}$$

From the above two expressions and using Eqn. 2.176, we can write the parameters θ_b and ϕ_b as the following:

$$\theta_b = \cos^{-1}\left(\frac{\cos(\theta)}{|\vec{r}|}\right) \tag{2.185}$$

$$\phi_b = \phi \tag{2.186}$$

Therefore, ϕ is the same as that of the azimuthal angle ϕ_b associated with the Bloch vector $\vec{r}$, but θ is not the same as the polar angle θ_b.

❑ **Interpreting the Physical Meanings of θ and ϕ in the (μ, θ, ϕ) Representation:** From Fig. 2.9, we see that the projection of the Bloch vector $\vec{OP} = \vec{r}$ on the z-axis is OS. Now, keeping the projection the same if we extend the line SP, which is normal to the z-axis, till it touches the surface of the sphere, then the point of intersection Q can be associated with a vector $\vec{OQ}$ of unit length. Therefore, $\vec{OQ}$ is the unit vector that has the same z-projection (OS) as the Bloch-vector $\vec{r} = \vec{OP}$ corresponding to the mixed state $\hat{\rho}$ and it has a projection $\vec{ON}$ on the $x - y$ plane, making the same angle with $\hat{x}$ as $\vec{OM}$. So, we can write

$$OS = \vec{OQ} \cdot \hat{z} = \vec{OP} \cdot \hat{z} = \vec{r} \cdot \hat{z} \tag{2.187}$$

$$\implies \quad \vec{OQ} \cdot \hat{z} = |\vec{r}| \cos(\theta_b) = \cos(\theta) \tag{2.188}$$

$$\implies \quad \vec{OQ} \cdot \hat{z} = \left|\vec{OQ}\right| \cos(\theta) \tag{2.189}$$

The above expression is obtained using Eqn. 2.183 and the value $\left|\vec{OQ}\right| = 1$. Hence, Eqn. 2.189 shows that θ is the angle that the unit vector $\vec{OQ}$ makes with $\hat{z}$. Therefore, ϕ is the angle that the projection of $\vec{OQ}$ in the $x - y$ plane makes with $\hat{x}$, which is the same as ϕ_b. Visualizing the state $\hat{\rho}$ in Cartesian co-ordinates, we can say that θ is the polar angle associated with a given mixed state $\hat{\rho}$ represented by a Bloch vector whose length has been normalized to one and ϕ is the azimuthal angle corresponding to the normalized unit Bloch vector. Therefore, any arbitrary state $\hat{\rho}(|\vec{r}|, \theta_b, \phi_b)$ in the Bloch sphere can be related to a point on the surface of the sphere.

In Fig. 2.9, P represents any arbitrary mixed state within the Bloch sphere, associated with a Bloch vector $\vec{r} = \vec{OP}$ that has a z-projection r_z same as the vector $\vec{OQ}$ of unit length, where Q lies on the surface of the sphere. From Eqn. 2.183, for any general state in two dimensions we can write,

$$\frac{\cos(\theta)}{\cos(\theta_b)} = |\vec{r}| \leq 1 \tag{2.190}$$

$$\implies \quad \cos(\theta) \leq \cos(\theta_b)$$

$$\implies \quad \theta \geq \theta_b \tag{2.191}$$

The equality holds for $|\vec{r}| = 1$, i.e., for the pure states. Therefore, for any mixed state the Bloch parameter θ_b would always be less than the parameter θ in the decoherence representation. This relation can be visualized using the Fig. 2.9 where any point, inside the Bloch sphere along the line SQ on the plane $z = r_z$, that represents a mixed state (say, $\hat{\rho}'$) is associated with a Bloch vector (say, $\vec{r}'$) having the length $\left|\vec{r}'\right|$ such that $r_z \leq \left|\vec{r}'\right| < 1$

with the polar angle θ_b varying as $0 \leq \theta_b < \theta$.

Further, since the Bloch parameter $\theta_b \in [0, \pi]$, for any general qubit we get

$$0 \leq \theta_b \leq \pi \quad \Longrightarrow \quad -1 \leq \cos(\theta_b) \leq 1$$

$$\Longrightarrow \quad -|\vec{r}| \leq |\vec{r}|\cos(\theta_b) \leq |\vec{r}| \quad \Longrightarrow \quad -|\vec{r}| \leq \cos(\theta) \leq |\vec{r}| \tag{2.192}$$

$$\text{giving,} \quad \cos^{-1}(|\vec{r}|) \leq \theta \leq \pi - \cos^{-1}(|\vec{r}|) \tag{2.193}$$

Since, for mixed states $|\vec{r}| < 1$, the above expression gives $0 < \theta < \pi$. So, θ can never have the value 0 or π for any mixed qubit state. Using the expression $|r| = \sqrt{\cos^2(\theta) + \mu^2 \sin^2(\theta)}$, for $\theta = 0$ or π, we get $|r| = 1$, i.e., pure states. $\theta = 0$ corresponds to pole P_0 giving the pure state $|0\rangle$ and $\theta = \pi$ corresponds to pole P_1 giving the pure state $|1\rangle$.

❑ Physical Significance of μ in the (μ, θ, ϕ) Representation:

So far, we have established how the parameters in the density matrix $\hat{\rho}$ in the (μ, θ, ϕ) representation are related to the co-ordinates in the Cartesian representation, as well as to the parameters in the Bloch representation. The expression of $\hat{\rho} \equiv \hat{\rho}(\mu, \theta, \phi)$ in Eqn. 2.9 represents a general qubit density matrix that can be constructed by writing a pure state density matrix (given in Eqn. 2.8) in spherical polar co-ordinates [20] and then introducing the effect of decoherence through the parameter μ in the off-diagonal terms. Decoherence does not affect the probabilities $|\alpha|^2 = \cos^2\left(\frac{\theta}{2}\right)$ and $|\beta|^2 = \sin^2\left(\frac{\theta}{2}\right)$ associated with the basis vectors, but causes loss in the system information, especially the phase information. Therefore, it attenuates the off-diagonal terms that represent quantum coherence and introduces mixedness in the system [29]. So, visualizing in $\mathbb{R}^3$ we can say, in presence of decoherence, the pure states that lie on the surface of the Bloch sphere (with $|\vec{r}| = 1$), evolve towards the z-axis along a plane given by $z = constant$ [30].

[20] Pure state density matrix is the same in both (μ, θ, ϕ) and $(|\vec{r}|, \theta_b, \phi_b)$ representations, as $|\vec{r}| = 1, \mu = 1, \theta = \theta_b$ and $\phi = \phi_b$ for pure states.

Consider a plane at S normal to the z-axis, as depicted in Fig. 2.9. Every point across this plane within the Bloch sphere would represent the qubit mixed states that emerges as a result of the non-unitary evolution (associated with decoherence) of the pure states lying along the points on the circumference of a circle formed at the intersection of $z = OS$ plane and the unit sphere. Decoherence does not change the azimuthal angle, i.e., $\phi_b = \phi$ and the z-projection i.e., $|\vec{r}|\cos(\theta_b) = \cos(\theta)$ associated with the pure state lying on the surface of the Bloch sphere, it only moves the points representing the system state from the surface of the sphere to the surface of an ellipsoid within the sphere, depending on the value of μ (known as correlation-damping factor) [6, 30]. The states with $\mu = 1$ lie on the surface of the sphere and the states with $\mu = 0$ lie along the z-axis.

Since, the shape of the ellipsoid changes from a sphere to a line along the z-axis as μ varies from 1 to 0, we can say that μ controls the purity of a qubit in (μ, θ, ϕ) representation. However, μ is not the same as the length of the Bloch vector $|\vec{r}|$, but is related to it as the following,

$$\mu = \sqrt{\frac{|\vec{r}|^2 - \cos^2(\theta)}{\sin^2(\theta)}} = \sqrt{\frac{|\vec{r}|^2(1 - \cos^2(\theta_b))}{1 - |\vec{r}|^2\cos^2(\theta_b)}} \tag{2.194}$$

From the above expression, it may appear that at $\theta = 0$ or π, the parameter μ blows up. But, this is not the case, since when θ tends to 0 or π, $\cos(\theta)$ tends to $|\vec{r}|$, giving a finite value of μ. Unlike $|\vec{r}|$ in the Bloch representation, μ does not scale uniformly with the purity of the state because of its θ dependence. For the states of constant purity, say $\mathcal{P}$, we can write

$$|\vec{r}| = \sqrt{2\mathcal{P} - 1} \quad \text{and} \quad \mu = \sqrt{1 + \frac{2\mathcal{P} - 2}{\sin^2(\theta)}} \tag{2.195}$$

Therefore, if we consider a plane $\phi_b = \phi = constant$, the locus of the states with same purity is circular about θ in $|\vec{r}|$, whereas the locus of the states with same purity about θ is the deformed elliptic toroidal or “baloon” shaped, as shown in Fig. 2.10b.

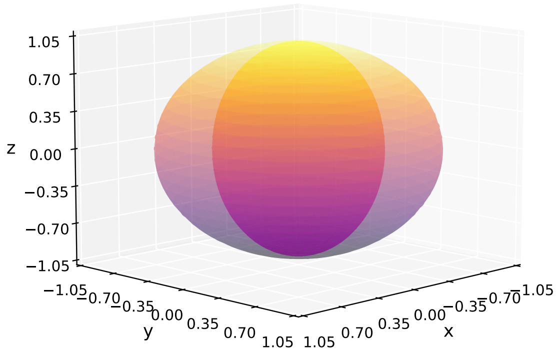

(a) Deformation of the Bloch sphere (with radius $|\vec{r}| = 1$) into an ellipsoid (shown for $\mu = 0.6$) within the sphere, in the presence of decoherence in an open quantum system, indicating the emergence of mixedness to the system.

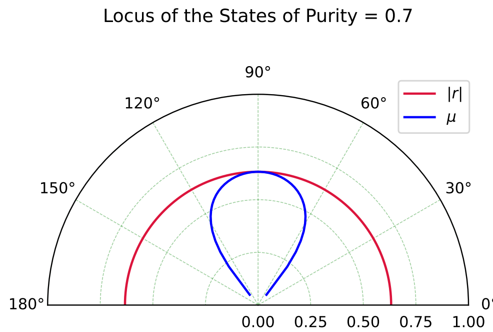

(b) Locus of points representing the qubits of constant purity (here, $\mathcal{P} = 0.7$) about the polar angle $\theta \in [0, \pi]$, at $\phi = const.$ plane, is circular in $|\vec{r}|$ ('red' curve) and is deformed elliptic toroidal or 'balloon' shaped in μ ('blue' curve).

Figure 2.10: Visualization of two-dimensional state space in two different representations, the Bloch sphere representation, and the decoherence representation.

In summary, representation of any arbitrary qubit using two sets of parameters $(|\vec{r}|, \theta_b, \phi_b)$ and (μ, θ, ϕ) are shown in Eqn. 2.16 and Eqn. 2.9 respectively and a discussion on their geometrical interpretation in terms of Cartesian co-ordinates is presented in this section. The Bloch sphere representation using $(|\vec{r}|, \theta_b, \phi_b)$, where any arbitrary density matrix is written as a linear combination of identity operator $(\hat{\mathbb{1}})$ and the Pauli operators ($\hat{\sigma}_i$ with $i = x, y, z$), is the most commonly used form for state characterization and study of coherent evolution of the system. On the other hand, (μ, θ, ϕ) provides the preferred form of representing a qubit for the characterization of the system when dynamics is concerned. Here, mixedness is introduced with the decay of the off-diagonal terms (of a pure state density matrix) using the factor μ, associated with the loss of system information through interaction with an environment for an open system. Therefore, the two sets of parameters simply denotes alternate notations for the same state, which fundamentally differ in terms of the visualization the two-dimensional Hilbert space in $\mathbb{R}^3$.

In $(|\vec{r}|, \theta_b, \phi_b)$ parameterization, a qubit is represented as a point in a unit 2-sphere $\mathbb{S}^{(2)}$ – Bloch sphere, embedded in $\mathbb{R}^3$. However, with (μ, θ, ϕ) parameters, a qubit is represented as a point on the surface an ellipsoid contained inside the Bloch sphere, formed due to the deformation of the unit sphere under decoherence, as shown in Fig. **2.10a**. The pure state space for both the representations is the same, given by the points $(\theta_b = \theta, \phi_b = \theta)$ on the surface of the unit sphere with the associated parameters $|\vec{r}| = 1$, $\mu = 1$. Its the mixed state space that visually differs in the two notations as can be seen in Fig. **2.10a**. In Bloch representation, as $|\vec{r}|$ tends to zero, the state becomes maximally mixed. However, in the decoherence representation, when μ tends to zero, the state is Non-maximally mixed, as the purity of the state has a dependence on θ. In the Bloch representation, as can be seen from Eqn. **2.17**, the states of same purity lies on the surface of the sphere of radius $|\vec{r}|$, independent of θ_b and ϕ_b. However, in decoherence representation, the states of the same purity lie on the surface of a deformed elliptical torus having a balloon-like cross-section at $\phi = constant$, with the shape of the balloon changing with the Purity.

References

[1] Fulvio Flamini, Nicolò Spagnolo, and Fabio Sciarrino. "Photonic quantum information processing: a review". In: *Reports on Progress in Physics* 82.1 (2018), p. 016001. DOI: 10.1088/1361-6633/aad5b2.

[2] Sergei Slussarenko and Geoff J. Pryde. "Photonic quantum information processing: A concise review". In: *Applied Physics Reviews* 6.4 (2019), p. 041303. DOI: 10.1063/1.5115814.

[3] Michael A. Nielsen and Isaac L. Chuang. *Quantum Computation and Quantum Information: 10th Anniversary Edition*. Cambridge University Press, 2010. DOI: 10.1017/CBO9780511976667.

[4] U. Fano. "Description of States in Quantum Mechanics by Density Matrix and Operator Techniques". In: *Rev. Mod. Phys.* 29 (1 1957), pp. 74–93. DOI: 10.1103/RevModPhys.29.74.

[5] George T. Gilbert. "Positive Definite Matrices and Sylvester's Criterion". In: *The American Mathematical Monthly* 98.1 (1991), pp. 44–46.

[6] W. H. Zurek. "Environment-induced superselection rules". In: *Phys. Rev. D* 26 (8 1982), pp. 1862–1880. DOI: 10.1103/PhysRevD.26.1862.

[7] W. Pauli. "Zur Quantenmechanik des magnetischen Elektrons". In: *Zeitschrift für Physik* 43 (9 1927), pp. 601–623. DOI: 10.1007/BF01397326.

[8] Yakir Aharonov, David Z. Albert, and Lev Vaidman. "How the result of a measurement of a component of the spin of a spin-1/2 particle can turn out to be 100". In: *Phys. Rev. Lett.* 60 (14 1988), pp. 1351–1354. DOI: 10.1103/PhysRevLett.60.1351.

[9] Arun Kumar Pati, Uttam Singh, and Urbasi Sinha. "Measuring non-Hermitian operators via weak values". In: *Phys. Rev. A* 92 (5 2015), p. 052120. DOI: 10.1103/PhysRevA.92.052120.

[10] David J. Griffiths and Darrell F. Schroeter. *Introduction to Quantum Mecanics*. Cambridge University Press, 2018.

[11] Brian C. Hall. *Lie Groups, Lie Algebras, and Representations: An Elementary Introduction*. Springer, 2015. DOI: 10.1007/978-3-319-13467-3.

[12] Richard Jozsa. "Complex weak values in quantum measurement". In: *Phys. Rev. A* 76 (4 2007), p. 044103. DOI: 10.1103/PhysRevA.76.044103.

[13] P. A. M. Dirac. *The Principles of Quantum Mecanics*. Oxford, Clarendon Press, 1981.

[14] Gaurav Nirala et al. "Measuring average of non-Hermitian operator with weak value in a Mach-Zehnder interferometer". In: *Phys. Rev. A* 99 (2 2019), p. 022111. DOI: 10.1103/PhysRevA.99.022111.

[15] L. Zehnderl. "Ein neuer interferenzrefraktor". In: *Zeitschrift für Instrumentenkunde* 11 (1891).

[16] L. Mach. "Ueber einen interferenzrefraktor". In: *Zeitschrift für Instrumentenkunde* 12 (1892).

[17] Z. Y. Ou and L. Mandel. "Derivation of reciprocity relations for a beam splitter from energy balance". In: *American Journal of Physics* 57.1 (1989), pp. 66–67. DOI: 10.1119/1.15873.

[18] Vittorio Degiorgio. "Phase shift between the transmitted and the reflected optical fields of a semireflecting lossless mirror is $\pi/2$". In: *American Journal of Physics* 48.1 (1980), pp. 81–81. DOI: 10.1119/1.12238.

[19] A. Zeilinger. "General properties of lossless beam splitters in interferometry". In: *American Journal of Physics* 49.9 (1981), pp. 882–883. DOI: 10.1119/1.12387.

[20] N. J. Cerf, C. Adami, and P. G. Kwiat. "Optical simulation of quantum logic". In: *Phys. Rev. A* 57 (3 1998), R1477–R1480. DOI: 10.1103/PhysRevA.57.R1477.

[21] S. Adhikari et al. "Toward secure communication using intra-particle entanglement". In: *Quantum Information Processing* 14.4 (2015), pp. 1451–1468. DOI: 10.1007/s11128-015-0941-0.

[22] Matteo Pasini et al. "Bell-inequality violation by entangled single-photon states generated from a laser, an LED, or a halogen lamp". In: *Phys. Rev. A* 102 (6 2020), p. 063708. DOI: 10.1103/PhysRevA.102.063708.

[23] R. Simon and N. Mukunda. "Universal SU(2) gadget for polarization optics". In: *Physics Letters A* 138.9 (1989), pp. 474–480. DOI: https://doi.org/10.1016/0375-9601(89)90748-2.

[24] R. Simon and N. Mukunda. “Minimal three-component SU(2) gadget for polarization optics”. In: *Physics Letters A* 143.4 (1990), pp. 165–169. DOI: https://doi.org/10.1016/0375-9601(90)90732-4.

[25] B. Neethi Simon, C. M. Chandrashekar, and Sudhavathani Simon. “Hamilton’s turns as a visual tool kit for designing single-qubit unitary gates”. In: *Phys. Rev. A* 85 (2 2012), p. 022323. DOI: 10.1103/PhysRevA.85.022323.

[26] Seymour Lipschutz and Marc Lipson. *Schaum’s Outline of Linear Algebra*. Fourth. McGraw-Hill, 2008. DOI: 10.1036/9780071543538.

[27] Robert T. Beyer John von Neumann and Nicholas A. Wheeler. *Mathematical Foundations of Quantum Mechanics: New Edition*. Princeton Landmarks in Mathematics and Physics, Princeton University Press, 2018.

[28] Arun Kumar Ajoy Ghatak. *Polarization of Light With Applications in Optical Fibers*. SPIE Press, 2011. DOI: 10.1117/3.861761.

[29] Aram Harrow. *Chapter 3: Entanglement, Density Matrices, and Decoherence*. https://ocw.mit.edu/courses/8-06-quantum-physics-iii-spring-2016/resources/mit8_06s16_chap3/. 2016.

[30] Wojciech Hubert Zurek. “Decoherence, einselection, and the quantum origins of the classical”. In: *Rev. Mod. Phys.* 75 (3 2003), pp. 715–775. DOI: 10.1103/RevModPhys.75.715.

Chapter 3

Experimental Reconstruction of Polarization Qubit using Quantum State Interferography

Contents

3.1 Comparison of Quantum State Interferography Technique in Various Interferometric Setups

3.2 Quantum State Interferography for Characterizing Polarization Qubits

3.3 Experimental Implementation of Polarization State Interferography With Mach-Zehnder Interferometer

3.4 Experimental Implementation of Polarization State Interferography With Sagnac Interferometer

3.5 Ensuring Physicality of the Reconstructed Density Matrix in Quantum State Interferography

3.6 Conclusion

3.A Circular Mean and Circular Standard Deviation

3.B Individual Plots for Phase Shift, Average Intensity and Visibility obtained from Sagnac Interferometer

3.C Variation of Fidelity of Qubits with the Mixedness

In the previous chapter, we have presented an interferometric scheme for quantum state reconstruction, in which, an unknown quantum state can be inferred employing the phenomena of quantum interference. We have discussed the theory for characterization of an unknown qubit, whether pure or mixed, from the phase shift, average intensity and visibility of an interference pattern obtained in a single setup without the need to change any experimental setting. The technique named as "Quantum State Interferography" (QSI) determines all the three state parameters $-$ $(|r|, \theta_b, \phi_b)$ in Bloch Sphere representation or (μ, θ, ϕ) in Decoherence representation $-$ that describes any arbitrary qubit, at once by processing a single interference pattern (also known as "interferogram"). When compared to the standard Quantum State Tomography (QST) technique, where a pure and a mixed qubit state reconstruction requires two and three projective measurements respectively, QSI reduces the number of measurements and hence the amount of data acquisition, needed for an unknown state reconstruction, which makes this technique useful for various applications in quantum information processing.

In this chapter, we will explore the practical application of Quantum State Interferography (QSI) technique and will experimentally demonstrate how a two-path interferometer can be used to reconstruct not only pure states but also mixed states of a two-dimensional quantum system. This chapter will present an implementation of this interferometric state determination scheme in polarization degree of freedom of light for characterizing different polarization qubits. A comparative analysis of the performance of QSI executed using two different interferometers: Mach-Zehnder interferometer and Sagnac interferometer (in displaced configuration) would be discussed. Here, we will establish one of the significant features of QSI $-$ its ability to offer a "true single-shot" state estimation technique for qubits, by practically showing that once the setup is aligned, no internal setting needs to be modified in between the incidence of photons in an unknown polarization state and the extraction of the state information.

This chapter will also present the physical realization of the operators $\hat{U}$ and $\hat{R}$, to be placed inside the interferometer in the QSI setup, with the components readily available in an optics lab. Lastly, we will report the fidelity of the experimentally reconstructed density matrices of the polarization qubits, demonstrating that QSI can be effectively implemented for unknown state characterization with high degree of accuracy.

3.1 Comparison of Quantum State Interferography Technique in Various Interferometric Setups

The state determination scheme − Quantum State Interferography (QSI) − characterizes any unknown quantum state using an interferometric setup and analyzing the information obtained from the interference patterns, generated when an ensemble of identical particles in the unknown quantum state evolves through the setup. The experiment, where we implement the QSI technique for inferring an unknown qubit in polarization degree of freedom of light, requires setting up a two path interferometer with operator $\hat{U} = \hat{\sigma}_x$ in one path and operator $\hat{R} = \hat{\Pi}_H$ in the other path. From the interference pattern formed at the end of the interferometer, the quantities such as the phase shift (Φ), visibility (V) and the average intensity $(\bar{I})$ have to be determined in order to reconstruct a density matrix $(\hat{\rho})$ associated with the polarization state incident on the interferometer. Depending on the state parameters of the incident polarization qubit, the intensity distribution as a function of phase, i.e., $I_d(\epsilon)$ changes across the transverse plane of the beam. Here, ϵ is the relative phase between the two paths of the interferometer, which can be controlled using a phase shifter in one of the paths of the interferometer. Alternatively, by introducing a path length difference between the two interfering beams across the detector plane through the alignment of the interferometer itself (in non-collinear geometry), the relative phase ϵ can be varied. Any change in the relative phase (i.e., $\epsilon \pm \Delta\epsilon$) inside the interferometer causes a redistribution of the intensity I_d in the detector plane. Since the phase shift of the interferogram (Φ) is determined as that value of phase which corresponds to maximum intensity (i.e., $I_d(\Phi) = I_d^{(max)}$) in the interference pattern, it is necessary to ensure that during the experiment, any phase shift occurs is solely dependent on the state parameters and not due to any change in the relative phase in the interferometer caused by the external influences or noises. Thus, to obtain the correct phase information, the interferometer needs to remain stable against any potential sources of phase fluctuation.

Hence, the qubit state reconstruction using QSI requires a two path interferometer of any kind, with a stable relative phase. In the previous chapter, we have discussed the theory for polarization state interferography using a Mach Zehnder Interferometer (MZI) setup [1, 2]. One of the disadvantages of using this interferometer is that any external vibration affects the two individual paths of the MZI differently, causing the path difference to change over time. The relative phase between the two interfering beams changes as a result of the path difference changing, which causes the redistribution of the interference pattern (a shift in the interference fringes for the non-collinear configuration of the interferometer) on the detector plane. Thus, when the state parameter (ϕ) is determined using the phase shift Φ obtained from the interferogram formed in a MZI, it gives an inaccurate value since it carries the effect due to the variation in the relative phase (i.e., $\pm\Delta\epsilon$) of the interferometer. Hence, obtaining any consistent phase information from the experiment performed using MZI requires stabilization of the path difference against external vibrations. Therefore, to accurately infer the phase shift (Φ) of the interferogram for reconstructing the state, we prefer those interferometers that are not prone to get affected by external vibrations, e.g., the double slit interferometer and the Sagnac interferometer.

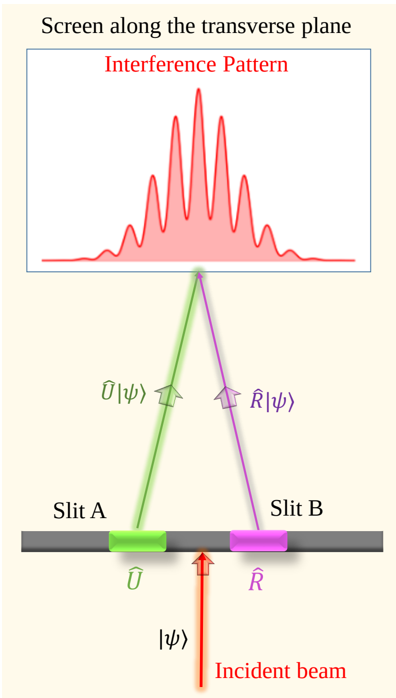

(a) Double Slit Version of QSI: Beam in an unknown quantum state $|\psi\rangle$ is incident on the Double Slit interferometer with slit A and slit B being filled with the operators $\hat{U}$ and $\hat{R}$, respectively.

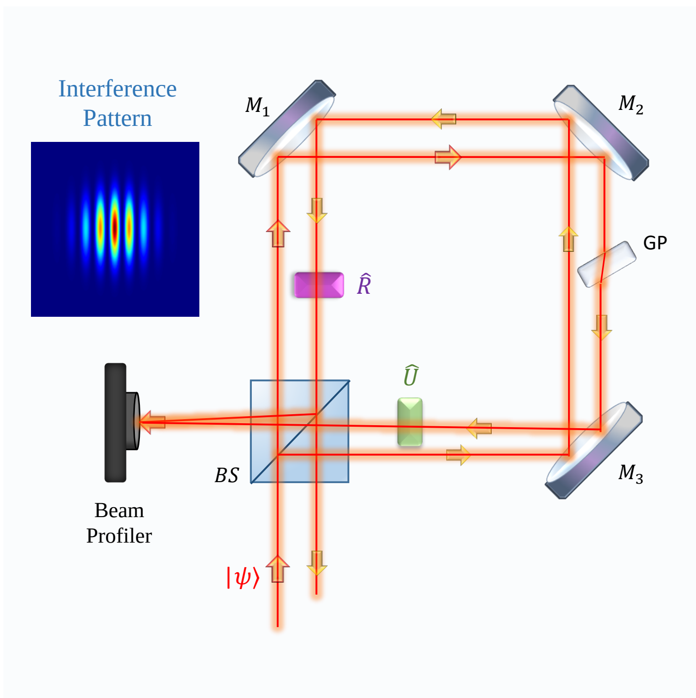

(b) Sagnac Version of QSI: Beam in an unknown quantum state $|\psi\rangle$ is incident on the Displaced Sagnac interferometer with operators $\hat{U}$ and $\hat{R}$ in respective arms. Double slit like interference pattern is obtained by aligning the interferometer in non-collinear geometry, with the overlap between the interfering beams being adjusted by tilting a glass plate GP.

Figure 3.1: Double Slit interferometer and Sagnac interferometer as alternatives to Mach Zehnder interferometer for unknown state characterization using QSI.

Characterization of a polarization qubit using quantum state interferography (QSI) technique can simply be performed using an equivalent double slit set up, with one slit attached with a polarizer having the transmission axis oriented along Horizontal to realize $\hat{\Pi}_H$ (i.e., $\hat{R}$) and the other slit filled with a half-wave plate (HWP) with its fast axis oriented at an angle $\frac{\pi}{4}$ with respect to Horizontal to realize $\hat{\sigma}_x$ (i.e., $\hat{U}$) as shown in Fig: 3.1a. The interference pattern formed here would be insensitive to external noise because the inter-slit distance is robust against any noise [1]. A double-slit interferometer appears to be the ideal device to give an interference pattern with stable fringes from which both visibility and phase shift can be accurately obtained. Average intensity, anyway, does get affected by the change in relative phase. Therefore, the QSI setup designed using a double-slit interferometer can give us consistent information about the state parameters.

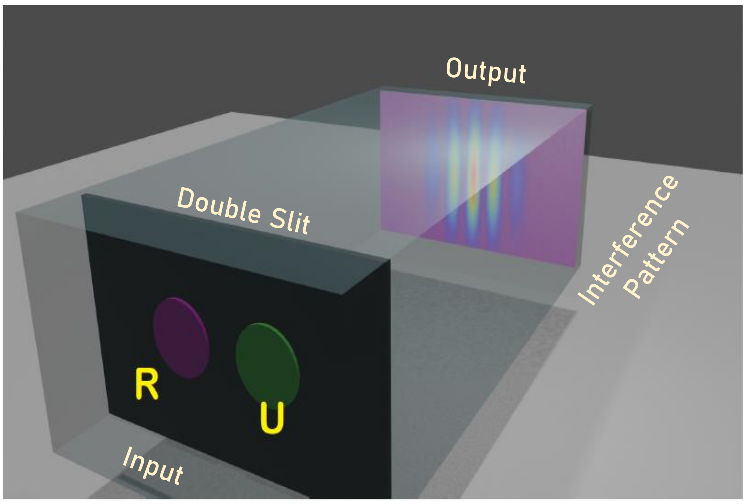

Figure 3.2: Miniaturization of Quantum State Estimating device using double slit interferometer with one slit filled with $\hat{U}$ and the other slit filled with $\hat{R}$. The entire device can be made a few *cm* long by designing the slits of sizes of the order of a few microns. Stream of identical particles in the unknown state (say, $\hat{\rho}$) enters the device through the *Input*, passes through the double slit with the respective operators, forms an interference pattern on a screen within the device. The interference pattern is post-processed using an inbuilt algorithm to produce the state information that is available at the *Output* of the device.

[1] Fringe width (ω) of the interference pattern generated at a distance D from a double slit interferometer with inter slit distance d, when the light at wavelength λ is incident on the interferometer, is given as $\omega = \frac{\lambda D}{d}$ [3].

The slit version of QSI can also miniaturize the state estimating device by having the slit width and the optics (i.e., the polarizer or the wave plate to realize the operators $\hat{R}$ and $\hat{U}$) with sizes of the order of few microns and making the entire module few cm long as shown in Fig **3.2**. To go for a miniaturized setup, it is best to custom design [2] the slits in the slit version of the experiment. But, in that case, the polarizer and the half-wave plate for the double-slit need to be carefully and specifically manufactured and placed appropriately on the slits. Any difference in the shape of the slits and that of the polarizer or the wave plate would lead to additional diffraction effects. Since QSI does not require any change in the experimental setting during the measurement procedure, it has the potential for future development of pocket sized devices with built-in slit interferometer setup along with a post-processing algorithm, using which one can extract the state information from the output when the beam in an unknown state is made incident at the input.

With a Sagnac interferometer, however, we can achieve phase stability against external low frequency vibrations due to its geometry [5]. The displaced configuration of the Sagnac Interferometer is used for setting up the QSI experiment, in order to place the components to realize the operators $\hat{U} = \hat{\sigma}_x$ and $\hat{R} = \hat{\Pi}_H$ in the two different paths of the interferometer. Since the same optical components are used to align both the paths in a displaced Sagnac interferometer (DSI), as shown in Fig: **3.1**b, the path difference here appears to be robust against any external influence [6]. The two interfering beams propagating through the same optics get affected in the similar manner in the presence of any external vibrations and thus, the effect of vibration on the relative phase gets nullified. However, the non-idealness of the optical components being used in the experiment still causes the relative phase to vary slightly. In the displaced Sagnac configuration though the two beams pass through the same optics, they do not hit the optics exactly at the same point due to the displacement between them. Therefore, the effects due to the surface roughness, scratch-dig, presence of dust on the optics, etc. comes into play and modifies the path lengths of the two beams in an uncorrelated manner [3] – causing the relative phase between the interfering beams to vary. However, a two path interferometer in the displaced Sagnac configuration is comparatively more stable than the Mach-Zehnder configuration and is more useful in getting consistent phase information for state determination using QSI.

[2]Such custom designed slits have been in use in experiments such as [4].

[3]This can cause a path length difference up to $100\mu m$.

3.2 Quantum State Interferography for Characterizing Polarization Qubits

As discussed in the last Chapter, inferring any state in a two-dimensional Hilbert space using the Quantum State Interferography technique requires the processing of an interference pattern generated in a two path interferometer setup with operator $\hat{U}$ in one path and operator $\hat{R}$ in the other path. Here, this interferometric state determination scheme is experimentally implemented in the polarization degree of freedom of light, which yields a single-shot method for the characterization of polarization qubits $-$ the technique being named as *polarization state interferography*. The density matrix representation of a general qubit using the parameters (μ, θ, ϕ), where $\mu \in [0,1]$, $\theta \in [0,\pi]$ and $\phi \in [-\pi, \pi)$, is given as follows:

$$\hat{\rho} = \begin{pmatrix} \cos^2\left(\dfrac{\theta}{2}\right) & \dfrac{1}{2}\mu e^{-i\phi}\sin(\theta) \\ \dfrac{1}{2}\mu e^{i\phi}\sin(\theta) & \sin^2\left(\dfrac{\theta}{2}\right) \end{pmatrix} \tag{3.1}$$

Here, μ governs the purity of the state, with $\mu = 1$ representing the pure states. The purity of the state $\hat{\rho}$ is given as,

$$\mathrm{Tr}(\hat{\rho}^2) = 1 - \frac{1-\mu^2}{2}\sin^2(\theta) = \frac{1}{4}\left[3 + \mu^2 + \left(1-\mu^2\right)\cos(2\theta)\right] \tag{3.2}$$

Therefore, if the state parameters (μ, θ, ϕ) are inferred from an experiment, the unknown qubit density matrix $(\hat{\rho})$ can be reconstructed.

We will present the experimental realization of the QSI scheme in an optical setup using two different interferometers to infer the polarization state of the light beam incident on the setup. We first demonstrate the protocol in a setup designed with a Mach-Zehnder Interferometer (MZI) using a light beam at wavelength 778 nm emitting from a Diode laser. We then implement the scheme using 632.8 nm Helium-Neon laser light in a setup with displaced Sagnac interferometer (DSI). The input state would be prepared by placing a half-wave plate at an angle α followed by a quarter-wave plate at an angle β in the path of a horizontally (or vertically) polarized beam before it enters the interferometer and the effectiveness of this interferometeric state determination scheme would be examined by computing the fidelity of the reconstructed state from QSI compared to the prepared state.

3.2.1 Effect of Linear Retarders in Polarization State Interferography:

Any pure state in polarization degree of freedom can be considered as a superposition of two orthogonal linearly polarized components $\{|H\rangle, |V\rangle\}$ with certain amplitudes and a relative phase between them, respectively governed by the parameters $\theta \in [0, \pi]$ and $\phi \in [-\pi, \pi)$ [7].

$$|\psi\rangle = \cos\left(\frac{\theta}{2}\right)|H\rangle + e^{i\phi}\sin\left(\frac{\theta}{2}\right)|V\rangle \tag{3.3}$$

The entire pure state space of polarization qubits can be scanned using a combination of linear retarders [8, 9] – a half-wave plate (HWP) that changes θ and a quarter-wave plate (QWP) that changes θ and ϕ both. HWP and QWP are made up of optically anisotropic materials that uses the phenomena of birefringence to introduce a phase difference δ (also known as *retardance*) between the ordinary and extra-ordinary components of light propagating through them, where $\delta = \delta_h = \pi$ for HWP and $\delta = \delta_q = \frac{\pi}{2}$ for QWP [10].

The 2×2 Unitary operators associated with the evolution through a linear retarder whose fast axis is oriented at an angle ϑ with respect to the horizontal is represented using Jones matrix [11], as the following:

$$\hat{S}_\delta(\vartheta) = e^{-\frac{i\delta}{2}} \begin{pmatrix} \cos^2(\vartheta) + e^{i\delta}\ \sin^2(\vartheta) & \left(1 - e^{i\delta}\right)\sin(\vartheta)\cos(\vartheta) \\ \left(1 - e^{i\delta}\right)\sin(\vartheta)\cos(\vartheta) & \sin^2(\vartheta) + e^{i\delta}\ \cos^2(\vartheta) \end{pmatrix} \tag{3.4}$$

where, δ is the relative phase introduced between the fast and slow axis associated with the retarder. Therefore, the Jones matrix of a HWP and a QWP can be obtained as, $\hat{S}_h = \hat{S}_{\delta=\delta_h=\pi}$ and $\hat{S}_q = \hat{S}_{\delta=\delta_q=\pi/2}$ respectively.

In the experiment designed to demonstrate the performance of the QSI technique, an arbitrary pure state $|\psi(\theta, \phi)\rangle$ is prepared by rotating a HWP and a QWP (at angles α and β respectively) in the path of a horizontally or vertically polarized beam, which, when passed through the QSI setup, generates a unique interference pattern characterized by distinct set of values for the phase shift (Φ), average intensity ($\bar{I}$) and visibility (V), that enables the unique identification of the corresponding state parameters. The unitary operator associated with the combined action of a HWP followed by a QWP is given as,

$$\hat{U}(\alpha, \beta) = \hat{S}_q(\beta)\ \hat{S}_h(\alpha) \tag{3.5}$$

$$\hat{U}(\alpha, \beta) = e^{-i\frac{3\pi}{4}} \begin{pmatrix} \cos^2(\beta) + i\sin^2(\beta) & (1-i)\sin(\beta)\cos(\beta) \\ (1-i)\sin(\beta)\cos(\beta) & \sin^2(\beta) + i\cos^2(\beta) \end{pmatrix} \begin{pmatrix} \cos(2\alpha) & \sin(2\alpha) \\ \sin(2\alpha) & -\cos(2\alpha) \end{pmatrix} \tag{3.6}$$

Fig. 3.3 and Fig. 3.4 show, how the interferometric quantities, i.e., the phase shift, average intensity and visibility of the interference pattern formed in a QSI setup, vary as a function of the parameters (α, β) corresponding to the orientations of HWP and QWP acting on the initial state $|H\rangle$ and $|V\rangle$ respectively.

❑ For $|H\rangle \to HWP(\alpha) \to QWP(\beta)$, The Input State: $|\psi(\theta, \phi)\rangle = \hat{U}(\alpha, \beta)\,|H\rangle$

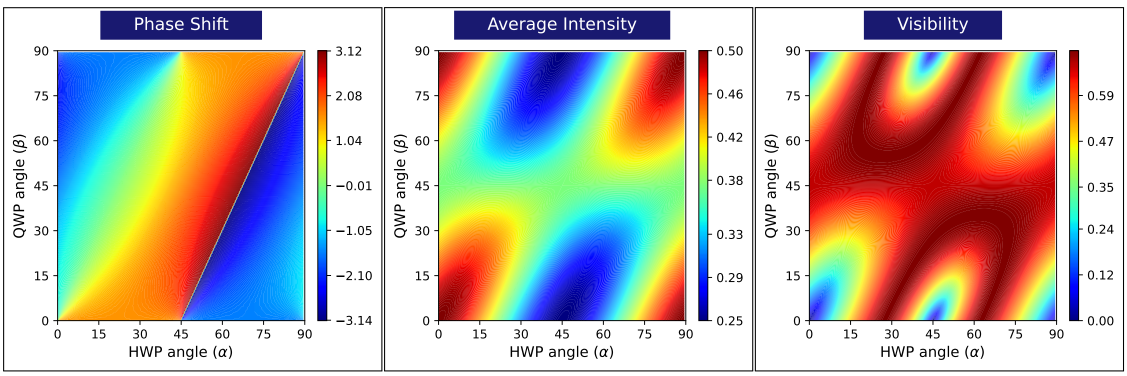

Figure 3.3: Phase Shift (Φ), Average Intensity ($\bar{I}$) and Visibility (V) for the states prepared by rotating a $HWP(\alpha)$ followed by a $QWP(\beta)$ in the path of Horizontally polarized beam.

❑ **For** $|V\rangle \rightarrow HWP(\alpha) \rightarrow QWP(\beta)$, **The Input State:** $|\psi(\theta,\phi)\rangle = \hat{U}(\alpha,\beta)\,|V\rangle$

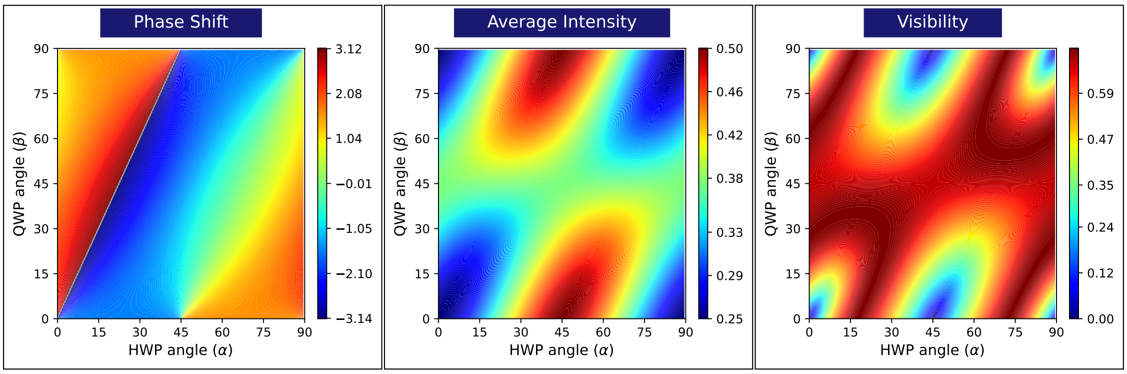

Figure 3.4: Phase Shift (Φ), Average Intensity ($\bar{I}$) and Visibility (V) for the states prepared by rotating a $HWP(\alpha)$ followed by a $QWP(\beta)$ in the path of a Vertically polarized beam.

3.3 Experimental Implementation of Polarization State Interferography With Mach-Zehnder Interferometer

The interferometric state determination scheme, Quantum State Interferography (QSI), is experimentally implemented using a Mach-Zehnder Interferometer (MZI) with the aim to provide a proof of principle demonstration of this technique for the characterization of the polarization state of light. An optical setup is designed with the components (i) to prepare an arbitrary polarization state to be inferred using QSI, (ii) to physically realize the operators $\hat{U}$ and $\hat{R}$ to be placed inside the interferometer and (iii) to record the generated interference pattern that is to be analyzed to infer the input state. Experimental realization of such a state determination scheme requires consistent recording of the interferometric information obtained at the output, when an ensemble of identical particles in an unknown state evolves through the setup, so that the state parameters inferred from the recorded data can be accurately applied to reconstruct the state of individual particles. Therefore, the experimental setup includes some additional components to ensure the stability of different parameters [4] that can impact the interference and hence, the experimental data.

[4] such as the wavelength of the light source, the relative interferometric phase, temperature and stress that slightly changes the polarization of the beam coming out of a polarization maintaining fiber etc.

As already discussed in Section. 3.2, the input state here is prepared by placing a half-wave plate (HWP) at an angle α followed by a quarter-wave plate (QWP) at an angle β in the path of a Horizontally polarized beam, i.e., the input state to the QSI setup can be expressed as $\hat{S}_q(\beta)\hat{S}_h(\alpha)\left|H\right\rangle = \hat{U}(\alpha,\beta)\left|H\right\rangle$. To reconstruct the states of various input polarization, one of the quantities that we need to obtain experimentally is the phase shift (Φ) of the interference pattern as (α, β) varies. Therefore, maintaining a constant phase relationship between the two paths of the interferometer throughout the experiment is necessary, so that the obtained phase shift Φ can be considered to be a function of state parameters only. So, the MZI needs to be phase stabilized against the external vibrations that change the path difference and hence, the relative phase between the interfering beams affecting the interference. The detailed experimental setup with the method of data acquisition and data analysis will be presented in the following.

3.3.1 The Experimental Setup

The beam from a diode laser of wavelength 778 $nm \pm 1$ nm is coupled to a polarization maintaining single mode fiber [12] ($PMSMF$) [$P5-780PM-FC-2$, $Thorlabs$], so that we have a Gaussian transverse profile of the beam [5] coming out of the collimator COL [$F240-FC-780$, $Thorlabs$]. The $PMSMF$ also reduces the pointing fluctuation across the transverse plane of the beam. The APC (Angle Physical Contact) end [6] of the fiber is used to couple the laser beam, for preventing any back-reflection from the fiber-tip from entering the laser cavity [14] and the PC end is used for the collimation. To ensure polarization stability at the collimation side, a polarizing beam splitter (PBS) [$PBS122$, $Thorlabs$] followed by a half-wave plate (HWP) [$WPA03H-810$, $Newlight$ $Photonics$] is placed just before the coupler and the HWP is rotated in small steps to align the input linear polarization (to the coupler) almost parallel to the fast or the slow axis of the polarization maintaining fiber [7]. The output from the collimator is made to be horizontally polarized ($\left|H\right\rangle$) by rotating the output end (i.e., the PC end) of the fiber attached to the collimating lens using a kinematic rotation mount [$K6XS$, $Thorlabs$] to which the lens is mounted.

[5] The field distribution of the fundamental mode for single mode fiber can be approximated to be a Gaussian [13].

[6] This APC connector has an 8° angle-polished fiber end face, used for minimizing the back reflection.

[7] When the polarization of the input beam is not along the fast or slow axis of a polarization maintaining fiber, the polarization of the output is likely to fluctuate with time.

In order to ensure purity of the polarization which may slightly fluctuate due to the effect of temperature and stress on the polarization maintaining fiber [15, 16], a polarizing beam splitter PBS_1 [$PBS122$, $Thorlabs$] is placed in the beam path after the COL. PBS_1 reflects the vertical polarization component (if any) of the beam incident on it, allowing only the Horizontal component to pass through. The variation in polarization after the COL can be monitored by recording the power fluctuation in the reflecting port of PBS_1 using a power meter sensor PM_1 [sensor: $S121C$, $Thorlabs$, meter: $PM100D$, $Thorlabs$].

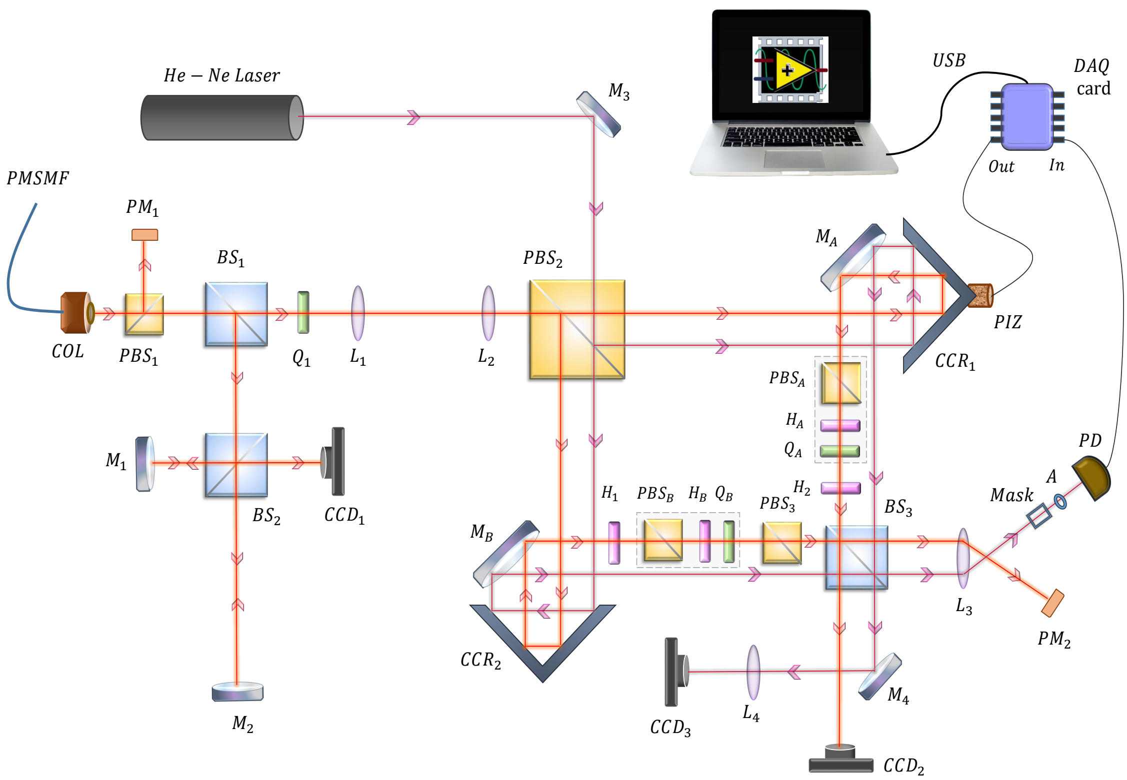

Figure 3.5: Experimental setup for the characterization of the polarization qubit of light using a stabilized Mach-Zehnder Interferometer aligned in non-collinear geometry.

Next, using a non-polarizing 50 : 50 beam splitter BS_1 [$BS014$, $Thorlabs$] a part of the beam (here, the reflected beam) is sent towards a Michelson interferometer that consists of a 50 : 50 beam splitter (BS_2) [$BS014$, $Thorlabs$] and two mirrors (M_1 and M_2) [$BB1-E03$, $Thorlabs$], as shown in Fig. 3.5. The Michelson interferometer is aligned in the non-collinear configuration so that we obtain the interference fringes on the beam profiler CCD_1 [$WinCamD-UCD12$]. The visibility of the interference pattern [8] obtained from the Michelson interferometer is used as a diagnostic tool to notice drifts or jumps in the frequency modes of the Diode laser. Since the polarization is Horizontal [9], any drop in visibility in this reference interference pattern, apart from rapid vibrations of the table, should indicate a multi-mode diode laser output. The two mirrors M_1 and M_2 are placed at different distances from the beam splitter BS_2 to achieve a longer path length difference between the interferometric arms, so that even a slight change in the mode is noticeable.

❑ **Setting up the Mach-Zehnder Interferometer:** The Mach-Zehnder Interferometer (MZI) is formed using two beam splittters – first one being a 2 *inch* polarizing beam splitter (PBS_2) [$PBS512$, $Thorlabs$] and the second one being a non-polarizing $50:50$ beam splitter BS_3 [$BS014$, $Thorlabs$]. The beam in the transmitting port of BS_1 serves as the input to the MZI. A quarter-wave plate Q_1 [$WPQ05M-808$, $Thorlabs$] is placed after BS_1 in the transmitting port, with the fast axis aligned in a way that makes the polarization of the beam in this path circular [10], so that the intensity gets equally divided in the two paths of the MZI after PBS_2. Alternately, a half-wave plate that is aligned to make the horizontal ($|H\rangle$) polarization of the beam diagonal ($|D\rangle$) or anti-diagonal ($|A\rangle$), could have been used instead of the quarter-wave plate Q_1. Then a lens combination L_1 and L_2 (of focal lengths $f_1 = 75\ mm$ and $f_2 = 50\ mm$ respectively) is placed in the beam path before the MZI to expand the beam to an appropriate size, retaining the collimation so that the beam does not hit the edges of any optical component in the setup. While ensuring minimum divergence of the beam, a beam size of about $2.5\ mm$ is achieved.

---

[8] The visibility is maintained to be at $> 99\%$ for 778 nm.

[9] Visibility might crawl not only due to changes in the laser mode, but also when the input polarization changes. Hence, the polarization purity of the input beam to the Michelson Interferometer needs to be ensured.

[10] A QWP (at λ) is a birefringent crystal that introduces a phase shift of $\delta_q = \frac{\pi}{2} = 0.50\pi$ between the e-ray and the o-ray of a beam of wavelength λ propagating through it. In general, QWP with the fast axis aligned at an angle $\frac{3\pi}{4}$ with respect to the horizontal, when acts on $|H\rangle$ gives a right circularly polarized light, $|R\rangle = \frac{1}{\sqrt{2}}\begin{pmatrix}1\\ i\end{pmatrix}$. However, since the QWP used here, i.e., Q_1 is meant for the wavelength $\lambda = 808\ nm$ and we are using it for a beam at wavelength $\lambda_s = 778\ nm$, the retardance at λ_s would be different ($\delta_q = 0.5204\pi$ at $\lambda_s = 778\ nm$) and hence, the angle at which the QWP needs to be rotated to obtain the left circular polarization would be different from $\frac{3\pi}{4}$.

Now, the beam with circular polarization when incident on the MZI, the power of the circularly polarized light is equally divided between the transmitting and reflecting ports of the polarizing beam splitter PBS_2. The two paths of the interferometer with the beams having horizontal and vertical polarization, corresponding to the transmission and reflection from PBS_2, are labelled as $path - A$ and $path - B$ respectively. The beams after PBS_2 are redirected towards the final beam splitter BS_3 using a combination of a mirror (M_A or M_B) [$BB2 - E03$, $Thorlabs$] and a corner cube retro-reflector (CCR_1 or CCR_2) [$PS976M - B$, $Thorlabs$] which is attached to a $3D$ translation stage, as shown in Fig. 3.5. The corner cube retro-reflector (CCR) uses the phenomena of total internal reflection (TIR) to reflect the beam that propagates parallel (within 3 $arcsec$) to the incident beam with a lateral displacement between them (in general), depending on the point where the incident beam hits the CCR [17]. Therefore, CCRs are used instead of mirrors to avoid any angular beam deviation upon translation which might be needed to adjust the path length difference [11]. To be able to control the interferometric path difference, which is very sensitive to environmental noise, we have attached a piezo PIZ [$osi - Stack$, $Piezomechanik$] to the corner cube retro-reflector (CCR_1) in $path - A$. The piezo expands and contracts depending on the voltage provided to it and hence, makes the CCR_1 move forward and backward in $path - A$ resulting in microscopic (about few nm) variations in the path length difference between the two paths of the MZI. The piezo PIZ and the retro-reflector CCR_1 assembly in $path - A$ is used for the active stabilization of the Mach-Zehnder Interferometer (details in SubSec. 3.3.2). The corner cube CCR_2 in $path - B$ compensates for the macroscopic (up to mm) path difference caused by the introduction of the corner cube CCR_1 in $path - A$.

The reflection from a corner cube retro-reflector (CCR), however, introduces an ellipticity in the polarization of the beam. Therefore, the polarizing beam splitters PBS_A and PBS_B [$PBS122$, $Thorlabs$] are placed after the CCRs in $path - A$ and $path - B$ respectively, to ensure the polarization thereafter is Horizontal [12]. The use of polarizing beam splitters after CCR prevents the propagation of any elliptic component that emerges

[11] Use of the CCRs are useful for maintaining a constant path length difference between the two arms of the interferometer, details of which will be presented in SubSec. 3.3.2.

[12] Alternately, the ellipticity in polarization after a CCR can be corrected using a half-wave plate followed by a quarter-wave plate placed in the path of the reflected beam to achieve any linear polarization [18]; Horizontal for this experiment.

due to multiple reflections within the corner cubes CCR_1 or CCR_2. A half-wave plate H_1 $[WPO02 - H - 810 - UM,\ Newlight\ Photonics]$ is placed in $path - B$ before PBS_B and is oriented such that the transmitted power after PBS_B becomes almost equal to the transmitted power after PBS_A. Therefore, the evolution of the beam from the input of PBS_2 to the outputs of PBS_A and PBS_B (considering only the transmission) in the respective paths of the interferometer, can be expressed as

$$|I_s\rangle \otimes |R\rangle \longrightarrow \frac{1}{\sqrt{2}}\left(|A\rangle \otimes |H\rangle + i\,|B\rangle \otimes |H\rangle\right) \tag{3.7}$$

This evolution is effectively similar to the evolution of a horizontally polarized beam through a non-polarizing $50:50$ beam splitter. Here, $|I_s\rangle$ represents the spatial mode associated with the input to PBS_2 from which the signal beam at 778 nm enters the MZI.

❑ **The State Preparation:** The unknown polarization states which are to be reconstructed experimentally using the QSI scheme, would be prepared by acting a half-wave plate (HWP) followed by a quarter-wave plate (QWP) on the horizontal polarization, ideally before the beam enters the MZI. However, if we do so, the presence of the CCRs in the two paths could change the polarization of the beam within the interferometer, resulting in an interferogram different from the intended one that would have been generated with the original prepared state entering the interferometer. Therefore, in this demonstration experiment, we have moved the stage of preparing the polarization states, to the individual paths within the interferometer at a position after the CCRs, ensuring the purity in polarization post transmission through PBS_A in $path - A$ and PBS_B in $path - B$ respectively. A combination of HWP [WPO02-H-810-UM, Newlight Photonics] and QWP [WPO02-Q-810-UM, Newlight Photonics] after the PBS in each path (H_A followed by Q_A in $path - A$ and H_B followed by Q_B in $path - B$), prepares the state to be characterized. The half-wave plates H_A and H_B, when rotated together in synchronization, create a situation equivalent to an effective HWP rotation before an ideal Mach-Zehnder interferometer. Similarly, the quarter-wave plates Q_A and Q_B are rotated together in a correlated manner to change the ellipticity of the polarization.

❑ **Realization of the Operators ($\hat{U}$ and $\hat{R}$):** The half-wave plate H_2 [WPO02-H-810-UM, Newlight Photonics] in the $path-A$ with its fast axis oriented at $\frac{\pi}{4}$ with respect to the horizontal, effectively realizes the operator $\hat{U} = \hat{\sigma}_x$ and the transmission through a polarizing beam splitter PBS_3 [$PBS122$, $Thorlabs$] in the $path-B$ serves as the operator $\hat{R} = \hat{\Pi}_H$. However, note that all the half-wave plates and quarter-wave plates used within the interferometer are meant for 810 nm, but are being used for the beam at wavelength 778 nm. Therefore, exact Jones matrices for the HWP and QWP operations need to be incorporated here, in order to estimate the effect of these wave plates on the polarization of a beam of $\lambda_s = 778\ nm$. According to the specification sheet of the wave plates used (i.e., for H_1, H_2, H_A, H_B, Q_A, Q_B), the phase shifts introduced by the HWP and the QWP are respectively $\delta_h = 179.7°$ and $\delta_q = 90.1°$ at $\lambda = 810\ nm$ and $\delta_h^{'} = 187.6°$ and $\delta_q^{'} = 94°$ at $\lambda_s = 778\ nm$. Therefore, from the Eqn. 3.4, we get the actual Jones matrix for these HWPs and QWPs acting on the 778 nm beam as $\hat{S}_h^{(a)} = \hat{S}_{\delta=\delta_h^{'}}$ and $\hat{S}_q^{(a)} = \hat{S}_{\delta=\delta_q^{'}}$ [13]. The effect of the use of these wave plates ($\hat{S}_h^{(a)}$ and $\hat{S}_q^{(a)}$) on the interferometric information, would be discussed in SubSec. 3.3.3.

❑ **Recording the Interferogram:** Now, the two beams from $path-A$ and $path-B$ are recombined at the beam splitter BS_3 that forms an interference pattern in both the output ports of BS_3. To be able to detect the intensity distribution I_d of the interference pattern as a function of the relative phase ϵ, the Mach-Zehnder Interferometer (MZI) is aligned in the non-collinear configuration that introduces a natural variation of the path difference between the two interfering beams. This produces a non-collinear interference pattern, i.e., alternate bright and dark fringes across the transverse plane of the beam within the beam width, as can be seen from Fig. 3.7. The non-collinearity in the interferometer can be introduced by rotating the mirror M_B at a small angle resulting in an angular deviation of the beam in $path-B$, which would then be merged with the beam coming from $path-A$ applying a slight tilt to the beam splitter BS_3. The interference pattern is recorded using a beam profiler CCD_2 [$WinCamD-UCD15$]. A power meter sensor PM_2 [sensor: $S121C$, $Thorlabs$, meter: $PM100D$, $Thorlabs$] records the average power of the interference pattern, in the other output port of BS_3, the data for which is compared with the average intensity recorded using CCD_2.

[13]The superscript '(a)' represents the actual Jones matrix of the wave plates to be used in this experiment.

❑ **The Collinear and Non-Collinear Interference Patterns:** The intensity distribution $I_d(\epsilon)$ can be recorded by varying the phase (ϵ) either in the time-domain for collinear configuration or in the space-domain for non-collinear configuration of the MZI.

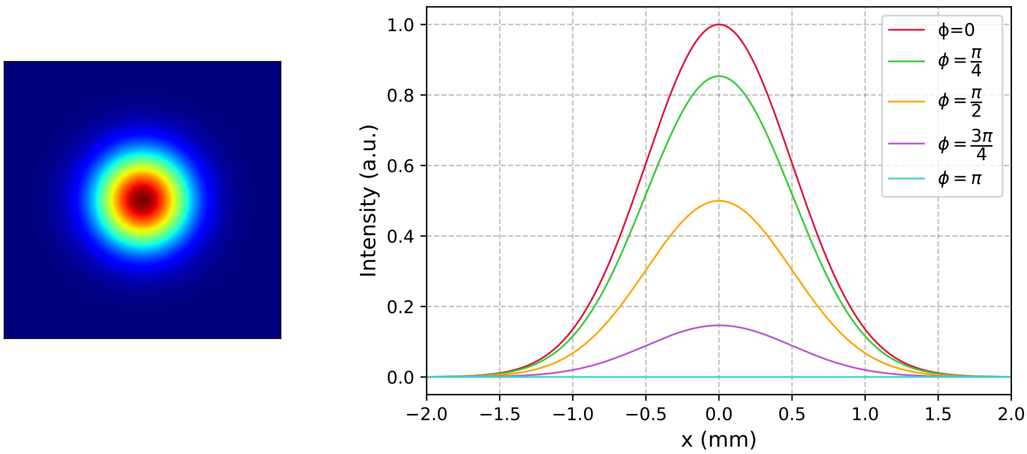

Figure 3.6: **Interference in Collinear geometry of Interferometer:** Collinear Interference pattern formed on the (local) $x - y$ plane when two Gaussian beams, with propagation vectors (along z) being parallel and on top of each other, interfere. As the phase changes from $\varphi = 0$ to $\varphi = \pi$, the intensity after the interference varies from 1 to 0.

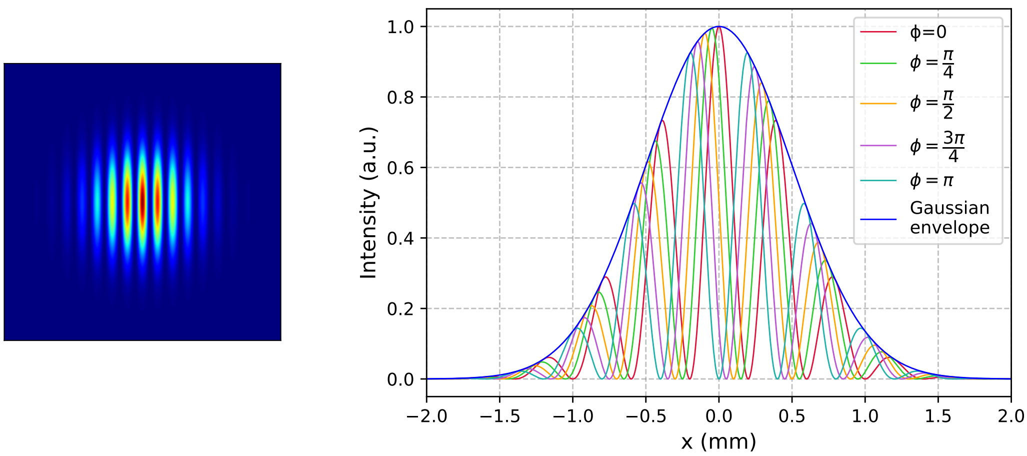

Figure 3.7: **Interference in Non-Collinear geometry of Interferometer:** Non-Collinear Interference pattern formed on the (local) $x - y$ plane when two Gaussian beams, with propagation vectors having an angle between them, overlap and interfere. The number of fringes and the fringe widths vary depending on the angle between the two propagation vectors. As the phase changes from $\varphi = 0$ to $\varphi = \pi$, the average intensity after interference remain the same, only the fringes are redistributed within the Gaussian Envelope.

3.3.2 Phase Stabilization of Mach-Zehnder Interferometer

As mentioned earlier, the relative phase between the two paths of the Mach Zehnder interferometer (MZI) varies over time due to the presence of mechanical and acoustic vibrations that affect the optical components in the two individual paths of the interferometer differently, thereby changing the path length difference with time. To maintain a constant phase relationship between the two paths of the interferometer as a function of time, the MZI is phase-stabilized [19, 20] using a Helium Neon Laser ($He - Ne$) [$LHX1 - 25 - LHP991 - 230,\ Melles\ Griot$] at wavelength $\lambda = 632.8\ nm$. The vertically polarized beam emitting from the $He - Ne$ laser source is made incident on the MZI through the other input port of PBS_2, which is distinct from the one receiving the $\lambda_s = 778\ nm$ beam, also referred to as the *signal beam*. The $He - Ne$ beam propagates through $path - A$ and $path - B$ of the interferometer, without encountering any optics meant for the signal beam (at λ_s). This is achieved by using half-inch wave plates (H_1, H_2, H_A, H_B, Q_A, Q_B) and half-inch polarizing beam splitters (PBS_A, PBS_B, PBS_3) with the mirrors (M_A, M_B) and the corner cube retro-reflectors (CCR_1, CCR_2) being of size two-inch. The choice of different-sized components within the setup ensures a gap of almost 1.2 cm between the beams of the two wavelengths (i.e., 778 nm and 632.8 nm). Now, the $He - Ne$ beams from the two paths are recombined at the final beam splitter BS_3 where they interfere and form non-collinear fringes in both the output ports. The interference pattern (formed with the $He - Ne$ beams) in one of the output ports is used to lock the interferometer at a particular reference value of the relative phase.

The stabilization of the MZI remains unaffected if, in case, the $He - Ne$ beam passes through the optical components (meant for λ_s) that remain in a fixed configuration during the experiment, such as the wave plates H_1 and H_2 and the polarizing beam splitters PBS_A, PBS_B, PBS_3. However, if the $He - Ne$ beam in $path - A$ or $path - B$ travels through the components which need to be rotated during the experiment, like the wave plates H_A, H_B, Q_A, Q_B, it results in a change in the reference interference signal (generated with $He - Ne$ beams) to be used to lock the interferometric phase and consequently disturbs the stabilization. This happens because (i) the rotation of the polarization optics in the beam path changes the polarization of the interfering beams, which would result in a fringe shift as well as a change in the average intensity of the interference pattern,

(ii) the rotation of the wave plates, sometimes, cause an angular deviation of the beam propagating through them, affecting the spatial overlap of the two interfering beams and thus, changes the interference. Hence, while stabilizing the MZI it is ensured that the $He-Ne$ beam does not pass through any of the optics, here the wave plates, that change its configuration during the course of data acquisition.

In order to stabilize the interferometer, the intensity of light ($He-Ne$) after the interference is detected with a fast photo-detector (PD) in one of the output ports of BS_3. Since the interferometer is aligned in non-collinear geometry, any change in the relative phase would only cause a fringe shift across the beam width, without affecting the average intensity of the interference pattern [14], as can be seen from Fig. **3.7**. Hence, the intensity from a small region of a particular fringe, recorded by the photo-detector PD, is used as the *set point* for the stabilization. This is achieved by placing a lens L_3 (focal length, $f_3 = 25\ mm$) in the beam path after BS_3 that magnifies the non-collinear interference pattern, from which a small portion of a specific fringe is selected using a narrow slit (of slit width 60 μm) from a $Mask$, followed by an aperture (A). The slit (in the $Mask$) is aligned along the fringes, so that the intensity recorded at the photo-detector PD after the aperture, becomes sensitive to any change in the phase (which causes a fringe shift) of the interference pattern formed with the $He-Ne$ beam. As a reference to the overall phase shift during the experiment, the $He-Ne$ beam from the other port of the beam splitter BS_3 is directed towards another beam profiling device (Monochrome Line Camera) CCD_3 [$LC100/M$, $Thorlabs$], which records the interference fringes for $He-Ne$ (after a magnification through the lens L_4) at specific intervals of time.

The interference intensity (say, $\mathcal{I}_0$) for 632.8 nm beam recorded by the photo-detector PD after the Mask and the aperture (A), for a particular alignment of the interferometer (say, at time $t = t_0$) with decent visibility, is chosen as the set point for stabilizing the Mach-Zehnder Interferometer (MZI). The phase shift of the interferometer at an instant t is inferred by comparing the detector signal $\mathcal{I}(t)$ collected using a $DAQ\ card$ [$NI\ USB-6003$] (at that instant) with the set point $\mathcal{I}_0$. A software [$NI\ LabView$] based PID algorithm is employed using a computer to correct for the phase difference in real

[14]For the collinear configuration of the interferometer, as the phase changes the intensities at each output port varies.

time [21]. Depending on the error signal $\mathcal{E}(t) = \mathcal{I}(t) - \mathcal{I}_0$, the PID [15] algorithm finds the appropriate voltage to be provided to the piezo (PIZ) to maintain the relative phase of the interferometer at the value associated with the set point. Upon receiving the voltage generated from the $DAQ\ card$, the piezo expands or contracts linearly causing the CCR_1 to move forward and backward in $path - A$ and hence, adjusting the path-length difference or the consequent relative phase within the MZI. The entire arrangement involving PIZ, PD, and the PID algorithm along with the $DAQ\ card$ that receives the voltage from the photo-detector PD and provides the required voltage to the piezo PIZ, forms a closed loop feed-back system for the stabilization of the MZI.

A triangular ramp voltage signal generated from the DAQ card is fed into the piezo PIZ, which scans the path length of $Path - A$ as the piezo expands and contracts depending on the voltage received and therefore, scans the relative phase between the two paths of the interferometer. As the relative phase between the interfering beams is periodically varied, the photo-detector records a sinusoidal voltage signal, of the form shown in Fig. 3.8, associated with the variation of interference intensity with the path difference. This step helps in understanding the possible range for the voltage within which the detected signal (corresponding to $\mathcal{I}(t)$) could vary due to a change in phase from 0 to π, i.e., a change in path length by $\frac{\lambda}{2}$. Adjusting the gain and the offset settings of the photo-detector PD, the sinusoidal signal is aligned symmetrically between $\pm 9.5\ V$ (almost) [16], in order to increase the sensitivity of detection of the photo-detector PD which would help in identifying even small phase changes within the interferometer. Using the optimal values for the co-efficients in the PID algorithm, the phase is locked at a point corresponding to either the rising or falling slope of the sinusoidal signal. Using the stabilization procedure, we can correct for the low frequency vibrations or the noises as the response of the control algorithm is limited by the sampling rate of the $DAQ\ card$ (which is 100 KHz) being used in this experiment.

[15] The PID, which stands for proportional-integral-derivative, is a control algorithm that uses three coefficients associated with each of these operations to generate an optimal response with the aim to minimize the error signal $\mathcal{E}(t)$. The error signal is calculated as the difference $\mathcal{E}(t) = PV - SP$, where PV denotes the process variable that changes over time and SP refers to the set point, the value at which we want to maintain our system.

[16] This specific range is chosen, as the $DAQ\ card$ that receives the voltage signal from the photo-detector, can operate for the voltage range of $\pm$ 10 V.

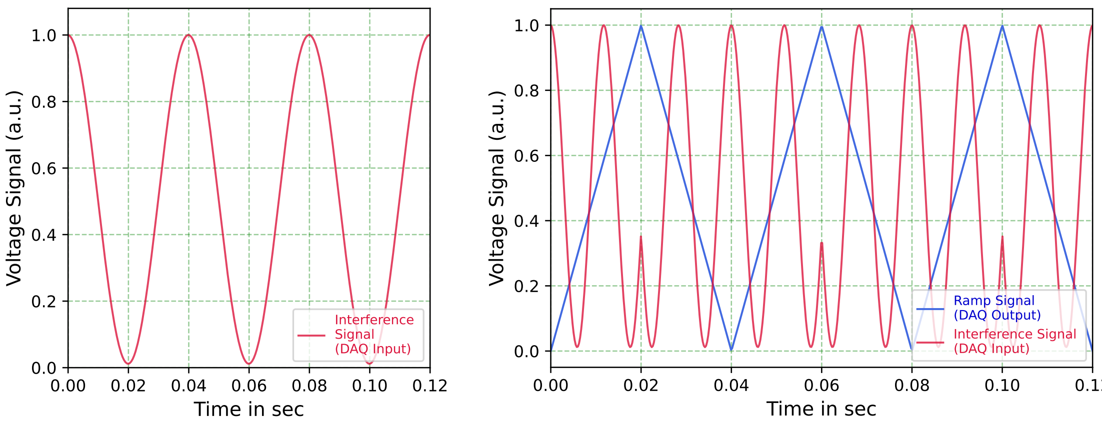

(a) Sinusoidal Voltage Signal recorded by the photo detector (PD) as the path difference of MZI changes monotonically in one particular direction.

(b) Sinusoidal Voltage Signal (in 'magenta') recorded by the photo detector (PD) as the path difference of MZI changes periodically with a Triangular Ramp Voltage Signal (in 'blue') of frequency 25 Hz.

Figure 3.8: Theoretically generated plots representing the Input signal (in 'magenta') and the Output signal (in 'blue') to the *DAQ card* as the interferometric phase varies. Subfigure (a) shows that when the piezo receives a voltage which is either increasing or decreasing, the *DAQ card* records a sinusoidally varying voltage signal with a constant amplitude. Next, Subfigure (b) shows the Input signal (in 'magenta') to the *DAQ card*, received from the photo-detector PD in the absence of any noise, as the relative phase (φ) of the interferometer is varied with a triangular ramp Output signal of the *DAQ card* which is fed to the piezo to scan the path length difference of the MZI. In the theoretical analysis, the detected signal at the photo-detector (PD) after a slit (of width Δx, say) for a particular phase (φ) of the interferometer is replicated by generating a non-collinear interference pattern from a Gaussian enveloped cosine function given as $F_{nc}(x) = A \exp\left(-\frac{(x-m)^2}{2\sigma^2}\right)(1+\cos(kx+\varphi))$, with an array of x variables $X = \{x_i\}$ where $i \in [1, N]$ and then taking the sum of the elements $x_i \in [m - \frac{\Delta x}{2},\ m + \frac{\Delta x}{2}] \subset X$ about the mean (m) of the Gaussian[17].

[17] Here, we have chosen $N = 4000$ with $x_1 = -2$ and $x_N = +2$, giving $x_{i+1} - x_i = 0.001$. Therefore, the collection of intensity data through the $60\mu m$ slit width can be mimicked by selecting a slice Δx of the array X, where $\Delta x = 60$ about the mean $m = 0$ of the Gaussian having amplitude $A = 1$ and width $\sigma = 0.5$.

3.3.3 Effect of the Use of Wave Plates meant for Different Wavelength

In the experimental implementation of the interferometric state determination scheme − *polarization state interferography*, the polarization states that are to be reconstructed using the QSI technique, are prepared by acting a half-wave plate (HWP) H_A or H_B followed by a quarter-wave plate (QWP) Q_A or Q_B in the path of a Horizontally polarized beam[18]. The prepared state $|\psi(\alpha,\beta)\rangle$ with the fast axis of the HWPs aligned at α and the fast axis of the QWPs aligned at β with respect to horizontal, is given as

$$|\psi(\alpha,\beta)\rangle = \hat{S}_q(\beta)\ \hat{S}_h(\alpha)\ |H\rangle \tag{3.8}$$

$$= e^{-\frac{i\pi}{4}} \begin{pmatrix} \cos^2(\beta) + i\sin^2(\beta) & (1-i)\sin(\beta)\cos(\beta) \\ (1-i)\sin(\beta)\cos(\beta) & \sin^2(\beta) + i\cos^2(\beta) \end{pmatrix} e^{-\frac{i\pi}{2}} \begin{pmatrix} \cos(2\alpha) & \sin(2\alpha) \\ \sin(2\alpha) & -\cos(2\alpha) \end{pmatrix} \begin{pmatrix} 1 \\ 0 \end{pmatrix}$$

where $\hat{S}_h(\alpha)$ and $\hat{S}_q(\beta)$ are respectively the Jones matrices of the HWP and the QWP obtained from Eqn. 3.4, with $\delta_h = \pi$ and $\delta_q = \dfrac{\pi}{2}$. Therefore, we get the input polarization state as

$$|\psi(\alpha,\beta)\rangle = \frac{-i}{\sqrt{2}} \begin{pmatrix} \cos(2\alpha) - i\cos(2\alpha - 2\beta) \\ \sin(2\alpha) + i\sin(2\alpha - 2\beta) \end{pmatrix} \tag{3.9}$$

As this state evolves through the operators $\hat{U} = \hat{\sigma}_x$ realized using another half-wave plate (H_2) with the fast axis at angle $\dfrac{\pi}{4}$ and $\hat{R} = \hat{\Pi}_H$ realized using a polarizing beam splitter (PBS_3) in the two paths A and B of the interferometer respectively, the polarization state at one of the output ports of the final beam splitter (BS_3) is obtained as,

$$|\psi(\alpha,\beta)\rangle_d = \frac{1}{2}\left(\hat{U} + e^{i\epsilon}\hat{R}\right)|\psi(\alpha,\beta)\rangle \tag{3.10}$$

$$|\psi(\alpha,\beta)\rangle_d = \frac{1}{2}\left(\hat{S}_h\left(\frac{\pi}{4}\right) + e^{i\epsilon}\ \hat{\Pi}_H\right)\hat{S}_q(\beta)\ \hat{S}_h(\alpha)\,|H\rangle \tag{3.11}$$

[18] For the state preparation, the wave plates in $path-A$ and $path-B$ of the interferometer are rotated in synchronization to achieve an effective wave plate rotation on the horizontally polarized beam incident on the setup.

Here, ϵ represents the relative phase between the two paths of the interferometer.

Now, as discussed in SubSec. 3.3.1, the wave plates that are used in the experiment are meant to behave ideally for the wavelength $\lambda = 810\ nm$. However, we have setup the experiment with a light source at $\lambda_s = 778\ nm\ (\pm\ 1\ nm)$. The corresponding phase shifts introduced (between the e-ray and o-ray of the beams) by the wave plates at λ_s are given by $\delta_h^{'} = 187.6^\circ \equiv 1.04222\pi$ and $\delta_q^{'} = 94^\circ \equiv 0.52222\pi$ [19]. These variations in the retardance values (i.e., $\delta_h^{'}$, $\delta_q^{'}$) would cause the wave plates to deviate from their ideal behavior. As a result, the states prepared in this experiment i.e., $|\psi^{(a)}(\alpha,\beta)\rangle = \hat{S}_q^{(a)}(\beta)\ \hat{S}_h^{(a)}(\alpha)\,|H\rangle$ would differ from the one shown in Eqn. **3.9**, where $\hat{S}_h^{(a)}$ and $\hat{S}_q^{(a)}$ are the Jones matrices of the wave plates representing their actual behavior at wavelength λ_s, obtained from Eqn. **3.4** with $\delta_h^{'}$ and $\delta_q^{'}$ respectively.

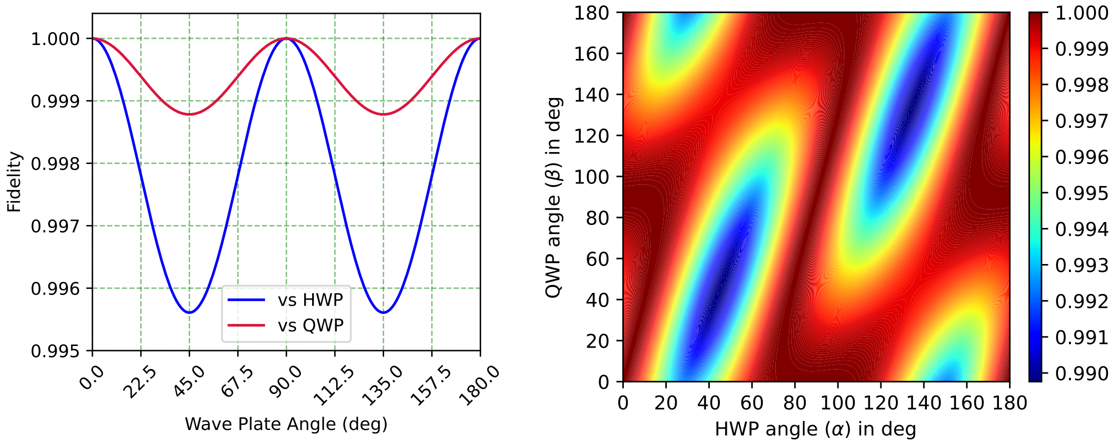

Figure **3.9**: Fidelity of the states produced by the action of the wave plates (meant for $\lambda = 810\ nm$) on Horizontal polarization of the beam at wavelength $\lambda_s = 778\ nm$, as compared to the states that would have been produced with the ideal wave plates acting on Horizontal polarization. The plot [in left] shows the fidelity of the prepared states by the action of the HWP or the QWP only, with the other one being absent. The fidelity $F(\alpha)$ or $F(\beta)$ for HWP or QWP alone appears to be symmetric about their fast and slow axis. However, if a QWP is placed after the HWP on the path of the Horizontally polarized beam at λ_s, the fidelity varies arbitrarily as shown in the plot [in right].

[19]The numbers are noted from the specification sheet of the wave plates, i.e., the HWP [WPO02-H-810-UM, Newlight Photonics] and QWP [WPO02-Q-810-UM, Newlight Photonics].

To quantify the effect of these wave plates on the 778 nm beam, we find the overlap of the prepared states $\left|\psi^{(a)}(\alpha,\beta)\right\rangle$ on the states expected with the ideal wave plate behaviors, i.e., on $|\psi(\alpha,\beta)\rangle$. The plot for the fidelity of the prepared states as functions of wave plate angles α and β can be seen in Fig. 3.9, where the fidelity is computed as the following

$$F(\alpha,\beta) = \left|\left\langle\psi(\alpha,\beta)\middle|\psi^{(a)}(\alpha,\beta)\right\rangle\right|^2 \tag{3.12}$$

$$F(\alpha,\beta) = \left|\langle H|\,\hat{S}_h^\dagger(\alpha)\;\hat{S}_q^\dagger(\beta)\;\hat{S}_q^{(a)}(\beta)\;\hat{S}_h^{(a)}(\alpha)\,|H\rangle\right|^2 \tag{3.13}$$

❑ Effect of the Use of Arbitrary Wave Plates on Experimental Results:

In the quantum state interferography (QSI) scheme, an unknown qubit is characterized using the phase shift, average intensity and visibility obtained from an interference pattern generated when the state evolves through a two path interferometer with operators $\hat{U}$ in one arm and $\hat{R}$ in the other arm. The experimental demonstration of the scheme in an optical setup, involves the preparation of polarization qubits for different combinations of the angles α and β, respectively associated with the orientations of a HWP and a QWP acting on Horizontally polarized beam. The intensity distribution, produced at the end of the interferometric setup, as a function of wave plate angles can be expressed as the following,

$$I_d(\epsilon,\alpha,\beta) = \left\|\frac{1}{2}\left(\hat{U}+e^{i\epsilon}\hat{R}\right)|\psi(\alpha,\beta)\rangle\right\|^2 \tag{3.14}$$

$$\begin{aligned} I_d(\epsilon,\alpha,\beta) = \frac{1}{16}\,[\;& 6+\cos(4\alpha)+\cos(4\alpha-4\beta) \\ &+2(\sin(4\alpha)-\sin(4\alpha-4\beta))\;\cos(\epsilon) \\ &+4\sin(4\alpha-2\beta)\;\sin(\epsilon)\;] \end{aligned} \tag{3.15}$$

where $|\psi(\alpha,\beta)\rangle = \hat{S}_q(\beta)\;\hat{S}_h(\alpha)\,|H\rangle$ is the state prepared with ideal wave plates in the experiment. The state parameters of this polarization state needs to be inferred by processing the interference pattern given above.

For a particular combination of wave plate angles (say, α, β), the phase shift (Φ) is obtained at that value of ϵ which maximizes $I_d(\epsilon, \alpha, \beta)$. This value of Φ is computed by solving for the ϵ, which satisfies the following conditions.

$$\left.\frac{\partial I_d(\epsilon, \alpha, \beta)}{\partial \epsilon}\right|_{\epsilon=\Phi} = 0 \quad \text{and} \quad \left.\frac{\partial^2 I_d(\epsilon, \alpha, \beta)}{\partial \epsilon^2}\right|_{\epsilon=\Phi} < 0 \tag{3.16}$$

The average intensity ($\bar{I}$) is obtained by integrating $I_d(\epsilon, \alpha, \beta)$ over all possible phases ϵ,

$$\bar{I}(\alpha, \beta) = \int_{\epsilon} I_d(\epsilon, \alpha, \beta)\; d\epsilon = \frac{1}{16}\left[6 + \cos(4\alpha) + \cos(4\alpha - 4\beta)\right] \tag{3.17}$$

Visibility (V) is obtained by computing the maximum and minimum intensities $I_d^{(max)}(\alpha, \beta)$ and $I_d^{(min)}(\alpha, \beta)$ respectively, from $I_d(\epsilon, \alpha, \beta)$ and then applying the values to the following expression,

$$V(\alpha, \beta) = \frac{I_d^{(max)}(\alpha, \beta) - I_d^{(min)}(\alpha, \beta)}{I_d^{(max)}(\alpha, \beta) + I_d^{(min)}(\alpha, \beta)} \tag{3.18}$$

However, in the experiment all these quantities ($\Phi, \bar{I}, V$) are inferred from the best fit parameters of the non-collinear interference pattern recorded using the beam profiler (CCD_2) after the interferometer.

Now, since here the wave plates behave differently from the ideal ones for the beam at wavelength λ_s, the same angles α, β of the HWP and QWP respectively would prepare a state different from $|\psi(\alpha, \beta)\rangle$ given in Eqn. 3.9. The use of a HWP, with the fast axis oriented at $\frac{\pi}{4}$ with respect to horizontal, to physically realize the operator $\hat{U} = \hat{\sigma}_x$ would also affect the overall evolution operator associated with the QSI setup. Therefore, due to the arbitrary behavior of the wave plates at λ_s, the polarization state at one of the output ports of BS_3 is obtained as,

$$\left|\psi^{(a)}(\alpha, \beta)\right\rangle_d = \frac{1}{2}\left(\hat{S}_h^{(a)}\left(\frac{\pi}{4}\right) + e^{i\epsilon}\,\hat{\Pi}_H\right)\hat{S}_q^{(a)}(\beta)\;\hat{S}_h^{(a)}(\alpha)\,|H\rangle \tag{3.19}$$

This would result in an interference pattern $I_d^{(a)}(\epsilon, \alpha, \beta)$, which is different from the one obtained using the ideal wave plates for the same (α, β) combination (i.e., $I_d(\epsilon, \alpha, \beta)$) as expressed in Eqn. 3.15. Consequently, the interferometric quantities that are derived from the interference pattern to infer the state parameters, would deviate from the ideal results. A comparison of the phase shift (Φ), average intensity $(\bar{I})$ and visibility (V) obtained from $I_d^{(a)}(\epsilon, \alpha, \beta)$ with the ideal values for various wave plate angles, is illustrated in Fig. 3.10 and Fig. 3.11.

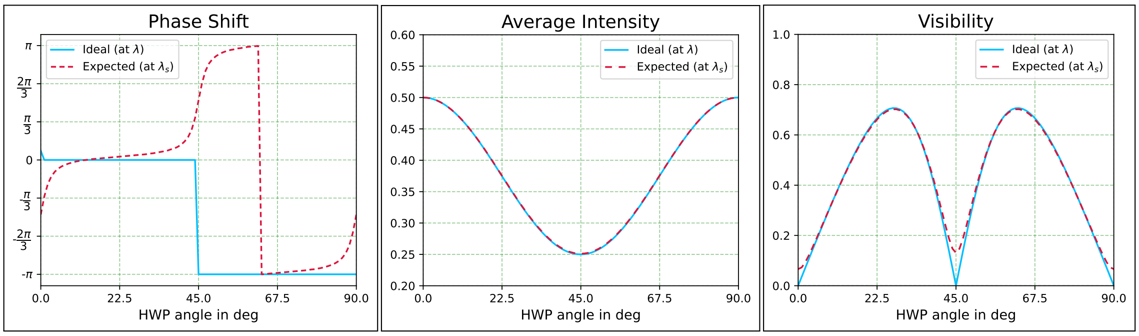

Figure 3.10: The *expected values* of the interferometric quantities with the use of HWP meant for $\lambda = 810$ nm (while the QWP is absent) on beam of wavelength $\lambda_s = 778$ nm, along with the associated *ideal results*. Due to the non-ideal behavior of the wave plate for the beam of wavelength 778 nm, the phase shift of the interferogram appears to be affected the most, while the average intensity remains unaffected when compared with the ideal results. The visibility obtained with 778 nm beam does not go to zero.

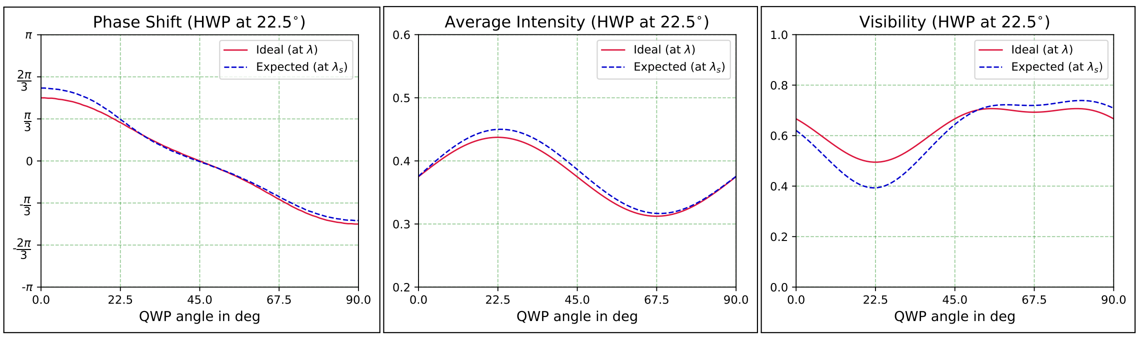

Figure 3.11: The *expected values* of the interferometric quantities obtained for the non-ideal behavior of the wave plates, that are meant for $\lambda = 810$ nm, acting on the beam of wavelength $\lambda_s = 778$ nm along with the associated *ideal results*, for a condition when the HWP is aligned at $\alpha = 22.5°$ with respect to horizontal and the QWP angle (β) is varied.

3.3.4 Experimental Method

After aligning the setup, the Mach Zehnder Interferometer (MZI) is stabilized at a specific intensity recorded by the photo detector (PD) corresponding to a particular path length difference of the interferometer. It is ensured that during the entire process of data acquisition the stabilization is not reset or disturbed. At first, in absence of the quarter-wave plates Q_A and Q_B, the two half-wave plates H_A and H_B are synchronously rotated in steps of $5°$ starting from $0°$ to $90°$. For each orientation of the HWP, the images of three different interference patterns are simultaneously captured (within 100 $micro\ sec$) using the devices CCD_1, CCD_2 and CCD_3. These three images include the interference patterns – (i) produced by the 778 nm beam after BS_2 in the Michelson interferometer, (ii) produced by 778 nm beam at one of the output ports of BS_3 in the MZI, (iii) produced by 632.8 nm $He-Ne$ beam at the other output port of BS_3 in the MZI, respectively referred to as, (i) Mode Reference, (ii) Signal, and (iii) Phase Reference. Here, the mode reference and the signal images are captured with a resolution of $16-bit$ [DataRay, $WinCamD-UCD15$], while the phase reference image is captured with a resolution of $8-bit$ [ThorCam, $LC100/M$, $Thorlabs$]. All the images consists of 30 rows corresponding to the respective intensity profile along the horizontal. For each HWP angle α, 30 images of each interference pattern are captured at an interval of 0.5 sec. The whole procedure is repeated for different HWP angles.

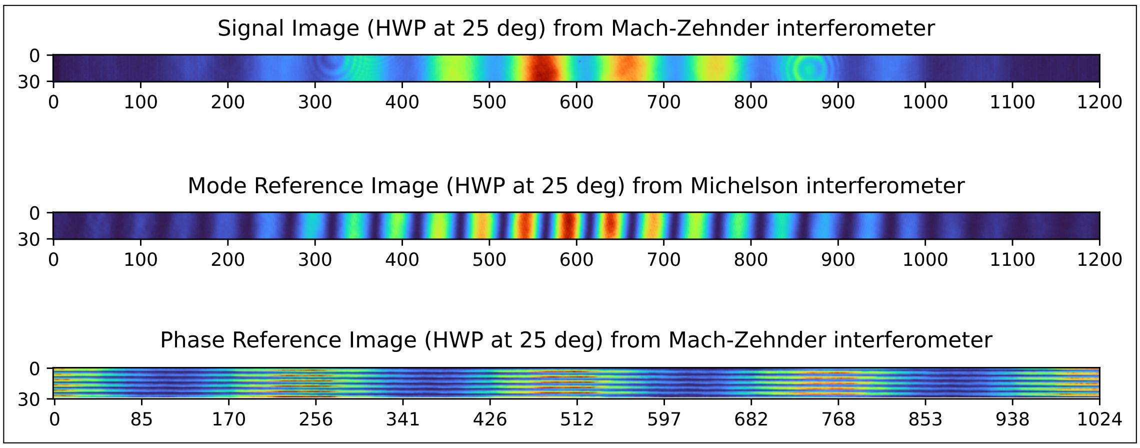

Figure 3.12: The 15-th image of all the three interference patterns captured for the condition when the fast axis of the half-wave plates (H_A, H_B) are oriented at $25°$ with respect to horizontal, in absence of the quarter-wave plates. Few diffraction patterns generated due to dusts on the optics or the sensor in the beam path, can be seen in the signal image.

Even though the Mode Reference images are captured simultaneously while recording the signal data (in MZI) for various HWP orientations, it is important to note that these interference patterns generated in the Michelson interferometer, are not influenced by the HWP angles. The mode reference data is acquired concurrently with the signal data to verify if there has been any changes in the frequency mode of the source. From each of the mode reference images, we find the visibility of the interference pattern by fitting the image data to a non-linear model $F_{nc}(x)$ as expressed in Eqn. 3.20. During the entire data collection process for various HWP angles (30 images per angle), the visibility of the interference patterns produced in the Michelson interferometer is observed to vary as presented in the plot in Fig. 3.13. The visibility is mostly maintained above 0.97, except for few images in between (the 360-th to 540-th images), as can be seen from the plot. For these images, the visibility slowly drops in the beginning and then fluctuates within 0.98 to 0.85 (approx), respectively corresponding to the mode crawl and mode hop of the laser. This shift in the laser mode, for that particular time, would impact the corresponding signal interference in the MZI as well, which in turn would alter the values of the phase shift, average intensity and visibility to be extracted from the interferogram to infer the polarization state.

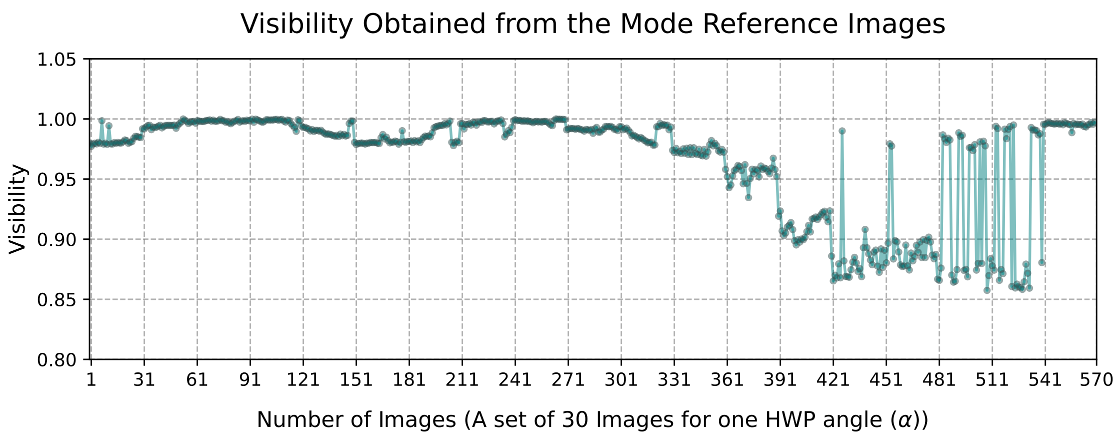

Figure 3.13: Visibility of the interferograms produced in the Michelson interferometer for monitoring the mode stability of the laser source, while acquiring the interferometric data from the MZI for the states prepared by rotating the HWPs (in absence of the QWPs) from $0°$ to $90°$ in steps of $5°$. Each set of consecutive 30 visibility values are obtained from the reference images, that are captured almost at the same time (within 100 *micro sec*) while capturing the signal interference pattern in MZI, for a particular HWP angle.

Next, in presence of the quarter-wave plates Q_A and Q_B, the combination of the wave plates i.e., (H_A, Q_A) and (H_B, Q_B) in the two different paths of the interferometer, are rotated in sync to prepare different polarization states. The quarter-wave plate angle (β) is varied in steps of $10°$ from $0°$ to $180°$ for various orientations (α) of the half-wave plates H_A and H_B. For each combination of (α, β), the entire procedure of capturing three different images [20] using three beam profiling devices is repeated.

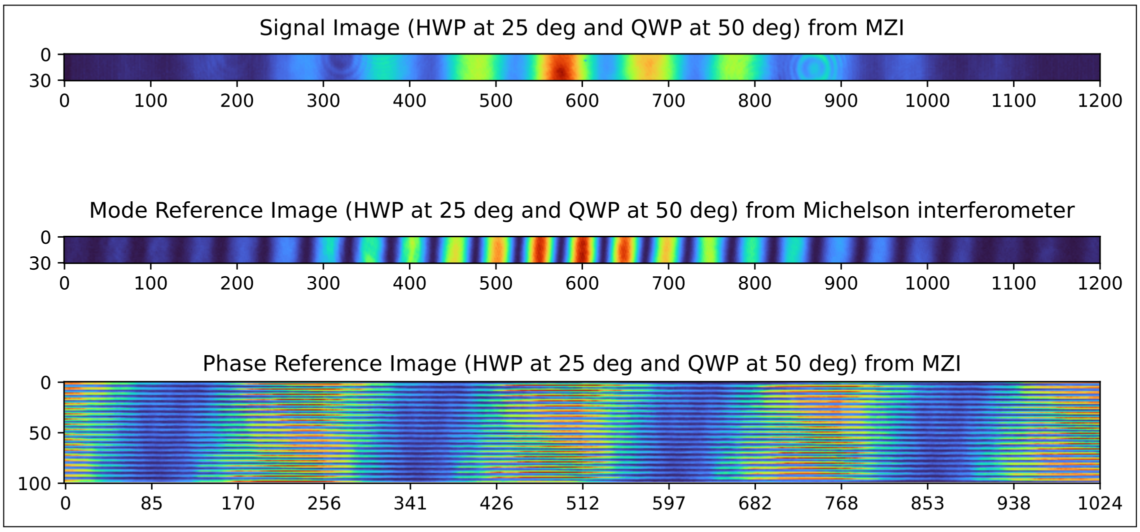

Figure 3.14: The 15-th image of all the three interference patterns captured for the condition when the half-wave plates (H_A, H_B) are oriented at $25°$ and the quarter-wave plates (Q_A, Q_B) are oriented at $50°$, with respect to horizontal. Few diffraction patterns due to dusts along the side fringes of the Signal Image can be seen. The phase reference image is captured with 8-bit CCD, hence the resolution is comparatively low. [21]

The intensity profiles of the interference patterns captured for different orientations of the HWPs and QWPs (also, for different angles of HWPs in absence of QWPs) are fit to a non-linear profile expressed with the formulae,

$$F_{nc}(x) = B + A \exp\left(-\frac{(x - x_m)^2}{2\sigma^2}\right)(1 + v \cos(k\ x + \varphi)) \tag{3.20}$$

[20] Here, the phase reference images consist of 100 row profiles, compare to 30 row profiles for the signal and mode reference images.

[21] Along with the vertical fringes, few horizontal lines are formed in the phase reference image, which could be due to the diffraction of the beam hitting the edge of any of the optical components meant for 778 nm beam or from the edge of the CCRs.

Here, $F_{nc}(x)$ is a Gaussian weighted cosine function with the parameters $[B, A, x_m, \sigma, v, k, \varphi]$. The parameter A represents the amplitude of the $1D$ Gaussian envelope (along x) centered at x_m having the standard deviation σ and B represents the background noise [22]. The visibility of the fringes within the Gaussian envelope are represented by v and the fringe constant k is related to the fringe width (ω) as $\omega = \dfrac{2\pi}{k}$. The parameter φ represents the phase shift, i.e., the position of the maximum intensity within the envelope [23].

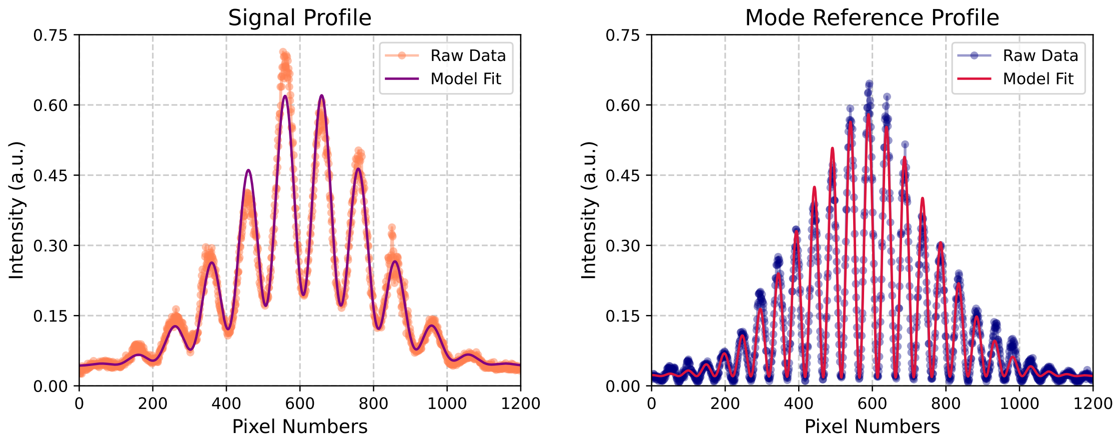

Figure 3.15: Profile fit of the 15-th row of Signal Image and Mode Reference Image captured when the half-wave plates are oriented at 25° in absence of quarter-wave plates.

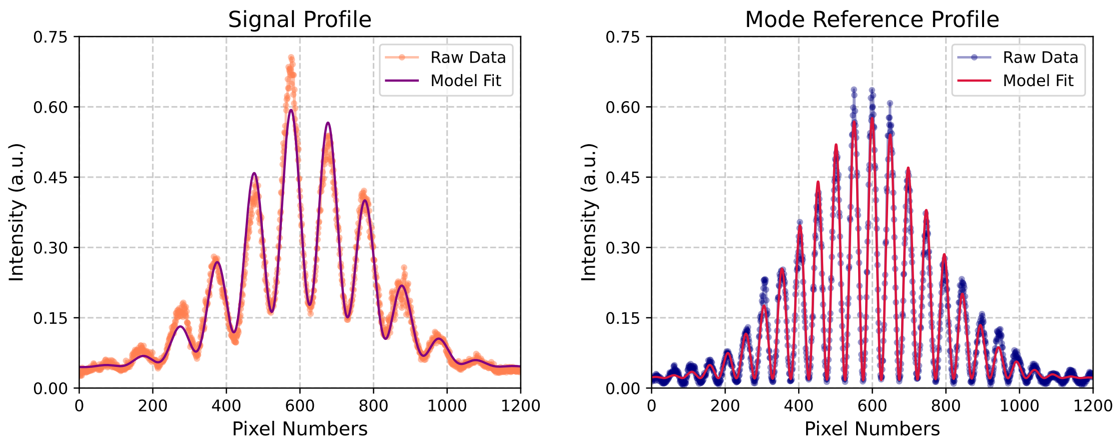

Figure 3.16: Profile fit of the 15-th row of the Signal Image and the Mode Reference Image captured when the half-wave plates are oriented at 25° and the quarter-wave plates are oriented at 50°.

[22] Background noise could be due to the ambient lights or the read-out noises of CCDs.

[23] The visibility and the phase shift can also be obtained by identifying the peaks and dips of the interference profile where ever peaks are prominent.

Note that, the model $F_{nc}(x)$ given in Eqn. **3.20** assumes the interference of two Gaussian beams having the same intensities and hence, produces an interference profile symmetric about the mean of the Gaussian (x_m) apart from the asymmetry arising due to the fringe shift with the phase (φ). However, in the experiment, the two interfering beams coming from $path - A$ and $path - B$ of the MZI have different intensities because of the presence of the projector to H ($\hat{\Pi}_H$) in $path - B$ of the interferometer, which introduces a loss in the beam coming from that path. As a result, the intensity profile that we obtain experimentally, appears to be asymmetric. This can be seen from the plots in Fig. **3.15** and Fig. **3.16**, presenting the non-linear model fitting to the intensity profile of a specific row of the signal and mode reference images taken for a particular α and β value.

The phase shift (Φ), visibility (V) and average intensity ($\bar{I}$) of the Signal Interference patterns for a particular prepared state with a combination of (α, β), are obtained from the best fit parameters φ, v and A respectively. The presence of dusts in the beam path on the sensor or on the optical components, changes the wavefront of the beam and creates diffraction patterns that affect the corresponding intensity profile. This effect can be observed in the signal images of both Fig. **3.12** and Fig. **3.14**. Therefore, to minimize the effect of dusts on the final results, we individually fit the intensity profiles for each of the 30 rows in the image instead of fitting the data from entire image. We then calculate the mean and standard deviation corresponding to a parameter over 30 values. So, for a particular (α, β) combination we get 30 mean values and 30 standard deviations for each of the parameters obtained from 30 images. The final result is reported as the mean (over 30 images) of the means (over 30 horizontal rows of an image) and the error in the final result is calculated as the rms value (over 30 images) of the standard deviations (over 30 rows of an image) after taking into account the error (if any) due to the change in the laser mode. Here, any change in the mode is inferred by examining the visibility of the Mode Reference interference patterns, obtained from the best best fit parameter v after the reference profile fitting. For finding the mean and the standard deviation of the phase shift Φ, for a particular state, we have used the circular statistics, discussed in Appendix. 3.A. The change in the relative phase of the Mach-Zehnder Interferometer while acquiring the Signal data for a prepared state is inferred from the corresponding Phase Reference images. With the active stabilization of the Mach-Zehnder Interferometer discussed in SubSec. 3.3.2, here we aim to achieve a phase uncertainty within $\frac{\pi}{16}$.

3.3.5 Experimental Results and Discussions

The experiment for the demonstration of quantum state interferography (QSI) scheme is performed with the aim to reconstruct different polarization qubits prepared in the lab, using the experimentally obtained values of phase shift (Φ), average intensity ($\bar{I}$) and visibility (V) of an interference pattern generated in a Mach-Zehnder interferometer (MZI) when the state evolves through the operators $\hat{\sigma}_x$ and $\hat{\Pi}_H$ in the respective paths of the interferometer. The interferometric data are collected for the two following situations:

(i) When the polarization states are prepared by rotating only the half-wave plates (H_A and H_B) in the paths of horizontally polarized beam, in absence of the quarter-wave plates (Q_A and Q_B), i.e., for the prepared states $|\psi(\alpha)\rangle$.

(ii) When the polarization states are prepared by rotating the quarter-wave plates (Q_A and Q_B) for a specific orientation of the half-wave plates (H_A and H_B) on the paths of horizontally polarized beam, i.e., for the states $|\psi(\alpha, \beta)\rangle$.

In the following, the quantities Φ, $\bar{I}$ and V are plotted as functions of HWP angle α and QWP angle β, for different polarization states evolving through the QSI setup. The dots and bars in the plots respectively represent the experimentally obtained values (the mean) and the corresponding uncertainty in determining the value (the statistical error). Theoretical expectations obtained by incorporating the actual behavior of the wave plates for 778 nm beam (SubSec: 3.3.3) are presented with the solid lines, whereas the dashed lines represent the ideal values computed considering the ideal behavior of the wave plates.

❑ **The Interferometric Quantities (Φ, $\bar{I}$, V) as Functions of Half-Wave Plate Angles (α) :** The resultant polarization state, when the HWP with the fast axis oriented at an angle α acts on the horizontal polarization, is given as

Ideal WP Behavior:
$$|\psi(\alpha)\rangle = \hat{S}_h |H\rangle = \begin{pmatrix} \cos(2\alpha) \\ \sin(2\alpha) \end{pmatrix} \tag{3.21}$$

Actual WP behavior:
$$\left|\psi^{(a)}(\alpha)\right\rangle = \hat{S}_h^{(a)} |H\rangle \tag{3.22}$$

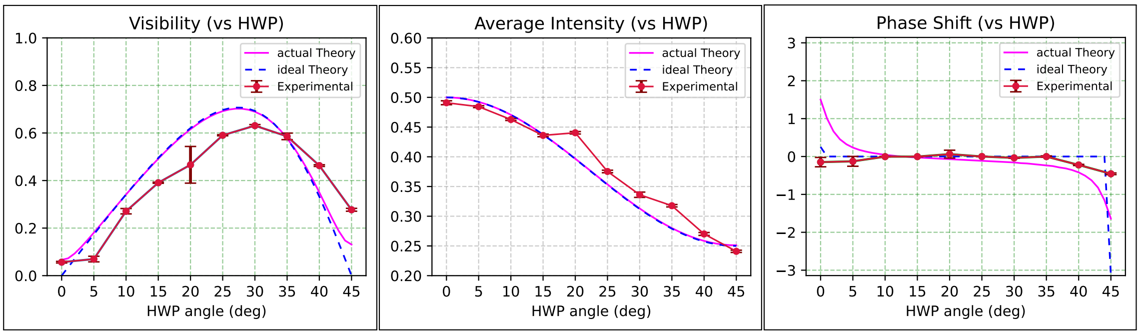

Figure 3.17: Visibility (V), Average Intensity ($\bar{I}$) and Phase Shift (Φ) of the states prepared for various orientations (α) of the HWP (in absence of QWP).

From Fig. 3.17, it can be seen that the experimentally obtained phase shift (Φ) for different polarization states corresponding to the variation of HWP angles α, is obtained to be a straight line about 0. This agrees with the expectation, since rotation of a HWP does not introduce any relative phase (ϕ) between the orthogonal components of polarization. At HWP angle 0° and 45° the phase is not well defined, since these values correspond to the states near the poles of the Bloch sphere. The state parameter θ can be inferred from the experimentally obtained visibility (V) and average intensity ($\bar{I}$). However, the visibility appears to have same values for two HWP angles. Since, the average intensity is monotonic, it can distinguish between the values of θ for which the visibility is the same.

❑ The Interferometric Quantities (Φ, $\bar{I}$, V) as Functions of Quarter-Wave Plate Angles (β) for a Specific Half-Wave Plate Angle (α):

The resultant polarization state, when a HWP oriented at an angle α followed by a QWP oriented at an angle β acts on the horizontal polarization, is given as

Ideal WP Behavior: $$|\psi(\alpha,\beta)\rangle = \hat{S}_q\hat{S}_h\,|H\rangle = \frac{-i}{\sqrt{2}}\begin{pmatrix}\cos(2\alpha) - i\cos(2\alpha-2\beta)\\ \sin(2\alpha) + i\sin(2\alpha-2\beta)\end{pmatrix} \tag{3.23}$$

Actual WP behavior: $$\left|\psi^{(a)}(\alpha,\beta)\right\rangle = \hat{S}_q^{(a)}\hat{S}_h^{(a)}\,|H\rangle \tag{3.24}$$

The experimental results determined by processing the interference patterns generated with the rotation of QWP for various HWP angles, are shown below.

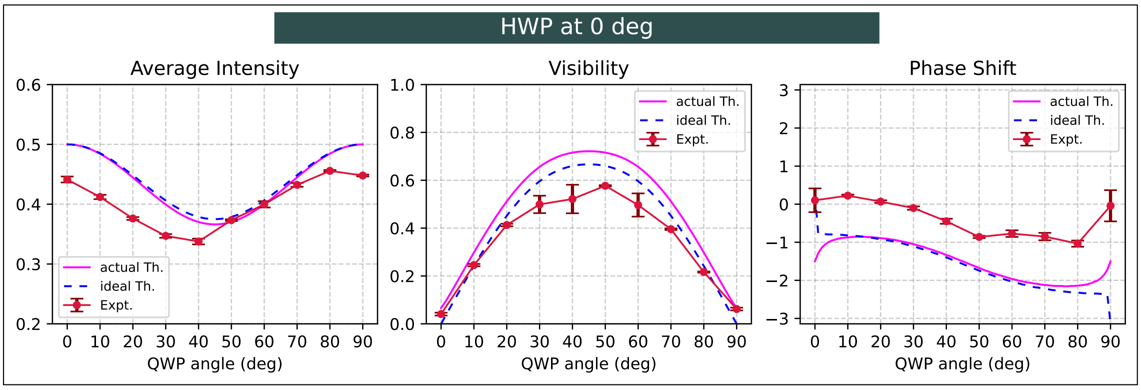
HWP at 0 deg
Average Intensity
Visibility
Phase Shift
actual Th.
ideal Th.
Expt.
QWP angle (deg)

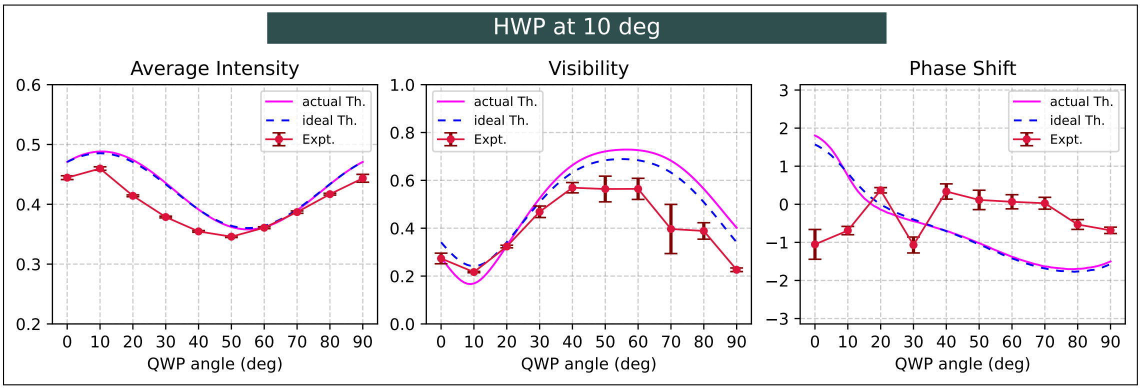
HWP at 10 deg
Average Intensity
Visibility
Phase Shift
actual Th.
ideal Th.
Expt.
QWP angle (deg)

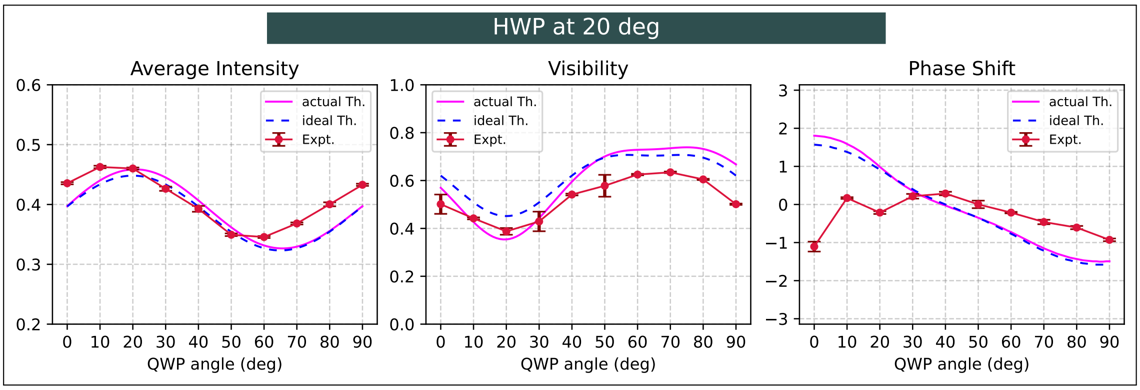
HWP at 20 deg
Average Intensity
Visibility
Phase Shift
actual Th.
ideal Th.
Expt.
QWP angle (deg)

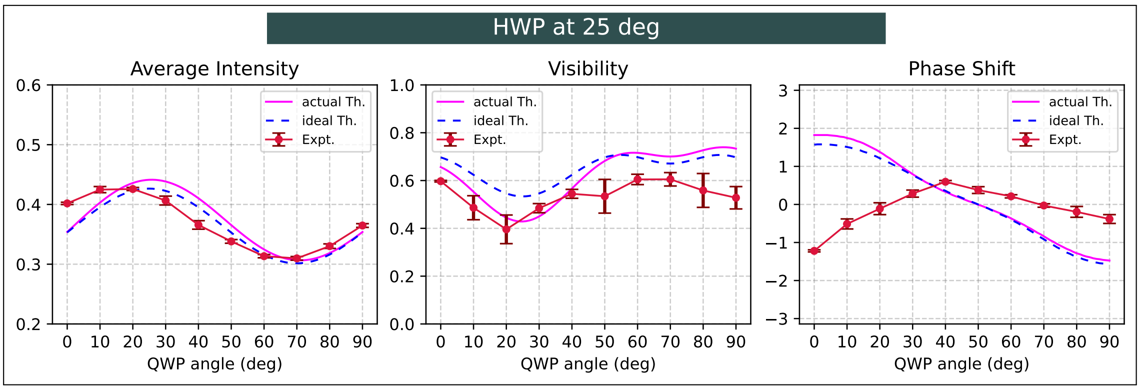
HWP at 25 deg
Average Intensity
Visibility
Phase Shift
actual Th.
ideal Th.
Expt.
QWP angle (deg)

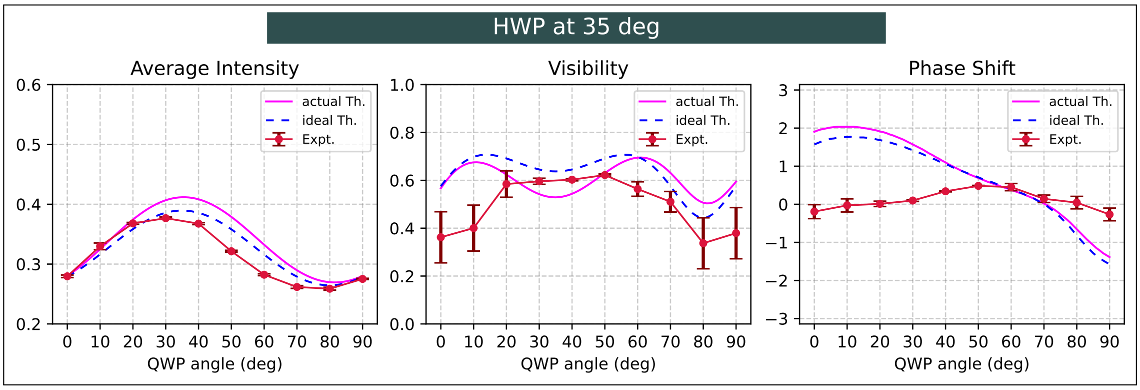

In the above, the plots of the interferometric quantities $(\bar{I}, V, \Phi)$ − both experimentally obtained (dots and bars) and the theoretical expectations (solid lines) − are shown for various polarization states prepared for different combinations of HWP angle α and QWP angle β. Though we have collected the data by varying the QWP from $0°$ to $180°$ for a fixed HWP angle, here we have only reported the interferometeric quantities $(\bar{I}, V, \Phi)$ for the QWP angles in the range $0°$ to $90°$, to maintain the uniqueness of the plots.

From the experimental results it can be seen that the average intensity and visibility obtained for various (α, β) combinations almost agrees with the theoretical expectations, but the phase shifts show a deviation from the expected values, for most of the cases. The disagreement in the results is majorly due to the instability in the frequency mode of the laser being used in the experiment, that keeps on varying during the course of data acquisition in an uncorrelated manner, affecting the interference. Apart from that there are some phase noises arising from the residual fluctuation of phase even after stabilization. The mismatch in the visibility with the QWP angle is due to the deviation of the behaviors of the wave plate for $\lambda_s = 778\ nm$ beam from the ideal ones (at λ). Again, any fluctuation in polarization from the collimation end, changes the overall power of the beam incident on the MZI and hence affects the experimentally obtained average intensity.

However, note that the half inch wave plates in the state preparation stage, in the two paths of the interferometer, are rotated manually in sync using a kinematic rotation mount with the least count of $2°$. A slight misalignment [24] of the fast axis of the wave plates from the desired angle or any relative error in the orientations of the wave plates in the

[24] which is possible because the orientation of a wave plate is subject to the visual acuity and judgment of the observer.

two paths, would produce a different interference pattern than the intended one. This in turn would affect the quantities $\bar{I}$, V and Φ processed from the interference patterns. Also, additional care needs to be taken while attempting to manually rotate the wave plates so that the $He - Ne$ beam does not get blocked accidentally, because this could reset the stabilization and therefore, the phase reference would be lost.

Since here, the obtained values of $\bar{I}$ and V matches well with the theoretical expectations (apart from few exceptions), this setup designed using a MZI could be used to correctly infer the state parameter θ, or even the mixedness parameter μ when an unknown mixed state is incident on the setup. However, since we could not control the interferometric phase in a consistent manner, this design can not be considered as a precise tool to infer the phase shift (Φ) and hence, the state parameter ϕ of the unknown quantum state. Therefore, based on the experimental results obtained from the QSI setup depicted in Fig. **3.5**, we can not provide an accurate complete description of the unknown qubit within the Bloch sphere. Nonetheless, the projection of the unknown qubit on the z-axis can be accurately determined. Hence, for inferring the parameter (ϕ) in a meaningful manner to accurately demonstrate the interferometric state determination scheme, we choose a different setup designed with a more stable source and interferometer, as discussed in Sec. 3.4.

In summary, polarization states prepared by acting a half-wave plate followed by a quarter-wave plate on the path of a horizontally polarized beam, when evolves through the operators $\hat{U}$ and $\hat{R}$ in the two paths of a MZI, gives the phase shift, average intensity and visibility of the interference patterns as function of the wave plate angles. To consistently determine the phase shift, the path difference of the MZI is stabilized and maintained throughout the experiment. However, the factors such as the mode instability of laser and the use of the wave plates designed for a different wavelength than that of the source, make the experimental results dependent on various parameters other than the HWP and QWP angles used for state preparation. This necessitates correction of the collected data against the possible sources of errors which makes the data analysis process for this experiment a cumbersome one. Due to the non-ideal nature of the components used, the phase shift and visibility may not be accurately applied to estimate the polarization. Nevertheless, this experiment demonstrates that a Mach-Zehnder Interferometer can, in principle, be used to determine an unknown polarization state employing the QSI technique.

3.4 Experimental Implementation of Polarization State Interferography With Sagnac Interferometer

In the last section, we have shown how a Mach Zehnder Interferometer (MZI) setup can be used to characterize the qubits in polarization degree of freedom of light. The interference pattern, generated at the end of the MZI when a beam in an arbitrary polarization state evolves through the setup, is analyzed to get the quantities such as phase shift (Φ), average intensity ($\bar{I}$) and visibility (V), which are further processed to infer the polarization state. Consistent determination of the state parameters for different polarization states, however, requires phase-stabilization of the MZI against vibrations that change the path difference and hence, the relative phase between the two paths of interferometer. To avoid the stabilization process and to remove the effects of some of the non-ideal parameters that influence experimental results as discussed in SubSec. 3.3.5, we choose to perform the experiment in a different setup with a stable source, here, Helium-Neon laser source ($He-Ne$) at 632.8 nm using the wave plates meant for that particular wavelength.

In order maintain a constant phase relationship between the two arms of the interferometer, i.e., to get stable interference fringes, we prefer the equivalent two path interferometers that are not prone to vibrations such as the Double Slit Interferometer, the Sagnac Interferometer etc.. In principle, for a double-slit interferometer, we can place a half-wave plate (as $\hat{\sigma}_x$ operation) in one slit and a polarizer with transmission axis along horizontal (as $\hat{\Pi}_H$ operation) in the other slit and record the interference pattern. However, designing such a setup appears to be challenging due to the manufacturing difficulties of slit-sized (of the order of few tens of μm) wave plates. Therefore, for the experiment in lab, we choose to use a Sagnac interferometer as described in Fig. 3.18.

3.4.1 The Experimental Setup

Beam from a Helium Neon Laser source [$LHX1-25-LHP991-230$, $Melles\ Griot$] at wavelength $\lambda = 632.8\ nm$ is incident on a $50:50$ non-polarizing beam splitter (BS) [$BS013$, $Thorlabs$] that forms a Sagnac Interferometer with the three mirrors M_1, M_2, M_3 [5101, $Newport$]. The output of $He-Ne$ laser used in this experiment is linearly polarized, which is oriented in a way that the emergent beam from the source is vertically polarized. The Sagnac interferometer is aligned in displaced configuration instead of common path configuration in order to place the optical components corresponding the operators $\hat{U} = \hat{\sigma}_x$ and $\hat{R} = \hat{\Pi}_H$ in the two different paths. The beam from the laser source when incident on the interferometer i.e., on the beam splitter BS, gets transmitted and reflected with equal intensities into the two paths of the interferometer. The paths are labelled as $path - A$ and $path - B$ that respectively correspond to the propagation of the beams in the clock-wise and counter clock-wise directions. A half-wave plate HWP $[WPH05M - 633,\ Thorlabs]$ with the fast axis oriented at an angle $\frac{\pi}{4}$ is placed in the clock-wise arm (i.e., $path - A$) to realize the operator $\hat{\sigma}_x$. A polarizing beam splitter PBS $[PBS122,\ Thorlabs]$ is placed in the counter clock-wise arm (i.e., $path - B$) to effectively realize $\hat{\Pi}_H$, when only transmission through PBS is considered. Alternatively, a polarizer with the transmission axis along the horizontal could have been used as the $\hat{\Pi}_H$ operator.

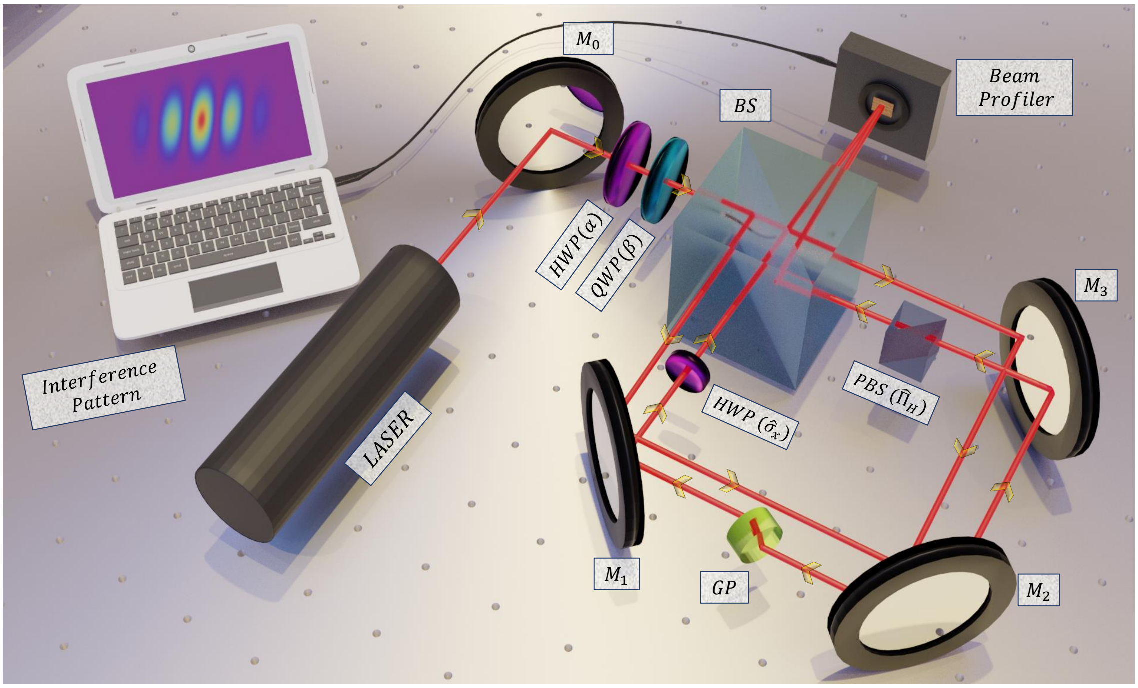

Figure 3.18: Experimental setup for Polarization State Interferography using a Non-Collinear Displaced Sagnac Interferometer.

In the displaced Sagnac configuration, the beams from the clock-wise and anti clock-wise paths recombine at the same beam splitter BS and interferes in both the sides of the BS – one in which the beam profiler is shown in Fig. 3.18 and the other being the one from which the $He - Ne$ beam enters the interferometer. The beam profiler (CCD) [$WinCamD - UCD15$] is placed in that output port to which the beam emerging from $\hat{R}$ (in $|H\rangle$) is reflected and the beam emerging from $\hat{U}$ is transmitted to avoid any change in the polarization due to reflection from the beam splitter [25]. The Displaced Sagnac Interferometer (DSI) is aligned in the non-collinear geometry [22] to directly obtain the intensity distribution as a function of the relative phase on the detector plane. This non-collinearity is achieved by tilting the beam splitter BS slightly, which results in a double-slit like interference pattern on the beam profiler. However, in the displaced Sagnac geometry, it is typically not possible obtain the non-collinear fringes while ensuring a good overlap between the two beams at the same time. Therefore, a glass plate GP, also known as parallel window [$WG40530-B$, $Thorlabs$] is placed in one of the paths (here, in $path-A$) and is tilted to achieve a displacement of the beam in that path to ensure maximum overlap of the two non-collinear beams at the beam profiler. A glass plate of thickness t (here, $t = 3\ mm$), when tilted at angle when θ_i with respect to the incident beam, causes a lateral displacement a in the beam propagating through it.

$$a = \frac{t\ \sin(\theta_i - \theta_r)}{\cos(\theta_r)} \tag{3.25}$$

where, θ_r is the angle of refraction, that satisfies the Snell's law $n_i \sin(\theta_i) = n_r \sin(\theta_r)$, with n_i and n_r being the refractive indices of the incident and refracted medium. Here, $n_i = 1$ for air and $n_r = n$ for the glass window.

The input polarization state is prepared by placing a half-wave plate ($HWP(\alpha)$) [$WPH05M - 633$, $Thorlabs$] at an angle α followed by a quarter-wave plate ($QWP(\beta)$) [$WPQ05M - 633$, $Thorlabs$] at angle β in the path of a vertically polarized beam coming from the Helium-Neon Laser source, before it enters the interferometer. In contrast to MZI, here we place the state preparation optics before the interferometer [26]. Both these

[25] Although, ideally we expect the non-polarizing beam splitters to have no effect on the polarization d.o.f. of light, the real beam splitters usually have a polarization dependent reflection and transmission coefficients, i.e., $t_p \neq t_s$ and $r_p \neq r_s$. Also, reflection from the beam splitter, in general, adds a relative phase between Horizontal (p-polarized) and Vertical (s-polarized) components of polarization, introducing an ellipticity in the polarization of the reflected beam.

[26] This could not be done in MZI because of the presence of the CCRs within the interferometeric arms that adds an elliptic component to the beams reflecting from it.

HWP and QWP are mounted on motorized rotation stages [$PRM1/MZ8$, $Thorlabs$, operated with $KDC101$, $Thorlabs$] which allows for precise control over the angle of rotation of the wave plates for the state preparation. The use of motorized mounts also enables us to perform the entire experiment, i.e., preparation of various polarization states and collection of interferometric data from the beam profiler for each state, through a simple software code ($LabView$) on a computer eliminating the need to adjust anything manually. Hence, the implementation of the displaced Sagnac Interferometer (DSI) greatly simplifies the experimental setup as well as the data collection process for reconstructing an unknown state using the QSI technique.

3.4.2 Experimental Method

Different polarization states that are to be reconstructed using the quantum state interferography (QSI) technique, are prepared by rotating the HWP and the QWP in the path of the vertically polarized beam emitting from the $He-Ne$ source (at $\lambda = 632.8\ nm$). Here, we aim to obtain the phase shift (Φ), visibility (V) and average intensity ($\bar{I}$) of the generated interference patterns, as a function of the HWP angle α and the QWP angle β. The polarization state, after the action of the wave plates on vertical polarization, that serves as the input to the displaced Sagnac Interferometer (DSI) is given by,

$$|\psi(\alpha,\beta)\rangle = \hat{S}_q(\beta)\ \hat{S}_h(\alpha)\ |V\rangle = \frac{e^{i\pi}}{\sqrt{2}}\begin{pmatrix}\sin(2\alpha-2\beta)+i\sin(2\alpha)\\ \\ \cos(2\alpha-2\beta)-i\cos(2\alpha)\end{pmatrix} \tag{3.26}$$

For a fixed angle α of the HWP, the QWP is rotated in steps of 2° and for each (α,β) combination, 5 images are recorded using the beam profiler at an interval of 500 ms. All the images are recorded using a 16-bit ADC for a cross-section of 600×600 pixels, with the pixel size being 4.4 μm. Before processing each image, the ADC values of all the pixels are normalized with respect to the maximum for 16-bit ADC, which is 2^{16}. Considering the interference patterns are generated along $x-y$ plane, we find that the recorded fringes are slightly tilted, almost at an angle 13.7 deg as can be seen in Fig. 3.19a. Hence, at first the images are rotated about their centroid (C_x, C_y) to orient the fringes along the horizontal i.e., along x. The horizontal and vertical centroids of an image are computed as,

$$C_x = \frac{\sum_{x=1}^{N}\sum_{y=1}^{N} x\, I_{xy}}{\sum_{x=1}^{N}\sum_{y=1}^{N} I_{xy}} \quad \text{and} \quad C_y = \frac{\sum_{x=1}^{N}\sum_{y=1}^{N} y\, I_{xy}}{\sum_{x=1}^{N}\sum_{y=1}^{N} I_{xy}} \tag{3.27}$$

Here, I_{xy} is the value of the pixel in the y-th row and the x-th column of the recorded image, with $N = 600$. In other words, I_{ij} represents the (i, j)-th element of the image matrix, where $i, j \in [1, 600]$.

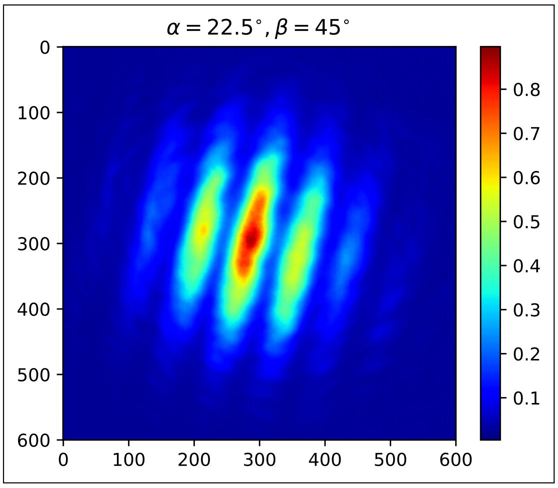

(a) Raw Image

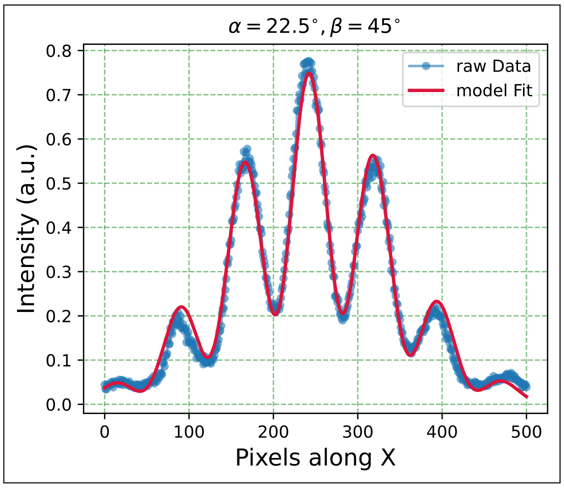

(b) Single Row of the Rotated Image

Figure 3.19: Interferometric data collected for the polarization state prepared by acting the HWP at 22.5° followed by the QWP at 45° on the state $|V\rangle$. **(a)** The image of the interference pattern formed after the QSI setup as captured by the Beam Profiler. The interference fringes are slightly tilted. **(b)** Intensity distribution across one of the horizontal slices of the image generated after rotating the raw image by 13.7 deg about its centroid and the non-linear model fit to the intensity distribution from which phase shift, average intensity and visibility would be inferred.

For each image, we select 101 horizontal slices about the vertical centroid of the rotated image (i.e., about $C_y^{(r)}$) and fit the data for each of the slices with a model which is a Gaussian weighted cosine function, as given below.

$$F_{nc} = B_f + A_f \exp\left(-c_f(x_f - m_f)^2\right)\left(1 + v_f \cos(k_f x_f + \phi_f)\right) \tag{3.28}$$

Here, x_f is the array of pixel along x direction, chosen symmetrically about the horizontal centroid (i.e., $C_x^{(r)}$) of the rotated image, for which the fitting function is applied. In the fitting model, B_f represents the background noise, A_f represents the amplitude of the Gaussian envelope centered at m_f having standard deviation of $\sigma_f = \sqrt{\frac{1}{2c_f}}$. The fringe width is given by $\omega_f = \frac{2\pi}{k_f}$. The quantities v_f and ϕ_f respectively represents the visibility and the phase shift of the interference pattern. From a single image we get 101 such parameters i.e., $[B_f, A_f, m_f, c_f, k_f, v_f, \phi_f]$ which are obtained by fitting the experimentally recorded intensity distribution across each row of the image (one of them is shown in Fig. 3.19b) to the above model.

We weigh the data, obtained from an image, with the vertical Gaussian profile (W_y) and then take the mean and standard deviation of each of the parameters over the 101 slices. For the determination of the vertical Gaussian profile, at first we evaluate the intensity distribution $I_y = \{I_{y_a}\}$ across the y direction of the rotated image, where I_{y_a} is the mean intensity of a given row y_a [27]. We then fit the data $I_y = \{I_{y_a}\}$ to the Gaussian model,

$$F_g = B_a + A_a e^{-c_a(y_a - m_a)^2} \tag{3.29}$$

where B_a represents the background noise associated with the Gaussian of amplitude A_a, centered at m_a having the standard deviation $\sigma_a = \sqrt{\frac{1}{2c_a}}$. Next, using the fit parameter c_a associated with the width of the Gaussian, obtained after fitting as shown in Fig. 3.20a, the vertical Gaussian profile $W_y = \{w_{y_a}\}$ is determined as the following,

$$w_{y_a} = \exp\left(-c_a\ (y_a - C_y^{(r)})^2\right) \tag{3.30}$$

where, y_a is the row number in the rotated image. For the 101 Horizontal slices about the vertical centroid $C_y^{(r)}$, we choose 101 values about the mean of the Gaussian weight function W_y, as shown in Fig. 3.20b.

---

[27]For a particular row y_a, the mean intensity is given by $I_{y_a} = \frac{\sum_{x=1}^{N_a} I_{xy_a}}{N_a}$, where N_a is number of pixels in each row of the rotated image.

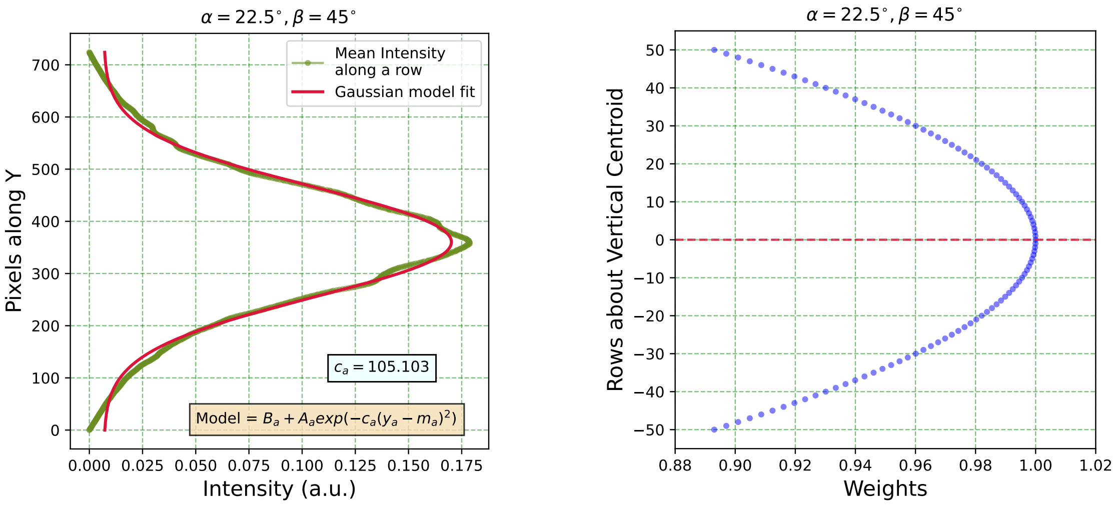

(a) Gaussian Model Fit to the vertical intensity distribution of the rotated image.

(b) Gaussian Weights to be assigned to each Horizontal Slices of the rotated image.

Figure 3.20: Determining the Vertical Gaussian Profile for weighing the parameters obtained by fitting the intensity distributions along different rows across the rotated image.

Now, while fitting the 101 rows about the vertical centroid of the rotated image, if the model F_{nc} does not fit any of the slices, i.e., if the adjusted R^2 of the fit is less than 0.99, we give it a zero weight. For a single image, we find the weighted mean and weighted standard deviation (over 101 slices) of each of the parameters (A_f, v_f, ϕ_f). For the phase shift ϕ_f, we use circular mean and circular standard deviation [23], discussed in Appendix. 3.A. The amplitude A_f is corrected against the vertical Gaussian weight.

Analyzing the five images captured for a particular HWP and QWP angle, i.e., for a particular polarization state, we evaluate the mean and standard deviation of phase shift (Φ), average intensity $(\bar{I})$ and visibility (V). The average (over 5 images) of the averages (over 101 slices) is used to represent the mean experimental value and the error bars are represented by the maximum between standard deviation (over 5 images) of the means (over 101 slices) or the RMS (over 5 images) of the standard deviations (over 101 slices) [28]. This entire process is repeated for different QWP angles at a given HWP angle.

[28]For a particular parameter (say, p), we derive a weighted (weights $= W_y$) mean $\mu_{\mathcal{I}}$ and weighted standard deviation $\sigma_{\mathcal{I}}$ over 101 values obtained by fitting 101 horizontal slices of a single image $(\mathcal{I})$. So, for a given state from 5 images, we have means $M = \{\mu_{\mathcal{I}_k}\}$ and stds $S = \{\sigma_{\mathcal{I}_k}\}$, where k ranges from 1 to 5. The experimental result is reported as $p = mean(M)$, with the error bar given as $p_{err} = \max[std(M),\ rms(S)]$.

We then repeat the same process for various HWP angles α. The HWP is rotated in steps of 5° and for each of the HWP angles the QWP is rotated in steps of 2°. Finally, we take a dataset with the QWP absent in the setup in order to find the the zero reference of the phase shift. The experimentally obtained quantities i.e., the phase shift (Φ), average intensity ($\bar{I}$) and visibility (V) for each (α, β) combination are then used to compute the state parameters θ, ϕ, μ of the polarization state being incident on the setup. Though the state prepared in the experiment is almost pure, we can use the visibility to show that the obtained μ value is close to 1.

3.4.3 Choice of Statistics for Data Acquisition and Data Analysis

The interference pattern in a Sagnac interferometer is not affected by the low frequency vibrations and hence, repetitions of image acquisition over time are reproducible. In the experiment, for each run, we set the specific angles α and β of the HWP and the QWP by rotating the motorized mounts. We then acquire five images with a fixed exposure of 13 ms at intervals of about 500 ms, for the given prepared state. Because of the stability of the interferometer over time, these recorded images give us consistent results ensuring the reproducibility. However, the envelope of the transverse profile of the beam is not perfectly Gaussian because of some dust on the optical components and on the imaging sensor. The presence of dusts changes the wavefront of the beam due to additional diffraction effects and hence, affects the intensity distribution recorded by the beam profiler. Therefore, instead of taking just one profile from an image, we take 101 horizontal slices about the vertical centroid of the image and find the best fit parameters for each of the slices by fitting the intensity distribution across a horizontal slice with the model given in Eqn. 3.28. Then, the averages of the fit parameters over all these 101 slices are computed. The slices which are far off the vertical centroid are affected the most due to lack of perfect overlap between the two beams coming from two different paths of the interferometer. Therefore, we optimally select the 101 slices, which fall within the full width half maximum (FWHM) of the vertical Gaussian envelope to have enough sampling of the beam in order to eliminate the irregularities. The experimental results are determined by weighing the fit parameters obtained from different slices with the vertical Gaussian profile to address the varying significance of these parameters across the beam width.

The standard deviation of the fit parameters over 101 slices quantifies how spread out the obtained values are from the average, for a particular image captured for a given state. From the values of the means and the standard deviations computed for all the five images, it is obtained that the variation of the fit parameters across the 101 slices for a given image is larger than the changes in mean of the fit parameters across the 5 images. This implies that there is more variability in the fit parameters within a single image (across different slices) than there is between different images. Because of this, capturing more images would not significantly improve the statistics or provide more information about the interferometric quantities. Therefore, 5 images give us the sufficient statistics for reliably inferring the experimental results.

3.4.4 Experimental Results

The experiment aims to demonstrate the polarization state interferography scheme by showing the reconstruction of different polarization qubits incident on the Quantum State Interferography (QSI) setup designed with a displaced Sagnac interferometer (DSI) depicted in Fig. **3.18**. As described in SubSec. 3.4.2, from the interference patterns formed in the DSI aligned in non-collinear geometry, we determine the phase shift (Φ), average intensity ($\bar{I}$) and visibility (V) for different polarization states prepared by rotating a HWP and a QWP at different angles (α and β) in the path of a vertically polarized beam. The obtained values of $(\Phi, \bar{I}, V)$ are used to infer the state parameters of the polarization qubits to reconstruct the input state. We then compute the fidelity of the reconstructed states comparing to the prepared ones. Here, we use 632.8 nm Helium Neon Laser as the source along with the wave plates meant for the wavelength 633 nm. Therefore, the results (i.e., Φ, $\bar{I}$, V) obtained from the experiment are expected to be close to the values evaluated from theory, unlike the QSI experiment with the Mach-Zehnder Interferometer (MZI).

We have presented the variations of the phase shift, averaged intensity and visibility of the interference patterns with respect to the HWP angle α and the QWP angle β – obtained from both, the experimentally recorded data and the theoretical computation as the state $|\psi(\alpha,\beta)\rangle = \hat{S}_q(\beta)\ \hat{S}_h(\alpha)\,|V\rangle$ evolves through the QSI setup, where $\hat{S}_h$ and $\hat{S}_q$ are the Unitary operators associated with the wave plates, given in Eqn. **3.4**. The plots for Φ, $\bar{I}$ and V as functions of the wave plate angles α and β are shown in Fig. **3.21**, Fig: **3.22** and Fig: 3.23 respectively. The solid lines in the plots represent the theoretical prediction while the dots and bars respectively represent the experimentally obtained mean and statistical error. The means and error bars of each of the quantities in the plots are derived from a statistical analysis of 101 horizontal slices from each of the five images captured for a specific combination of (α, β). The black curves (at $\beta = 0$) in each plot represent the respective quantities as a function of the HWP angle α, obtained for the experiment where the QWP is absent from the state preparation stage and the polarization states, that are incident on the QSI setup, are prepared by action of the HWP only on the state $|V\rangle$. The individual plots for different states prepared by (i) rotating HWP only and (ii) rotating QWP with the HWP fixed at different angles, can be seen in Appendix. 3.B.

❑ **Phase Shift (Φ) :** The phase shift of the interference pattern represents the value of the relative phase that corresponds to the maximum intensity of the intensity distribution obtained from the interferometric setup.

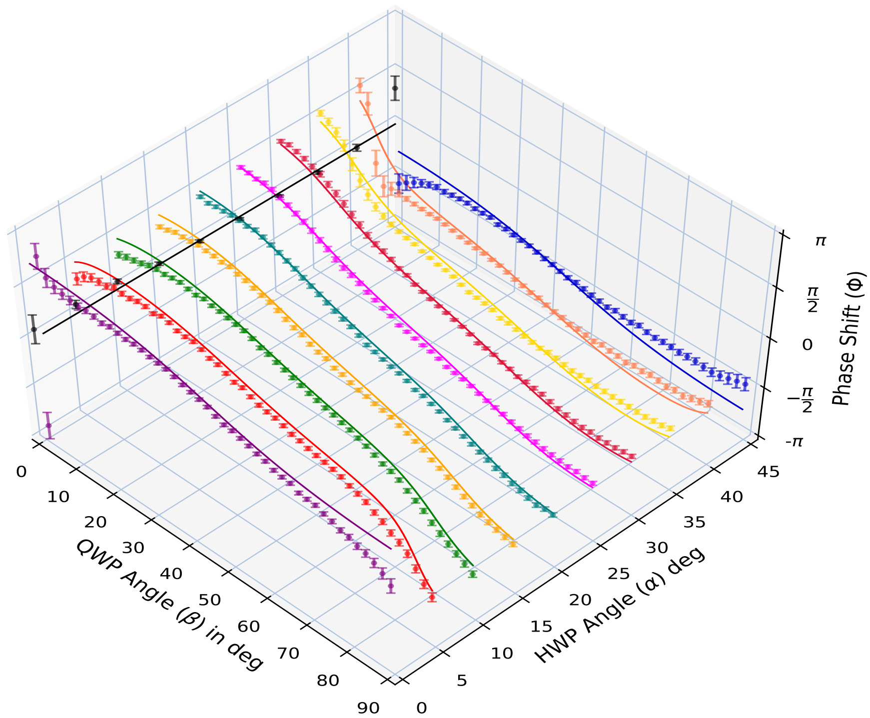

Figure 3.21: Phase shift of the interference pattern obtained from non-collinear displaced Sagnac interferometer as a function of α and β. The black curve corresponds to the phase shift obtained for the experiment where only HWP is rotated in absence of the QWP.

In the experimental condition where the QWP is not present, the phase shift as a function of HWP angle α is obtained to be a straight line (shown in 'black'). This result agrees well with the theory, according to which, in absence of QWP the value of phase shift is expected to remain constant with respect to α. This is because, a half-wave plate does not introduce any relative phase (ϕ) between the horizontal and vertical components of an incident linear polarization, it only transforms one linear polarization to another. However, in the displaced Sagnac geometry, the two interfering beams have an arbitrary but constant path difference, resulting in a phase shift which is not exactly zero but some constant. This value is considered as the zero reference for determining the phase shift under all other experimental conditions, i.e., for different (α, β) combinations.

As the state parameter θ approaches the values 0 or π, the phase shifts obtained from the interference patterns have more errors, since $\theta = 0$ and $\theta = \pi$ correspond to the states at the poles of the Bloch sphere, where the parameter ϕ is undefined. This is manifested in noticeable deviations of the experimental graphs from the theory for the HWP angles $\alpha = 0°$ and $\alpha = 45°$.

❑ **Average Intensity ($\bar{I}$) :** Average intensity of the interference pattern represents the phase averaged value of the intensity distribution obtained from the interferometric setup. Average intensity is obtained to be a function of the state parameter θ and independent of ϕ. The black dots in $\beta = 0$ plane, represents the experimentally obtained average intensities for the states prepared with different orientations of the HWP while the QWP is absent. All the experimentally obtained averaged intensities for different combinations of (α, β) are normalized (with norm $= 0.5$) with respect to the corresponding maximum of the average intensity obtained as a function of the HWP in the absence of QWP. This step for normalization can be avoided if the detector is calibrated against known input intensity.

The average intensity ($\bar{I}$) of an interference pattern, generated in the QSI setup for a given polarization state, does not depend on the interference and hence, it is not prone to errors that could potentially affect the visibility and phase shift. Average intensity is solely determined by the intensities of the two interfering beams, which are dependent on the polarization state being incident on the QSI setup. The factors such as the spatial overlap of the beams, stability of the interferometer, wavefront or the beam shape that can influence the interference, have no effect on $\bar{I}$. Therefore, the experimentally obtained values for $\bar{I}$ shows a better match with the theoretical predictions, as shown in the plots.

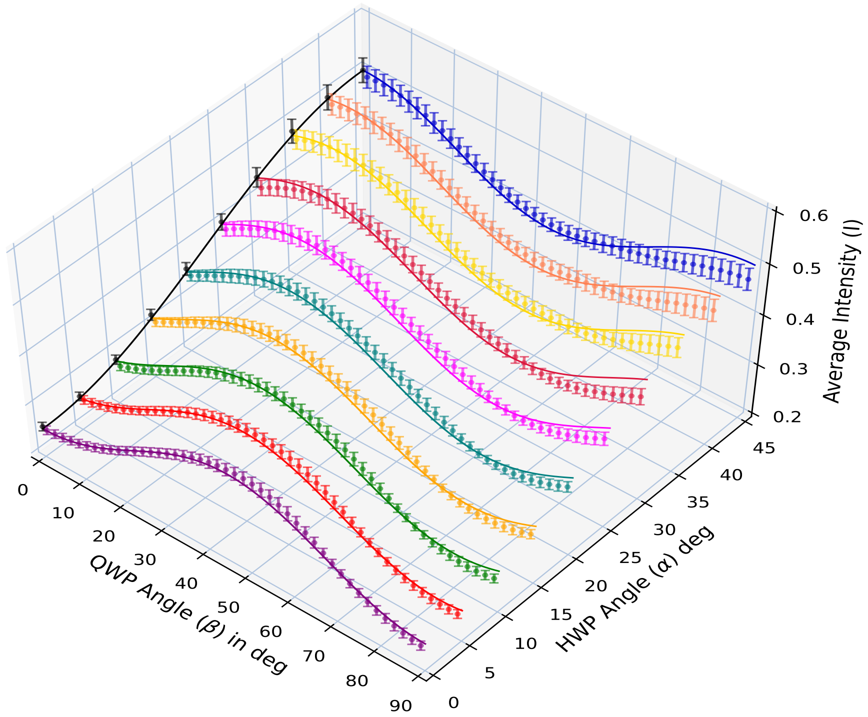

Figure 3.22: Average Intensity (average over phase) of the interference pattern obtained from non-collinear displaced Sagnac interferometer as a function of α and β. The black curve corresponds to the phase averaged intensity obtained for the experiment where only HWP is rotated in absence of the QWP.

❑ **Visibility (V) :** Visibility of the interference pattern represents the degree of coherence between the two interfering beams in an interferometric setup. It depends on how well the two beams overlap in different degrees of freedom including the spatial overlap, the polarization, the transverse coherence, which is related to the shape of the wavefront of the two interfering beams etc.. From the plot of visibility as a function of wave plate angles α, β, it can be seen that the experimentally obtained visibility is systematically lower than the theoretical prediction because of various experimental imperfections and the factors that change the interference.

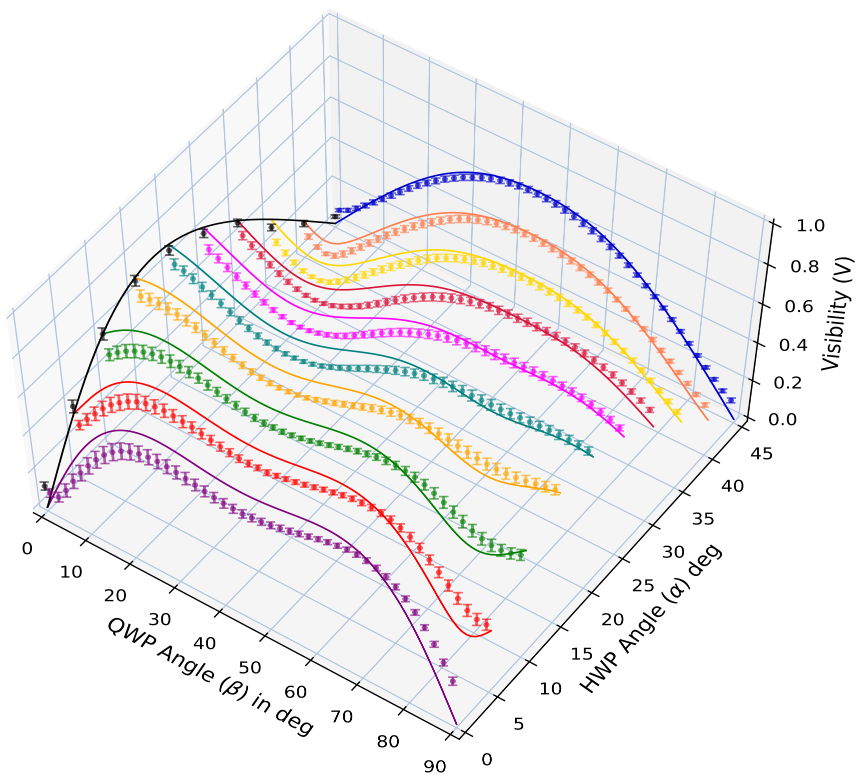

Figure **3.23**: Visibility of the interference pattern obtained from non-collinear displaced Sagnac interferometer as a function of α and β. The black curve corresponds to the visibility obtained for the experiment where only HWP is rotated in absence of the QWP.

The particular HWP and QWP used in this experiment for the state preparation, cause a slight angular deviation (almost about 10 $arcsec$) of the beam as they are rotated. As a result, the spatial overlap of the two beams at the detector plane changes for different orientations of the wave plates, that leads to the experimentally obtained visibility to be systematically lower than the theoretical predictions at certain angles of the wave plate. Also, the beam splitter BS has the transmission and reflection probabilities dependent on polarization by about 2.7%, which introduces an ellipticity in the polarization of the beams. These effects, along with other minor effects such as the averaging of the intensity over the area of the pixels are the reasons why the experimentally obtained visibility is systematically lower.

3.4.5 Inferring the State Parameters from Interferometric Information

In this experiment, we prepare different polarization states using a half-wave plate (HWP) followed by a quarter-wave plate (QWP), for different combinations of their angles α and β respectively, acting on the polarization state $|V\rangle$. The resulting states, denoted as $|\psi(\alpha,\beta)\rangle$, are made incident on the optical setup, as shown in Fig. 3.18 and the state parameters are inferred by analyzing the interference patterns recorded at the end of the setup using a CCD. Applying the Jones matrices of the respective wave plates, given in Eqn. 3.4, the prepared state $|\psi(\alpha,\beta)\rangle$ can be expressed as follows,

$$|\psi(\alpha,\beta)\rangle = \hat{S}_q(\beta)\ \hat{S}_h(\alpha)\ |V\rangle \tag{3.31}$$

$$= e^{-\frac{i\pi}{4}} \begin{pmatrix} \cos^2(\beta) + i\sin^2(\beta) & (1-i)\sin(\beta)\cos(\beta) \\ (1-i)\sin(\beta)\cos(\beta) & \sin^2(\beta) + i\cos^2(\beta) \end{pmatrix} e^{-\frac{i\pi}{2}} \begin{pmatrix} \cos(2\alpha) & \sin(2\alpha) \\ \sin(2\alpha) & -\cos(2\alpha) \end{pmatrix} \begin{pmatrix} 0 \\ 1 \end{pmatrix}$$

$$= e^{-i\frac{3\pi}{4}} \begin{pmatrix} \cos^2(\beta) + i\sin^2(\beta) & (1-i)\sin(\beta)\cos(\beta) \\ (1-i)\sin(\beta)\cos(\beta) & \sin^2(\beta) + i\cos^2(\beta) \end{pmatrix} \begin{pmatrix} \sin(2\alpha) \\ -\cos(2\alpha) \end{pmatrix}$$

$$\implies \qquad |\psi(\alpha,\beta)\rangle = \frac{e^{i\pi}}{\sqrt{2}} \begin{pmatrix} \sin(2\alpha - 2\beta) + i\sin(2\alpha) \\ \cos(2\alpha - 2\beta) - i\cos(2\alpha) \end{pmatrix} = \begin{pmatrix} \psi_H \\ \psi_V \end{pmatrix} \tag{3.32}$$

Here, ψ_H and ψ_V respectively represent the horizontal and vertical components of the polarization state which would be reconstructed using the interferometric setup employing Quantum State Interferography (QSI) technique. Therefore, in terms of the wave plate angles α and β, the respective polarization components are expressed as,

$$\psi_H = |\psi_H| e^{i\,\arg(\psi_H)} = \frac{e^{i\pi}}{\sqrt{2}} \left(\sin(2\alpha - 2\beta) + i\sin(2\alpha)\right) \tag{3.33}$$

$$\psi_V = |\psi_V| e^{i\,\arg(\psi_V)} = \frac{e^{i\pi}}{\sqrt{2}} \left(\cos(2\alpha - 2\beta) - i\cos(2\alpha)\right) \tag{3.34}$$

So, we have $|\psi_H|^2 + |\psi_V|^2 = \frac{1}{2}\left(\sin^2(2\alpha - 2\beta) + \sin^2(2\alpha) + \cos^2(2\alpha - 2\beta) + \cos^2(2\alpha)\right) = 1$. Now, ignoring the global phase [29] from the expression in Eqn. 3.32, we get

$$|\psi(\alpha,\beta)\rangle = \begin{pmatrix} |\psi_H| \\ \\ |\psi_V| \exp\left(i(\arg(\psi_V) - \arg(\psi_H))\right) \end{pmatrix} \tag{3.35}$$

In terms of the state parameters $\theta \in [0, \pi]$ and $\phi \in [-\pi, \pi)$, a general pure state in two dimensions is represented as,

$$|\psi(\theta,\phi)\rangle = \begin{pmatrix} \cos\left(\frac{\theta}{2}\right) \\ \\ e^{i\phi}\sin\left(\frac{\theta}{2}\right) \end{pmatrix} \tag{3.36}$$

Therefore, from element wise comparison between the expressions for the pure qubit in Eqn. 3.36 and Eqn. 3.35, we get the relation between the state parameters θ, ϕ with the wave plate angles α, β as shown below,

$$\theta = 2\cos^{-1}\left(|\psi_H|\right) \quad \text{and} \quad \phi = \arg(\psi_V) - \arg(\psi_H) \tag{3.37}$$

$$\text{where,} \quad |\psi_H| = \sqrt{\frac{\sin^2(2\alpha - 2\beta) + \sin^2(2\alpha)}{2}} \tag{3.38}$$

$$\arg(\psi_H) = \tan^{-1}\left(\frac{\sin(2\alpha)}{\sin(2\alpha - 2\beta)}\right) \tag{3.39}$$

$$\arg(\psi_V) = -\tan^{-1}\left(\frac{\cos(2\alpha)}{\cos(2\alpha - 2\beta)}\right) \tag{3.40}$$

The state parameters, however, would be determined from the information extracted from an interference pattern formed in the QSI setup.

[29] As global phase does not have any physically observable significance upon measurement.

As the state evolves through the QSI setup which consists of a displaced Sagnac interferometer (DSI) having the operators $\hat{\sigma}_x$ and $\hat{\Pi}_H$ in the respective arms, we get the intensity distribution as a function of relative phase ϵ as, $I_d(\epsilon) = \langle\psi(\alpha,\beta)|\hat{\mathcal{E}}^\dagger\hat{\mathcal{E}}|\psi(\alpha,\beta)\rangle$. Here, $\hat{\mathcal{E}}$ is the effective evolution operator of the QSI setup, given as $\hat{\mathcal{E}} = \frac{1}{2}\left(\hat{\sigma}_x + e^{i\epsilon}\,\hat{\Pi}_H\right)$. Therefore, as a function of the wave plate angles (α,β), the intensity distribution obtained at the end of the setup can be expressed as the following,

$$I_d(\alpha,\beta,\epsilon) = \left\|\hat{\mathcal{E}}\,|\psi(\alpha,\beta)\rangle\right\|^2 = \left\|\frac{1}{2}\begin{pmatrix} e^{i\epsilon} & 1 \\ 1 & 0 \end{pmatrix}\begin{pmatrix} \psi_H \\ \psi_V \end{pmatrix}\right\|^2 \tag{3.41}$$

$$I_d(\alpha,\beta,\epsilon) = \frac{1}{4}\left[1 + |\psi_H|^2 + 2|\psi_H||\psi_V|\cos\left(\epsilon - (\arg(\psi_V) - \arg(\psi_H))\right)\right] \tag{3.42}$$

Processing the above intensity distribution, recorded by the beam profiler, we determine the phase shift (Φ), phase averaged intensity ($\bar{I}$) and visibility (V) of the interferogram,

$$\Phi = \arg(\psi_V) - \arg(\psi_H) \tag{3.43}$$

$$\bar{I} = \frac{1}{4}(1 + |\psi_H|^2) \tag{3.44}$$

$$V = \frac{2|\psi_H||\psi_V|}{1 + |\psi_H|^2} = \frac{2|\psi_H|}{\sqrt{1 + |\psi_H|^2}} \tag{3.45}$$

Therefore, from Eqn. 3.37 and using the above interferometric information the state parameters θ and ϕ can be determined as the following,

$$\theta = 2\cos^{-1}(|\psi_H|) = 2\cos^{-1}\left(\sqrt{4\bar{I} - 1}\right) \tag{3.46}$$

$$\phi = \arg(\psi_V) - \arg(\psi_H) = \Phi \tag{3.47}$$

So, the parameters θ and ϕ associated with the pure polarization state $|\psi(\alpha,\beta)\rangle$ can be directly inferred from experimentally obtained average intensity ($\bar{I}$) and phase shift (Φ) of the interference pattern. Though the determination of $\bar{I}$ and Φ are sufficient for a pure polarization state reconstruction using the QSI scheme, determination of visibility (V) is useful for the complete characterization of a mixed polarization qubit. The parameter μ which describes the mixedness of a state $\hat{\rho}(\theta, \phi, \mu)$ in two dimensions, can be inferred from the experimentally obtained visibility.

3.4.6 Purity and Fidelity of the States Reconstructed Using QSI

The Quantum State Interferography (QSI), an interferometric state determination scheme, has been experimentally demonstrated through the reconstruction of various polarization states using the interferometric information obtained from a non-collinear displaced Sagnac interferometer. To evaluate the effectiveness of this technique, in terms of the accuracy of the reconstructed states, we compute the fidelity of the experimentally determined states by comparing them with the states incident on the QSI setup. Fidelity provides a quantitative measure of the closeness between two the states, (i) $|\psi_i\rangle$: the state prepared in the lab and made incident on the QSI setup, and (ii) $|\psi_r\rangle$: the state reconstructed using the QSI technique. For pure quantum state reconstruction, the fidelity is computed as $\mathcal{F}_p = |\langle\psi_i|\psi_r\rangle|^2$, which is the same as the transition probability of the state $|\psi_r\rangle$ to $|\psi_i\rangle$. The fidelity ranges between 0 and 1 [30], with a higher fidelity indicating a more accurate reconstruction (of the incident state). Therefore, the higher the fidelity is, better is the performance of the state determination scheme. In the density matrix representation of the quantum states, the fidelity [24] is computed as,

$$\mathcal{F}(\hat{\rho}_i, \hat{\rho}_r) = \left(\mathrm{Tr}\left(\sqrt{\sqrt{\hat{\rho}_i}\ \hat{\rho}_r\ \sqrt{\hat{\rho}_i}}\right)\right)^2 \tag{3.48}$$

Here, $\hat{\rho}_i$ is the density matrix associated with the prepared state and $\hat{\rho}_r$ is the density matrix associated with the state reconstructed using QSI. The analysis of fidelity in this experiment is significant, as it not only validates our experimental results but also provides an insight into the potential utility of this interferometric scheme for quantum state characterizations.

[30] The fidelity value 1 implies the two quantum states, that are being compared, are identical and a fidelity value 0 denotes the two states are orthogonal.

Presuming that the polarization state of the incident beam is pure, we compute the fidelity of the state reconstructed from θ and ϕ, respectively determined using the experimentally obtained average intensity $\bar{I}$ and phase shift Φ of the interference pattern generated in the QSI setup. Therefore, the fidelity for pure states ($\mathcal{F}_p$) appears to be a function of $\bar{I}$ and Φ, which are necessary for inferring the pure state in two dimensions, as discussed in SubSec. 3.4.5. The mean fidelity ($\mathcal{F}_p$) calculated from experimentally obtained mean phase shift (Φ) and mean average intensity ($\bar{I}$) are plotted on the surface of a Bloch sphere at the corresponding θ and ϕ values of the prepared states, where $\theta \in [0, \pi]$ and $\phi \in [-\pi, \pi)$ respectively represent the polar angle and the azimuthal angle associated with the Bloch vector of the state. The errors obtained in the determination of $\bar{I}$ and Φ are propagated to the calculation of fidelity for a single state. The plot of the mean fidelity $\mathcal{F}_p$, for different reconstructed states ($|\psi(\theta, \phi)\rangle$) related to the states prepared experimentally ($|\psi(\alpha, \beta)\rangle$) for various orientations of the wave plates acting on the vertically polarized beam, can be seen in Fig. **3.24** [Left] with the values indicated by the colorbar. The average fidelity over all the prepared states is obtained to be greater than 98%.

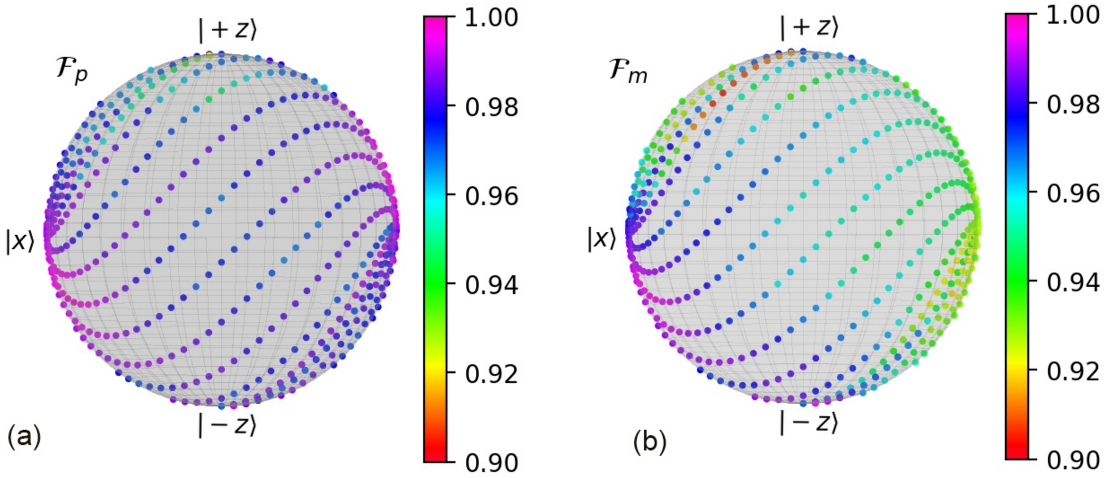

Figure **3.24**: [Left] Fidelity with assumption that the various prepared states at different θ and ϕ over the Bloch Sphere are pure. [Right] Fidelity of reconstructed density matrices of various prepared states at different θ and ϕ over the Bloch Sphere.

Although, in this experiment, the polarization of the incident beam is almost pure (since the initial vertical polarization of the beam before the wave plates has a purity better than 99%), this interferometric method for state determination can be used in experiments involving mixed states as well. To illustrate, we reconstruct the density matrix $\hat{\rho}(\theta, \phi, \mu)$ using the experimentally obtained values of average intensity ($\bar{I}$), phase shift (Φ) and visibility (V) of the interference pattern. The parameter μ, which is related to the purity of the state, is determined from the visibility (V), with the restriction that it makes the reconstructed density matrix physical, i.e., ensuring the condition $\mathrm{Tr}(\hat{\rho}^2) \leq 1$ is satisfied. This is achieved by substituting μ with $\min[\mu, 1]$ during the construction of the density matrix $\hat{\rho}$ [31] from the experimentally inferred parameters. It is because, for any physical state in two dimensions the parameter μ lies between 0 and 1, i.e., $0 \leq \mu \leq 1$, with $\mu = 1$ corresponding to the pure states.

However, since the experimentally obtained visibility is systematically lower than the theory due to several experimental imperfections, the reconstructed density matrix $\hat{\rho}_r = \hat{\rho}(\theta, \phi, \mu)$ has a lower purity. Consequently, the fidelity of the reconstructed density matrix slightly drops but still remains greater than 90% for all the prepared states, even in the worst case as can be seen from the Table. **3.1**. The plots for the fidelity $\mathcal{F}_m$, computed using Eqn. **3.48**, of the reconstructed density matrices ($\hat{\rho}_r$) on a Bloch sphere, at the θ and ϕ values of the corresponding prepared states ($\hat{\rho}_i$), is shown in Fig. **3.24** [Right] with the values indicated by the colorbar. From the plot, it can be seen that the fidelity $\mathcal{F}_m$ for the reconstructed density matrices using the experimentally obtained phase shift, average intensity and visibility is lower than the case with pure state assumption. However, for ideal conditions how the fidelity of an arbitrary state $\rho(\mu, \hat{\theta}, \phi)$ compared to the pure states $\rho(\mu = \hat{1}, \theta, \phi)$, varies with the mixedness parameter μ is discussed in Appendix. 3.C.

Here, we report median analysis as the errors introduced during the computation of fidelity are dependent on the state that is being evolved through the QSI setup. For instance, there is more uncertainty in determining the phase shift whenever the visibility is low. In the Table **3.1** we present the best case and worst case scenarios for the reconstruction of the states using QSI technique. The optimal scenario indicates that by reducing both systematic and random errors − for example, with the use of cage mount assembly for achieving better stability of the optics and by miniaturizing the setup to avoid effects due to pointing fluctuations of the beam and the angular deviations caused due to wave

[31] The details of how μ affects the fidelity of the reconstructed state and other methods to infer μ from experiment that makes the density matrix $\hat{\rho}$ physical, is discussed in Sec. 3.5.

plate rotations, having a sensor with smaller pixel sizes etc. − this state reconstruction method could potentially provide state estimations with the fidelity exceeding 98%. The median of the average mixed state fidelity ($\mathcal{F}_m$) over all the states reconstructed in the experiment, is obtained to be lower than the corresponding median of the average fidelity for the reconstructed pure states ($\mathcal{F}_p$). This is because of the introduction of the errors in determining μ from the visibility of the recorded interference pattern, which is affected by the pixel averaging, the spatial overlap of the two interfering beams and change in ellipticity of polarization at each reflection. Since the reconstruction of pure states does not require the determination of visibility, these errors only impact the reconstruction of the mixed states, resulting in a reduction of their purity as well as the fidelity [32].

	Average	**Best Case**	**Worst Case**
Purity: $\mathrm{Tr}\left(\hat{\rho}^2\right)$	$0.92(5)^{+0.03(7)}_{-0.03(7)}$	$0.98(0)^{+0.01(9)}_{-0.02(7)}$	$0.85(7)^{+0.06(5)}_{-0.03(1)}$
Mixed state Fidelity: $\mathcal{F}_m$	$0.94(1)^{+0.02(5)}_{-0.01(3)}$	$0.98(1)^{+0.00(9)}_{-0.01(2)}$	$0.90(2)^{+0.03(2)}_{-0.01(4)}$
Pure state Fidelity: $\mathcal{F}_p$	$0.98(3)^{+0.00(4)}_{-0.00(6)}$	$0.99(5)^{+0.00(2)}_{-0.00(5)}$	$0.97(0)^{+0.00(6)}_{-0.00(6)}$

Table 3.1: Purity and Fidelity: This table presents the median of the average fidelity and the purity computed over all the prepared states, along with the upper and lower quartile deviations. It also includes the best case and worst case, which are determined from the highest and lowest values of purity and fidelity obtained after error (derived from the statistics of the average intensity, phase shift and visibility of the interference patterns) propagation of half standard deviation about the mean quantities.

[32] However, errors such as change in polarization due to reflection can be avoided in the miniaturized slit based QSI setup, discussed in Sec. 3.1.

3.5 Ensuring Physicality of the Reconstructed Density Matrix in Quantum State Interferography

A general density matrix in two-dimensions can be represented using the parameters (μ, θ, ϕ) as the following,

$$\hat{\rho}(\mu,\theta,\phi) = \begin{pmatrix} \cos^2\left(\frac{\theta}{2}\right) & \frac{1}{2}\mu e^{-i\phi}\sin(\theta) \\ \\ \frac{1}{2}\mu e^{i\phi}\sin(\theta) & \sin^2\left(\frac{\theta}{2}\right) \end{pmatrix} \tag{3.49}$$

where the coordinates $\theta \in [0,\pi]$ and $\phi \in [-\pi,\pi)$ describe the direction of the Bloch vector associated with the state (in Bloch sphere representation) and $\mu \in [0,1]$ is related to the length of the Bloch vector and governs the purity of the density matrix $\hat{\rho}$. The purity of the state $\hat{\rho}$ is given as,

$$\mathrm{Tr}\left(\hat{\rho}^2\right) = 1 - \left(\frac{1-\mu^2}{2}\right)\sin^2(\theta) = \frac{1}{4}\left[3+\mu^2+\left(1-\mu^2\right)\cos(2\theta)\right] \tag{3.50}$$

Therefore, $\mu = 1$ corresponds to purity 1, which represent the pure states. Since, $\theta \in [0,\pi]$ and $\mu \in [0,1]$, we get the Purity, $\mathrm{Tr}(\hat{\rho}^2) \in [0.5,1]$, with $\mathrm{Tr}(\hat{\rho}^2) = 1$ representing pure states $\hat{\rho} = |\psi\rangle\langle\psi|$ and $\mathrm{Tr}(\hat{\rho}^2) = 0.5$ representing the maximally mixed state $\hat{\rho} = \dfrac{|H\rangle\langle H| + |V\rangle\langle V|}{2}$.

For all values of θ and ϕ, the density matrix $\hat{\rho}$ is inherently physical for the range $0 \leq \mu \leq 1$, by virtue of its construction. Experimentally, we determine θ and ϕ directly from the average intensity $\bar{I}$ and the phase shift Φ of the recorded interference pattern as,

$$\theta = \cos^{-1}\left(8\bar{I}-3\right) \qquad \text{and} \qquad \phi = \Phi \tag{3.51}$$

Once θ is determined, we can compute the parameter μ from the experimentally obtained visibility V as the following,

$$\mu = \left(\frac{3+\cos(\theta)}{2\sin(\theta)}\right)V \tag{3.52}$$

Therefore, using experimentally obtained values of average intensity $\bar{I}$ and visibility V, we can infer μ for a given incident state. When θ approaches close to 0 or π, the denominator tends to 0. In this situation, the experimentally obtained visibility must be sufficiently low to ensure that the condition $\mu \leq 1$ holds. However, due to several experimental imperfections and noises, the visibility derived experimentally can sometimes be slightly higher or lower than what one would expect with ideal experimental components and ideal laboratory conditions. This slight discrepancy in visibility between the experimentally observed value and the expected value, can result in the obtained μ values to be more than 1 (i.e., $\mu > 1$) when computed simply using the formula given in Eqn. 3.52.

These situations, where we obtain μ values larger than 1, mostly occurs when the state is close to the poles of the Bloch sphere, i.e., when θ nears 0 or π. At the values $\theta = 0$ and $\theta = \pi$ (the states are $|H\rangle$ and $|V\rangle$ respectively), the off-diagonal terms in $\hat{\rho}$ (magnitude of which is given by $\frac{1}{2}\mu\sin(\theta)$) tend to zero. Hence, for the reconstruction of these states, if the value of μ is clipped between 0 and 1, the error in $\hat{\rho}$ seems to be minimal.

We have seen that in the experiment performed using a displaced Sagnac Interferometer, the values of μ computed from average intensity $\bar{I}$ and visibility V, is almost always found to be within 1, with only a few exceptions. Fig. 3.25a and Fig. 3.25b present the variation of μ as a function of the states prepared by changing the QWP angle β for the HWP angle fixed at $\alpha = 0°$ and $\alpha = 22.5°$ respectively. For the few instances, where $\mu > 1$ as computed using Eqn. 3.52, we have constrained the value to 1 by taking $\mu \equiv \min[\mu, 1]$. This adjustment does not significantly affect the reconstruction of $\hat{\rho}$, as the off-diagonal terms are anyways small because of θ being closer to 0 or π. Further, a generic procedure is outlined, using which μ can be obtained systematically without the need of clipping the value between 0 and 1.

In the experiment, the non-collinear interference pattern generated at the end the interferometric setup for a given incident state, is analyzed by fitting the recorded intensity distribution to a non-linear function F_{nc} given in Eqn. 3.28, which is

$$F_{nc} = B_f + A_f e^{-c_f(x_f - m_f)^2}(1 + v_f \cos(k_f x_f + \phi_f)) \tag{3.53}$$

We find the average intensity, visibility and phase shift of an interference pattern from mean of the respective best fit parameters A_f, v_f and ϕ_f obtained from 101 horizontal slices about the vertical centroid of the recorded (and rotated) image. Now, instead of finding the best fit for the parameters A_f and v_f along with other parameters for each of the slices, we can directly substitute $A_f = \frac{\mathcal{N}}{8}(3+\cos(\theta))$ and $v_f = \frac{2\mu\sin(\theta)}{3+\cos(\theta)}$. Here, $\mathcal{N}$ is the normalization or scaling factor associated with intensity measurement and is determined from the experimental setup. In this way, now we can directly find the best fit values for θ and μ instead of A_f and v_f. The fitting algorithm is essentially a constrained optimization with the bounds for θ being $[0, \pi]$ and that for μ being $[0, 1]$. Thus, the requirement that $0 \leq \mu \leq 1$ can be directly imposed in the fitting algorithm rather than imposing the constraints on the computed value of μ from v_f and A_f.

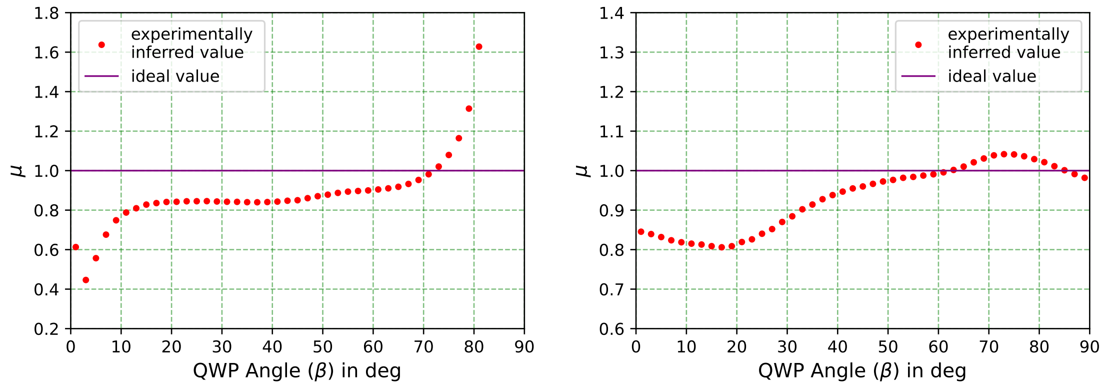

(a) HWP angle $\alpha = 0°$

(b) HWP angle $\alpha = 22.5°$

Figure 3.25: The mixedness parameter μ obtained as a function of prepared states parameterized by the QWP angle β for different HWP angles α. **(a)** For HWP set at $\alpha = 0°$, the angle θ varies between 85.55° to 172.81° as β changes. Except for few points in the region where β approaches 90°, we obtain $\mu < 1$, i.e., the reconstructed density matrices are physical. Here, the value of μ mostly lies within 0.8 to 1 (for $11° < \beta < 73°$). As β nears 0° or 90° the smaller and the higher values of μ does not affect the state reconstruction, as for these values of β the state is close to $|V\rangle$, for which the off-diagonal elements of the corresponding density matrix are 0. **(b)** For the HWP set at $\alpha = 22.5°$, the angle θ varies between 55.24° to 120.43° as β changes. Since here θ lies well away from 0° or 180° (i.e., 0 or π rad), the parameter μ does not show any abrupt rise or fall in its value. The μ values obtained for different states for $\alpha = 22.5°$ lies within 0.8 to 1.04.

This additional post-processing for ensuring the physicality of the reconstructed state, is not some thing special for Quantum State Interferography (QSI) technique. It is also worth noting that the reconstructed density matrix from Quantum State Tomography (QST) also requires additional post-processing so that the inferred density matrix becomes physical, i.e., $\mathrm{Tr}\left(\hat{\rho}^2\right) \leq 1$ [25, 26].

3.6 Conclusion

In this chapter, we have presented the experimental realization of the interferometric state determination scheme, Quantum State Interferography (QSI), for inferring the two-dimensional quantum states in the polarization degree of freedom of light. We have shown how a single interference pattern, generated when an unknown state evolves through the QSI setup, can be processed to get the interferometric quantities from which the state can be reconstructed. The experimental demonstration of polarization state interferography is presented for two different interferometric setups, one with a Mach-Zehnder Interferometer (MZI) and the other one with a Displaced Sagnac Interferometer (DSI). High fidelity of the reconstructed states (compared to the prepared states) obtained from the DSI setup validates the efficacy of this scheme with a stable interferometric arrangement. From both these experiments, we can conclude that QSI provides a “true single shot” state estimation technique for qubits, where in between the incidence of the photon in the unknown state and extraction of the state information, no internal setting needs to be modified.

In various applications like quantum communication or information protocols, it is essential to have the knowledge of the state of the quantum particle we are dealing with. However, while determining the state using the QSI technique, it is important to note that a single particle can not produce an interference pattern and it is described only with a statistical ensemble of particles. Since the average statistical properties of light are equivalent for an ensemble of identical photons and for a coherent beam [27], the interference pattern obtained from a stream of single photons would be identical to the one formed with the coherent laser light [28]. Therefore, the interferometric method of state reconstruction described in this chapter using a laser light source would be applicable for determining the state of an identically prepared ensemble of single photons as well.

Appendix

3.A Circular Mean and Circular Standard Deviation

Circular statistics is used while dealing with the data of periodic nature, like angles or time or phase etc. [23]. The traditional statistical measures of central tendency and dispersion such as the mean and standard deviation, in general, can not provide an accurate description of such periodic data since they do not account for the cyclical variation of the data. For example, here in this experiment, we aim to determine the phase shift Φ of the interference pattern which is periodic in nature with the periodicity being 2π. Here, Φ values of 0 and 2π are effectively the same, but the simple arithmetic mean of these two values would yield $\frac{0+2\pi}{2} = \pi$, which is incorrect. Therefore, to accurately determine the mean and standard deviation of the phase shift of the interference pattern obtained from the 101 horizontal slices of an image, we employ circular statistics.

Consider an array A_ϕ containing the list of circular variable φ. Then the circular mean for a list of N values is given by

$$\mu_c^\phi = \arctan\left(\frac{\sum_{i=1}^{N}\cos\left(A_\phi^i\right)}{N}, \frac{\sum_{i=1}^{N}\sin\left(A_\phi^i\right)}{N}\right). \tag{3.54}$$

Here, $\arctan(x, y)$ gives $\tan^{-1}\left(\frac{y}{x}\right)$ after taking into account the quadrant to which the pair belongs to. The circular standard deviation provides a measure how spread out the cyclical data is around the circular mean. The circular standard deviation σ_c^{ϕ} is obtained as the square root of the circular variance and is computed as follows:

$$\sigma_c^{\phi} = \sqrt{1 - \frac{\sqrt{\left(\sum_{i=1}^{N} \cos\left(A_{\phi}^{i}\right)\right)^2 + \left(\sum_{i=1}^{N} \sin\left(A_{\phi}^{i}\right)\right)^2}}{N}} \tag{3.55}$$

3.B Individual Plots for Phase Shift, Average Intensity and Visibility obtained from Sagnac Interferometer

The plots in Fig. 3.21, Fig. 3.22 and Fig. 3.23 respectively present the experimentally obtained phase shift (Φ), average intensity ($\bar{I}$) and visibility (V) of the interference patterns generated for various polarization states in the non-collinear displaced Sagnac Interferometer with $\hat{\sigma}_x$ operator in one arm and $\hat{\Pi}_H$ operator in the other arm. These $3D$ plots for Φ, $\bar{I}$ and V offers a comprehensive comparison, all together, of the respective parameters determined by analyzing the recorded interference patterns for all the states prepared in the experiment.

However, although the $3D$ plots aid in visualizing the variations of the interferometric parameters for different polarization states, they are susceptible to parallax errors. As a result, for some states, the parameters may appear slightly shifted from their actual values. To address this, here we present the individual $2D$ plots corresponding to different polarization states obtained for the conditions (i) when QWP angle β varies in steps of $2°$ at a specific HWP angle α and the same repeated for α varying in steps of $5°$, (ii) when only HWP angle α is varied in absence of QWP. These plots, similar to their $3D$ representations, feature solid lines representing the theoretical predictions and dots and bars representing the experimentally obtained mean and statistical error respectively. The curve in 'black' showcase the variation of the experimentally obtained quantities as a function of HWP angle α only.

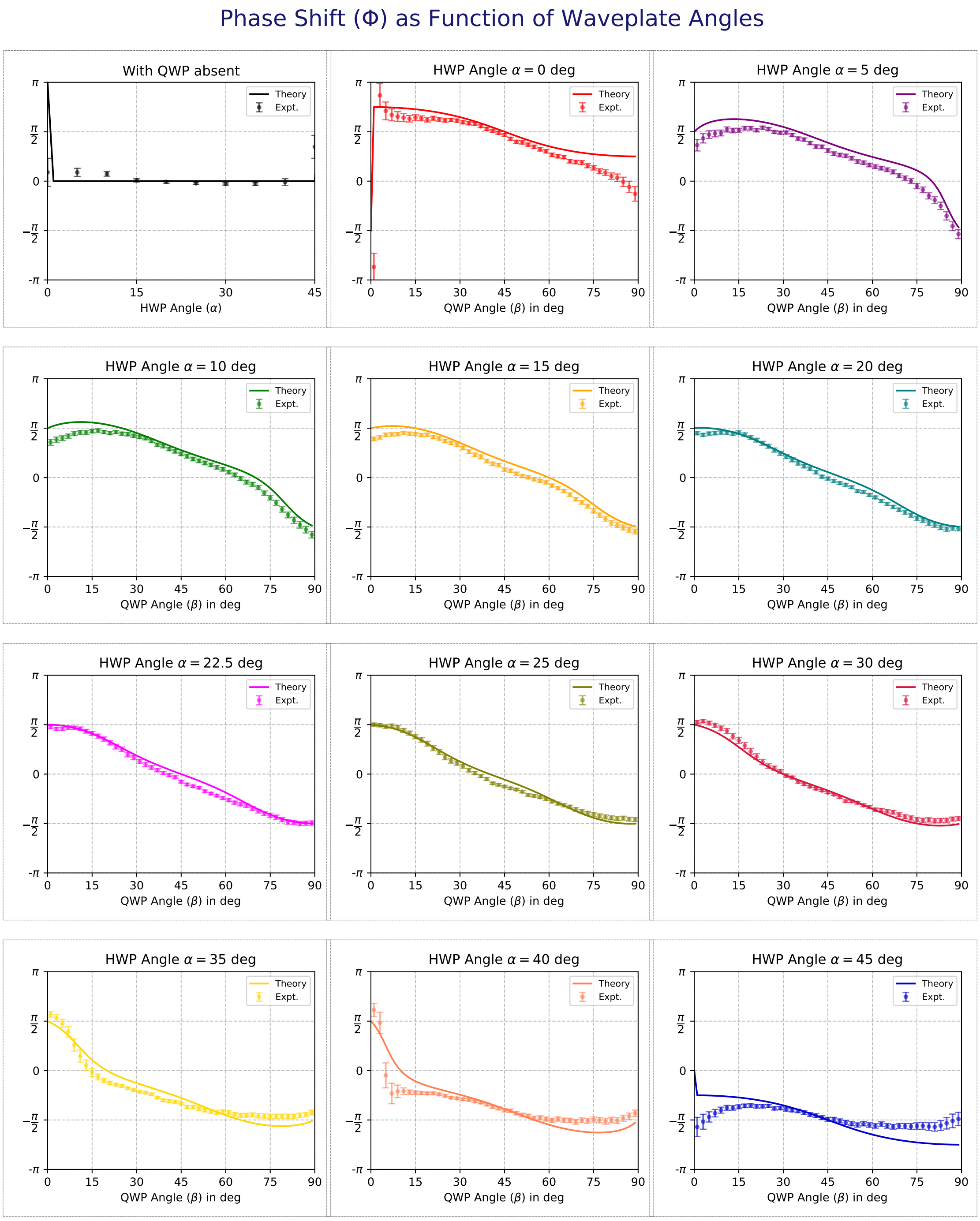

Figure 3.26: Phase Shift (Φ) of the interference patterns generated in the QSI setup for different polarization qubits prepared by rotating the HWP (at α) followed by the QWP (at β) in the path of a vertically polarized beam. In absence of QWP, the experimentally obtained value of phase is expected to be a constant with respect to α, which is considered as the zero reference for all the measurements. The mean and standard deviations associated with phase are obtained from the experimental datasets using circular statistics.

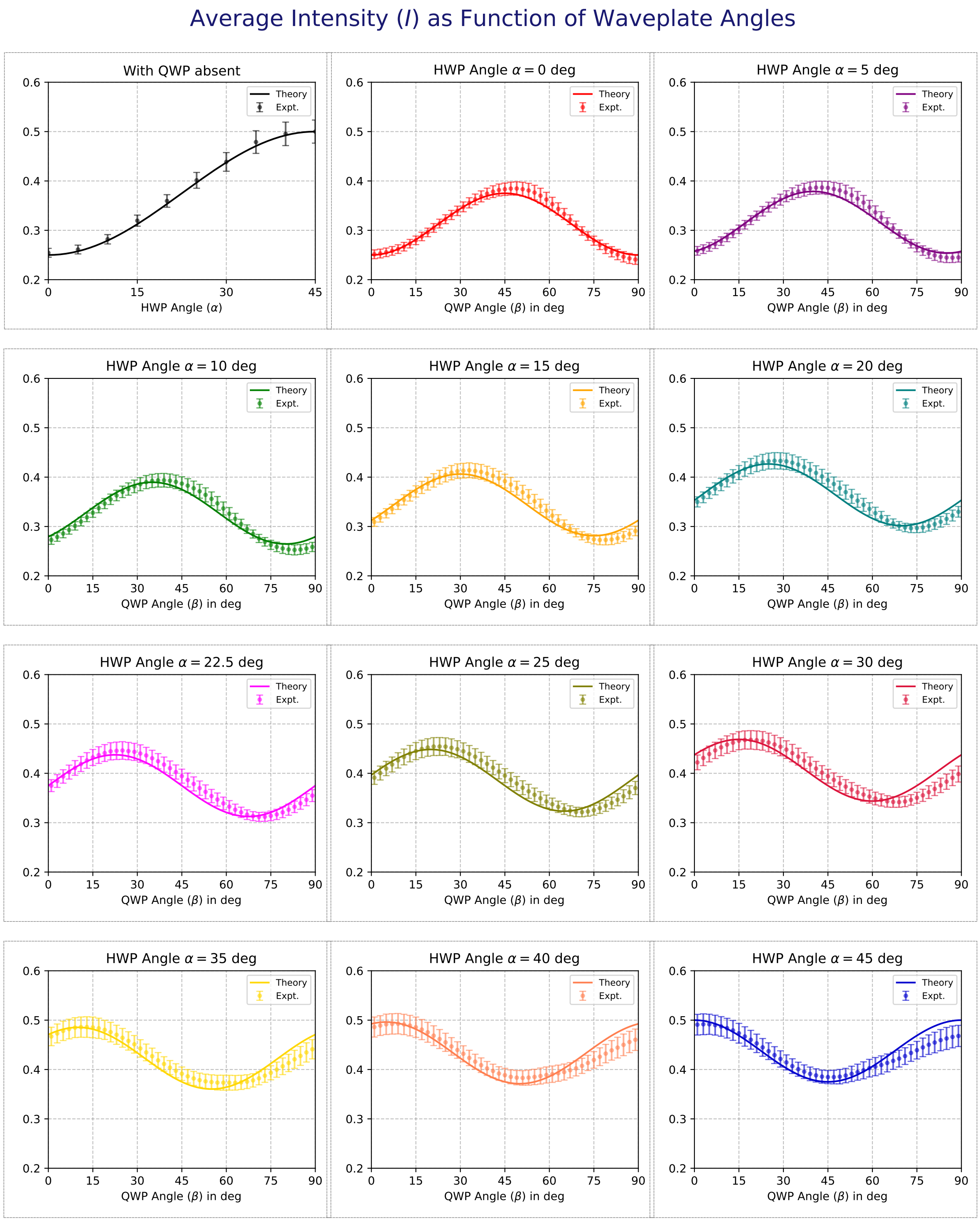

Figure 3.27: Average Intensity ($\bar{I}$) of the interference patterns generated in the QSI setup for different polarization qubits prepared by rotating the HWP (at α) followed by the QWP (β) in the path of a vertically polarized beam. All the experimentally average intensities are normalized with respect to the $norm = 0.5$ corresponding to the maximum value when only HWP is rotated in absence of the QWP.

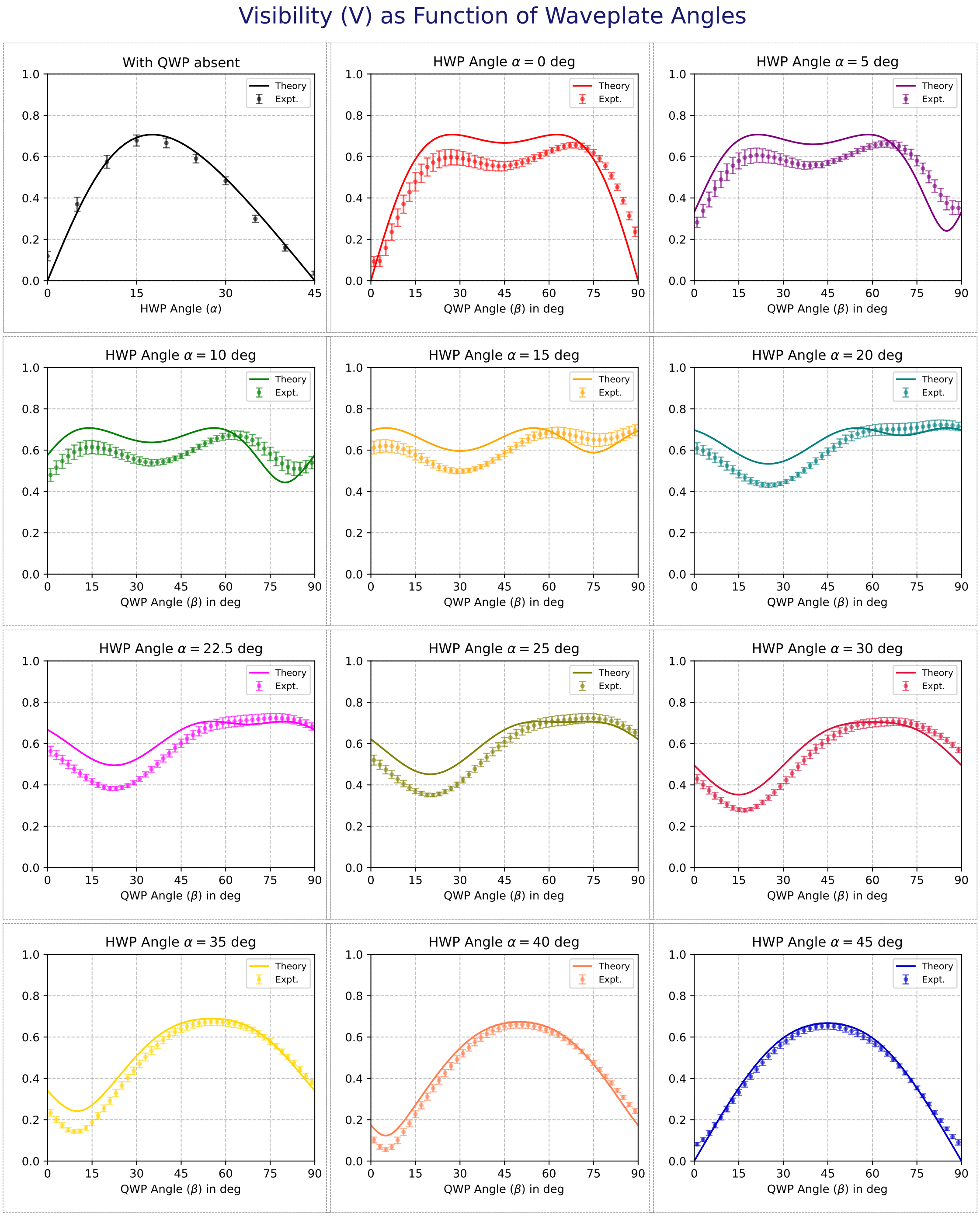

Figure 3.28: Visibility of the interference patterns generated in the QSI setup for different polarization qubits prepared by rotating the HWP (at α) followed by the QWP (β) in the path of a vertically polarized beam. The experimentally obtained visibility is systematically lower than the theoretical predictions due to different non-idealness in the experiment, such as angular deviation of the beam with wave plate rotation changing the spatial overlap, polarization dependent splitting ratio of the beam splitter, intensity averaging over the sensor area, distortion of the wavefront due to dusts on the optics and the sensor etc.

3.C Variation of Fidelity of Qubits with the Mixedness

In the experiment for polarization state interferography, we have prepared the states by acting a half-wave plate (HWP) and a quarter-wave plate (QWP) on the path of a beam with horizontal polarization $|H\rangle$ for the setup with MZI or vertical polarization $|V\rangle$ for the setup with DSI, which prepares a pure state $|\psi(\alpha,\beta)\rangle$. However, in general, the states that we deal with in an experiment are not always pure. For a qubit, the mixedness is parameterized with the factor μ. Here we will show how the fidelity of $\hat{\rho}_{pure}$ − the density matrix for a pure state (i.e., $\hat{\rho}_{pure} = \hat{\rho}(\mu = 1, \theta, \phi)$) with $\hat{\rho} = \hat{\rho}(\mu, \theta, \phi)$ − the density matrix for an arbitrary state (can be mixed or pure), changes as a function of μ. The fidelity of the state $\hat{\rho}_{pure}$ with the state $\hat{\rho}$ is computed as,

$$\mathcal{F}(\hat{\rho}_{pure}, \hat{\rho}) = \mathrm{Tr}\left(\sqrt{\sqrt{\hat{\rho}_{pure}}\ \hat{\rho}\ \sqrt{\hat{\rho}_{pure}}}\right)^2 \tag{3.56}$$

$$\implies \quad \mathcal{F}(\hat{\rho}_{pure}, \hat{\rho}) = 1 - \frac{1-\mu}{2}\sin^2(\theta) = \frac{1}{4}(3 + \mu + (1-\mu)\cos(2\theta)) \tag{3.57}$$

Therefore, the fidelity is a function of the parameters θ and μ and is independent of ϕ. Thus, the mixedness of a two-dimensional state does not affect the determination of the phase ϕ. At $\theta = 0$ or $\theta = \pi$, we get the fidelity as $\mathcal{F} = 1$, which is expected as θ values 0 and π respectively represent the pure states $|H\rangle$ and $|V\rangle$. When $\theta = \frac{\pi}{2}$, we get $\mathcal{F} = \frac{1+\mu}{2}$. Now, when μ tends to zero with $\theta = \frac{\pi}{2}$, i.e., when the state in the two dimensions approaches the maximally mixed state, the fidelity $\mathcal{F}$ tends to $\frac{1}{2}$.

The density plot for the fidelity as a function of μ and θ is shown in Fig. 3.29. From the plot, it can be observed that the fidelity $\mathcal{F}$ is close to 1 as μ approaches 1 corresponding to the pure states. Further, the value of $\mathcal{F}$ is close to 1 irrespective of the value of μ, when θ is close to 0 or π. The fidelity drops significantly, only when θ is close to $\frac{\pi}{2}$ and $\mu << 1$, i.e., when the mixedness of the state increases. For a small amount of mixedness introduced during the state preparation, we have the experimentally obtained fidelity $\mathcal{F} > 0.9$ for $\mu > 0.8$.

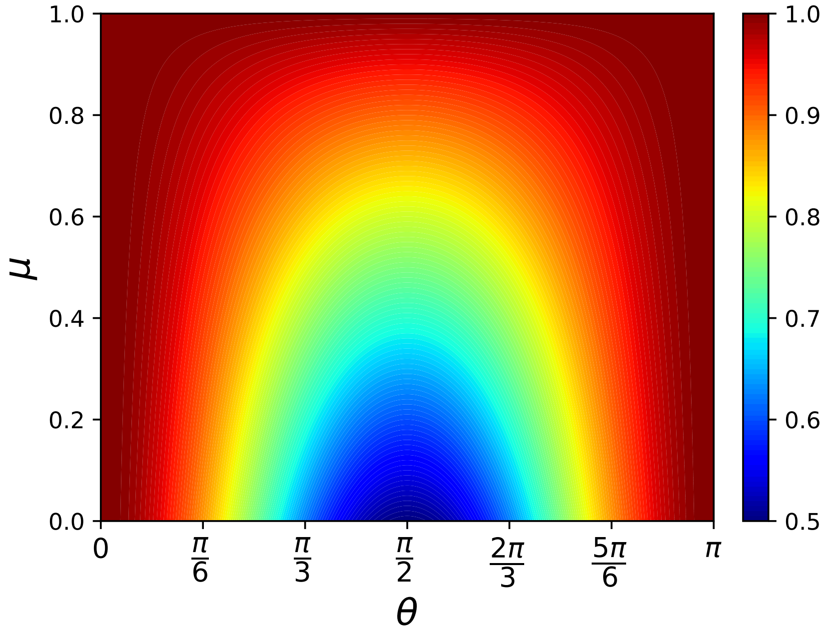

Figure 3.29: Density plot of Fidelity between a pure state $\hat{\rho}_{pure}$ and any arbitrary state $\hat{\rho}$ parameterized by μ. Note that the colors scale from 0.5 (blue) to 1 (red) corresponding to the values obtained for maximally mixed state and the pure state respectively.

References

[1] L. Zehnderl. "Ein neuer interferenzrefraktor". In: *Zeitschrift für Instrumentenkunde* 11 (1891).

[2] L. Mach. "Ueber einen interferenzrefraktor". In: *Zeitschrift für Instrumentenkunde* 12 (1892).

[3] A.K. Ghatak. *Optics*. Tata McGraw-Hill Publishing Company Limited, 2009.

[4] S. P. Walborn et al. "Double-slit quantum eraser". In: *Phys. Rev. A* 65 (3 2002), p. 033818. DOI: 10.1103/PhysRevA.65.033818.

[5] Masud Mansuripur. "The Sagnac interferometer". In: *Classical Optics and its Applications*. 2nd ed. Cambridge University Press, 2009, pp. 182–196. DOI: 10.1017/CBO9780511803796.017.

[6] Michal Mičuda et al. "Highly stable polarization independent Mach-Zehnder interferometer". In: *Review of Scientific Instruments* 85.8 (2014), p. 083103. DOI: 10.1063/1.4891702.

[7] Michael A. Nielsen and Isaac L. Chuang. *Quantum Computation and Quantum Information: 10th Anniversary Edition*. Cambridge University Press, 2010. DOI: 10.1017/CBO9780511976667.

[8] R. Simon and N. Mukunda. "Universal SU(2) gadget for polarization optics". In: *Physics Letters A* 138.9 (1989), pp. 474–480. DOI: https://doi.org/10.1016/0375-9601(89)90748-2.

[9] R. Simon and N. Mukunda. "Minimal three-component SU(2) gadget for polarization optics". In: *Physics Letters A* 143.4 (1990), pp. 165–169. DOI: https://doi.org/10.1016/0375-9601(90)90732-4.

[10] Arun Kumar Ajoy Ghatak. *Polarization of Light With Applications in Optical Fibers*. SPIE Press, 2011. DOI: 10.1117/3.861761.

[11] R. Clark Jones. "A New Calculus for the Treatment of Optical SystemsI. Description and Discussion of the Calculus". In: *J. Opt. Soc. Am.* 31.7 (1941), pp. 488–493. DOI: 10.1364/JOSA.31.000488.

[12] Ajoy Ghatak and K. Thyagarajan. *An Introduction to Fiber Optics*. Cambridge University Press, 1998. DOI: 10.1017/CBO9781139174770.

[13] D. Marcuse. "Gaussian approximation of the fundamental modes of graded-index fibers". In: *J. Opt. Soc. Am.* 68.1 (1978), pp. 103–109. DOI: 10.1364/JOSA.68.000103.

[14] Dr. Rüdiger Paschotta. *Fiber Connectors*. https://www.rp-photonics.com/fiber_connectors.html.

[15] Paul B. Ruffin. "Stress and temperature effects on the performance of polarization-maintaining fibers". In: *Polarimetry: Radar, Infrared, Visible, Ultraviolet, and X-Ray*. Ed. by Russell A. Chipman and John W. Morris. Vol. 1317. International Society for Optics and Photonics. SPIE, 1990, pp. 324–332. DOI: 10.1117/12.22068.

[16] M.P. Varnham et al. "Analytic solution for the birefringence produced by thermal stress in polarization-maintaining optical fibers". In: *IEEE Journal of Lightwave Technology* 1.2 (1983), pp. 332–9.

[17] *TIR Retroreflector Prisms, Thorlabs.*

[18] Surya Narayan Sahoo et al. "Unambiguous joint detection of spatially separated properties of a single photon in the two arms of an interferometer". In: *Communications Physics* 6.1 (2023), p. 203. DOI: 10.1038/s42005-023-01317-7.

[19] Gregor Jotzu, Tim J. Bartley, Hendrik B. Coldenstrodt-Ronge, Brian J. Smith and Ian A. Walmsley. "Continuous phase stabilization and active interferometer control using two modes". In: *Journal of Modern Optics* 59.1 (2012), pp. 42–45. DOI: 10.1080/09500340.2011.621033.

[20] Esben Ravn Andresen et al. "An active interferometer-stabilization scheme with linear phase control". English. In: *Optics Express* 14.12 (2006), pp. 1328–1330.

[21] I. J. Nagrath and M. Gopal. *Control Systems Engineering*. 2nd. USA: Halsted Press, 1982.

[22] Gaurav Nirala et al. "Measuring average of non-Hermitian operator with weak value in a Mach-Zehnder interferometer". In: *Phys. Rev. A* 99 (2 2019), p. 022111. DOI: 10.1103/PhysRevA.99.022111.

[23] N. I. Fisher. *Statistical Analysis of Circular Data*. Cambridge University Press, 1993. DOI: 10.1017/CBO9780511564345.

[24] Richard Jozsa. “Fidelity for Mixed Quantum States”. In: *Journal of Modern Optics* 41.12 (1994), pp. 2315–2323. DOI: 10.1080/09500349414552171.

[25] K. Banaszek, M. Cramer, and D. Gross. “Focus on quantum tomography”. In: *New Journal of Physics* 15.12 (2013), p. 125020. DOI: 10.1088/1367-2630/15/12/125020.

[26] Daniel F. V. James et al. “Measurement of qubits”. In: *Physical Review A* 64.5 (2001), p. 052312. DOI: 10.1103/PhysRevA.64.052312.

[27] E. C. G. Sudarshan. “Equivalence of Semiclassical and Quantum Mechanical Descriptions of Statistical Light Beams”. In: *Phys. Rev. Lett.* 10 (7 1963), pp. 277–279. DOI: 10.1103/PhysRevLett.10.277.

[28] Bo-Sture K Skagerstam. “On the three-slit experiment and quantum mechanics”. In: *Journal of Physics Communications* 2.12 (2018), p. 125014. DOI: 10.1088/2399-6528/aaf683.

Chapter 4

Quantum State Interferography for Higher Dimensional and Bipartite Quantum Systems

Contents

4.1 Parametric Representation of Higher Dimensional Quantum States – The Qudits

4.2 Quantum State Interferography for Qutrit

4.3 Quantum State Interferography for Qudit: The General Scheme

4.4 Quantum State Interferography for Qudit: The Scheme Employing Two Interferometers

4.5 Quantum State Interferography for Bipartite Qubits

4.6 Quantification of Entanglement using QSI Scheme

4.7 Conclusion

4.A Quantum State Interferography for Pure Qudits: Discussion With Normalization

4.B QSI for Qudit: Estimating Losses in Schemes with (d-1) Interferometers vs Two Interferometers

Quantum State Interferography (QSI), discussed in the previous chapters, is an interferometric state determination scheme that utilizes the information processed from interference patterns to characterize an unknown quantum state. For two-dimensional quantum systems, QSI appears to be a *single shot* state determination technique − that characterizes any unknown qubit by measuring the expectation values of the operators $\hat{\Pi}_0$ and $\hat{\sigma}_-$ in an interferometric setup. The last chapter presents the experimental implementation of this scheme for the reconstruction of the states in the polarization degree of freedom of light, which demonstrates QSI to be an effective technique for characterizing any arbitrary qubit with high fidelity, from a single interference pattern. In this chapter, we will introduce an extension of the scheme for characterizing the unknown states of d-dimensional quantum systems, referred to as *qudits*, as well as, for characterizing the unknown states of two qubit systems, also known as the *bipartite qubits*. The chapter will include the experimental proposals for inferring the d-dimensional pure spin qudit $|\psi\rangle^{(d)}$ from $(d-1)$ measurements, and for determining the pure bipartite qubit $|\Psi\rangle_{AB}$ of a photonic system with three measurements in two experimental settings.

The process of characterizing an unknown quantum state, be it a qudit or a bipartite qubit, using quantum state interferography (QSI) involves extracting the state parameters from the phase shift, average intensity, and visibility of a number of interference patterns generated in an interferometric setup with several necessary operators. In this chapter we will first present, the parametric representations of qudit states within a d-dimensional Hilbert space and bipartite qubit states within a 2×2 dimensional Hilbert space. Then, we will explore the interferometric scheme for inferring the state parameters of an arbitrary d-dimensional pure qudit $|\psi\rangle^{(d)}$ from $(d-1)$ interferograms that can be produced using merely two interferometers, without the need to change any experimental settings, i.e., in a *single shot* method. Next, we will present an experimental scheme for the reconstruction of pure bipartite qubits (labeled as $|\Psi\rangle_{AB}$) employing interferometry, where the unknown bipartite state can be inferred by performing single qubit QSI on the respective subsystems A and B and a heralded QSI with the heralding subject to a constraint. We then go on to show that QSI is more resource efficient than standard quantum state tomography (QST) for the quantification of entanglement in pure bipartite qubits.

4.1 Parametric Representation of Higher Dimensional Quantum States – The Qudits

In the Bloch sphere representation, a pure state for a qubit can be represented as a point on the surface of a unit 2-sphere $\mathbb{S}^{(2)}$ - the Bloch sphere [1]. The polar angle $\theta_b \in [0, \pi]$ and the azimuthal angle $\phi_b \in [-\pi, +\pi)$ in the spherical polar co-ordinate completely describes $|\psi\rangle^{(2)}$, the state for a pure qubit. However, a state for mixed qubit is represented by a point inside the Bloch sphere. So, the Bloch vector associated with a mixed qubit should span the entire volume of the Bloch sphere and hence, requires one additional parameter for its representation, which corresponds to the length of the Bloch vector ($|\vec{r}| = r_b$). Thus in general, an arbitrary qubit state can be represented by 3 real parameters (θ_b, ϕ_b, r_b), where $r_b = 1$ for pure qubits and $0 \leq r_b < 1$ for mixed qubits. Hence, $\mathbb{S}^{(2)}$ needs to be embedded in three dimensions.

Now, if we aim to extend the idea intuitively to d-dimensional qudit, we may attempt to represent a pure state in d-dimension as a point on the surface of a unit d-sphere ($\mathbb{S}^{(d)}$) and a mixed state as a point within the volume of the unit d-sphere, with the corresponding ray spanning the entire volume of $\mathbb{S}^{(d)}$. By analogy, $\mathbb{S}^{(d)}$ is considered to be embedded in $(d+1)$-dimensional Euclidean space. However, such generalizations do not hold. Employing a geometric representation similar to the Bloch-sphere for the visualization of higher dimensional quantum states would be beneficial in the filed of quantum information and computation, but implementing such a generalization for the qudits is not that simple and seems to be challenging [2, 3, 4].

A pure qubit state is described by a two-dimensional complex-valued vector with unit norm i.e., the state being $\begin{pmatrix} \alpha_1 \\ \alpha_2 \end{pmatrix}$ with the constraint that $|\alpha_1|^2 + |\alpha_2|^2 = 1$. The information in two complex numbers, given one constraint (the normalization), can be represented by $(2 \times 2 - 1) = 3$ real numbers. However, the global phase can also be ignored since only the relative phase between the two basis vectors in the Hilbert space has any physical consequence [1]. Thus, the number of real quantities to be specified for a pure qubit can be reduced to 2. Hence, the co-ordinates of a point i.e., (θ_b, ϕ_b) on the surface of $\mathbb{S}^{(2)}$ suffices

[1]in terms of the outcomes of projective measurements.

to represent the pure state of a qubit.

Now, if we consider a pure qutrit, i.e., a state of a three level quantum system, 3 complex numbers $(\alpha_1, \alpha_2, \alpha_3)$ are required to represent a vector in the 3-dimensional Hilbert space. Provided, we have one constraint of normalization i.e., $\sum_{j=1}^{3} |\alpha_j|^2 = 1$ and we can ignore the global phase here as well, makes the number of real parameters needed for a complete description of a pure state of a three-dimensional quantum system to be $(3 \times 2 - 2) = 4$. So, a pure qutrit can be specified as a point on the surface of a unit 4-sphere ($\mathbb{S}^{(4)}$) [5] embedded in $4 + 1 = 5$ dimensions in Euclidean geometry [6]. Usually, one can parameterize a point on the 4-sphere with four Euler angles (the angles that the ray makes with the basis vectors). But they do not help much in visualizing the state.

Similarly, for a d-dimensional pure qudit we will have one normalization constraint i.e., $\sum_{j=1}^{d} |\alpha_j|^2 = 1$ where $\alpha_j \in \mathbb{C}^2$ and can ignore the global phase; making the number of real parameters needed to describe a pure qudit to be $(2 \times d - 2) = 2(d - 1)$. So, a pure state in d-dimensional Hilbert space can be represented as a point on the surface of a unit $2(d - 1)$-sphere i.e., $\mathbb{S}^{(2(d-1))}$ embedded in $2d - 1$ dimensional Euclidean space [7]. Even though there are various existing representations for the qudits, the attempts to visualize the higher dimensional states within the Bloch-sphere in $\mathbb{R}^3$ is still a subject of ongoing research [8, 9]. Here, in this section we will focus on the widely recognized representation − the Majorana representation of qudits and will explore the possibilities of inferring the state parameters in this representation through the use of interferometric techniques.

4.1.1 Majorana Representation

Since the number of real parameters needed for the description of a d-dimensional pure qudit is $2(d - 1)$, instead of representing a single point on the surface of $2(d - 1)$-sphere, i.e., on $\mathbb{S}^{(2(d-1))}$, we can represent a set of $(d - 1)$ points on unit 2-sphere i.e., on $\mathbb{S}^{(2)}$ [10, 11]. The $\mathbb{S}^{(2)}$ is embedded in the three-dimensional space $\mathbb{R}^3$ with the two antipodal points representing the eigenstates associated with the extreme eigenvalues for a given eigen basis, when all the $(d - 1)$ points lie on the surface. So, the point on the +ve z-axis (the north pole) of the unit sphere represents the eigenvector corresponding to the largest eigenvalue and the point on the −ve z-axis (the south pole) of the unit sphere represents the eigenvector corresponding to the smallest eigenvalue for the given eigen basis. The protocol is to place an Argand plane at the $z = 0$ plane in Cartesian three-dimensional space $\mathbb{R}^3$. In general, the $(d-1)$ points on the 2-sphere are obtained by stereographic projections (with respect to the south pole) of the $(d-1)$ complex roots of the Majorana polynomial represented on the extended Argand plane [12].

The roots of the Majorana polynomial for a system with spin [2] $s = \dfrac{d-1}{2}$ are given by the solutions of the following expression [10],

$$\sum_{r=0}^{2s} a_r \; \xi^{2s-r} = 0 \tag{4.1}$$

$$\Longrightarrow \qquad a_0\xi^{2s} + a_1\xi^{2s-1} + \ldots + a_{2s-1}\xi + a_{2s} = 0 \tag{4.2}$$

$$\text{where,} \qquad a_r = (-1)^r \frac{C_{s-r}}{\sqrt{(2s-r)!\; r!}} \tag{4.3}$$

Eqn. 4.2 represents the relationship between the $(2s+1)$ coefficients a_r and the $2s = d-1$ roots of the Majorana polynomial. C_k's are the complex coefficients of the qudit state $|\psi\rangle^{(d)}$ represented in a given eigenbasis $\{|-s\rangle, |-s+1\rangle, \ldots, |0\rangle, \ldots, |s-1\rangle, |s\rangle\}$, i.e.,

$$|\psi\rangle^{(d)} = \sum_{k=-s}^{s} C_k \, |k\rangle \, . \tag{4.4}$$

The state $|\psi\rangle^{(d)}$ can be represented by the points $P_1, P_2, \ldots, P_{d-1}$ on the surface of the unit 2-sphere [13], with $\{\theta_m, \phi_m\}$ being the spherical polar co-ordinates of a point P_m. The roots ξ_m (with $m = 1, 2, \ldots, 2s$) of the Majorana polynomial satisfies the following relation with θ_m, ϕ_m.

$$\xi_m = \tan\left(\frac{\theta_m}{2}\right) e^{i\phi_m} \tag{4.5}$$

[2]Usually, a system with spin s is described in a $(2s+1)$-dimensional Hilbert space, thus we get the dimensionality to be $d = 2s+1$.

Thus the pure state $|\psi\rangle^{(d)}$ of a d-dimensional quantum system has a bijective correspondence with the complex roots ξ_m of the Majorana polynomial and these roots belonging to the Argand plane at $z = 0$ of $\mathbb{R}^3$ have bijective correspondence to the points given by (θ_m, ϕ_m) on the surface of $\mathbb{S}^{(2)}$ through stereographic projections.

For example, the set of two points $\{P_1 \equiv (\theta_1, \phi_1),\ P_2 \equiv (\theta_2, \phi_2)\}$ on the Bloch sphere, represents the pure state of a qutrit $|\psi\rangle^{(3)}$ [14]. A three-dimensional system $(d = 3)$ can be considered as a system with $s = 1$; thus the $2s = 2$ roots of the Majorana polynomial associated with this three level system i.e., ξ_1 and ξ_2 can be obtained by solving the following expression,

$$a_0\xi^2 + a_1\xi + a_2 = 0 \tag{4.6}$$

$$C_1\xi^2 - \sqrt{2}C_0\xi + C_{-1} = 0 \tag{4.7}$$

Here, C_1, C_0, C_{-1} are respectively the probability amplitudes associated with basis vectors $\{|1\rangle, |0\rangle, |-1\rangle\}$ that spans the three-dimensional Hilbert space. Therefore the qutrit is represented as, $|\psi\rangle^{(3)} = C_1|1\rangle + C_0|0\rangle + C_{-1}|-1\rangle$. Both ξ_1 and ξ_2 satisfies the relation shown in Eqn. 4.5 with (θ_1, ϕ_1) and (θ_2, ϕ_2) respectively [3], giving the pure state of a qutrit in the Majorana representation as the following,

$$|\psi\rangle^{(3)} = \Gamma \begin{pmatrix} \sqrt{2}\cos\left(\frac{\theta_1}{2}\right)\cos\left(\frac{\theta_2}{2}\right) \\ e^{i\phi_1}\sin\left(\frac{\theta_1}{2}\right)\cos\left(\frac{\theta_2}{2}\right) + e^{i\phi_2}\cos\left(\frac{\theta_1}{2}\right)\sin\left(\frac{\theta_2}{2}\right) \\ \sqrt{2}\, e^{i(\phi_1+\phi_2)}\sin\left(\frac{\theta_1}{2}\right)\sin\left(\frac{\theta_2}{2}\right) \end{pmatrix} \tag{4.8}$$

$$\text{where,} \qquad \Gamma = \sqrt{\frac{2}{3 + \cos(\theta_1)\cos(\theta_2) + \sin(\theta_1)\sin(\theta_2)\cos(\phi_1 - \phi_2)}} \tag{4.9}$$

The factor Γ in front of the vector is the normalization factor and the ray in the 3-dimensional Hilbert space is completely determined by the vector itself.

[3]The roots ξ_1 and ξ_2 are given as, $\xi_1 = \tan\left(\frac{\theta_1}{2}\right)e^{i\phi_1}$ and $\xi_2 = \tan\left(\frac{\theta_2}{2}\right)e^{i\phi_2}$.

❑ Expectation Values of the Spin Ladder Operators:

As presented in Chapter. 2, the state of an unknown qubit $|\psi\rangle^{(2)}$ could be determined from the expectation value of the spin ladder operators $\hat{\sigma}_{\pm} = \frac{1}{2}(\hat{\sigma}_x \pm i\hat{\sigma}_y)$. The argument of the complex expectation value $\langle\hat{\sigma}_{\pm}\rangle$ in the Argand plane appears to be the same as the relative phase of the qubit state in the Bloch sphere, i.e., $\arg(\langle\hat{\sigma}_{\pm}\rangle) = \pm\phi$. The magnitude of $\langle\hat{\sigma}_{\pm}\rangle$ gives the polar angle θ of the two-dimensional state. Here, for the qudits, we aim to achieve something similar i.e., we will first check if we can obtain the azimuthal angles i.e., ϕ_m (for $m = 1, 2, \dots (d-1)$) from the expectation values of the spin ladder operators.

The spin ladder operators $\hat{\sigma}^{[3]}_{\pm} = \frac{1}{2}\left(\hat{\sigma}^{[3]}_x \pm i\hat{\sigma}^{[3]}_y\right)$ that acts on the 3-dimensional Hilbert space [4] and their polar decomposition into Unitary and Hermitian are given as below.

$$\hat{\sigma}^{[3]}_{+} = \sqrt{2}\begin{pmatrix} 0 & 1 & 0 \\ 0 & 0 & 1 \\ 0 & 0 & 0 \end{pmatrix} = \hat{U}^{[3]}_{+}\ \hat{R}^{[3]}_{+} \tag{4.10}$$

$$\text{with} \quad \hat{U}^{[3]}_{+} = \begin{pmatrix} 0 & 1 & 0 \\ 0 & 0 & 1 \\ 1 & 0 & 0 \end{pmatrix} \quad \text{and} \quad \hat{R}^{[3]}_{+} = \sqrt{2}\begin{pmatrix} 0 & 0 & 0 \\ 0 & 1 & 0 \\ 0 & 0 & 1 \end{pmatrix} \tag{4.11}$$

$$\hat{\sigma}^{[3]}_{-} = \sqrt{2}\begin{pmatrix} 0 & 0 & 0 \\ 1 & 0 & 0 \\ 0 & 1 & 0 \end{pmatrix} = \hat{U}^{[3]}_{-}\ \hat{R}^{[3]}_{-} \tag{4.12}$$

$$\text{with} \quad \hat{U}^{[3]}_{-} = \begin{pmatrix} 0 & 0 & 1 \\ 1 & 0 & 0 \\ 0 & 1 & 0 \end{pmatrix} \quad \text{and} \quad \hat{R}^{[3]}_{-} = \sqrt{2}\begin{pmatrix} 1 & 0 & 0 \\ 0 & 1 & 0 \\ 0 & 0 & 0 \end{pmatrix} \tag{4.13}$$

[4] The pauli matrices in SU(3) are obtained using Kramer's method and are as follows:

$$\hat{\sigma}^{[3]}_x = \sqrt{2}\begin{pmatrix} 0 & 1 & 0 \\ 1 & 0 & 1 \\ 0 & 1 & 0 \end{pmatrix}, \quad \hat{\sigma}^{[3]}_y = i\sqrt{2}\begin{pmatrix} 0 & -1 & 0 \\ 1 & 0 & -1 \\ 0 & 1 & 0 \end{pmatrix}, \quad \hat{\sigma}^{[3]}_z = 2\begin{pmatrix} 1 & 0 & 0 \\ 0 & 0 & 0 \\ 0 & 0 & -1 \end{pmatrix}$$

From the above expressions note that, in the three dimensions neither the Hermitian component $\hat{R}_{\pm}^{[3]}$ of the spin ladder operator is a projector nor the Unitary component $\hat{U}_{\pm}^{[3]}$ is Pauli-X operator $\hat{\sigma}_x^{[3]}$, when compared to the two dimensional operators. In two dimensions, the 2×2 non-Hermitian spin ladder operators $\hat{\sigma}_{\pm}$ and their polar decomposition into positive semi-definite Hermitian $(\hat{R})$ and Unitary $(\hat{U})$ are given as, $\hat{\sigma}_{-}^{[2]} = \hat{U}_{-}^{[2]}\ \hat{R}_{-}^{[2]} = \hat{\sigma}_x^{[2]}\ \hat{\Pi}_0^{[2]}$ and $\hat{\sigma}_{+}^{[2]} = \hat{U}_{+}^{[2]}\ \hat{R}_{+}^{[2]} = \hat{\sigma}_x^{[2]}\ \hat{\Pi}_1^{[2]}$, where $\hat{\Pi}_0^{[2]}$ and $\hat{\Pi}_1^{[2]}$ are the 2×2 projectors associated with the basis states $|0\rangle$ and $|1\rangle$. The expectation values of the ladder operators $\hat{\sigma}_{\pm}^{[3]}$ in the qutrit state given in the Majorana representation in Eqn. 4.8 is obtained as,

$$\left\langle \hat{\sigma}_{+}^{[3]} \right\rangle = \left\langle \psi^{(3)} \middle| \hat{\sigma}_{+}^{[3]} \middle| \psi^{(3)} \right\rangle = \Gamma^2 \left(e^{i\phi_1} \sin(\theta_1) + e^{i\phi_2} \sin(\theta_2) \right) \tag{4.14}$$

$$= \frac{2\left(e^{i\phi_1}\sin(\theta_1) + e^{i\phi_2}\sin(\theta_2)\right)}{3 + \cos(\theta_1)\cos(\theta_2) + \sin(\theta_1)\sin(\theta_2)\cos(\phi_1 - \phi_2)} \tag{4.15}$$

$$\left\langle \hat{\sigma}_{-}^{[3]} \right\rangle = \left\langle \psi^{(3)} \middle| \hat{\sigma}_{-}^{[3]} \middle| \psi^{(3)} \right\rangle = \Gamma^2 \left(e^{-i\phi_1} \sin(\theta_1) + e^{-i\phi_2} \sin(\theta_2) \right) \tag{4.16}$$

$$= \frac{2\left(e^{-i\phi_1}\sin(\theta_1) + e^{-i\phi_2}\sin(\theta_2)\right)}{3 + \cos(\theta_1)\cos(\theta_2) + \sin(\theta_1)\sin(\theta_2)\cos(\phi_1 - \phi_2)} \tag{4.17}$$

So, the expectation values $\left\langle \hat{\sigma}_{\pm}^{[3]} \right\rangle$ are the function of all the four parameters $\{\theta_1, \phi_1, \theta_2, \phi_2\}$ associated with the qutrit and none of the individual parameters can be directly extracted from the magnitude, Argand phase, real part or imaginary part of the complex expectation values of the spin ladder operators. It seems that, if we rewrite the spin ladder operators in terms of two ladder-like [5] operators, we may be able to obtain $e^{i\phi_1}\sin(\theta_1)$ and $e^{i\phi_2}\sin(\theta_2)$ separately from the complex expectation values. Sadly, that is not the case with Majorana representation, as shown in the computations below.

❑ Expectation Values of the Ladder-Like Operators:

Now, let us consider the three-dimensional Hilbert space is spanned by the basis states $\{|1\rangle, |2\rangle, |3\rangle\}$, where

[5] Strictly, they are not the spin ladder operators because they do not follow from $\frac{1}{2}(\hat{\sigma}_x \pm i\hat{\sigma}_y)$.

$$|1\rangle = \begin{pmatrix} 1 \\ 0 \\ 0 \end{pmatrix}, \qquad |2\rangle = \begin{pmatrix} 0 \\ 1 \\ 0 \end{pmatrix}, \qquad |3\rangle = \begin{pmatrix} 0 \\ 0 \\ 1 \end{pmatrix} \tag{4.18}$$

Therefore, for the qutrits, we can consider the ladder-like [6] non-Hermitian operators $\hat{\mathcal{A}}^{3\to1}, \hat{\mathcal{A}}^{2\to1}$ and $\hat{\mathcal{A}}^{3\to2}$ as given in the following, where $\hat{\mathcal{A}}^{i\to j}$ is an operator similar to the raising operator that takes the basis state $|i\rangle$ to the state $|j\rangle$.

$$\hat{\mathcal{A}}^{3\to1} = \begin{pmatrix} 0 & 0 & 1 \\ 0 & 0 & 0 \\ 0 & 0 & 0 \end{pmatrix}, \qquad \hat{\mathcal{A}}^{2\to1} = \begin{pmatrix} 0 & 1 & 0 \\ 0 & 0 & 0 \\ 0 & 0 & 0 \end{pmatrix}, \qquad \hat{\mathcal{A}}^{3\to2} = \begin{pmatrix} 0 & 0 & 0 \\ 0 & 0 & 1 \\ 0 & 0 & 0 \end{pmatrix} \tag{4.19}$$

The expectation values of the above ladder-like operators in the state $|\psi\rangle^{(3)}$ given in Eqn. 4.8 are computed as the following,

$$\left\langle \hat{\mathcal{A}}^{3\to1} \right\rangle = \frac{\Gamma^2}{2}\, e^{i(\phi_1+\phi_2)} \sin(\theta_1) \sin(\theta_2) \tag{4.20}$$

$$\left\langle \hat{\mathcal{A}}^{2\to1} \right\rangle = \frac{\Gamma^2}{\sqrt{2}} \left[e^{i\phi_1} \sin(\theta_1) \cos^2\left(\frac{\theta_2}{2}\right) + e^{i\phi_2} \sin(\theta_2) \cos^2\left(\frac{\theta_1}{2}\right) \right] \tag{4.21}$$

$$\left\langle \hat{\mathcal{A}}^{3\to2} \right\rangle = \frac{\Gamma^2}{\sqrt{2}} \left[e^{i\phi_1} \sin(\theta_1) \sin^2\left(\frac{\theta_2}{2}\right) + e^{i\phi_2} \sin(\theta_2) \sin^2\left(\frac{\theta_1}{2}\right) \right] \tag{4.22}$$

Again all the expectation values computed above are functions of all the four parameters, i.e., $\{\theta_1, \theta_2, \phi_1, \phi_2\}$. Thus, the state parameters can not be determined individually from the expectation values of the ladder-like operators as well. This implies that identifying the state parameters associated with a qudit in Majorana representation is not that straight forward. Therefore, we require an alternative representation for qudits and aim to obtain

[6] Since the dimension is discreet, and there is a prior hierarchy or non-degeneracy among states, the ladder operator that raises the state $\begin{pmatrix} 1 & 0 & 0 \end{pmatrix}^T$ to $\begin{pmatrix} 0 & 1 & 0 \end{pmatrix}^T$ is on the same footing as the operator that takes $\begin{pmatrix} 0 & 0 & 1 \end{pmatrix}^T$ to $\begin{pmatrix} 1 & 0 & 0 \end{pmatrix}^T$.

the relative phases directly as the phase in the Argand plane in the complex expectation values of the ladder-like operators.

4.1.2 Episphere Representation

In the last subsection, we have seen the Majorana representation of a d-dimensional qudit where a pure qudit is represented as a set of $(d-1)$ points on the surface of a unit 2-sphere i.e., the Bloch sphere. $(2d-2)$ quantities $\{\theta_j, \phi_j\}$ with $j = 1, 2, \ldots, (d-1)$, can completely describe the pure qudit $|\psi\rangle^{(d)}$, where each set (θ_m, ϕ_m) with $\theta_m \in [0, \pi]$ and $\phi_m \in [-\pi, \pi)$ represents the polar angle and azimuthal angle associated with a point P_m on $\mathbb{S}^{(2)}$. Here, we will propose another way of parameterizing the d-dimensional states, where each pure state $|\psi\rangle^{(d)}$ in d-dimension would be represented as *a chain of vectors* within *epispheres*. The name "Episphere" is considered along the terms of 'epicycles' which represent a circle whose center lies on the circumference of another circle. Thus, here the term "Episphere" is used to represent the sphere which originates at a point lying on the surface of another previously existing sphere.

In the proposed Episphere representation of a qudit, any d-dimensional pure state $|\psi\rangle^{(d)}$ can be represented as a sequence of $(d-1)$ Bloch vectors, defined within what we term as 'Epispheres'. For a d-dimensional qudit, we construct $(d-1)$ spheres, with the origin of the k-th sphere being located at the tip of the $(k-1)$-th Bloch vector defined in the $(k-1)$-th sphere, where $1 \leq k \leq d-1$ as shown in Fig. 4.1. Each sphere represents a subsequent two-dimensional subspace of the d-dimensional Hilbert space. The $1st$ sphere represents the first two-dimensional sub-space spanned by the states $\{|1\rangle, |2\rangle\}$. The tip of the Bloch vector associated with the first sub-space, located at (θ_1, ϕ_1) on the surface of this sphere, is considered as the origin of the $2nd$ sphere, which is the first episphere in the sequence. The $2nd$ sphere in the sequence represents the sub-space spanned by the states $\{|2\rangle, |3\rangle\}$ and the corresponding Bloch vector has the tip at (θ_2, ϕ_2) on the surface of this sphere. Consequently, the n-th sphere in the sequence (i.e., the $(n-1)$-th episphere) represents the n-th two-dimensional subspace spanned by the basis states $|n\rangle$ and $|n+1\rangle$. Therefore, in the Episphere representation, we parameterize the state $|\psi\rangle^{(d)}$ in terms of the $(d-1)$ two-dimensional sub-spaces of the d-dimensional space in a specific sequence.

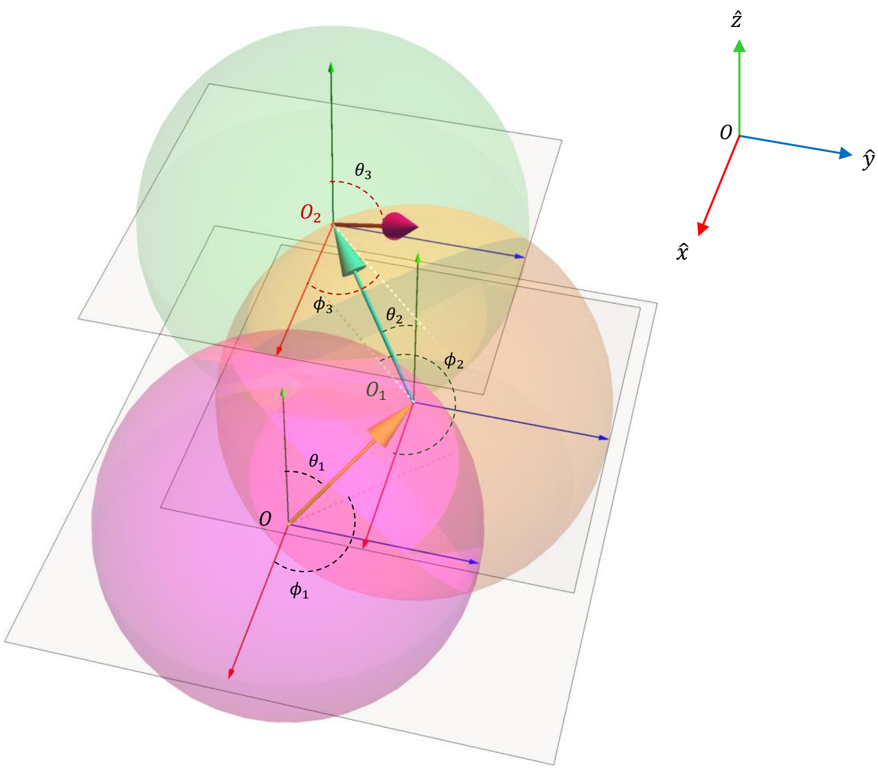

Figure 4.1: Episphere representation of a qudit (with d=4): Representation of a pure state $|\psi\rangle^{(d=4)}$ as a chain of three Bloch vectors presented with orange, green and maroon arrows. The 'orange' Bloch vector spans the $1st$ two-dimensional subspace with basis vectors $\{|1\rangle, |2\rangle\}$. The $2nd$ subspace with basis vectors $\{|2\rangle, |3\rangle\}$ is represented by the episphere (shown in 'orange') that originates from the tip of the 'orange' vector at (θ_1, ϕ_1) and is spanned by the 'green' Bloch vector. The $3rd$ subspace with basis states $\{|3\rangle, |4\rangle\}$ is spanned by the 'maroon' vector within the episphere (shown in 'green') whose origin lies at the tip of the 'green' Bloch vector at (θ_2, ϕ_2). θ_i and ϕ_i in each sphere represent the polar and azimuthal angles corresponding to different Bloch vectors.

4.1.3 Episphere Representation of Qutrits

The Majorana representation of a qutrit involves the description of two points on $\mathbb{S}^{(2)}$ – the Bloch sphere. Instead of using the same Bloch sphere, in Episphere representation we construct two Bloch spheres and the qutrit is represented by a chain of two Bloch vectors. The tip of the first Bloch vector lies on the surface of the first Bloch sphere (with center at O) at any point O_1 denoted by the parameters (θ_1, ϕ_1) where $\theta_1 \in [0, \pi]$ and $\phi_1 \in [-\pi, \pi)$

respectively represent the angle that the Bloch vector ($\overrightarrow{OO_1}$) makes with $\hat{z}$ and the angle that the projection of Bloch vector on $x-y$ plane makes with $\hat{x}$. The tip of the second Bloch vector ($\overrightarrow{O_1O_2}$) represents a point O_2 denoted by (θ_2, ϕ_2) on the surface of the second Bloch sphere which originate at the point $O_1 \equiv (\theta_1, \phi_1)$. We can very well represent the two vectors on a single Bloch sphere or two separate Bloch spheres as long as the ordering of the vectors is clear. Representing the vectors as a chain makes the collection of the Bloch vectors an ordered set, which will be important in the representation of 3-dimensional state.

Each Bloch-vector (say, $\vec{v}_j$) defined in a Bloch sphere that represents the pure state space of the corresponding two-dimensional subspace (say, j-th subspace where $j = 1, 2$ for qutrit), can be represented in terms of polar co-ordinates (θ_j, ϕ_j) as the following.

$$\vec{v}_j = \begin{pmatrix} \cos\left(\frac{\theta_j}{2}\right) \\ \\ e^{i\phi_j} \sin\left(\frac{\theta_j}{2}\right) \end{pmatrix} \tag{4.23}$$

Therefore, the episphere representation of the three-dimensional pure state $|\psi\rangle^{(3)}$ in the form of a chain of two Bloch vectors, is given by,

$$|\psi\rangle^{(3)} = \begin{pmatrix} \cos\left(\frac{\theta_1}{2}\right) \\ \\ e^{i\phi_1} \sin\left(\frac{\theta_1}{2}\right) \begin{pmatrix} \cos\left(\frac{\theta_2}{2}\right) \\ \\ e^{i\phi_2} \sin\left(\frac{\theta_2}{2}\right) \end{pmatrix} \end{pmatrix} = \begin{pmatrix} \cos\left(\frac{\theta_1}{2}\right) \\ \\ e^{i\phi_1} \sin\left(\frac{\theta_1}{2}\right) \cos\left(\frac{\theta_2}{2}\right) \\ \\ e^{i(\phi_1+\phi_2)} \sin\left(\frac{\theta_1}{2}\right) \sin\left(\frac{\theta_2}{2}\right) \end{pmatrix} \tag{4.24}$$

Here, the second two-dimensional subspace spanned by the second Bloch vector $\vec{v}_2$ parameterized with (θ_2, ϕ_2) is multiplied with the second element of the first Bloch vector $\vec{v}_1$ parameterized with (θ_1, ϕ_1) to generate a vector $|\psi\rangle^{(3)}$ in the three dimensions.

❑ Does $|\psi(\theta_1, \theta_2, \phi_1, \phi_2)\rangle^{(3)}$ spans the entire 3-dimensional Hilbert space?

In order to show that the above representation spans all the rays in the 3-dimensional Hilbert space, we have to show that we can construct a set of three arbitrary complex numbers $\{\alpha_1, \alpha_2, \alpha_3\}$ that represent a three dimensional vector $\vec{a}$ up to a global phase and with the constraint of normalization, i.e., $\sum_{k=1}^{3} |\alpha_k|^2 = 1$. So, we can write a vector $\vec{a}$ in three dimensions as,

$$\vec{a} = \begin{pmatrix} \alpha_1 \\ \alpha_2 \\ \alpha_3 \end{pmatrix} = \begin{pmatrix} |\alpha_1| e^{i\arg(\alpha_1)} \\ |\alpha_2| e^{i\arg(\alpha_2)} \\ |\alpha_3| e^{i\arg(\alpha_3)} \end{pmatrix} = e^{i\arg(\alpha_1)} \begin{pmatrix} |\alpha_1| \\ |\alpha_2| e^{i(\arg(\alpha_2)-\arg(\alpha_1))} \\ |\alpha_3| e^{i(\arg(\alpha_3)-\arg(\alpha_1))} \end{pmatrix} \tag{4.25}$$

First, we can always multiply the vector $\vec{a}$ with $e^{-i\arg(\alpha_1)}$ as $\phi_g = \arg(\alpha_1)$ is considered as the global phase of the state, which gives a new vector $\vec{a'} = e^{-i\phi_g}\ \vec{a} = \begin{pmatrix} \alpha & \beta & \gamma \end{pmatrix}^T$. The first element of the new vector is given as $\alpha = |\alpha_1|$ which is a positive real quantity. Due to normalization constraint, i.e., $\sum_{k=1}^{3} |\alpha_k|^2 = 1$, we will always have $|\alpha_1| \leq 1$ and thus $|\alpha_1|$ can be parameterized by $\cos\left(\frac{\theta_1}{2}\right)$, where, $0 \leq \theta_1 \leq \pi$ ensures that $0 \leq |\alpha_1| \leq 1$. So, we have the first element of the vector $\vec{a'}$ as $\alpha = \cos\left(\frac{\theta_1}{2}\right)$.

The second element of the new vector $\vec{a'}$ is, $\beta = |\alpha_2| e^{i\varphi_{21}}$ where $\varphi_{21} = \arg(\alpha_2) - \arg(\alpha_1)$. Thus, β is a new complex number with magnitude $|\beta| = |\alpha_2|$ and argument $\arg(\beta) = \varphi_{21}$. The normalization constraint imposes that $|\beta| \leq \sqrt{1 - |\alpha|^2}$. Now we have $\sqrt{1 - |\alpha|^2} = \sqrt{1 - \cos^2\left(\frac{\theta_1}{2}\right)} = \sin\left(\frac{\theta_1}{2}\right)$, making the above condition to be $|\beta| \leq \sin\left(\frac{\theta_1}{2}\right)$. Thus, the magnitude of the complex number β can be represented as $|\beta| = \sin\left(\frac{\theta_1}{2}\right)\cos\left(\frac{\theta_2}{2}\right)$ which ensures $0 \leq |\beta| \leq \sin\left(\frac{\theta_1}{2}\right)$, given $\theta_2 \in [0, \pi]$. The argument of the quantity β can be arbitrary and hence can be represented by ϕ_1 with $\phi_1 \in [-\pi, \pi)$. Therefore, it gives $\phi_1 = \arg(\beta) = \varphi_{21}$, i.e., $\phi_1 = \arg(\alpha_2) - \arg(\alpha_1)$. So, we have the second element of the vector $\vec{a'}$ as $\beta = e^{i\phi_1}\sin\left(\frac{\theta_1}{2}\right)\cos\left(\frac{\theta_2}{2}\right)$.

The last element of the vector $\vec{a'}$ is another complex number, $\gamma = |\alpha_3| e^{i\varphi_{31}}$, where $\varphi_{31} = \arg(\alpha_3) - \arg(\alpha_1)$. The magnitude of γ is constrained by the normalization condition and hence has to be $|\gamma| = \sqrt{1 - |\alpha|^2 - |\beta|^2} = \sqrt{1 - \cos^2\left(\frac{\theta_1}{2}\right) - \sin^2\left(\frac{\theta_1}{2}\right)\cos^2\left(\frac{\theta_2}{2}\right)} = \sqrt{\sin^2\left(\frac{\theta_1}{2}\right) - \sin^2\left(\frac{\theta_1}{2}\right)\cos^2\left(\frac{\theta_2}{2}\right)} = \sin\left(\frac{\theta_1}{2}\right)\sin\left(\frac{\theta_2}{2}\right)$. The argument of γ is given by $\arg(\gamma) = \varphi_{31} = \arg(\alpha_3) - \arg(\alpha_1) = (\arg(\alpha_3) - \arg(\alpha_2)) + (\arg(\alpha_2) - \arg(\alpha_1)) = \phi_2 + \phi_1$, where we considered $\phi_2 = \arg(\alpha_3) - \arg(\alpha_2)$. Thus, the phase of γ in the Argand plane can be spanned by $(\phi_1 + \phi_2)$, where $\phi_2 \in [-\pi, \pi)$. So, we have the last element of the vector as $\gamma = e^{i(\phi_1+\phi_2)} \sin\left(\frac{\theta_1}{2}\right) \sin\left(\frac{\theta_2}{2}\right)$.

Hence, the vector $\vec{a'}$ in three dimensions can be written in terms of the parameters $\{\theta_1, \theta_2, \phi_1, \phi_2\}$ as the following,

$$\vec{a'} = \begin{pmatrix} \alpha \\ \beta \\ \gamma \end{pmatrix} = \begin{pmatrix} \cos\left(\frac{\theta_1}{2}\right) \\ e^{i\phi_1} \sin\left(\frac{\theta_1}{2}\right) \cos\left(\frac{\theta_2}{2}\right) \\ e^{i(\phi_1+\phi_2)} \sin\left(\frac{\theta_1}{2}\right) \sin\left(\frac{\theta_2}{2}\right) \end{pmatrix} \tag{4.26}$$

The vector $\vec{a'}$ in three dimensions has the same representation as the state $|\psi\rangle^{(3)}$ given in Eqn. 4.24. Thus, we have shown that the state $|\psi\rangle^{(3)}$ can be represented by any set of three arbitrary complex numbers, up to a global phase. By varying the state parameters $\{\theta_1, \theta_2, \phi_1, \phi_2\}$ one can make $|\psi\rangle^{(3)}$ span the entire ray space in three dimensions.

❑ Expectation Values of the Ladder Operators and the Ladder-Like Operators in the State $|\psi\rangle^{(3)}$:

Next, let us check if we can determine the individual parameters of the qutrit from the expectation values of the ladder operators $\hat{\sigma}_+^{[3]}$, $\hat{\sigma}_-^{[3]}$ given in Eqn. 4.10, Eqn. 4.12 respectively or from the expectation values of ladder-like operators $\hat{\mathcal{A}}^{3\to1}, \hat{\mathcal{A}}^{2\to1}$ and $\hat{\mathcal{A}}^{3\to2}$ given in Eqn. 4.19. The expectation values of these non-Hermitian operators in the three dimensions, computed for the state $|\psi\rangle^{(3)}$ given in the Episphere representation as shown in Eqn. 4.24, are expressed as the following,

$$\left\langle \hat{\sigma}_+^{[3]} \right\rangle = \frac{1}{\sqrt{2}} \left[e^{i\phi_1} \sin(\theta_1) \cos\left(\frac{\theta_2}{2}\right) + e^{i\phi_2} \sin^2\left(\frac{\theta_1}{2}\right) \sin(\theta_2) \right] \tag{4.27}$$

$$\left\langle \hat{\sigma}_-^{[3]} \right\rangle = \frac{1}{\sqrt{2}} \left[e^{-i\phi_1} \sin(\theta_1) \cos\left(\frac{\theta_2}{2}\right) + e^{-i\phi_2} \sin^2\left(\frac{\theta_1}{2}\right) \sin(\theta_2) \right] \tag{4.28}$$

$$\left\langle \hat{\mathcal{A}}^{3\to1} \right\rangle = \frac{1}{2} e^{i(\phi_1+\phi_2)} \sin(\theta_1) \sin\left(\frac{\theta_2}{2}\right) \tag{4.29}$$

$$\left\langle \hat{\mathcal{A}}^{2\to1} \right\rangle = \frac{1}{2} e^{i\phi_1} \sin(\theta_1) \cos\left(\frac{\theta_2}{2}\right) \tag{4.30}$$

$$\left\langle \hat{\mathcal{A}}^{3\to2} \right\rangle = \frac{1}{2} e^{i\phi_2} \sin^2\left(\frac{\theta_1}{2}\right) \sin(\theta_2) \tag{4.31}$$

So, the expectation values of the ladder operators $\left\langle \hat{\sigma}_{\pm}^{[3]} \right\rangle$ involves all the four state parameters $\{\theta_1, \phi_1, \theta_2, \phi_2\}$, thus would not help much in extracting the individual parameters. However, by measuring the complex expectation values of any two of the above three ladder-like operators, we can infer the relative phases in Bloch spheres i.e., ϕ_1 and ϕ_2 from their arguments. For example, if we have $\left\langle \hat{\mathcal{A}}^{2\to1} \right\rangle$ and $\left\langle \hat{\mathcal{A}}^{3\to1} \right\rangle$ then we get the phases as,

$$\phi_1 = \arg\left(\left\langle \hat{\mathcal{A}}^{2\to1} \right\rangle\right) \quad \text{and} \quad \phi_2 = \arg\left(\left\langle \hat{\mathcal{A}}^{3\to1} \right\rangle\right) - \phi_1 \tag{4.32}$$

Also, we can obtain ϕ_2 directly from $\left\langle \hat{\mathcal{A}}^{3\to2} \right\rangle$ as, $\phi_2 = \arg\left(\left\langle \hat{\mathcal{A}}^{3\to2} \right\rangle\right)$. Now, we can infer θ_1 and θ_2 from the magnitudes of these complex expectation values, as the following:

$$\left|\left\langle \hat{\mathcal{A}}^{3\to1} \right\rangle\right|^2 + \left|\left\langle \hat{\mathcal{A}}^{2\to1} \right\rangle\right|^2 = \frac{1}{4} \sin^2(\theta_1) \tag{4.33}$$

$$\implies \qquad \theta_1 = \sin^{-1}\left(2\sqrt{\left|\left\langle \hat{\mathcal{A}}^{3\to1} \right\rangle\right|^2 + \left|\left\langle \hat{\mathcal{A}}^{2\to1} \right\rangle\right|^2}\right) \tag{4.34}$$

Knowing θ_1, we can find out θ_2 from the magnitude of the expectation value of any one of the ladder-like operators.

$$\theta_2 = 2\sin^{-1}\left(\frac{2\left|\left\langle \hat{\mathcal{A}}^{3\to1} \right\rangle\right|}{\sin(\theta_1)}\right) = 2\cos^{-1}\left(\frac{2\left|\left\langle \hat{\mathcal{A}}^{2\to1} \right\rangle\right|}{\sin(\theta_1)}\right) = \sin^{-1}\left(\frac{2\left|\left\langle \hat{\mathcal{A}}^{3\to2} \right\rangle\right|}{\sin^2\left(\frac{\theta_1}{2}\right)}\right) \tag{4.35}$$

Hence, from the above discussion, we can conclude that the parameters $\{\theta_1, \theta_2, \phi_1, \phi_2\}$ associated with any pure qutrit can be inferred from the expectation values of the two ladder-like operators $\hat{\mathcal{A}}^{2\to 1}$ and $\hat{\mathcal{A}}^{3\to 1}$. Experimentally, the expectation values of the above non-Hermitian operators can be obtained from the interference pattern formed in a Mach-Zehnder interferometer with each arm having the components corresponding to the operators obtained from the polar decomposition of the non-Hermitian operators.

4.1.4 Episphere Representation of Qudits

Here, we aim to extend the idea presented in SubSec. 4.1.3 for the parameterization of qutrits to d-dimensional qudits. In the Episphere representation, any pure state in the d-dimensional Hilbert space is depicted as a chain of $(d-1)$ Bloch vectors, instead of having $(d-1)$ points on a single Bloch sphere as in the Majorana representation. Each Bloch vector, in this parameterization, is defined within a Bloch sphere that represents a subsequent two-dimensional subspace of the d-dimensional Hilbert space. Out of the $(d-1)$ spheres constructed for any d-dimensional pure state, $(d-2)$ are the epispheres (except for the first one), where the origin of the k-th Bloch sphere (with $k > 1$) lies at the tip of the $(k-1)$-th Bloch vector, located on the surface of the $(k-1)$-th Bloch sphere.

Any ray in d-dimensional Hilbert space can be characterized by $(2d-2)$ real parameters $\{\theta_j, \phi_j\}$ with $j = 1, 2, \ldots, (d-1)$. Here, $\theta_j \in [0, \pi]$ and $\phi_j \in [-\pi, \pi)$ respectively represent the polar angle and the azimuthal angle associated with the j-th Bloch vector defined within the j-th Bloch sphere in the sequence. Eqn. **4.23** presents the Bloch vector $\vec{v}_j$ for the j-th two dimensional subspace, spanned by $|j\rangle$ and $|j+1\rangle$. Similar to the expression in Eqn. **4.24**, the Episphere representation of the pure qudit $|\psi\rangle^{(d)}$ can be derived by multiplying the k-th Bloch vector $\vec{v}_k$ with the second element of $(k-1)$-th Bloch vector $\vec{v}_{k-1}$ for all k's varying from 2 to $(d-1)$ in that particular sequence. Thus, the Episphere representation of the state for the k-th two-dimensional subspace is obtained as,

$$|\psi\rangle_k^{(2;d)} = \left(\prod_{j=1}^{k-1} \exp(i\phi_j) \sin\left(\frac{\theta_j}{2}\right)\right) \begin{pmatrix} \cos\left(\frac{\theta_k}{2}\right) \\ \exp(i\phi_k) \sin\left(\frac{\theta_k}{2}\right) \cos\left(\frac{\theta_{k+1}}{2}\right) \end{pmatrix} \tag{4.36}$$

The first Bloch vector $\vec{v}_1$ defined within the 1st Bloch sphere spans the first two-dimensional subspace given by the states $\{|1\rangle, |2\rangle\}$ and the tip of this Bloch vector lies at a point with the co-ordinates (θ_1, ϕ_1) on the surface of this Bloch sphere. The second Bloch vector $\vec{v}_2$ parameterized by (θ_2, ϕ_2) is defined within the 2nd Bloch sphere (which is the $1st$ episphere) that originate from the point (θ_1, ϕ_1) and spans the 2nd two-dimensional subspace given by $\{|2\rangle, |3\rangle\}$. In this way, the $(d-1)$-th Bloch vector spans the last two-dimensional subspace of the d-dimensional space with states $\{|d-1\rangle, |d\rangle\}$ and is parameterized by $(\theta_{d-1}, \phi_{d-1})$. So, in the Episphere representation, a pure qudit can be parameterized with $(d-1)$ polar angles θ_j's and $(d-1)$ azimuthal angles ϕ_j's, with each pair of parameters arranged in a particular sequence.

Therefore, the Episphere representation of the pure state $|\psi\rangle^{(d)}$ in the d-dimensions can be obtained as,

$$|\psi\rangle^{(d)} = \begin{pmatrix} \cos\left(\frac{\theta_1}{2}\right) \\ e^{i\phi_1}\sin\left(\frac{\theta_1}{2}\right) \begin{pmatrix} \cos\left(\frac{\theta_2}{2}\right) \\ e^{i\phi_2}\sin\left(\frac{\theta_2}{2}\right) \begin{pmatrix} \ddots \\ \begin{pmatrix} \cos\left(\frac{\theta_k}{2}\right) \\ e^{i\phi_k}\sin\left(\frac{\theta_k}{2}\right) \begin{pmatrix} \ddots \\ \begin{pmatrix} \cos\left(\frac{\theta_{d-1}}{2}\right) \\ e^{i\phi_{d-1}}\sin\left(\frac{\theta_{d-1}}{2}\right) \end{pmatrix} \end{pmatrix} \end{pmatrix} \end{pmatrix} \end{pmatrix} \end{pmatrix} \tag{4.37}$$

Hence, from the above expression, we can see that in terms of the parameters $\{\theta_j, \phi j\}$ corresponding to the $(d-1)$ Bloch vectors, a d-dimensional pure qudit is expressed in the form of a nested column vector. Now, omitting the nested brackets from Eqn. 4.37 we can write the state $|\psi\rangle^{(d)}$ as the following single column vector in the Episphere representation.

$$|\psi\rangle^{(d)} = \begin{pmatrix} \cos\left(\dfrac{\theta_1}{2}\right) \\ e^{i\phi_1}\ \sin\left(\dfrac{\theta_1}{2}\right)\ \cos\left(\dfrac{\theta_2}{2}\right) \\ \vdots \\ \prod_{j=1}^{k-1} e^{i\phi_j}\ \sin\left(\dfrac{\theta_j}{2}\right)\ \cos\left(\dfrac{\theta_k}{2}\right) \\ \vdots \\ \prod_{j=1}^{d-1} e^{i\phi_j}\ \sin\left(\dfrac{\theta_j}{2}\right) \end{pmatrix} \tag{4.38}$$

❑ Does $|\psi\rangle^{(d)}$ in Episphere representation spans the entire d-dimensional Hilbert space?

Next, we need to show that the Episphere representation of the vector $|\psi\rangle^{(d)}$ shown above spans all the rays in the d-dimensional Hilbert space. A general pure state (say, $|\Psi\rangle^{(d)}$) in d-dimensions can be represented by a set of d arbitrary complex numbers α_i's, where $\alpha_i \in \mathbb{C}^2$ with $i = 1, 2, \ldots, d$. Therefore, we have an arbitrary pure qudit as,

$$|\Psi\rangle^{(d)} = \alpha_1 |1\rangle + \alpha_2 |2\rangle + \ldots\ldots + \alpha_d |d\rangle \tag{4.39}$$

provided the normalization constraint as given below:

$$|\alpha_1|^2 + |\alpha_2|^2 + \ldots\ldots + |\alpha_d|^2 = 1 \qquad \Longrightarrow \qquad \sum_{i=1}^{d} |\alpha_i|^2 = 1 \tag{4.40}$$

The first term of the vector $|\Psi\rangle^{(d)}$ can always be considered as a positive real number (say, $\alpha = |\alpha_1|$) because the global phase has no physically observable consequence upon measurement and hence, can be ignored. The normalization constraint restricts the maximum possible value of this real positive quantity to be 1, i.e., $|\alpha_1| \leq 1$. Therefore the term α can always be expressed as $\alpha = \cos\left(\dfrac{\theta_1}{2}\right)$, where $\theta_1 \in [0, \pi]$. The second term, say β, can be in general complex but can have the maximum possible magnitude as $\sqrt{1-|\alpha_1|^2} = \sqrt{1-\cos^2\left(\frac{\theta_1}{2}\right)} = \sin\left(\frac{\theta_1}{2}\right)$. Hence, the magnitude of the second term β can be written as $|\beta| = \sin\left(\frac{\theta_1}{2}\right)\cos\left(\frac{\theta_2}{2}\right) \in [0,\ \sin\left(\frac{\theta_1}{2}\right)]$ given $\theta_2 \in [0,\pi]$. So, in the polar form [15] the second term of the vector can be written as $e^{i\phi_1}\sin\left(\frac{\theta_1}{2}\right)\cos\left(\frac{\theta_2}{2}\right)$, where ϕ_1 is the argument of the complex number β. Similarly, the k-th term in the vector can be written as $\left(\prod_{j=1}^{k-1} e^{i\phi_j}\sin\left(\frac{\theta_j}{2}\right)\right)\cos\left(\frac{\theta_k}{2}\right)$, with the argument being $\sum_{j=1}^{k-1}\phi_j$. The magnitude of the final term i.e., the d-th term for the d-dimensional state, is determined by all the previous terms due to the given normalization condition and hence, is expressed as $\prod_{j=1}^{d-1} e^{i\phi_j}\sin\left(\frac{\theta_j}{2}\right)$. Therefore, the polar representation of a pure state $|\Psi\rangle^{(d)}$ in d-dimensional Hilbert space will be the same as given in Eqn. 4.38, i.e., $|\Psi\rangle^{(d)} \equiv |\psi\rangle^{(d)}$.

Also, we have already verified that in this representation $|\psi\rangle^{(2)}$ spans the Hilbert space for $d=2$ (Bloch sphere for qubits) and $|\psi\rangle^{(3)}$ spans the Hilbert space for $d=3$ (two sequential Bloch spheres for qutrit, where the second sphere originates from the surface of the first sphere). Here, we will prove that the set of $(2d-2)$ parameters $\{\theta_j,\phi_j\}$ with $j=1,2,\ldots,(d-1)$ makes $|\psi\rangle^{(d)}$ span the entire vector space in d-dimension by the use of principle of mathematical induction. For this, first we assume that the state $|\psi\rangle^{(m)}$ spans the entire m-dimensional Hilbert space and then we aim to argue that, by implication, $|\psi\rangle^{(m+1)}$ spans all the rays in the $(m+1)$-dimensional Hilbert space. So, we have

$$|\psi\rangle^{(m)} = \begin{pmatrix}\alpha_1\\ \alpha_2\\ \vdots\\ \alpha_m\end{pmatrix} = \begin{pmatrix}\cos\left(\frac{\theta_1}{2}\right)\\ e^{i\phi_1}\sin\left(\frac{\theta_1}{2}\right)\cos\left(\frac{\theta_2}{2}\right)\\ \vdots\\ \prod_{j=1}^{m-1} e^{i\phi_j}\sin\left(\frac{\theta_j}{2}\right)\end{pmatrix} \tag{4.41}$$

Since, $|\psi\rangle^{(m)}$ spans the m-dimensional Hilbert space, here we have $\{\alpha_1,\alpha_2,\ldots,\alpha_m\}$ as the set of arbitrary complex numbers that represent the state $|\psi\rangle^{(m)}$ up to a global phase and constrained to normalization, $\sum_{i=1}^{m}|\alpha_i|^2 = 1$. Therefore, we now have to show that α_{m+1} is an arbitrary complex number as well, so that the set $\{\alpha_1,\alpha_2,\ldots,\alpha_m,\alpha_{m+1}\}$ can completely represent the $(m+1)$ dimensional state $|\psi\rangle^{(m+1)}$.

The pure state in $(m+1)$ dimension can be written as,

$$|\psi\rangle^{(m+1)} = \begin{pmatrix} \cos\left(\frac{\theta_1}{2}\right) \\ \vdots \\ \prod_{j=1}^{m-1} e^{i\phi_j} \sin\left(\frac{\theta_j}{2}\right) \begin{pmatrix} \cos\left(\frac{\theta_m}{2}\right) \\ e^{i\phi_m} \sin\left(\frac{\theta_m}{2}\right) \end{pmatrix} \end{pmatrix} = \begin{pmatrix} \beta_1 \\ \vdots \\ \beta_m \\ \beta_{m+1} \end{pmatrix} \tag{4.42}$$

Here, we have to show that $\{\beta_1, \beta_2, \ldots, \beta_m, \beta_{m+1}\}$ are a set of arbitrary complex numbers, that can span any ray in the $(m+1)$-dimensional Hilbert space. Comparing the vectors shown in Eqn. 4.41 and Eqn. 4.42, we get the elements of the vectors are same up to the $(m-1)$-th term, i.e., $\beta_n = \alpha_n$ for $n = 1, 2, \ldots, (m-1)$. Therefore, from analogy the set, $\{\beta_1, \beta_2, \ldots, \beta_{m-1}\}$ are arbitrary complex numbers. Next, we have $\beta_m = \alpha_m \cos\left(\frac{\theta_m}{2}\right)$, i.e., β_m is obtained by scaling α_m with $\cos\left(\frac{\theta_m}{2}\right)$ that ranges between 0 to 1. Therefore, β_m represents an arbitrary complex number as well, given $\theta_m \in [0, \pi]$ which makes $\beta_m \in [0, \alpha_m]$. Thus, we now have to show that β_{m+1} can be any arbitrary complex number.

Here, we have $\beta_{m+1} = \left(\prod_{j=1}^{m-1} e^{i\phi_j} \sin\left(\frac{\theta_j}{2}\right)\right) e^{i\phi_m} \sin\left(\frac{\theta_m}{2}\right) = \alpha_m \; e^{i\phi_m} \sin\left(\frac{\theta_m}{2}\right)$. Since α_m is an arbitrary complex number as defined for the description of $|\psi\rangle^{(m)}$, the conditions that $\theta_m \in [0, \pi]$ and $\phi_m \in [-\pi, \pi)$ makes β_{m+1} an arbitrary complex number as well with the magnitude $|\beta_{m+1}|$ bounded by $\left|\prod_{j=1}^{m} e^{i\phi_j} \sin\left(\frac{\theta_j}{2}\right)\right|$. Thus $|\psi\rangle^{(m+1)}$ spans the entire $(m+1)$-dimensional Hilbert space.

This way of representing a qudit forms an intuitive map between the dynamics of qudits with dynamics of N-pendulums joined serially end to end [16, 17]. Although in Fig. 4.1 we have represented the z-axis of all the Bloch spheres along the z-axis of the first Bloch sphere, this is not a requirement and the subsequent Bloch spheres can be rotated along the direction of the previous Bloch vector. The crucial component of this description is the sequence in which the Bloch vectors representing the state are arranged.

4.1.5 Implication from the Normalization Condition for Qudit

Any pure state $|\psi\rangle^{(d)}$ in the d-dimensional Hilbert space can be expressed as the superposition of all the basis states $\{|k\rangle\,; k = 1, 2, \ldots, d\}$, i.e., $|\psi\rangle^{(d)} = \sum_{k=1}^{d} \alpha_k |k\rangle$. Here, α_k's are complex coefficients representing the probability amplitudes associated with the respective basis states and are constrained by the normalization condition $\sum_{k=1}^{d} |\alpha_k|^2 = 1$. Therefore, any pure qutrit spanned by the three basis states $\{|1\rangle, |2\rangle, |3\rangle\}$ can be written as,

$$|\psi\rangle^{(3)} = \alpha_1 |1\rangle + \alpha_2 |2\rangle + \alpha_3 |3\rangle \tag{4.43}$$

$$\text{satisfying} \qquad |\alpha_1|^2 + |\alpha_2|^2 + |\alpha_3|^2 = 1 \tag{4.44}$$

The Episphere representation of the qudit given in Eqn. 4.38 parameterizes the state with $\{\theta_j, \phi_j\}$, where $j = 1, 2, \ldots, (d-1)$ and $\theta_j \in [0, \pi]$, $\phi_j \in [-\pi, \pi)$. The k-th term of the vector $|\psi\rangle^{(d)}$ in this representation is given as the following,

$$\alpha_k = \left(\prod_{j=1}^{k-1} \exp(i\phi_j) \sin\left(\frac{\theta_j}{2}\right) \right) \cos\left(\frac{\theta_k}{2}\right) \tag{4.45}$$

Thus, expanding the expression of α_k as shown in Eqn. 4.45 for the determination of the complex coefficients α_1, α_2 and α_3 for a qutrit, we get

$$\alpha_1 = \cos\left(\frac{\theta_1}{2}\right) \tag{4.46}$$

$$\alpha_2 = \exp(i\phi_1) \sin\left(\frac{\theta_1}{2}\right) \cos\left(\frac{\theta_2}{2}\right) \tag{4.47}$$

$$\alpha_3 = \exp(i\phi_1) \sin\left(\frac{\theta_1}{2}\right) \exp(i\phi_2) \sin\left(\frac{\theta_2}{2}\right) \cos\left(\frac{\theta_3}{2}\right) \tag{4.48}$$

Putting these values in the normalization condition $\sum_{k=1}^{3} |\alpha_k|^2 = 1$, we get

$$\cos^2\left(\frac{\theta_1}{2}\right) + \sin^2\left(\frac{\theta_1}{2}\right) \cos^2\left(\frac{\theta_2}{2}\right) + \sin^2\left(\frac{\theta_1}{2}\right) \sin^2\left(\frac{\theta_2}{2}\right) \cos^2\left(\frac{\theta_3}{2}\right) = 1 \tag{4.49}$$

Rearranging the above expression we get the following,

$$\sin^2\left(\frac{\theta_1}{2}\right)\left[\cos^2\left(\frac{\theta_2}{2}\right)+\sin^2\left(\frac{\theta_2}{2}\right)\cos^2\left(\frac{\theta_3}{2}\right)\right]=1-\cos^2\left(\frac{\theta_1}{2}\right)=\sin^2\left(\frac{\theta_1}{2}\right)$$

$$\implies \qquad \cos^2\left(\frac{\theta_2}{2}\right)+\sin^2\left(\frac{\theta_2}{2}\right)\cos^2\left(\frac{\theta_3}{2}\right)=1$$

$$\implies \qquad \sin^2\left(\frac{\theta_2}{2}\right)\cos^2\left(\frac{\theta_3}{2}\right)=1-\cos^2\left(\frac{\theta_2}{2}\right)=\sin^2\left(\frac{\theta_2}{2}\right)$$

$$\implies \qquad \cos^2\left(\frac{\theta_3}{2}\right)=1$$

Therefore, from the above expression obtained using the normalization condition of qutrit, we get

$$\theta_3 = 2\cos^{-1}(\pm 1) \tag{4.50}$$

$$\theta_3 = 2n\pi, \qquad \text{with} \qquad n = 0, 1, 2, \ldots \text{positive integer} \tag{4.51}$$

Since $\theta_j \in [0, \pi]$, the only value that θ_3 can take is $\theta_3 = 0$. Using the same logic we can show that a d-dimensional pure state spanned by the basis vectors $\{|1\rangle, |2\rangle, \ldots, |d\rangle\}$ when represented in polar co-ordinates, the normalization condition gives:

$$\theta_d = 0 \tag{4.52}$$

Therefore, from Eqn. 4.45 the complex coefficient α_d for a pure state in d-dimensions can be expressed as,

$$\alpha_d = \left(\prod_{j=1}^{d-1} \exp(i\phi_j)\sin\left(\frac{\theta_j}{2}\right)\right)\cos\left(\frac{\theta_d}{2}\right) = \prod_{j=1}^{d-1} \exp(i\phi_j)\sin\left(\frac{\theta_j}{2}\right) \tag{4.53}$$

This value $\theta_d = 0$ will appear to be very useful in the discussion of the next sections in this chapter where we will attempt to infer the state parameters from the experimentally obtained interferometric quantities using the scheme Quantum State Interferography.

4.2 Quantum State Interferography for Qutrit

Characterization of an arbitrary pure state in 3-dimensional Hilbert space requires 4 real quantities. In the Episphere representation, as discussed in SubSec. 4.1.3, a pure qutrit is expressed with $\{\theta_1, \theta_2, \phi_1, \phi_2\}$ as the following,

$$|\psi\rangle^{(3)} = \begin{pmatrix} \cos\left(\frac{\theta_1}{2}\right) \\ e^{i\phi_1}\sin\left(\frac{\theta_1}{2}\right)\cos\left(\frac{\theta_2}{2}\right) \\ e^{i(\phi_1+\phi_2)}\sin\left(\frac{\theta_1}{2}\right)\sin\left(\frac{\theta_2}{2}\right) \end{pmatrix} \tag{4.54}$$

Here, the four parameters $\{\theta_1, \theta_2, \phi_1, \phi_2\}$ with $\theta_j \in [0, \pi]$ and $\phi_j \in [-\pi, \pi)$ can span the entire three dimensional ray space. Thus, an unknown state $|\psi\rangle^{(3)}$ can be inferred by experimentally determining the values of these four parameters that represent the state.

This section will introduce an interferometric scheme using which one can infer the four parameters associated with a qutrit $|\psi\rangle^{(3)}$ – the scheme is termed as Quantum State Interferography for qutrits. This technique is an extension of the concept discussed in Chapter. **2** which involves the determination of an unknown quantum state in 2-dimensions (i.e., any arbitrary qubit), to any pure state in 3-dimensions. Employing Quantum State Intererography (QSI), any pure qutrit can be reconstructed by processing two interference patterns – one obtained by performing single qubit QSI on the 1st two dimensional subspace spanned by $\{|1\rangle, |2\rangle\}$ and the other obtained by performing single qubit QSI on the 2nd two dimensional subspace spanned by $\{|2\rangle, |3\rangle\}$. We will illustrate the method for the reconstruction of a pure state in spin degrees of freedom, using the schematic in Fig 4.2.

4.2.1 Theory

The three dimensional Hilbert space spanned by $\{|1\rangle, |2\rangle, |3\rangle\}$ can be considered to have 2 two dimensional subspaces – the $1st$ subspace consisting of the basis states $\{|1\rangle, |2\rangle\}$ and the $2nd$ subspace consisting of the basis states $\{|2\rangle, |3\rangle\}$. Let, $|\psi\rangle_1^{(2;3)}$ and $|\psi\rangle_2^{(2;3)}$ are the components of the states $|\psi\rangle^{(3)}$ in the $1st$ and $2nd$ two dimensional subspaces respectively, which in general are not normalized and can be expressed as,

$$|\psi\rangle_1^{(2;3)} = \begin{pmatrix} \cos\left(\frac{\theta_1}{2}\right) \\ e^{i\phi_1}\sin\left(\frac{\theta_1}{2}\right)\cos\left(\frac{\theta_2}{2}\right) \end{pmatrix} \tag{4.55}$$

$$|\psi\rangle_2^{(2;3)} = \begin{pmatrix} e^{i\phi_1}\sin\left(\frac{\theta_1}{2}\right)\cos\left(\frac{\theta_2}{2}\right) \\ e^{i(\phi_1+\phi_2)}\sin\left(\frac{\theta_1}{2}\right)\sin\left(\frac{\theta_2}{2}\right) \end{pmatrix} = e^{i\phi_1}\sin\left(\frac{\theta_1}{2}\right)\begin{pmatrix} \cos\left(\frac{\theta_2}{2}\right) \\ e^{i\phi_2}\sin\left(\frac{\theta_2}{2}\right) \end{pmatrix} \tag{4.56}$$

The superscripts $(2;3)$ in $|\psi\rangle_1^{(2;3)}$ and $|\psi\rangle_2^{(2;3)}$ indicates that the states are defined for the 2-dimensional subspaces of the 3-dimensional Hilbert space.

Let, $\hat{\sigma}_\pm^{(1)}$ represent the spin ladder operator that acts on the $1st$ two dimensional subspace, i.e., $\hat{\sigma}_+^{(1)}$ raises the state $|1\rangle$ to $|2\rangle$ and $\hat{\sigma}_-^{(1)}$ lowers the state $|2\rangle$ to $|1\rangle$. Similarly, $\hat{\sigma}_\pm^{(2)}$ represent the spin ladder operator for the $2nd$ two dimensional subspace. The expectation value of $\hat{\sigma}_\pm^{(1)}$ for the state $|\psi\rangle_1^{(2;3)}$ shown in Eqn. 4.55 can be computed as,

$$\left\langle \hat{\sigma}_\pm^{(1)} \right\rangle = \left\langle \psi_1^{(2;3)} \middle| \hat{\sigma}_\pm^{(1)} \middle| \psi_1^{(2;3)} \right\rangle = \frac{1}{2}\exp(\pm i\phi_1)\sin(\theta_1)\cos\left(\frac{\theta_2}{2}\right) \tag{4.57}$$

Similarly, the expectation value of $\hat{\sigma}_\pm^{(2)}$ for the state $|\psi\rangle_2^{(2;3)}$ expressed in Eqn. 4.56 is computed to be,

$$\left\langle \hat{\sigma}_\pm^{(2)} \right\rangle = \left\langle \psi_2^{(2;3)} \middle| \hat{\sigma}_\pm^{(2)} \middle| \psi_2^{(2;3)} \right\rangle = \frac{1}{2}\exp(\pm i\phi_2)\sin^2\left(\frac{\theta_1}{2}\right)\sin(\theta_2) \tag{4.58}$$

Therefore, the parameters ϕ_1 and ϕ_2 can be determined directly from the arguments of the expectation values of the spin ladder operators i.e., $\left\langle \hat{\sigma}_{\pm}^{(1)} \right\rangle$ defined for the $1st$ two dimensional subspace and $\left\langle \hat{\sigma}_{\pm}^{(2)} \right\rangle$ defined for the $2nd$ two dimensional subspace.

$$\phi_1 = \pm \arg\left(\left\langle \hat{\sigma}_{\pm}^{(1)} \right\rangle\right) \tag{4.59}$$

$$\phi_2 = \pm \arg\left(\left\langle \hat{\sigma}_{\pm}^{(2)} \right\rangle\right) \tag{4.60}$$

Next, the parameters θ_1 and θ_2 can be determined from the magnitudes of the complex expectation values $\left\langle \hat{\sigma}_{\pm}^{(1)} \right\rangle$ and $\left\langle \hat{\sigma}_{\pm}^{(2)} \right\rangle$ given in Eqn. 4.57 and Eqn. 4.58 respectively.

$$\left|\left\langle \hat{\sigma}_{\pm}^{(1)} \right\rangle\right| = \frac{1}{2}\sin(\theta_1)\cos\left(\frac{\theta_2}{2}\right) \tag{4.61}$$

$$\left|\left\langle \hat{\sigma}_{\pm}^{(2)} \right\rangle\right| = \frac{1}{2}\sin^2\left(\frac{\theta_1}{2}\right)\sin(\theta_2) \tag{4.62}$$

One possible way of determining the two quantities θ_1 and θ_2 is by simultaneous solution of the above two expressions given in Eqn. 4.61 and Eqn. 4.62. Alternatively, as in the case for qubits, we can determine the expectation values of the projector operators $\hat{\Pi}_0^{(1)}$ and $\hat{\Pi}_0^{(2)}$ that acts on the $1st$ and $2nd$ two dimensional sub-spaces of the 3-dimensional Hilbert space, respectively. $\hat{\Pi}_0^{(1)}$ projects any state in the $1st$ subspace spanned by $\{|1\rangle, |2\rangle\}$ on to the state $|1\rangle$, thus, can be defined as $\hat{\Pi}_0^{(1)} = |1\rangle\langle 1|$. Similarly, $\hat{\Pi}_0^{(2)}$ projects any state in the $2nd$ subspace spanned by $\{|2\rangle, |3\rangle\}$ on to the state $|2\rangle$, thus, can be defined as $\hat{\Pi}_0^{(2)} = |2\rangle\langle 2|$.

The expectation value of the operator $\hat{\Pi}_0^{(1)}$ for the state $|\psi\rangle_1^{(2;3)}$ can be computed as,

$$\left\langle \hat{\Pi}_0^{(1)} \right\rangle = \left\langle \psi_1^{(2;3)} \middle| \hat{\Pi}_0^{(1)} \middle| \psi_1^{(2;3)} \right\rangle = \cos^2\left(\frac{\theta_1}{2}\right) \tag{4.63}$$

Thus, the parameter θ_1 can be obtained directly from $\left\langle \hat{\Pi}_0^{(1)} \right\rangle$ and knowing θ_1 we can determine θ_2 either from Eqn. 4.61 or from Eqn. 4.62.

$$\theta_1 = 2\cos^{-1}\left(\sqrt{\left\langle \hat{\Pi}_0^{(1)} \right\rangle}\right) \tag{4.64}$$

$$\theta_2 = 2\cos^{-1}\left(\frac{2\left|\left\langle \hat{\sigma}_{\pm}^{(1)} \right\rangle\right|}{\sin(\theta_1)}\right) = \sin^{-1}\left(\frac{2\left|\left\langle \hat{\sigma}_{\pm}^{(2)} \right\rangle\right|}{\sin^2\left(\frac{\theta_1}{2}\right)}\right) \tag{4.65}$$

Alternatively, we can also determine the expectation value of $\hat{\Pi}_0^{(2)}$ for the state $|\psi\rangle_2^{(2;3)}$ in the second two dimensional subspace and can determine θ_2 from $\left\langle \hat{\Pi}_0^{(2)} \right\rangle$ using the already known value of θ_1 determined from $\left\langle \hat{\Pi}_0^{(1)} \right\rangle$.

$$\left\langle \hat{\Pi}_0^{(2)} \right\rangle = \left\langle \psi_2^{(2;3)} \middle| \hat{\Pi}_0^{(2)} \middle| \psi_2^{(2;3)} \right\rangle = \sin^2\left(\frac{\theta_1}{2}\right)\cos^2\left(\frac{\theta_2}{2}\right) \tag{4.66}$$

$$\text{giving,} \qquad \theta_2 = 2\cos^{-1}\left(\sqrt{\frac{\left\langle \hat{\Pi}_0^{(2)} \right\rangle}{\sin^2\left(\frac{\theta_1}{2}\right)}}\right) = 2\cos^{-1}\left(\sqrt{\frac{\left\langle \hat{\Pi}_0^{(2)} \right\rangle}{1-\left\langle \hat{\Pi}_0^{(1)} \right\rangle}}\right) \tag{4.67}$$

Thus, the state parameters associated with an unknown qutrit can be inferred from the expectation values of the spin ladder operators ($\hat{\sigma}_{\pm}^{(1)}$ and $\hat{\sigma}_{\pm}^{(2)}$) and any of the projector operators ($\hat{\Pi}_0^{(1)}$ or $\hat{\Pi}_0^{(2)}$) defined to act on the respective sub-spaces of the 3-dimensional space.

4.2.2 Experimental Protocol

In order to experimentally determine a pure qutrit $|\psi\rangle^{(3)}$ employing the Quantum State Interferography (QSI) technique, one needs to design two interferometers, one on each of the two dimensional sub-spaces of the 3-dimensional space arranged in the sequence in which we parameterize the three-dimensional vector in the Episphere representation. Here, we present a generic scheme to construct all the necessary operators in each subspace from the Pauli operators in the 3-dimensional Hilbert space in order to infer $|\psi\rangle^{(3)}$. The proposal is to use two Mach-Zehnder interferometers (or any equivalent two path interferometers) with the required operators in each arms, designed to act on the two individual sub-spaces as shown in Fig. 4.2 and obtain two interferograms – the post-processing of which will give the 4 state parameters corresponding to the unknown state $|\psi\rangle^{(3)}$.

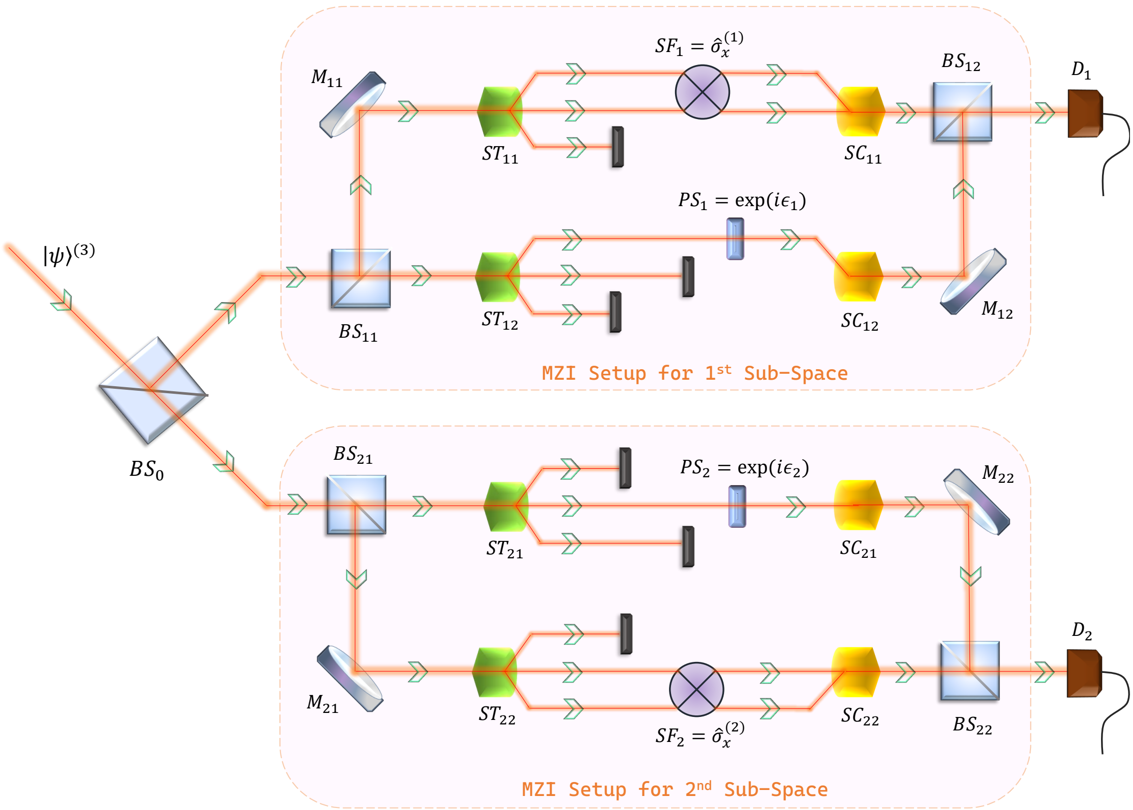

Figure 4.2: Schematic of the setup to characterize the pure state of a three-dimensional quantum system, i.e., a pure qutrit using Quantum State Interferography technique. The beam in the state $|\psi\rangle^{(3)}$ is divided into two spatial modes using the beam splitter BS_0. Each mode is made incident on a two path interferometer (here, a Mach-Zehnder Interferometer formed with beam splitters BS_{i1} and BS_{i2} and mirrors M_{i1} and M_{i2}, where $i = 1, 2$) to act on the k-th two-dimensional subspace with $\hat{\Pi}_0^{(k)}$ operator in one arm and $\hat{\sigma}_x^{(k)}$ operator in the other arm of the interferometer; where $k = 1, 2$ labels the two-dimensional sub-spaces for $d = 3$. The intensity distribution I_k as a function of relative phase ϵ_k of the interferometer is recorded by the detector D_k placed at the end of each interferometer [7].

[7]Note that, we have used $\hat{\mathcal{O}}^{[d]}$ to represent the operator that acts on the d-dimensional Hilbert space and $\hat{\mathcal{O}}^{(k)}$ to represent the operator that acts on the k-th two dimensional subspace.

Let us consider the stream of particles in the state $|\psi\rangle^{(3)}$ is incident on the QSI setup shown in Fig. 4.2. First, the input beam is divided into two spatial modes and each such mode is used to select a particular two dimensional subspace (of the 3-dimensional space) for which we need to obtain one interferogram. For a qutrit, a $50:50$ Beam splitter BS_0 can be used to divide the incident beam into two spatial modes. For each beam corresponding to a spatial mode, we construct one Mach-Zehnder interferometer (MZI) which acts on a particular two dimensional subspace. Here, the beam splitters BS_{11} and BS_{12} along with the mirrors M_{11} and M_{12} forms the MZI for the $1st$ subspace consisting of spin modes $\{|1\rangle, |2\rangle\}$. This is achieved by splitting the beams in the respective paths of the MZI (after BS_{11}), into three spin modes $|1\rangle$, $|2\rangle$ and $|3\rangle$ by the Spin Tritters ST_{11} and ST_{12} placed in the two individual paths of the MZI and then blocking the beam in the mode $|3\rangle$. The spin tritter ST is nothing but the $\hat{\sigma}_z^{[3]}$ operation on the beam in the state $|\psi\rangle^{(3)}$, which splits the incident beam into three beams each with one of the eigenstates of the $\hat{\sigma}_z^{[3]}$ operator. Here, $\hat{\sigma}_z^{[3]}$ is the Pauli spin matrix that acts on the 3-dimensional Hilbert space. By blocking the beam in the mode $|3\rangle$ in each path of this MZI we effectively select the two modes $|1\rangle$ and $|2\rangle$ which comprises the first two dimensional subspace.

As in the case for qubit, here also, we polar decompose the non-Hermitian ladder operator $\hat{\sigma}_-^{(1)}$ for the $1st$ two dimensional subspace into unitary $\hat{U}^{(1)} = \hat{\sigma}_x^{(1)}$ which is the spin flip operator for the modes $\{|1\rangle, |2\rangle\}$ and Hermitian $\hat{R}^{(1)} = \hat{\Pi}_0^{(1)}$ which is the projector to mode $|1\rangle$ for the $1st$ space, i.e.,

$$\hat{\sigma}_-^{(1)} = \hat{U}^{(1)}\ \hat{R}^{(1)} = \hat{\sigma}_x^{(1)}\ \hat{\Pi}_0^{(1)} \tag{4.68}$$

In order to experimentally obtain the expectation value of $\hat{\sigma}_-^{(1)}$ operator for the $1st$ subspace, we need to place the polar decomposed components $\hat{\sigma}_x^{(1)}$ and $\hat{\Pi}_0^{(1)}$ in each path of the Mach Zehnder Interferometer (MZI).

Experimentally, the operator $\hat{\Pi}_0^{(1)}$ for the $1st$ two-dimensional subspace with $\{|1\rangle, |2\rangle\}$ can be effectively realized by blocking the mode $|2\rangle$ in one of the arms of the interferometer. We then add a phase shifter PS_1 in the spin mode $|1\rangle$ in the same arm of the MZI, which introduces a relative phase ϵ_1 between the two interferometric paths. So, the effective operator in this arm of the MZI is given by $\exp(i\epsilon_1)\hat{\Pi}_0^{(1)}$. In the other arm of the

MZI, we use the spin flip operator (SF_1) to swap the mode $|1\rangle$ with $|2\rangle$ and vice-versa. Thus, the effective operator in this path is $\hat{\sigma}_x^{(1)}$. Finally, the spin modes in each arm are recombined using the spin combiners (reverse of spin tritter) SC_{11} and SC_{12} respectively. Then the beam splitter BS_{12} recombines the two spatial modes associated with the two paths of the MZI and the interference pattern generated at the end of this MZI is recorded using a detector. The detector D_1 records the intensity I_1 as a function of relative phase ϵ_1 of the interferometer, from which we obtain the visibility, phase shift and phase averaged intensity corresponding to the interference pattern formed for the $1st$ subspace.

Similarly, the second MZI constructed for the $2nd$ two dimensional spin subspace spanned by $\{|2\rangle, |3\rangle\}$ consists of the two beam splitters BS_{21}, BS_{22} and two mirrors M_{21}, M_{22}. The $2nd$ subspace is effectively selected by passing the beams in the two arms of the interferometer (after BS_{21}) through the spin tritters ST_{21} and ST_{22} respectively and then blocking the beam in the spin mode $|1\rangle$. In one arm of MZI, the beam in the spin mode $|3\rangle$ is blocked and a phase shifter $\exp(i\epsilon_2)$ is placed in the spin mode $|2\rangle$, that effectively realizes the operator $\exp(i\epsilon_2)\hat{\Pi}_0^{(2)}$ in this arm. Here ϵ_2 controls the relative phase between the two paths of the MZI. On the other arm we have a spin-flip operator SF_2 which performs the $\hat{\sigma}_x^{(2)}$ operation that swaps the mode $|2\rangle$ with $|3\rangle$ and vice-versa. The spin modes in each paths of the interferometer are recombined into a single beam using the spin combiners SC_{21} and SC_{22}. Then the beams from the two paths of the MZI are combined in BS_{22} and the intensity I_2 as a function of the relative phase ϵ_2 is recorded using the detector D_2. The interference pattern obtained for the $2nd$ subspace is further processed to determine the interferometric quantities from which state parameters are inferred.

4.2.3 Inferring the State Parameters to Reconstruct a Pure Qutrit

The MZI designed for the $1st$ two-dimensional subspace consists of $\hat{\Pi}_0^{(1)}$ operator in one arm and $\hat{\sigma}_x^{(1)}$ operator in the other arm, with the relative phase between the two interferometeric arms being ϵ_1. This makes the overall evolution operator associated the first MZI to be,

$$\hat{\mathcal{O}}^{(1)} = \frac{1}{2}\left(\exp(i\epsilon_1)\ \hat{\Pi}_0^{(1)} + \hat{\sigma}_x^{(1)}\right) = \frac{1}{2}\begin{pmatrix} \exp(i\epsilon_1) & 1 \\ 1 & 0 \end{pmatrix}$$

When the mode $|\psi\rangle_1^{(2;3)}$ associated with the $1st$ two dimensional subspace propagates through the Mach Zehnder Interferometer described above, we get the intensity distribution I_1 as a function of ϵ_1 at the end of the interferometer as the following,

$$I_1 = \left\| \hat{\mathcal{O}}^{(1)} |\psi\rangle_1^{(2;3)} \right\|^2 = \left\langle \psi_1^{(2;3)} \middle| \hat{\mathcal{O}}^{(1)\dagger} \hat{\mathcal{O}}^{(1)} \middle| \psi_1^{(2;3)} \right\rangle \tag{4.69}$$

$$I_1 = \frac{1}{4} \left[\left\langle \hat{\mathbb{1}}^{(1)} \right\rangle + \left\langle \hat{\Pi}_0^{(1)} \right\rangle + 2 \left| \left\langle \hat{\sigma}_-^{(1)} \right\rangle \right| \cos\left(\epsilon_1 + \arg\left(\left\langle \hat{\sigma}_-^{(1)} \right\rangle \right) \right) \right] \tag{4.70}$$

where $\hat{\mathbb{1}}^{(1)}$ is the 2×2 identity operator for the $1st$ two dimensional subspace whose expectation value in the state $|\psi\rangle_1^{(2;3)}$ is not equal to 1, since here we have not considered the normalization of the state. Computing the expectation values of the operators $\hat{\mathbb{1}}^{(1)}$, $\hat{\Pi}_0^{(1)}$ and $\hat{\sigma}_-^{(1)}$ for the state $|\psi\rangle_1^{(2;3)}$ represented in Eqn. 4.55, the intensity I_1 as a function of the relative phase ϵ_1 for the $1st$ subspace can be expressed as,

$$I_1(\epsilon_1) = \frac{1}{16} \left[5 + \cos(\theta_2) + \cos(\theta_1)(3 - \cos(\theta_2)) + 4\sin(\theta_1)\cos\left(\frac{\theta_2}{2}\right)\cos(\epsilon_1 - \phi_1) \right] \tag{4.71}$$

Similarly, the mode $|\psi\rangle_2^{(2;3)}$ given in Eqn. 4.56 associated with the $2nd$ two dimensional subspace when propagates through the Mach Zehnder Interferometer with $\hat{\Pi}_0^{(2)}$ operator in one arm and $\hat{\sigma}_x^{(2)}$ operator in the other arm, the intensity distribution obtained at the end of the interferometer as a function of the relative phase ϵ_2 can be expressed as,

$$I_2 = \left\| \hat{\mathcal{O}}^{(2)} |\psi\rangle_2^{(2;3)} \right\|^2 = \left\langle \psi_2^{(2;3)} \middle| \hat{\mathcal{O}}^{(2)\dagger} \hat{\mathcal{O}}^{(2)} \middle| \psi_2^{(2;3)} \right\rangle \tag{4.72}$$

$$I_2(\epsilon_2) = \frac{1}{4} \left[\left\langle \hat{\mathbb{1}}^{(2)} \right\rangle + \left\langle \hat{\Pi}_0^{(2)} \right\rangle + 2 \left| \left\langle \hat{\sigma}_-^{(2)} \right\rangle \right| \cos\left(\epsilon_2 + \arg\left(\left\langle \hat{\sigma}_-^{(2)} \right\rangle \right) \right) \right] \tag{4.73}$$

$$I_2(\epsilon_2) = \frac{1}{8} \sin^2\left(\frac{\theta_1}{2}\right) [3 + \cos(\theta_2) + 2\sin(\theta_2)\cos(\epsilon_2 - \phi_2)] \tag{4.74}$$

where $\hat{\mathcal{O}}^{(2)}$ is the overall evolution operator corresponding to the MZI designed to act on the $2nd$ two dimensional subspace and is given as the following:

$$\hat{\mathcal{O}}^{(2)} = \frac{1}{2}\left(\exp(i\epsilon_2)\ \hat{\Pi}_0^{(2)} + \hat{\sigma}_x^{(2)}\right) = \frac{1}{2}\begin{pmatrix}\exp(i\epsilon_2) & 1\\ 1 & 0\end{pmatrix} \tag{4.75}$$

From each of the two interference patterns we need to determine the phase shift (Φ_k), phase averaged intensity ($\bar{I}_k$) and visibility (V_k) associated with the particular sub-spaces.

❑ **Phase Shift:** For the $1st$ subspace, the phase shift Φ_1 of the interference pattern generated in the MZI, is determined at the value of phase ϵ_1 that maximizes the intensity I_1. Thus, Φ_1 can be obtained by solving for ϵ_1 in the equation $\frac{\partial I_1(\epsilon_1)}{\partial \epsilon_1} = 0$ and ensuring that $\left.\frac{\partial^2 I_1(\epsilon_1)}{\partial {\epsilon_1}^2}\right|_{\epsilon_1=\Phi_1} < 0$. From Eqn. 4.71 we get,

$$\left.\frac{\partial I_1(\epsilon_1)}{\partial \epsilon_1}\right|_{\epsilon_1=\Phi_1} = -\frac{1}{4}\sin(\theta_1)\cos\left(\frac{\theta_2}{2}\right)\sin(\Phi_1-\phi_1) = 0 \tag{4.76}$$

The above expression gives $\Phi_1 - \phi_1 = n\pi$, where n is any integer. When $n = 0$, we get $\Phi_1 = \phi_1$, for which we ensure that

$$\left.\frac{\partial^2 I_1(\epsilon_1)}{\partial {\epsilon_1}^2}\right|_{\epsilon_1=\Phi_1=\phi_1} = -\frac{1}{4}\sin(\theta_1)\cos\left(\frac{\theta_2}{2}\right) < 0 \tag{4.77}$$

given $0 \leq \sin(\theta_1) \leq 1$ for $\theta_1 \in [0,\pi]$ and $0 \leq \cos\left(\frac{\theta_2}{2}\right) \leq 1$ for $\theta_2 \in [0,\pi]$. Thus, we get the phase shift of the interference pattern generated for the first subspace at $\epsilon_1 = \phi_1$. So, the state parameter ϕ_1 can be directly obtained from the phase shift of the first interference pattern $I_1(\epsilon_1)$, i.e.,

$$\phi_1 = \Phi_1 \tag{4.78}$$

Next, the phase shift Φ_2 of the interference pattern obtained for the $2nd$ subspace is determined at the value of ϵ_2 for which the intensity I_2 is maximum. Thus, Φ_2 can be obtained from $I_2(\epsilon_2)$ gven in Eqn. 4.74 using the same method discussed for finding Φ_1.

$$\left.\frac{\partial I_2(\epsilon_2)}{\partial \epsilon_2}\right|_{\epsilon_2=\Phi_2} = -\frac{1}{4}\sin^2\left(\frac{\theta_1}{2}\right)\sin(\theta_2)\sin(\Phi_2-\phi_2)=0 \tag{4.79}$$

$$\left.\frac{\partial^2 I_2(\epsilon_2)}{\partial {\epsilon_2}^2}\right|_{\epsilon_2=\Phi_2=\phi_2} = -\frac{1}{4}\sin^2\left(\frac{\theta_1}{2}\right)\sin(\theta_2)<0 \tag{4.80}$$

provided $\sin^2\left(\frac{\theta_1}{2}\right)$ is always positive and $0 \leq \sin(\theta_2) \leq 1$ as $\theta_2 \in [0,\pi]$. Hence, the phase shift of the interference pattern $I_2(\epsilon_2)$ is obtained at $\epsilon_2 = \phi_2$. So, the state parameter ϕ_2 can be directly obtained from the phase shift Φ_2 of the interferogram, i.e.,

$$\phi_2 = \Phi_2 \tag{4.81}$$

❑ **Average Intensity:** Now, the phase averaged intensities $\bar{I}_1$ and $\bar{I}_2$ can be obtained by integrating the interference patterns $I_1(\epsilon_1)$ and $I_2(\epsilon_2)$ over all possible phases.

$$\bar{I}_1 = \int_{\epsilon_1} I_1(\epsilon_1)d\epsilon_1 = \frac{1}{16}\left[5+\cos(\theta_2)+\cos(\theta_1)(3-\cos(\theta_2))\right] \tag{4.82}$$

$$\bar{I}_2 = \int_{\epsilon_2} I_2(\epsilon_2)d\epsilon_2 = \frac{1}{8}\sin^2\left(\frac{\theta_1}{2}\right)\left[3+\cos(\theta_2)\right] \tag{4.83}$$

Here, both $\bar{I}_1$ and $\bar{I}_2$ are functions of the polar angles θ_1 and θ_2 respectively. Therefore, we can obtain the state parameters θ_1, θ_2 from the simultaneous solutions of the above two expressions using the experimentally obtained quantities $\bar{I}_1$ and $\bar{I}_2$. Hence, the four state parameters $\{\theta_1, \theta_2, \phi_1, \phi_2\}$ can be obtained from the phase shifts and the average intensities of the two interference patterns obtained for the two sub-spaces.

❑ **Visibility:** The visibility of an interference pattern can be computed using the maximum intensity $I^{(max)}$ and the minimum intensity $I^{(min)}$, as the following:

$$V = \frac{I^{(max)} - I^{(min)}}{I^{(max)} + I^{(min)}} \tag{4.84}$$

Now, if we compute the visibilities of the two interference patterns $I_1(\epsilon_1)$ and $I_2(\epsilon_2)$ obtained at the end of the QSI setup for qutrit depicted in Fig. 4.2, we get

$$V_1 = \frac{4\sin(\theta_1)\cos\left(\frac{\theta_2}{2}\right)}{5+\cos(\theta_2)+\cos(\theta_1)(3-\cos(\theta_2))} \tag{4.85}$$

$$V_2 = \frac{2\sin(\theta_2)}{3+\cos(\theta_2)} \tag{4.86}$$

From the above expressions of visibility we can see that V_2 is a unique function of θ_2. Therefore, the parameter θ_2 can be directly obtained from the visibility V_2 of the interference pattern obtained for the $2nd$ two dimensional subspace. Knowing θ_2 we can determine θ_1 from the visibility V_1. Thus, the 4 state parameters associated with a pure qutrit can also be determined from the experimentally obtained phase shifts and visibilities of the interference patterns. Alternatively, θ_1 can also be computed from the experimentally determined average intensity $\bar{I}_1$ using Eqn. 4.82 or $\bar{I}_2$ using 4.83, considering we have already determined the value of θ_2 from the visibility V_2.

In summary, the Quantum State Interferography technique can be employed to characterize an unknown pure state of a 3-dimensional quantum system. In this protocol, the 4 state parameters $\{\theta_1, \theta_2, \phi_1, \phi_2\}$ with $\theta_1, \theta_2 \in [0, \pi]$ and $\phi_1, \phi_2 \in [-\pi, \pi)$, representing the state $|\psi\rangle^{(3)}$ can be obtained from the post-processing of two interference patterens only. The two interferograms are formed at the end of the interferometric setup with 2 two path interferometers designed to act on each of the two dimensional sub-spaces $\{|1\rangle, |2\rangle\}$ and $\{|2\rangle, |3\rangle\}$ of the 3-dimensional Hilbert space. The parameters ϕ_1 and ϕ_2 can be inferred directly from the phase shifts of the two interference patterns and the parameters θ_1 and θ_2 can be determined either from the visibilities or from the phase averaged intensities of the two interferograms. This scheme can be further generalized to d-dimensions where the state parameters for an unknown qudit $|\psi\rangle^{(d)}$ can be inferred from $(d-1)$ interferograms associated with the $(d-1)$ two dimensional sub-spaces. The respective sub-spaces can be selected by blocking all the components after a spin splitter (eqivalent to Spin Tritter ST for qutrit) except for the desired pair $-$ details will be discussed in the next section.

4.3 Quantum State Interferography for Qudit: The General Scheme

We have already seen how the Quantum State Interferography technique can be employed for the reconstruction of any arbitrary qubit ($d = 2$), whether mixed or pure, as well as the pure state of a qutrit ($d = 3$). In this section, we will present an extension of the scheme to generalize the characterization of an unknown qudit ($d > 2$) using interferometry as the tool. This extended protocol, however, is only applicable for pure state reconstructions in d-dimension and does not work for mixed states in general.

In the Episphere representation, a pure state in a d-dimensional Hilbert space i.e., a pure qudit can be expressed in the polar spherical form with $(2d-2)$ parameters $\{\theta_j, \phi_j\}$, discussed in SubSec. 4.1.4, as the following:

$$|\psi\rangle^{(d)} = \begin{pmatrix} \cos\left(\frac{\theta_1}{2}\right) \\ \exp(i\phi_1)\sin\left(\frac{\theta_1}{2}\right)\cos\left(\frac{\theta_2}{2}\right) \\ \vdots \\ \prod_{j=1}^{n-1}\exp(i\phi_j)\sin\left(\frac{\theta_j}{2}\right)\cos\left(\frac{\theta_n}{2}\right) \\ \vdots \\ \prod_{j=1}^{d-1}\exp(i\phi_j)\sin\left(\frac{\theta_j}{2}\right) \end{pmatrix} \tag{4.87}$$

Now, if we consider that the d-dimensional Hilbert space is spanned by the basis vectors $\{|1\rangle, |2\rangle, \ldots, |d\rangle\}$, then the complex co-efficient α_n associated with the n-th basis state ($|n\rangle$) can be written as,

$$\alpha_n = \left(\prod_{j=1}^{n-1}\exp(i\phi_j)\sin\left(\frac{\theta_j}{2}\right)\right)\cos\left(\frac{\theta_n}{2}\right) \tag{4.88}$$

The d-dimensional space can be considered to have $(d-1)$ two dimensional sub-spaces arranged in a particular sequence, each sub-space consisting of two consecutive basis states in that sequence. For example, the 1st two dimensional subspace consists of the basis states $\{|1\rangle, |2\rangle\}$. The component of the state $|\psi\rangle^{(d)}$ associated with this subspace is labeled as $|\psi\rangle_1^{(2;d)}$ which, in general, is not normalized and can be expressed as $|\psi\rangle_1^{(2;d)} = \begin{pmatrix} \alpha_1 \\ \alpha_2 \end{pmatrix}$. Similarly, the 2nd subspace consists of the basis states $\{|2\rangle, |3\rangle\}$ and the component of $|\psi\rangle^{(d)}$ in this subspace is written as $|\psi\rangle_2^{(2;d)} = \begin{pmatrix} \alpha_2 \\ \alpha_3 \end{pmatrix}$ and so on. Thus, the k-th two dimensional subspace would be spanned by the basis states $\{|k\rangle, |k+1\rangle\}$ with the associated complex coefficients α_k and α_{k+1} being expressed as,

$$\alpha_k = \left(\prod_{j=1}^{k-1} \exp(i\phi_j) \sin\left(\frac{\theta_j}{2}\right)\right) \cos\left(\frac{\theta_k}{2}\right) \tag{4.89}$$

$$\alpha_{k+1} = \left(\prod_{j=1}^{k} \exp(i\phi_j) \sin\left(\frac{\theta_j}{2}\right)\right) \cos\left(\frac{\theta_{k+1}}{2}\right) \tag{4.90}$$

Therefore, the component of $|\psi\rangle^{(d)}$ associated with the k-th two-dimensional subspace in the Episphere representation, can be written as the following:

$$|\psi\rangle_k^{(2;d)} = \begin{pmatrix} \alpha_k \\ \alpha_{k+1} \end{pmatrix} = \left(\prod_{j=1}^{k-1} \exp(i\phi_j) \sin\left(\frac{\theta_j}{2}\right)\right) \begin{pmatrix} \cos\left(\frac{\theta_k}{2}\right) \\ \exp(i\phi_k) \sin\left(\frac{\theta_k}{2}\right) \cos\left(\frac{\theta_{k+1}}{2}\right) \end{pmatrix} \tag{4.91}$$

In order to infer the state $|\psi\rangle^{(d)}$ experimentally, we need to determine the $(2d-2)$ state parameters $\{\theta_j, \phi_j\}$ with $j = 1, 2, \ldots, (d-1)$, where $\theta_j \in [0, \pi]$ and $\phi_j \in [-\pi, \pi)$. The determination of all these $(2d-2)$ parameters associated with the state $|\psi\rangle^{(d)}$ using the interferometric scheme – the quantum state interferography (QSI) for d-dimensional systems requires post-processing of the quantities obtained from $(d-1)$ interferograms. To achieve this, we need to construct $(d-1)$ interferometers, one acting on each of the two dimensional sub-spaces (arranged in a particular order) of the d-dimensional space and need to perform single qubit QSI on each of the sub-spaces.

Although, here we shall be formulating the protocol of QSI for qudits using $(d-1)$ interferometers for ease of conceptualization, in principle and for many physical systems in practice, the state can be inferred from $(d-1)$ interferograms obtained with a setup involving only two interferometers. This is achieved by using the same interferometer for all the two dimensional sub-spaces and getting all the information required to infer $|\psi\rangle^{(d)}$ at once at the end of the interferometer; the details of which will be discussed in Section 4.4.

4.3.1 Theory

The component $|\psi\rangle_k^{(2;d)}$ of the pure qudit $|\psi\rangle^{(d)}$, in the k-th two dimensional subspace spanned by $\{|k\rangle, |k+1\rangle\}$ is given in the Eqn. **4.91**. Now, let us consider $\hat{\sigma}_{\pm}^{(k)}$ be the spin ladder operator for the k-th two-dimensional subspace, [8] i.e., $\hat{\sigma}_{+}^{(k)}$ raises the state $|k\rangle$ to $|k+1\rangle$ and $\hat{\sigma}_{-}^{(k)}$ lowers the state $|k+1\rangle$ to $|k\rangle$. The complex expectation values of the spin ladder operators $\hat{\sigma}_{\pm}^{(k)}$ in the k-th two dimensional subspace can be computed as,

$$\left\langle \hat{\sigma}_{\pm}^{(k)} \right\rangle = \left\langle \psi_k^{(2;d)} \middle| \hat{\sigma}_{\pm}^{(k)} \middle| \psi_k^{(2;d)} \right\rangle$$

$$= \frac{1}{2} \left(\prod_{j=1}^{k-1} \sin^2\left(\frac{\theta_j}{2}\right) \right) \exp(\pm i\phi_k) \sin(\theta_k) \cos\left(\frac{\theta_{k+1}}{2}\right) \tag{4.92}$$

$$\left\langle \hat{\sigma}_{\pm}^{(k)} \right\rangle = \frac{1}{2}\xi(k) \exp(\pm i\phi_k) \sin(\theta_k) \cos\left(\frac{\theta_{k+1}}{2}\right) \tag{4.93}$$

where, we have considered $\xi(k) = \prod_{j=1}^{k-1} \sin^2\left(\frac{\theta_j}{2}\right)$. So, from the above expression, we get the argument and the magnitude of the complex expectation values $\left\langle \hat{\sigma}_{\pm}^{(k)} \right\rangle$ as,

$$\arg\left(\left\langle \hat{\sigma}_{\pm}^{(k)} \right\rangle\right) = \pm\, \phi_k \tag{4.94}$$

[8]Here, the notation $\hat{\mathcal{O}}^{(k)}$ is used to denote the operator $\hat{\mathcal{O}}$ meant for the qubit associated with the k-th two dimensional subspace. The operators for d-dimensional qudits are represented as $\hat{\mathcal{O}}^{[k]}$.

$$\left|\left\langle \hat{\sigma}_{\pm}^{(k)} \right\rangle\right| = \frac{\xi(k)}{2} \sin(\theta_k) \cos\left(\frac{\theta_{k+1}}{2}\right) \tag{4.95}$$

So, from Eqn. 4.94 we directly get the relative phase ϕ_k of the k-th two-dimensional subspace from the argument of the matrix element of the spin ladder operator in that subspace. From Eqn. 4.95, however, we can see that the determination of θ_k requires the knowledge of θ_{k+1} and $\xi(k)$, which is a function of $\{\theta_1, \theta_2, \ldots, \theta_{k-1}\}$. For the 1st sub-space (i.e., $k = 1$), where $\xi(1) = 1$, the magnitude of the expectation value $\left\langle \psi_1^{(2;d)} \middle| \hat{\sigma}_{\pm}^{(1)} \middle| \psi_1^{(2;d)} \right\rangle$ is a function of both θ_1 and θ_2, as can be seen from the expression below and hence, can not be determined without any additional information.

$$\left|\left\langle \hat{\sigma}_{\pm}^{(1)} \right\rangle\right| = \left|\left\langle \psi_1^{(2;d)} \middle| \hat{\sigma}_{\pm}^{(1)} \middle| \psi_1^{(2;d)} \right\rangle\right| = \frac{1}{2} \sin(\theta_1) \cos\left(\frac{\theta_2}{2}\right) \tag{4.96}$$

Nevertheless, as in the case for qubits, we can compute the matrix element of $\hat{\Pi}_0^{(k)}$ in the k-th two-dimensional subspace, where $\hat{\Pi}_0^{(k)}$ is the projector to the first mode in that subspace. Thus, for the k-th subspace spanned with $\{|k\rangle, |k+1\rangle\}$, we have $\hat{\Pi}_0^{(k)} = |k\rangle\langle k|$. The expectation value of this projector computed for the state $|\psi\rangle_k^{(2;d)}$ is given as,

$$\left\langle \hat{\Pi}_0^{(k)} \right\rangle = \left\langle \psi_k^{(2;d)} \middle| \hat{\Pi}_0^{(k)} \middle| \psi_k^{(2;d)} \right\rangle = \xi(k) \cos^2\left(\frac{\theta_k}{2}\right) \tag{4.97}$$

Therefore, θ_k can be determined from the above expression provided we already know $\xi(k)$, i.e., $\{\theta_1, \theta_2, \ldots, \theta_{k-1}\}$. Now, for the 1st subspace consisting of the basis vectors $\{|1\rangle, |2\rangle\}$ if we determine the expectation value of $\hat{\Pi}_0^{(1)}$ which is the projector to state $|1\rangle$, we get

$$\left\langle \hat{\Pi}_0^{(1)} \right\rangle = \left\langle \psi_1^{(2;d)} \middle| \hat{\Pi}_0^{(1)} \middle| \psi_1^{(2;d)} \right\rangle = \cos^2\left(\frac{\theta_1}{2}\right) \tag{4.98}$$

Thus, from the above equation we can determine θ_1 as the following,

$$\theta_1 = 2\cos^{-1}\left(\sqrt{\left\langle \hat{\Pi}_0^{(1)} \right\rangle}\right) \tag{4.99}$$

Once θ_1 is known, subsequently we can determine θ_2 using the values of either $\left|\left\langle\hat{\sigma}_{\pm}^{(1)}\right\rangle\right| = \left|\left\langle\psi_1^{(2;d)}\middle|\hat{\sigma}_{\pm}^{(1)}\middle|\psi_1^{(2;d)}\right\rangle\right|$ or $\left\langle\hat{\Pi}_0^{(2)}\right\rangle = \left\langle\psi_2^{(2;d)}\middle|\hat{\Pi}_0^{(2)}\middle|\psi_2^{(2;d)}\right\rangle$.

$$\theta_2 = 2\cos^{-1}\left(\frac{2\left|\left\langle\hat{\sigma}_{\pm}^{(1)}\right\rangle\right|}{\sin(\theta_1)}\right) \tag{4.100}$$

or

$$\theta_2 = 2\cos^{-1}\left(\sqrt{\frac{\left\langle\hat{\Pi}_0^{(2)}\right\rangle}{\sin^2\left(\frac{\theta_1}{2}\right)}}\right) \tag{4.101}$$

Similarly, θ_3 can be determined from the already known values of θ_1 and θ_2 using either $\left|\left\langle\hat{\sigma}_{\pm}^{(2)}\right\rangle\right|$ or $\left\langle\hat{\Pi}_0^{(3)}\right\rangle$.

Hence, for inferring a d-dimensional pure state $|\psi\rangle^{(d)}$ the state parameters ϕ_k's can be determined directly from the arguments of the expectation values of the spin ladder operators in the respective sub-spaces, i.e., from $\arg\left(\left\langle\hat{\sigma}_{\pm}^{(k)}\right\rangle\right)$. The polar angle θ_1 is determined using the value of $\left\langle\hat{\Pi}_0^{(1)}\right\rangle$ and θ_2 is determined either from $\left|\left\langle\hat{\sigma}_{\pm}^{(1)}\right\rangle\right|$ or from $\left\langle\hat{\Pi}_0^{(2)}\right\rangle$, using the value of θ_1. Therefore, once θ_k is determined, θ_{k+1} can be obtained sequentially either from the magnitude of $\left\langle\hat{\sigma}_{\pm}^{(k)}\right\rangle$ or from the value of $\left\langle\hat{\Pi}_0^{(k+1)}\right\rangle$. So, the state parameters of $|\psi\rangle^{(d)}$ are inferred as,

$$\left.\begin{aligned} \phi_k &= \pm\arg\left(\left\langle\hat{\sigma}_{\pm}^{(k)}\right\rangle\right) \\ \theta_k &= 2\cos^{-1}\left(\sqrt{\frac{\left\langle\hat{\Pi}_0^{(k)}\right\rangle}{\xi(k)}}\right) \end{aligned}\right\} \quad k = 1, 2, 3, \ldots, d-1$$

or

$$\theta_{k'} = 2\cos^{-1}\left(\frac{2\left|\left\langle\hat{\sigma}_{\pm}^{(k'-1)}\right\rangle\right|}{\xi(k'-1)\sin\left(\theta_{k'-1}\right)}\right) \quad \Big\} \quad k' = 2, 3, \ldots, d-1 \tag{4.102}$$

4.3.2 Experimental Protocol

So far we have discussed how the $(2d-2)$ parameters $\{\theta_j, \phi_j\}$ with $j = 1, 2, \ldots, (d-1)$, necessary to characterize a pure state in the d-dimensions, can be inferred from the expectation values of the spin ladder operators $\left\langle \hat{\sigma}_{\pm}^{(k)} \right\rangle$ and the projector $\left\langle \hat{\Pi}_0^{(k)} \right\rangle$, obtained for the individual two dimensional sub-spaces. In this subsection, we will present a generic protocol for experimentally determining the expectation values of the sequence of spin ladder operators and the projectors in order to reconstruct the pure qudit $|\psi\rangle^{(d)}$ using the interferometric state determination technique, quantum state interferography (QSI). The protocol involves constructing $(d-1)$ Mach Zehnder interferometers (or an equivalent two path interferometer) on each of the two-dimensional sub-space of the d-dimensional state $|\psi\rangle^{(d)}$, in the sequence in which we represent the vector. Each interferometer yields an interferogram (i.e., the intensity distribution over the relative phase between the two interferometric paths) and the information from these $(d-1)$ interferograms is post-processed to obtain the state parameters $\{\theta_j, \phi_j\}$.

The QSI setup for reconstructing a d-dimensional pure state would be similar to the setup for reconstructing a qutrit i.e., a state in $d = 3$, as shown in Fig. 4.2, but with $(d-1)$ Mach-Zehnder interferometers (MZI) instead of just two. In the interferometric setup for d-dimensional pure qudit reconstruction, the incident beam in the unknown state $|\psi\rangle^{(d)}$ is split into $(d-1)$ spatial modes. Each spatial mode, for example the k-th mode, selects a specific two dimensional sub-space spanned by the states $\{|k\rangle, |k+1\rangle\}$ of the d-dimensional space. A MZI, with the respective operators in its two paths, is aligned for each of the spatial modes on which single qubit QSI is performed that generates an interference pattern corresponding to a particular subspace. This method is scalable to any higher dimensional system.

We employ the same scheme of polar decomposing the non-Hermitian spin ladder operator $\hat{\sigma}_{-}^{(k)}$ in the two-dimensional k-th subspace into the Unitary $\hat{\sigma}_x^{(k)}$ and positive semi-definite Hermitian $\hat{\Pi}_0^{(k)}$, as the following

$$\hat{\sigma}_{-}^{(k)} = \hat{\sigma}_x^{(k)}\ \hat{\Pi}_0^{(k)} \tag{4.103}$$

To experimentally determine $\left\langle \hat{\sigma}_{-}^{(k)} \right\rangle$ for the two dimensional subspace with $\{|k\rangle, |k+1\rangle\}$, we place the polar decomposed components of this non-Hermitian operator in the two respective arms of a Mach Zehnder interferometer (or any equivalent two path interferometer). On one arm of the interferometer, we have the operator $\exp(i\epsilon_k)\hat{\Pi}_0^{(k)}$, i.e., a phase shifter PS_k that controls the relative phase ϵ_k between the two arms of the k-th interferometer and a projector $\hat{\Pi}_0^{(k)}$ on the mode $|k\rangle$ in k-th two dimensional subspace. In the other arm of the interferometer, we have the operator $\hat{\sigma}_x^{(k)}$ which is the spin-flip operator in the k-th subspace that swaps $|k\rangle$ with $|k+1\rangle$ and vice versa. Experimentally we have to design $(d-1)$ such Mach-Zehnder interferometer (MZI) setups for estimating the state of a d-dimensional pure qudit. From each such MZI, we can effectively obtain the expectation value of the ladder operator $\hat{\sigma}_{-}^{(k)}$ for k-th subspace.

Let's consider that a stream of identically prepared quantum particles in the state $|\psi\rangle^{(d)}$ is incident on the experimental setup with $(d-1)$ Mach-Zehnder interferometers, each having the operators $\hat{\sigma}_x^{(k)}$ and $\exp(i\epsilon_k)\hat{\Pi}_0^{(k)}$ associated with the respective sub-spaces in the individual arms. First, the beam is divided into $(d-1)$ spatial modes and each such spatial mode is used to select one of the two dimensional sub-spaces. If the initial beam is incident on the setup with the intensity $\mathcal{I}$, then each of the spatial mode would have the intensity $\dfrac{\mathcal{I}}{d-1}$ (ideally). Now, $(d-1)$ components of $|\psi\rangle^{(d)}$ corresponding to each subspace, i.e., the states $|\psi\rangle_n^{(2;d)}$ where $n = 1, 2, \ldots, (d-1)$, associated with the individual two-dimensional sub-spaces are prepared from each of the spatial modes. For example, consider the state $|\psi\rangle_k^{(2;d)}$ associated with the k-th two dimensional subspace spanned by the basis $\{|k\rangle, |k+1\rangle\}$ is prepared from one of the spatial modes. This state preparation in a particular spatial mode of the beam is done in three steps;

(i) First, decomposing the d-dimensional state into the basis states i.e., $\{|1\rangle, |2\rangle, \ldots, |d\rangle\}$ using a spin-splitter (say, SS_k). This can be achieved by applying the $\hat{\sigma}_z^{[d]}$ operator on the k-th spatial mode of the beam.

(ii) Then, blocking all the eigen states of $\hat{\sigma}_z^{[d]}$ operator except the desired pair, i.e., except $|k\rangle$ and $|k+1\rangle$ for selecting the k-th subspace.

(iii) Lastly, recombining the beams in the two states $|k\rangle$ and $|k+1\rangle$ into a single beam using a spin-combiner (say, SC_k).

The beam in the k-th spatial mode is now prepared in the state $|\psi\rangle_k^{(2;d)}$, given in Eqn. 4.91. Next, this beam in the particular state $|\psi\rangle_k^{(2;d)}$ associated with the k-th two-dimensional subspace is made incident on the Mach-Zehnder interferometer (MZI) constructed to act on that particular subspace. The MZI designed using two beam splitters BS_{k1}, BS_{k2} and two mirrors M_{k1}, M_{k2}, consists of the operators $\exp(i\epsilon_k)\hat{\Pi}_0^{(k)}$ in one arm and the operator $\hat{\sigma}_x^{(k)}$ in the other arm. The intensity I_k at one of the output ports of the final beam splitter BS_{k2} of the MZI, is recorded as a function of the relative phase ϵ_k, which is processed to get the state parameters.

The effective evolution operator, from the input port of the beam splitter BS_{k1} to one of the output ports of the final beam splitter BS_{k2}, of the two path interferometer acting on the k-th subspace, can be written as

$$\hat{\mathcal{O}}^{(k)} = \frac{1}{2}\Big(\exp(i\epsilon_k)\ \hat{\Pi}_0^{(k)} + \hat{\sigma}_x^{(k)}\Big) \tag{4.104}$$

$$\Longrightarrow \qquad \hat{\mathcal{O}}^{(k)} = \frac{1}{2}\begin{pmatrix} \exp(i\epsilon_k) & 1 \\ 1 & 0 \end{pmatrix}_k^{(2;d)} \tag{4.105}$$

Therefore, when a beam in the state $|\psi\rangle_k^{(2;d)}$ propagates through an interferometer with the corresponding evolution operator $\hat{\mathcal{O}}^{(k)}$, the final state at one of the output ports after the interferometer is obtained to be,

$$|\Psi\rangle_k^{(2;d)} = \hat{\mathcal{O}}^{(k)}\ |\psi\rangle_k^{(2;d)} \tag{4.106}$$

Thus, the intensity I_k recorded by the detector D_k at the end of the interferometer constructed to act on k-th two dimensional subspace is given by,

$$I_k = \Big\| |\Psi\rangle_k^{(2;d)} \Big\|^2 = \left| \left\langle \Psi_k^{(2;d)} \middle| \Psi_k^{(2;d)} \right\rangle \right|^2 \tag{4.107}$$

Using the expressions given in Eqn. 4.104 and Eqn. 4.106 we get the expression for intensity as a function of the relative phase ϵ_k as the following:

$$I_k(\epsilon_k) = \left\langle \psi_k^{(2;d)} \middle| \hat{\mathcal{O}}^{(k)\dagger} \hat{\mathcal{O}}^{(k)} \middle| \psi_k^{(2;d)} \right\rangle \tag{4.108}$$

$$\begin{aligned} &= \frac{1}{4} \left\langle \psi_k^{(2;d)} \right| \left[\left(\hat{\sigma}_x^{(k)} \right)^\dagger \hat{\sigma}_x^{(k)} + \left(\hat{\Pi}_0^{(k)} \right)^\dagger \hat{\Pi}_0^{(k)} + \exp(i\epsilon_k) \left(\hat{\sigma}_x^{(k)} \right)^\dagger \hat{\Pi}_0^{(k)} \right. \\ &\qquad \left. + \ \exp(-i\epsilon_k) \left(\hat{\Pi}_0^{(k)} \right)^\dagger \hat{\sigma}_x^{(k)} \right] \left| \psi_k^{(2;d)} \right\rangle \end{aligned} \tag{4.109}$$

Here, $\hat{\sigma}_x^{(k)}$ is a Hermitian operator, i.e., $\left(\hat{\sigma}_x^{(k)}\right)^\dagger = \hat{\sigma}_x^{(k)}$. So, we get $\left(\hat{\sigma}_x^{(k)}\right)^\dagger \hat{\sigma}_x^{(k)} = \left(\hat{\sigma}_x^{(k)}\right)^2 = \hat{\mathbb{1}}^{(k)}$. Again, since $\hat{\Pi}_0^{(k)}$ is the projector on to the k-th mode in the corresponding two dimensional subspace, we have $\left(\hat{\Pi}_0^{(k)}\right)^\dagger = \hat{\Pi}_0^{(k)}$ and $\left(\hat{\Pi}_0^{(k)}\right)^\dagger \hat{\Pi}_0^{(k)} = \hat{\Pi}_0^{(k)}$. Therefore, the above expression of intensity can be written as,

$$\begin{aligned} I_k(\epsilon_k) &= \frac{1}{4} \left[\left\langle \hat{\mathbb{1}}^{(k)} \right\rangle + \left\langle \hat{\Pi}_0^{(k)} \right\rangle + 2\,\mathrm{Re} \left(\exp(i\epsilon_k) \left\langle \hat{\sigma}_x^{(k)}\ \hat{\Pi}_0^{(k)} \right\rangle \right) \right] \\ &= \frac{1}{4} \left[\left\langle \hat{\mathbb{1}}^{(k)} \right\rangle + \left\langle \hat{\Pi}_0^{(k)} \right\rangle + 2\,\mathrm{Re} \left(\exp(i\epsilon_k) \left\langle \hat{\sigma}_-^{(k)} \right\rangle \right) \right] \\ &= \frac{1}{4} \left[\left\langle \hat{\mathbb{1}}^{(k)} \right\rangle + \left\langle \hat{\Pi}_0^{(k)} \right\rangle + 2 \left| \left\langle \hat{\sigma}_-^{(k)} \right\rangle \right| \cos \left(\epsilon_k + \arg \left(\left\langle \hat{\sigma}_-^{(k)} \right\rangle \right) \right) \right] \end{aligned} \tag{4.110}$$

Note that, here the expectation value of the identity operator in the two dimensional k-th subspace is not unity, i.e., $\langle \hat{\mathbb{1}}^{(k)} \rangle \neq 1$. This is because the mode $\left| \psi_k^{(2;d)} \right\rangle$ for which the expectation value is being computed, is a component of the state $|\psi\rangle^{(d)}$ and it is not normalized. The expectation value of $\hat{\mathbb{1}}^{(k)}$ in the state $\left| \psi_k^{(2;d)} \right\rangle$ is computed to be,

$$\left\langle \hat{\mathbb{1}}^{(k)} \right\rangle = \left\langle \psi_k^{(2;d)} \middle| \hat{\mathbb{1}}^{(k)} \middle| \psi_k^{(2;d)} \right\rangle = \xi(k) \left[\cos^2 \left(\frac{\theta_k}{2} \right) + \sin^2 \left(\frac{\theta_k}{2} \right) \cos^2 \left(\frac{\theta_{k+1}}{2} \right) \right] \tag{4.111}$$

Putting the values of $\langle \hat{\mathbb{1}}^{(k)} \rangle$, $\left\langle \hat{\Pi}_0^{(k)} \right\rangle$, the argument and magnitude of $\left\langle \hat{\sigma}_-^{(k)} \right\rangle$ from Eqn. 4.111, Eqn. 4.97, Eqn. 4.94 and Eqn. 4.95 respectively, in the expression given in Eqn. 4.110 we get the intensity I_k as a function of relative phase ϵ_k obtained at the end of the interferometer designed for the two dimensional k-th subspace.

$$
\begin{aligned}
&I_k(\epsilon_k) \\
&= \frac{\xi(k)}{4}\left[2\cos^2\left(\frac{\theta_k}{2}\right)+\sin^2\left(\frac{\theta_k}{2}\right)\cos^2\left(\frac{\theta_{k+1}}{2}\right)+\sin(\theta_k)\cos\left(\frac{\theta_{k+1}}{2}\right)\cos(\epsilon_k-\phi_k)\right] \\
&= \frac{\xi(k)}{16}\left[5+\cos(\theta_{k+1})+\cos(\theta_k)(3-\cos(\theta_{k+1}))+4\sin(\theta_k)\cos\left(\frac{\theta_{k+1}}{2}\right)\cos(\epsilon_k-\phi_k)\right]
\end{aligned} \tag{4.112}
$$

Experimentally this intensity I_k is measured as a function of the relative phase ϵ_k between the two paths of the k-th interferometer and the interferometric quantities such as the visibility (V_k), phase shift (Φ_k) and phase averaged intensity ($\bar{I}_k$) are obtained for the k-th subspace from $I_k(\epsilon_k)$. This is repeated for all the $(d-1)$ subspaces, i.e, one intensity distribution (called the interferogram) each is recorded from one interferometer designed to act on a particular subspace. The information collected from $(d-1)$ interferograms are analyzed to infer the $(2d-2)$ state parameters associated with the state $|\psi\rangle^{(d)}$ which was incident on the setup. The details of the analysis is discussed next, in SubSec. 4.3.3. Further, the derivation of the expectation values of the operators $\hat{\sigma}_{\pm}^{(k)}$, $\hat{\Pi}_0^{(k)}$ corresponding to the k-th two dimensional subspace and the associated intensity distribution $I_k(\epsilon_k)$ obtained from the single qubit QSI performed on that subspace, considering *normalization* of the state $|\psi\rangle_k^{(2;d)}$ is presented in Appendix 4.A.

4.3.3 Inferring the State Parameters to Reconstruct the Pure Qudit

The mode $|\psi\rangle_k^{(2;d)}$ associated with the k-th two dimensional subspace of the d-dimensional space, spanned by $\{|k\rangle, |k+1\rangle\}$ with $k = 1, 2, \ldots, (d-1)$ provided $\theta_d = 0$, can be expressed in terms of the Episphere co-ordinates as the following,

$$
|\psi\rangle_k^{(2;d)} = \left(\prod_{j=1}^{k-1}\exp(i\phi_j)\sin\left(\frac{\theta_j}{2}\right)\right)\begin{pmatrix}\cos\left(\frac{\theta_k}{2}\right) \\ \exp(i\phi_k)\sin\left(\frac{\theta_k}{2}\right)\cos\left(\frac{\theta_{k+1}}{2}\right)\end{pmatrix} \tag{4.113}
$$

The first term outside the matrix form is nothing but a global factor multiplied with the amplitude of the vector in the k-th subspace. Hence, the intensity modulation I_k obtained by evolving the state $|\psi\rangle_k^{(2;d)}$ through the interferometer designed for that subspace, would not be affected by the factor but would be scaled by the factor $\prod_{j=1}^{k-1} \sin^2\left(\frac{\theta_j}{2}\right)$.

The intensity pattern $I_k(\epsilon_k)$ for the k-th subspace, formed at the end when the mode $|\psi\rangle_k^{(2;d)}$ is incident on the MZI having $\hat{\Pi}_0^{(k)}$ operator in one arm and $\hat{\sigma}_x^{(k)}$ operator in the other arm, with a relative phase ϵ_k between the two interferometric arms is given as,

$$I_k = \frac{\xi(k)}{16}\left[5 + \cos(\theta_{k+1}) + \cos(\theta_k)(3 - \cos(\theta_{k+1})) + 4\sin(\theta_k)\cos\left(\frac{\theta_{k+1}}{2}\right)\cos(\epsilon_k - \phi_k)\right] \tag{4.114}$$

where the factor $\xi(k)$ is given by,

$$\xi(k) = \prod_{j=1}^{k-1} \sin^2\left(\frac{\theta_j}{2}\right) \tag{4.115}$$

❑ **Phase Shift:** The phase shift Φ_k of the interferogram is determined from the value of relative phase ϵ_k that corresponds to the maximum intensity. Say, for $\epsilon_k = \epsilon_k^{(m)}$, we have $I_k(\epsilon_k = \epsilon_k^{(m)}) = I_k^{(max)}$. Therefore,

$$\left.\frac{\partial I_k(\epsilon_k)}{\partial \epsilon_k}\right|_{\epsilon_k=\epsilon_k^{(m)}} = -\frac{\xi(k)}{4}\sin(\theta_k)\cos\left(\frac{\theta_{k+1}}{2}\right)\sin\left(\epsilon_k^{(m)} - \phi_k\right) = 0 \tag{4.116}$$

From the above equation we get, $\epsilon_k^{(m)} - \phi_k = n\pi$, where n can take the values either 0 giving $\epsilon_k^{(m)} = \phi_k$ or 1 giving $\epsilon_k^{(m)} = \phi_k + \pi$. Now, at the phase $\epsilon_k^{(m)}$ that corresponds to the maximum intensity, the double derivative of $I_k(\epsilon_k)$ with respect to ϵ_k would be negative. So, the criteria that needs to be satisfied would be,

$$\left.\frac{\partial^2 I_k(\epsilon_k)}{\partial {\epsilon_k}^2}\right|_{\epsilon_k=\epsilon_k^{(m)}} = -\frac{\xi(k)}{4}\sin(\theta_k)\cos\left(\frac{\theta_{k+1}}{2}\right)\cos\left(\epsilon_k^{(m)} - \phi_k\right) < 0 \tag{4.117}$$

Provided $\theta_k \in [0, \pi]$, both $\sin(\theta_k)$ and $\cos\left(\frac{\theta_{k+1}}{2}\right)$ are always positive and we have $\xi(k) > 0$, as well. Thus, in order to satisfy the condition presented in Eqn. 4.117 we must have $\cos\left(\epsilon_k^{(m)} - \phi_k\right) > 0$, i.e., $0 \leq \epsilon_k^{(m)} - \phi_k < \frac{\pi}{2}$. Therefore, the value $\epsilon_k^{(m)} = \phi_k$ ensures

$$\left.\frac{\partial^2 I_k(\epsilon_k)}{\partial {\epsilon_k}^2}\right|_{\epsilon_k^{(m)}=\phi_k} < 0 \tag{4.118}$$

giving $I_k(\epsilon_k = \phi_k) = I_k^{(max)}$. Hence, the phase shift of the interference pattern generated for the k-th subspace, would be

$$\Phi_k = \phi_k \tag{4.119}$$

Thus, the state parameters $\{\phi_k\}$ with $k = 1, 2, \ldots, (d-1)$ for a d-dimensional pure qudit can be directly obtained from the experimentally observed phase shifts $\{\Phi_k\}$ of the $(d-1)$ interference patterns generated at the end of the Mach Zehnder Interferometers, each designed to act on a particular two dimensional subspace.

❑ **Average Intensity:** The phase averaged intensity is obtained by integrating the intensity distribution $I_k(\epsilon_k)$ over all possible phases (ϵ_k), i.e.,

$$\bar{I}_k = \int_{\epsilon_k} I_k(\epsilon_k) d\epsilon_k = \frac{\xi(k)}{16}\left[5 + \cos(\theta_{k+1}) + \cos(\theta_k)(3 - \cos(\theta_{k+1}))\right] \tag{4.120}$$

So, the average intensity $\bar{I}_k$ of the interferogram obtained for the k-th subspace is a function of $\{\theta_1, \theta_2, \ldots, \theta_k, \theta_{k+1}\}$. Using the above equation, the parameter θ_k can be determined from the experimentally obtained value of $\bar{I}_k$ for a given θ_{k+1} and known $\xi(k)$. But in order to reconstruct the state, all the unknown parameters need to be determined from the experiment, i.e., from the information recorded in the interferograms.

From $(d-1)$ interference patterns we have $(d-1)$ measured values of $\bar{I}_k$ and need to infer $(d-1)$ values of θ_k's. The determination of the θ_k's is not straight forward because of the presence of the term $\xi(k) = \prod_{j=1}^{k-1} \sin^2\left(\frac{\theta_j}{2}\right)$. In order to eliminate the product of sines the ratio of $\bar{I}_k$ to $\bar{I}_{k-1}$ can be taken.

$$\frac{\bar{I}_k}{\bar{I}_{k-1}} = \frac{\sin^2\left(\frac{\theta_{k-1}}{2}\right)\left[5+\cos(\theta_{k+1})+\cos(\theta_k)(3-\cos(\theta_{k+1}))\right]}{5+\cos(\theta_k)+\cos(\theta_{k-1})(3-\cos(\theta_k))} \tag{4.121}$$

The above ratio of average intensities for the k-th and $(k-1)$-th sub-spaces is a function of three variables θ_{k-1} , θ_k and θ_{k+1}. Here k represents the chosen two-dimensional subspace, thus can take values from 1 to $(d-1)$.

If we take the ratio of average intensities $\bar{I}_{d-1}$ and $\bar{I}_{d-2}$ obtained from the interference patterns generated for the modes $|\psi\rangle_{d-1}^{(2;d)}$ and $|\psi\rangle_{d-2}^{(2;d)}$ associated with $(d-1)$-th and $(d-2)$-th subspace respectively, we get

$$\frac{\bar{I}_{d-1}}{\bar{I}_{d-2}} = \frac{\sin^2\left(\frac{\theta_{d-2}}{2}\right)\left[5+\cos(\theta_d)+\cos(\theta_{d-1})(3-\cos(\theta_d))\right]}{5+\cos(\theta_{d-1})+\cos(\theta_{d-2})(3-\cos(\theta_{d-1}))} \tag{4.122}$$

From the normalization criteria for the state $|\psi\rangle^{(d)}$, we have $\theta_d = 0$ as shown in SubSec. 4.1.5. Thus, putting the value $\cos(\theta_d) = 1$ in the above equation we get,

$$\frac{\bar{I}_{d-1}}{\bar{I}_{d-2}} = \frac{2\sin^2\left(\frac{\theta_{d-2}}{2}\right)(3+\cos(\theta_{d-1}))}{5+\cos(\theta_{d-1})+\cos(\theta_{d-2})(3-\cos(\theta_{d-1}))} \tag{4.123}$$

Therefore, using only the average intensities $\bar{I}_k$ of the $(d-1)$ interferograms we can not determine the state parameters $\{\theta_k\}$. However, if any of the parameters θ_{d-1} or θ_{d-2} are known, the other parameter can be determined from the above ratio of the average intensities $\frac{\bar{I}_{d-1}}{\bar{I}_{d-2}}$ using Eqn. 4.123. Once $\theta_{d-1}, \theta_{d-2}$ are known, the parameter θ_{d-3} can be obtained from the ratio, $\frac{\bar{I}_{d-2}}{\bar{I}_{d-3}}$ and so on.

$$\frac{\bar{I}_{d-2}}{\bar{I}_{d-3}} = \frac{\sin^2\left(\frac{\theta_{d-3}}{2}\right)\left[5+\cos(\theta_{d-1})+\cos(\theta_{d-2})(3-\cos(\theta_{d-1}))\right]}{5+\cos(\theta_{d-2})+\cos(\theta_{d-3})(3-\cos(\theta_{d-2}))} \tag{4.124}$$

❑ **Visibility:** The visibility of the interference pattern for the k-th subspace can be determined by computing,

$$V_k = \frac{I_k^{(max)} - I_k^{(min)}}{I_k^{(max)} + I_k^{(min)}} \tag{4.125}$$

where $I_k^{(max)}$ and $I_k^{(min)}$ represents the maximum and minimum values of the intensities obtained experimentally from the interferogram $I_k(\epsilon_k)$ corresponding to the k-th subspace.

Varying the phase ϵ_k in the expression given in Eqn. 4.114 we get the maximum and minimum intensity values as the following,

$$I_k^{(max)} = \frac{\xi(k)}{16}\left[5 + \cos(\theta_{k+1}) + \cos(\theta_k)(3 - \cos(\theta_{k+1})) + 4\sin(\theta_k)\cos\left(\frac{\theta_{k+1}}{2}\right)\right] \tag{4.126}$$

$$I_k^{(min)} = \frac{\xi(k)}{16}\left[5 + \cos(\theta_{k+1}) + \cos(\theta_k)(3 - \cos(\theta_{k+1})) - 4\sin(\theta_k)\cos\left(\frac{\theta_{k+1}}{2}\right)\right] \tag{4.127}$$

Thus the visibility of the interference pattern for the k-th subspace can be computed as,

$$V_k = \frac{4\sin(\theta_k)\cos\left(\frac{\theta_{k+1}}{2}\right)}{5 + \cos(\theta_{k+1}) + \cos(\theta_k)(3 - \cos(\theta_{k+1}))} \tag{4.128}$$

This quantity V_k, which is obtained to be a function of θ_k and θ_{k+1}, is experimentally determined from the interferogram for the k-th subspace and can be used to infer the state parameters $\{\theta_j\}$ with $j = 1, 2, \ldots, (d-1)$. Visibility for $(d-1)$-th subspace, provided $\theta_d = 0$, can be expressed as

$$V_{d-1} = \frac{4\sin(\theta_{d-1})\cos\left(\frac{\theta_d}{2}\right)}{5 + \cos(\theta_d) + \cos(\theta_{d-1})(3 - \cos(\theta_d))} = \frac{2\sin(\theta_{d-1})}{3 + \cos(\theta_{d-1})} \tag{4.129}$$

So, the value of θ_{d-1} can be determined from the experimentally obtained value of V_{d-1} using the Eqn. 4.129 by solving the expression as shown in the following.

$$
\begin{aligned}
&(3+\cos(\theta_{d-1}))\, V_{d-1} = 2\sin(\theta_{d-1}) \\
\implies \quad & \left(V_{d-1}^2+4\right)\cos^2(\theta_{d-1}) + 6V_{d-1}^2\cos(\theta_{d-1}) + \left(9V_{d-1}^2-4\right) = 0
\end{aligned}
\tag{4.130}
$$

Then the obtained value of θ_{d-1} can be put into Eqn. 4.123 to compute the value of θ_{d-2}. Alternatively, θ_{d-2} can be determined using the experimentally obtained value of visibility V_{d-2} of the interferogram generated for the $(d-2)$-th subspace and the known value of θ_{d-1}, from the following expression

$$
V_{d-2} = \frac{4\sin(\theta_{d-2})\cos\left(\dfrac{\theta_{d-1}}{2}\right)}{5+\cos(\theta_{d-1})+\cos(\theta_{d-2})(3-\cos(\theta_{d-1}))} \tag{4.131}
$$

Knowing θ_{d-2}, the value for θ_{d-3} can be inferred from the experimentally obtained quantity V_{d-3} as shown in the following or from the ratio $\dfrac{\bar{I}_{d-2}}{\bar{I}_{d-3}}$ as shown in Eqn. 4.124.

$$
V_{d-3} = \frac{4\sin(\theta_{d-3})\cos\left(\dfrac{\theta_{d-2}}{2}\right)}{5+\cos(\theta_{d-2})+\cos(\theta_{d-3})(3-\cos(\theta_{d-2}))} \tag{4.132}
$$

Therefore, the characterization of a d-dimensional pure state $|\psi\rangle^{(d)}$ using Quantum State Interferography technique requires processing of $(d-1)$ interferograms generated for each individual two dimensional sub-spaces of the d-dimensional space. The $(d-1)$ values of the azimuthal angles $\{\phi_k\}$ can be directly obtained from the phase shifts Φ_k of the respective interferograms. However, the state parameter θ_{d-1} can be inferred from the experimentally obtained visibility V_{d-1} of the interferogram produced for $(d-1)$-th two dimensional subspace. Once θ_{d-1} is determined, all the other polar angles θ_j (where $j = 1, 2, \ldots, (d-2)$) can be determined in the backward sequence as described above, either from the visibility V_j or from the ratio of the average intensities $\dfrac{\bar{I}_{j+1}}{\bar{I}_j}$.

❑ Alternative Method for Determining the Polar Angles:

In the method discussed above, the determination of θ_j's for $|\psi\rangle^{(d)}$ require post-processing of the interferogram for the $(d-1)$-th subspace first, so that the already known information $\theta_d = 0$ can be utilized while inferring θ_{d-1}. Once θ_{d-1} is known all the other polar angles $\theta_{d-2}, \theta_{d-3}, \ldots, \theta_1$ can be determined sequentially. Alternatively, we can directly obtain θ_1 and θ_2 from the simultaneous solution of the expressions,

$$V_1 = \frac{4\sin(\theta_1)\cos\left(\dfrac{\theta_2}{2}\right)}{5 + \cos(\theta_2) + \cos(\theta_1)(3 - \cos(\theta_2))} \tag{4.133}$$

$$\bar{I}_1 = \frac{1}{16}\left[5 + \cos(\theta_2) + \cos(\theta_1)(3 - \cos(\theta_2))\right] \tag{4.134}$$

given $\xi(1) = 1$. Here both the quantities V_1 and $\bar{I}_1$ are obtained experimentally from the interferogram recorded at the end of the interferometer designed to act on the $1st$ two dimensional subspace spanned by the states $|1\rangle$ and $|2\rangle$.

The advantage in this process is that once we know the parameters θ_1 and θ_2, we can infer θ_3 from the experimental quantities $\bar{I}_2$ or V_2. In this method, we only have to solve the simultaneous equations *once* for the interferometric quantities V_1 and $\bar{I}_1$ obtained for the first subspace. Then the recursive property of $\bar{I}_k$ and V_k can be used to infer θ_{k+1} and subsequently the other θ_j's. Note that, from above we may have multiple solutions in which case we have to resort to solving for θ_k and θ_{k+1} using V_k and $\bar{I}_k$.

4.3.4 Quantum State Interferography for Mixed Qudit

After discussing the scheme for the successful reconstruction of an arbitrary pure qudit state from $(d-1)$ interference patterns generated in a single setup with $(d-1)$ interferometers using quantum state interferography (QSI), the natural question that follows is: *Whether this Interferometric Protocol can be applied to infer any Mixed State of a Qudit?*

❑ **Inferring Mixed Qudits using QSI:** A mixed state in d-dimensional Hilbert space, say $\hat{\rho}^{[d]}$, can be completely described with (d^2-1) number of independent real quantities.

Thus, to reconstruct a mixed state in d-dimensions using the interferometric technique, we need to infer (d^2-1) quantities from a number of interference patterns produced when the state $\hat{\rho}^{[d]}$ evolves through an interferometric setup with the necessary operators. The protocol described above for the pure state reconstruction, involves $(d-1)$ interferometers and three distinct real quantities i.e., phase shift, phase averaged intensity and visibility to be obtained from each of the interference patterns generated at the end of the interferometer. Thus, using this particular setup we can have a total of $3(d-1)$ experimental quantities. For $d \geq 3$, we have $d^2-1 > 3(d-1)$, and hence this protocol, in the current form, cannot be extended to infer mixed state of qudits.

Thus, **in summary**, an unknown pure state in d-dimensions can be determined using an interferometric technique by analyzing $(d-1)$ interference patterns produced in a single setup. A qudit state $|\psi\rangle^{(d)}$, when evolved through an experimental setup with $(d-1)$ two path interferometers, each designed to act on a particular two dimensional subspace of the d-dimensional Hilbert space arranged in a particular sequence, having a projector to the first mode of the subspace in one path and a spin flip operator for that subspace in the other path, we obtain $(d-1)$ interference patterns at the end. All the state parameters $\{\theta_j, \phi_j\}$ with $j = 1, 2, \ldots, (d-1)$ that specify the d-dimensional pure state as a chain of $(d-1)$ Bloch vectors in Episphere representation, can be inferred experimentally from the phase shifts, average intensities and visibilities of the $(d-1)$ interference patterns. Once the $(2d-2)$ state parameters are known from the experiment, the state $|\psi\rangle^{(d)}$ can be constructed using the Eqn. 4.87. Therefore, quantum state interferography provides a *single shot* state determination protocol for qudits, where an unknown pure qudit can be characterized from a number of interference patterns obtained in a single setup without the need to alter any internal settings within the setup during the experiment. Further, for an unknown pure state characterization quantum state interferography (QSI) demands the number of data acquisitions to be $(d-1)$ as compared to $(5d-7)$ in quantum state tomography (QST) [18] with the pure state assumption, that provides a scaling advantage as the dimensionality of the Hilbert space increases.

4.4 Quantum State Interferography for Qudit: The Scheme Employing Two Interferometers

In the last section, we have presented how the Quantum State Interferography (QSI) technique can be employed to infer a pure quantum state $|\psi\rangle^{(d)}$ in d-dimensions from the $(d-1)$ interference patterns. The scheme is described with the use of $(d-1)$ Mach Zehnder interferometers designed for each one of the two-dimensional sub-spaces, spanned by two consecutive basis states of the d-dimensional Hilbert space. The use of Mach Zehnder interferometer (MZI) in experiments is not trivial because of the need to stabilize the path length difference of the interferometer against the noises. MZI is very sensitive to the external vibrations (such as acoustic or mechanical) which changes the path lengths inside the interferometer over time, affecting the relative phase between the two interferometric arms. Thus, to obtain any consistent phase information from the interference pattern formed at the end of the interferometer, it needs to be phase stabilized. Also, aligning the interferometer in a non-collinear configuration gives the intensity as function of phase difference directly, without requiring to change any settings in the experimental set-up.

As discussed in the Sec. 4.3, it seems that we need to construct $(d-1)$ Mach Zehnder interferometers for inferring the d-dimensional pure qudit state $|\psi\rangle^{(d)}$. Hence, it would appear experimentally challenging to set up that many interferometers with the components corresponding to the respective operators in each interferometric path, mostly from two perspectives − one for the increase in the requirement of resources (the optical and opto-mechanical components) as the dimensionality increases and the other, for the increase in the complexity in maintaining a constant phase for each of the MZI through phase stabilization. Depending on the system, it could be experimentally easier to switch to other types of interferometers, like Sagnac interferometer or double slit interferometer, which do not require stabilization and hence are relatively easy to set up in practice.

However, it is not always necessary to have $(d-1)$ interferometers to get $(d-1)$ interference patterns. To reconstruct a pure qudit state using QSI one needs more and more *interference patterns* as the dimension goes higher and higher. But the scaling is linear i.e., $(d-1)$ interferograms are required to infer the state of d-dimensional pure qudit. All these interference patterns can be obtained at once using only *two interferometers*, if we observe the interference patterns on a camera i.e., using a $2D$ imaging sensor. The key idea is to stack the interference patterns vertically (assuming each interferogram is formed along the horizontal) so that the same interferometer can be used for obtaining the required interferometric information from each subspace.

4.4.1 Experimental Protocol for Single-Shot Characterization of Pure Qudit: $2D$ Imaging with Two Interferometers

The scheme presented in Sec. 4.3 is a conceptual extension of QSI for qubits discussed in Chapter. 2, to higher dimensions where the beam (in the state $|\psi\rangle^{(d)}$) incident on the setup is divided into $(d-1)$ spatial modes and each mode is sent through one MZI designed to act on a particular two dimensional subspace. Since, in the process of selecting a particular two-dimensional subspace from each spatial mode, we discard all particles that do not belong to the basis states within the desired subspace, the proposed scheme is a lossy one. From a stream of identical particles incident on the setup, only $\mathcal{O}\left(\dfrac{2}{d}\right)$ particles are used to perform QSI for d-dimensional qudits because after the $\hat{\sigma}_z^{[d]}$ operation in each spatial mode, we block all the beams except the two corresponding to the two dimensional sub-spaces inside an interferometer. However, if we make the modification in the experimental setup as shown in Fig. **4.3**, not only the requirement of the interferometer goes down to *two* for all $d > 2$ but also the interferometric technique (QSI) for inferring $|\psi\rangle^{(d)}$ becomes more efficient. The key idea is to obtain all the interferograms, required to infer the state parameters θ_j's and ϕ_j's, from the same interferometer designed to act on all the sub-spaces at once and record all of them using the $2D$-imaging technique.

First, the d-dimensional qudit, say $|\psi\rangle^{(d)}$, incident on the QSI setup is decomposed into the eigen states of $\hat{\sigma}_z^{[d]}$ operator. This could be implemented for spin degree of freedom by applying an inhomogeneous magnetic field along $\hat{z}$ so that the components of the state split along the z direction, i.e., vertically [19, 20]. In this way the beam in the unknown state $|\psi\rangle^{(d)}$ is divided into d number of spatial modes, each in one of the eigenstates $|n\rangle$, where $n = 1, 2, \ldots, d$. Next, the Bragg mirrors (labeled as M_V in the diagram) make all the beams in different states propagate along the y-direction i.e., make the beams parallel to each other arranged along z direction. The beams now pass through the Bragg beam splitter $\mathrm{BS}_{\mathrm{V}_1}$ which then splits each of the beam vertically into two beams with equal intensities. So, after the beam splitter $\mathrm{BS}_{\mathrm{V}_1}$ we have $2d$ number of beams along z; vertically from top the first two beams are in the state $|1\rangle$ (labeled as $|1\rangle_1, |1\rangle_2$), the 3rd and 4th beams are in the state $|2\rangle$ (labeled as $|2\rangle_3, |2\rangle_4$) and so on. Thus in general $(2n-1)$-th and $2n$-th beam after $\mathrm{BS}_{\mathrm{V}_1}$ are in the state $|n\rangle$, labeled as $|n\rangle_{2n-1}$ and $|n\rangle_{2n}$ respectively.

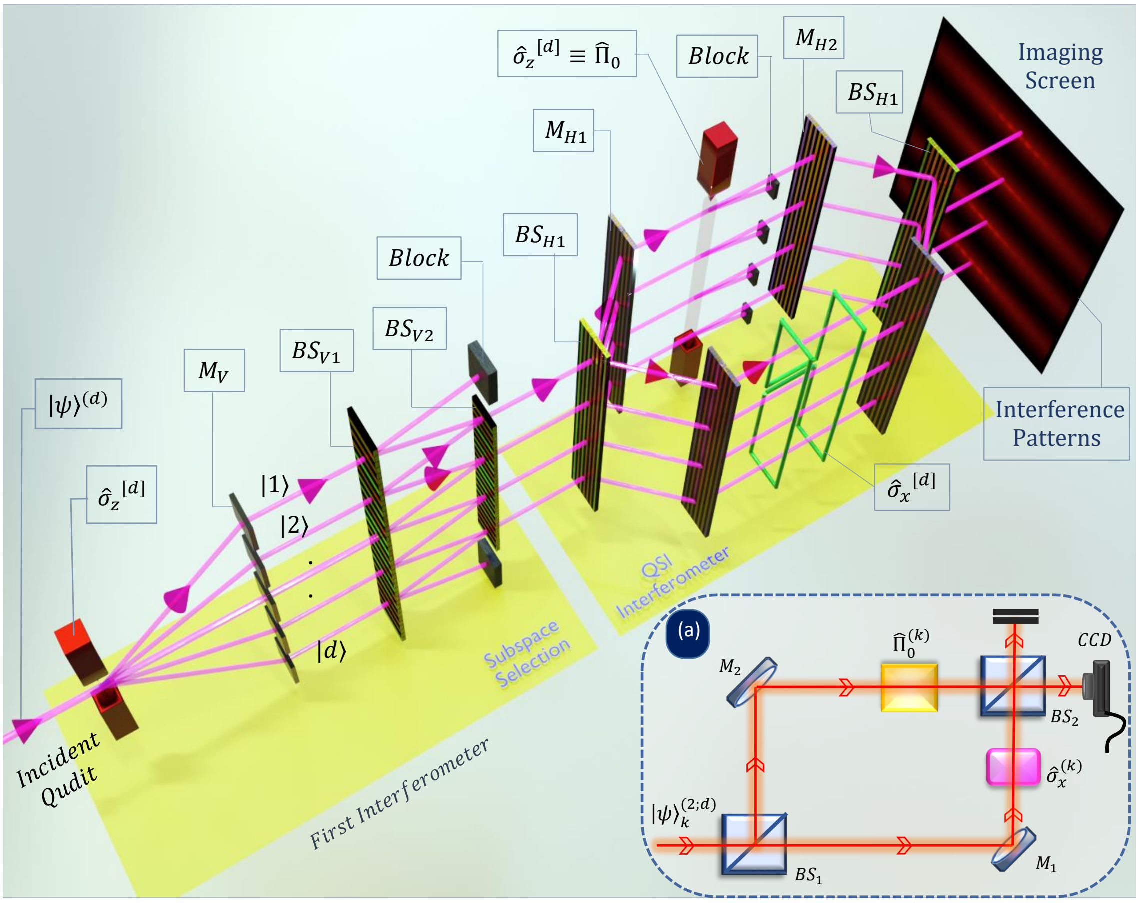

Figure 4.3: Schematic of the interferometric setup for characterizing a state in the d-dimensional Hilbert space using Quantum State Interferography technique. The pure qudit $|\psi\rangle^{(d)}$ evolving through the setup can be inferred from $(d-1)$ interferograms obtained with the use of only two interferometers. The first interferometer is used to select the two dimensional sub-spaces on which the required operations can be performed using the second interferometer to get the interference patterns associated with each of the sub-spaces.

The beams from the adjacent eigenstates $|k\rangle$ and $|k+1\rangle$ $\forall$ $k = 1, 2 \ldots, (d-1)$ are combined using the Bragg beam combiner $\mathrm{BS}_{\mathrm{V}_2}$. Thus, after $\mathrm{BS}_{\mathrm{V}_2}$ we have $(d-1)$ beams, each associated with one of the two dimensional sub-spaces of the d-dimensional Hilbert space. Here, the combination needs to be coherent and hence the spin splitter $\hat{\sigma}_z^{[d]}$ and the beam combiner $\mathrm{BS}_{\mathrm{V}_2}$ forms the first interferometer using which $(d-1)$ sub-spaces can be selected simultaneously by stacking the beams vertically. Half of the intensity of the beams in the eigen modes $|1\rangle$ and $|d\rangle$ are blocked so that each two dimensional subspace has *apriori* unbiased contribution from the two eigenstates. So, after $\mathrm{BS}_{\mathrm{V}_2}$ the k-th beam from top is in the state $|\psi\rangle_k^{(2;d)}$ which is a component of $|\psi\rangle^{(d)}$ in the k-th two dimensional subspace spanned by the basis states $\{|k\rangle, |k+1\rangle\}$.

❖ The evolution of the state $|\psi\rangle^{(d)}$ through the First Interferometer:

Evolution of the d-dimensional qudit incident on the QSI setup shown in Fig. 4.3 from $\hat{\sigma}_z^{[d]}$ operator to BS_{V_2} is shown from left to right in the following,

$$
|\psi\rangle^{(d)} \xrightarrow{\hat{\sigma}_z^{[d]}}
\begin{array}{l}
\left.\begin{array}{l}
|1\rangle \xrightarrow{BS_{\mathrm{V}_1}} \dfrac{(|1\rangle_1 + |1\rangle_2)}{\sqrt{2}} \\[3ex]
|2\rangle \xrightarrow{BS_{\mathrm{V}_1}} \dfrac{(|2\rangle_3 + |2\rangle_4)}{\sqrt{2}}
\end{array}\right\} \xrightarrow{BS_{\mathrm{V}_2}} \dfrac{(|1\rangle_2 + |2\rangle_3)}{\sqrt{2}} = |\psi\rangle_1^{(2;d)} \\
\vdots \\
\left.\begin{array}{l}
|k\rangle \xrightarrow{BS_{\mathrm{V}_1}} \dfrac{(|k\rangle_{2k-1} + |k\rangle_{2k})}{\sqrt{2}} \\[3ex]
|k+1\rangle \xrightarrow{BS_{\mathrm{V}_1}} \dfrac{(|k+1\rangle_{2k+1} + |k+1\rangle_{2k+2})}{\sqrt{2}}
\end{array}\right\} \xrightarrow{BS_{\mathrm{V}_2}} \begin{array}{l} \dfrac{(|k\rangle_{2k} + |k+1\rangle_{2k+1})}{\sqrt{2}} \\ = |\psi\rangle_k^{(2;d)} \end{array} \\
\vdots \\
\left.\begin{array}{l}
\vdots \\
|d\rangle \xrightarrow{BS_{\mathrm{V}_1}} \dfrac{(|d\rangle_{2d-1} + |d\rangle_{2d})}{\sqrt{2}}
\end{array}\right\} \xrightarrow{BS_{\mathrm{V}_2}} \dfrac{(|d-1\rangle_{2d-2} + |d\rangle_{2d-1})}{\sqrt{2}} = |\psi\rangle_{d-1}^{(2;d)}
\end{array}
\tag{4.135}
$$

Once the sub-spaces are selected across the individual beams along z after BS_{V_2}, we need to obtain the interferograms for each of the subspaces. For this, as shown in the inset (a) of Fig. 4.3, the state $|\psi\rangle_k^{(2;d)}$ associated with the k-th two dimensional subspace of the qudit needs to be made incident and evolved through a two path interferometer, such as a Mach Zehnder Interferometer (MZI). On one arm of the interferometer, we need to have the projector $\hat{\Pi}_0^{(k)}$ for the k-th subspace (which projects a state to the mode $|k\rangle$ in that subspace) and on the other arm we need to implement the evolution operator $\hat{\sigma}_x^{(k)}$ (which is the spin-flip operator that swaps the state $|k\rangle$ with $|k+1\rangle$ and vice-versa) for the k-th subspace. In the QSI setup for qudit, the Bragg beam splitter $\mathrm{BS}_{\mathrm{H}_1}$ which splits an incident beam horizontally into two beams of equal intensities, along with the beam combiner $\mathrm{BS}_{\mathrm{H}_2}$ forms the Mach Zehnder interferometer to be acting on all the sub-spaces at once. The interferometer can be made non-collinear such that the interference pattern is obtained along the horizontal (i.e., along x) as a function of the relative phase ϵ between the two paths of the interferometer, as shown in Fig. 4.3.

The $(d-1)$ interferograms can be obtained using the same interferometer as the beams corresponding to the $(d-1)$ subspaces are stacked vertically. The use of same pair of beam splitter and beam combiner (i.e., BS_{H_1} and BS_{H_2}) for all the $(d-1)$ sub-spaces implies that instead of stabilizing the otherwise $(d-1)$ MZIs now we need to stabilize only one. Also, the operators $\hat{\Pi}_0^{(k)}$ for the k-th two dimensional subspace can be realized by simply using the $\hat{\sigma}_z^{[d]}$ measurement operator for the qudit in one arm of the interferometer. This operator will split the beam in each subspace into two eigenstates. For the k-th subspace, $\hat{\sigma}_z^{[d]}$ decomposes the state $|\psi\rangle_k^{(2;d)}$ into $|k\rangle$ and $|k+1\rangle$. Now to effectively realize the operator $\hat{\Pi}_0^{(k)}$ for k-th subspace, the beam in the state $|k+1\rangle$ can be blocked and the beam in the state $|k\rangle$ can be allowed through the interferometer. The evolution operator $\hat{\sigma}_x^{(k)}$ for the k-th subspace is the same as the $\hat{\sigma}_x^{[d]}$ evolution operator for the d-dimensional qudit. Thus, the operations $\hat{R} = \hat{\Pi}_0^{(k)}$ and $\hat{U} = \hat{\sigma}_x^{(k)}$, that needs to be performed on a state to obtain the interferograms in all the two-dimensional sub-spaces can have the same physical implementation. Therefore, in the second interferometer each beam in the respective state $|\psi\rangle_k^{(2;d)}$ evolves through the effective operator $\hat{\mathcal{O}}^{(k)}$ as described below.

$$\hat{\mathcal{O}}^{(k)} = \frac{1}{2}\left(\exp(i\epsilon)\hat{\Pi}_0^{(k)} + \hat{\sigma}_x^{(k)}\right) = \frac{1}{2}\begin{pmatrix}\exp(i\epsilon) & 1 \\ 1 & 0\end{pmatrix} \tag{4.136}$$

where, ϵ is the relative phase between the two paths of the MZI formed with BS_{H_1} and BS_{H_2} and the mirrors M_{H_1} and M_{H_2} that redirects the beams.

❖ Evolution through the Second Interferometer:

As the state $|\psi\rangle_k^{(2;d)}$ evolves through the second interferometer, we have the following:

$$|\psi\rangle_k^{(2;d)} \xrightarrow{MZI} \hat{\mathcal{O}}^{(k)} |\psi\rangle_k^{(2;d)}$$

This evolution gives the intensity distribution $I_k(\epsilon)$ for each of the two dimensional subspaces on a $2D$ imaging screen as computed below,

$$\begin{aligned} I_k(\epsilon) &= \left\| \hat{\mathcal{O}}^{(k)} |\psi\rangle_k^{(2;d)} \right\|^2 = \left\langle \psi_k^{(2;d)} \middle| \hat{\mathcal{O}}^{(k)\dagger} \hat{\mathcal{O}}^{(k)} \middle| \psi_k^{(2;d)} \right\rangle \\ &= \frac{1}{4} \left[\left\langle \hat{\mathbb{1}}^{(k)} \right\rangle + \left\langle \hat{\Pi}_0^{(k)} \right\rangle + 2\,\mathrm{Re}\left(\exp(i\epsilon) \left\langle \hat{\sigma}_x^{(k)}\ \hat{\Pi}_0^{(k)} \right\rangle \right) \right] \end{aligned} \tag{4.137}$$

In terms of the state parameters $\{\theta_j, \phi_j\}$, for $j = 1, 2, \ldots, (d-1)$, we can express

$$I_k(\epsilon) = \frac{\xi(k)}{16} \left[5 + \cos(\theta_{k+1}) + \cos(\theta_k)(3 - \cos(\theta_{k+1})) + 4 \sin(\theta_k) \cos\left(\frac{\theta_{k+1}}{2}\right) \cos(\epsilon - \phi_k) \right] \tag{4.138}$$

where, the factor $\xi(k)$ is expressed as, $\xi(k) = \prod_{j=1}^{k-1} \sin^2\left(\frac{\theta_j}{2}\right)$. Processing the k-th interference pattern $I_k(\epsilon)$ formed on the screen, we obtain the quantities such as the phase shift (Φ_k), phase-averaged intensity $(\bar{I}_k)$ and visibility (V_k) as presented in Eqn. 4.119, Eqn. 4.120 and Eqn. 4.128 respectively. All these interferometric information, obtained experimentally from the $(d-1)$ interferograms recorded simultaneously at the end of the setup using $2D$ imaging technique, are further utilized to infer the state parameters to characterize $|\psi\rangle^{(d)}$ as discussed in detail in SubSec. 4.3.3.

4.4.2 Operator Descriptions for d-dimensions:

Here, we will present how the operators $\hat{\Pi}_0^{[d]}$ and $\hat{\sigma}_x^{[d]}$ described to act on the d-dimensional Hilbert space, can effectively function as the operators $\hat{\Pi}_0^{(k)}$ and $\hat{\sigma}_x^{(k)}$ for the k-th two dimensional subspace. For a d-dimensional system, the matrix elements of $\hat{\sigma}_x^{[d]}$ and $\hat{\sigma}_z^{[d]}$ operators are given as [21],

$$\hat{\sigma}_x\Big|_{i,j}^{[d]} = (\delta_{i+1,j} + \delta_{i,j+1})\sqrt{(s+1)(i+j-1) - ij} \tag{4.139}$$

$$\hat{\sigma}_z\Big|_{i,j}^{[d]} = 2\delta_{i,j}(s+1-i) \tag{4.140}$$

where, we have $i, j = 1, 2, \ldots d$ for d-dimensions. The dimensionality of the Hilbert space is given by $d = 2s+1$, with s representing the spin quantum number [9] associated with the spin angular momentum S of the quantum system [22] (where, $\mathrm{S} = \hbar\sqrt{s(s+1)}$ with $\hbar$ being the reduced Plank Constant, i.e., $\hbar = \dfrac{h}{2\pi}$). For example, the dimension $d = 5$ corresponds to $s = 2$.

For the k-th two dimensional subspace, we have $i = k, k+1$ and $j = k, k+1$. Thus, using Eqn. 4.139 we can compute the corresponding matrix elements $\hat{\sigma}_x\big|_{i,j}^{[d]}$ of the $\hat{\sigma}_x^{[d]}$ operator for that subspace. The elements are as expressed in the following:

$$\hat{\sigma}_x\Big|_{k,k}^{[d]} = (\delta_{k+1,k} + \delta_{k,k+1})\sqrt{(s+1)(2k-1) - k^2} = 0 \tag{4.141}$$

$$\hat{\sigma}_x\Big|_{k,k+1}^{[d]} = (\delta_{k+1,k+1} + \delta_{k,k+2})\sqrt{(s+1)(2k) - k(k+1)} = \sqrt{k(d-k)} \tag{4.142}$$

$$\hat{\sigma}_x\Big|_{k+1,k}^{[d]} = (\delta_{k+2,k} + \delta_{k+1,k+1})\sqrt{(s+1)(2k) - (k+1)k} = \sqrt{k(d-k)} \tag{4.143}$$

$$\hat{\sigma}_x\Big|_{k+1,k+1}^{[d]} = (\delta_{k+2,k+1} + \delta_{k+1,k+2})\sqrt{(s+1)(2k+1) - (k+1)^2} = 0 \tag{4.144}$$

Therefore, using the elements computed above, the 2×2 spin-flip operator $\hat{\sigma}_x^{(k)}$ for the k-th two dimensional subspace of the d-dimensional space can be written as,

[9] The spin quantum number s can take integer or half-integer values, i.e., $s = \dfrac{n}{2}$, where n is any non-negative integer.

$$\hat{\sigma}_x^{(k)} = \begin{pmatrix} \hat{\sigma}_x\big|_{k,k}^{[d]} & \hat{\sigma}_x\big|_{k,k+1}^{[d]} \\ \hat{\sigma}_x\big|_{k+1,k}^{[d]} & \hat{\sigma}_x\big|_{k+1,k+1}^{[d]} \end{pmatrix} = \sqrt{k(d-k)} \begin{pmatrix} 0 & 1 \\ 1 & 0 \end{pmatrix} \tag{4.145}$$

The factor $\sqrt{k(d-k)}$ only modifies the amplitude of the states after the evolution through the $\hat{\sigma}_x^{(k)}$ operation which swaps $|k\rangle$ with $|k+1\rangle$ and vice-versa. Hence, when the input is restricted to the subspace $\{|k\rangle, |k+1\rangle\}$, the $\hat{\sigma}_x^{[d]}$ operator for the d-dimensional Hilbert space also acts as the $\hat{\sigma}_x^{(k)}$ operator for the two dimensional k-th subspace. Thus, the $\hat{\sigma}_x^{(k)}$ operators for all the two dimensional sub-spaces can be realized by the action of $\hat{\sigma}_x^{[d]}$ operator within the $2nd$ interferometer.

As we can see from the example below, for the operator $\hat{\sigma}_x^{[5]}$ described within $d = 5$ dimensional Hilbert space, the highlighted two-dimensional matrices $\hat{\sigma}_x^{(k)}$ are a scalar times the $\hat{\sigma}_x$ operation in the respective two dimensional sub-spaces. This holds true for all the sequential pairwise two-dimensional sub-spaces for arbitrary d-dimensions.

$$\hat{\sigma}_x^{[5]} = \begin{pmatrix} 0 & 2 & 0 & 0 & 0 \\ 2 & 0 & \sqrt{6} & 0 & 0 \\ 0 & \sqrt{6} & 0 & \sqrt{6} & 0 \\ 0 & 0 & \sqrt{6} & 0 & 2 \\ 0 & 0 & 0 & 2 & 0 \end{pmatrix}$$

Next, we will determine the $\hat{\sigma}_z^{[d]}$ operator and the respective $\hat{\sigma}_z^{(k)}$ operators corresponding to the two-dimensional sub-spaces. From the expression of matrix elements $\hat{\sigma}_z\big|_{i,j}^{[d]}$ shown in Eqn. 4.140, we can imply that only the diagonal elements of $\hat{\sigma}_z^{[d]}$ operator would survive. For the k-th subspace, for which $i = k, k+1$ and $j = k, k+1$ we can compute the matrix elements as,

$$\hat{\sigma}_z\Big|_{k,k}^{[d]} = 2\delta_{k,k}(s+1-k) = 2(s+1-k) \tag{4.146}$$

$$\hat{\sigma}_z\Big|_{k,k+1}^{[d]} = 2\delta_{k,k+1}(s+1-k) = 0 \tag{4.147}$$

$$\hat{\sigma}_z\Big|_{k+1,k}^{[d]} = 2\delta_{k+1,k}(s+1-k-1) = 0 \tag{4.148}$$

$$\hat{\sigma}_z\Big|_{k+1,k+1}^{[d]} = 2\delta_{k+1,k+1}(s+1-k-1) = 2(s-k) \tag{4.149}$$

Using the elements of $\hat{\sigma}_z^{[d]}$ operator computed above, we can write the $\hat{\sigma}_z^{(k)}$ operator for the k-th two dimensional subspace as follows,

$$\hat{\sigma}_z^{(k)} = \begin{pmatrix} \hat{\sigma}_z\big|_{k,k}^{[d]} & \hat{\sigma}_z\big|_{k,k+1}^{[d]} \\ \hat{\sigma}_z\big|_{k+1,k}^{[d]} & \hat{\sigma}_z\big|_{k+1,k+1}^{[d]} \end{pmatrix} = 2\begin{pmatrix} s+1-k & 0 \\ 0 & s-k \end{pmatrix} \tag{4.150}$$

As an example, the operator $\hat{\sigma}_z^{[d]}$ described for the $d=5$ dimensional Hilbert space can be obtained as a diagonal matrix with the diagonal elements representing the values of spin-magnetic quantum number $m_s = \{2, 1, 0, -1, -2\}$ for a spin $s = 2$ system [10].

$$\hat{\sigma}_z^{[5]} = 2\begin{pmatrix} 2 & 0 & 0 & 0 & 0 \\ 0 & 1 & 0 & 0 & 0 \\ 0 & 0 & 0 & 0 & 0 \\ 0 & 0 & 0 & -1 & 0 \\ 0 & 0 & 0 & 0 & -2 \end{pmatrix}$$

In the matrix representation of the operator $\hat{\sigma}_z^{[d]}$ shown above, the operators $\hat{\sigma}_z^{(k)}$ for the two dimensional sub-spaces of the 5-dimensional space are highlighted with different colours, which are all diagonal matrices associated with the states $|k\rangle$ and $|k+1\rangle$ that span the corresponding subspace. Therefore, the $\hat{\sigma}_z^{[d]}$ operator for any arbitrary value of d, can serve as the $\hat{\sigma}_z^{(k)}$ operator for any subspace k with the input state $|\psi\rangle_k^{(2;d)}$.

[10]Spin-magnetic quantum number m_s represents the projection of the spin angular momentum S along z-direction as $\mathrm{S}_z = m_s\hbar$. Hence, m_s is also referred to as the spin-projection quantum number along z.

4.4.3 Quantum State Interferography for Pure Qudit: An Alternate Approach with Two Interferometers

So far in this Section, we have seen how a d-dimensional pure state $|\psi\rangle^{(d)}$ can be characterized using the Quantum State Interferography (QSI) technique from $(d-1)$ interferograms, produced with only two interferometers – one used to prepare the states corresponding to the two-dimensional sub-spaces and the other used to perform single qubit QSI on those sub-spaces. The protocol described in SubSec. 4.4.1 provides a single shot state estimation scheme for the qudits, in which all the $(d-1)$ interference patterns required to reconstruct the state can be obtained employing a $2D$-imaging technique without the need to make any changes in the experimental settings once the setup is aligned. However, if capturing a $2D$ image is not possible for some specific system, we can alternatively change the experimental settings for $(d-1)$ times in the two interferometer setup to obtain $(d-1)$ interferograms as shown in Fig. 4.4 and discussed in detail in the context of a $d = 5$ dimensional pure state reconstruction.

Let us consider an unknown state in 5-dimensions $|\psi\rangle^{(d=5)}$ needs to be characterized experimentally using the interferometric technique for a system where any one of the following is satisfied, i.e, where,

(i) it is impossible to physically realize the operators $\hat{\Pi}_0^{[5]}$ and $\hat{\sigma}_x^{[5]}$ that can act on all the two-dimensional sub-spaces of the 5-dimensional space at the same time,

(ii) there is no scope to prepare the beams in the states $|\psi\rangle_k^{(2;5)}$ associated with different two dimensional sub-spaces all together,

(iii) it is impossible to capture a $2D$ image in that system.

For such a system, the stream of particles in the state $|\psi\rangle^{(5)}$ incident on the setup, is first resolved into the $d = 5$ eigenstates of the $\hat{\sigma}_z^{[5]}$ operator that acts on the 5-dimensional Hilbert space, as expressed in Eqn. 4.4.2. Any two adjacent beams in the states $|k\rangle$ and $|k+1\rangle$ where $k = 1, 2, 3, 4$, (say, in states $|2\rangle$ and $|3\rangle$, as shown in schematic of Fig. 4.4), can be allowed to pass through in order to select one of the two-dimensional sub-spaces (here, the $2nd$ subspace spanned by $\{|2\rangle, |3\rangle\}$) and the rest (here, $|1\rangle, |4\rangle$ and $|5\rangle$) can be blocked using beam blockers. Those two beams are combined into a single beam using a beam combiner to effectively prepare the state for a particular two dimensional subspace (here, $|\psi\rangle_2^{(2;5)}$ for $2nd$ subspace). This needs to be a coherent combination and effectively the beam combiner along with $\hat{\sigma}_z^{[5]}$ would form one interferometer. The setting inside the interferometer needs to be changed for $(d-1)$ times (4 times for this example) to select $(d-1)$ sub-spaces for performing QSI in d-dimension. For each setting the beam blockers need to be moved between the beams such that only one pair of adjacent beams in states $|k\rangle$ and $|k+1\rangle$ passes through and recombines into a single beam in the state $|\psi\rangle_k^{(2;d)}$.

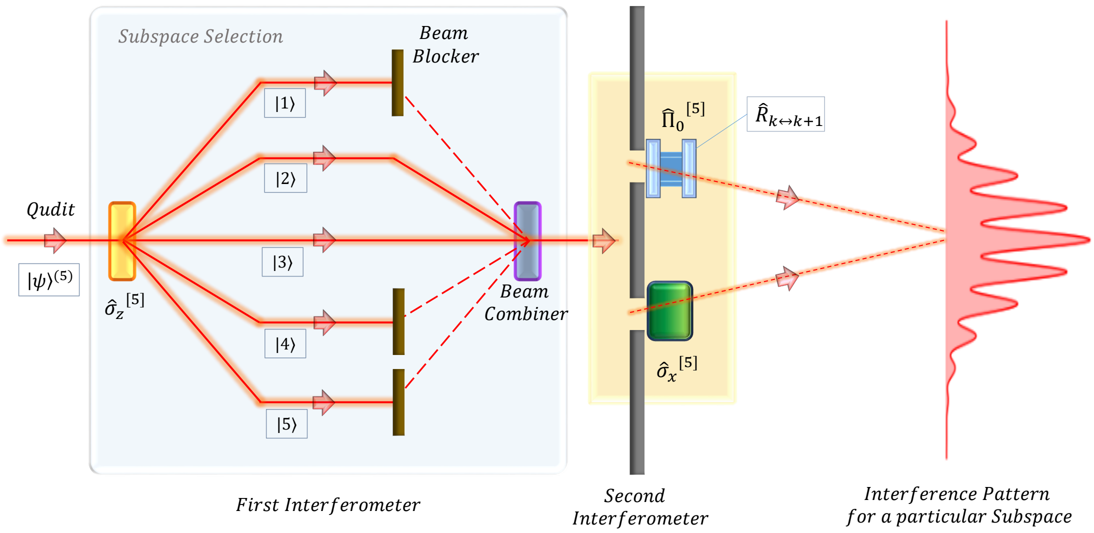

Figure 4.4: Schematic of the Quantum State Interferography setup for a generic d-dimensional qudit (here, $d = 5$) state reconstruction with two interferometers. All the state parameters of a pure state in d-dimensions are inferred by processing $(d-1)$ interferograms obtained by changing the settings of the two interferometers $(d-1)$ times. The first interferometer selects one particular subspace and the second interferometer performs the single qubit QSI on that subspace at a particular time.

Next, to perform QSI on the selected subspace k, we need one more interferometer with the polar decomposed components of non-Hermitian $\hat{\sigma}_-^{(k)}$ operator in the two respective paths. Here, in the setup shown in Fig. 4.4 a double slit interferometer is used, with $\hat{\sigma}_x^{(k)}$ operator on one of the slits and $\hat{\Pi}_0^{(k)}$ operator on the other slit. The spin-flip operator $\hat{\sigma}_x^{(k)}$ can simply be the $\hat{\sigma}_x^{[5]}$ operator on the $d = 5$ dimensional Hilbert space, as shown in SubSec. 4.4.2. The projector $\hat{\Pi}_0^{(k)}$ for the k-th two dimensional subspace can be constructed from $\hat{\Pi}_0^{[5]}$ operator with the rotation of basis using the operators $\hat{R}_{k\leftrightarrow k+1}$. The operator $\hat{\Pi}_0^{[5]}$

is effectively realized with a $\hat{\sigma}_z^{[5]}$ operator with all the beams except the beam in the first eigenstate being blocked. By changing the orientation of the components corresponding to these rotation operations $\hat{R}_{k\leftrightarrow k+1}$, different $\hat{\Pi}_0^{(k)}$ operators for the choice of subspace with $\{|k\rangle, |k+1\rangle\}$ can be realized.

Hence, overall for the reconstruction of arbitrarily high d-dimensional qudits, only two interferometers are needed to be set up − one for choosing one particular subspace i.e., decomposing the incident unknown state into its basis states and combining the beams in a selected subspace (this can be a Sagnac interferometer) and the other being the double slit interferometer that performs single qubit QSI on the selected two dimensional subspace. The cost, however is that, we need to move the blocks $(d-1)$ times to allow a certain pair of states, say $|k\rangle$ and $|k+1\rangle$, to pass through and for each such combination the projector needs to be rotated so that it is set to $\hat{\Pi}_0^{(k)}$. Therefore, unlike the scheme presented in SubSec. 4.4.1, this QSI scheme without the use of $2D$ imaging does not provide a single-shot state estimation technique for the qudits. However, both the QSI schemes with the use of two interferometers, described in this section appear to be more efficient than the scheme described in Sec. 4.3 (details in Appendix. 4.B).

In summary, the pure state reconstruction in a d-dimensional Hilbert space using Quantum State Interferography technique requires post-processing of $(d-1)$ interferograms which can be obtained from as low as two interferometers. The state $|\psi\rangle^{(d)}$ can be inferred in a single shot where there is no need to change the internal settings of the setup and all the interferograms are recorded at once using a $2D$ imaging screen i.e., using a camera. The operators for the subspace can be realized with the operators available for d-dimensional Hilbert space. Alternatively the state can be inferred from two interferometers by changing the setup for $(d-1)$ times and recording a single interference pattern at a time − each time selecting a different subspace using the first interferometer and performing QSI on that subspace using the second interefrometer. Although, the above schemes are discussed in the context of spin degree of freedom, characterization of the pure qudit can be achieved for most systems with the realization of the suitable operators.

4.5 Quantum State Interferography for Bipartite Qubits

So far, Quantum State Interferography technique has been discussed as an interferometric tool to determine arbitrary (pure or mixed) states of qubits ($d = 2$) and pure states of qudits ($d > 2$). It has appeared as a single-shot state determination scheme for qubits as well as for qudits, which does not require any change in the experimental setting in between the incidence of the unknown state and extraction of the state information. In this section, the scope of the Quantum State Interferography (QSI) technique will be extended for the determination of the unknown state of bipartite systems. The interferometric scheme for characterizing the bipartite states in polarization degree of freedom of light will be presented. The method shall be applicable to all bipartite systems once one identifies the realization of relevant operators required in this protocol.

First, the general state of a two qubit system would be parameterized in terms of the Bloch sphere co-ordinates and then an experimental protocol with the post-processing analysis techniques to determine those parameters associated with the unknown bipartite qubit state will be presented, in this section. Here, the protocol for the reconstruction of the polarization state associated with a pair of photons, say signal photon A and idler photon B, generated by Spontaneous Parametric Down Conversion (SPDC) process [23, 24] will be worked out. We will explore that an unknown bipartite state reconstruction using Quantum State Interferography (QSI) requires post-processing of 3 interference patterns $--$ two interference patterns obtained by performing single qubit QSI on the two individual particles A and B respectively and one heralded interference pattern obtained from the single qubit QSI of the B particles conditioned to A particles being projected to state $|H\rangle$. Just for comparison, the conventional and widely used technique $-$ Quantum State Tomography (QST) for bipartite qubit state assuming that the state is pure would require 9 measurement settings [25, 26] whereas Quantum State Interferography requires only 2 experimental settings to generate those 3 interference patterns to infer a pure qubit state associated with the bipartite system.

Performing the single qubit QSI on either particles A or B to obtain the unheralded i.e., singles interference pattern can give us the reduced density matrix (ρ_A or ρ_B) associated with the respective subsystems. This makes QSI an efficient technique for quantification of entanglement of pure bipartite states using a single setup, the details of which will be discussed in the section 4.6.

4.5.1 Parameterization of Pure Bipartite Qubit

The state of a two qubit system, represented in the polarization degree of freedom, is considered to belong to the joint Hilbert space of the individual subsystems. The subsystems A and B are described within the two dimensional Hilbert spaces $\mathcal{H}_A$ and $\mathcal{H}_B$ respectively, where $\mathcal{H}_A$ is spanned by the basis vectors $\{|H\rangle_A, |V\rangle_A\}$ and $\mathcal{H}_B$ is spanned by the basis vectors $\{|H\rangle_B, |V\rangle_B\}$. Thus, the bipartite qubit states are described as the vectors in the $2 \times 2 = 4$ dimensional composite vector space $\mathcal{H}_{AB} = \mathcal{H}_A \otimes \mathcal{H}_B$ associated with the bipartite system and is spanned by the four basis states $\{|HH\rangle_{AB}, |HV\rangle_{AB}, |VH\rangle_{AB}, |VV\rangle_{AB}\}$, where $|HH\rangle_{AB} = |H\rangle_A \otimes |H\rangle_B = |H\rangle_A |H\rangle_B$ and so on.

In general, the pure state of a bipartite system can be written as the superposition of the four basis states of $\mathcal{H}_{AB}$ as the following,

$$|\Psi\rangle_{AB} = \alpha_1 |HH\rangle_{AB} + \alpha_2 |HV\rangle_{AB} + \alpha_3 |VH\rangle_{AB} + \alpha_4 |VV\rangle_{AB} \tag{4.151}$$

$$= \alpha_1 |H\rangle_A |H\rangle_B + \alpha_2 |H\rangle_A |V\rangle_B + \alpha_3 |V\rangle_A |H\rangle_B + \alpha_4 |V\rangle_A |V\rangle_B \tag{4.152}$$

Here, $\alpha_1, \alpha_2, \alpha_3, \alpha_4$ are the four complex coefficients ($\alpha_j \in \mathbb{C}^2$) or the probability amplitudes associated with the four basis states in the Hilbert space $\mathcal{H}_{AB}$ and are constrained to the normalization condition that $\sum_{j=1}^{4} |\alpha_j|^2 = 1$. Therefore,

$$|\Psi\rangle_{AB} = \begin{pmatrix} \alpha_1 \\ \alpha_2 \\ \alpha_3 \\ \alpha_4 \end{pmatrix} = \begin{pmatrix} |\alpha_1|\ e^{i\varphi_1} \\ |\alpha_2|\ e^{i\varphi_2} \\ |\alpha_3|\ e^{i\varphi_3} \\ |\alpha_4|\ e^{i\varphi_4} \end{pmatrix} = e^{i\varphi_1} \begin{pmatrix} |\alpha_1| \\ |\alpha_2|\ e^{i\varphi_{21}} \\ |\alpha_3|\ e^{i\varphi_{31}} \\ |\alpha_4|\ e^{i\varphi_{41}} \end{pmatrix} \tag{4.153}$$

where, we have expressed each complex quantity α_j in terms of its magnitude $|\alpha_j|$ and argument $\arg(\alpha_j) = \varphi_j$ as $\alpha_j = |\alpha_j|e^{i\varphi_j}$. Also we have considered $e^{i\varphi_{mn}} = e^{i(\varphi_m - \varphi_n)}$. The factor $e^{i\varphi_1}$ is associated with the global phase φ_1 and has no physically observable effects, thus can be ignored. Hence, $4 \times 2 - 2 = 6$ real quantities are required to completely describe a pure bipartite qubit state $|\Psi\rangle_{AB}$.

From the expression of $|\Psi\rangle_{AB}$ presented in Eqn. 4.152, we can can collect the polarization of the subsystem A, so that it helps to parameterize the state in terms of the angles in a single qubit Bloch sphere. So, we get

$$|\Psi\rangle_{AB} = |H\rangle_A (\alpha_1 |H\rangle_B + \alpha_2 |V\rangle_B) + |V\rangle_A (\alpha_3 |H\rangle_B + \alpha_4 |V\rangle_B) \tag{4.154}$$

Hence, when the signal (the subsystem A) state is projected to $|H\rangle_A$ or $|V\rangle_A$, the idler (the subsystem B) state respectively becomes $|\psi\rangle_B^{(H)}$ or $|\psi\rangle_B^{(V)}$. Therefore,

$$|\psi\rangle_B^{(H)} = \alpha_1 |H\rangle_B + \alpha_2 |V\rangle_B \tag{4.155}$$

$$|\psi\rangle_B^{(V)} = \alpha_3 |H\rangle_B + \alpha_4 |V\rangle_B \tag{4.156}$$

Note that, if we start with a pure bipartite state $|\Psi\rangle_{AB}$, the state of the idler also reduces to a pure state once the signal is projected to a particular pure polarization state.

The states $|\psi\rangle_B^{(H)}$ and $|\psi\rangle_B^{(V)}$ appear to have the same form as a single qubit, but we have to keep in mind that these states are not normalized to 1, i.e., $|\alpha_1|^2 + |\alpha_2|^2 \neq 1$ and $|\alpha_3|^2 + |\alpha_4|^2 \neq 1$. Let, for the state $|\psi\rangle_B^{(H)}$ the normalization factor be γ, which is the probability of the particle A to be projected to the state $|H\rangle_A$. Thus, the probability of the particle A being projected to the state $|V\rangle_A$ would be $(1 - \gamma)$, which will be the normalization factor for the idler state $|\psi\rangle_B^{(V)}$. Therefore,

$$|\alpha_1|^2 + |\alpha_2|^2 = \gamma \tag{4.157}$$

$$|\alpha_3|^2 + |\alpha_4|^2 = 1 - \gamma \tag{4.158}$$

For the subsystem B, the single qubit state $|\psi\rangle_B^{(H)} = \alpha_1 |H\rangle_B + \alpha_2 |V\rangle_B$ can be parameterized in terms of the Bloch sphere angles $\theta_H \in [0, \pi]$ and $\phi_H \in [-\pi, \pi)$ with the normalization being $\gamma \leq 1$. So, we can write the complex coefficients as the following:

$$\alpha_1 = \sqrt{\gamma}\ \cos\left(\frac{\theta_H}{2}\right) \tag{4.159}$$

$$\alpha_2 = \sqrt{\gamma}\ e^{i\phi_H}\ \sin\left(\frac{\theta_H}{2}\right) \tag{4.160}$$

The phase of the complex number α_1 is absorbed as the global phase. The subscript 'H' in the parameters θ_H and ϕ_H reminds us that the state $|\psi\rangle_B^{(H)}$ in the Bloch sphere represents the state for the idler qubit when the signal is projected to $|H\rangle_A$.

Similarly, when the signal is projected to $|V\rangle_A$, we can have the parameterization of the reduced idler state $|\psi\rangle_B^{(V)} = \alpha_3 |H\rangle_B + \alpha_4 |V\rangle_B$ in terms of the Bloch sphere angles $\theta_V \in [0, \pi]$ and $\phi_V \in [-\pi, \pi)$ with the normalization being $(1 - \gamma)$. Therefore, the complex coefficients α_3 and α_4 can be expressed as,

$$\alpha_3 = e^{i\phi_r}\ \sqrt{1-\gamma}\ \cos\left(\frac{\theta_V}{2}\right) \tag{4.161}$$

$$\alpha_4 = e^{i\phi_r}\ \sqrt{1-\gamma}\ e^{i\phi_V}\ \sin\left(\frac{\theta_V}{2}\right) \tag{4.162}$$

Here, ϕ_r is the relative phase between the Bloch vectors $\sqrt{\gamma}\left[\cos\left(\frac{\theta_H}{2}\right) + e^{i\phi_H}\ \sin\left(\frac{\theta_H}{2}\right)\right]$ and $\sqrt{1-\gamma}\left[\cos\left(\frac{\theta_V}{2}\right) + e^{i\phi_V}\ \sin\left(\frac{\theta_V}{2}\right)\right]$ associated with the idler states $|\psi\rangle_B^{(H)}$ and $|\psi\rangle_B^{(V)}$, which are normalized to γ and $(1 - \gamma)$ respectively. Again the subscript 'V' in the parameters θ_V and ϕ_V refers to the idler state $|\psi\rangle_B^{(V)}$ in the Bloch sphere, when the signal state is projected to $|V\rangle_A$.

We can choose $\gamma = \cos^2(\theta_r)$ provided $\theta_r \in [0, \pi]$ to explicitly make $\gamma \leq 1$ which will help in algebraic simplification later. Consequently, we get $(1 - \gamma) = \sin^2(\theta_r)$. Thus, in terms of θ's and ϕ's the complex coefficients $\{\alpha_j\}$ with $j = 1, 2, 3, 4$ can be written as,

$$\alpha_1 = \cos(\theta_r)\ \cos\left(\frac{\theta_H}{2}\right) \tag{4.163}$$

$$\alpha_2 = \cos(\theta_r)\ e^{i\phi_H}\ \sin\left(\frac{\theta_H}{2}\right) \tag{4.164}$$

$$\alpha_3 = e^{i\phi_r}\ \sin(\theta_r)\ \cos\left(\frac{\theta_V}{2}\right) \tag{4.165}$$

$$\alpha_4 = e^{i\phi_r}\ \sin(\theta_r)\ e^{i\phi_V}\ \sin\left(\frac{\theta_V}{2}\right) \tag{4.166}$$

So, any pure bipartite qubit state $|\Psi\rangle_{AB}$ can be parameterized in terms of the 6 real quantities $\{\theta_H, \phi_H, \theta_V, \phi_V, \theta_r, \phi_r\}$ with $\theta_H, \theta_V, \theta_r \in [0, \pi]$ and $\phi_H, \phi_V, \phi_r \in [-\pi, \pi)$. The parametric representation of any arbitrary bipartite pure state is given as,

$$|\Psi\rangle_{AB} = \begin{pmatrix} \cos(\theta_r)\ \cos\left(\frac{\theta_H}{2}\right) \\ e^{i\phi_H}\ \cos(\theta_r)\ \sin\left(\frac{\theta_H}{2}\right) \\ e^{i\phi_r}\ \sin(\theta_r)\ \cos\left(\frac{\theta_V}{2}\right) \\ e^{i\phi_r}\ e^{i\phi_V}\ \sin(\theta_r)\ \sin\left(\frac{\theta_V}{2}\right) \end{pmatrix} \tag{4.167}$$

4.5.2 Experimental Protocol

Any pure bipartite qubit state can be parameterized using 6 real quantities, as shown in Eqn. 4.167. In this subsection, a generic interferometric scheme for the reconstruction of a pure bipartite qubit in the polarization degree of freedom of light will be presented, along with the discussion on the required analysis of the experimental quantities extracted from the interference patterns for the determination of the 6 unknown state parameters.

Let, a pair of photons A and B, are generated by Spontaneous Parametric Down Conversion (SPDC) process [11]. The combined state of the two particles generated from SPDC, i.e., $|\Psi\rangle_{AB}$ in the polarization degree of freedom (which is an element of bipartite space $\mathcal{H}_{AB}$) needs to be identified experimentally. The two particles, the signal A and the idler B, of the bipartite system can be at two spatially separated locations with two different parties. Therefore, for inferring the unknown state associated with the particles A and B, we shall avoid performing any global operation. So that the parties, say Alice (with signal particle A) and Bob (with idler particle B), can perform local single qubit operations on the respective particles with them and later by classical communication i.e., post-processing with coincidence logic, can determine the state of the bipartite system.

For this, one single qubit QSI setup, i.e., a Mach-Zehnder interferometer (or any equivalent two path interferometer) with one arm having $\hat{\sigma}_x$ operator and the other arm having $\hat{\Pi}_H$ operator needs to be designed for each subsystems A and B respectively. $\hat{\sigma}_x$ is the Pauli-X operator that swaps the polarization states $|H\rangle$ with $|V\rangle$ and $|V\rangle$ with $|H\rangle$, which can be realized using a half-wave plate (HWP) with the fast axis oriented at 45° with respect to the horizontal. $\hat{\Pi}_H$ is the projector to the polarization $|H\rangle$, which can be effectively realized by transmitting the beam through a polarizing beam splitter (PBS).

As shown in Fig. 4.5, the interferometer in Alice's setup is formed with two beam splitters BS_{A1}, BS_{A2} and two mirrors M_{A1}, M_{A2}, having HWP_A (as $\hat{\sigma}_x^{(A)}$) in one path and PBS_A (as $\hat{\Pi}_H^{(A)}$) in the other path along with a CCD array (CCD_A) placed at one of the output ports of BS_{A2}. Similarly, the interferometer in Bob's setup is formed with two beam splitters BS_{B1}, BS_{B2} and two mirrors M_{B1}, M_{B2}, having HWP_B (as $\hat{\sigma}_x^{(B)}$) and PBS_B (as $\hat{\Pi}_H^{(B)}$) in the two respective paths, along with a CCD array (CCD_B) placed at one of the output ports of BS_{B2}. The operators $\{\hat{\sigma}_x^{(A)}, \hat{\Pi}_H^{(A)}\}$ and $\{\hat{\sigma}_x^{(B)}, \hat{\Pi}_H^{(B)}\}$, that acts on the two dimensional polarization spaces $\mathcal{H}_A$ and $\mathcal{H}_B$ respectively, are placed at the respective arms of the Alice's and Bob's interferometer. Both Alice and Bob need to perform single qubit quantum state interferography on their respective signal (A) and idler (B) photons and record the time-stamps of the particles forming the interference

[11]SPDC is a non-linear optical process, where a pair of daughter photons (say, A and B) are generated from a pump photon (say, P) within a non-linear optical media, obeying the law of conservation of energy (i.e., $E_P = E_A + E_B$ or $\hbar\omega_P = \hbar\omega_A + \hbar\omega_B$) and the law of conservation of momentum (i.e., $\vec{k}_P = \vec{k}_A + \vec{k}_B$).

pattern. One of the parties, here Bob, needs to perform quantum state interferography with the heralded B particles subject to A particles being projected on to $|H\rangle_A$, which can be achieved by blocking the interferometer arm containing $\hat{\sigma}_x^{(A)}$ operator in Alice's setup. Bob can extract the heralded intensity pattern by correlating the time-stamps of the idler photons (B) with that of the signal photons (A) projected to $|H\rangle_A$. The information about the timestamps can be shared via classical communication.

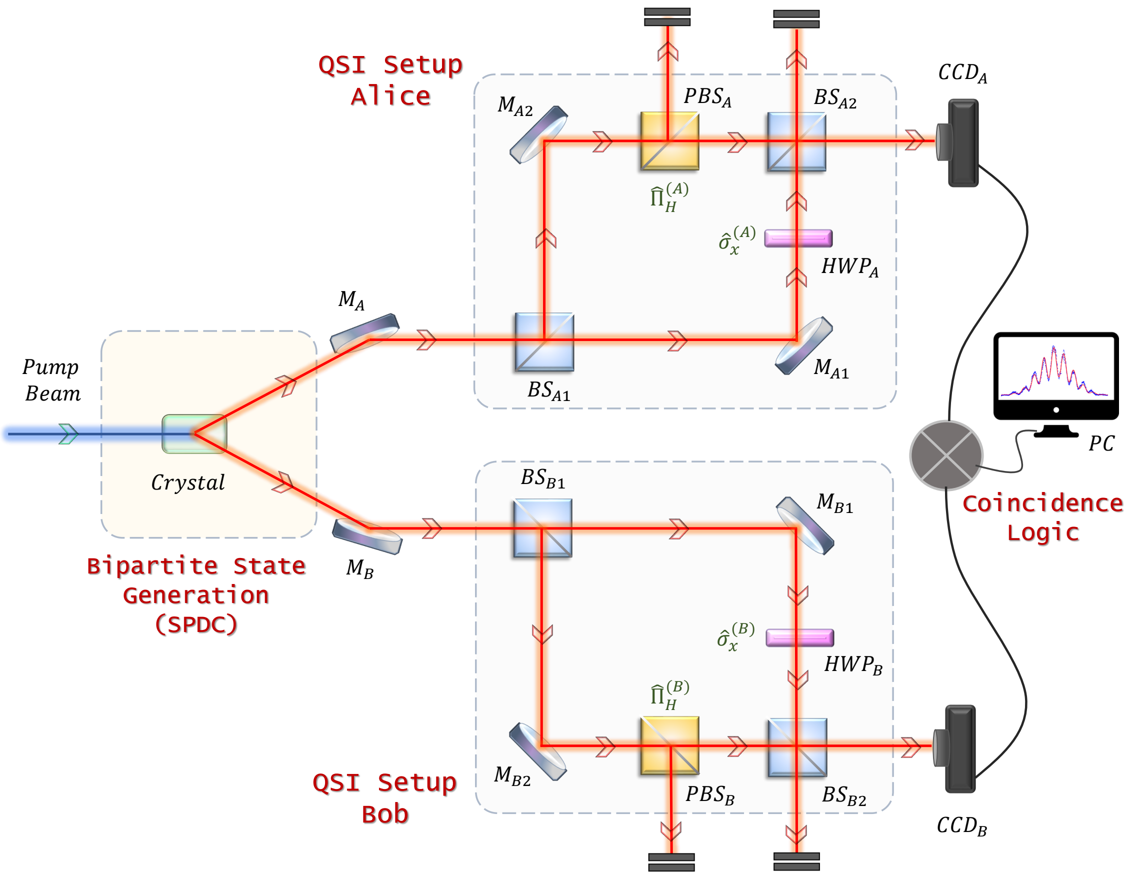

Figure 4.5: Quantum State Interferography (QSI) for bipartite state characterization: The two spatially separated parties Alice and Bob perform single qubit QSI on the respective particles A and B with them. Bob additionally performs single qubit QSI with the heralded B particles subject to A particles being projected to $|H\rangle$.

Thus, in total, for the pure qubit state reconstruction of a bipartite system, Alice and Bob would just need *two* experimental settings to obtain *three* interference patterns from which all the *six* state parameters for specifying the unknown bipartite state can be determined. So, overall the QSI for bipartite system requires,

(i) Intensity pattern ($I_B^{(h)}$) generated from heralded B particles conditioned to particle A being projected on to $|H\rangle_A$ − *Heralded single qubit QSI for* B,

(ii) Interference pattern (I_B) generated from singles of idler particle B − *Unheralded single qubit QSI for* B,

(iii) Interference pattern (I_A) generated from singles of signal particle A *Unheralded single qubit QSI for* A.

4.5.3 Method and Inferring the State Parameters

Here, we will discuss how the three intensity profiles $I_B^{(h)}$, I_B and I_A obtained for the three different cases mentioned above, can be processed to infer the state parameters $\{\theta_H, \phi_H, \theta_V, \phi_V, \theta_r, \phi_r\}$ to reconstruct the bipartite state $|\Psi\rangle_{AB}$.

❑ Single Qubit QSI with Heralded B Particles:

The general form of the bipartite qubit state $|\Psi\rangle_{AB}$ in terms of the complex coefficients $\{\alpha_1, \alpha_2, \alpha_3, \alpha_4\}$ is shown in Eqn. 4.152, provided the normalization $\sum_{j=1}^{4} |\alpha_j|^2 = 1$.

$$|\Psi\rangle_{AB} = \alpha_1 |H\rangle_A |H\rangle_B + \alpha_2 |H\rangle_A |V\rangle_B + \alpha_3 |V\rangle_A |H\rangle_B + \alpha_4 |V\rangle_A |V\rangle_B$$

The parametric representation of the state $|\Psi\rangle_{AB}$ in terms of $\{\theta_H, \phi_H, \theta_V, \phi_V, \theta_r, \phi_r\}$, where $\theta_H, \theta_V, \theta_r \in [0, \pi]$ and $\phi_H, \phi_V, \phi_r \in [-\pi, \pi)$, is shown in Eqn. 4.167. When Alice projects the particles A to the state $|H\rangle_A$, the state of the particle B becomes

$$|\psi\rangle_B^{(H)} = \alpha_1 |H\rangle_B + \alpha_2 |V\rangle_B = \begin{pmatrix} \alpha_1 \\ \alpha_2 \end{pmatrix}$$

$$|\psi\rangle_B^{(H)} = \begin{pmatrix} \cos(\theta_r) \cos\left(\dfrac{\theta_H}{2}\right) \\ e^{i\phi_H} \cos(\theta_r) \sin\left(\dfrac{\theta_H}{2}\right) \end{pmatrix} = \cos(\theta_r) \begin{pmatrix} \cos\left(\dfrac{\theta_H}{2}\right) \\ e^{i\phi_H} \sin\left(\dfrac{\theta_H}{2}\right) \end{pmatrix} \tag{4.168}$$

Here, $\cos(\theta_r)$ is the global factor and would only affect the normalization of the state $|\psi\rangle_B^{(H)}$. This factor has no effect on the intensity modulation with respect to the relative interferometric phase generated by the heralded B particles at the end of the two path interferometer (with Bob), formed with the beam splitters BS_{B1} and BS_{B2}, having the operators $\hat{\sigma}_x^{(B)}$ in one path and $\hat{\Pi}_H^{(B)}$ in the other path.

The evolution of the state $|\psi\rangle_B^{(H)}$ through the QSI setup of Bob to one of the output ports of the second beam splitter (BS_{B2}) with CCD_B, can be described using the effective evolution operator $\hat{\mathcal{E}}_B$, which is given by

$$\hat{\mathcal{E}}_B = \frac{1}{2}\left(\exp(i\epsilon)\ \hat{\Pi}_H^{(B)} + \hat{\sigma}_x^{(B)}\right) \tag{4.169}$$

$$\hat{\mathcal{E}}_B = \frac{1}{2}\left[\exp(i\epsilon)\begin{pmatrix}1 & 0\\ 0 & 0\end{pmatrix}_B + \begin{pmatrix}0 & 1\\ 1 & 0\end{pmatrix}_B\right] = \frac{1}{2}\begin{pmatrix}e^{i\epsilon} & 1\\ 1 & 0\end{pmatrix}_B \tag{4.170}$$

Here, ϵ is the relative phase between the two paths of the interferometer. This evolution operator is non-Unitary because of the losses associated with the operator $\hat{\Pi}_H^{(B)}$ and the fact that we are detecting the particles only in one of the two ports of the second beam splitter BS_{B2} of the interferometer. Note that, $\hat{\mathcal{E}}_B$ is only employed here as a short-cut to the detailed derivation (the Unitary description of the evolution) shown in **Chapter. 2**.

Experimentally, the A particles can be projected to state $|H\rangle_A$ by blocking the path with $\hat{\sigma}_x^{(A)}$ operator in Alice's setup, since the other path of the interferometer already has the projector $\hat{\Pi}_H^{(A)}$. The interferometer in Bob's setup can be made non-collinear so that the intensity can be directly obtained as a function of phase difference ϵ in the CCD array CCD_B. Here, we can consider CCD_B to be a camera that can be gated, so that CCD_B only records the B particles when it is triggered by the signal from CCD_A generated upon the detection of the A particle in state $|H\rangle_A$. Alternatively, we can consider that both the CCD arrays CCD_A and CCD_B can record time-stamps of the detected photons, so that the correlation of the detected B particles in Bob's setup can be obtained with the detected A particles in the Alice's setup. In this way, the intensity pattern generated by the heralded B particles conditioned to A particles being projected to $|H\rangle_A$ can be obtained.

At this setting of the setup, the intensity recorded by CCD_B is given as,

$$I_B^{(h)} = \left\| \hat{\mathcal{E}}_B \left|\psi\right\rangle_B^{(H)} \right\|^2 \tag{4.171}$$

Now, using the expressions of $\hat{\mathcal{E}}_B$ and $|\psi\rangle_B^{(H)}$ given in Eqn. 4.170 and Eqn. 4.168 we get,

$$\hat{\mathcal{E}}_B \left|\psi\right\rangle_B^{(H)} = \frac{\cos(\theta_r)}{2} \begin{pmatrix} e^{i\epsilon} \cos\left(\frac{\theta_H}{2}\right) + e^{i\phi_H} \sin\left(\frac{\theta_H}{2}\right) \\ \cos\left(\frac{\theta_H}{2}\right) \end{pmatrix} \tag{4.172}$$

Hence, the heralded intensity pattern $I_B^{(h)}$ as a function of relative phase ϵ recorded by Bob conditioned to Alice detecting the particles A in the state $|H\rangle_A$, can be expressed as

$$I_B^{(h)}(\epsilon) = \frac{1}{8}\cos^2(\theta_r)\left[3 + \cos(\theta_H) + 2\sin(\theta_H)\cos(\epsilon - \phi_H)\right] \tag{4.173}$$

The superscript '(h)' in $I_B^{(h)}$ indicates that this intensity distribution obtained for the B particles from Bob's QSI setup is subject to heralding of the A particles in the state $|H\rangle_A$. The above expression of intensity is similar to the intensity distribution obtained when a pure qubit state evolves through the QSI setup, as presented in Chapter. 2, except for the additional scaling factor $\cos^2(\theta_r)$ which is associated with the normalization of the qubit corresponding to the subsystem B (with $\mu = 1$ due to assumption that the bipartite state is pure, causing $|\psi\rangle_B^{(H)}$ to be pure).

Experimentally, $\cos^2(\theta_r)$ can be determined from the observed probability of A particles being projected to $|H\rangle_A$. If Alice just blocks the arm with $\hat{\sigma}_x^{(A)}$ operation to effectively perform this projection on A particles and computes the probability of detecting the horizontally projected particles to be $P_{d_A}^{(H)}$ from the number of particles reaching the CCD array CCD_A, then the normalization factor γ can be obtained as $\gamma = 4\, P_{d_A}^{(H)}$. The factor 4 is introduced to compensate for the losses in the particles due to the presence of two $50:50$ beam splitters, BS_{A1} and BS_{A2}, which in a ideal situation allows only 25% of the photons incident on Alice's setup to reach to CCD_A. Therefore, accounting for the particles that are not being collected by CCD_A due to the fact that we have the projector $\hat{\Pi}_H^{(A)}$ in one of the output ports of BS_{A1} and are detecting the particles at one output port of BS_{A2}, we get the normalization factor γ as:

$$\gamma = \cos^2(\theta_r) = 4\ P_{d_A}^{(H)} \tag{4.174}$$

$$\implies \qquad \theta_r = \cos^{-1}\left(\sqrt{4\ P_{d_A}^{(H)}}\right) \tag{4.175}$$

Since Alice can determine θ_r by experimentally observing $P_{d_A}^{(H)}$, Bob can use it to suitably normalize his state from the observed intensity.

The phase shift $(\Phi_B^{(h)})$ of the heralded interference pattern can be obtained by finding the value of phase ϵ at which the intensity $I_B^{(h)}(\epsilon)$ is maximum. This is obtained by solving the equation $\dfrac{\partial I_B^{(h)}(\epsilon)}{\partial \epsilon} = 0$ for ϵ and ensuring that $\left.\dfrac{\partial^2 I_B^{(h)}(\epsilon)}{\partial \epsilon^2}\right|_{\epsilon=\Phi_B^{(h)}} < 0$. From the expression of heralded intensity in Eqn. 4.173, we get

$$\left.\frac{\partial I_B^{(h)}(\epsilon)}{\partial \epsilon}\right|_{\epsilon=\Phi_B^{(h)}} = -\frac{1}{4}\cos^2(\theta_r)\sin(\theta_H)\sin\left(\Phi_B^{(h)} - \phi_H\right) = 0 \tag{4.176}$$

$$\left.\frac{\partial^2 I_B^{(h)}(\epsilon)}{\partial \epsilon^2}\right|_{\epsilon=\Phi_B^{(h)}} = -\frac{1}{4}\cos^2(\theta_r)\sin(\theta_H)\cos\left(\Phi_B^{(h)} - \phi_H\right) \tag{4.177}$$

So, for $\Phi_B^{(h)} = \phi_H$, we get the expression in Eqn. 4.177 to be $\left.\dfrac{\partial^2 I_B^{(h)}(\epsilon)}{\partial \epsilon^2}\right|_{\epsilon=\Phi_B^{(h)}=\phi_H} < 0$, given that $\sin(\theta_H)$ is positive for $\theta_H \in [0,\pi]$ and $\cos^2(\theta_r) > 0$ for all θ_r.

Therefore, at the phase $\epsilon = \phi_H$, we obtain the heralded intensity to be the maximum, giving the phase shift of the interference pattern as $\Phi_B^{(h)} = \phi_H$. So, the state parameter $\phi_H \in [-\pi,\pi)$ can be directly obtained from the phase shift $\Phi_B^{(h)}$ of the heralded intensity distribution $I_B^{(h)}(\epsilon)$ of the B particles.

$$\phi_H = \Phi_B^{(h)} \tag{4.178}$$

The phase averaged intensity of the intensity distribution is obtained by integrating $I_B^{(h)}(\epsilon)$ over all possible phases ϵ and is given as,

$$\bar{I}_B^{(h)} = \int_\epsilon I_B^{(h)}(\epsilon)\; d\epsilon = \frac{1}{8}\cos^2(\theta_r)\,(3+\cos(\theta_H)) \tag{4.179}$$

Since Alice can determine $\cos^2(\theta_r)$ from the probability of detecting the particle A in the state $|H\rangle_A$ as shown in Eqn. 4.174, Bob can use that information to determine θ_H from the above expression as the following,

$$\theta_H = \cos^{-1}\left(\frac{8\;\bar{I}_B^{(h)}}{\cos^2(\theta_r)} - 3\right) \tag{4.180}$$

Thus, from the setting which projects the A particles to $|H\rangle_A$ and generates the heralded interference pattern $I_B^{(h)}(\epsilon)$ of B particles, Alice and Bob can determine 3 state parameters θ_r, θ_H and ϕ_H associated with the unknown state $|\Psi\rangle_{AB}$.

❑ Single Qubit QSI with Unheralded B Particles:

Now, if Bob considers all the particles detected in the CCD array CCD_B without any heralding, we get the unheralded interference pattern (I_B) generated at the end of the QSI setup that is with Bob. In this case, we need to consider the reduced state of the particle B which, in general, is mixed. Thus, here we need to deal with the density matrix $\hat{\rho}_{AB}$, associated with the pure state of the bipartite system, from which we can obtain the reduced density matrix for particle B after performing partial trace [27] over A, i.e., $\hat{\rho}_B = \mathrm{Tr}_A(\hat{\rho}_{AB})$.

In terms of the complex amplitudes $\{\alpha_j\}$, the density matrix for the pure state of the two qubit system can be written as,

$$\hat{\rho}_{AB} = |\Psi\rangle_{AB}\langle\Psi|_{AB} = \begin{pmatrix} |\alpha_1|^2 & \alpha_1\alpha_2^* & \alpha_1\alpha_3^* & \alpha_1\alpha_4^* \\ \alpha_2\alpha_1^* & |\alpha_2|^2 & \alpha_2\alpha_3^* & \alpha_2\alpha_4^* \\ \alpha_3\alpha_1^* & \alpha_3\alpha_2^* & |\alpha_3|^2 & \alpha_3\alpha_4^* \\ \alpha_4\alpha_1^* & \alpha_4\alpha_2^* & \alpha_4\alpha_3^* & |\alpha_4|^2 \end{pmatrix} \tag{4.181}$$

Now, in terms of the state parameters $\{\theta_H, \phi_H, \theta_V, \phi_V, \theta_r, \phi_r\}$, the elements of the density matrix $\hat{\rho}_{AB}$ are computed as the following,

$$|\alpha_1|^2 = \cos^2(\theta_r)\ \cos^2\left(\frac{\theta_H}{2}\right) \tag{4.182}$$

$$|\alpha_2|^2 = \cos^2(\theta_r)\ \sin^2\left(\frac{\theta_H}{2}\right) \tag{4.183}$$

$$|\alpha_3|^2 = \sin^2(\theta_r)\ \cos^2\left(\frac{\theta_V}{2}\right) \tag{4.184}$$

$$|\alpha_4|^2 = \sin^2(\theta_r)\ \sin^2\left(\frac{\theta_V}{2}\right) \tag{4.185}$$

$$\alpha_1\alpha_2^* = (\alpha_2\alpha_1^*)^* = \frac{1}{2}\cos^2(\theta_r)\ \sin(\theta_H)\ e^{-i\phi_H} \tag{4.186}$$

$$\alpha_1\alpha_3^* = (\alpha_3\alpha_1^*)^* = \frac{1}{2}\sin(2\theta_r)\ \cos\left(\frac{\theta_H}{2}\right)\ \cos\left(\frac{\theta_V}{2}\right)\ e^{-i\phi_r} \tag{4.187}$$

$$\alpha_1\alpha_4^* = (\alpha_4\alpha_1^*)^* = \frac{1}{2}\sin(2\theta_r)\ \cos\left(\frac{\theta_H}{2}\right)\ \sin\left(\frac{\theta_V}{2}\right)\ e^{-i(\phi_V+\phi_r)} \tag{4.188}$$

$$\alpha_2\alpha_3^* = (\alpha_3\alpha_2^*)^* = \frac{1}{2}\sin(2\theta_r)\ \sin\left(\frac{\theta_H}{2}\right)\ \cos\left(\frac{\theta_V}{2}\right)\ e^{i(\phi_H-\phi_r)} \tag{4.189}$$

$$\alpha_2\alpha_4^* = (\alpha_4\alpha_2^*)^* = \frac{1}{2}\sin(2\theta_r)\ \sin\left(\frac{\theta_H}{2}\right)\ \sin\left(\frac{\theta_V}{2}\right)\ e^{i(\phi_H-\phi_V-\phi_r)} \tag{4.190}$$

$$\alpha_3\alpha_4^* = (\alpha_4\alpha_3^*)^* = \frac{1}{2}\sin^2(\theta_r)\ \sin(\theta_V)\ e^{-i\phi_V} \tag{4.191}$$

Therefore, the reduced density matrix $\hat{\rho}_B$ associated with the subsystem B can be computed as,

$$\hat{\rho}_B = \mathrm{Tr}_A\left(\hat{\rho}_{AB}\right) = \begin{pmatrix} |\alpha_1|^2 + |\alpha_3|^2 & \alpha_1\alpha_2^* + \alpha_3\alpha_4^* \\ \\ \alpha_2\alpha_1^* + \alpha_4\alpha_3^* & |\alpha_2|^2 + |\alpha_4|^2 \end{pmatrix} \tag{4.192}$$

In terms of the state parameters $\hat{\rho}_B$ can be expressed as,

$$\begin{aligned} \hat{\rho}_B(\theta_r, \theta_H, \theta_V, \phi_H, \phi_V) \; &= \\ &\begin{pmatrix} \begin{array}{l} \cos^2(\theta_r)\cos^2\left(\dfrac{\theta_H}{2}\right) \\ \qquad + \sin^2(\theta_r)\cos^2\left(\dfrac{\theta_V}{2}\right) \end{array} & \begin{array}{l} \dfrac{1}{2}[\cos^2(\theta_r)\sin(\theta_H)\, e^{-i\phi_H} \\ \qquad + \sin^2(\theta_r)\sin(\theta_V)\, e^{-i\phi_V}] \end{array} \\ \\ \begin{array}{l} \dfrac{1}{2}[\cos^2(\theta_r)\sin(\theta_H)\, e^{i\phi_H} \\ \qquad + \sin^2(\theta_r)\sin(\theta_V)\, e^{i\phi_V}] \end{array} & \begin{array}{l} \cos^2(\theta_r)\sin^2\left(\dfrac{\theta_H}{2}\right) \\ \qquad + \sin^2(\theta_r)\sin^2\left(\dfrac{\theta_V}{2}\right) \end{array} \end{pmatrix} \end{aligned} \tag{4.193}$$

As the B particles travel through the single qubit QSI setup of Bob, an unconditional interference pattern is generated at the end of the interferometer. This intensity distribution I_B in the port with CCD_B, can be derived by evolving the state $\hat{\rho}_B$ through the effective evolution operator $\hat{\mathcal{E}}_B = \dfrac{1}{2}\left(\exp(i\epsilon_B)\ \hat{\Pi}_H^{(B)} + \hat{\sigma}_x^{(B)}\right)$, where ϵ_B is the relative phase between the two paths of the interferometer. So, we compute I_B as,

$$I_B = \mathrm{Tr}\left(\hat{\mathcal{E}}_B\ \hat{\rho}_B\ \hat{\mathcal{E}}_B^\dagger\right) \tag{4.194}$$

The unheralded intensity distribution as a function of the phase difference ϵ_B, recorded by Bob at one of the output ports of BS_{B2} can be written as follows:

$$\begin{aligned} I_B(\epsilon_B) = \frac{1}{8}\Big[\ 3\ +\ & \cos^2(\theta_r)\left(\ \cos(\theta_H) + 2\sin(\theta_H)\cos(\epsilon_B - \phi_H)\ \right) \\ & +\ \sin^2(\theta_r)\left(\ \cos(\theta_V) + 2\sin(\theta_V)\cos(\epsilon_B - \phi_V)\ \right)\ \Big] \end{aligned} \tag{4.195}$$

The unheralded intensity $I_B(\epsilon_B)$ is a function of the state parameters $\theta_r, \theta_H, \phi_H, \theta_V, \phi_V$ apart from the relative phase ϵ_B. Post-processing the intensity distribution obtained due to the detection of heralded B particles subject to A particles being projected to $|H\rangle_A$, i.e., from $I_B^{(h)}$, we have already determined the parameters θ_r, θ_H and ϕ_H. Now, if we compute the phase averaged intensity from the unheralded intensity distribution I_B, we get

$$\bar{I}_B = \frac{1}{8}\left[\, 3 + \cos^2(\theta_r)\cos(\theta_H) + \sin^2(\theta_r)\cos(\theta_V)\,\right] \tag{4.196}$$

So, the average intensity $\bar{I}_B$ varies depending on the parameters θ_r, θ_H and θ_V. Since, θ_r and θ_H are already known, we can infer θ_V from the above expression of average intensity.

$$\theta_V = \cos^{-1}\left(\frac{8\ \bar{I}_B - 3 - \cos^2(\theta_r)\cos(\theta_H)}{\sin^2(\theta_r)}\right) \tag{4.197}$$

Again, the phase shift Φ_B of the interference pattern $I_B(\epsilon_B)$ can be obtained experimentally by finding the phase ϵ_B for which I_B has the maximum value. Analytically the value Φ_B can be determined by solving the equation $\left.\frac{\partial I_B(\epsilon_B)}{\partial \epsilon_B}\right|_{\epsilon_B=\Phi_B} = 0$ and ensuring $\left.\frac{\partial^2 I_B(\epsilon_B)}{\partial {\epsilon_B}^2}\right|_{\epsilon_B=\Phi_B} < 0$. Thus, using the expression in Eqn. 4.195 we get,

$$\left.\frac{\partial I_B(\epsilon_B)}{\partial \epsilon_B}\right|_{\epsilon_B=\Phi_B} = 0 \tag{4.198}$$

$$\implies \quad -\frac{1}{4}\left[\, \cos^2(\theta_r)\sin(\theta_H)\sin(\Phi_B - \phi_H) + \sin^2(\theta_r)\sin(\theta_V)\sin(\Phi_B - \phi_V)\,\right] = 0$$

$$\implies \quad \frac{\sin(\Phi_B - \phi_V)}{\sin(\Phi_B - \phi_H)} = -\frac{\cos^2(\theta_r)\sin(\theta_H)}{\sin^2(\theta_r)\sin(\theta_V)} \tag{4.199}$$

$$\implies \quad \sin(\Phi_B - \phi_V) = -\cot^2(\theta_r)\left(\frac{\sin(\theta_H)}{\sin(\theta_V)}\right)\sin(\Phi_B - \phi_H) \tag{4.200}$$

Once, the phase shift Φ_B of the interference pattern is experimentally determined from the phase corresponding to the maximum intensity I_B, the state parameter ϕ_V can be obtained from Eqn. 4.200 using the already known values of $\theta_r, \theta_H, \theta_V$ and ϕ_H. Thus we get ϕ_V as the following,

$$\phi_V = \Phi_B + \sin^{-1}\left(\cot^2(\theta_r)\, \frac{\sin(\theta_H)}{\sin(\theta_V)}\, \sin(\Phi_B - \phi_H)\right) \tag{4.201}$$

Care should be taken to verify that ϕ_V maximizes I_B for the values of θ_H, θ_V and ϕ_H determined earlier, i.e. need to ensure

$$\left.\frac{\partial^2 I_B(\epsilon_B)}{\partial {\epsilon_B}^2}\right|_{\epsilon_B = \Phi_B} < 0 \tag{4.202}$$

If I_B gets minimized instead, π must be added for consistency. Therefore, from the average intensity $\bar{I}_B$ and the phase shift Φ_B of the unheralded interference pattern obtained experimentally by performing single qubit QSI on the subsystem B, we can determine the state parameters θ_V and ϕ_V respectively.

So far, we have determined all the state parameters except ϕ_r. Although without the knowledge of ϕ_r, the state $|\Psi\rangle_{AB}$ can not be determined completely, we can infer some important properties about the state from the already obtained parameters – such as whether the pure state $|\Psi\rangle_{AB}$ is entangled or not. The von Neumann entropy S of the reduced density matrix $\hat{\rho}_B$ is a unique measure of the entanglement for the bipartite pure state $|\Psi\rangle_{AB}$. Since, the reduced state $\hat{\rho}_B$ of the subsystem B is a function of $\{\theta_r, \theta_H, \theta_V, \phi_H, \phi_V\}$; we can construct $\hat{\rho}_B$ using the already determined values of the state parameters from the Eqn. 4.193.

❑ Single Qubit QSI with Unheralded A Particles:

Next, for the complete state reconstruction, we need to perform Quantum State Interferography on the unheralded A particles in Alice's setup. The reduced density matrix $\hat{\rho}_A$ associated with the subsystem A is obtained as,

$$\hat{\rho}_A = \mathrm{Tr}_B\left(\hat{\rho}_{AB}\right) = \begin{pmatrix} |\alpha_1|^2 + |\alpha_2|^2 & \alpha_1\alpha_3^* + \alpha_2\alpha_4^* \\ \alpha_3\alpha_1^* + \alpha_4\alpha_2^* & |\alpha_3|^2 + |\alpha_4|^2 \end{pmatrix} \tag{4.203}$$

In terms of the state parameters the density matrix $\hat{\rho}_A$ can be expressed as,

$$
\hat{\rho}_A(\theta_H,\theta_V,\theta_r,\phi_H,\phi_V,\phi_r) \;=
$$

$$
\begin{pmatrix}
\cos^2(\theta_r) & \begin{array}{r}\frac{1}{2}\sin(2\theta_r)e^{-i\phi_r}\left[\cos\left(\frac{\theta_H}{2}\right)\cos\left(\frac{\theta_V}{2}\right)\right.\\ \left. +\sin\left(\frac{\theta_H}{2}\right)\sin\left(\frac{\theta_V}{2}\right)e^{i(\phi_H-\phi_V)}\right]\end{array} \\
\begin{array}{r}\frac{1}{2}\sin(2\theta_r)e^{i\phi_r}\left[\cos\left(\frac{\theta_H}{2}\right)\cos\left(\frac{\theta_V}{2}\right)\right.\\ \left. +\sin\left(\frac{\theta_H}{2}\right)\sin\left(\frac{\theta_V}{2}\right)e^{-i(\phi_H-\phi_V)}\right]\end{array} & \sin^2(\theta_r)
\end{pmatrix}
\tag{4.204}
$$

Now, when the A particles travel through the single qubit QSI setup of Alice, having the operators $\hat{\sigma}_x^{(A)}$ and $\hat{\Pi}_H^{(A)}$ in the respective paths of the two path interferometer with Alice, an interference pattern is generated at the end of the setup. The corresponding intensity distribution I_A in the output port of BS_{A2} with CCD_A can be obtained by evolving the state $\hat{\rho}_A$ through the effective evolution operator $\hat{\mathcal{E}}_A$ as given below. Therefore,

$$
I_A = \mathrm{Tr}\Big(\hat{\mathcal{E}}_A\;\hat{\rho}_A\;\hat{\mathcal{E}}_A^{\dagger}\Big) \tag{4.205}
$$

$$
\text{where,} \qquad \hat{\mathcal{E}}_A = \frac{1}{2}\left(\exp(i\epsilon_A)\;\hat{\Pi}_H^{(A)} + \hat{\sigma}_x^{(A)}\right) \tag{4.206}
$$

where ϵ_A is the relative phase between the two paths of the interferometer in Alice's setup.

The intensity distribution as a function of ϵ_A as recorded by Alice, can computed to be

$$
\begin{aligned}
I_A(\epsilon_A) = \frac{1}{8}\Bigg[\, 3+\cos(2\theta_r)+2\sin(2\theta_r)\Bigg(\cos\left(\frac{\theta_H}{2}\right)\cos\left(\frac{\theta_V}{2}\right)\cos(\epsilon_A-\phi_r) \\
+\sin\left(\frac{\theta_H}{2}\right)\sin\left(\frac{\theta_V}{2}\right)\cos(\epsilon_A+\phi_H-\phi_V-\phi_r)\Bigg)\Bigg]
\end{aligned}
\tag{4.207}
$$

The average intensity of the interference pattern $I_A(\epsilon_A)$ is obtained by integrating it over all possible phases ϵ_A and is given by,

$$\bar{I}_A = \frac{1}{8}(3 + \cos(2\theta_r)) \tag{4.208}$$

Thus, the state parameter θ_r can also be determined from the experimentally obtained average intensity $\bar{I}_A$ of the interference pattern produced by performing single qubit QSI on A particles, i.e.,

$$\theta_r = \frac{\cos^{-1}\left(8\bar{I}_A - 3\right)}{2} \tag{4.209}$$

Next, we obtain the phase shift Φ_A of the interference pattern by experimentally finding the phase ϵ_A for which I_A is maximum. The parameter ϕ_r can be determined by considering the relation $\left.\frac{\partial I_A(\epsilon_A)}{\partial \epsilon_A}\right|_{\epsilon_A = \Phi_A} = 0$, since we know all other parameters. From Eqn. 4.207, we get

$$\left.\frac{\partial I_A(\epsilon_A)}{\partial \epsilon_A}\right|_{\epsilon_A = \Phi_A} = 0 \tag{4.210}$$

$$\cos\left(\frac{\theta_H}{2}\right)\cos\left(\frac{\theta_V}{2}\right)\sin(\Phi_A - \phi_r) + \sin\left(\frac{\theta_H}{2}\right)\sin\left(\frac{\theta_V}{2}\right)\sin(\Phi_A + \phi_H - \phi_V - \phi_r) = 0$$

$$\implies \quad \frac{\sin(\Phi_A + \phi_H - \phi_V - \phi_r)}{\sin(\Phi_A - \phi_r)} = -\cot\left(\frac{\theta_H}{2}\right)\cot\left(\frac{\theta_V}{2}\right) \tag{4.211}$$

Expanding the above expression using $\sin(C + D) = \sin(C)\cos(D) + \cos(C)\sin(D)$, we get

$$\frac{\sin(\Phi_A - \phi_r)\cos(\phi_H - \phi_V) + \cos(\Phi_A - \phi_r)\sin(\phi_H - \phi_V)}{\sin(\Phi_A - \phi_r)} = -\cot\left(\frac{\theta_H}{2}\right)\cot\left(\frac{\theta_V}{2}\right)$$

$$\implies \quad \cot(\Phi_A - \phi_r)\sin(\phi_H - \phi_V) = -\left[\cos(\phi_H - \phi_V) + \cot\left(\frac{\theta_H}{2}\right)\cot\left(\frac{\theta_V}{2}\right)\right] \tag{4.212}$$

Thus, the state parameter ϕ_r can be obtained using experimentally obtained phase shift Φ_A and the other state parameters from the expression in Eqn. 4.212, as the following

$$\phi_r = \Phi_A + \cot^{-1}\left(\cot(\phi_H - \phi_V) + \frac{\cot\left(\frac{\theta_H}{2}\right)\cot\left(\frac{\theta_V}{2}\right)}{\sin(\phi_H - \phi_V)}\right) \tag{4.213}$$

The above expression must be picked with appropriate signs which maximizes I_A for a given set values of other parameters obtained earlier.

Therefore, from the average intensity $\bar{I}_A$ and the phase shift Φ_A of the unheralded interference pattern produced experimentally by performing single qubit QSI on the subsystem A, we can determine the state parameters θ_r and ϕ_r respectively.

In summary, the interferometric state determination scheme − Quantum State Interferography allows the complete characterization of a pure state associated with a two qubit system within the Hilbert space $\mathcal{H}_{AB} = \mathcal{H}_A \otimes \mathcal{H}_B$, using the information processed from three interference patterns generated in two experimental settings. In one setting, the path of the interferometer with $\hat{\sigma}_x^{(A)}$ operator in Alice's setup for subsystem A is blocked, that allows the particles to undergo $|H\rangle_A$ projection through the operator $\hat{\Pi}_H^{(A)}$ present in the other interferometric path. At this condition without changing the experimental setting, the parameters θ_r, θ_H, ϕ_H, θ_V and ϕ_V are determined from the two intensity patterns obtained by Bob in the same single qubit QSI setup − (i) one intensity pattern formed with the B particles heralded to $|H\rangle_A$ projection of the A particles and (ii) the other formed with the unheralded B particles. Another setting of the interferometric setup, where Alice performs single qubit QSI on the subsystem A by allowing the particles to evolve through the interferometric setup (that is with Alice) having the respective operators in the two arms, is required to determine the parameter ϕ_r. Thus, for the complete reconstruction of the pure bipartite qubit state $|\Psi\rangle_{AB}$ by identifying the six quantities that describe the state, QSI requires two experimental settings as compared to nine measurement settings required for Quantum State Tomography (QST). Nevertheless, the entanglement of the bipartite pure state can be quantified from a single setting of this setup, the details of which will be discussed next.

4.6 Quantification of Entanglement using QSI Scheme

The phenomena of entanglement is one of the most fundamental features of quantum mechanics that represents a non-classical correlation between the sub-systems of a composite quantum system, which persists regardless of the spatial separation between the sub-systems [28, 29]. Quantum entanglement has been the subject of extensive research over decades, due to both its inherent properties that do not have any classical counterpart and its potential applications in advancing quantum technologies; especially in the fields of quantum information processing [30, 31, 32] and in the development of secure quantum communication protocols [33, 34, 35]. A state of a two-particle system, say $|\Psi\rangle_{AB}$, defined within a composite Hilbert space $\mathcal{H}_{AB} = \mathcal{H}_A \otimes \mathcal{H}_B$ of two subsystems A and B, is said to be entangled if it can not be expressed as a product of two separable states $|\psi\rangle_A$ and $|\psi\rangle_B$ corresponding to the two sub-systems, i.e., $|\Psi\rangle_{AB} \neq |\psi\rangle_A \otimes |\psi\rangle_B$ [36].

One of the most challenging and fundamental aspects of entanglement theory concerns the quantification of entanglement [37]. The quantification of entanglement becomes important, while dealing with entangled systems, as it characterizes the degree of non-classical correlation present in the quantum system [38]. This knowledge is essential for manipulating the quantum states and for gauging the eventual fidelity or the efficiency of the quantum computation or communication protocols involving entanglement. Interestingly, the Quantum State Interferography (QSI) technique can be used to quantify the entanglement of bipartite states from a single measurement.

Entanglement of a bipartite system, with the prior knowledge about the bipartite state being pure, can be quantified by the von-Neumman entropy of the reduced density matrix of one of the subsystems [39, 40]. Consider, A and B are the two subsystems of a pure bipartite system and $|\Psi\rangle_{AB}$ is an element of the composite vector space $\mathcal{H}_{AB}$, then the entanglement of the state can be quantified by the measure E, computed as the following:

$$\mathrm{E}(\hat{\rho}_{AB}) = S(\hat{\rho}_A) = S(\hat{\rho}_B) \tag{4.214}$$

Therefore, the knowledge of the $\hat{\rho}_A$ and $\hat{\rho}_B$ can be used individually to compute the entanglement measure $\mathrm{E}(\hat{\rho}_{AB})$.

$$\mathrm{E}(\hat{\rho}_{AB}) = S(\hat{\rho}_A) = -\operatorname{Tr}\left(\hat{\rho}_A \log(\hat{\rho}_A)\right) \tag{4.215}$$

$$\text{or,} \qquad \mathrm{E}(\hat{\rho}_{AB}) = S(\hat{\rho}_B) = -\operatorname{Tr}\left(\hat{\rho}_B \log(\hat{\rho}_B)\right) \tag{4.216}$$

Here, $\hat{\rho}_{AB}$ is the density matrix characterizing the composite system. $\hat{\rho}_A$ and $\hat{\rho}_B$ are the reduced density matrices [1] associated with the subsystems A and B respectively, which are in general mixed, i.e., $\operatorname{Tr}\big(\hat{\rho}_A^2\big) < 1$ and $\operatorname{Tr}\big(\hat{\rho}_B^2\big) < 1$. The reduced density matrix for one of the subsystems (say, i) is derived from the composite system state $\hat{\rho}_{ij}$ by tracing out the basis states in the associated degree of freedom of the rest of the system (i.e., j), such that $\hat{\rho}_i = \operatorname{Tr}_j(\hat{\rho}_{ij})$. Therefore, we have $\hat{\rho}_A$ and $\hat{\rho}_B$ given as the following:

$$\hat{\rho}_A = \operatorname{Tr}_B(\hat{\rho}_{AB}) \qquad \text{and} \qquad \hat{\rho}_B = \operatorname{Tr}_A(\hat{\rho}_{AB}) \tag{4.217}$$

$$\text{where,} \qquad \hat{\rho}_{AB} = |\Psi\rangle_{AB} \langle\Psi|_{AB} \tag{4.218}$$

In the last section, we have shown with a single experimental setting of the QSI setup for the B particles, the reduced density matrix $\hat{\rho}_B$ can be determined. Therefore, this interferometric technique can be used to quantify the entanglement of pure states of bipartite qubits from Eqn. 4.216. With alternative procedures like quantum state tomography (QMT) one would require 9 measurements to be performed on the entire system to quantify the entanglement of the associated state. For entanglement quantification from Bell inequality violation, one would need at least 3 measurement settings if the basis is known, else the optimization procedure requires many more measurements. Thus, Quantum State Interferography (QSI) provides a single-shot entanglement quantification technique using which one can measure the entanglement from a single experimental setting without the need to change any internal settings during the procedure.

4.7 Conclusion

In this chapter, we have established Quantum State Interferography (QSI) as an efficient state determination scheme for higher dimensional ($d > 2$) and bipartite quantum systems employing interferometry as a tool. In this technique, an unknown state can be characterized by finding the associated state parameters from the phase shift, phase averaged intensity and visibility of a number of interference patterns produced in an interferometric setup. Here, we introduce a parametric representation of a d-dimensional pure qudit $|\psi\rangle^{(d)}$ as a chain of $(d-1)$ Bloch vectors within the sequence of Epispheres which are the unit $\mathbb{S}^{(2)}$ spheres, each defined for one of the two-dimensional sub-spaces of the d-dimensional space, having their origin at the location of the tip of the Bloch vector defined within the previous sphere. This chapter presents three different experimental setups involving either $(d-1)$ or 2 interferometers that can be employed to infer the $(2d-2)$ state parameters of a general qudit, without the need to change the experimental settings during the process of data acquisition. Therefore, Quantum State Interfergraphy appears as a true single shot state determination scheme for qudits, which require post-processing of $(d-1)$ interferograms generated at the end of the setup. Also, QSI can be considered to be an efficient state determination technique for higher dimensional pure states and can serve as a less cumbersome and promising alternative to QST. Further, we have shown that this interferometric protocol can be employed to infer the unknown states of a bipartite system with the prior knowledge about the system state being pure by analyzing only three interference patterns generated with two experimental settings, as compared to nine measurement settings required in Quantum State Tomography (QST). Lastly, we have presented Quantum state Interferography as a *single shot entanglement quantification scheme* for pure bipartite states using which the entanglement measure of a pure bipartite qubit can be determined from the von-Neumann entropy of the reduced density matrix of one of the subsystems.

Appendix

4.A Quantum State Interferography for Pure Qudits: Discussion With Normalization

In the Section. 4.3 we have discussed how an unknown pure qudit $|\psi\rangle^{(d)}$ can be inferred from $(d-1)$ interferograms produced using the Quantum State Interferography technique. The theory for the state determination from the complex expectation values of the spin-ladder operators $\hat{\sigma}_{\pm}^{(k)}$ in each of the two-dimensional sub-spaces of the d-dimensional space given by $k = 1, 2, \ldots, (d-1)$ (in SubSec. 4.3.1) and the calculations corresponding to the post-processing of the experimentally obtained quantities such as the phase shift (Φ_k), average intensity $(\bar{I}_k)$ and visibility (V_k) of the interferograms obtained for different sub-spaces (in SubSec. 4.3.3), are presented considering the evolution of the component of $|\psi\rangle^{(d)}$ in k-th two dimensional subspace. In the discussion presented in Sec. 4.3, the component of the qudit in the k-th two-dimensional subspace spanned by $\{|k\rangle, |k+1\rangle\}$, is represented by the state $|\psi\rangle_k^{(2;d)}$ expressed in Eqn. **4.91**, which is not normalized. Further, we have not considered the normalization while computing the expectation values of different operators both in theory and in the post-processing of collected data. In this section, we will present the same scheme for characterizing the qudit $|\psi\rangle^{(d)}$, with all the calculations performed taking normalization into account.

The state $|\psi\rangle_k^{(2;d)}$ can be considered as the projection of the state $|\psi\rangle^{(d)}$ on the k-th two dimensional subspace. Apriori, there is no need for normalization because the projection of a vector need not have any pre-defined norm. However, the norm of the vector $|\psi\rangle_k^{(2;d)}$ given in Eqn. **4.91** can be computed as,

$$\left\| |\Psi\rangle_k^{(2;d)} \right\| = \sqrt{\xi(k) \left[\cos^2\left(\frac{\theta_k}{2}\right) + \sin^2\left(\frac{\theta_k}{2}\right) \cos^2\left(\frac{\theta_{k+1}}{2}\right) \right]} \qquad (4.219)$$

$$\implies \quad \left\| |\Psi\rangle_k^{(2;d)} \right\| = \sqrt{\frac{\xi(k)}{4}\left[3+\cos(\theta_{k+1})+\cos(\theta_k)(1-\cos(\theta_{k+1}))\right]} \qquad (4.220)$$

where, $\xi(k) = \prod_{j=1}^{k-1} \sin^2\left(\frac{\theta_j}{2}\right)$. Therefore the normalized vector, represented as $\left|\psi^{(n)}\right\rangle_k^{(2;d)}$, in the two dimensional k-th subspace can be expressed as the following:

$$\left|\psi^{(n)}\right\rangle_k^{(2;d)} = \frac{\left(\prod_{j=1}^{k-1} \exp(i\phi_j)\sin\left(\frac{\theta_j}{2}\right)\right)}{\sqrt{\frac{\xi(k)}{4}\left[3+\cos(\theta_{k+1})+\cos(\theta_k)(1-\cos(\theta_{k+1}))\right]}} \begin{pmatrix} \cos\left(\frac{\theta_k}{2}\right) \\ e^{i\phi_k}\sin\left(\frac{\theta_k}{2}\right)\cos\left(\frac{\theta_{k+1}}{2}\right) \end{pmatrix} \qquad (4.221)$$

4.A.1 Theory Considering Normalization

If we compute the expectation value of the spin ladder operator $\hat{\sigma}_\pm^{(k)}$ for the state $\left|\psi^{(n)}\right\rangle_k^{(2;d)}$ or in other words express the expectation value of $\hat{\sigma}_\pm^{(k)}$ in normalized form, we get

$$\left\langle \hat{\sigma}_\pm^{(k)} \right\rangle^{(n)} = \frac{\left\langle \psi_k^{(2;d)} \middle| \hat{\sigma}_\pm^{(k)} \middle| \psi_k^{(2;d)} \right\rangle}{\left\langle \psi_k^{(2;d)} \middle| \psi_k^{(2;d)} \right\rangle} = \frac{2\exp(\pm i\phi_k)\sin(\theta_k)\cos\left(\frac{\theta_{k+1}}{2}\right)}{3+\cos(\theta_{k+1})+\cos(\theta_k)(1-\cos(\theta_{k+1}))} \qquad (4.222)$$

The above form assumes that the factor $\xi(k) = \prod_{j=1}^{k-1}\sin^2\left(\frac{\theta_j}{2}\right)$ cancel out between the numerator and denominator requiring that $\theta_j \neq 0 \; \forall \; j < k$. It should be pointed out that in the limiting case, the terms always cancel out. However, when $\theta_k = \pi$ and $\theta_{k+1} = \pi$ simultaneously, $|\psi\rangle_k^{(2;d)}$ cannot be normalized.

The argument and the magnitude of the expectation value of $\hat{\sigma}_\pm^{(k)}$ in the normalized form can be written as,

$$\arg\left(\left\langle \hat{\sigma}_{\pm}^{(k)} \right\rangle^{(n)}\right) = \pm\phi_k \tag{4.223}$$

$$\left|\left\langle \hat{\sigma}_{\pm}^{(k)} \right\rangle^{(n)}\right| = \frac{2\sin(\theta_k)\cos\left(\frac{\theta_{k+1}}{2}\right)}{3+\cos(\theta_{k+1})+\cos(\theta_k)(1-\cos(\theta_{k+1}))} \tag{4.224}$$

Thus, even in the normalized form, the argument of the complex expectation value of the ladder operator $\hat{\sigma}_{\pm}^{(k)}$ directly gives the relative phase ϕ_k associated with the k-th two dimensional subspace. The magnitude $\left|\left\langle \hat{\sigma}_{\pm}^{(k)} \right\rangle^{(n)}\right|$ is a function of θ_k and θ_{k+1}. So, the polar angle θ_k can be determined from the value of $\left|\left\langle \hat{\sigma}_{\pm}^{(k)} \right\rangle^{(n)}\right|$ if θ_{k+1} is known.

For $(d-1)$-th subspace spanned by the states $\{|d-1\rangle, |d\rangle\}$, the magnitude of the expectation value of the ladder operator $\left|\left\langle \hat{\sigma}_{\pm}^{(d-1)} \right\rangle^{(n)}\right|$ would be a function of θ_{d-1} and θ_d. Now the normalization condition of the qudit pure state gives $\theta_d = 0$, as shown in SubSec. 4.1.5. Thus, for the $(d-1)$-th subspace we have,

$$\left|\left\langle \hat{\sigma}_{\pm}^{(d-1)} \right\rangle^{(n)}\right| = \frac{2\sin(\theta_{d-1})\cos\left(\frac{\theta_d}{2}\right)}{3+\cos(\theta_d)+\cos(\theta_{d-1})(1-\cos(\theta_d))} = \frac{\sin(\theta_{d-1})}{2} \tag{4.225}$$

$$\implies \qquad \theta_{d-1} = \sin^{-1}\left(2\left|\left\langle \hat{\sigma}_{\pm}^{(d-1)} \right\rangle^{(n)}\right|\right) \tag{4.226}$$

Hence, from the value of the magnitude of the expectation value $\left\langle \hat{\sigma}_{\pm}^{(d-1)} \right\rangle^{(n)}$ for the $(d-1)$-th subspace we can compute the polar angle θ_{d-1}. Once θ_{d-1} is known, we can compute θ_{d-2} from the value of expectation of spin ladder operator $\left|\left\langle \hat{\sigma}_{\pm}^{(d-2)} \right\rangle^{(n)}\right|$ obtained for the $(d-2)$-th subspace from the following expression.

$$\left|\left\langle \hat{\sigma}_{\pm}^{(d-2)} \right\rangle^{(n)}\right| = \frac{2\sin(\theta_{d-2})\cos\left(\frac{\theta_{d-1}}{2}\right)}{3+\cos(\theta_{d-1})+\cos(\theta_{d-2})(1-\cos(\theta_{d-1}))} \tag{4.227}$$

In this manner, using the recursive relations all the polar angles $\{\theta_j\}$ (with $\theta_j \in [0,\pi]$) describing the state $|\psi\rangle^{(d)}$ can be determined sequentially from the magnitude of the normalized form of the expectation values of spin ladder operators associated with two dimensional sub-spaces. All the azimuthal angles $\{\phi_j\}$ (with $\phi_j \in [-\pi, \pi)$) are directly determined from the argument of the expectation values of $\hat{\sigma}_{\pm}^{(k)}$ as given in Eqn. 4.223. Thus, when normalization of the states $|\psi\rangle_k^{(2;d)}$ are taken into account, all the state parameters are obtained from the expectation values of spin-ladder operators, i.e, $\left\langle \hat{\sigma}_{\pm}^{(k)} \right\rangle^{(n)}$. Hence, the state $|\psi\rangle^{(d)}$ can be inferred from the $(d-1)$ complex valued quantities derived for $(d-1)$ two dimensional sub-spaces of d-dimensional Hilbert space.

4.A.2 Experimental protocol and Inferring the State Parameters Considering Normalization

If we consider a beam in the state $\left|\psi^{(n)}\right\rangle_k^{(2;d)}$ associated with two dimensional k-th subspace propagates through a Mach-Zehnder (or any equivalent two path) interferometer having the operator $\hat{\sigma}_x^{(k)}$ in one arm and the effective operator $\exp(i\epsilon_k)\hat{\Pi}_0^{(k)}$ in the other arm, where ϵ_k is the relative phase between the two arms of the interferometer, then the intensity profile obtained at one of the output ports of the interferometer is given as follows,

$$I_k^{(n)} = \frac{\left\langle \psi_k^{(2;d)} \middle| \hat{\mathcal{O}}^{(k)\dagger}\hat{\mathcal{O}}^{(k)} \middle| \psi_k^{(2;d)} \right\rangle}{\left\langle \psi_k^{(2;d)} \middle| \psi_k^{(2;d)} \right\rangle} \tag{4.228}$$

Here $\hat{\mathcal{O}}^{(k)}$ is the overall evolution operator (non-unitary) corresponding to the action of the MZI with the respective operators given by Eqn. 4.104,

$$\hat{\mathcal{O}}^{(k)} = \frac{1}{2}\left(\exp(i\epsilon_k)\ \hat{\Pi}_0^{(k)} + \hat{\sigma}_x^{(k)}\right) = \frac{1}{2}\begin{pmatrix} \exp(i\epsilon_k) & 1 \\ 1 & 0 \end{pmatrix}_k^{(2;d)} \tag{4.229}$$

Considering normalization of the state, the intensity $I_k^{(n)}$ as a function of the relative phase ϵ_k recorded from one of the output ports of the MZI acting on k-th two dimensional subspace is given by,

$$I_k^{(n)}(\epsilon_k) = \frac{1}{4}\left[\left\langle \hat{\mathbb{1}}^{(k)} \right\rangle^{(n)} + \left\langle \hat{\Pi}_0^{(k)} \right\rangle^{(n)} + 2\,\mathrm{Re}\left(\exp(i\epsilon_k)\left\langle \hat{\sigma}_x^{(k)}\ \hat{\Pi}_0^{(k)} \right\rangle^{(n)}\right)\right] \tag{4.230}$$

$$I_k^{(n)}(\epsilon_k) = \frac{1}{4}\left[\left\langle \hat{\mathbb{1}}^{(k)} \right\rangle^{(n)} + \left\langle \hat{\Pi}_0^{(k)} \right\rangle^{(n)} + 2\,\mathrm{Re}\left(\exp(i\epsilon_k)\left\langle \hat{\sigma}_-^{(k)} \right\rangle^{(n)}\right)\right] \tag{4.231}$$

$$= \frac{5+\cos(\theta_{k+1})+\cos(\theta_k)(3-\cos(\theta_{k+1}))+4\sin(\theta_k)\cos\left(\frac{\theta_{k+1}}{2}\right)\cos(\epsilon_k-\phi_k)}{4\left[3+\cos(\theta_{k+1})+\cos(\theta_k)(1-\cos(\theta_{k+1}))\right]} \tag{4.232}$$

Here, $\langle \hat{\mathbb{1}}^{(k)} \rangle^{(n)}$ and $\left\langle \hat{\Pi}_0^{(k)} \right\rangle^{(n)}$ respectively represent the normalized form of the expectation values of 2×2 identity operator and projection operator corresponding to the k-th two-dimensional subspace. The above form of intensity assumes that the factor $\xi(k) = \prod_{j=1}^{k-1}\sin^2\left(\dfrac{\theta_j}{2}\right)$ cancel out between the numerator and denominator requiring that $\theta_j \neq 0\ \forall j < k$.

The value of phase ϵ_k, for which the intensity distribution $I_k^{(n)}(\epsilon_k)$ have the maximum value, determines the phase shift $\Phi_k^{(n)}$ of the interferogram. The expression of intensity given in Eqn. 4.232 has the maximum value for $\epsilon_k = \phi_k$, given $\theta_k, \theta_{k+1} \in [0,\pi]$. So, the azimuthal angle ϕ_k can be directly obtained from the phase shift of the interefrogram generated for k-th two dimensional subspace, i.e.,

$$\Phi_k^{(n)} = \phi_k \tag{4.233}$$

Similarly, the phase averaged intensity $\bar{I}_k^{(n)}$ can be obtained by integrating $I_k^{(n)}(\epsilon_k)$ over all the phases ϵ_k and is expressed in the normalized form as follows,

$$\bar{I}_k^{(n)} = \frac{5+\cos(\theta_{k+1})+\cos(\theta_k)(3-\cos(\theta_{k+1}))}{4\left[3+\cos(\theta_{k+1})+\cos(\theta_k)(1-\cos(\theta_{k+1}))\right]} \tag{4.234}$$

The advantage of having the normalized form is that the quantity $\bar{I}_k^{(n)}$ now only involves θ_k and θ_{k+1} and does not carry the effect of all θ_j's in the form of $\xi(k) = \prod_{j=1}^{k-1}\sin^2\left(\dfrac{\theta_j}{2}\right)$.

Therefore, provided that we already know $\theta_d = 0$, the state parameter θ_{d-1} can be computed directly using the experimentally obtained quantity $\bar{I}_{d-1}^{(n)}$, which is the average intensity of the interferogram generated for $(d-1)$-th subspace.

$$\bar{I}_{d-1}^{(n)} = \frac{5+\cos(\theta_d)+\cos(\theta_{d-1})(3-\cos(\theta_d))}{4\left[3+\cos(\theta_d)+\cos(\theta_{d-1})(1-\cos(\theta_d))\right]} = \frac{3+\cos(\theta_{d-1})}{8} \tag{4.235}$$

$$\implies \qquad \theta_{d-1} = \cos^{-1}\left(8\ \bar{I}_{d-1}^{(n)} - 3\right) \tag{4.236}$$

Knowing θ_{d-1}, we can compute θ_{d-2} from the experimentally obtained quantity $\bar{I}_{d-2}^{(n)}$ and then iteratively all the θ_k's can be found.

$$\bar{I}_{d-2}^{(n)} = \frac{5+\cos(\theta_{d-1})+\cos(\theta_{d-2})(3-\cos(\theta_{d-1}))}{4\left[3+\cos(\theta_{d-1})+\cos(\theta_{d-2})(1-\cos(\theta_{d-1}))\right]} \tag{4.237}$$

Additionally, we can make use of the visibility of the interference pattern to infer the polar angles θ_j's. The visibility of the interferogram $I_k^{(n)}(\epsilon_k)$ for the k-th two dimensional subspace can be computed as,

$$V_k^{(n)} = \frac{I_k^{(n)(max)} - I_k^{(n)(min)}}{I_k^{(n)(max)} + I_k^{(n)(min)}} = \frac{4\sin(\theta_k)\cos\left(\dfrac{\theta_{k+1}}{2}\right)}{5+\cos(\theta_{k+1})+\cos(\theta_k)(3-\cos(\theta_{k+1}))} \tag{4.238}$$

Visibility $V_k^{(n)}$ computed from the maximum intensity $I_k^{(n)(max)}$ and minimum intensity $I_k^{(n)(min)}$ obtained for the evolution of the normalized state $\left|\psi^{(n)}\right\rangle_k^{(2;d)}$ through the k-th MZI has the same form as the visibility V_k obtained for the evolution of the state $|\psi\rangle_k^{(2;d)}$ through the same setup as given in Eqn. 4.128.

Similar to the procedure discussed in SubSec. 4.3.3, the polar angle θ_{d-1} can be determined using the experimentally obtained quantity $V_{d-1}^{(n)}$ of the interferogram formed for the k-th two dimensional subspace.

$$V_{d-1}^{(n)} = \frac{4\sin(\theta_{d-1})\cos\left(\dfrac{\theta_d}{2}\right)}{5+\cos(\theta_d)+\cos(\theta_{d-1})(3-\cos(\theta_d))} = \frac{2\sin(\theta_{d-1})}{3+\cos(\theta_{d-1})} \tag{4.239}$$

Once θ_{d-1} is determined, we can use this value to determine θ_{d-2} from the value of experimentally obtained visibility $V_{d-2}^{(n)}$ for the $(d-2)$-th subspace using the following expression,

$$V_{d-2}^{(n)} = \frac{4\sin(\theta_{d-2})\cos\left(\dfrac{\theta_{d-1}}{2}\right)}{5+\cos(\theta_{d-1})+\cos(\theta_{d-2})(3-\cos(\theta_{d-1}))} \tag{4.240}$$

Knowing θ_{d-2}, we can infer θ_{d-3} from $V_{d-3}^{(n)}$ and so on. In this sequential method we can determine all the polar angles θ_j's that specifies the state $|\psi\rangle^{(d)}$.

❑ Alternative Method to Infer the Polar Angles:

Here again, the θ_j's are determined by post-processing the interferograms obtained for $(d-1)$-th subspace, $(d-2)$-th subspace and so on in this particular sequence, as determination of θ_k requires the knowledge of θ_{k+1} and here we can use the already known information that $\theta_d = 0$. But, alternatively we can directly obtain θ_1 and θ_2 by simultaneously solving the following expressions,

$$V_1^{(n)} = \frac{4\sin(\theta_1)\cos\left(\dfrac{\theta_2}{2}\right)}{5+\cos(\theta_2)+\cos(\theta_1)(3-\cos(\theta_2))} \tag{4.241}$$

$$\bar{I}_1^{(n)} = \frac{5+\cos(\theta_2)+\cos(\theta_1)(3-\cos(\theta_2))}{4\left[3+\cos(\theta_2)+\cos(\theta_1)(1-\cos(\theta_2))\right]} \tag{4.242}$$

Once we know θ_1, θ_2 we can obtain θ_3 from experimentally obtained quantities $\bar{I}_2^{(n)}$ or $V_2^{(n)}$.

In summary, considering the normalized form of the expectation values or considering normalization of the state $|\psi\rangle_k^{(2;d)}$, the azimuthal angles ϕ_j's and the polar angles θ_j's can be determined from the argument and the magnitude of the expectation value of the spin ladder operator $\hat{\sigma}_{\pm}^{(k)}$ only. Experimentally, ϕ_j's can be determined from the phase shift of the interferograms associated with respective subspaces and θ_j's can be determined either from the visibility or the average intensity computed from the interferograms. The advantage of considering the normalization is that the polar angle determination requires any one quantity, either average intensity or the visibility, to be computed from the interferograms, thus it reduces the amount of post-processing required for inferring the unknown qudit state $|\psi\rangle^{(d)}$ compare to the method without normalization.

4.B QSI for Qudit: Estimating Losses in Schemes with (d-1) Interferometers vs Two Interferometers

In Sec. 4.3 and Sec. 4.4 we have shown how a single interferometric setup can be employed to characterize a pure state of a d-dimensional quantum system, i.e., a pure qudit $|\psi\rangle^{(d)}$. The interferometric information such as the phase shift, phase averaged intensity, and visibility obtained from $(d-1)$ interferograms produced in the setup, are processed to infer the $(2d-2)$ parameters required to uniquely specify a state $|\psi\rangle^{(d)}$. However, the scheme presented in Sec. 4.3 requires setting up $(d-1)$ two path interferometers (described using MZI), each for one of the two-dimensional sub-spaces of the d-dimensional space arranged in a particular sequence. A single interferometer (say, the k-th interferometer) produces one interferogram $I_k(\epsilon_k)$ by performing single qubit QSI on the component $|\psi\rangle_k^{(2;d)}$ associated with the k-th two-dimensional subspace spanned by $\{|k\rangle, |k+1\rangle\}$. In order to select the component related to a particular subspace (say, k-th subspace) within one interferometer, the incident beam in the state $|\psi\rangle^{(d)}$ is split into d beams in the d eigen modes of $\hat{\sigma}_z^{[d]}$ operator and all the beams except the two beams in states $|k\rangle$ and $|k+1\rangle$ are blocked. Therefore, this scheme for inferring an unknown pure qudit utilizes only $\left(\dfrac{2}{d}\right) \cdot N$ number of particles out of N particles incident on the setup in the state $|\psi\rangle^{(d)}$.

However, the scheme described in Sec. 4.4 utilizes only two interferometers to infer the unknown state $|\psi\rangle^{(d)}$ incident on the setup. Here, $(d-1)$ interferograms are generated by performing single qubit QSI on all the two-dimensional components $|\psi\rangle_k^{(2;d)}$ of $|\psi\rangle^{(d)}$ (where k ranges from 1 to $(d-1)$) at once, applying the necessary operators altogether. The first interferometer in the setup selects the component states $|\psi\rangle_k^{(2;d)}$ associated with two-dimensional subspaces, by blocking only half of the particles belonging to the extreme eigenstates of $\hat{\sigma}_z^{[d]}$ operator. Therefore, $\left(\dfrac{d-1}{d}\right) \cdot N$ number of particles evolve through the second interferometer, which generates $(d-1)$ interferograms at the end of the setup, processing which the unknown qudit state can be inferred. Thus, the loss associated with the QSI scheme employing 2 interferometers is $\mathcal{O}\left(\dfrac{1}{d}\right)$ as compared to loss $\mathcal{O}\left(\dfrac{d-2}{d}\right)$ for the scheme employing $(d-1)$ interferometers. Therefore, the comparison shows that the losses are negligible for the scheme with two interferometers for higher dimensional state reconstruction and hence it provides an efficient single shot qudit state determination procedure over the procedure with $(d-1)$ interferometers.

References

[1] Michael A. Nielsen and Isaac L. Chuang. *Quantum Computation and Quantum Information: 10th Anniversary Edition*. Cambridge University Press, 2010. DOI: 10.1017/CBO9780511976667.

[2] Julio A. López-Saldívar et al. “Qubit representation of qudit states: correlations and state reconstruction”. In: *Quantum Information Processing* 18.7 (2019), p. 210. DOI: 10.1007/s11128-019-2327-1.

[3] Rahul Bijurkar. *Representation of Qudits on a Riemann Sphere*. 2007.

[4] Gen Kimura. “The Bloch vector for N-level systems”. In: *Physics Letters A* 314.5 (2003), pp. 339–349. DOI: 10.1016/S0375-9601(03)00941-1.

[5] Jeffrey R. Weeks. *The shape of space: how to visualize surfaces and three-dimensional manifolds*. Monographs and textbooks in pure and applied mathematics 96. M. Dekker, 1985.

[6] Marvin Jay Greenberg. *Euclidean and Non-Euclidean Geometries. Development and History*. Third Edition. W. H. Freeman, 1993.

[7] Sommerville D. *An introduction to the geometry of N dimensions*. Methuen, 1959.

[8] Gen Kimura and Andrzej Kossakowski. “The Bloch-Vector Space for N-Level Systems: the Spherical-Coordinate Point of View”. In: *Open Systems & Information Dynamics* 12.03 (2005), pp. 207–229. DOI: 10.1007/s11080-005-0919-y.

[9] Christopher Eltschka et al. “The shape of higher-dimensional state space: Bloch-ball analog for a qutrit”. In: *Quantum* 5 (2021), p. 485. DOI: 10.22331/q-2021-06-29-485.

[10] Ettore Majorana. “Atomi orientati in campo magnetico variabile”. In: *Il Nuovo Cimento (1924-1942)* 9 (1932), pp. 43–50. DOI: 10.1007/BF02960953.

[11] J. Schwinger. “The Majorana Formula”. In: *Transactions of the New York Academy of Sciences* 38 (1977), pp. 170–184.

[12] N. Wheeler. “Majorana Representation of Higher Spin States”. In: *Reed College* (2000).

[13] F. Bloch and I. I. Rabi. "Atoms in Variable Magnetic Fields". In: *Rev. Mod. Phys.* 17 (2-3 1945), pp. 237–244. DOI: 10.1103/RevModPhys.17.237.

[14] Shruti Dogra, Kavita Dorai, and Arvind. "Majorana representation, qutrit Hilbert space and NMR implementation of qutrit gates". In: *Journal of Physics B: Atomic, Molecular and Optical Physics* 51.4 (2018), p. 045505. DOI: 10.1088/1361-6455/aaa69f.

[15] L. E. Blumenson. "A Derivation of n-Dimensional Spherical Coordinates". In: *The American Mathematical Monthly* 67.1 (1960), pp. 63–66.

[16] Ryan A. Rubenzahl. "Small Oscillations of the n-Pendulum and the "Hanging Rope" Limit $n \to \infty$". In: 2017.

[17] David Acheson. *From calculus to chaos: an introduction to dynamics*. Oxford University Press, 1997.

[18] Jianxin Chen et al. "Uniqueness of quantum states compatible with given measurement results". In: *Phys. Rev. A* 88 (1 2013), p. 012109. DOI: 10.1103/PhysRevA.88.012109.

[19] Walther Gerlach and Otto Stern. "Der experimentelle Nachweis der Richtungsquantelung im Magnetfeld". In: *Zeitschrift für Physik* 9.1 (1922), pp. 349–352. DOI: 10.1007/BF01326983.

[20] J. F. Van Huele and Jared R. Stenson. "Stern-Gerlach experiments : past , present , and future". In: 2004.

[21] David J. Griffiths and Darrell F. Schroeter. *Introduction to Quantum Mecanics*. eng. Third edition. Cambridge University Press, 2018.

[22] B. H. Bransden and C. J. Joachain. *Physics of atoms and molecules*. eng. 2nd ed. Harlow, England: Prentice Hall Harlow, England, 2003.

[23] Christophe Couteau. "Spontaneous parametric down-conversion". In: *Contemporary Physics* 59.3 (2018), pp. 291–304. DOI: 10.1080/00107514.2018.1488463.

[24] Robert W. Boyd. *Nonlinear Optics, Third Edition*. 3rd. USA: Academic Press, Inc., 2008.

[25] J.B. Altepeter, E.R. Jeffrey, and P.G. Kwiat. “Photonic State Tomography”. In: ed. by P.R. Berman and C.C. Lin. Vol. 52. Advances In Atomic, Molecular, and Optical Physics. Academic Press, 2005, pp. 105–159. DOI: https://doi.org/10.1016/S1049-250X(05)52003-2.

[26] Daniel F. V. James et al. “Measurement of qubits”. In: *Phys. Rev. A* 64 (5 2001), p. 052312. DOI: 10.1103/PhysRevA.64.052312.

[27] Mark M. Wilde. *Quantum Information Theory*. Cambridge University Press, 2013. DOI: 10.1017/CBO9781139525343.

[28] A. Einstein, B. Podolsky, and N. Rosen. “Can Quantum-Mechanical Description of Physical Reality Be Considered Complete?” In: *Phys. Rev.* 47 (10 1935), pp. 777–780. DOI: 10.1103/PhysRev.47.777.

[29] E. Schrödinger. “Discussion of Probability Relations between Separated Systems”. In: *Mathematical Proceedings of the Cambridge Philosophical Society* 31.4 (1935), pp. 555–563. DOI: 10.1017/S0305004100013554.

[30] Charles H. Bennett and Stephen J. Wiesner. “Communication via one- and two-particle operators on Einstein-Podolsky-Rosen states”. In: *Phys. Rev. Lett.* 69 (20 1992), pp. 2881–2884. DOI: 10.1103/PhysRevLett.69.2881.

[31] Charles H. Bennett et al. “Teleporting an unknown quantum state via dual classical and Einstein-Podolsky-Rosen channels”. In: *Phys. Rev. Lett.* 70 (13 1993), pp. 1895–1899. DOI: 10.1103/PhysRevLett.70.1895.

[32] Dik Bouwmeester et al. “Experimental quantum teleportation”. In: *Nature* 390.6660 (1997), pp. 575–579. DOI: 10.1038/37539.

[33] Artur K. Ekert. “Quantum cryptography based on Bell’s theorem”. In: *Phys. Rev. Lett.* 67 (6 1991), pp. 661–663. DOI: 10.1103/PhysRevLett.67.661.

[34] Charles H. Bennett, Gilles Brassard, and N. David Mermin. “Quantum cryptography without Bell’s theorem”. In: *Phys. Rev. Lett.* 68 (5 1992), pp. 557–559. DOI: 10.1103/PhysRevLett.68.557.

[35] Klaus Mattle et al. “Dense Coding in Experimental Quantum Communication”. In: *Phys. Rev. Lett.* 76 (25 1996), pp. 4656–4659. DOI: 10.1103/PhysRevLett.76.4656.

[36] Gilbert Grynberg et al. *Introduction to Quantum Optics: From the Semi-classical Approach to Quantized Light*. Cambridge University Press, 2010. DOI: 10.1017/CBO9780511778261.

[37] Matteo Fadel et al. “Entanglement Quantification in Atomic Ensembles”. In: *Phys. Rev. Lett.* 127 (1 2021), p. 010401. DOI: 10.1103/PhysRevLett.127.010401.

[38] Ryszard Horodecki et al. “Quantum entanglement”. In: *Rev. Mod. Phys.* 81 (2 2009), pp. 865–942. DOI: 10.1103/RevModPhys.81.865.

[39] Charles H. Bennett et al. “Concentrating partial entanglement by local operations”. In: *Phys. Rev. A* 53 (4 1996), pp. 2046–2052. DOI: 10.1103/PhysRevA.53.2046.

[40] R. D. Sorkin. “On the Entropy of the Vacuum Outside a Horizon”. In: *General Relativity and Gravitation, Volume 1*. Ed. by B. Bertotti, F. de Felice, and A. Pascolini. Vol. 1. 1983, p. 734.

Chapter 5

Quantum Measure Theory and Measuring the Quantum Measure

Contents

5.1 Introduction: Conventional Quantum Theory to Quantum Measure Theory

5.2 Quantum Measure Space: A Brief Overview

5.3 Generalized Experimental Scheme for Measuring the Quantum Measure

5.4 Determination of Quantum Measure in Photonic Systems

5.5 Inferring the Quantum Measure of a Photonic Event: An Experimental Demonstration

5.6 Conclusion

5.A Histories Approach to Quantum Theory: State Based Formalism to History Based Formalism

In standard quantum physics, the comprehensive description of a micro-system is centered around the wave function, the knowledge of which enables one to make predictions about the probabilistic outcomes of a measurement performed on the system. However, wave functions, so far, are complex-valued abstract mathematical constructs without any tangible physical meaning assigned to them. As a result, we still lack a realistic description of the micro-world. Over the decades, several alternative interpretations of quantum theory have been introduced, each attempting to provide a more "realistic" understanding of the micro-system from different perspectives. Quantum Measure Theory (QMT), introduced in 1994, is one such alternative viewpoint to quantum theory based on the path-integral or the related sum over histories approach. It considers the histories of a micro-system as the elements of reality and interprets the probabilistic behavior of a quantum system from the perspective of a suitably generalized theory of Stochastic processes. Unlike the customary point of view, QMT provides an observer-independent and space-time realist interpretation of quantum theory, characterizing micro-systems in terms of histories instead of wave functions. The histories in this approach take into account the entire physical processes of the micro-systems from the start, thereby connecting the micro-world with practical scenarios. This history-based formalism generalizes the concept of probability measure to accommodate quantum interference and assigns a 'generalized probability', also referred to as 'quantum measure', to the set of histories associated with the system. The 'quantum measure' differs from the traditional probability measure and can even surpass the classical upper limit of one, revealing non-classical behaviors in the presence of interference.

In this chapter, we present a study of a two-site hopper within the context of QMT and develop the concepts that would be useful to perform a table-top experiment for measuring the 'quantum measure' associated with a chosen set of histories. Here, at first, we provide some background helpful for understanding the significance of reformulating quantum theory as history-based generalized probability theory, along with highlighting the key concepts that makes QMT different from the standard quantum theory. Next, a discussion on the existing theoretical proposal for inferring the value of 'quantum measure' will be presented, including an introduction to ideas such as event filtering and ancilla based path marking etc. within an experimental scenario. Finally, we explore potential designs for an 'event filter' in an optical setup allowing interference, for a specific hopper event, with an objective of capturing the non-classical nature of the 'quantum measure'.

5.1 Introduction: Conventional Quantum Theory to Quantum Measure Theory

A micro-system, in the conventional mathematical formalism of quantum theory, is described by a wave function that is defined within a Hilbert space, and the dynamics of the system is governed by the Schrödinger wave equation that allows a unitary time evolution of the wave function under a particular Hamiltonian. A property of the system manifests itself through the outcome of a measurement [1], performed on the given system, of an observable − a Herimitian operator. The probability distribution of different possible outcomes of a measurement can be obtained using the Born rule [2] from the knowledge of the wave function and the observable that is being measured. Although the predictions made by this formalism have always been found to be consistent with the experimental results, the theory appears to be inadequate as it fails to comment on the reality of the micro-system, prior to an observation. Consequently, the physical procedures occurring at intermediate times between the preparation and the detection associated with the measurement process remain a mystery. The two questions − "*Is it possible to assign an ontological meaning to the wave function?*" [3, 4] and "*What exactly happens during a measurement procedure from the preparation to the observation?*" − have remained a subject of continuing debates [5] and lie at the core of the quantum measurement problem [6].

Here, a non-perturbing, minimally disturbing, measurement scheme − weak measurement (WM) [7, 8], described within the standard formalism, comes to the rescue providing a tool that attempts to extract the system information at an intermediate time during its evolution from the pre-measurement state (i.e., the pre-selection) to the final state (i.e., the post-selection). However, the information obtained from the WM can not be considered to be complete as the results of this measurement i.e., the 'weak values' are limited up to the first-order approximation. Also, from the weak value one can only infer the average system property between an initial state and a *given* final state − no answers could be provided to the question asking for the mechanism or the physical process behind the state reduction.

Amidst all the interpretational debates and the attempts to provide a complete description of the quantum system and its behaviors, there lies the fact that the conventional theory of quantum mechanics puts significant emphasis on the process of measurement, based on an apriori division of the universe into an observer (classical system) and observed (quantum system). However, the theory presumes this division without providing any coherent account of the "Heisenberg's cut" [9, 10]. This led to the need for establishing a more realistic and unified approach to quantum theory that can extend its field of applicability beyond the experiments or observations and consistently describe physical systems in both the micro and macro worlds within a single framework.

In quantum mechanics, wave functions are conceptualized as functions of space evolving continuously over time. In contrast, the covariant description of gravitational physics involves concepts that are global to space-time. This space-time description is more intuitive in the context of Quantum Field Theory and High Energy Physics. Therefore, it has been argued that Feynman's path integral approach [11] or more generally, the sum over histories approach [12] towards quantum dynamics is more appropriate in adapting quantum mechanics in the framework of general relativity [13]. This allies with the philosophy of "gravitizing quantum mechanics" [14] i.e., modifying quantum mechanics in a way that fits well with the description of general relativity. This is in contrast to "quantization of gravity" (alternately referred to as "quantizing gravity") i.e., making the description of gravitational physics fit along the lines of the existing formulation of quantum mechanics and quantum field theory [15].

Moreover, getting rid of the concepts like wave functions, observables, observers and state reduction in a new quantum formalism would render it more applicable in the context of cosmology and study of the early universe [16]. This is due to the fact that the physics of the early universe, where quantum effects cannot be neglected, do not present any natural way to discriminate state preparation and measurement, unlike a laboratory setting. Additionally, in the realm of cosmology no recognizable observer or concepts like measurement could exist, nor could any aspect of physics of that epoch be associated with these concepts. The quantum measure theory (QMT) is such a formalism that allows the description without any inherent need for functions evolving in time providing the correct dynamical framework for quantum gravity [17, 18]. This space-time history based formalism offers a fresh perspective to the behavior of the micro-system and attempts to resolve the existing interpretational challenges.

5.1.1 Quantum Measure Theory: An Alternate Formulation

Quantum Measure Theory (QMT) appears to provide a realist space-time formulation to quantum mechanics based on sum over histories [12] or path integral approach [11]. It interprets the behavior of a quantum system from the perspective of generalized stochastic theory [19]. According to this approach, the kinematics of a micro-system is described in terms a 'history' and the dynamics is governed by a kind of quantum stochastic law of motion for the histories [20]. A *history* in this framework is considered as the basic element of reality throughout space-time and is defined as the finest piece of information, conceivable in the theory, which can provide the most complete description of the physical reality of a given system. For example, the history of a particle would be its potential space-time trajectories; for a field, the history would be the possible space-time configurations, and so on. In general, the definition of history depends on the system one is dealing with and the context or any adopted model that can best describe the system. An *event* is then defined as a set of histories related to the system, which is mapped to a non-negative real number called the *quantum measure* that encodes the inherently probabilistic nature of the micro-system. Quantum measure generalizes the classical notion of probability measure, so as to incorporate quantum interference. This history-based formulation of the quantum theory is akin to the generalization of classical stochastic dynamics rather than classical Hamiltonian dynamics [21] and presents itself as a global realist approach toward quantum foundations. To be compatible with relativity, the 'events' in the history space, rather than measurement outcomes in quantum descriptions need to respect the causal structure.

5.2 Quantum Measure Space: A Brief Overview

A measure space is fundamental to measure theory which consists of a *measurable space* and a *measure* on it [22]. Classical measure space, such as a probability space in probability theory, is composed of the triple $(\Omega, \mathcal{A}, \mathbb{P})$; where Ω is the *sample space* which is the space over possible realities, $\mathcal{A}$ is the *set algebra* which is a set of all possible measurable subsets of the sample space Ω i.e., a σ-algebra on Ω, and $\mathbb{P}$ is the *measure* which is a function that systematically assigns numerical values to the elements of $\mathcal{A}$. The set algebra $\mathcal{A}$ is a subset of the power set $\mathcal{P}(\Omega)$ of Ω. When Ω is finite, we have $\mathcal{A} = \mathcal{P}(\Omega)$. In the context of probability theory, the classical measure is a probability measure over the sample space having the values between 0 to 1, i.e., $\mathbb{P} : \mathcal{A} \mapsto [0, 1]$. The probability measure $\mathbb{P}$ obeys the probability sum rule. Hence, the probability of occurrence of the events A or B, where A and B are the elements of the set algebra $\mathcal{A}$, is the same as the sum of the probabilities of occurrences of the individual events, i.e., $\mathbb{P}(A \cup B) = \mathbb{P}(A) + \mathbb{P}(B)$.

Similarly, the measure space in quantum measure theory for a *given* system is defined by the triple $(\Omega, \mathcal{A}, \mu)$; where Ω is the *history space* which is a space over all possible realities of the system, $\mathcal{A}$ is the *event algebra* which is the set of all possible sets of histories in Ω (in other words all possible subsets of Ω) including the empty set Φ and the complete set Ω itself, to which a measure can be assigned and μ is the *quantum measure* which is a function that maps each element of the event algebra to a real positive number, i.e., $\mu : \mathcal{A} \mapsto \mathbb{R}^+$. The elements of $\mathcal{A}$ are the potential *events* associated with the given system. Unlike classical measure space, quantum measure space allows for interference, and hence, the values of quantum measure can not simply be interpreted as the probability measure in the usual sense (except for some special cases). Quantum measure (μ) neither obeys the probability sum rule nor has an upper bound of one.

The quantum measure μ can be characterized by certain positivity conditions that generalize the Kolmogorov sum rule for probabilities. The mathematical expression for the quantum measure of an event $E = \{\gamma^1, \gamma^2, ...\}$ comprising of a finite number number of histories γ^k is given by,

$$\mu(E) = \sum_{\gamma^i, \gamma^j \in E} A(\gamma^i) A^*(\gamma^j) \delta_{\gamma^i_{end}, \gamma^j_{end}} \tag{5.1}$$

The above formula is obtained by using the path integral formalism within the framework of quantum measure theory. Here, $A(\gamma^i)$ represent the amplitude of the history γ^i that comprise the event E (similarly, $A(\gamma^j)$ is the amplitude of the history γ^j). The delta-function $\delta_{\gamma^i_{end}, \gamma^j_{end}}$ restricts the interference between the histories that end at the same point. The knowledge of the quantum measures for all the events of a given system enables one to make predictions about the system behavior similar to the Born rule probability in standard quantum formalism.

The concept of Preclusion is the central theme behind the interpretation of Quantum Mechanics from the perspective of generalized stochastic theory. The concept of preclusion says that a real history does not belong to a null set, i.e., a set with measure zero. Hence, if a real history $\gamma_r \in \Omega$, then $\mathbb{P}(E) = 0$ implies that $\gamma_r \notin E$.

5.2.1 Quantum Measure as Generalized Probability

Quantum measure theory generalizes the mathematical description of measure space by incorporating quantum interference. Consequently, the 'quantum measure' provides a broader perspective following a generalized sum rule and allowing the values beyond the classical upper limit of one related to the conventional probability measure. Here, we will illustrate how the intuitive concept of probabilities can be generalized to quantum measure. We would use the slit system as an example because the path integral is equivalent to the familiar Huygens scalar wave theory.

In Young's double slit experiment, the resultant wave at the detector plane when two slits are open is often calculated as the superposition of the two waves associated with the conditions when each individual slit is open. Thus, if $|\psi_A(x)\rangle$ represents the wavefunction when only slit A is open (slit B is closed) and $|\psi_B(x)\rangle$ represents the wavefunction when only slit B is open (slit A is closed), then according to the superposition principle the wave function $|\psi_{AB}(x)\rangle$ when both slit A and slit B are open, is given by

$$|\psi_{AB}(x)\rangle = |\psi_A(x)\rangle + |\psi_B(x)\rangle \tag{5.2}$$

However, in this new approach to quantum theory based on the path integrals, we aim to do away with wave functions. Instead, we would aim to describe the system directly in terms of the probabilities, which according to the standard formalism is given by the Born rule [23]. This would be comparable with the experimental results as well because, unlike the wave functions, the probability measures can be determined directly in an experiment.

According to the standard formalism of quantum theory, the probabilities that a system would travel through slit A and slit B are respectively given as $P_A(x) = |\psi_A(x)|^2$ and $P_B(x) = |\psi_B(x)|^2$, which could be obtained by placing detectors just after the respective slits. However, we know that in quantum mechanics, the probability of detection when both the slits are open is not the same as the sum of the individual probabilities, i.e., $P_{AB}(x) \neq P_A(x) + P_B(x)$. Therefore, the way the probabilities are added needs to be generalized. In the new formalism, instead of standard Kolmogorov probabilities, we would associate a non-negative real number, called the *quantum measure*, to each individual set of histories, i.e., to each 'event'.

Here in the two-slit example, a non-negative real number $\mu_{\mathcal{A}}$ [and $\mu_{\mathcal{B}}$] is assigned to the set $\mathcal{A} \equiv \{\gamma_A\}$ [and $\mathcal{B} \equiv \{\gamma_B\}$] of histories γ_A [and γ_B] corresponding to a quantum particle going through slit A [and slit B]. When the two slits are open, the measures $\mu_{\mathcal{A}}$ and $\mu_{\mathcal{B}}$ cannot be simply added to get the measure $\mu_{\mathcal{A}\cup\mathcal{B}}$, where $\mathcal{A} \cup \mathcal{B}$ represents the disjoint union of the two sets $\mathcal{A}$ and $\mathcal{B}$. The measure $\mu_{\mathcal{A}\cup\mathcal{B}}$ is associated with the 'event' $\mathscr{E} = \mathcal{A} \cup \mathcal{B} \equiv \{\gamma_A, \gamma_B\}$ corresponding to a particle going through any one of the slits A or B producing an interference pattern at the end (i.e., on the detection plane). To account for the interference when both the slits are open, an interference term $\mathcal{I}^{(2)}_{\mathcal{A},\mathcal{B}}$ needs to be included in the description of $\mu_{\mathcal{A}\cup\mathcal{B}}$. The superscript represents the order of interference, i.e., here for $\mathcal{I}^{(2)}_{\mathcal{A},\mathcal{B}}$ the superscript '(2)' implies that the interference is to be expressed in terms of the pairs of the alternatives (here the paths through the individual slits). For two slits (A and B), this interference term is defined as follows,

$$I^{(2)}_{\mathcal{A},\mathcal{B}} = \mu_{\mathcal{A}\cup\mathcal{B}} - (\mu_{\mathcal{A}} + \mu_{\mathcal{B}}) \tag{5.3}$$

From the double-slit interference experiments, we know that the difference between the measure when both slits A and B are open simultaneously and the sum of the individual measures when individual slits A or B is open, is non-zero, i.e., $\mu_{\mathcal{A}\cup\mathcal{B}} - (\mu_{\mathcal{A}} + \mu_{\mathcal{B}}) \neq 0$. This implies that the second-order interference term is non-zero, i.e., $\mathcal{I}^{(2)}_{\mathcal{A},\mathcal{B}} \neq 0$. Therefore, for a quantum system the second-order sum rule [1] does not hold true. Hence,

[1]For a double slit, where there can be two sets of histories $\mathcal{A} \equiv \{\gamma_A\}$ and $\mathcal{B} \equiv \{\gamma_B\}$, a sum rule would indicate $\mu_{\mathcal{A}\cup\mathcal{B}} = \mu_{\mathcal{A}} + \mu_{\mathcal{B}}$.

$$\mu_{\mathcal{A}\cup\mathcal{B}} \neq \mu_{\mathcal{A}} + \mu_{\mathcal{B}} \tag{5.4}$$

However, the above sum rule associated with two-path interference can be extended to higher-order sum rules. For a three-slit system (say, the slits are A, B, C), the interference term by generalized extension of the expression in Eqn. 5.3 can be written as,

$$\mathcal{I}^{(3)}_{\mathcal{A},\mathcal{B},\mathcal{C}} = \mu_{\mathcal{A}\cup\mathcal{B}\cup\mathcal{C}} - (\mu_{\mathcal{A}\cup\mathcal{B}} + \mu_{\mathcal{B}\cup\mathcal{C}} + \mu_{\mathcal{C}\cup\mathcal{A}}) + (\mu_{\mathcal{A}} + \mu_{\mathcal{B}} + \mu_{\mathcal{C}}) \tag{5.5}$$

The above expression for the third-order interference term $\mathcal{I}^{(3)}_{\mathcal{A},\mathcal{B},\mathcal{C}}$ is obtained by subtracting the measures for all possible combinations of two-slit configurations (i.e., at a time two slits are open with the other one being blocked) from the measure for the three-slit configuration (i.e., all the three slits are open at the same time) and adding the measures for all possible one-slit configurations (i.e., only one slit out of the three is open at a time) to the result. The additive properties of quantum measures can be completed with the two-path interference terms, if $\mathcal{I}^{(3)}_{\mathcal{A},\mathcal{B},\mathcal{C}} = 0$. Using the expressions for the second-order interferences given in Eqn. 5.3, in the Eqn. 5.5 with the consideration $\mathcal{I}^{(3)}_{\mathcal{A},\mathcal{B},\mathcal{C}} = 0$, we get

$$\mu_{\mathcal{A}\cup\mathcal{B}\cup\mathcal{C}} = \mu_{\mathcal{A}} + \mu_{\mathcal{B}} + \mu_{\mathcal{C}} + \mathcal{I}^{(2)}_{\mathcal{A},\mathcal{B}} + \mathcal{I}^{(2)}_{\mathcal{B},\mathcal{C}} + \mathcal{I}^{(2)}_{\mathcal{C},\mathcal{A}} \tag{5.6}$$

Further, expanding the expression for measure with three alternatives in terms of the measure of two alternatives, i.e, expressing $\mu_{\mathcal{A}\cup\mathcal{B}\cup\mathcal{C}} = \mu_{(\mathcal{A}\cup\mathcal{B})\cup\mathcal{C}} = \mu_{\mathcal{A}\cup\mathcal{B}} + \mu_{\mathcal{C}} + \mathcal{I}^{(2)}_{\mathcal{A}\cup\mathcal{B},\mathcal{C}}$ and using $\mu_{\mathcal{A}\cup\mathcal{B}} = \mu_{\mathcal{A}} + \mu_{\mathcal{B}} + \mathcal{I}^{(2)}_{\mathcal{A}\cup\mathcal{B}}$ we get the third-order interference term from Eqn. 5.5 as the following,

$$\mathcal{I}^{(3)}_{\mathcal{A},\mathcal{B},\mathcal{C}} = \mathcal{I}^{(2)}_{\mathcal{A}\cup\mathcal{B},\mathcal{C}} - \mathcal{I}^{(2)}_{\mathcal{A},\mathcal{C}} - \mathcal{I}^{(2)}_{\mathcal{B},\mathcal{C}} \tag{5.7}$$

The above expression would have a similar form if instead of considering overlap between the sets $\mathcal{A}$ and $\mathcal{B}$, we have considered the measure $\mu_{\mathcal{A}\cup\mathcal{B}\cup\mathcal{C}}$ as $\mu_{\mathcal{A}\cup(\mathcal{B}\cup\mathcal{C})}$ or $\mu_{(\mathcal{A}\cup\mathcal{C})\cup\mathcal{B}}$. Therefore, given the third order sum rule, i.e., $\mathcal{I}^{(3)}_{\mathcal{A},\mathcal{B},\mathcal{C}} = 0$, the second order interference terms appears to be *bi-additive*, equivalent to the inner products in the Hilbert space theory of the standard quantum formalism [19].

$$\mathcal{I}^{(2)}_{\mathcal{A}\cup\mathcal{B},\mathcal{C}} = \mathcal{I}^{(2)}_{\mathcal{A},\mathcal{C}} + \mathcal{I}^{(2)}_{\mathcal{B},\mathcal{C}} \tag{5.8}$$

Generalizing the expression of third-order interference term in Eqn. 5.7, preserving the bi-additivity, the $(n+1)$-th order interference term $\mathcal{I}^{(n+1)}$ can be related with the n-th order interference terms $\mathcal{I}^{(n)}$ as the following:

$$\mathcal{I}^{(n+1)}_{(\{\mathcal{A}_k\})} = \mathcal{I}^{(n)}_{(\mathcal{A}_i\cup\mathcal{A}_j,\{\mathcal{A}_k\}|k\neq i,j)} - \mathcal{I}^{(n)}_{(\{\mathcal{A}_k\}|k\neq j)} - \mathcal{I}^{(n)}_{(\{\mathcal{A}_k\}|k\neq i)} \tag{5.9}$$

Therefore, if $\mathcal{I}^{(n)} = 0$ then we get $\mathcal{I}^{(n+1)} = 0$; i.e., all higher-order interference terms would be inductively shown to be zero if any one of the interference terms in the hierarchy of the sum rules becomes zero [18].

In the standard description of the wave mechanics, if we assume the validity of the superposition principle for the wave function in the slit based interference experiments along with the Born rule from which we can compute the probability as the modulus square of the wave functions [24], then for the triple slit experiment we get the interference term $\mathcal{I}^{(3)}_{\mathcal{A},\mathcal{B},\mathcal{C}} = 0$. Although, till now there has been no observed deviation from the Born rule where amplitude division has been used [25], the fact that the superposition principle cannot be naively applied with wavefront divisions leads to a deviation which has been reported both in classical [26] and quantum domain [27]. The deviation, however, can be accounted for if the higher-order Feynman paths are considered in the theory.

The superposition principle is applicable if we restrict ourselves to the set of paths that cross the slit plane once. When we include paths that cross the slit plane more than once, the deviation of the results from the superposition principle can be qualitatively explained [28, 29]. It can be hypothesized that the deviation can be exactly characterized when all possible Feynman paths are included. The sum over histories approach of Quantum Measure Theory (QMT) is closer to the Feynman path integral formalism and aims to not use the wave functions and the associated superposition principle and the Born rule as a core part of the formalism. Thus, Quantum measure theory can be considered as an alternative formulation for quantum mechanics based on the path-integral approach that gives a generalized form of the probability theory and the 'quantum measure' can be considered as the 'generalized probability'.

5.2.2 Different Types of Events and the Quantum Measure

An event, in Quantum Measure Theory, is defined as a set of histories that can be mapped to a 'generalized probability' or 'quantum measure'. Here, the events are broadly classified into two categories, (i) Instrument events and (ii) Non-instrument events, which might also be referred to as system events. *Instrument events* are those that only consider the histories of an instrument. By "instrument" here we mean a piece of measuring apparatus that exhibits macroscopic behavior and by instrument's history we refer to the elements that describe this macroscopic behavior corresponding to different outputs of the instrument. For example, a detector can have a history space defined as $\Omega_I \equiv \{\checkmark, \times\}$; where $\checkmark$ and $\times$ are the two histories of the detector respectively corresponding to the two classically admissible outputs of the instrument, which are "click" and "not-click" of the detector. Hence, the event algebra $\mathcal{A}_I$ would consist of four possible instrument events $\Phi, \{\checkmark\}, \{\times\}, \{\checkmark, \times\}$, with the measures of the first and the last events being 0 and 1 respectively. The measure $\mu_\checkmark$ of the event $\{\checkmark\}$ gives the probability of 'click', directly implying the probability of detection in an experiment provided $\mu_\checkmark + \mu_\times = 1$.

Non-instrument events, on the other hand, are those that consider the histories not associated with an instrument, specifically any measuring apparatus. For example, the photonic events associated with a photon encountering a lossless optical beam splitter. Here, the two histories $\mathcal{T}$ and $\mathcal{R}$, respectively representing the paths of the photon undergoing transmission or reflection through the beam splitter, form the history space $\Omega_{NI} \equiv \{\mathcal{T}, \mathcal{R}\}$. The associated event algebra $\mathcal{A}_{NI}$ consists of four possible non-instrument (photonic) events $\Phi, \{\mathcal{T}\}, \{\mathcal{R}\}, \{\mathcal{T}, \mathcal{R}\}$ with the measures $\mu(\Phi) = 0$ and $\mu(\{\mathcal{T}, \mathcal{R}\}) = 1$. Further, for an ideal lossless beam splitter $\mu_\mathcal{T} + \mu_\mathcal{R} = 1$, where $\mu_\mathcal{T} = \mu(\{\mathcal{T}\})$ and $\mu_\mathcal{R} = \mu(\{\mathcal{R}\})$ respectively represent the probabilistic behavior of the photon. This is an example of the simplest non-instrument event involving one device (here, a beam splitter), where the quantum measures $\mu_\mathcal{T}$ and $\mu_\mathcal{R}$ are the same as the probabilities of transmission and reflection.

Non-instrument events, however, can be more complex in the presence of multiple devices with multiple output ports in the path of the system. Interference might be involved in non-instrument events consisting of the histories that terminate at the same point. The quantum measure might not be interpreted as the ordinary probability measure for these non-instrument events. Note that microscopic events similar to the photonic events in the above example also take place inside a measuring apparatus, like the events related to the motion of the electrons within the electrical circuit of the detector. However, as long as the detector functions properly, these microscopic events are of secondary importance as they do not significantly impact the macroscopic behavior of the instrument.

Although the non-instrument events are not directly observable, some of them can be inferred from instrument events. A simple example would be the following − when a photon encounters a beam splitter, we don't immediately know whether it has transmitted or reflected until a detector registers the photon either in the transmitting or in the reflecting port of the beam splitter. However, this kind of inference can only be made based on the assumption that the detector has high efficiency, i.e., the 'click' of the detector upon arrival of the photon has higher accuracy. Further, the dark counts of the detector can falsely imply photon arrivals, leading to non-instrument events being mistakenly identified. Therefore, inferring the occurrence of a non-instrument event from an instrument event relies on the assumption that there exists a perfect correlation between the two classes of events considering the specifications of the instrument (detector) being used.

The non-instrument events or the system events are further classified as (i) Serial events and (ii) Non-serial events. *Serial events* are those that could, in principle, be directly inferred from an instrument event or from a sequence of instrument events, without the need for any ancilla. For example, in a setup with two beam splitters arranged in series, the event where a photon incident on the setup transmits through both the beam splitters is a serial event. Mathematically, a serial event can be realized with a sequence of projection operators and therefore, the occurrence of such an event can be directly identified from one of the outcomes of a measurement (as defined in standard formalism). The quantum measure of the serial events can not exceed unity. In contrast, *non-serial events* are those that can not be directly identified from the instrument events, as they can not be assigned with any physically realizable operation or a succession of operations. Detection of such events requires the use of ancilla. The information about the occurrence of the event can be processed through coupling ancillas to the system and designing an 'event filter' to extract the intended set of histories associated with the event. A detailed discussion on this will be provided in Section. 5.3.

Here, we present a practical scenario to clarify the distinction between serial and non-serial events. Consider a particle passing through two double slit setups, placed one after the other with a definite gap in between. Let A_1, B_1 represent the upper and lower slits in the first double slit-setup and A_2, B_2 represent the same in the second double slit-setup. So, for a particle traveling through this dual double-slit setup, the history space would be defined as $\Omega = \{A_1A_2,\ A_1B_2,\ B_1A_2,\ B_1B_2\}$. Now, the events like $E_1 = \{A_1A_2,\ B_1A_2\}$ or $E_2 = \{A_1A_2,\ A_1B_2\}$ are considered as the serial events, as they can be simply detected by a placing an instrument (here, a detecting screen) after the second slit-setup while blocking the slit B_2 for E_1 and A_2 for E_2. Even more simply, all the single history events, i.e., $\{A_1A_2\}$, $\{A_1B_2\}$, $\{B_1A_2\}$, $\{B_1B_2\}$ are serial events. All these serial events can be realized by blocking a subset of the slits to allow the particle to pass only through the desired set of paths. On the other hand, events like $E_3 = \{A_1A_2,\ B_1B_2\}$ or $E_4 = \{A_1B_2,\ B_1A_2\}$ are considered as non-serial events, as these events can not be realized simply by blocking a subset of slits, or the undesired paths. In the attempts to detect the events E_3 or E_4 on the screen, the effect of the other two paths that are not a part of this event can not be eliminated. All the three history events like $E_5 = \{A_1A_2,\ A_1B_2,\ B_1A_2\}$ or $\{A_1A_2,\ B_1A_2,\ B_1B_2\}$ are examples of non-serial events as well.

The standard Quantum Mechanics (QM) interprets the probability of an event from the probability of an outcome of a measurement or in this case, from the possible detection by an instrument. Hence, according to standard QM, probabilities are only meaningfully attributed to instrument events and the dynamics of a micro-system undergoing serial events can only be interpreted. Quantum Measure Theory (QMT), on the other hand, goes beyond standard QM by providing information about all kinds of events including non-serial events. By employing ancilla coupling and designing event filters, QMT broadens the scope of possible measurements beyond conventional definitions, which could pave the way for a deeper understanding of the micro-world.

5.3 Generalized Experimental Scheme for Measuring the Quantum Measure

The probabilistic behavior of a quantum system owing to its stochastic dynamics is characterized in terms of the 'generalized probability' or the 'quantum measure', which within the framework of Quantum Measure Theory (QMT) assigns a non-negative real number to every 'event' of the micro-system. The quantum measure, in general, provides a kind of non-classical probability that can not be interpreted as the ordinary probability measure (the Kolmogorov probability), since the value of quantum measure can exceed the classical upper limit of one due to interference permitted in QMT. However, in order to understand the practical significance of this quantity, which remained an abstract theoretical concept so far, the reference [30] proposes a generalized experimental procedure to determine the value of the 'quantum measure' of any desired event (instrument or non-instrument, serial or non-serial) associated with a quantum system. A successful implementation of this scheme, providing a more direct experimental footing to 'quantum measure', would take us a step forward toward resolving the foundational issues of quantum theory.

Here, we will describe the experimental scheme simply by considering the physical system to be a particle that passes through a succession of N similar devices, each with multiple (say, m number of) output ports. The particle incident on a device can be found in any one of the m output ports after emerging from the device. Thus, within this (N, m) kind of experimental setup, there would be m^N possible paths for the particle to take and they would form the history space $\Omega^{(N,m)}$ for the particle. Visualizing in terms of the standard quantum mechanics, each of the devices can be associated with an observable, which when acted on the system would reduce the system state to one of the eigen states of the observable defined within the m-dimensional Hilbert space. A history $\gamma \in \Omega^{(N,m)}$ in this scenario, could be viewed as a sequence of N eigenvalues, associated with the measurement outcomes of a set of N observables at successive moments of times $T_\gamma = \{t_1, t_2, \ldots, t_N\}$.

One of the examples for such a system-device combination could be a spin s particle traversing through N number of Stern-Gerlach (SG) devices oriented in different directions such that $d_i \neq d_{i+1}$. Here, d_i represents one of the possible local directions (in a plane transverse to the direction of propagation of the particles) of the inhomogeneous magnetic field of i-th SG device; eg. for a stream of particles propagating along local y direction, d_i could be any direction on the transverse $x-z$ plane. When the particle passes through any such device, it can be found in one of the $(2s+1)$ possible paths after the device, associated with the eigenvalues of the spin projection operator being filtered. Consider a setup, where a spin-1/2 particle passes through two SG devices oriented in z and x directions respectively. After the first device, the particle can be found either in the state $|\uparrow\rangle$ or in the state $|\downarrow\rangle$, corresponding to the eigenvalues $+1$ or -1 of the observable $\hat{Z}$. Next, when the particle enters the second device, it comes out in either $|\nearrow\rangle$ or $|\swarrow\rangle$ associated with the eigenvalues $+1$ or -1 of the observable $\hat{X}$ [2]. So, for this setup the possible paths that the particle can take are as follows: $\Omega_{SG}^{(2,2)} = \{Z_{+1}X_{+1},\ Z_{+1}X_{-1},\ Z_{-1}X_{+1},\ Z_{-1}X_{-1}\}$. The same situation can be achieved with a photon passing through two optical beam splitters (BS) placed one after the other. A photon incident on a beam splitter either gets transmitted or gets reflected, with the chance depending on the splitting ratio $T : R$ of the beam splitter [3]. The history space for the photon can be defined as $\Omega_{BS}^{(2,2)} = \{\mathcal{T}_1\mathcal{T}_2,\ \mathcal{T}_1\mathcal{R}_2,\ \mathcal{R}_1\mathcal{T}_2,\ \mathcal{R}_1\mathcal{R}_2\}$, where $\mathcal{R}_1\mathcal{T}_2$ represents the path of the photon undergoing reflection from first BS and transmission through second BS etc..

In the following, the working principle of the proposed measurement scheme is outlined that would allow one to interpret the non-classical behavior of a micro-system from the value of the 'quantum measure' of an event, defined in the history-based formalism. For simplicity, here we will choose our system to pass through N devices, each with two output ports, i.e., $m = 2$, giving $(N, 2)$ kind of setup, as shown in the following figure.

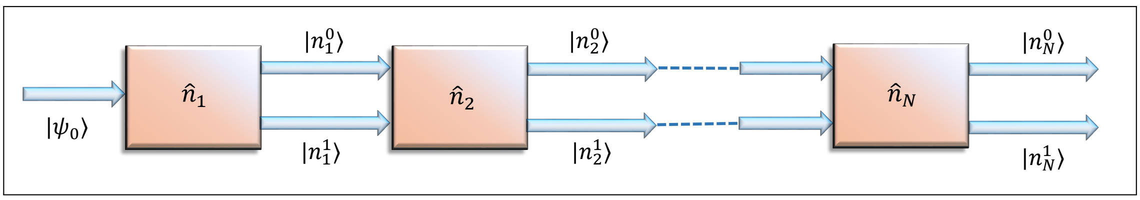

Figure 5.1: Schematic of a N-device setup, with each device having two output ports.

[2]The operators $\hat{X}$ and $\hat{Z}$ are the spin-projection operators in the two-dimensional Hilbert space, along x and z direction respectively. The relation between the eigen states of the observables $\hat{X}$ and $\hat{Z}$ are given as, $|\nearrow\rangle = \dfrac{|\uparrow\rangle + |\downarrow\rangle}{\sqrt{2}}$ and $|\nearrow\rangle = \dfrac{|\uparrow\rangle - |\downarrow\rangle}{\sqrt{2}}$.

[3]For a beam splitter, T and R respectively represents Transmissivity and Reflectivity of it, provided $T + R = 1$.

5.3.1 Finding the Amplitude of a History

Let, $|\psi_0\rangle$ represents the initial state of the system incident on the N-device setup as shown in Fig. 5.1. Here, each device with two output ports can be associated with an observable with two eigenvalues, labelled as 0 and 1 (say) corresponding to the system emerging in the upper and the lower output ports of the device. Let, the i-th device be represented by the observable $\hat{n}_i$ having two eigenvalues $\gamma_i = 0, 1$ associated with the eigen states $|n_i^0\rangle$ and $|n_i^1\rangle$, respectively representing the state of the system in the upper path and the lower path after the device. A history γ, in this setup, is one of the 2^N trajectories that the particle can follow and is given by a chain of N-bits as the following,

$$\gamma = (\gamma_1,\ \gamma_2,\ \ldots,\ \gamma_N) \equiv \{\gamma_i\} \quad \text{with} \quad i = 1, 2, \ldots, N \quad \text{and} \quad \gamma_i = 0 \text{ or } 1 \tag{5.10}$$

Here, $\gamma \in \Omega^{(N,2)}$ where $\Omega^{(N,2)}$ is the history space for the system propagating through the $(N, 2)$ setup, consisting of a total of 2^N histories.

According to the standard Quantum Mechanics, the action of the operator $\hat{n}_i$ on the particle state $|\psi_s\rangle$ can be shown as,

$$\hat{n}_i |\psi_s\rangle \to |n_i^{\gamma_i}\rangle \langle n_i^{\gamma_i}|\psi_s\rangle \quad \text{with} \ \ \gamma_i = 0 \text{ or } 1 \tag{5.11}$$

Therefore, for the N-device setup shown in Fig. 5.1, the system states $|\psi_1\rangle$ and $|\psi_2\rangle$ after the first and the second devices respectively, can be expressed as the following:

$$\text{After} \ \ \hat{n}_1 : \qquad |\psi_1\rangle = |n_1^{\gamma_1}\rangle \langle n_1^{\gamma_1}|\psi_0\rangle \tag{5.12}$$

$$\text{After} \ \ \hat{n}_2 : \qquad |\psi_2\rangle = |n_2^{\gamma_2}\rangle \langle n_2^{\gamma_2}|\psi_1\rangle = |n_2^{\gamma_2}\rangle \langle n_2^{\gamma_2}|n_1^{\gamma_1}\rangle \langle n_1^{\gamma_1}|\psi_0\rangle \tag{5.13}$$

$$= |n_2^{\gamma_2}\rangle \prod_{k=1}^{2} \langle n_k^{\gamma_k}|n_{k-1}^{\gamma_{k-1}}\rangle \tag{5.14}$$

Here, in the above expression, we have considered $|n_0^{\gamma_0}\rangle = |\psi_0\rangle$, which is the state of the system at the time of incidence on the setup. Hence, after the N-th device (i.e., the operation through $\hat{n}_N$) the state of the system would be,

$$|\psi_N\rangle = \left(\prod_{k=1}^{N} \left\langle n_k^{\gamma_k} \middle| n_{k-1}^{\gamma_{k-1}} \right\rangle\right) \left|n_N^{\gamma_N}\right\rangle \tag{5.15}$$

Now, relating the histories formalism of quantum mechanics to the standard formalism, a 'history' (γ) of the given system can be considered as a chain of outcomes associated with the action of a set of observables $\{\hat{n}_1, \hat{n}_2, \ldots \hat{n}_N\}$ on the initial system state $|\psi_0\rangle$ at times $T_\gamma = \{t_1, t_2, \ldots, t_N\}$, where $t_i < t_{i+1}$. The final state of the micro-system at the end of the setup would be dependent on the history γ i.e., the path that the system has taken within the setup, giving $\left|\psi_f^{(\gamma)}\right\rangle = |\psi_N\rangle = A(\gamma)\left|n_N^{\gamma_N}\right\rangle$. Hence, from Eqn. 5.15 the amplitude $A(\gamma)$ associated with the history $\gamma = (\gamma_1,\ \gamma_2,\ \ldots,\ \gamma_N)$ can be expressed as,

$$A(\gamma) = \prod_{k=1}^{N} \left\langle n_k^{\gamma_k} \middle| n_{k-1}^{\gamma_{k-1}} \right\rangle \tag{5.16}$$

where, $|n_0^{\gamma_0}\rangle = |\psi_0\rangle$ and $\gamma_k \in \gamma$. γ_k can take the value 0 or 1 depending on the eigen value of the observable $\hat{n}_k$ being emerged out.

Therefore, the quantum measure $\mu(E)$ for a set of histories $\{\gamma^p\}$ (where, p can be any integer between 1 to 2^N) i.e., for an event $E = \{\gamma^p\} \subseteq \Omega^{(N,2)}$, evaluated according to the expression in Eqn. 5.1, is obtained to be

$$\mu(E) = \sum_{\gamma^p, \gamma^q \in E} A(\gamma^p) A^*(\gamma^q) \delta_{\gamma_N^p, \gamma_N^q} \tag{5.17}$$

$$\mu(E) = \sum_{\gamma^p, \gamma^q \in E} \prod_{k,l=1}^{N} \left\langle n_k^{\gamma_k^p} \middle| n_{k-1}^{\gamma_{k-1}^p} \right\rangle \left\langle n_{l-1}^{\gamma_{l-1}^q} \middle| n_l^{\gamma_l^q} \right\rangle \delta_{\gamma_N^p, \gamma_N^q} \tag{5.18}$$

Here, $A(\gamma^p)$ is the amplitude associated with the history $\gamma^p = (\gamma_1^p,\ \gamma_2^p,\ \ldots,\ \gamma_N^p)$, with γ_N^p representing the end point of the history γ^p. Similarly, $A(\gamma^q)$ represents the amplitude associated with the history γ^q ending at γ_N^q. The delta function $\delta_{\gamma_N^p, \gamma_N^q}$ ensures interference between the histories $\gamma^p \in E$ and $\gamma^q \in E$ ending at the same location (i.e., γ_N).

Thus, from the viewpoint of standard Quantum Mechanics, the quantum measure $\mu(E)$ for a set of histories $E = \{\gamma^p\}$ depends on (i) the initial state $|\psi_0\rangle$ of the micro-system with which the system enters the setup, (ii) the histories that comprise the event i.e., the outcomes of the set of observables associated with the devices through which the system has traveled and (iii) the transition amplitudes between the eigen states of the successive observables. The phenomena of interference come into play for those trajectories where the system exit through the same port of the final device i.e., the N-th apparatus. The value of the quantum measure, as shown in Eqn. 5.18, is computed using the amplitudes of the histories from the mathematical expression of quantum measure given in QMT obtained employing the sum-over histories approach. Next, an experimental methodology will be established to determine the value of the "measure" through the measurements delineated in the conventional formalism.

5.3.2 Marking Outcomes via Ancilla Coupling

In order to keep track of the trajectory followed by the particle within the setup consisting of N-devices, an ancilla is coupled to the system after each device. The ancilla coupled to a particular device (say, i-th device) undergoes a state transition in accordance with the outcome of the action of the observable $\hat{n}_i$ associated with the device, enabling the identification of the particle's path after the device. The action of the i-th device and ancilla in combination can be expressed as,

$$|\psi_s\rangle\,|r_i\rangle_{a_i} \xrightarrow{\textit{Device}} |n_i^{\gamma_i}\rangle\,|r_i\rangle_{a_i} \xrightarrow{\textit{Ancilla}} |n_i^{\gamma_i}\rangle\,|\gamma_i\rangle_{a_i} \tag{5.19}$$

Here, $|\psi_s\rangle$ is the system state incident on the i-th device (n_i) and $|r_i\rangle_{a_i}$ is the initial state of the i-th ancilla coupled to this device, also known as 'ready state' of the ancilla which can be any state belonging to any basis corresponding to a Hilbert space that can be different from that of the system space.

Since we have considered a system hopping between two sites of the devices (a two-site hopper) here, the particle has been chosen to be a two-level quantum system. Therefore, the ancilla can be a qubit with the states $|0\rangle_{a_i}$ and $|1\rangle_{a_i}$, or any system in the higher dimension. The ready state of this ancilla can be chosen to be $|0\rangle_{a_i}$ or $|1\rangle_{a_i}$ for a two-level ancilla or any state orthogonal to $|0\rangle_{a_i}$ and $|1\rangle_{a_i}$ for an ancilla in the Hilbert space of dimension $d > 2$. However, the multi-level ancillas are useful for identifying the events of higher dimensional quantum systems. When the ready state is considered to be $|0\rangle_{a_i}$, the system-ancilla coupling can be mimicked as a $CNOT$ operation with the system state being the trigger, i.e.,

$$\text{Particle in the upper path:} \quad \left|n_i^0\right\rangle |0\rangle_{a_i} \rightarrow \left|n_i^0\right\rangle |0\rangle_{a_i} \tag{5.20}$$

$$\text{Particle in the lower path:} \quad \left|n_i^1\right\rangle |0\rangle_{a_i} \rightarrow \left|n_i^1\right\rangle |1\rangle_{a_i} \tag{5.21}$$

Hence, the path information of a particle after a device n_i is encoded in the state of the ancilla a_i. So, for the N-device setup, N number of ancillas are to be coupled one after each device as can be seen from the Fig. 5.2 and the joint state of all the N ancillas would represent the history chosen by the system.

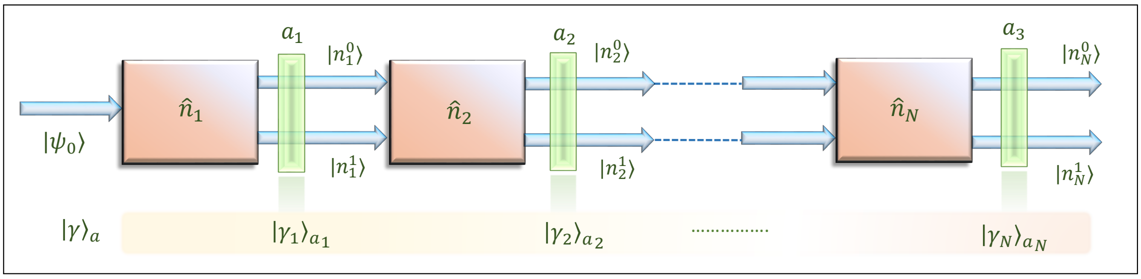

Figure 5.2: Schematic of an N-device setup, with the system after each device coupled to an individual ancilla undergoing state transition depending on the outcome of the device.

5.3.3 Joint State of System-Ancilla After Coupling

Let, the ready state of the ancillas $\{a_i\}$, coupled after the respective devices $\{n_i\}$ (with $i = 1, 2, \ldots, N$), when the system is incident on the $(N, 2)$ setup is $\{|r_i\rangle_{a_i}\}$. So, the initial joint state ($|\Psi_I\rangle \equiv |\Psi(t_0)\rangle$) of the system and N ancillas at time $t = t_0$ is given by,

$$|\Psi_I\rangle = |\psi_0\rangle |r_1\rangle_{a_1} |r_2\rangle_{a_2} \ldots\ldots |r_N\rangle_{a_N} = |\psi_0\rangle \prod_{i=1}^{N} |r_i\rangle_{a_i} \tag{5.22}$$

Here, $|\psi_0\rangle$ is the initial state of the system. As the system passes through the devices in the setup, its state is altered based on the outcomes of the actions of the observables $\{\hat{n}_i\}$ at times $T_\gamma = \{t_i\}$ where $i = 1, 2, \dots, N$ and $t_i < t_{i+1}$, and subsequently the state of the ancillas are modified one by one. Therefore, for a history $\gamma = (\gamma_1, \gamma_2, \dots, \gamma_N)$, the evolution of the joint system-ancilla state through the setup can be expressed as,

$$|\Psi_I\rangle = |\psi_0\rangle \prod_{i=1}^{N} |r_i\rangle_{a_i}$$

After 1st device-ancilla:

$$\rightarrow \;\; \left(\langle n_1^{\gamma_1}|\psi_0\rangle\right) |n_1^{\gamma_1}\rangle\, |\gamma_1\rangle_{a_1} \prod_{i=2}^{N} |r_i\rangle_{a_i}$$

After 2nd device-ancilla:

$$\rightarrow \;\; \left(\langle n_2^{\gamma_2}|n_1^{\gamma_1}\rangle \langle n_1^{\gamma_1}|\psi_0\rangle\right) |n_2^{\gamma_2}\rangle\, |\gamma_1\rangle_{a_1} |\gamma_2\rangle_{a_2} \prod_{i=3}^{N} |r_i\rangle_{a_i}$$

$$= \left(\prod_{k=1}^{2} \langle n_k^{\gamma_k}|n_{k-1}^{\gamma_{k-1}}\rangle\right) |n_2^{\gamma_2}\rangle\, |\gamma_1\rangle_{a_1} |\gamma_2\rangle_{a_2} \prod_{i=3}^{N} |r_i\rangle_{a_i}$$

$$\vdots \qquad\qquad \vdots \qquad\qquad \vdots$$

After N-th device-ancilla:

$$\rightarrow \;\; \left(\prod_{k=1}^{N} \langle n_k^{\gamma_k}|n_{k-1}^{\gamma_{k-1}}\rangle\right) |n_N^{\gamma_N}\rangle\, |\gamma_1\rangle_{a_1} |\gamma_2\rangle_{a_2} \dots |\gamma_N\rangle_{a_N}$$

Hence, after the system propagates through all the devices and gets coupled to the individual ancillas, the final joint state of system-ancilla at the end of the $(N, 2)$ setup for a particular history γ would be:

$$\left|\Psi_f^{(\gamma)}\right\rangle = \left(\prod_{k=1}^{N} \langle n_k^{\gamma_k}|n_{k-1}^{\gamma_{k-1}}\rangle\right) |n_N^{\gamma_N}\rangle \left(\prod_{i=1}^{N} |\gamma_i\rangle_{a_i}\right) \tag{5.23}$$

Here, we have assumed $|n_0^{\gamma_0}\rangle = |\psi_0\rangle$ representing the initial state of the system and $\left|n_N^{\gamma_N}\right\rangle$ is the final state of the system after emerging out of the setup. The state at $t = t_N$, i.e., $\left|\Psi_f^{(\gamma)}\right\rangle \equiv |\Psi(t_N)\rangle$ is the final joint state of system-ancilla associated with a particular history $\gamma = (\gamma_1, \gamma_2, \ldots, \gamma_N)$. Using the expression for amplitude $A(\gamma)$ of the history γ from Eqn. 5.16, we can write

$$\left|\Psi_f^{(\gamma)}\right\rangle = A(\gamma)\left|n_N^{\gamma_N}\right\rangle |\gamma\rangle_a \tag{5.24}$$

$$\text{with} \qquad |\gamma\rangle_a = |\gamma_1\rangle_{a_1} |\gamma_2\rangle_{a_2} \ldots\ldots |\gamma_N\rangle_{a_N} = \prod_{i=1}^{N} |\gamma_i\rangle_{a_i} \tag{5.25}$$

$|\gamma\rangle_a$ represents the joint state of N ancillas that encodes the path information of the system within the setup for the history γ. So, measurements performed on the joint ancilla states $\{|\gamma^p\rangle_a\}$, where p is any integer between 1 to 2^N, in a suitable basis enables us to comment on the system behavior between the time $t = t_0$ to $t = t_N$ without affecting the system.

5.3.4 Determining the Quantum Measure via Projective Measurements on Suitable Ancilla Basis

So far we have designed a setup consisting of N-apparatus having two output ports each, enabling a quantum system to follow one of the 2^N possible trajectories within the setup and registered this path information in the states of N ancillas coupled to the system, one after each apparatus. Here our goal is to find the value of the quantum measure $\mu(E)$ associated with a given set of histories $E = \{\gamma^p\}$, through the experimental determination of probability of a certain outcome of a projective measurement, identified as the standard measurement procedure in the conventional framework of quantum mechanics. Since the information regarding any history i.e., any path chosen by the system is encoded in the joint ancilla state $|\gamma\rangle_a$, the measurements needs to be performed on joint ancilla states in an appropriate basis defined in the joint Hilbert space of ancillas, while ensuring minimal disturbance caused to the system. So, once all the ancillas have recorded the paths chosen by the system after the devices, a suitable unitary transformation needs to be performed to the joint ancilla basis, so that a "click" in the detector associated with one of the states in the new basis confirms the occurrence of the desired event and the probability of the "click" corresponding to this particular outcome would be related to the 'quantum measure' of the event with a known factor of proportionality.

Let, $|E\rangle_a$ be that joint ancilla state in the new basis after the Unitary transformation which corresponds to the desired outcome of a projective measurement, the probability of which would be related to the measure $\mu(E)$ for the event E. The operator that projects the joint ancilla state to $|E\rangle_a$ leaving the system undisturbed is given by,

$$\hat{\Pi}_E = \hat{\mathbb{1}}_s \otimes |E_a\rangle\langle E_a| \tag{5.26}$$

Here, $\hat{\mathbb{1}}_s$ represents the identity operator (2×2 matrix for 2-level quantum system) that acts on the system state.

The expression in Eqn. 5.24 is the final system-ancilla joint state as the system propagates through the path γ (anyone among the 2^N paths) within the setup as shown in Fig 5.1, where $\gamma = (\gamma_1, \gamma_2, \ldots, \gamma_N)$ is a particular sequence of outcomes of the set of observables $\{\hat{n}_i\}$. However, according to the wavefunction description of the conventional quantum framework, prior to an observation, a quantum system is characterized to exist in a superposition of all possible eigen states of the observable simultaneously. Hence, in the N-device setup while traversing through the i-th device (the associated operator being $\hat{n}_i$), the system state is described as a superposition of being in the two output ports (with the associated eigen states $|n_i^0\rangle$ and $|n_i^1\rangle$) of the device at the same time, i.e., $|\psi_s\rangle = \alpha_{i0}\,|n_i^0\rangle + \alpha_{i1}\,|n_i^1\rangle$ with $|\alpha_{i0}|^2$ and $|\alpha_{i1}|^2$ respectively representing the probabilities of finding the particle in the upper and lower paths after the i-th device, upon detection. So, as per the conventional formalism, before any observation or detection is made, the joint system-ancilla state corresponding to the device n_i would be given as,

$$|\psi_s\rangle\,|r_i\rangle_{a_i} \rightarrow \langle n_i^0|\psi_s\rangle\,|n_i^0\rangle\,|0\rangle_{a_i} + \langle n_i^1|\psi_s\rangle\,|n_i^1\rangle\,|1\rangle_{a_i} = \alpha_{i0}\,|n_i^0\rangle\,|0\rangle_{a_i} + \alpha_{i1}\,|n_i^1\rangle\,|1\rangle_{a_i} \tag{5.27}$$

From the above expression, it can be seen that coupling between the system and ancilla after a device results in an entangled state.

For a two device (say, n_1, n_2) setup with each device having two output ports, the evolution of the joint system-ancilla state $|\Psi_I\rangle$ is given as,

$$|\Psi_I\rangle = |\psi_0\rangle\, |r_1\rangle_{a_1} |r_2\rangle_{a_2}$$

After 1st device:

$$\rightarrow \left(\langle n_1^0|\psi_0\rangle\, |n_1^0\rangle\, |0\rangle_{a_1} + \langle n_1^1|\psi_0\rangle\, |n_1^1\rangle\, |1\rangle_{a_1}\right) |r_2\rangle_{a_2}$$

After 2nd device:

$$\rightarrow \langle n_2^0|n_1^0\rangle \langle n_1^0|\psi_0\rangle\, |n_2^0\rangle\, |0\rangle_{a_1} |0\rangle_{a_2} + \langle n_2^1|n_1^0\rangle \langle n_1^0|\psi_0\rangle\, |n_2^1\rangle\, |0\rangle_{a_1} |1\rangle_{a_2}$$

$$+ \langle n_2^0|n_1^1\rangle \langle n_1^1|\psi_0\rangle\, |n_2^0\rangle\, |1\rangle_{a_1} |0\rangle_{a_2} + \langle n_2^1|n_1^1\rangle \langle n_1^1|\psi_0\rangle\, |n_2^1\rangle\, |1\rangle_{a_1} |1\rangle_{a_2}$$

Therefore, the final joint state of system-ancilla after the $2nd$ device can be expressed as,

$$|\Psi_f\rangle = A(00)\, |n_2^0\rangle\, |00\rangle_a + A(01)\, |n_2^1\rangle\, |01\rangle_a + A(10)\, |n_2^0\rangle\, |10\rangle_a + A(11)\, |n_2^1\rangle\, |11\rangle_a \tag{5.28}$$

Here, $A(\gamma)$ represents the amplitude of the history $\gamma = (\gamma_1, \gamma_2)$. The final joint state $|\Psi_f\rangle$ is an entangled state denoting a superposition of system-ancilla joint states associated with $2^2 = 4$ possible histories that form the history space $\Omega^{(2,2)} = \{00, 01, 10, 11\}$.

Now, a projective measurement on the combined system-ancilla state in the joint ancilla basis $\{|00\rangle_a, |01\rangle_a, |10\rangle_a, |11\rangle_a\} \equiv \{|\gamma\rangle_a\}$, reveals that the path 00 occurs with probability $\mathcal{P}(00) = |A(00)|^2$ with the system state being projected to $|n_2^0\rangle$, the path 01 occurs with probability $\mathcal{P}(01) = |A(01)|^2$ with the system state being projected to $|n_2^1\rangle$ and so on. For a desired event $E = \{00, 10\}$, measurements in the $\{|\gamma\rangle_a\}$ basis results in the probability of the event to be $\left|(\hat{\mathbb{1}}_s \otimes |00\rangle\langle 00|)\, |\Psi_f\rangle\right|^2 + \left|(\hat{\mathbb{1}}_s \otimes |10\rangle\langle 10|)\, |\Psi_f\rangle\right|^2 = |A(00)|^2 + |A(10)|^2 = \mathcal{P}(00) + \mathcal{P}(10)$, which does not contain the information of interference between the paths 00 and 10 ending at the same location, i.e., at the upper path (with the associated system state $|n_2^0\rangle$) of the device n_2. Hence, within the framework of QMT for the event $E = \{00, 10\}$

$$\mathcal{P}(E) \neq |A(00)|^2 + |A(10)|^2$$

$$\implies \quad \mathcal{P}(E) \neq \mathcal{P}(00) + \mathcal{P}(10) \tag{5.29}$$

The above expression of probability for the event $E = \{00, 10\}$ clearly shows that within the context of QMT, the probability $\mathcal{P}(E)$ does not follow the probability sum rule. However, we need to capture this effect through the outcome of the measurements on the joint ancilla states, leaving the system state undisturbed.

The expression in Eqn. 5.29 implies that the measurement on the joint ancilla states in the basis $\{|\gamma\rangle_a\}$ disturbs the evolution of the system, resulting in no interference. Now, let $\{|\gamma_u\rangle_a\}$ be another joint ancilla basis, the measurement on which gives the probability of the desired event $E = \{00, 10\}$ as the probability of one of the outcomes $\frac{|00\rangle_a + |10\rangle_a}{\sqrt{2}}$ of the projective measurement, without affecting the interference between 00 and 10. Here,

$$|\gamma_u\rangle_a = \hat{U}\,|\gamma\rangle_a \quad \text{with} \quad \hat{U}^\dagger\hat{U} = \hat{U}\hat{U}^\dagger = \hat{\mathbb{1}} \tag{5.30}$$

$\hat{U}$ is the unitary operator that transforms the joint ancilla basis $\{|\gamma\rangle_a\}$ to $\{|\gamma_u\rangle_a\}$.

The orthonormal basis $\{|\gamma_u\rangle_a\} \equiv \{\frac{|00\rangle_a + |10\rangle_a}{\sqrt{2}}, \frac{|01\rangle_a + |11\rangle_a}{\sqrt{2}}, \frac{|00\rangle_a - |10\rangle_a}{\sqrt{2}}, \frac{|01\rangle_a - |11\rangle_a}{\sqrt{2}}\}$, which is chosen appropriate for the final measurement on the ancillas, can be obtained from the transformation of the basis $\{|\gamma\rangle_a\} \equiv \{|00\rangle_a, |01\rangle_a, |10\rangle_a, |11\rangle_a\}$ through the unitary operator $\hat{U}$ as follows,

$$\hat{U} = \frac{1}{\sqrt{2}}\begin{pmatrix} 1 & 0 & 1 & 0 \\ 0 & 1 & 0 & 1 \\ 1 & 0 & -1 & 0 \\ 0 & 1 & 0 & -1 \end{pmatrix} = \frac{1}{\sqrt{2}}\begin{pmatrix} 1 & 1 \\ 1 & -1 \end{pmatrix} \otimes \begin{pmatrix} 1 & 0 \\ 0 & 1 \end{pmatrix} \tag{5.31}$$

Therefore, using the expression of $|\Psi_f\rangle$ from Eqn. 5.28, the probability of obtaining the state $|x_1\rangle_a = \frac{|00\rangle_a + |10\rangle_a}{\sqrt{2}}$ can be computed as,

$$\mathcal{P}(x_1) = \left\|(\hat{\mathbb{1}}_s \otimes |x_1\rangle\langle x_1|)\,|\Psi_f\rangle\right\|^2 = \frac{1}{2}(|A(00) + A(10)|^2) = \frac{\mu(E)}{2} \tag{5.32}$$

Here, $\mu(E)$ denotes the quantum measure of the event $E = \{00, 10\}$, as computed using the theoretical formula given in Eqn. 5.1. The above expression shows that the probability

$\mathcal{P}(x_1)$ of the outcome $|x_1\rangle_a = \dfrac{|00\rangle_a + |10\rangle_a}{\sqrt{2}}$ of the projective measurement is related to $\mu(E)$ for the event $E = \{00, 10\}$ by a factor $\dfrac{1}{2}$, allowing us to infer $\mu(E)$ from the probability $\mathcal{P}(x_1)$ determined experimentally.

Similar to the final joint state associated with a $(2, 2)$ setup shown in Eqn. 5.28, the final joint state of the system-ancilla prior to observation for a N-device setup i.e., for a $(N, 2)$ setup depicted in Fig. 5.2, would be in a superposition over the states $\left|n_N^{\gamma_N^p}\right\rangle |\gamma^p\rangle_a$ associated with all the 2^N possible paths $\gamma^p \in \Omega^{(N,2)}$. So, according to the conventional formalism, the final joint system-ancilla entangled state after the system has traveled through all the devices in a $(N, 2)$ setup is,

$$|\Psi_f\rangle = \sum_{p=1}^{2^N} A(\gamma^p) \left|n_N^{\gamma_N^p}\right\rangle |\gamma^p\rangle_a \tag{5.33}$$

Here, $A(\gamma^p)$ is the amplitude related to the history γ^p within the $(N, 2)$ setup and $|\gamma^p\rangle_a$ is the combined state of all ancillas $\{a_i\}$ within the setup after coupling with the system, i.e., $|\gamma^p\rangle_a = \prod_{i=1}^{N} |\gamma_i^p\rangle_{a_i}$.

The preceding discussion on the event $\{00, 10\}$ makes us conclude that in order to find the quantum measure of an event E, a projective measurement needs to be performed on the combined ancilla state in an appropriately chosen basis $\{|\gamma_u\rangle_a\}$. This basis must include a state that would be in unbiased (i.e., with equal weight) superposition of the joint ancilla states (represented in $\{|\gamma\rangle_a\}$ basis) corresponding to the histories that comprise the desired event E, with either no relative phase between them or a relative phase between those histories that end at different points, so that the interference remains unaffected. Therefore, for finding the measure of an event $E = \{\gamma^1, \gamma^2, \ldots, \gamma^k\}$ which is a set of k number of histories $\gamma^q \in \Omega^{(N,2)}$, the transformed basis must include the state $|E\rangle_a$ which would be the intended outcome of the projective measurement. This joint ancilla state $|E\rangle_a$ can be represented as,

$$|E\rangle_a = \frac{1}{\sqrt{k}} \sum_{q=1}^{k} |\gamma^q\rangle_a \tag{5.34}$$

The probability of the desired outcome E_a (with the associated state $|E\rangle_a$) of the projective measurement is obtained by acting the projector $\hat{\Pi}_E$ given in Eqn. 5.26 on the final state $|\Psi_f\rangle$ expressed in Eqn. 5.33, i.e.,

$$\mathcal{P}(E) = \left\|\hat{\Pi}_E \left|\Psi_f\right\rangle\right\|^2 = \left\|(\hat{\mathbb{1}}_s \otimes |E_a\rangle\langle E_a|)\left|\Psi_f\right\rangle\right\|^2 \tag{5.35}$$

$$= \left|\frac{1}{k}\left(\hat{\mathbb{1}}_s \otimes \sum_{q'=1}^{k}\sum_{q=1}^{k}\left|\gamma^{q'}\right\rangle\!\left\langle\gamma^{q}\right|\right)\left(\sum_{p=1}^{2^N} A(\gamma^p)\left|n_N^{\gamma_N^p}\right\rangle\left|\gamma^p\right\rangle_a\right)\right|^2$$

$$= \left|\frac{1}{k}\sum_{q'=1}^{k}\sum_{q=1}^{k}\sum_{p=1}^{2^N} A(\gamma^p)\left\langle\gamma^q|\gamma^p\right\rangle\left|n_N^{\gamma_N^p}\right\rangle\left|\gamma^{q'}\right\rangle_a\right|^2$$

$$= \left|\frac{1}{k}\sum_{q'=1}^{k}\sum_{q=1}^{k} A(\gamma^q)\left|n_N^{\gamma_N^q}\right\rangle\left|\gamma^{q'}\right\rangle_a\right|^2$$

$$= \frac{1}{k^2}\sum_{q'=1}^{k}\sum_{q=1}^{k}\sum_{r'=1}^{k}\sum_{r=1}^{k} A(\gamma^q)A^*(\gamma^r)\left\langle n_N^{\gamma_N^r}\middle|n_N^{\gamma_N^q}\right\rangle\left\langle\gamma^{r'}\middle|\gamma^{q'}\right\rangle$$

From the orthonormality condition of the ancilla states in the basis $\{|\gamma\rangle_a\}$, we get $\sum_{q'=1}^{k}\sum_{r'=1}^{k}\left\langle\gamma^{r'}\middle|\gamma^{q'}\right\rangle = \sum_{q'=1}^{k}\sum_{r'=1}^{k}\delta_{q',r'} = k$. Also, we have $\left\langle n_N^{\gamma_N^r}\middle|n_N^{\gamma_N^q}\right\rangle = \delta_{\gamma_N^q,\gamma_N^r}$ implying the interference of the particles ending at the same point after the N-th device in the setup.

Therefore, the probability of the outcome $|E\rangle_a$ of a projective measurement on the joint ancilla state, is obtained to be:

$$\mathcal{P}(E) = \frac{1}{k}\sum_{q=1}^{k}\sum_{r=1}^{k} A(\gamma^q)A^*(\gamma^r)\,\delta_{\gamma_N^q,\gamma_N^r} = \frac{\mu(E)}{k} \tag{5.36}$$

Thus, the probability of an event E can be experimentally determined from the probability of a particular outcome $|E\rangle_a$ of a projective measurement on the joint ancilla state leaving the system undisturbed. However, in principle, there may not exist a physically realizable observable in the joint Hilbert space of the ancillas having an eigenstate $|E\rangle_a$ associated with the desired outcome for an event, necessitating a modification of the setup depending on the event for which the quantum measure is to be determined.

So, The quantum measure for an event E can be inferred experimentally from the probability of the event $\mathcal{P}(E)$ by multiplying a known factor k as the following,

$$\mu(E) = k\ \mathcal{P}(E) \tag{5.37}$$

Here, in the above expression, k appears to be a proportionality factor representing the number of histories that comprise the event E of interest. However, in practice, the factor may vary depending on the design of the setup, i.e., on the choice of the event, the design of the event filter to select a particular set of the histories from the history space and to some extent on the choice of the components to be used in configuring the setup − further details will be discussed in the next chapter.

5.4 Determination of Quantum Measure in Photonic Systems

The last section outlines a generalized experimental scheme for inferring the value of the quantum measure of an event described for a particle traveling through a setup having N devices, each with two outputs. Here, we aim to implement the scheme in a photonic system propagating through an optical setup. This section provides the possibilities of a table-top demonstration of the scheme for determining the quantum measure of a specific event in an experimental scenario with the components available in an optics lab. It also discusses certain limitations and challenges in the applicability of the scheme, which is described with the assumptions of an idealized system-device combination in a real scenario. Here, we present the possible design of an event filter (involving interference) that helps filter the desired set of histories and gives a non-classical quantum measure for the event of interest associated with the photonic system.

5.4.1 Overview of the Scheme for Photonic System

In order to experimentally determine the value of quantum measure $\mu(E)$ for an event E associated with a photonic system, an optical arrangement needs to be made such that it relates one of the outcomes of a projective measurement to confirm the occurrence of the event E. Hence such a setup ensures that the probability of the event E is obtained from the probability of a measurement outcome, which is then used to infer the value of $\mu(E)$. Here, our system will be a photon that will pass through a succession of non-polarizing beam splitters, which is the device with two input ports and two output ports. The beam splitter (BS) setup can be treated as a two-site hopper [31] setting, i.e., a photon entering a BS would occupy one of its two output ports based on whether it transmits through or reflects from the BS. In this kind of setup, a BS serves the dual purpose i.e., (i) it causes amplitude division of the beam being incident on it from any input port, depending on the transmissivity (T) and reflectivity (R) of the BS, (ii) it recombines the beams entering the BS from the two input ports, allowing for interference in case of coherent combination.

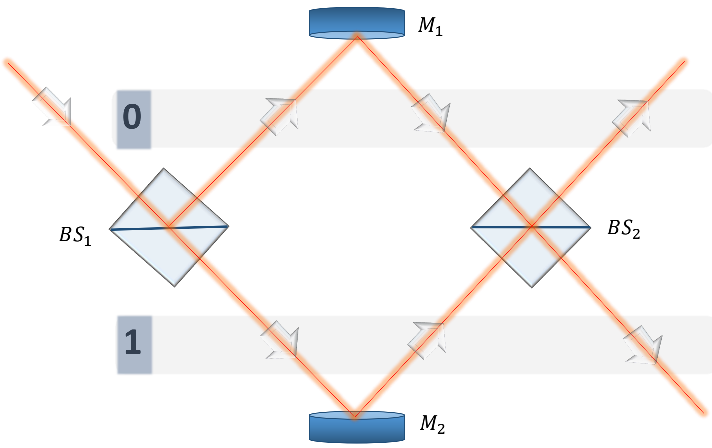

Figure 5.3: An optical two-site hopper setup consisting of two non-polarizing beam splitters arranged in a sequence allowing a photon to take four possible paths within the setup.

To demonstrate the scheme for a photonic event, let us consider a setup consisting of two beam splitters BS_1 and BS_2, arranged in the form of a Mach-Zehnder Interferometer [32, 33], as depicted in Fig. 5.3, where M_1 and M_2 are mirrors that redirect the photons at the output of BS_1 toward BS_2. A photon encountering the first beam splitter BS_1

from the top can take either the upper path through reflection or the lower path through transmission. Both the paths recombine at the second beam splitter BS_2, from where the photon again can take either the upper path or the lower path. Thus, there are 4 possible trajectories that a photon entering the setup can take, depending on the transmission or reflection from each device. If the photons in the upper and lower paths after each beam splitter are labeled as 0 and 1 respectively, then the history space for the photonic system can be described as $\Omega = \{00, 01, 10, 11\}$.

Let, the beam splitters BS_1 and BS_2 in the setup are lossless and symmetric, i.e, a photon incident on the beam splitters either gets transmitted or reflected (with possibilities defined by the splitting ratio $T : R$) without having any possibility of getting absorbed in the material of the BS and the reflection amplitudes (and the transmission amplitudes as well) are the same irrespective of which input port the photon is incident from [34]. Consider, t_i and r_i respectively represents the transmission and reflection coefficients of i-th beam splitter BS_i, provided $|t_i|^2 + |r_i|^2 = 1$ when no loss is associated with BS_i. For simplicity, we assume t_i and r_i to be real and a phase φ_i is acquired by the photon upon reflection, where $\{t_i, r_i, \varphi_i\} \in \mathbb{R}$. The possible amplitudes associated with the histories of the photon in this setup, are given as follows:

$$A(00) = r_1 e^{i\varphi_1} r_2 e^{i\varphi_2} \ , \ A(01) = r_1 e^{i\varphi_1} t_2 \ , \ A(10) = t_1 t_2 \ , \ A(11) = t_1 r_2 e^{i\varphi_2} \quad (5.38)$$

Here, we have not considered any relative phase in the setup related to the path difference between the upper path and lower path of the interferometer.

To demonstrate the applicability of the scheme discussed in the previous section, here we will choose an event E from the possible non-serial events that can not be associated with a physically realizable observable, implying that the probability of the event can not be directly determined from the expectation value of a self-adjoint operator or by simply blocking the undesired set of paths. Hence, we tend to select an event for which the scheme manifests its true potential through the use of ancilla. For the setup in Fig. **5.3**, where the photon travels through two beam splitters, the possible non-serial events are $\{00, 11\}$, $\{10, 01\}$, $\{00, 10, 01\}$, $\{00, 10, 11\}$, $\{00, 01, 11\}$, $\{10, 01, 11\}$. Also, the fact that the value of the quantum measure for certain events can go beyond the upper limit of the classical probability measure (which is one), inspires us to choose one of those events that involve interference and for which the non-classical nature of the quantum measure can be captured. Therefore, for the demonstration purpose here we select the three history event $E = \{00, 01, 11\}$ as our event of interest, for which two histories $01, 11$ ending at the same port would interfere. From the Eqn. 5.1, for the desired event $E = \{00, 01, 11\}$ we get

$$\begin{aligned}
\mu(E = \{00, 01, 11\}) &= A(00)A^*(00)\delta_{0,0} + A(00)A^*(01)\delta_{0,1} + A(00)A^*(11)\delta_{0,1} \\
&\quad + A(01)A^*(00)\delta_{1,0} + A(01)A^*(01)\delta_{1,1} + A(01)A^*(11)\delta_{1,1} \\
&\quad + A(11)A^*(00)\delta_{1,0} + A(11)A^*(01)\delta_{1,1} + A(11)A^*(11)\delta_{1,1} \\
&= |A(00)|^2 + |A(01)|^2 + A(01)A^*(11) + A(11)A^*(01) + |A(11)|^2
\end{aligned}$$

$$\implies \qquad \mu(E) = |A(00)|^2 + |A(01) + A(11)|^2 \tag{5.39}$$

Putting the expressions of the amplitudes given in Eqn. 5.38 for the photonic system, the quantum measure $\mu(E)$ for the event $E = \{00, 01, 11\}$ is obtained as,

$$\mu(E) = \left|r_1 r_2 e^{i\varphi_1} e^{i\varphi_2}\right|^2 + \left|r_1 t_2 e^{i\varphi_1} + t_1 r_2 e^{i\varphi_2}\right|^2 \tag{5.40}$$

For symmetric lossless $50:50$ beam splitters [4] $t_i = r_i = \frac{1}{\sqrt{2}}$ and $\varphi_i = \frac{\pi}{2}$, [5] [35, 34] giving the value of measure for the lossless system to be,

$$\mu(E) = \left|\frac{i}{\sqrt{2}}\frac{i}{\sqrt{2}}\right|^2 + \left|\frac{i}{\sqrt{2}}\frac{1}{\sqrt{2}} + \frac{1}{\sqrt{2}}\frac{i}{\sqrt{2}}\right|^2 = \frac{1}{4} + 1 = \frac{5}{4} \tag{5.41}$$

Hence, for an ideal, lossless system-device combination, the quantum measure for the event $E = \{00, 01, 11\}$ of a photonic system is obtained to be $\mu(E) = \frac{5}{4} = 1.25$, that exceeds the classical upper limit $\mu_{C,max} = 1$. The interference between the histories 01 and 11 makes

[4] The unitary evolution operator represented as, $BS_{sym} = \begin{pmatrix} t_i & r_i e^{i\varphi_i} \\ r_i e^{i\varphi_i} & t_i \end{pmatrix} = \frac{1}{\sqrt{2}}\begin{pmatrix} 1 & i \\ i & 1 \end{pmatrix}$.

[5] The relative phase φ_i between the reflected and transmitted modes of a real BS varies depending on the uncertainty in the beam splitter thickness, the surface flatness and thickness of the cement etc.

the value of the measure to be non-classical, the nature of which is aimed to be captured in an experimental scenario, as discussed in the following.

5.4.2 Measuring the Quantum Measure for Photonic Systems: Design of an Event filter, Choice of Ancilla and Measurements

Here, we present an experimental setup allowing interference, the analysis of which would give the quantum measure for a desired event $E = \{00, 01, 11\}$ when the system (here a photon) passes through two optical BS. To experimentally determine the quantum measure of an event, the setup with the two beam splitters needs to be modified and arranged in such a way that only the desired set of histories are filtered out from the history space (Ω) that consists of 4 possible paths. This modified setup is referred to as the "Event Filter" − the arrival of a photon at the output of the event filter confirms that the photon has taken one of the paths that comprise the event of interest, not necessarily revealing the exact path information. Projective measurement at the end of the event filter on an ensemble of identical systems gives the probability of occurrence of the event from which the quantum measure of the event can be inferred.

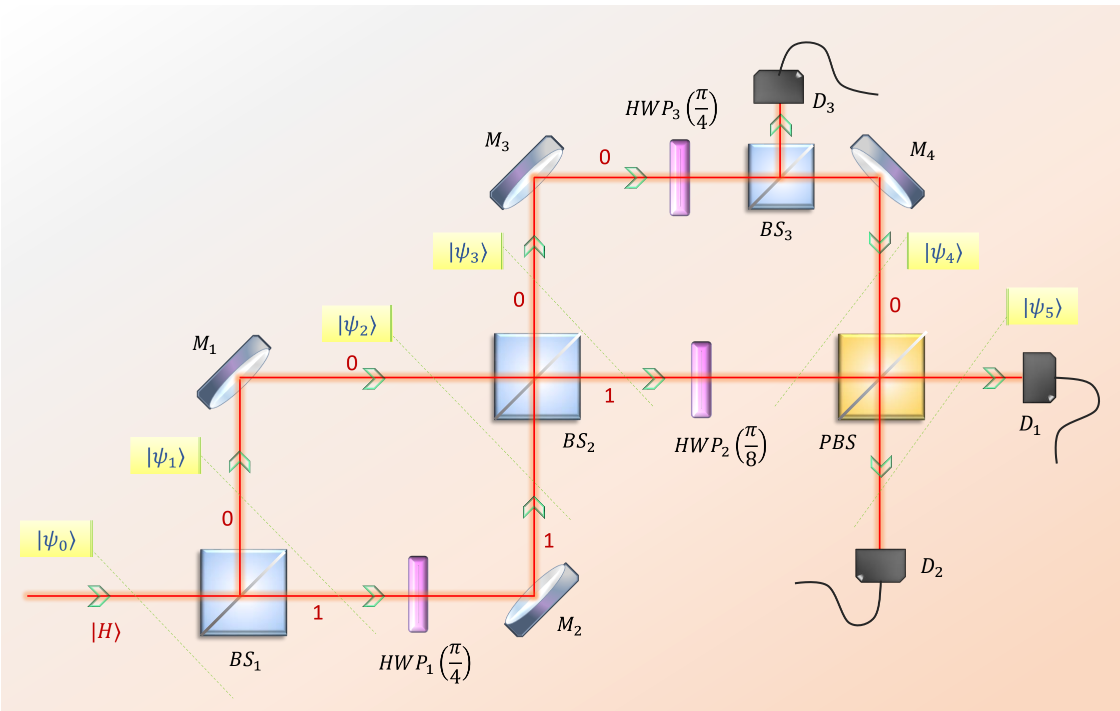

Figure 5.4: A possible design of an event filter for $E = \{00, 01, 11\}$ for a photonic system.

A possible design of an "Event Filter" for the desired event $E = \{00, 01, 11\}$ is shown in the Fig. 5.4. The path degree of freedom of the photon is chosen to represent the histories and operations are performed on the polarization degree of freedom to selectively allow only the photons from 00, 01, 11 paths to reach the output of the event filter ensuring interference between 01 and 11. The two devices i.e., the two beam splitters BS_1 and BS_2 forms a Mach-Zehnder Interferometer (MZI) with the two mirrors M_1, M_2 that redirects the two spatial modes after BS_1 towards BS_2. The two paths after BS_1 are labelled as $path-U$ and $path-L$ and the same after BS_2 are labelled as $path-T$ and $path-B$. The potential histories of a photon entering the setup are given as a chain of 2-bits, with 0 and 1 respectively representing the photon in the upper and lower paths after each BS.

Let, a beam of horizontally polarized light is made incident on the setup (on BS_1) at time t_0. The horizontal polarization is achieved by passing the beam emitting from a source through a linear polarizer with the pass axis along the horizontal or transmitting through a polarizing beam splitter (PBS) or a Glan Thompson polarizer (GT) in a particular orientation [6]. The unitary evolution operator for a symmetric lossless beam splitter BS_i, with transmission and reflection coefficients being t_i and $r_i e^{i\varphi_i}$ provided $|t_i|^2 + |r_i|^2 = 1$, is given as

$$BS_i = \begin{pmatrix} t_i & r_i e^{i\varphi_i} \\ r_i e^{i\varphi_i} & t_i \end{pmatrix} \tag{5.42}$$

The state of the system at time t_0 is $|\psi_0\rangle = |H\rangle$. When the horizontally polarized beam is incident on the beam splitter BS_1, the polarization of the beams in $path-U$ and $path-L$, right after the beam splitter is also horizontal, giving the state at time t_1 to be,

$$|\psi_1\rangle = (r_1 e^{i\varphi_1} |U\rangle |H\rangle)^{(0)} + (t_1 |L\rangle |H\rangle)^{(1)} \tag{5.43}$$

[6] A polarizer allows the component of polarization along its transmission axis to pass through it, while absorbing the rest. A PBS, on the other hand, transmits and reflects the horizontal and vertical components of polarization respectively, of a beam incident on it. A GT, transmits the s-polarized component and reflects the p-polarized component of the beam incident on it. Hence, horizontally polarized beam transmits through the GT depending on the orientation of its optic axis. In general, a GT has a relatively higher extinction ratio than a PBS, thus for better polarization purity a GT is preferred.

The two terms in $|\psi_1\rangle$ represent the states of the photon in the upper and lower paths after BS_1 [7], with the superscripts representing the trajectory of the photon.

In order to mark the paths within the interferometer in terms of ancillas, the polarization in one arm can be made orthogonal to the other (say, polarization in $path - L$ is made $|V\rangle$), so that any polarization measurement on the basis $\{|H\rangle, |V\rangle\}$ reveals which path the photon has taken. For that, a half-wave plate HWP_1 is inserted in $path - L$ with its fast axis oriented to $\frac{\pi}{4}$, i.e., in σ_x configuration which transforms the polarization of the photon in this arm from $|H\rangle$ to $|V\rangle$. The Jones matrix representation [36] of HWP with the fast axis oriented at ϑ with respect to the horizontal is given as,

$$HWP(\vartheta) = \begin{pmatrix} cos(2\vartheta) & sin(2\vartheta) \\ sin(2\vartheta) & -cos(2\vartheta) \end{pmatrix} \implies HWP(\vartheta = \frac{\pi}{4}) = \begin{pmatrix} 0 & 1 \\ 1 & 0 \end{pmatrix} = \sigma_x \quad (5.44)$$

If the relative phase due to the path length difference (ΔL) between the two paths of the interferometer is given by $\varphi_r = \frac{2\pi}{\lambda}\Delta L$, the state at time t_2 just before BS_2, can be written as

$$|\psi_2\rangle = (r_1 e^{i\varphi_1} |U\rangle |H\rangle)^{(0)} + (t_1 e^{i\varphi_r} |L\rangle |V\rangle)^{(1)} \quad (5.45)$$

Immediately after BS_2 at t_3, the state becomes

$$\begin{aligned} |\psi_3\rangle = &(r_1 r_2 e^{i\varphi_1} e^{i\varphi_2} |T\rangle |H\rangle)^{(00)} + (r_1 t_2 e^{i\varphi_1} |B\rangle |H\rangle)^{(01)} \\ &+ (t_1 t_2 e^{i\varphi_r} |T\rangle |V\rangle)^{(10)} + (t_1 r_2 e^{i\varphi_2} e^{i\varphi_r} |B\rangle |V\rangle)^{(11)} \end{aligned} \quad (5.46)$$

Here, $|T\rangle$ and $|B\rangle$ are the states associated with the spatial mode of the photon in the top and bottom paths after BS_2. Thus, from the time t_0 to t_3, a photon can travel through any one of the 4 possible paths, with the corresponding amplitudes

$$A(00) = r_1 r_2 e^{i\varphi_1} e^{i\varphi_2}, \;\; A(01) = r_1 t_2 e^{i\varphi_1}, \;\; A(10) = t_1 t_2 e^{i\varphi_r}, \;\; A(11) = t_1 r_2 e^{i\varphi_2} e^{i\varphi_r} \quad (5.47)$$

[7] Here, $|U\rangle$ and $|L\rangle$ are the states corresponding to the two spatial modes after BS_1

Hence, using the theoretical formula in Eqn. 5.39 the quantum measure for the event $E = \{00, 01, 11\}$ can be computed as,

$$\mu(E) = \left|r_1 r_2 e^{i\varphi_1} e^{i\varphi_2}\right|^2 + \left|r_1 t_2 e^{i\varphi_1} + t_1 r_2 e^{i\varphi_2} e^{i\varphi_r}\right|^2 \tag{5.48}$$

$$\mu(E) = |r_1 r_2|^2 + \left|r_1 t_2 + t_1 r_2 e^{i(\varphi_2 - \varphi_1)} e^{i\varphi_r}\right|^2 \tag{5.49}$$

The region within the setup which the photon travels between the time t_0 to t_3, i.e., the region from the input of BS_1 to the output of BS_2 can be called as "system propagation region", where the system is free is choose any of the paths γ^k belonging to the history space Ω with $k = 1, 2, 3, 4$; associated with the propagation of the system through the series of two devices BS_1, BS_2. The region next to it, i.e., after BS_2 to the end of the setup is labelled as "filtration region" where the desired set of paths are filtered out in order to determine the value of the quantum measure for the event E. As the photon enters this region after time t_3, operations on polarization d.o.f. of the photon are performed (i) to select the photons corresponding to the histories $00, 01, 11$ while rejecting the photons from the undesired history 10, (ii) to ensure interference between the histories $01, 11$ that emerge at the same output of the last device, and (iii) to combine the three histories such that a 'click' in the detector at the output of the event filter (i.e., at the detector D_1) confirms that the desired event has happened. Hence, in this design, the polarization d.o.f. of the photon behaves as the effective ancilla.

In the bottom port of BS_2, the photons from the two paths 01 and 11 arrive with horizontal and vertical polarizations respectively $-$ hence, they can not interfere. In order to make the two histories interfere, a half-wave plate (HWP_2) and PBS combination can be used. The action of HWP_2 with its fast axis oriented at θ with respect to horizontal, on $|H\rangle$ and $|V\rangle$ states result,

$$HWP(\theta)\,|H\rangle = \cos(2\theta)\,|H\rangle + \sin(2\theta)\,|V\rangle \tag{5.50}$$

$$HWP(\theta)\,|V\rangle = \sin(2\theta)\,|H\rangle - \cos(2\theta)\,|V\rangle \tag{5.51}$$

With a PBS placed right after HWP_2, both 01 and 11 beams are projected to polarization $|H\rangle$ in the transmitting port and to polarization $|V\rangle$ in the reflecting port of the PBS – causing interference between the two beams. Let, the output port of the PBS, where $01, 11$ are projected to $|H\rangle$ i.e., where the detector D_1 is located in Fig. 5.4, is chosen as the output to the event filter as well.

Therefore, from the beam in $path-T$, only the photons from 00 path need to be directed towards D_1, while preventing the photons from 10 path from reaching the detector. This is achieved by placing another half-wave plate HWP_3 with its fast axis at $\frac{\pi}{4}$ with respect to the horizontal, i.e., as σ_x evolution operator in $path-T$ after BS_2. The HWP_3 changes the polarization of 00 beam from $|H\rangle$ to $|V\rangle$, and 10 beam from $|V\rangle$ to $|H\rangle$, so that 00 beam gets reflected from PBS towards the port with D_1 and 01 beam gets transmitted through PBS towards the other port. Thus, any click in the detector D_1 confirms that the detected photon has not traveled from 10 path, i.e., the event E has happened. With HWP_2 and HWP_3 in the setup, the state of the photon just before the PBS becomes,

$$|\psi_4\rangle' = (r_1 r_2 e^{i\varphi_1} e^{i\varphi_2} |T\rangle |V\rangle)^{(00)} + (r_1 t_2 e^{i\varphi_1} |B\rangle (\cos(2\theta) |H\rangle + \sin(2\theta) |V\rangle))^{(01)}$$
$$+ (t_1 t_2 e^{i\varphi_r} |T\rangle |H\rangle)^{(10)} + (t_1 r_2 e^{i\varphi_2} e^{i\varphi_r} |B\rangle (\sin(2\theta) |H\rangle - \cos(2\theta) |V\rangle))^{(11)} \tag{5.52}$$

To avoid any bias for any paths comprising the event $E = \{00, 01, 11\}$ during the detection, the angle of HWP_2 is chosen to be $\theta = \frac{\pi}{8}$ so that the half-wave plate behaves as a Hadamard operator that transforms the states $|H\rangle$ and $|V\rangle$ associated with 01 and 11 beams to $|+\rangle$ and $|-\rangle$ respectively [8], as can be seen by putting $\theta = \frac{\pi}{8}$ to Eqn. 5.50 and 5.51. Hence, as the beams from $01, 11$ are projected to $|H\rangle$ in the output of the event filter, the amplitudes $A(01)$ and $A(11)$ are modified by a factor $\frac{1}{\sqrt{2}}$. Similarly, to remove the bias from 00 beam, a $50:50$ (non-polarizing) beam splitter BS_3 is placed in $path-T$, which modifies the amplitude of the beam in this path by $\frac{1}{\sqrt{2}}$ as well. Hence, at this condition the state just before the PBS becomes,

[8] where $|+\rangle = \frac{|H\rangle + |V\rangle}{\sqrt{2}}$ and $|-\rangle = \frac{|H\rangle - |V\rangle}{\sqrt{2}}$, represents an unbiased superposition of $|H\rangle$ and $|V\rangle$.

$$|\psi_4\rangle = \frac{1}{\sqrt{2}}\Big[(r_1 r_2 e^{i\varphi_1} e^{i\varphi_2}\,|T\rangle\,|V\rangle)^{(00)} + (r_1 t_2 e^{i\varphi_1}\,|B\rangle\,(|H\rangle + |V\rangle))^{(01)} \\ +(t_1 t_2 e^{i\varphi_r}\,|T\rangle\,|H\rangle)^{(10)} + (t_1 r_2 e^{i\varphi_2} e^{i\varphi_r}\,|B\rangle\,(|H\rangle - |V\rangle))^{(11)}\Big] \tag{5.53}$$

As the beam passes through the PBS, the states in the two output ports of it with detectors D_1 and D_2 respectively, are given as

$$|\psi_5\rangle_{d_1} = \frac{1}{\sqrt{2}}\left[r_1 r_2 e^{i\varphi_1} e^{i\varphi_2}\,|V\rangle + r_1 t_2 e^{i\varphi_1}\,|H\rangle + t_1 r_2 e^{i\varphi_2} e^{i\varphi_r}\,|H\rangle\right] \tag{5.54}$$

$$|\psi_5\rangle_{d_2} = \frac{1}{\sqrt{2}}\left[r_1 t_2 e^{i\varphi_1}\,|V\rangle + t_1 t_2 e^{i\varphi_r}\,|H\rangle - t_1 r_2 e^{i\varphi_2} e^{i\varphi_r}\,|V\rangle\right] \tag{5.55}$$

Hence at the position of D_1, the beams from 01 and 11 paths reach with the polarization $|H\rangle$ and the beam from 00 path reaches with polarization $|V\rangle$, i.e., at the output of the event filter $01, 11$ beams interfere. The probability of detection at D_1 is,

$$\mathcal{P}_{d_1} = \left|\langle\psi_5|\psi_5\rangle_{d_1}\right|^2 = \frac{1}{2}\left(\left|r_1 r_2 e^{i\varphi_1} e^{i\varphi_2}\right|^2 + \left|r_1 t_2 e^{i\varphi_1} + t_1 r_2 e^{i\varphi_2} e^{i\varphi_r}\right|^2\right) \tag{5.56}$$

$$\mathcal{P}_{d_1} = \frac{1}{2}\left(\left|r_1 r_2\right|^2 + \left|r_1 t_2 + t_1 r_2 e^{i(\varphi_2-\varphi_1)} e^{i\varphi_r}\right|^2\right) \tag{5.57}$$

In an ideal scenario, the detector D_1 clicks in the arrival of a photon from any one of 00, 01, or 11 paths, i.e., D_1 clicks when the event E happens. Thus, the probability of D_1 clicking is the same as the probability of occurrence of the event E. Comparing the probability $\mathcal{P}_{d_1}$ with the expression in Eqn. 5.49, we get $\mathcal{P}_{d_1} = \dfrac{\mu(E)}{2}$. The factor $\dfrac{1}{2}$ arises owing to the design of the event filter, where half of the photons that belong to the particular event E can not reach the detector D_1. This factor appears in the attempt to combine the histories $00, 01, 11$ ensuring interference only between 01 and 11, as we aim to measure the probability $\mathcal{P}_{d_1}$ at the particular output. The second term in the expression of $\mathcal{P}_{d_1}$ in Eqn. 5.57 represents the interference between the two paths 01 and 11 with the relative phase being $\varphi = \varphi_r + \varphi_2 - \varphi_1$. For maximum interference intensity, the phase φ can be made to zero by adjusting the path lengths within the MZI, so that beams from 01 and 11 constructively interfere [9]. Thus experimentally, the probability of click on detector D_1 can be obtained by recording the number of photons that arrive at D_1 from an ensemble of identical photons being incident on the setup in a condition when $\varphi = 0$. Upon determining the probability, the quantum measure $\mu(E)$ for the event E is obtained by multiplying it with the factor (here, 2) owing to the design of the event filter.

5.4.3 Comparing the Original Scheme and the Proposed Experiment: Addressing Potential Challenges and Limitations

The setup outlined in Fig. 5.4 can be considered as a toy model of the ancilla-based event filter described in [30] for the table top demonstration of determining the quantum measure of an event. In the original scheme, independent ancillas are coupled to the system after each device. Path information of the system after a device or the outcome of an observable corresponding to a device is encoded in the corresponding ancilla state and the probability of occurrence of an event is obtained non-destructively through measurements on the joint state of ancillas. Therefore, for a N-device setup, N number of independent ancillas are to be coupled to the system in a way that coupling of one ancilla does not affect the information already encoded by the previous ancillas, so that the joint ancilla state directly represents the trajectory of the system within the setup.

However, the scheme does not talk about any potential interactions between the ancillary systems or does not account for any loss in the combined system-ancilla setup. But in the real scenario, the evolution of the system throughout the setup is not always unitary, hence losses are associated. Also, depending on the choice of the ancillas, they can interact and even affect each others operation causing loss in the information. On top, if variables corresponding to different degrees of freedom other than the path degree of freedom of the same system that is propagating through the setup are selected to represent the ancillas, then observations on the combined ancilla variables to know if the intended event has

[9] For experiments with single photons, that has finite and small longitudinal coherence length, compensation of the additional path length in 11 beam due to the propagation through the thickness of HWP_1 (which is accounted in φ_r) is important to maintain the longitudinal coherence between the interfering beams and to get higher interference visibility.

occurred or not, would lead to destructive measurements, i.e., the particle would be lost during the detection.

In the setup shown in Fig. 5.4, a click in the detector D_1 would correspond to a destructive verification of the occurrence of the event. Affirmation of the occurrence of the event in a non-invasive manner is however possible, through the observation of "no clicks" in the detectors D_2 and D_3 once a photon had entered the setup. Here, there will be no detector at the output of the event filter (i.e., at the location of D_1), which would allow the photons belonging to the desired event E to continue its process without getting affected. For the setup in 5.4, a photon propagating through it, in a single run of the experiment, would end up either at D_1 or D_2 or D_3 (in ideal conditions without any loss). Thus, no click in detectors D_2 and D_3 would directly imply the arrival of the photon at the location of D_1, i.e., implies the success of the event E. This procedure, where an outcome of an experiment is inferred when the detector(s) does not register any count, is known as the "Negative Result Measurement" [37], employed to ensure non-invasive measurability up to a point where neither the current state nor the subsequent dynamics of the system are affected by an interaction during the measurement [38]. In this case, the probability of the event E is given as $\mathcal{P}_E \equiv \mathcal{P}_{d_1} = \mathcal{P}^{'}_{d_2}\mathcal{P}^{'}_{d_3} = 1 - \mathcal{P}_{d_2} - \mathcal{P}_{d_3}$, where $\mathcal{P}_{d_i}$ and $\mathcal{P}^{'}_{d_i}$ represents the probability of "click" and probability of "no click" of the detector D_i respectively. Thus, the probability of the event can be determined from experimentally obtained probabilities $\mathcal{P}_{d_2}$ and $\mathcal{P}_{d_3}$. However, in a real scenario affirming the success of the desired event from no clicks of the detectors D_2 and D_3, is subjected to the characterization of the setup for the possible losses and efficiency of the detectors being used.

Again according to the original scheme, in the setup where a photonic system encounters two beam splitters one after the other, two independent ancillas need to be coupled so that the joint state of the ancillas, once the system has come out of the setup, could be associated with the exact path taken by the system. One of the possible choices of the ancillas could have been the transverse displacement of the system along the two orthogonal directions, one direction variable each indicating the outputs of one device. Let, the local z-direction is considered as the direction of propagation of the beam with a Gaussian cross section along the local $x - y$ plane. The spatial distribution of the system at time t_0, when it incidents on BS_1 of the setup in Fig. 5.5 can be expressed as,

$$\psi_0(x,y) = A\exp\left(-\frac{x^2}{4\sigma^2}\right)\exp\left(-\frac{y^2}{4\sigma^2}\right) \tag{5.58}$$

Here, σ represents the width of the Gaussian beam assumed to be centered about $(x_0, y_0) = (0,0)$ and A is the amplitude of the beam at the time of incidence on BS_1 [10].

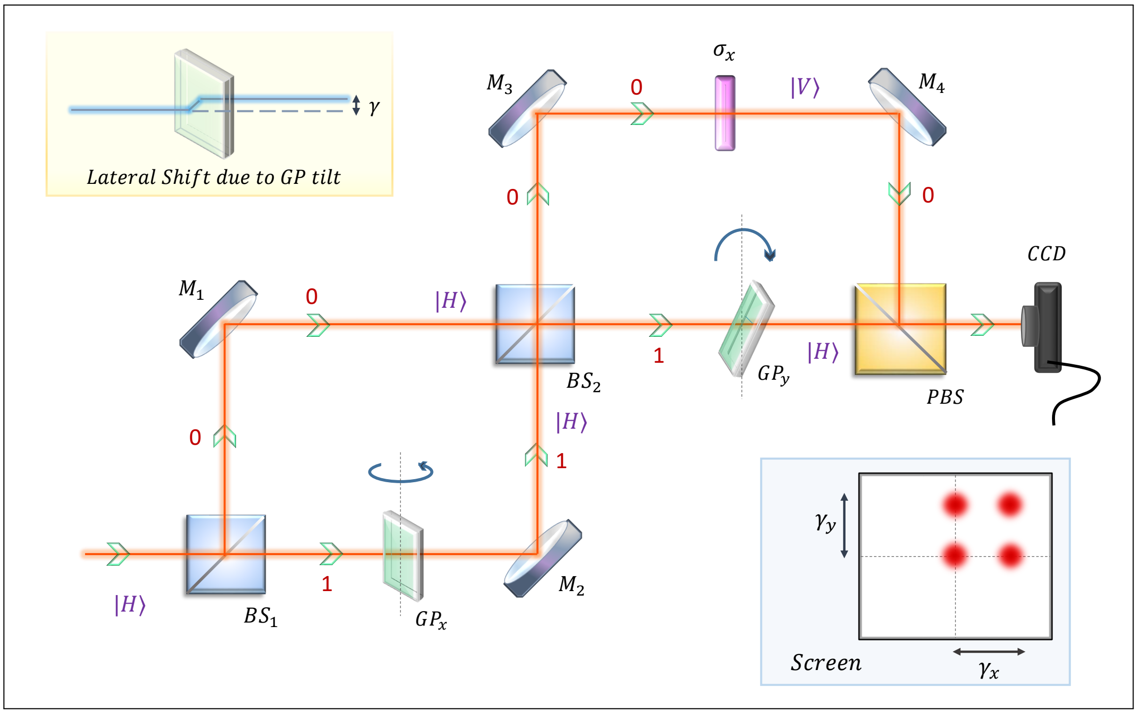

Figure 5.5: Schematic of the setup with two devices BS_1 and BS_2, each having two output ports. The four possible paths of a photon, which is incident on the setup with horizontal polarization ($|H\rangle$), are combined using a HWP realized as a σ_x evolution operator (i.e., having the fast axis oriented at $\frac{\pi}{4}$ w.r.to the horizontal) in the upper path after BS_2 and a polarizing beamsplitter PBS. The 01, 11 beams in $|H\rangle$ would get transmitted through the PBS and the 00, 10 beams that are transformed by the HWP from $|H\rangle$ to $|V\rangle$ would get reflected from the PBS to the same port. The spatial distribution of the photon reaching the output taking any of the four paths, when captured by a CCD camera gives the location of the center/centroid of the beam. The history of the photon within the setup can be identified by observing the relative displacement of the center/centroid when two glass plates GP_x – tilted to give a transverse shift γ_x along x and GP_y – tilted to give a transverse shift γ_y along y are placed respectively in the bottom paths after BS_1 and BS_2.

[10]The Gaussian is assumed to be symmetric along the $x - y$ plane, giving $\sigma_x = \sigma_y = \sigma$.

Now, let one glass plate each be placed in the lower paths after the beam splitters, as can be seen from Fig. 5.5, so that whenever the system emerges out in the lower path after a device, its center/centroid undergoes a transverse shift. The glass plates GP_x after BS_1 and GP_y after BS_2 are respectively tilted in such a way that GP_x cause a transverse shift γ_x along the $x-$direction and GP_y causes a transverse shift γ_y along the $y-$direction of the beams passing through them [11]. Thus, at the end of the setup observing the combined ancilla variables i.e., the combined displacements caused by the two glass plates, the trajectory of the photon within the setup can be inferred.

After BS_1, the ancilla coupling makes the spatial distribution of the system associated with the spatial modes $|U\rangle$ and $|L\rangle$ to be,

$$\textbf{Upper path:} \quad \psi_2^{(0)}(x,y) = Ar_1 e^{i\varphi_1} \exp\left(-\frac{x^2}{4\sigma^2}\right) \exp\left(-\frac{y^2}{4\sigma^2}\right) \tag{5.59}$$

$$\textbf{Lower path:} \quad \psi_2^{(1)}(x,y) = At_1 \exp\left(-\frac{(x-\gamma_x)^2}{4\sigma^2}\right) \exp\left(-\frac{y^2}{4\sigma^2}\right) \tag{5.60}$$

The above states just before BS_2 are represented without considering the relative phase φ_r due to the path length difference between the two paths $path - U$ and $path - L$ within the interferometer.

Next, after BS_2 and coupling of the $2nd$ ancilla, the spatial distribution of the beams from $00, 01, 10, 11$ are respectively represented as,

$$\textbf{Path-00:} \quad \psi_4^{(00)}(x,y) = Ar_1 r_2 e^{i\varphi_1} e^{i\varphi_2} \exp\left(-\frac{x^2}{4\sigma^2}\right) \exp\left(-\frac{y^2}{4\sigma^2}\right) \tag{5.61}$$

$$\textbf{Path-01:} \quad \psi_4^{(01)}(x,y) = Ar_1 t_2 e^{i\varphi_1} exp\left(-\frac{x^2}{4\sigma^2}\right) \exp\left(-\frac{(y-\gamma_y)^2}{4\sigma^2}\right) \tag{5.62}$$

[11] Alternately, in the two output ports of a beam splitter two glass plates could have been placed with the respective tilts causing shifts along $+x$ and $-x$ directions (i.e., $x_0 \pm \gamma_x$) to the center/centroid of the system emerging in the upper path and lower path after BS_1 and causing shifts along $+y$ and $-y$ directions (i.e., $y_0 \pm \gamma_y$) to the system emerging in the upper and lower paths after BS_2.

$$\textbf{Path-10:} \quad \psi_4^{(10)}(x,y) = At_1t_2 \exp\left(-\frac{(x-\gamma_x)^2}{4\sigma^2}\right) \exp\left(-\frac{y^2}{4\sigma^2}\right) \tag{5.63}$$

$$\textbf{Path-11:} \quad \psi_4^{(11)}(x,y) = At_1r_2e^{i\varphi_2} \exp\left(-\frac{(x-\gamma_x)^2}{4\sigma^2}\right) \exp\left(-\frac{(y-\gamma_y)^2}{4\sigma^2}\right) \tag{5.64}$$

Once all the beams are recombined (say, at time t_5), the four possible trajectories of the system within the setup can be identified by observing the location of the center/centroid of the beam or the location of the photon on a detecting screen in a single run. So, looking at the ancilla variables jointly we can comment that the photons that show no shift, a $y-$shift, a $x-$shift and a diagonal shift respectively belong to the paths $00, 01, 10, 11$.

Thus, in order to determine the probability of the event $E = \{00, 01, 11\}$, the statistics of the photons at t_5 need to be determined except for those that show only horizontal (x-) shift. Again, to ensure the interference between 01 and 11, quantitatively the displacement caused by GP_x needs to be much smaller than the beam width, i.e., $\gamma_x << \sigma$. However, contrary to that the photons coming from the 10 path can not be distinguished (from the photons from the 00 path) unless the displacement γ_x is larger than the beam width σ. A larger transverse shift along x would affect the overlap between $01, 11$ beams and hence the interference, changing the obtained probability of the event. Thus, to avoid the contest between the requirement of $\gamma_x << \sigma$ to make the histories $01, 11$ interfere and the requirement of $\gamma_x > \sigma$ to identify the photons 10 in order to eliminate them from the determination of probability, we have chosen a design where the polarization of the photon behaves as the effective ancilla.

In the design given in Fig. 5.4 operations on the polarization d.o.f. are performed to ensure interference between the desired set of histories and reject the undesired history along with associating a particular outcome of a projective measurement on the polarization basis to the occurrence of the event E of interest. Here, we have given up on the idea of relating different paths with a separate combination of independent ancilla variables to identify them individually, rather we constructed the setup to identify the event, i.e., to confirm the arrival of the photon from any one of the desired set of paths that comprises the event without actually knowing which path.

❑ **Inferring the measure of a non-serial event from the measures of serial events:** Again, the non-serial event $E = \{00, 01, 11\}$ can be considered as the disjoint union of two serial events, $E_1 = \{00\}$ (where a photon emerges in the upper path after each device) and $E_2 = \{01, 11\}$ (where a photon randomly chooses any of the two paths after the first device, then emerges at the lower path of the second device). Thus, the event E can be expressed as $E = E_1 \cup E_2$, implying $\mu(E) = \mu(E_1) + \mu(E_2)$. Therefore in an experimental scenario, the measure $\mu(E)$ can be determined by adding the measures for E_1 and E_2 obtained individually. The measure for a serial event can be directly obtained through standard measurement procedure, i.e., through the sequence of suitable projective measurements without the need to use any ancilla, as shown in the Fig. 5.6.

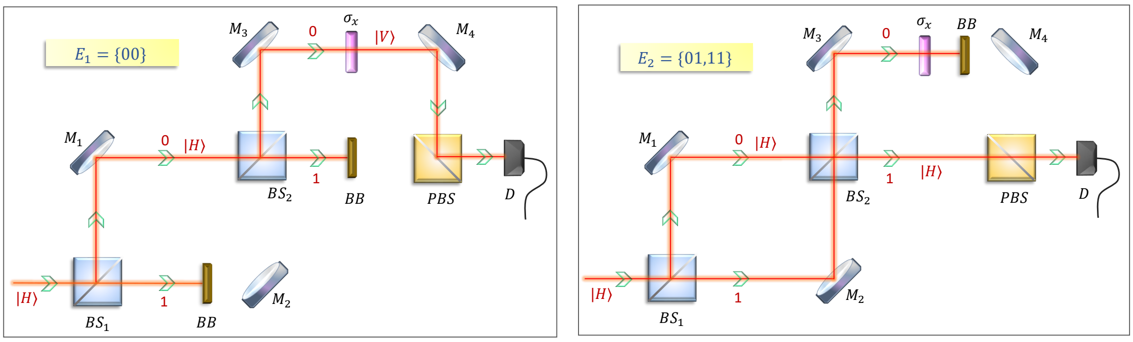

(a) Setting to determine $\mu(E_1)$ for $E_1 = \{00\}$ (b) Setting to determine $\mu(E_2)$ for $E_2 = \{01, 11\}$

Figure 5.6: Experimental determination of $\mu(E)$ for non-serial event $E = \{00, 01, 11\}$ from the sum of the measures $\mu(E_1)$ and $\mu(E_2)$ associated with the serial events $E_1 = \{00\}$ and $E_2 = \{01, 11\}$, obtained from the two different settings of the experimental setup where the undesired paths for each event are blocked by beam blockers (BB).

When a horizontally polarized photon enters the setup shown in Fig. 5.6, it can take four possible paths, all of which are combined using a HWP (with its fast axis at $\frac{\pi}{4}$ w.r.to horizontal) as σ_x operator which transforms $|H\rangle$ to $|V\rangle$ and vice versa and a PBS. The determination of $\mu(E)$ from $\mu(E_1)$ and $\mu(E_2)$ requires detection to be made at two different experimental settings – each corresponding to a serial event, where the photons are made to follow certain paths by blocking the other possible paths using the beam blockers (BB). For the setting shown in Fig. 5.6a, i.e., when the lower path after BS_1 and lower path after BS_2 are blocked, the probability of click in the detector D gives the measure for $E_1 = \{00\}$. Next, in another setting when the upper path after BS_2 is blocked as shown in Fig. 5.6b, the probability of click in the detector gives the measure for $E_2 = \{01, 11\}$. The effect of interference for this event is captured by the detector D in this setting. Though, the determination of quantum measure in this manner appears to be quantitatively equivalent (i.e., produces similar results) to those procedures involving the ancillas, this technique does not ensure that the detected photons actually belong to the event E, i.e., it does not confirm the occurrence of the desired event. This is just a computation of the measure value $\mu(E)$ from the two values $\mu(E_1)$ and $\mu(E_2)$. Hence, this procedure can not be considered as a demonstration of the determination of quantum measure of an event, however can be used for the verification of the value of $\mu(E)$ obtained experimentally from the measurements performed in an "event filter" based setup shown in Fig. 5.4.

5.5 Inferring the Quantum Measure of a Photonic Event: An Experimental Demonstration

The last section discusses the applicability of the experimental scheme presented in Sec. 5.3 for the determination of the quantum measure of an event associated with a photonic system. Potential design of "event filter" for an event $E = \{00, 01, 11\}$ is presented in Fig. 5.4, where a photonic system encounters two devices i.e., two beam splitters BS_1 and BS_2 with the two output ports labelled as 0 and 1 respectively. The histories of the system are represented by its spatial degree of freedom, while the polarization degree of freedom of the same system acts as an effective ancilla. Operations on the polarization d.o.f. are performed in such a way that detection at the output of the event filter reveals that the desired event E has happened. Determining the probability of the occurrence of the event E experimentally, the quantum measure $\mu(E)$ is inferred. Here, we aim to experimentally demonstrate the idea of event filtering that would extract the desired set of histories from the history space and determine the quantum measure of a photonic event by implementing the model with the components commonly available in an optics lab.

To be able to determine the quantum measure in a laboratory setting would provide an experimental footing to the quantity that so far has only the theoretical construct. The knowledge of the quantum measure obtained from the implementation of an ancilla based event filter setup would help in interpreting the micro-system and predicting its dynamics, especially when it undergoes non-serial events like $E = \{00, 01, 11\}$, as the probability for such an event can not be determined from the expectation value of an operator as described by standard quantum formalism. Additionally, the effect of interference between 01 and 11 paths with a relative phase within a certain range, has the potential to take the value of the quantum measure of the event E beyond the classical upper limit of one (i.e., $\mu_{C,max} = 1$). Therefore, a successful demonstration of the proposal would present an experimental scenario capable of capturing the non-classical nature of the quantity, paving the way for further tests on fundamental aspects of quantum mechanics.

5.5.1 The Experimental Setup:

Here, we will present an experimental setup allowing interference, the analysis of which can give the value of the quantum measure of a particular event E associated with a photonic system. For the experimental demonstration within the two-hopper model designed with two beam splitters, few modifications are made in the optical setup as compared to the setup shown in Fig. 5.4. Mostly the changes are made in the "system propagation region", i.e., in the arrangement of the devices through which the photon has to propagate. Instead of a Mach-Zehnder Interferometer (MZI) configuration, here the two beam splitters BS_1 and BS_2 are arranged in the form of a displaced Sagnac Interferometer (DSI), as depicted in Fig. 5.7. The interferometer is modified to a DSI to achieve better interferometric stability against the mechanical or acoustic vibrations, noises, temperature variation etc. that affect the alignment of the optical components [12] and hence, impact the performance of the setup [39]. Interference in MZI is very sensitive to the ambient condition changes, as the two paths in the MZI encounter different optical components. Any external vibration impacts the individual paths differently, resulting in a randomly varying path length difference that affects the relative phase between the interfering beams, changing the interference intensity for the collinear configuration of the interferometer [13]. One of the possible ways of maintaining a consistent phase throughout the experiment is to actively

[12] The optomechanics on which the optical components are mounted show a temperature dependent alignment stability as well, i.e., as the temperature changes its alignment changes.

[13] For the non-collinear configuration of the interferometer a fluctuating relative phase causes a shift in the interference fringes over the beam width.

stabilize the MZI, using a real time closed loop feedback system and a piezo [14] driven path correcting mechanism [41]. In order to avoid the complexity in the setup, for the demonstration purpose, we have chosen the displaced Sagnac configuration for designing the interferometer, which is considered to be more stable than MZI due to its geometry [42, 43]. In displaced Sagnac configuration, both the interfering paths interact with the same optical components [44] and hence, any external vibration affects the two paths simultaneously in a similar manner, maintaining a constant phase relationship between them.

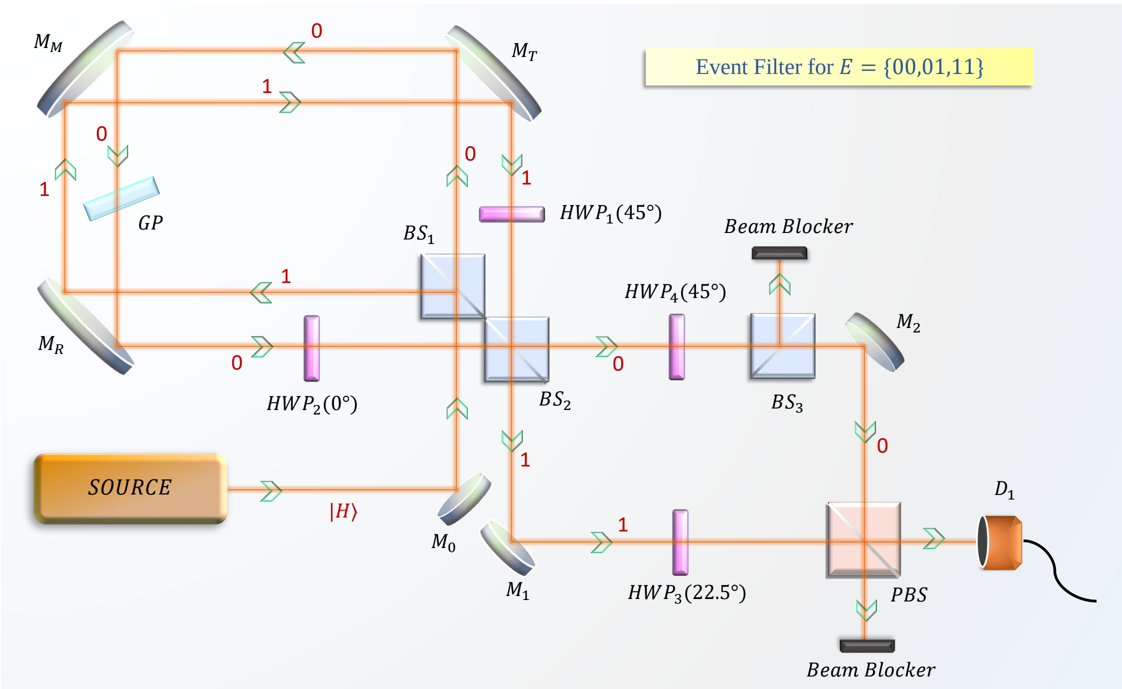

Figure 5.7: Schematic of an optical setup for the table top demonstration of inferring the value of quantum measure of an event $E = \{00, 01, 11\}$ associated with a photonic system that passes through two non-polarizing beam splitters, each with two output ports labelled as 0 and 1, arranged in the displaced Sagnac geometry.

[14] A piezo-electric device expands or contracts linearly depending on the voltage provided to it. Hence, a piezo when attached to a mirror in one of the paths of the MZI, its expansion or contraction causes the mirror to move forward or backward, compensating for the path length difference within the interferometer. However, to avoid the lateral shift (and any angular shift) of the beam reflecting from the mirror as it moves, it is preferred to have the piezo mounted on a Corner Cube Retroreflector (CCR) that reflects a beam parallel to the incident beam with a lateral shift between them depending on the point where the incident beam hits the CCR [40].

The experimental setup for the determination of the quantum measure of a particular event $E = \{00, 01, 11\}$ of a photonic system is shown in Fig. 5.7, where the system successively encounters two $50:50$ non-polarizing beam splitters BS_1 and BS_2. The upper or lower paths, taken by the system while emerging from each beam splitter, are labelled as 0 or 1 respectively. The two beam splitters are arranged to form a dispaced Sagnac Interferometer (DSI) with the mirrors M_T, M_R and M_M that directs the system from the output ports of BS_1 to the input ports of BS_2 through clockwise and counter-clockwise paths. Within the "system propagation region", i.e., from the input to BS_1 till the output of BS_2, the system is free to choose any of the four trajectories $\{00, 01, 10, 11\}$. After BS_2 the event of interest $E = \{00, 01, 11\}$ would be filtered out by acting on the polarization d.o.f. of the system in the "event filtration region", exactly the same manner described for setup in Fig. 5.4. The value of quantum measure $\mu(E)$ would be inferred by analyzing the counts in the detector D_1 at the output of the event filter.

A photon incident on BS_1 from one of the input ports, as shown the Fig. 5.7, would either undergo a counter-clockwise path $|\circlearrowleft\rangle$ (labelled as 0) after transmission or undergo a clockwise path $|\circlearrowright\rangle$ (lablled as 1) following reflection – both the paths recombine at BS_2. The amplitudes associated with the possible histories within the system propagation region, would be

$$A(00) = t_1 t_2, \quad A(01) = t_1 r_2 e^{i\varphi_2}, \quad A(10) = r_1 r_2 e^{i\varphi_1} e^{i\varphi_2}, \quad A(11) = r_1 t_2 e^{i\varphi_1} \tag{5.65}$$

where t_i and $r_i e^{i\varphi_i}$ respectively represent the transmission and reflection coefficients of BS_i. For the event of interest $E = \{00, 01, 11\}$, the quantum measure can be computed using the expression in Eqn. 5.39, as the following:

$$\mu(E) = |t_1 t_2|^2 + \left| t_1 r_2 e^{i\varphi_2} + r_1 t_2 e^{i\varphi_1} \right|^2 \tag{5.66}$$

For $50:50$ symmetric beam splitters, $t_i = \dfrac{1}{\sqrt{2}}$ and $r_i e^{i\varphi_i} = \dfrac{i}{\sqrt{2}}$, giving the measure to be

$$\mu(E) = \left| \frac{1}{\sqrt{2}} \frac{1}{\sqrt{2}} \right|^2 + \left| \frac{1}{\sqrt{2}} \frac{i}{\sqrt{2}} + \frac{i}{\sqrt{2}} \frac{1}{\sqrt{2}} \right|^2 = \frac{1}{4} + 1 = \frac{5}{4} = 1.25 \tag{5.67}$$

The paths $\{|\circlearrowleft\rangle, |\circlearrowright\rangle\}$ taken by the system within the interferometer are marked by the polarization states $\{|H\rangle, |V\rangle\}$. This is achieved for a system incident on the setup with horizontal polarization ($|H\rangle$) by evolving it through half-wave plates HWP_1 in the clockwise path and HWP_2 in the counter-clockwise path, with their fast axis respectively at 45° and 0° with respect to the horizontal. HWP_1 at 45° realizes a $\hat{\sigma}_x$ operator that changes $|H\rangle$ to $|V\rangle$ and vice versa, while HWP_2 at 0° forms a $\hat{\sigma}_z$ operator that leaves $|H\rangle$ unaffected and introduces a phase π to $|V\rangle$. Hence, the state of the photon just before BS_2 would be, $t_1 |\circlearrowleft\rangle |H\rangle + r_1 e^{i\varphi_1} |\circlearrowright\rangle |V\rangle$. The presence of HWP_2 in the counter-clockwise path (i.e., path 0) is important for single photon interferometry in order to compensate for the additional optical path length introduced in path 1 during the propagation through HWP_1, since the single photons generated through processes like spontaneous parametric down-conversion (SPDC) typically have smaller coherence lengths (of the order of few hundreds of μm). However, HWP_2 may not be required for the interferometric experiment with beams having higher coherence lengths (as presented in the next chapter).

The determination non-classical value of measure, i.e., $\mu(E) = 1.25$ as obtained in Eqn. **5.67**, demands constructive interference to occur between the systems coming from the two paths 01 and 11 that correspond to the same output port of BS_2. However, after the DSI the photons from 01 and 11 paths in the setup have orthogonal polarizations $|H\rangle$ and $|V\rangle$ respectively, hence do not interfere. They are made to interfere by evolving through a half-wave plate HWP_3 with its fast axis at 22.5° that transforms $\{|H\rangle, |V\rangle\}$ to $\{|+\rangle, |-\rangle\}$ and then projecting them to $|H\rangle$ in the transmitting port of a PBS, which is considered as the output of the event filter. Generally, in an ideal DSI there should not be any relative phase arising due to the path length difference between the two paths of the interferometer, because of the given geometry. However, the non-idealness of the optical components like the scratches, surface roughness, dust on the optics, etc. introduces a path length difference between the beams in the two paths, as they hit the optics at two different points due to the displacement between them. This results in a relative phase between the interfering beams. Therefore, to ensure the constructive interference between 01 and 11, a glass plate GP is placed in any one of the paths within the interferometer and the tilt of it is adjusted to set any relative phase between the interfering beams to zero [15].

[15]Details of the effect of the GP is given in Chapter. 6

Next, in the upper path after BS_2, a half-wave plate (HWP_4) as $\hat{\sigma}_x$ and a $50:50$ non-polarizing beam splitter BS_3 are placed that direct the photons from 00 path towards the output of the filter with the same normalizing factor as 01 and 11 paths, while rejecting the photons from 10. Operations on the polarization d.o.f. combines the three paths in such a way that any click at detector D_1 placed at the output of the event filter reveals that the detected photon has travelled from any of the three paths $00, 01, 11$. The quantum measure $\mu(E)$ of the event E is inferred from the probability of occurrence of the event which can be determined from the ratio of the obtained counts at the output of the event filter and at the input to the setup.

However, arranging the two beam splitters BS_1 and BS_2 experimentally to form a displaced Sagnac geometry in collinear configuration requires fine adjustments to align them in a way that the cuts of the beam splitters are exactly parallel to each other or at best, lies along a same straight line. Any relative vibration between the two would change the overlap of the interfering beams and the relative phase, affecting the interference intensity. Therefore, to further increase the stability of the setup and to reduce the alignment complexity, the arrangement of two beam splitters (BS_1 and BS_2) in the design in Fig. 5.7 can be replaced with a single big-sized beam splitter (say, BS). This re-arrangement in the setup would provide the same experimental demonstration of determining the quantum measure of a photonic event (here, $E = \{00, 01, 11\}$) from the probability of an outcome of a projective measurement. However, due to this modification, in this case the photon would encounter a single device (a $50:50$ BS) twice instead of encountering two identical devices (i.e., two $50:50$ beam splitters) one after the other, resulting in the same value for quantum measures for all the events. Modifying the transmission and reflection amplitudes with the substitution $t_1 = t_2 = t$ and $r_1 e^{i\varphi_1} = r_2 e^{i\varphi_2} = re^{i\varphi}$, we get the expression in Eqn. 5.66 giving the quantum measure for event $E = \{00, 01, 11\}$ to be $\mu(E) = |t|^2 + \left|tre^{i\varphi} + rte^{i\varphi}\right|^2 = \left|\frac{1}{\sqrt{2}}\right|^2 + \left|\frac{1}{\sqrt{2}}\frac{i}{\sqrt{2}} + \frac{i}{\sqrt{2}}\frac{1}{\sqrt{2}}\right|^2 = \frac{5}{4} = 1.25$, which remain the same as before.

A design of the 'event-filter' in a displaced Sagnac configuration with the use of a single beam splitter, is experimentally implemented in the next chapter of this thesis which presents a table-top demonstration to determine the value of the quantum measure for the particular event $E = \{00, 01, 11\}$ in a laboratory setting.

5.6 Conclusion

In this chapter, we have attempted to address the foundational interpretational puzzles of standard quantum theory from the perspective of a space-time realistic framework, Quantum Measure Theory that involves a generalization of probability − the ‘quantum measure’ to describe the dynamics of a quantum particle. Here, we have formally defined the constitutes of this framework, such as the histories which describe the kinematics of a system or the events associated with a system, and shown that the ‘quantum measure’ may differ from the Kolmogorov probability when interference is involved. An experimental method to identify the event through which the quantum system has undergone is presented using the concept of event-filtering employing ancillas, extending it further to infer the value of the ‘quantum measure’ of that event. A successful determination of quantum measure provides an immediate experimental footing to this theoretical notion so far, which opens up avenues for future tests on quantum foundations. For the demonstration, we have considered a two-site hopper setting in an optical setup. We have implemented it using amplitude division (instead of wavefront division) so that there would not be a need to assume whether the higher-order interference terms vanish or not and can be relied simply on the second-order interference for photons. In the next chapter, a toy model of the experiment will be presented, which could demonstrate an experimental scenario that can give a non-classical measure.

Appendix

5.A Histories Approach to Quantum Theory: State Based Formalism to History Based Formalism

Histories approach to Quantum Mechanics was introduced by Dirac and Feynman who aimed to formulate the quantum theory from an observer-independent perspective and with a space-time way of describing the reality. Histories are fundamental in this approach as compared to the state vectors or the wave functions in the standard formalism of quantum theory. Conventional non-relativistic quantum mechanics deals with wave functions, observables, measurement, etc. and puts a heavy emphasis on the notion of time that determines the events at individual instances. Therefore the histories in terms of standard theory can be described as a series of events at successive moments of time in between an initial and final time. Before the history-based formulations, the histories approach in quantum theory was discussed from the perspective of "standard" QM as discussed below.

5.A.1 Defining Histories in Standard Formalism

At an instant t_0, the standard quantum mechanical theory considers the system to be described by a state $|\psi(t_0)\rangle$ evolving in time under a given Hamiltonian $H(t)$ according to the Unitary evolution operator $U(t_1, t_0) = \exp\left(-\frac{1}{\hbar}\int_{t_0}^{t_1} H(t)dt\right)$ within a Hilbert space $\mathcal{H}$. The evolution is given by, $|\psi(t_1)\rangle = U(t_1, t_0)\,|\psi(t_0)\rangle$, where the evolution operator satisfies the relation $U(t_1, t_0) = U(t_1, t^{'})U(t^{'}, t_0)$ for $t_0 < t^{'} < t_1$. Measurement at an instant t corresponds to the projection onto a subspace of the Hilbert space $\mathcal{H}$ giving a particular outcome. Thus, every measurement outcome or an "event" according to [15] can be associated with projection operation, which may or may not be physically realizable. From the viewpoint of Hilbert space theory in the standard formalism of QM, a history is described as a sequence of events at successive moments of time i.e., a sequence of outcomes of a time-ordered set of projection operators [45]. A history $\gamma = (\alpha_1, \alpha_2, \ldots, \alpha_n)$ can be described by a set of projectors $\mathcal{P}_\gamma = \{P_{\alpha_1}, P_{\alpha_2}, \ldots, P_{\alpha_n}\}$, where α_i is the outcome of the projection operation P_{α_i} made at time t_i (where $t_i < t_{i+1}$). The final state of the quantum system at time t_n at the end of the history is given by,

$$\left|\psi_f^\gamma(t_n)\right\rangle = \frac{\hat{C}_\gamma \left|\psi(t_0)\right\rangle}{\left\|\hat{C}_\gamma \left|\psi(t_0)\right\rangle\right\|} \tag{5.68}$$

$$\text{where,} \qquad \hat{C}_\gamma = P_{\alpha_n} U(t_n, t_{n-1}) \ldots\ldots P_{\alpha_2} U(t_2, t_1) P_{\alpha_1} U(t_1, t_0) \tag{5.69}$$

Here, in the above expression, $|\psi(t_0)\rangle$ represents the initial state of the system at time t_0 and $\left\|\hat{C}_\gamma |\psi(t_0)\rangle\right\|$ defines the norm of the final state within the Hilbert space. The expression 5.69 for the operator (given in the Schrodinger picture) can be represented in the Heisenberg picture as follows,

$$\hat{C}_\gamma = U(t_n, t_0) P_{\alpha_n}(t_n) \ldots\ldots P_{\alpha_2}(t_2) P_{\alpha_1}(t_1) \tag{5.70}$$

$$\text{where,} \qquad P_{\alpha_i}(t) = U^\dagger(t, t_0) P_{\alpha_i} U(t, t_0) \tag{5.71}$$

Here, We would like to formulate a theory that can describe the classical macro world and the micro world consistently without any discrepancy. The decoherent histories approach can describe a system whose micro states follow quantum dynamics and it behaves classically at the macro level. For a decoherent set of histories, the non-diagonal terms of the decoherence functional matrix are zero, and the diagonal terms can be interpreted as probabilities. Thus, the decoherent histories formalism allows us to assign probabilities to a set of decoherent or consistent histories, without any requirement for any measurement, observation, measuring apparatus, etc. Thus this theory can be considered as a generalization of the Copenhagen interpretation in describing the entire universe as a whole from an observer independent perspective, though this theory still applies the notion of state vectors evolving in a Hilbert space.

References

[1] John Archibald Wheeler and Wojciech Hubert Zurek. *Quantum Theory and Measurement*. Princeton Series in Physics. Princeton: Princeton University Press, 1983.

[2] Nicolaas P. Landsman. "Born Rule and its Interpretation". In: *Compendium of Quantum Physics*. Ed. by Daniel Greenberger, Klaus Hentschel, and Friedel Weinert. Springer Berlin Heidelberg, 2009, pp. 64–70. DOI: 10.1007/978-3-540-70626-7_20.

[3] Matthew Leifer. "Is the Quantum State Real? An Extended Review of Ψ-ontology Theorems". In: *Quanta* 3.1 (2014), pp. 67–155. DOI: 10.12743/quanta.v3i1.22.

[4] Y. Aharonov, J. Anandan, and L. Vaidman. "Meaning of the wave function". In: *Phys. Rev. A* 47 (6 1993), pp. 4616–4626. DOI: 10.1103/PhysRevA.47.4616.

[5] Lluís Masanes, Thomas D. Galley, and Markus P. Müller. "The measurement postulates of quantum mechanics are operationally redundant". In: *Nature Communications* 10.1 (2019), p. 1361. DOI: 10.1038/s41467-019-09348-x.

[6] Maximilian Schlosshauer. "Decoherence, the measurement problem, and interpretations of quantum mechanics". In: *Rev. Mod. Phys.* 76 (4 2005), pp. 1267–1305. DOI: 10.1103/RevModPhys.76.1267.

[7] Yakir Aharonov, David Z. Albert, and Lev Vaidman. "How the result of a measurement of a component of the spin of a spin-1/2 particle can turn out to be 100". In: *Phys. Rev. Lett.* 60 (14 1988), pp. 1351–1354. DOI: 10.1103/PhysRevLett.60.1351.

[8] I. M. Duck, P. M. Stevenson, and E. C. G. Sudarshan. "The sense in which a "weak measurement" of a spin-1/2 particle's spin component yields a value 100". In: *Phys. Rev. D* 40 (6 1989), pp. 2112–2117. DOI: 10.1103/PhysRevD.40.2112.

[9] Wojciech H. Zurek. "Decoherence and the Transition from Quantum to Classical". In: *Physics Today* 44.10 (1991), pp. 36–44. DOI: 10.1063/1.881293.

[10] George F.R. Ellis. "On the limits of quantum theory: Contextuality and the quantum–classical cut". In: *Annals of Physics* 327.7 (2012), pp. 1890–1932. DOI: https://doi.org/10.1016/j.aop.2012.05.002.

[11] R. P. Feynman. "Space-Time Approach to Non-Relativistic Quantum Mechanics". In: *Rev. Mod. Phys.* 20 (2 1948), pp. 367–387. DOI: 10.1103/RevModPhys.20.367.

[12] Paul A. M. Dirac. "The Lagrangian in quantum mechanics". In: *Phys. Z. Sowjetunion* 3 (1933), pp. 64–72.

[13] James B. Hartle. "The spacetime approach to quantum mechanics". In: *Vistas in Astronomy* 37 (1993), pp. 569–583. DOI: https://doi.org/10.1016/0083-6656(93)90097-4.

[14] Roger Penrose. "On the Gravitization of Quantum Mechanics 1: Quantum State Reduction". In: *Foundations of Physics* 44.5 (2014), pp. 557–575. DOI: 10.1007/s10701-013-9770-0.

[15] C. J. Isham and N. Linden. "Quantum temporal logic and decoherence functionals in the histories approach to generalized quantum theory". In: *Journal of Mathematical Physics* 35.10 (1994), pp. 5452–5476. DOI: 10.1063/1.530759.

[16] J. B. Hartle. "Quantum kinematics of spacetime. II. A model quantum cosmology with real clocks". In: *Phys. Rev. D* 38 (10 1988), pp. 2985–2999. DOI: 10.1103/PhysRevD.38.2985.

[17] Rafael D. Sorkin. "On the Role of Time in the Sum Over Histories Framework for Gravity". In: *Int. J. Theor. Phys.* 33 (1994), pp. 523–534. DOI: 10.1007/BF00670514.

[18] Rafael D. Sorkin. *Quantum Measure Theory and its Interpretation*. 1997.

[19] Rafael D. Sorkin. "Quantum Mechanics as Quantum Measure Theory". In: *Modern Physics Letters A* 09.33 (1994), pp. 3119–3127. DOI: 10.1142/S021773239400294X.

[20] Sukanya Sinha and Rafael D. Sorkin. "A sum-over-histories account of an EPR(B) experiment". In: *Foundations of Physics Letters* 4.4 (1991), pp. 303–335. DOI: 10.1007/BF00665892.

[21] L. D. Landau and E. M. Lifshitz. *Mechanics, Third Edition: Volume 1 (Course of Theoretical Physics)*. Butterworth-Heinemann, 1976.

[22] R.B. Griffiths. *Consistent Quantum Theory*. Cambridge University Press, 2003.

[23] Max Born. "Quantenmechanik der Stoßvorgänge". In: *Zeitschrift für Physik* 38.11 (1926), pp. 803–827. DOI: 10.1007/BF01397184.

[24] Urbasi Sinha et al. "Testing Born's Rule in Quantum Mechanics with a Triple Slit Experiment". In: *AIP Conference Proceedings* 1101.1 (2009), pp. 200–207. DOI: 10.1063/1.3109942.

[25] Thomas Kauten et al. "Obtaining tight bounds on higher-order interferences with a 5-path interferometer". In: *New Journal of Physics* 19.3 (2017), p. 033017. DOI: 10.1088/1367-2630/aa5d98.

[26] G Rengaraj et al. "Measuring the deviation from the superposition principle in interference experiments". In: *New Journal of Physics* 20.6 (2018), p. 063049. DOI: 10.1088/1367-2630/aac92c.

[27] Omar S Magaña-Loaiza et al. "Exotic looped trajectories of photons in three-slit interference". In: *Nature Communications* 7.1 (2016). DOI: 10.1038/ncomms13987.

[28] Rahul Sawant et al. "Nonclassical Paths in Quantum Interference Experiments". In: *Phys. Rev. Lett.* 113 (12 2014), p. 120406. DOI: 10.1103/PhysRevLett.113.120406.

[29] Aninda Sinha, Aravind H. Vijay, and Urbasi Sinha. "On the superposition principle in interference experiments". In: *Scientific Reports* 5.1 (2015). DOI: 10.1038/srep10304.

[30] Álvaro Mozota Frauca and Rafael Dolnick Sorkin. "How to Measure the Quantum Measure". In: *International Journal of Theoretical Physics* 56.1 (2017), pp. 232–258. DOI: 10.1007/s10773-016-3181-x.

[31] Stanley P. Gudder and Rafael D. Sorkin. "Two-site quantum random walk". In: *General Relativity and Gravitation* 43.12 (2011), pp. 3451–3475. DOI: 10.1007/s10714-011-1245-z.

[32] L. Zehnder. "Ein neuer interferenzrefraktor". In: *Zeitschrift für Instrumentenkunde* 11 (1891).

[33] L. Mach. "Ueber einen interferenzrefraktor". In: *Zeitschrift für Instrumentenkunde* 12 (1892).

[34] A. Zeilinger. "General properties of lossless beam splitters in interferometry". In: *American Journal of Physics* 49.9 (1981), pp. 882–883. DOI: 10.1119/1.12387.

[35] Vittorio Degiorgio. "Phase shift between the transmitted and the reflected optical fields of a semireflecting lossless mirror is $\pi/2$". In: *American Journal of Physics* 48.1 (1980), pp. 81–81. DOI: 10.1119/1.12238.

[36] Arun Kumar Ajoy Ghatak. *Polarization of Light With Applications in Optical Fibers*. SPIE Press, 2011. DOI: 10.1117/3.861761.

[37] A. J. Leggett. "Experimental Approaches to the Quantum Measurement Paradox". In: *Foundations of Physics* 18.9 (1988), pp. 939–952. DOI: 10.1007/bf01855943.

[38] A J Leggett. "Realism and the physical world". In: *Reports on Progress in Physics* 71.2 (2008), p. 022001. DOI: 10.1088/0034-4885/71/2/022001.

[39] Michal Mičuda et al. "Highly stable polarization independent Mach-Zehnder interferometer". In: *Review of Scientific Instruments* 85.8 (2014), p. 083103. DOI: 10.1063/1.4891702.

[40] *TIR Retroreflector Prisms, Thorlabs.*

[41] Surya Narayan Sahoo et al. "Unambiguous joint detection of spatially separated properties of a single photon in the two arms of an interferometer". In: *Communications Physics* 6.1 (2023), p. 203. DOI: 10.1038/s42005-023-01317-7.

[42] Kaushik Joarder et al. "Loophole-Free Interferometric Test of Macrorealism Using Heralded Single Photons". In: *PRX Quantum* 3 (1 2022), p. 010307. DOI: 10.1103/PRXQuantum.3.010307.

[43] Surya Narayan Sahoo et al. "Quantum State Interferography". In: *Phys. Rev. Lett.* 125 (12 2020), p. 123601. DOI: 10.1103/PhysRevLett.125.123601.

[44] Masud Mansuripur. "The Sagnac interferometer". In: *Classical Optics and its Applications*. 2nd ed. Cambridge University Press, 2009, pp. 182–196. DOI: 10.1017/CBO9780511803796.017.

[45] H. F. Dowker and J. J. Halliwell. "Quantum mechanics of history: The decoherence functional in quantum mechanics". In: *Phys. Rev. D* 46 (4 1992), pp. 1580–1609. DOI: 10.1103/PhysRevD.46.1580.

Chapter 6

Experimental Determination of Quantum Measure in Photonic Systems

Contents

6.1 The Quantum Measure

6.2 Experimental Implementation of an Event Filter for Determining the Quantum Measure

6.3 Experimental Data Analysis: Dealing with Errors

6.4 Determination of the Experimental Distribution of Quantum Measure

6.5 Determination of the Theoretical Distribution of Quantum Measure

6.6 Quantum Measure of a Photonic Event: A Comparison of Experimental and Theoretical Distributions

6.7 Statistical Significance Analysis and Hypothesis Testing

6.8 Conclusion

Quantum Measure Theory (QMT) provides an alternative history-based formulation to quantum mechanics based on the sum over histories or path-integral approach, in which a quantum system can be described from a more realistic space-time perspective. Here, the ontology of a micro-system is described in terms of histories − a *history* gives the most complete description of the physical reality of a given system. The dynamics of the system is governed by the stochastic laws of motion for the histories and is presented in terms of a function − the *quantum measure*, that assigns a non-negative real number (which can exceed unity under certain circumstances) to a set of histories (i.e., an *event*) associated with the system. The knowledge of the quantum measures of the events for a given micro-system enables one to make predictions about the system behavior in a similar way to how the Born rule probability does in standard formalism.

As discussed in the previous chapter, though the quantum measure can be interpreted as the Born rule probability for certain events, in general, it goes beyond and presents itself as a *generalized probability* for all kinds of events, including those which can not be associated with a physically realizable observable. Therefore, *quantum measure* can not be simply interpreted as the expectation value of a self-adjoint operator and finding the value of it from an experiment seems unfeasible. However, the paper "How to Measure the Quantum Measure" [1] proposes a generalized experimental scheme that would allow one to determine the value of the quantum measure for any set of histories related to a given system. According to the scheme, for a quantum system propagating through a series of devices − recording the path information in the states of a group of ancillas (each coupled to the system after a device) and performing a projective measurement on the joint state of ancillas in a suitably chosen basis, one can infer the quantum measure of a desired event from the probability of one of the outcomes of the measurement. This chapter will present a table-top experimental demonstration of the scheme using a toy model of the ancilla-based event filtering setup for a photonic event. The significance of the experimentally obtained result would be analyzed through Hypothesis testing with respect to the classical-quantum boundary in order to establish the non-classical nature of the quantum measure obtained for an event involving interference.

6.1 The Quantum Measure

The expression for quantum measure (μ) for an event $E = \{\gamma^1, \gamma^2, ...\}$ obtained using the path integral formalism in Quantum Measure Theory [2], is given as

$$\mu(E) = \sum_{\gamma^i, \gamma^j \in E} A(\gamma^i) A^*(\gamma^j) \delta_{\gamma^i_{end}, \gamma^j_{end}} \tag{6.1}$$

where γ^i (similarly, γ^j) is one of the histories having the amplitude $A(\gamma^i)$ (similarly, the amplitude for γ^j being $A(\gamma^j)$) that comprises the event E. The quantity $\delta_{\gamma^i_{end}, \gamma^j_{end}}$ ensures the interference between the histories that end at the same point.

Hence, for the desired event $E = \{00, 01, 11\}$ [1] the two histories 01 and 11 would interfere and the quantum measure $\mu(E)$ for this event can be expressed as,

$$\mu(E) = |A(00)|^2 + |A(01) + A(11)|^2 \tag{6.2}$$

Experimentally we will design an event filter that will ensure the detection of beams coming from 00, 01 or 11 paths and not from 10 path. Then depending on the amplitudes associated with each detected path the value of the quantum measure would be determined.

Unlike classical measure theory, Quantum Measure Theory (QMT) allows for interference and because of that, quantum measure can not in general be interpreted as ordinary probability measure. Unlike classical probability measures, quantum measures (μ) do not follow the probability sum rule and can take values greater than one. The classical theory bounds the maximum possible value of measure to be one. Hence, any value of measure for an event obtained to be greater than one makes it non-classical. Here we aim to capture this non-classical nature of the measure associated with a quantum system by designing an experiment that gives μ value to be greater than one. From this experiment we will also be able to comment on the effect of interference in a quantum system.

[1] The reason for choosing this event is discussed in the previous chapter, i.e., Chapter 3.

6.2 Experimental Implementation of an Event Filter for Determining the Quantum Measure

In this section we will discuss the optical implementation of an 'event filter' for a photonic system using the idea similar to two-site hopper [3]. Here, the device would be a $50:50$ beam splitter (BS) which has two possible output ports (say, labelled as 0 and 1) $-$ any single photon incident on the beam splitter can either get transmitted through it or can get reflected from it. Thus the photon can be found in any one of the two possible spatial modes after the BS. Depending on the output port at which the photon emerges, the path of the photon is labelled as 0 or 1. Now, if a photon encounters such a beam splitter twice, there would be overall 4 possible paths ($\gamma^1 = 00, \gamma^2 = 01, \gamma^3 = 10, \gamma^4 = 11$) that the photon can access, making the history space to be $\Omega = \{00, 01, 10, 11\}$. We intent to design a setup, called the "Event Filter", such that we only get the photons coming from the paths that belong to the desired event E (here, $E = \{00, 01, 11\}$) i.e., any detection at the end of the setup confirms the occurrence of the event E.

This concept of "event filter" strictly applies to a single photon. A single photon entering an optical setup consisting of components that have multiple output ports would take any one of the n possible paths that comprise the entire history space Ω. In order that an event filter designed for the event $E^{'} = \{\gamma^1, \gamma^2, \ldots, \gamma^m\}$ succeeds, the detected photon should have traveled through any one the m (where $m \leq n$) paths that comprise the particular event $E^{'}$. Thus, while designing an "event filter" for the event E, the path of the single photon after each beam splitter BS is something that we are looking for. If many photons are incident on a beam splitter at once, some of the photons would get transmitted and some would get reflected depending on the splitting ratio of the given beam splitter. In other words, some of the photons would take path 0 and some would take path 1, causing all possible paths to be populated at a given point of time. Thus, the notion of "event filter" for a laser light source, the emitted beam from which is in the coherent state [4, 5], may appear inappropriate.

However, here in this experiment, our ultimate aim after designing the event filter is to obtain the value of measure μ associated with the particular event E. This requires us to determine the probability of the event. Also, while setting up the filter, the histories that end at the same point need to be made to interfere as well. Both these phenomena, i.e., (i) quantum interference, and (ii) probability measure, are described for an ensemble and can not be obtained from a single particle. These average statistical properties of light are equivalent for an ensemble of discrete photons and for a coherent beam, [6]. Therefore, the quantity of interest i.e, the value of the quantum measure for a particular event will be the same whether determined using a laser light source or a stream of single photons.

In this experiment, we have used laser light to demonstrate the working principle of an 'event filter' modeled for a photonic system and infer the value of the 'quantum measure' for a particular event. The system would be passing through a device, a beam splitter BS, twice within a Displaced Sagnac Interferometer geometry. The path degree of freedom of the system would be considered to label the histories associated with the system and the polarization degree of freedom of the same system would be considered as an effective ancilla, operations on which would filter out the desired event. The intensity of the beam would be measured at the input and the output of the event filter and the value of quantum measure would be obtained by post-processing the experimentally obtained data.

6.2.1 Aim of the Experiment:

In this experiment, we aim to demonstrate the determination of the value of the "measure" for an event $E = \{00, 01, 11\}$ associated with a photonic system by designing an event filter employing ancilla-coupling. Here, we also aim to establish the non-classical nature of the experimentally obtained quantity for the photonic system by analyzing its significance with respect to the classical-quantum boundary defined for "measure".

6.2.2 The Experimental Setup

An optical implementation of the event filter for an event $E = \{00, 01, 11\}$ is shown in Fig. 6.2. Light at wavelength $\lambda = 810\ nm$ emitting from a narrow bandwidth (linewidth typically $< 300\ kHz$) diode laser [$Toptica\ DL\ Pro$] is used as the source for this experiment. The laser beam is coupled to a FC/PC to FC/APC Polarization Maintaining Single Mode Fiber ($PMSMF$) [$P5-780PM-FC-2$, $Thorlabs$] using a fixed focus lens

[$F220APC - 780$, $Thorlabs$] mounted in a $6 - axis$ kinematic mount [$K6XS$, $Thorlabs$] with an adapter [$AD11F$, $Thorlabs$]. The APC (Angled Physical Contact) [7] end of the $PMSMF$ is connected to the coupling lens to minimize the back reflection and to prevent the back-reflected beam from entering into the laser cavity. The Polarization Maintaining Single Mode Fiber [8] is used to (i) maintain the polarization while the beam propagates through the fiber and hence to get stability in power after any polarization component placed at the fiber output, (ii) to reduce the pointing fluctuation about the transverse plane of the beam (compare to the bare beam), (iii) also to get the spatial mode at the output of the fiber as much Gaussian as possible [2].

At the output end of the $PMSMF$, an adjustable fiber collimator [3] [$CFC11P - B$, $Thorlabs$] is used to minimize (to be less than 1 $mrad$) the beam divergence. Here, the collimator COL is fixed for a condition where we obtain a beam width of around 1750 μm as recorded using a beam profiler [$WinCamD - UCD12$], while obtaining a beam divergence ≈ 0.43 $mrad$. The collimating lens is mounted on a $6 - axis$ kinematic mount [$K6XS$, $Thorlabs$] with an adapter [$AD15F2$, $Thorlabs$]. The beam from the $Collimator$ is redirected towards the setup for the event filter using the mirror M_0 [5102, $Newport$] mounted in [$SU100 - F2K$, $Newport$].

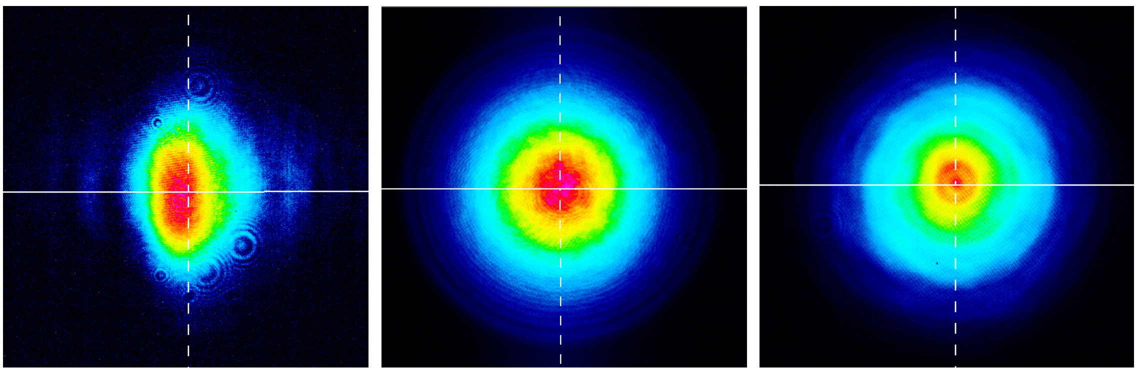

(a) Bare beam shape i.e., beam shape at the laser output.

(b) Beam shape after the Collimator i.e., at fiber output.

(c) Beam shape after GT i.e., at the input to the Event filter

Figure 6.1: Transverse beam profiles at different locations of the experimental setup as recorded by the beam profiler.

[2] The field distribution of the fundamental mode for single mode fiber can be approximated to be Gaussian [9, 10] (the transverse profile of the bare beam was not a Gaussian as can be seen in Fig. 6.1)

[3] In adjustable collimator the distance between the aspheric lens and the tip of the fiber can be adjusted.

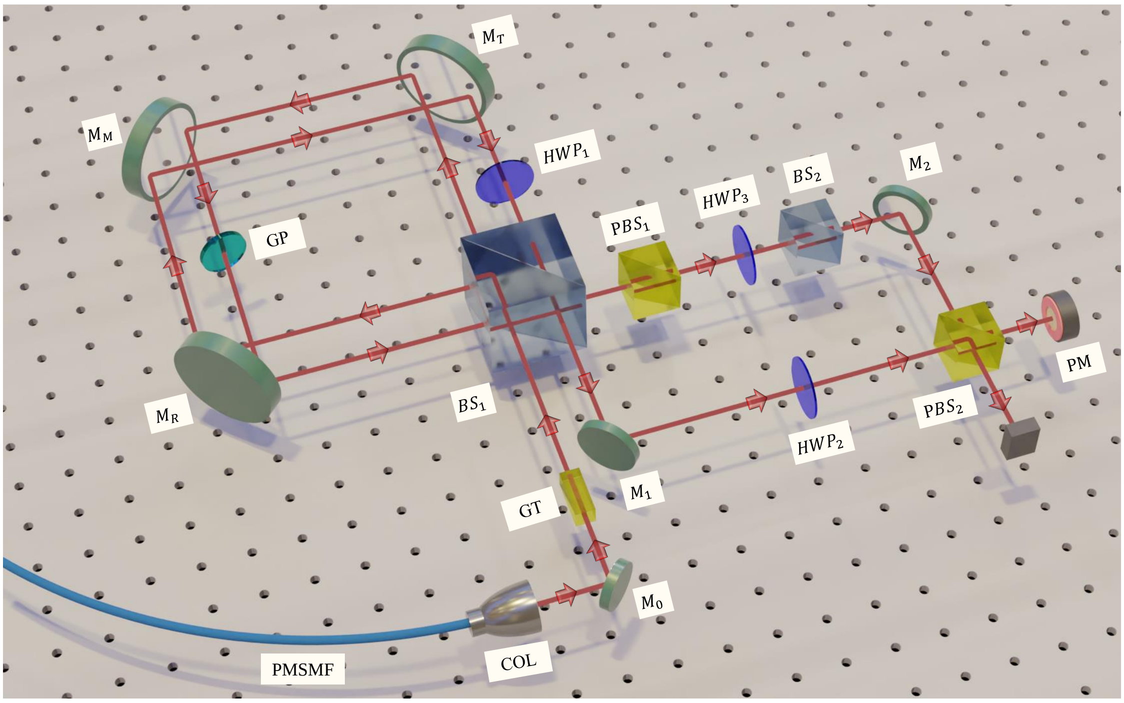

Figure 6.2: Experimental Setup of the event filter for the photonic event $E = \{00, 01, 11\}$. The system is allowed to pass through the beam splitter (BS_1) twice inside the Displaced Sagnac Interferometer (DSI) setup aligned in collinear geometry. The glass plate GP in one of the paths inside the interferometer controls the relative phase. The upper and lower paths taken by the photon after each pass through the beam splitter are labeled as 0 and 1 respectively. The system propagating through the interferometer can choose any one of the 4 possible trajectories; 3 desired trajectories among them are filtered out at the end of the setup at the location where the PM (here a power meter sensor, can be a single photon detector as well) is shown.

Before entering the event filter the collimated beam is passed through a Glan-Thompson polarizer [4] GT [$GTH5M-B$, $Thorlabs$], mounted inside a lens tube [$SM05L10$, $Thorlabs$] attached to a $6-axis$ kinematic mount [$K6X5$, $Thorlabs$], to ensure high degree in polarization purity. The optic axis of the GT is oriented with respect to the incident beam in a way that it transmits the horizontal ($|H\rangle$) component of polarization of the beam and the transmission is maximized by rotating the output end of the fiber attached to the collimating lens (COL). The performance of the $PMSMF$ is very sensitive to the external stress and ambient temperature; any change in these parameters can cause the

[4] A Glan Thompson polarizer transmits the $s-$polarized component (the $e - ray$) and reflects the $p-$polarized component (the $o - ray$) of any unpolarized beam incident on it.

polarization of the beam at the output of the fiber to vary causing a power fluctuation after the Glan-Thompson Polarizer (GT). The transmitted beam through the GT serves as the input to the Sagnac interferometer in the event filter.

The horizontally polarized beam after the GT is made incident on the beam splitter BS_1 [$20BC17MB.2$, $Newport$] which forms the Displaced Sagnac interferometer (DSI) with the mirrors M_T, M_R and M_M (all of them are [5122, $Newport$]; M_T, M_R are mounted in [$Polaris$ $K2T$, $Thorlabs$], M_M is mounted in [$KS2D$, $Thorlabs$]). A part of the beam incident on BS_1 is transmitted and another part is reflected, depending on the splitting ratio ($T : R$) of BS_1. Lets consider the paths for the transmitted beam and the reflected beam inside the interferometer ate labelled as $path - U$ and $path - L$ respectively. M_T is the mirror that the transmitted beam encounters the first, similarly M_R is the mirror that the reflected beam encounters the first and M_M is the mirror that sits in the middle and redirects the transmitted beam from M_T to M_R and reflected beam from M_R to M_T respectively. By adjusting the tilt of M_T and M_R and the beam splitter BS_1 while looking at the interference fringes in both the output ports of the interferometer, the DSI is aligned in collinear geometry, i.e., in each of the output ports of the interferometer the propagation vectors associated with the two beams coming from the individual paths of the interferometer are made to be collinear and are always on top of each other. In collinear configuration, the intensity at individual output ports after the interference varies depending upon the relative phase (φ) between the two paths of the interferometer.

The relative phase of the interferometer is controlled by tilting a Glass Plate GP [$WG40530$, $Thorlabs$] placed in one of the arms of the interferometer, here in $path - U$. The GP is mounted on a lens mount [$LMR05/M$, $Thorlabs$] attached to a base rotation mount [$PR01/M$, $Thorlabs$] with an adapter [$BA2S5/M$, $Thorlabs$] which enables us to tilt the GP with the surface normal being in a plane parallel to the optical table causing a longitudinal path delay (say, $\Delta p = p_U - p_L$) for the beam propagating in $path - U$ compare to the beam propagating in $path - L$. Adjusting the angle of tilt of the GP with respect to the propagation vector of the beam, the relative phase φ [5] between the two paths of the interferometer can be tuned. For the GP of thickness t (here, $t = 3$ mm) tilted at angle θ

[5]Phase φ is computed considering the path difference Δp introduced due to the presence of a titled glass plate (of thickness t) in $path - U$ and nothing in $path - L$.

with respect to the incident beam, the relative phase (φ) is obtained to be,

$$\varphi = \frac{2\pi}{\lambda}\Delta p = \frac{2\pi x}{\lambda}(n_r - n_i \cos(\theta_i - \theta_r)) \tag{6.3}$$

$$\text{where,} \qquad x = \frac{t}{\cos(\theta_r)} \tag{6.4}$$

$$\text{provided,} \qquad \theta_r = \sin^{-1}\left(\frac{n_i}{n_r}\sin(\theta_i)\right) = \sin^{-1}\left(\frac{\sin(\theta)}{n}\right) \tag{6.5}$$

where x is the path length of the beam (after refraction) inside the GP when it is tilted at an angle θ. The angle of incidence θ_i would be the same as the angle of tilt θ, i.e., $\theta_i = \theta$.

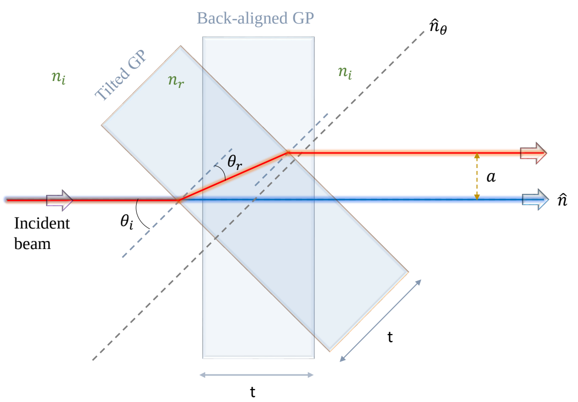

(a) A beam incident normally on a glass-plate (GP), labelled as "Back-aligned GP" (surface normal along $\hat{n}$), propagates straight though it as shown by the blue line. When the GP is tilted at an angle $\theta = \theta_i$ (surface normal along $\hat{n}_\theta$) the beam incident on it undergoes refraction and the propagation of the beam through the "Tilted GP" is shown using the red line. The tilt of the GP introduces a longitudinal path delay and a lateral displacement a to the beam in red compare to the beam in blue.

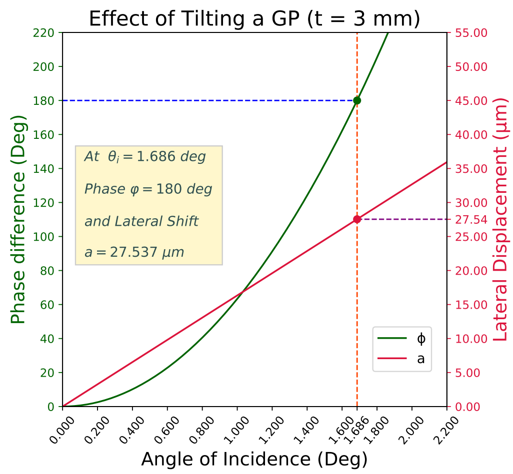

(b) The relative phase φ (in green) and the lateral displacement a (in magenta) introduced due the tilt of a GP of thickness $t = 3\ mm$, placed in one of the paths of the interferometer, is shown as a function of the angle of tilt $\theta = \theta_i$. A phase change of $\varphi = 180°$ occurs when the GP is tilted at angle $\theta = 1.686°$ with respect to the incident beam which results in a lateral displacement of $a = 27.537\ \mu m$ in the beam propagating through the GP.

Figure 6.3: Beam propagation through a tilted Glass plate

The angle of refraction θ_r in Eqn. 6.3 follows the Snell's law $n_i \sin(\theta_i) = n_r \sin(\theta_r)$, where n_i and n_r are the refractive indices of the incident medium (here, air with $n_i = 1$) and the refraction medium (here, UV-fused silica with $n_r = 1.4531$ at 810 nm [11]). Here, we have considered $\dfrac{n_r}{n_i} = n$.

The tilt in the GP also causes a lateral displacement (say, a) of the beam going through the GP as shown in Fig. 6.3a. From Fig 6.3b it can be seen that even for changing the phase from 0 to π rad (or 180°), i.e., to change the interference from a constructive to a destructive one or vice versa, the 3 mm thick GP used in the experiment needs to be tilted at an angle ≈ 1.686 $degree$ that gives a lateral shift a (horizontally) in the order of few tens of microns ($\approx 27.537 \mu m$) which is much smaller than the beam width (≈ 1.7 mm). Thus the two interfering beams still have a good overlap that maintains a high degree of collinearity and the loss in visibility due to the lateral shift in the beam in $path - U$ would be small enough that it can be ignored. The lateral displacement a of the beam propagating through the GP of thickness t due to the tilt at an angle $\theta = \theta_i$ can be expressed as,

$$a = x \ \sin(\theta_i - \theta_r) = \frac{t \ \sin(\theta_i - \theta_r)}{\cos(\theta_r)} \tag{6.6}$$

In one of the paths (here in $path - L$) of the Sagnac interferometer a half-wave plate (HWP_1) [$WPO02 - H - 810 - UM$, $NewlightPhotonics$] is placed with its fast axis oriented at $\dfrac{\pi}{4}$ with respect to the horizontal. The HWP oriented this way realizes the σ_x operator [6] which changes the H polarization of the beam in that path to V and acts as a marker to the path. So, any polarization measurement in the basis $\{|H\rangle, |V\rangle\}$ at the output of BS_1 can give information about the path of the photon inside the interferometer. After each encounter of the system with the device i.e., with BS_1, the path of the system is labelled by 0 or 1 depending on the upper path or lower path chosen by the system. Therefore, there are four possible paths that the system can take after passing through BS_1 twice. The event filter for the event $E = \{00, 01, 11\}$ is designed by selecting only the paths $00, 01, 11$ and discarding the path 10 by acting on the polarization d.o.f. after DSI.

[6] Jones matrix representation of a HWP whose fast axis is oriented at ϑ with respect to the horizontal is given by, $\hat{S}_h(\vartheta) = \begin{pmatrix} \cos(2\vartheta) & \sin(2\vartheta) \\ \sin(2\vartheta) & -\cos(2\vartheta) \end{pmatrix}$. Hence, $\hat{S}_h(\frac{\pi}{4}) = \begin{pmatrix} 0 & 1 \\ 1 & 0 \end{pmatrix} = \hat{\sigma}_x$.

The polarizing beam splitter PBS_1 [$PBS122$, $Thorlabs$] placed in the top arm (as seen in Fig. 6.2) after the DSI reflects the history 10 away from the setup. This is because the trajectory 10 corresponds to $path - L$ (hence the first bit is 1) inside the interferometer having the HWP_1 behaving as σ_x, which makes the polarization of the system in this path to be $|V\rangle$ that gets reflected by the polarizing beam splitter. PBS_1 allows the history 00 (with $|H\rangle$ polarization) to pass through it which is redirected towards the event filter output using a mirror M_2 [5102, $Newport$] mounted in [$SU100 - F2K$, $Newport$]. A half-wave plate HWP_2 [$RZQ2.15L.0810$, $B.\ Halle$] (mounted in kinematic rotation mount [$KS1RS$, $Thorlabs$]) and a polarizing beam splitter (PBS_2) [$PBS122$, $Thorlabs$] combination is placed in the bottom arm after the DSI that makes the two histories 01, 11 interfere, which otherwise have orthogonal polarizations ($|H\rangle$ and $|V\rangle$ respectively) after the Sagnac interferometer. HWP_2 has its fast axis oriented at $\frac{\pi}{8}$ with respect to the Horizontal which physically realizes a Hadamard operator that changes $|H\rangle$ to $|D\rangle$ for the history 01 and $|V\rangle$ to $|A\rangle$ for the history 11. After HWP_2, the two beams coming from two different paths of the interferometer with $|D\rangle$ and $|A\rangle$ polarizations respectively are projected onto $|H\rangle$ in one output port of the PBS_2 and into $|V\rangle$ in the other output port of it. The event $E = \{00, 01, 11\}$ can be detected at one of the output ports of PBS_2 using a detector (here a power meter sensor, PM [sensor: $S121C$, $Thorlabs$, meter: $PM100D$, $Thorlabs$]) as is shown in Fig. 6.2.

Here, the port of PBS_2 at which the beams from 01 and 11 are projected horizontally is selected as the output of the event filter − hence we need to ensure that the photons coming from 00 path reaches that port as well. In order to achieve this, another half-wave plate HWP_3 [$RZQ2.15L.0810$, $B.\ Halle$] (mounted in kinematic rotation mount [$KS1RS$, $Thorlabs$]) with its fast axis at $\frac{\pi}{4}$ (i.e., as σ_x operator) is placed in the top arm just after PBS_1. This HWP_3 changes the polarization of the 00 beam from $|H\rangle$ to $|V\rangle$ so that it gets reflected from PBS_2 and reaches PM. A $50:50$ beam splitter BS_2 [$BS005$, $Thorlabs$] placed in the top path reduces the intensity of the 00 beam to half, in order to remove any bias at the detection associated with any path. The detector (PM) detects the beams coming from any of the three paths $00, 01, 11$ and any detection at this position confirms that the system being detected belongs to the event $E = \{00, 01, 11\}$.

6.2.3 Method and Data Acquisition

In the experimental setup after ensuring that a decent transverse profile of the beam is emerging out of the Glan-Thompson GT and the polarization is Horizontal with a high degree in purity, first the Displaced Sagnac Interferometer (DSI) is aligned in collinear configuration with a back-aligned glass plate (GP) being present in one of the paths (here, $path - U$). The collinearity is achieved by looking at the individual beams (when separated) and the interference (when overlapped) using two beam profilers (BP) – one placed at a position very near to BS_1 in one port and the other at a position far from BS_1 in the other port of it, so that we can ensure the beams do not cross each other and remain parallel while propagating the distance from a near position to a far position. Next, the event filter is set up by placing different polarization optics at different locations keeping in mind that only the beams from $00, 01, 11$ paths need to be detected at the output and the beams from 01 and 11 need to be made to interfere. Then, the power of the beam after the Glan-Thompson Polarizer (GT) is measured using a power meter. This power (consider P_{input}) represents the intensity of the beam being incident on the device (i.e., BS_1) through which the system has to propagate twice. Also, the power at the output of the event filter (consider, P_{event}) is measured when the beams from the paths 01 and 11 constructively interfere. Constructive interference is ensured by tuning the tilt of the GP (which earlier was back-aligned) while observing the power at the output end with the top path after DSI being blocked and fixing the GP at an angle for which the power after the interference becomes maximum. Using the power data, i.e., $P_{event}-$ power associated with the beams coming from $00, 01, 11$ paths at the end of the setup and $P_{input}-$ power associated with the beam being incident on the setup, the probability of detection of the event E is obtained, from which quantum measure $\mu(E)$ for the particular event E is inferred.

Other than these two power data, additionally the powers P_{int}, P_{01}, P_{11} are monitored at the output of the event filter in order to get an idea about the interferometric phase fluctuation over a long period of time. Here,

- P_{int} is the power associated with the interference between the beams from the paths 01 and 11, measured with the top arm after DSI being blocked.
- P_{01} is the power associated with the beam in 01 path, measured with $path - L$ inside the interferometer and top path after the interferometer being blocked.

- P_{11} is the power associated with the beam in path 11, measured with $path-U$ inside the interferometer and top path after the interferometer being blocked.

Also, the power P_{00} associated with the beam in 00 path is measured at the output while the bottom path after DSI is blocked. Experimentally, a few other observations are made in order to get an idea how different parameters can impact the experimental data and how the quantity being determined from the experiment gets affected compared to the expected theoretical value, the details of which will be discussed in the following section.

6.3 Experimental Data Analysis: Dealing with Errors

Experimental data is always associated with some real limitations, imperfections, noise, fluctuations, losses, etc.. The lab conditions and different parameters of the environment like temperature, pressure, humidity, air current, etc. impact the experimental data as well. All these effects on the collected data in an experiment are responsible for the deviation in the value of the quantity being measured experimentally from the theoretical value computed considering ideal conditions and effectively manifest as an error in the experimentally determined quantity. Thus, while analyzing the experimental data different possible sources of errors need to be kept in mind and corrections for some parameters are required depending on the degree it affects the experiment.

6.3.1 Types of Experimental Error

In an experiment in quantum mechanics, there would be some inherent random noise which can originate due to the fundamental nature of quantum mechanics or from classical sources which are chaotic and hard to trace [12]. Also, high frequency acoustic vibrations may appear as random noise if the sampling rate is low [13, 14]. However many experimental parameters, although accessible to the one performing the experiment, may not be precisely controlled during the experiment. In an optical experiment, variation in temperature and pressure often impacts the opto-mechanics affecting the optical alignment and a slight change in the alignment mostly affects the outcome of an interferometry based experiment. For a short time scale the recorded data for these parameters may appear as showing a drift but if we wait for long enough time they may appear to be visibly oscillatory. Depending on the variation of the parameters, be it a slow drift or oscillation, the required data for the experiment varies. Thus, the time scale at which the data is acquired in an experiment plays an important role in determining whether and how the data affects the quantity to be experimentally determined.

Further, there are systematic instrumental errors, which are a matter of characterization. The non-linear response of a detector, the power meter sensor (or any sensor being used in the experiment) and its calibration accuracy may be one of these errors. In an experiment where we record the powers (or the intensity) using those instruments, some of the errors like the calibration accuracy, may not affect the experiment as long as we are interested in the ratio of powers and not in absolute power value. But factors like the detector's non-linear response would affect the ratio as well. Some real limitations like the efficiency of the detector, spatial averaging over a certain pixel size of the camera etc. affects the experimental result as well.

Also, in optical experiments, there are always some losses associated with absorption in the material of the optical element. Imperfections in the optical components being used modify the outcome of the experiment; like deviation in the splitting ratio ($T : R$) for the beam splitters from the quoted value modifies the intensities of the transmitted and reflected beams, the polarization dependence of reflection [7] from mirrors, beam splitters etc. adds ellipticity to the polarization of the beam, extinction ratio of optical elements impacts the polarization purity, surface quality of the optical components causes distortion in the wavefront of the beam that changes the spatial overlap of the beams during interference etc.

Additionally, in an interferometric experiment, the phase instability inside the interferometer, beam wander of the two overlapping beams, etc. will also lead to experimental errors, and their contribution needs to be accounted for in the theory of optics. Also, some misalignment of the optics, specks of dust or any imperfections present on the surface of

[7] In most of the optical elements $R_s \neq R_p$, i.e., the reflectivity is not the same for $s-$ and $p-$ polarizations and also reflection adds a relative phase between $s-$ and $p-$polarized components of the beam.

optics (like the scratches, uneven surfaces, roughness, quality of anti-reflection coatings, etc.) modifies the beam path as well as changes the wavefront which affects the interference and hence impacts the result obtained from any interferometry based experiment. All these parameters need to be considered while analyzing experimental data in order to determine the quantity of interest.

6.3.2 Data Analysis Considering Experimental Non-idealness

In Sec. 6.2 we have presented the experimental implementation of an "event filter" in an optical setup for the particular event $E = \{00, 01, 11\}$, for which we want to determine the quantum measure. After setting up the event filter we aim to demonstrate how the value of quantum measure $\mu(E)$ for the event E can be inferred from the data collected at different positions of the event filter as discussed in 6.2.3. Ideally, $\mu(E)$ could have been inferred from the ratio $\frac{P_{event}}{P_{input}}$, where P_{input} and P_{event} are respectively the powers at the input and at the output of the event filter. However, in practice, the collected data often suffers from various non-idealnesses that can cause deviations between the experimentally determined value and its theoretical prediction. Consequently, a more rigorous analysis of the data is necessary to accurately determine $\mu(E)$, taking into account the potential sources of non-idealnesses.

The theoretical formula given in Eqn. 6.2 computes the value of the quantum measure $\mu(E)$, for the event $E = \{00, 01, 11\}$ for a photonic system that encounters a $50 : 50$ beam splitter (BS) twice, to be 1.25. This is the value of measure for that event obtained by considering the system to be lossless and in ideal lab conditions. Any loss within the setup would only reduce the amplitudes associated with the paths, which would effectively lower the value of the quantum measure to be obtained experimentally. Also, the value $\mu(E) = 1.25$ is obtained considering constructive interference between the beams from 01 and 11, i.e., when the relative phase between the two paths of the interferometer is $\varphi = 0$. Hence, any variation in the phase from zero would only reduce the obtained interference intensity and would effectively reduce the value of $\mu(E)$. So, considering the limitations and errors associated with an experiment the value of the quantum measure to be obtained experimentally is expected to be less than the value 1.25.

During an experiment, different sources of experimental errors, as discussed in SubSec. 6.3.1 affect the data acquisition and give the value of the experimentally obtained quantity within a certain uncertainty range. The experimentally collected data can be corrected for some of the known sources of errors but for most of the parameters correction would not be feasible and the errors need to be propagated during the analysis [15]. Also while computing the quantity of interest theoretically, we can modify our expectation by accounting for the non-idealnesses associated with different parameters in the theory. Some of the non-idealnesses arise due to the beam wander about a certain mean value in the transverse plane, temperature and humidity variation within a certain range, wavelength fluctuation of the laser source, beam shape not being perfectly Gaussian, the polarization of the beam not being linear, polarization fluctuation, slight non-collinearity in the aligned interferometer, phase noise in the interferometer and imperfections associated with the components being used in the experiment (like the losses in optical components, deviation from surface flatness, real transmission and reflection efficiency, detector efficiency etc.).

Here, in the analysis for obtaining the value of $\mu(E)$ for the event E,

(i) The effects of phase instability in the interferometer, beam wander causing lack of overlap of beams, detector non-linearity and imperfections associated with different components would be accounted for in the theoretical computation in order to have a more accurate estimate of the quantity to be determined experimentally.

(ii) The loss in the overall power due to absorption of light by optical components would be accounted and corrected for in the experimental data analysis along with the analysis for uncertainty due to various drifts.

In summary, the data analysis in this experiment would involve,

(1) Determining the value of quantum measure (say, $\mu_{exp}(E)$) associated with the event E from the experimentally obtained distribution of probability of occurrence of the event with the necessary corrections in the experimental data; presented in Sec. 6.4.

(2) Comparison of the obtained experimental distribution $\mu_{exp}(E)$ with the theoretical distribution (say, $\mu_{th}(E)$) estimated using the direct formula for quantum measure considering real parameters and experimental non-idealnesses; discussed in Sec. 6.5.

(3) The statistical significance analysis of the quantity obtained from the experiment (i.e., $\mu_{exp}(E)$) with respect to the classical-quantum boundary ($\mu_{C(max)} = 1$) as well as the theoretically computed quantity ($\mu_{th}(E)$) using the concepts of evidence-based hypothesis-testing, presented in Sec. 6.7.

6.4 Determination of the Experimental Distribution of Quantum Measure

The experimental determination of quantum measure for $E = \{00, 01, 11\}$, which is a non-serial event for the history space $\Omega = \{00, 01, 10, 11\}$ associated with a photonic system, an optical setup must be implemented as outlined in Sec. 6.2 such that any successful detection at its output assures that the detected particle has travelled through any one of three paths 00, 01 or 11 within the setup. Such a setup is called an "Event filter" for the particular event E. Next, the probability of the event E occurring needs to be determined from the ratio of the powers obtained at the output and the input of the event filter. However, various experimental parameters cause the power to fluctuate over time and affect the experimental data, as a result, the probability is obtained as a distribution with an uncertainty band. Further, to report the uncertainty, we need to understand if the fluctuations in power exhibit any periodicity or are random in nature. Thus, understanding the temporal behavior of the power data is essential, which is presented in SubSec. 6.4.1.

Upon determining the probability $\mathcal{P}_{exp}(E)$ associated with the event E, the value of the quantum measure $\mu(E)$ can be obtained by multiplying this probability with the loss factor associated with the design of the event filter. But, here we need to account that a fraction of the power gets absorbed in the components, mainly in BS_1 that due to its thickness (2 *inch* thick) causes significant attenuation in the powers in each path. Hence, the probability distribution $\mathcal{P}_{exp}(E)$ obtained from the ratio of the powers is corrected after taking into account the absorption loss in the material of the beam splitter BS_1. The experimental quantum measure $\mu_{exp}(E)$ is then inferred from this corrected probability distribution ($\mathcal{P}^{(c)}_{exp}(E)$).

6.4.1 Understanding the Nature of Power Data

Experimentally, the power at the input to the event filter (P_{input}) is measured at a position after the Glan Thompson Polarizer (GT) and the power at the output to the event filter P_{event} is measured after PBS_2 at the position where the power meter sensor (PM) is shown in Fig. 6.2. Under ideal conditions, the probability could have been obtained by simply taking the ratio of the two powers, i.e., $prob(E) = \frac{P_{event}}{P_{input}}$, provided both the powers are measured simultaneously and remain unchanged over the time. As discussed in the SubSec. 6.3.1, the ambient conditions and other factors affect different experimental parameters which cause the powers to change over time. Also, in this experimental setup P_{input} and P_{event} can not be measured at the same time because putting a power meter at the input i.e., after GT for recording P_{input} would block the beam from entering into the interferometer. Ideally, simultaneous measurement of both the powers could have been done by placing a non-polarizing beam splitter in between the GT and DSI, which would transmit a fraction of the beam into the interferometer so that P_{event} can be recorded and reflect the rest of the beam so that P_{input} can be estimated by measuring the power at the reflecting port of this beam splitter [8]. However, given the power fluctuation, P_{event} can not simply be expected to be mere proportional to P_{input} as many of the fluctuations in P_{event} may get overridden by the interference effects.

The fluctuation of power P_{input} (i.e., the power after the Glan Thompson polarizer) would be a combination of three things:

(i) Since the power is measured after a Glan Thompson polarizer GT, any polarization fluctuation after the collimator COL can result in power fluctuation. The polarization after a polarization maintaining single mode fiber ($PMSMF$) can get slightly affected when the fiber gets subjected to a change in temperature or stress [9] [16, 17]. Thus there would be drifts in power corresponding to the time scale of the

[8] This further requires the characterization of the beam splitter for its $T : R$ ratio, the absorption loss through it etc..

[9] The operating temperature and stress conditions of the $PMSMF$ changes its birefringence that causes a variation in the delay along the orthogonal fast and slow axes of the fiber. So, any fluctuation in the lab parameters adds a relative phase between the orthogonal polarizations that are being maintained along the fast and slow axes of the $PMSMF$, resulting an elliptic output polarization from the $PMSMF$ with the ellipticity changing over time depending on the temperature cycle.

temperature and humidity cycle (as determined by the air-conditioner).

(ii) The centroid/center of the beam before the coupler can drift in the transverse plane, which would affect the coupling efficiency and hence the power after the Glan Thompson polarizer.

(iii) The overall power from the source can vary depending on the temperature and humidity of the surrounding, since variation in these ambient parameters linearly effects the cavity parameters of the diode laser.

The power data recorded at the end of the event filter (P_{event}) would be affected depending on the variation in the input power. Additionally it would be affected by the phase shift in the interferometer (the phase stability is very sensitive to the ambient parameters), beam wander of the two interfering beams that can cause a drop in the degree of overlap, any variation in laser wavelength etc. The power P_{int} which corresponds to the interference between 01 and 11, measured at the end of the filter with the upper path after BS_1 being blocked, would also be affected by the parameters mentioned above. Thus it can give an estimation of the error in the P_{event} data.

All the power data recorded in the experiment would also have some random noise in the process of detection, along with the drifts due to the above causes. Further, the measured value, of course, can differ from the true power due to the detector non-linearity or calibration uncertainty.

❑ Characterizing the Power Data:

As we record the powers P_{input} and P_{event} at different times, it is important that the powers remain stable over time so that no bias is introduced in inferring the measure $\mu_{exp}(E)$ from the ratio of the two. Though the interferometric phase fluctuation or the change in the visibility due to beam wander of the interfering beams affects P_{event}, computation of the ratio would be mostly affected if there is a time-dependent drift or oscillation in the input power. Any variation in P_{input} affects P_{event} as well, thus a periodic drift over a long time in the input power data would cause the ratio to have a bias depending on the time when the data were acquired. Here, we have recorded both the data for a duration of approximately $T = 2\ hours$ and then analyzed to understand the nature of their variation with time. This would give us an idea, how to proceed with the data analysis in order to minimize the bias.

The P_{input} data, as presented in the plot in Fig. 6.4a, shows a sinusoidal variation with the average power over a cycle having a slow upward drift. The power oscillates with a periodicity of $9 - 11$ $mins$ which correlates with the temperature cycle of the Air Conditioning Unit in the lab. In general, we have the temperature and the humidity going as a triangular ramp function as the units periodically turns on and off. The length of the grating cavity of the diode laser changes linearly with the periodic rise and fall of the temperature, causing the resonating wavelength to change slowly. This results the power emitting from the laser to vary.

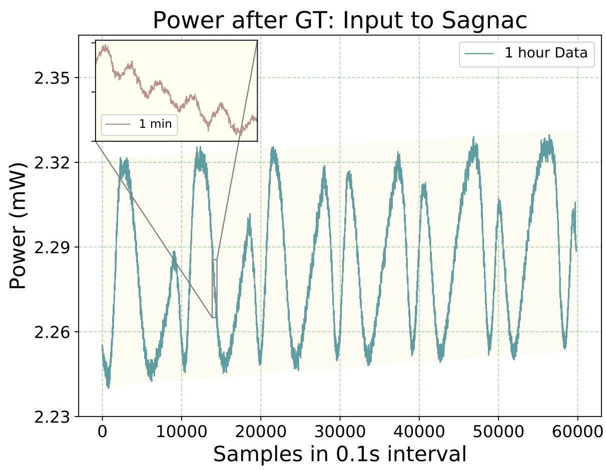

(a) Short and Long time Variation of Data

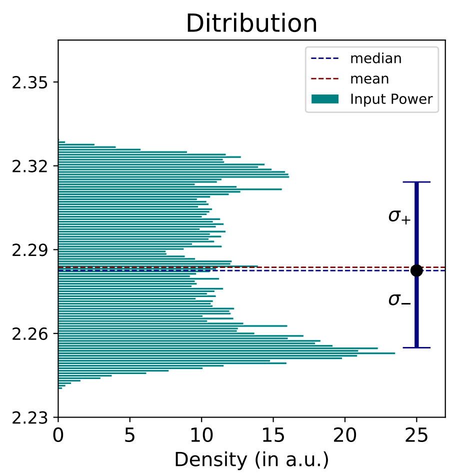

(b) Histogram Plot of the Data

Figure 6.4: Temporal variation of the power (P_{input}) incident on the setup as recorded in the experiment.

Also, since P_{input} is the power of the beam after the GT which projects the polarization into Horizontal, the sinusoidal variation in it is mostly due to the change in polarization before GT. The external temperature (and also stress) causes the birefringence of the $PMSMF$ to change, which results in the variation of the output polarization of the $PMSMF$ depending on the temperature cycle. The power after GT is found to be oscillating by around 3% about the mean owing to the polarization fluctuation of the beam exiting the fiber. Also, we have seen a slow increase ($\approx 0.525\%$) in the average power over the 2 *hours* of acquisition time. On top of the sinusoidal variation, the data also shows some short period random fluctuations which appear as the noise on the sine curve. This, high frequency random fluctuations can be seen in the inset plot of Fig. 6.4a showing the data for for $t = 1$ *min* timescale chosen randomly from P_{input}.

The histogram plot in Fig. 6.4b shows that P_{input} is not a normal distribution, which implies that the experimentally recorded powers do have a combination of both − random fluctuations along with some systematic and periodic drifts. The drift in power seems to occur at a different time scale than the random fluctuations in power, most likely due to the temperature cycle. Since the nature of the distribution is not normal, the *standard deviation* can not be considered as the measure of spread of the data and *median* instead of *mean* would be a better choice to describe the measure for central tendency of the data. The uncertainty of the distribution would be defined as the range for the 68.26% confidence interval and would be represented with $\sigma_{\pm}$, where σ_+ and σ_- are respectively the ranges of the 84.13^{th} and the 15.87^{th} percentiles of the data with respect to the median. Since the average power for P_{input} rises with time, the uncertainty in this distribution is obtained to be high. For a small enough time, the power variation is random, as seen from the histogram plot of a block of data for a period $t << T$ chosen randomly from P_{input} which seems to have a normal distribution.

6.4.2 Fast Fourier Transformation of the Recorded Data

In order to understand the nature of the power variation over time and to get an idea about the frequencies at which the power tends to fluctuate, Fourier transformation can be performed on the recorded data. This information will also guide us in choosing the correct time scale for data analysis so that the uncertainty associated with the measured probability can be minimized.

In this experiment, we have recorded the powers at the input (P_{input}) and the output (P_{event}) of the event filter for about 2 *hours* at a sampling rate of 10 Hz. Given the data acquisition was sampled at $0.1s$, the maximum frequency for which we can comment is 5 Hz (the Nyquist frequency) [18]. The time for which the data were acquired limits the minimum frequency about which we can comment on to be of the order of mHz. The spectral intensity distribution obtained from the Fast Fourier Transformation (FFT) of both the data P_{input} and P_{event}, shows there are no significant fluctuations beyond 0.008 Hz. So, both the low frequency drifts and high frequency vibrations will mostly come into effect while acquiring data for more than $125s$. Thus, statistics up to $125s$ can be drawn in order to minimize the effects of power fluctuation. Here, for the data analysis in this experiment, all the data sets are chosen for the time scale of $100s$.

6.4.3 Determination of Probability Distribution

Experimentally the value of quantum measure $\mu_{exp}(E)$ for the event E would be determined from the probability ($\mathcal{P}_{exp}(E)$) obtained using the data P_{event} and P_{input}. However, the powers recorded at different times can not, in general, be combined to determine the probability because the powers have some random fluctuations along with some periodic drifts over time, as shown in 6.4.2. Depending on the time scale of data acquisition some random fluctuations (even some high frequency oscillations) in power can be averaged out, but the effect due to the drift in power over a long period would remain. This would introduce a systematic error to the experimentally obtained quantity $\mathcal{P}_{exp}(E)$ which would also propagate to $\mu_{exp}(E)$.

The data acquisition time plays an important role in minimizing the uncertainty in the measured quantity caused due to the power fluctuation. The spectral intensity distribution, obtained from the FFT of the power data P_{input} and P_{event}, shows that no significant fluctuation exists within about $\approx 125s$. Hence, we draw short time scale (over $100s < 125s$) statistics (say, pI and pE) randomly from the long time data P_{input} and P_{event} respectively for determining the probability $\mathcal{P}(E)$. The process is repeated for $\mathcal{N}$ times [10] in order to get the probability distribution $\mathcal{P}_{exp}(E)$, which signifies that the probability computed from the ratio of the powers would have values within a certain range owing to the facts that both the powers (i) are subject to fluctuation and (ii) are not recorded simultaneously. To completely avoid the effect due to the systematic drift, ideally both the powers P_{event} and P_{input} should have been measured simultaneously. Since this was not the case here, we had performed statistical analysis on the randomly chosen data. In each trial, pI and pE are drawn randomly from P_{input} and P_{event} and the probability is determined as,

[10] Here, $\mathcal{N} = 10^5$ samples each are drawn randomly from the distributions P_{input} and P_{event}.

$$\mathcal{P}^{(k)}(E) = mean\left(\frac{pE^{(k)}}{pI^{(k)}}\right) \tag{6.7}$$

The above expression shows the computation of the probability $\mathcal{P}^{(k)}(E)$ for the k-th trial.

Now, while determining the probability we need to account that a fraction of the powers in different paths get absorbed in the components present in the paths, which affect the power measured at any position after the interferometer. Among all the components inside the interferometer, the power gets absorbed the most in the material of the 2 *inch* beam splitter BS_1 because of its thickness. In the Sagnac Interferometer, designed with a beam splitter BS_1 and three mirrors M_T, M_R and M_M, the system passes through the beam splitter twice, causing a significant drop in the overall power after the interferometer. The loss due to absorption affects the P_{event} data when compared to P_{input}, which modifies the quantity to be determined from the experiment. Thus, a correction for the probability is needed to account for the loss due to the absorption.

If η is the overall transmission factor (where $0 \leq \eta \leq 1$) of the interferometer [11], then the power associated with each path (γ) after the system leaves the interferometer becomes, $P_\gamma = \eta\ P_\gamma^0$. Here, P_γ is the power experimentally recorded at any point after the DSI and P_γ^0 is the power at the same location without any loss in the interferometer (i.e., in ideal case). Thus, the corrected probability distribution can be obtained as,

$$\mathcal{P}^{(c)}_{exp}(E) = \frac{\mathcal{P}_{exp}(E)}{\eta} \tag{6.8}$$

Experimentally the overall transmission factor η of the interferometer can be determined using two methods:

(1) Finding the transmission factor η_s of BS_1 when the incident beam passes through it once (i.e., during single pass) from the power values measured at the input port, transmitting port and reflecting port of the beam splitter. Here, η_s is computed

[11] $Here, \eta$ is the ratio between the total power at the outputs of the interferometer, i.e., $(P_{O_1} + P_{O_2})$ and at the input of the interferometer, i.e. P_I, where O_1 and O_2 are the two output ports after the DSI.

as, $\eta_s = \dfrac{P_T + P_R}{P_I} = T_{abs} + R_{abs}$, where P_I is the power of the beam incident on BS_1, P_T and P_R are respectively the powers of the beams transmitted and reflected from BS_1. Considering the absorption, T_{abs} and R_{abs} are the absolute values of the Transmittance and Reflectance of the BS_1, provided $T_{abs} + R_{abs} < 1$[12]. Since the system in each path (γ) passes through the BS twice, the transmission factor of the interferometer η can be considered as $\eta = \eta_s^2$. Thus, the probability distribution corrected after accounting for the loss due to absorption in the 2 *inch* BS should be,

$$\mathcal{P}^{(c)}_{exp}(E) = \frac{\mathcal{P}_{exp}(E)}{\eta_s^2} \tag{6.9}$$

(2) Finding the overall transmission factor η_d from the powers measured at the outputs of the interferometer i.e., after each beam has travelled through the BS twice (double pass). Here, η_d is computed as, $\eta_d = \dfrac{P_{00} + P_{10} + P_{01} + P_{11}}{P_I}$. Here, P_{ij} (with $i = 0, 1$ and $j = 0, 1$) is the power of the beam from $\gamma = ij$ path recorded after the DSI. The beams in the top path and the bottom path after each pass through the beam splitter are labelled as 0 and 1. Thus, P_{11} is the beam that respectively reflects and transmits through the BS_1 during its first and second pass. So, here we get $\eta = \eta_d$ and the corrected probability after accounting for the loss due to BS_1 becomes,

$$\mathcal{P}^{(c)}_{exp}(E) = \frac{\mathcal{P}_{exp}(E)}{\eta_d} \tag{6.10}$$

Here in this experiment, for the analysis of the probability $\mathcal{P}^{(c)}_{exp}(E)$, the first method discussed above is used. The overall transmission factor of BS_1, i.e., η_s is determined from the recorded data P_I, P_T and P_R. Since the value of η_s obtained experimentally relies on the measured power values at different locations, it also gets affected by the fluctuations in power. To minimize the uncertainty in determining η_s, random $100s$ statistics pI, pT, pR are drawn from each of the recorded power data and then the mean of the ratio $\dfrac{pT + pR}{pI}$ is

[12]For BS_1 experimentally we obtain $T_{abs} = 49.21\%$ and $R_{abs} = 44.34\%$.

computed. The process is repeated for $\mathcal{N}$ times, to obtain a distribution for η_s from which we get $\eta_s = 0.9356^{+0.0015}_{-0.0031}$. Hence, a single pass of the beam through the beam splitter BS_1 results in 93.56% transmission of the incident beam, with the remainder being lost. Then, the correction factor $\frac{1}{\eta_s^2}$ is multiplied with the probability $\mathcal{P}_{exp}(E)$ to determine $\mathcal{P}^{(c)}_{exp}(E)$.

6.4.4 Quantum Measure Inferred from the Experiment

The quantum measure $\mu(E)$ for the event E is determined from the corrected distribution of probability as the following,

$$\mu_{exp}(E) = 2\ \mathcal{P}^{(c)}_{exp}(E) = 2\left(\frac{1}{\eta_s^2}\right)\mathcal{P}_{exp}(E) \tag{6.11}$$

The probability $\mathcal{P}^{(c)}_{exp}(E)$ is multiplied with the factor 2 because the design of the event filter (mainly the "event filtration region") makes half of the photons, associated with the event E, move away from the setup. $\mu_{exp}(E)$ represents the distribution of measure for a certain event E associated with a photonic system, inferred from an experiment designed allowing the interference – therefore, we expect $\mu_{exp}(E)$ to have values beyond the classical limit i.e., values greater than 1 under certain conditions.

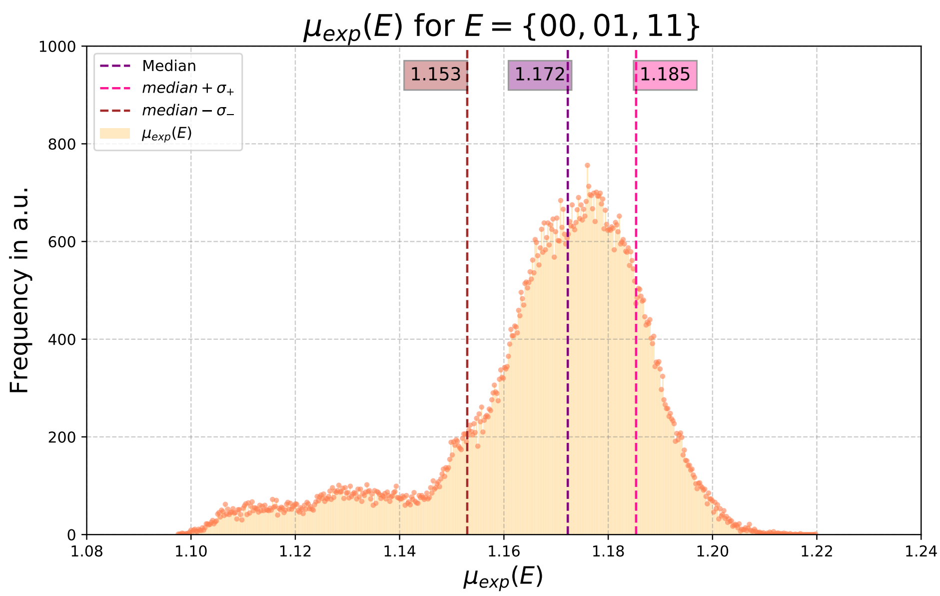

Figure 6.5: The histogram plot of the experimentally obtained distribution of the quantum measure for an event $E = \{00, 01, 11\}$ of a photonic system.

The plot in Fig. 6.5 shows the distribution of the quantum measure for the event $E = \{00, 01, 11\}$, obtained experimentally by determining the probability distribution of the event. The histogram plot of the distribution $\mu_{exp}(E)$ is asymmetric in nature, the asymmetry arising from the use of the power data P_{event} and P_{input} in the determination of the probability, both having systematic drifts over time. The tail towards the left of the distribution can be associated with the mode hop [13] in the cavity laser, causing interferometric phase to vary slowly from zero and hence, reducing the power associated with the interference, giving lower values of the quantum measure. From the distribution of $\mu_{exp}(E)$, the experimentally obtained measure can be reported using the median value of the distribution with 1σ uncertainty which is $\mu_e(E) = 1.172^{+0.013}_{-0.019}$.

6.5 Determination of the Theoretical Distribution of Quantum Measure

According to Quantum Measure Theory (QMT), the value of the quantum measure associated with an event $E = \{00, 01, 11\}$ for a photonic system passing through two $50:50$ beam splitters or passing twice through a single $50:50$ beam splitter (as in this experiment) should be $\mu_{th}^{ideal} = 1.25$. This value is derived from the theoretical expression of the quantum measure μ given in Eqn. 6.2 considering the ideal system, ideal devices and laboratory conditions. However, due to the limitations, imperfections and noises associated with an experiment and the losses associated with the real physical components, the experimentally obtained value of $\mu(E)$ is expected to be less than 1.25. It is important to have an estimation of the quantity to be determined in an experiment, considering the parameters that impact the measurement. In this section, we will theoretically estimate the range within which we can expect the $\mu(E)$ value to lie.

The experiment for the determination of the quantum measure of a specific event for a photonic system using an optical setup, as outlined in Sec. 6.2, is influenced by various factors that alter the value of the measure to be inferred from the experiment from its the-

[13]Mode hop is observed to happen in every $\approx$ $40 mins$ interval, due to the changes in the cavity parameters of the laser.

oretical value μ_{th}^{ideal}. Some of the factors are listed here: losses due to absorption during the transmission through different optical elements that causes a reduction in the power to be measured; the transmittance (T) and reflectance (R) of the real beam splitter(s) being different from 50 : 50 (i.e., $T \neq R$) that modifies the amplitudes of the different paths; polarization dependence of T and R of the beam splitters, polarization dependence of the reflectivity of the mirrors (i.e., $R_s \neq R_p$) which introduces ellipticity in the polarization of the beam; temperature and humidity variations that impacts the alignment as well as the laser parameters; temperature and stress affecting properties of $PMSMF$, hence the output polarization; fluctuations, noises and drifts in the power which results in an uncertainty in the quantity to be determined; external vibrations (mostly acoustic); phase fluctuations within the interferometer that affects the interference and hence the power; beam wander that changes the overlap of the interfering beams; surface quality of the optical components being used and dusts on the components that causes wavefront distortion affecting the interference; the non-linear response of the detector to high powers, calibration uncertainties etc.

In the following, we will determine the possible distribution for the measure $\mu_{th}(E)$ corresponding to the desired event E, taking into account different parameters that influence the experimental result. $\mu_{th}(E)$ can be called as the theoretical expectation considering the experimental uncertainties.

6.5.1 The Quantum Measure: Theoretical Expression Considering Various Experimental Parameters

According to quantum measure theory, as obtained using the path-integral approach, the quantum measure associated with the event $E = \{00, 01, 11\}$ can be expressed as,

$$\mu(E) = |A(00)|^2 + |A(01) + A(11)|^2 \tag{6.12}$$

where $A(00)$, $A(01)$ and $A(11)$ are the amplitudes associated with the respective histories 00, 01 and 11. The second term in the above expression represents interference between the two histories 01 and 11 corresponding to the beams that emerges out in the same port after the device.

The expression for $\mu(E)$ assumes constructive interference between the two histories 01 and 11, i.e., the relative phase between 01 and 11 is considered to be $\varphi = 0$. But in general, an interferometric experiment is affected by the relative phase change (φ) between the interfering paths. Thus, considering the phase dependence of the interference between 01 and 11, makes $\mu(E)$ a function of φ. Therefore,

$$\mu_{\varphi}(E) = |A(00)|^2 + |A(01) + \exp(i\varphi)A(11)|^2 \tag{6.13}$$

The amplitudes $A(\gamma^k)$ associated with different paths γ^k are computed considering the effects of different optical components present in the respective paths, as the beam transmits through them. Consider, the amplitudes $A_e(\gamma^k)$ correspond to the history γ^k where $k = 1, 2, 3, 4$ with real components in the experimental design as shown in Fig. 6.2 up to the "system propagation region", i.e., up to DSI. Thus, for this two-site hopper setting, the expression for measure becomes,

$$\mu^e_{\varphi}(E) = |A_e(00)|^2 + |A_e(01) + \exp(i\varphi)A_e(11)|^2 \tag{6.14}$$

$\mu^e_{\varphi}(E)$ is the theoretically computed value of the measure for the event $E = \{00, 01, 11\}$ considering different experimental parameters that affect the outcome. The absorption of a fraction of the beam in different optics, the reflection from optical surfaces will cause reduction in the respective amplitudes, i.e., $\left|A_e(\gamma^k)\right| < \left|A(\gamma^k)\right|$. The variation in phase from $\varphi = 0$ and the losses associated with different paths result in the measure having a value less than 1.25 for this event. Again, the uncertainty inherent in the parameters corresponding to the real optical components and the laboratory environment causes $\mu^e_{\varphi}(E)$ to have a range of possible values. This results in a distribution, represented by $\mu_{th}(E)$, for the event E. So, the quantity to be obtained from the experiment is expected to fall within the distribution of $\mu_{th}(E)$ and the degree of overlap between the distributions $\mu_{exp}(E)$ and $\mu_{th}(E)$ will be analyzed in the next section 6.7.

6.5.2 Computing the Measure from Modified Amplitudes: Accounting for Real Optical Components

First, we will determine the distribution of the measure (say, $\mu^1_{th}(E)$) for the event $E = \{00, 01, 11\}$ considering the effects of the real optical components present in the paths. For this computation we disregard the phase fluctuation and choose the relative phase to be maintained at $\varphi = 0$. Thus, the measure as given in Eqn. 6.14 would become,

$$\mu^e_{\varphi=0}(E) = |A_e(00)|^2 + |A_e(01) + A_e(11)|^2 \tag{6.15}$$

Here, $A_e(\gamma^k)$ are the amplitudes of the paths γ^k for the experimental setup. The presence of the real optical components in different paths modifies the amplitudes, represented by $A_e(\gamma^k)$, in comparison to the amplitudes $A(\gamma^k)$ obtained considering ideal components.

The experimental setup in Fig. 6.2 shows that within the DSI the beams in all the three paths $00, 01, 11$ interact with a beam splitter BS_1 twice and encounters three mirrors M_T, M_R, M_M. Paths 00 and 01 have a 3 mm glass plate GP, while path 10 has a half-wave plate HWP_1. All these components are associated with some losses mostly due to absorption in the material and reflection from the surfaces etc.. The amplitudes of the paths get affected by the absorption loss depending on the refractive index and the thickness of the material [19]. The overall transmission factor (η) of a component is either obtained from its specification sheet or determined experimentally from the ratio of the measured powers at its output and input. In some cases, the transmission factor (η) of a component can be calculated using the Beer-Lambert law from the known transmission factor of another component composed of the same material.

❑ **Beer Lambert Law:** According to Beer Lambert Law, as light propagates through an optical media its intensity diminishes along the thickness of the media and the loss in intensity is linearly proportional to the incident intensity and the length of the media [20, 21]. If I_0 is the intensity of light incident on an optical element with thickness l, then the transmitted intensity after passing through the element would be $I = I_0 \exp(-A)$, where A is the absorbance of the material. Absorbance (A) is a measure of attenuation in intensity when a beam of a particular wavelength passes through an optical element. For a material with a uniform concentration across its thickness (l), absorbance is given by $A = al$, where a is the attenuation coefficient of the material. Thus, according to Beer-Lambert law,

$$I = I_0 \exp(-A) = I_0 \exp(-al) \tag{6.16}$$

The transmittance (η) (or the transmission factor) of the material is defined as the fraction of light being transmitted through the material and is given by,

$$\eta = \frac{I}{I_0} = \exp(-al) \tag{6.17}$$

From the above expression for η we can write, $\ln(\eta) = -al$ [22]. Now, if we have a material of known thickness l_1 and known transmittance η_1, the transmittance η_2 of the same material with a different thickness l_2 can be determined as the following,

$$\eta_2 = \exp\left[\left(\frac{l_2}{l_1}\right)\ln(\eta_1)\right] \tag{6.18}$$

Here, the transmission factor η_g for the GP, which is an AR coated [14] 3 mm thick glass window composed of UV-fused silica, is determined from the known transmission factor (η') of an uncoated 10 mm thick glass window [25] made of the same material. The anti-reflection coating on our GP improves the transmittance η_g of it by minimizing the loss due to reflection, compared to an uncoated GP for which the Reflectance at wavelength $\lambda = 810\ nm$ is $R_s = R_p = 3.4122\ \%$ at $0°$ angle of incidence [26]. Thus, η' is corrected for the presence of anti-reflection coating and the corrected value is used to compute η_g from the Beer-Lambert law as expressed in Eqn. 6.18. The transmission factor η_h for the half-wave plates is chosen from the specification sheet accounting for the reflection from the anti-reflection coatings. For BS_1 the transmission factor η_s is determined using the

[14] AR coating or anti-reflection coating [23] is applied to the optical surfaces to minimize the reflection from the surfaces, hence to increases the transmission through the component. The performance of the AR coatings is dependent on the wavelength of the light and the angle of incidence. The GP used in the experiment has B-coating [24] which reduces the reflection loss for the wavelength range $650 - 1050\ nm$.

experimentally recorded power data at the outputs and at the input of the BS as described in Sec. 6.4.

Apart from the transmission loss, the parameters that modify the amplitudes are mainly the $T : R$ ratio of the BS and the polarization dependent reflectivity of the mirrors, where $R_p \neq R_s$. Depending on the splitting ratio ($T : R$) of BS_1, a part of the beam incident on it gets transmitted and another part gets reflected, where $T + R = 1$. Though in the specification sheet, BS_1 is mentioned as a $50 : 50$ beam splitter, from the experimental data we found that it has a Transmittance, $T \approx 52.62$ and Reflectance, $R \approx 47.38$, when normalized to the total power at the output of BS_1. However, as the beam propagates through the beam splitter, due to the absorption loss we get absolute transmittance $T_{abs} = \eta_s T$ and absolute reflectance $R_{abs} = \eta_s R$, where $T_{abs} + R_{abs} < 1$. For BS_1 we get, $T_{abs} = 49.21$ % and $R_{abs} = 44.34$ %, giving $\eta_s = 93.55$ %. Since we have already accounted for the transmission loss through the 2 *inch* beam splitter BS_1 in the analysis for obtaining the experimental distribution $\mu_{exp}(E)$ and corrected for it, we have not considered the absorption loss in BS_1 while computing the amplitudes for finding the theoretical distribution.

In this experiment, we are interested in finding the measure for the event $E = \{00, 01, 11\}$, similar to finding the probability of the system choosing any one of the paths $00, 01, 11$ while traveling through the beam splitter BS_1 twice. Thus ideally, the theoretical computation of measure should consider the amplitudes of the paths up to the outputs of DSI, i.e., up to the system propagation region. The amplitudes A_e associated with the desired paths i.e., $00, 01$ and 11 are determined from the parameters of real optical components, and the measure is computed from these amplitudes using the Eqn. **6.15**. The distribution, $\mu_{th}^{(1)}(E)$ of the measure values, is obtained by accounting for the inherent uncertainties associated with the parameters of optical components. Considering only the effects of real optical components present up to DSI in the setup while assuming constructive interference between the paths 01 and 11, we obtain the theoretical value of measure to be 1.2348 ± 0.0015.

However, this section aims to find a distribution of the values of measures for the event E computed theoretically considering the limitations and uncertainties associated with the experiment. This provides an estimate of the range in which the quantity to be determined experimentally is expected to lie. Since the determination of experimental quantity involves measuring the power at the end of the event filter, the parameters associated with the optics in the event filtration region after the DSI would also come into play and affect the experimental result. So, the amplitudes of the paths up to the detector, let $A_e^{(d)}(\gamma^k)$, need to be computed and accounted for in the determination of $\mu_{th}^{(1)}(E)$.

The splitting ratio $T : R$ and transmission factor (η_{bs}) of BS_2 are determined from the experimentally measured powers at its input and outputs. Since, the paths after DSI involve polarization projection, any change in the polarization in the paths will affect the final power. Thus, a small disorientation of the fast axes of the half-wave plates would change the amplitudes $A_e^{(d)}(\gamma^k)$ and hence $\mu_{th}^{(1)}(E)$. The setup for the event filter has three HWPs; the fast axis of HWP_1 and HWP_3 are to be oriented at $\theta = 45°$ w.r.to the horizontal in order to realize σ_x operator and the fast axis of the HWP_2 is to be oriented at 22.5° w.r.to the horizontal to realize a Hadamard operator which transforms the polarization basis from $\{H, V\}$ to $\{D, A\}$. Each of the HWPs is mounted on a kinematic rotation mount [$KS1RS$, $Thorlabs$] which has a least count of 2°. Thus there can be an associated uncertainty in the orientation of the fast axis with respect to the desired angle, which would modify the evolution of the state through the HWPs affecting the interference intensity.

However, for the analysis of the theoretical distribution of μ the error corresponding to the HWP orientation is ignored. This could be done because in the experiment the fast-axes of different HWPs are aligned by looking at the desired outcomes, not simply looking into the labels on the mount. HWP_1 and HWP_3 are to be oriented to realize as σ_x operator, which is achieved by placing a PBS after the HWP and monitoring the power at the transmitting port of it when a horizontally polarized beam is made incident on the HWP. The fast axis of the HWP is rotated in small steps and is fixed at the angle for which the transmitted power through the PBS becomes minimum. For aligning HWP_2, a PBS is placed after it and the powers at both the output ports of it are monitored simultaneously. The HWP is rotated in small steps and is fixed at the angle that corresponds to equal powers in the reflecting and transmitting ports of the PBS when a horizontally or vertically polarized beam is made incident on the HWP. At this setting HWP_2 behaves as a Hadamard operator. So, the HWPs are aligned observing the intensities (powers) after the PBSs and not looking at the label on the mount. This makes the uncertainty associated with the half-wave plate orientation to be related to the random detection noises and random power variations, the effect of which on the theoretical computation of μ is considered in the next subsection 6.5.3.

The amplitudes $A_e^{(d)}$ are determined for the paths $00,\ 01,\ 11$ considering the real parameters of the components present in the paths and the distribution $\mu_{th}^{(1)}(E)$ is obtained from the values computed using Eqn. **6.15** keeping in mind that the design of the event filter causes loss in half of the photons in the paths after the interferometer. Thus, $\mu_{th}^{(1)}(E)$ is the theoretical distribution of expected values of measure with the real optical components and without any phase fluctuation, assuming constructive interference between 01 and 11. From the obtained distribution, we get the theoretically expected measure value to be 1.2095 ± 0.0015 [15]. Thus the value of measure obtained from the amplitudes up to the detector i.e., $A_e^{(d)}(\gamma^k)$, is less than the one obtained using amplitudes up to DSI i.e., $A_e(\gamma^k)$ which is expected as there are several other components in the paths from DSI to the detector, all associated with some transmission loss [16].

6.5.3 Computing the Measure from the Intensities: Accounting for Power Fluctuations and Real Optical Components

The modified expression for measure for the event $E = \{00, 01, 11\}$ obtained from theory considering real experimental parameters without the phase fluctuation (assuming constructive interference between the histories 01 and 11) is given by Eqn. **6.15**,

$$\mu^e_{\varphi=0}(E) = |A_e(00)|^2 + |A_e(01) + A_e(11)|^2$$

Here, $A_e(\gamma^k)$ are the amplitudes associated with the paths γ^k for the experimental setup. In terms of intensities, where $I_e(\gamma^k) = \left|A_e(\gamma^k)\right|^2$ represent the intensity of the beam in the path γ^k, the above expression can be written as,

[15] Since the obtained distribution $\mu_{th}^{(1)}(E)$ is a normal distribution we report $mean \pm std$, where std is the standard deviation of the distribution.

[16] Here, we have ignored the effects of the disorientation (if any) of the HWPs . The least count of 2° of a HWP mounts implies that the fast axis of that HWP lies somewhere between $\vartheta + 1^\circ$ to $\vartheta - 1^\circ$ with ϑ being the desired angle [27]. Considering this uncertainty in the orientation of the fast axes of the HWPs, we get the value to be 1.2090 ± 0.034. This implies that any error in the orientation of the HWPs would increase the uncertainty i.e., the spread of the distribution $\mu_{th}^{(1)}(E)$.

$$\mu^e_{\varphi=0}(E) = I_e(00) + I_e(01) + I_e(11) + 2\sqrt{I_e(01)\ I_e(11)} \tag{6.19}$$

In general, $A_e(\gamma^k) = \left|A_e(\gamma^k)\right| \exp\big(i \arg(A_e(\gamma^k))\big)$. Since we can always adjust the relative phase between the two histories 01 and 11 by adjusting the tilt of the GP, we can choose $\arg(A_e(01)) - \arg(A_e(11)) = 0$ for the above expression to have constructive interference.

So far we have determined the theoretical distribution $\mu^{(1)}_{th}(E)$ of measure for the desired event E considering only the effects of the real optical components present in the setup. The inherent uncertainties associated with different parameters of the components make $\mu^{(1)}_{th}(E)$ an almost symmetric distribution about the mean 1.2095 with a standard deviation of 0.0015. Experimentally, the measure μ for the event E is determined from the powers P_{input} and P_{event} recorded at the input and the output of the designed event filter. As discussed in 6.4.1, the experimentally recorded powers have high frequency random fluctuations along with some periodic drifts that affect the quantity to be obtained from the experiment. Here, we would find the theoretical distribution $\mu^{(2)}_{th}(E)$ accounting for the effect of the power fluctuations along with the effects of the real components. Experimentally, the powers $P_{00},\ P_{01},\ P_{11}$ are recorded for the individual histories $00,\ 01,\ 11$ that comprise the event E, at different experimental settings. The intensities $I_e(\gamma^k)$ are computed after correcting the powers P_{γ^k} accounting for the transmission loss through BS_1 and then normalizing the corrected powers with the incident power P_I.

$$I_e(\gamma^k) = \frac{1}{\eta_s^2}\left(\frac{P_{\gamma^k}}{P_I}\right) \tag{6.20}$$

The measure $\mu^e_{\varphi=0}(E)$ for the event is calculated from the intensities $I_e(\gamma^k)$ using the expression given in Eqn. 6.19. The uncertainties associated with the power data gives a distribution of $\mu^e_{\varphi=0}$ values, which is the distribution obtained from the theoretical expression of measure considering parameters of the real optical components and power fluctuations when there is no phase fluctuation. The drifts in the power introduces an asymmetry in the distribution for $\mu^{(2)}_{th}$, thus the expected theoretical value of measure obtained from the distribution is reported as $median^{+\sigma_+}_{-\sigma_-}$, where $median$ corresponds to 50^{th} percentile of the distribution, σ_+ and σ_- respectively represent the ranges of 84.13^{th}

and 15.87^{th} percentile of the distribution with respect to the median. Given the temporal variation of power we get the theoretical estimation for measure to be $1.1981^{+0.0084}_{-0.0075}$. The drift in the power broadens the theoretical distribution for measure $\mu^{(2)}_{th}(E)$, i.e., increases the uncertainty in the estimated theoretical value and makes the distribution a skewed one.

6.5.4 Computing the Measure with Experimental Uncertainties: Accounting for Real Optical Components, Power Variation and Interferometric Phase Fluctuation

So far, we have theoretically determined the distribution of measure μ for the event $E = \{00, 01, 11\}$ from the modified amplitudes $A_e(\gamma^k)$ of the paths γ^k accounting for non-idealnesses of the optical components. We have also estimated how the drifts and fluctuations in power (along with the detection noises) would affect the quantity to be obtained experimentally. From the distributions, $\mu^{(1)}_{th}(E)$ and $\mu^{(2)}_{th}(E)$, it can be seen that the transmission loss associated with different components causes a reduction in the value of the measure from the one computed considering ideal components ($\mu^{(ideal)}_{th}(E) = 1.25$), while the power variations mostly cause broadening in the distribution. Computation of both the distributions assumes a stable interferometric phase at $\varphi = 0$ i.e., constructive interference between the histories 01 and 11. However, any interferometric experiment is affected by the relative phase fluctuation unless the phase is actively stabilized. Here, we will find how the phase fluctuations modify the theoretical distribution of measure for the desired event while considering other parameters that influence the experimental result.

For the event $E = \{00, 01, 11\}$, the experimental determination of measure relies on the measurement of intensity of the beam at the end of the event filter where the two beams from the paths 01 and 11 interfere. For collinear geometry of the interferometer, the interference intensity varies depending on the relative phase φ between the interfering paths [17]. The interference intensity is maximum at phase $\varphi = 0$ and it drops as the phase varies in either direction from zero. The theoretical expression for quantum measure for the event $E = \{00, 01, 11\}$ accounting for experimental non-idealnesses including the phase variation is given by,

[17] For non-collinear geometry, as the relative phase varies the interference fringes redistribute themselves across the beam width i.e., fringe shift occurs with the average power remaining the same.

$$\mu^e_\varphi(E) = |A_e(00)|^2 + |A_e(01) + \exp(i\varphi)A_e(11)|^2 \tag{6.21}$$

where $A_e(\gamma^k)$ are the modified amplitudes of the histories γ^k for the particular design of the event filter i.e., the experimental setup shown in Fig. 6.2.

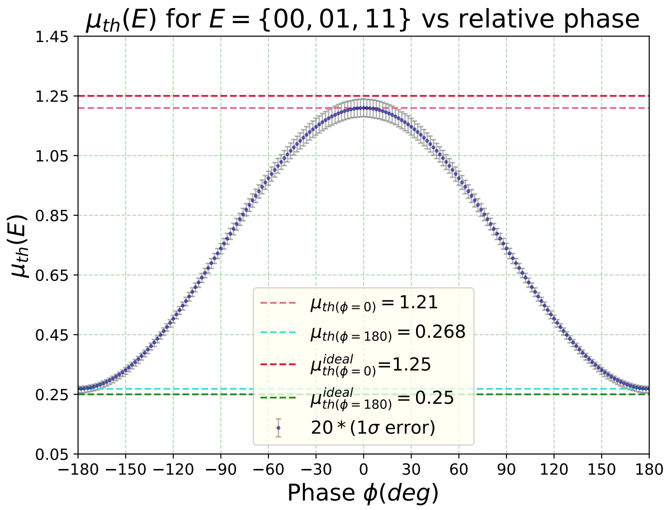

Figure 6.6: Theoretical distribution of the measure ($\mu_{th}(E)$) varying as a function of the relative phase $\varphi \in [-\pi, \pi)$ between the two interfering paths 01 and 11. The blue dots and gray lines respectively represent the median and 20 times the 1σ error bar of the distribution [18]computed for a particular phase. The horizontal lines show the maximum and minimum possible values of the measure for the event E as the interference changes from constructive ($\varphi = 0°$) to destructive ($\varphi = \pm 180°$), obtained for both an ideal scenario as well as the experimental scenario.

Since the powers are measured at the end of the filter where the detector is placed, the amplitudes up to the detector i.e., $A^{(d)}_e(\gamma^k)$ are computed considering non-idealness of all the components present in the respective paths as discussed in 6.5.2 and from the amplitudes μ^e_φ is obtained for a particular phase φ using Eqn. 6.21 taking into account the fact that half of the photons contributing to the event are lost in the filtration region

[18]The uncertainties associated with each distribution are multiplied by 20 in order to make them visually noticeable.

owing to its design. With the phase φ varying within a certain range during the experiment, the theoretical distribution of the measure $\mu_{th}^{(3)}(E)$ is obtained. Fig. 6.6 shows how the variation of the relative phase from $-180°$ to $+180°$ (or $-\pi$ to $+\pi$) changes the theoretical distribution of measure for the event E obtained considering the effect of real optical components present in the setup. The value of the measure decreases as the phase changes in either direction from 0, implying that any change in phase from $0°$ during the experiment would result in a reduction in the value of the measure. Additionally, the plot shows that for a certain range of phase, the measure can take values greater than 1 i.e., beyond the classical limit. This indicates that the phenomena of "interference" allowed in Quantum Measure Theory is the cause of μ having values in the non-classical region.

❏ Finding the Interferometric Phase from the Experiment:

In order to find the theoretical distribution of measure considering the effect of experimental phase fluctuation, we need to find the potential range of the interferometric phase within which it can vary during the experiment. This is achieved from the recorded power data P_{01}, P_{11} and P_{int} [19], respectively representing the powers associated with 01 path, 11 path and the interference between 01 and 11 paths. When two beams of intensities I_1 and I_2 interferes with each other, the interference intensity I as a function of relative phase can be expressed as,

$$I(\varphi) = I_1 + I_2 + 2\sqrt{I_1 I_2}\cos(\varphi) \tag{6.22}$$

Experimentally, the intensities I_1 and I_2 are obtained from P_{01} and P_{11} data and the interference intensity $I(\varphi)$ is obtained from the power P_{int} recorded at the end of the event filter with the top arm after DSI being blocked. As the power P_I (i.e., P_{input}) incident on the setup varies as a combination of high frequency random fluctuations along with low frequency periodic drift because of the reasons listed in Sec. 6.4, P_{01} and P_{11} vary accordingly having their own distributions for the time of data acquisition. Similarly, we have a distribution for P_{int} data as well. There are several factors that causes the power data P_{int} to vary over time as listed in the following.

[19] Detail of the data acquisition procedure is given in the subsection 6.2.3 titled "Method and Data Acquisition".

(i) The fluctuation in the powers P_{01}, P_{11} associated with the two interfering beams,

(ii) The beam wander and the beam drift of the two interfering beams that changes the degree of overlap of the beams on the detector plane affecting the collinearity and hence the interference intensity,

(iii) The fluctuation in relative phase between two interfering beams as a result of the vibrations in any opto-mechanical components inside the interferometer and any drift in the laser wavelength (mode hopping) that affect the interference[20].

If the powers associated with two interfering beams were equal i.e., $I_1 = I_2 = I_0$ say, then the relative phase φ between them could have been found only from the interference intensity i.e., from P_{int} data over time. In this case, the interference intensity as a function of phase can be written as,

$$I(\varphi) = 2I_0(1 + \cos(\varphi)) \tag{6.23}$$

$$\text{giving,} \qquad I_{max} = I(\varphi = 0) = 4I_0 \tag{6.24}$$

Using the above expressions the relative phase φ can be obtained as the following,

$$\frac{I(\varphi)}{I_{max}} = \frac{1 + \cos(\varphi)}{2} \tag{6.25}$$

$$\implies \qquad \varphi = \arccos\left(\frac{2I(\varphi)}{I_{max}} - 1\right) \tag{6.26}$$

The variation of phase φ during the experiment can be obtained from the interference intensity $I(\varphi)$ provided both the interfering beams have equal powers that remain constant throughout the data acquisition. However, this assumption may not hold true in practice.

[20] We have seen a periodic drop in the interference power I_{int} (and also for P_{event}) for very short duration at an interval of ≈ 40 $mins$, this happens because the change in the cavity parameters causes instability in the resonating Laser mode which fluctuates for a small time and then again gets stabilized at a particular value. This is called mode hop of the Laser that happens periodically.

In reality, the beams associated with the two paths 01 and 11 pass through different optical components and thus, encounter different amounts of losses in their intensities, resulting in $I_1 \neq I_2$. Ignoring the power fluctuations, we can express the intensities as, $I_1 = \left|A_e^{(d)}(01)\right|^2 P_I$ and $I_2 = \left|A_e^{(d)}(11)\right|^2 P_I$, where P_I is the power of the beam incident on the setup which is assumed to be constant here and $A_e^{(d)}(01)$, $A_e^{(d)}(11)$ represent the amplitudes of the respective histories $01, 11$ up to the detector, computed using the real parameters of the components present in each path. For the case when $I_1 \neq I_2$, the relative phase (φ) is determined from the interference intensity $I(\varphi)$ as,

$$\varphi = \arccos\left(\frac{I(\varphi) - I_1 - I_2}{2\sqrt{I_1 I_2}}\right) \tag{6.27}$$

provided the following condition is satisfied,

$$I(\varphi) \leq I_1 + I_2 + 2\sqrt{I_1 I_2} \tag{6.28}$$

However, in the experiment, the recorded power data P_{01} and P_{11} of the interfering beams (01 and 11) exhibit temporal variations that cause I_1 and I_2 to have their own distributions as well. Thus, the determination of the quantity φ for a particular $I(\varphi)$ from Eqn. 6.27 using the data from the distributions of I_1 and I_2, would result in multiple values of φ within a certain range.

Hence, the interferometric phase fluctuation during the experiment can be determined using the distribution of interference intensity $I \equiv I(\varphi)$ and the individual intensities $I_1,\ I_2$ associated with the interfering beams. These intensities are obtained from P_{int}, P_{01}, andP_{11} data, ideally to be recorded at the same time. However, since these data are collected at different times experimentally, the systematic drift of power over time introduces an error when determining the phase directly from the data. To avoid any time dependence and minimize the systematic error in computing φ, random samples (say, $I_s,\ I_{1s},\ I_{2s}$) are drawn from each distribution $I,\ I_1,\ I_2$ and the phase $\varphi^{(k)}$ is determined as,

$$\varphi^{(k)} = \arccos\left(\frac{Is - I_{1s} - I_{2s}}{2\sqrt{I_{1s} I_{2s}}}\right) \tag{6.29}$$

$$\text{provided,} \qquad I_s \leq (I_{1s} + I_{2s} + 2\sqrt{I_{1s}I_{2s}}) \tag{6.30}$$

where $\varphi^{(k)}$ is the phase determined for the $k-$th trial. This process is repeated several times to get the distribution of phase, say Φ, for the experiment. This distribution, in general, carries the effect of both power and interferometric phase fluctuations. From the obtained data P_{int} the effects due to these two factors, i.e., power fluctuation and phase fluctuation, can not separated from each other.

For a particular trial, the quantity $(I_{1s} + I_{2s} + 2\sqrt{I_{1s}I_{2s}})$ gives the maximum possible value of the interference intensity when beams of intensities I_{1s} and I_{2s} interferes. Thus for I_1 and I_2 obtained from the experimental data, we will have a particular distribution, say I_{max}, of the maximum interference intensities. Now, since the power shows a slow drift and oscillation over time, it can so happen that P_{01} or/and P_{11} are recorded during the falling slope of the average intensity and P_{int} is recorded during the rising slope of the average intensity. This situation may cause $(I_{1s} + I_{2s} + 2\sqrt{I_{1s}I_{2s}})$ to have a value smaller than I_s for certain data, which ideally is not possible. Thus, while determining the phase, we choose only those data for which the condition given in Eqn. 6.30 is satisfied.

❏ Theoretical Distribution of Measure Considering Interferometric Phase Fluctuation:

For the event $E = \{00, 01, 11\}$, the theoretical value of the measure is calculated to be 1.2095 ± 0.0015 considering only the effect of the real optical components and disregarding the power and phase fluctuations while assuming $\varphi = 0$. Next, considering the effects of real components and the power variation while ignoring phase fluctuation, the expected theoretical value of the measure is computed to be $1.1981^{+0.0084}_{-0.0075}$. Now, the measure for the event E will be estimated accounting for the phase fluctuations in the interferometer as well. After finding the distribution for phase (Φ), we calculate μ^e_φ from Eqn. 6.21 using random samples drawn from Φ and $A^{(d)}_e(\gamma^k)$ for $\gamma^k = 00, 01, 11$ and repeat the process multiple times (here, $\mathcal{N} = 10^5$ times) to get the theoretical distribution $\mu^{(3)}_{th}(E)$ of different μ^e_φ values. Ideally, the obtained distribution Φ should only reflect the relative phase between the interfering beams [21], but due to the involvement of the intensities in the expression of φ, the obtained value of phase carries the effect of power fluctuation as well. Therefore, $\mu_{th}^{(3)}(E)$ is the distribution of measure obtained theoretically that incorporates all parameters having a significant impact on the experimental outcome.

At first, while determining Φ, we assume that the variation in interference intensity $I(\varphi)$ only results from the phase fluctuation ignoring the power fluctuations. Here, we consider I_1 and I_2 to remain constant at the median of their respective distributions $\left|A_e^{(d)}(01)\right|^2 P_I$ and $\left|A_e^{(d)}(11)\right|^2 P_I$. Thus here, Φ is obtained from P_{int} data for which the criteria mentioned in Eqn. 6.28 is fulfilled and then the distribution $\mu_{th}^{(3)}(E)$ is determined for Φ using the amplitudes $A_e^{(d)}$ s. The theoretical value of measure obtained in this case is given by $1.2020^{+0.0052}_{-0.0043}$ [22]. Here, the distributions for the interfering intensities are obtained from the incident intensity distribution P_I and propagating it to the end of the setup through different optical components accounting for the inherent uncertainties in their parameters, i.e., using the distributions of $A_e^{(d)}(\gamma^k)$ for $\gamma^k = 01, 11$.

Next, the measure is theoretically computed using the distribution of phase (Φ) determined using $I(\varphi)$ (obtained from P_{int} data), and the intensities I_1 and I_2 of the interfering beams (obtained from experimentally recorded P_{01}, P_{11} data). In this case, at first, I_1 and I_2 are considered to remain constant at the median values of P_{01} and P_{11} respectively and Φ is determined using the data P_{int} which is assumed to vary only due to the phase fluctuations. Since the interfering intensities are chosen to be constant, the maximum possible value of interference intensity $I_{max} = I_1 + I_2 + 2\sqrt{I_1 I_2}$ is a constant as well. Here, the distribution of phase (Φ) is obtained from P_{int} data for which the condition $I(\varphi) \leq I_{max}$ is satisfied. Hence, ignoring the effect of experimental power fluctuations, the theoretical value of the measure is calculated to be $1.1828^{+0.0125}_{-0.0097}$.

However, in reality, the interference intensity $I(\varphi)$ varies over time not only because of the interferometric phase fluctuation but due to the temporal variation of the powers

[21] due to the variation in the path difference between the two interfering beams or due to the variation in laser wavelength etc..

[22] When I_1, I_2 are chosen to be $I_1 = \left|A_e^{(d)}(01)\right|^2 pI_{(m)}$ and $I_2 = \left|A_e^{(d)}(11)\right|^2 pI_{(m)}$, where $pI_{(m)}$ is the median value of the data P_I recorded at the input of the setup, the theoretical measure value is calculated to be $1.1993^{+0.0064}_{-0.0048}$.

associated with the interfering beams as well. The experimentally recorded powers P_{01} and P_{11} fluctuate over time, causing the resultant intensity P_{int} to vary even in the absence of phase fluctuations [23]. From the distributions of I_1 and I_2, Φ is obtained using Eqn. 6.29. Interference between two beams with varying intensities I_1 and I_2 results in a distribution for I_{max}, with the maximum value of $I(\varphi)$ expected to fall anywhere within the distribution. Thus, considering the effect of power fluctuations of the interfering beams along with the interferometric phase fluctuation, we get the theoretical value of measure to be $1.1824^{+0.0134}_{-0.0106}$. This value represents the median and $\pm 1\sigma$ error of the distribution $\mu_{th}^{(3)}(E)$ for $E = \{00, 01, 11\}$ obtained theoretically using the distributions of amplitudes associated with different paths (i.e., $00, 01, 11$) accounting for the transmission losses and real parameters of different optical components and the distribution of phase Φ derived considering the interferometric phase fluctuation and the temporal variation of the powers.

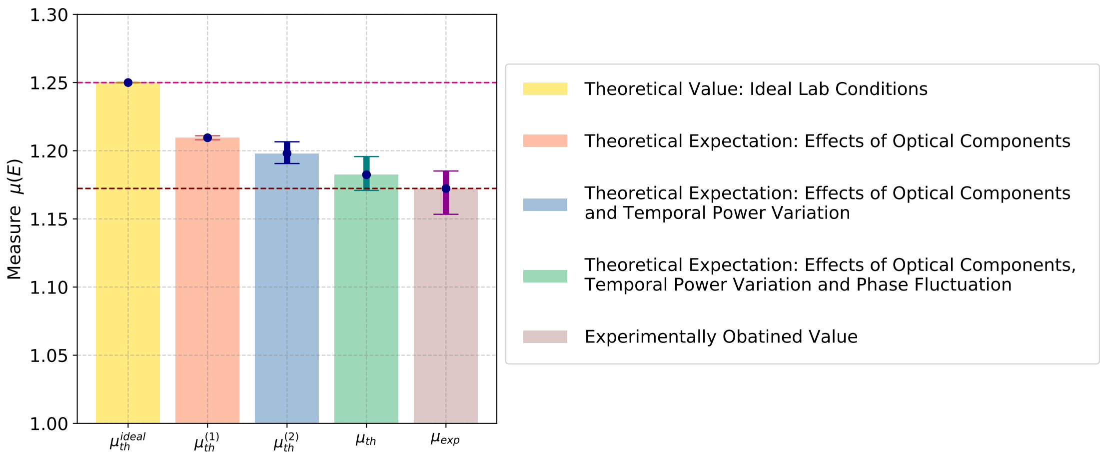

Figure 6.7: Comparison of the measures for the event $E = \{00, 01, 11\}$ associated with a photonic system for different conditions. Each bar height represents the value of the measure either obtained or expected to be obtained experimentally for a certain condition and the solid lines represent the uncertainty associated with the distribution at that condition. The bar in "yellow", "red", "blue", "green", and "violet" respectively correspond to the distributions $\mu_{th}^{(ideal)}(E) = 1.25$, $\mu_{th}^{(1)}(E) = 1.2095 \pm 0.0015$, $\mu_{th}^{(2)}(E) = 1.1981^{+0.0084}_{-0.0075}$, $\mu_{th}^{(3)}(E) = 1.1824^{+0.0134}_{-0.0106}$ and $\mu_{exp}(E) = 1.1723^{+0.0129}_{-0.0194}$.

[23] The determination of the theoretical value of measure, considering only the power fluctuations assuming phase to remain constant at $\varphi = 0$, using the recorded powers P_{00}, P_{01}, P_{11} associated with the individual paths comprising the event E is given in 6.5.3.

6.6 Quantum Measure of a Photonic Event: A Comparison of Experimental and Theoretical Distributions

The histogram plot for the experimentally obtained distribution of the quantum measure $\mu_{exp}(E)$ for the event $E = \{00, 01, 11\}$ associated with a photonic system is shown in Fig. 6.8. Since the distribution $\mu_{exp}(E)$ is not a *Normal distribution*, the central tendency and the measure of spread of it are reported with the *median* and $\sigma_{\pm}$ values instead of the *mean* and *standard deviation* (i.e., $\pm\sigma$). Here the uncertainty of the distribution is given by $\Delta\sigma = \sigma_+ - (-\sigma_-) = \sigma_+ + \sigma_-$. The *median* represents the 50^{th} percentile of the data and σ_+, σ_- respectively represent the range of 84.13^{th} percentile and 15.87^{th} percentile of the data w.r.to the *median*. The 68.26%, 95.44% and 99.74% confidence intervals CI (associated with the 1σ, 2σ and 3σ of a Normal distribution) are presented in the plot with three different shaded regions. Here, the "red" line shows the theoretical expectation of measure $\mu^{(ideal)}(E) = 1.25$ under ideal lab conditions and the "green" line shows the upper bound of the probability measure in the classical measure space at $\mu_{C,max} = 1$.

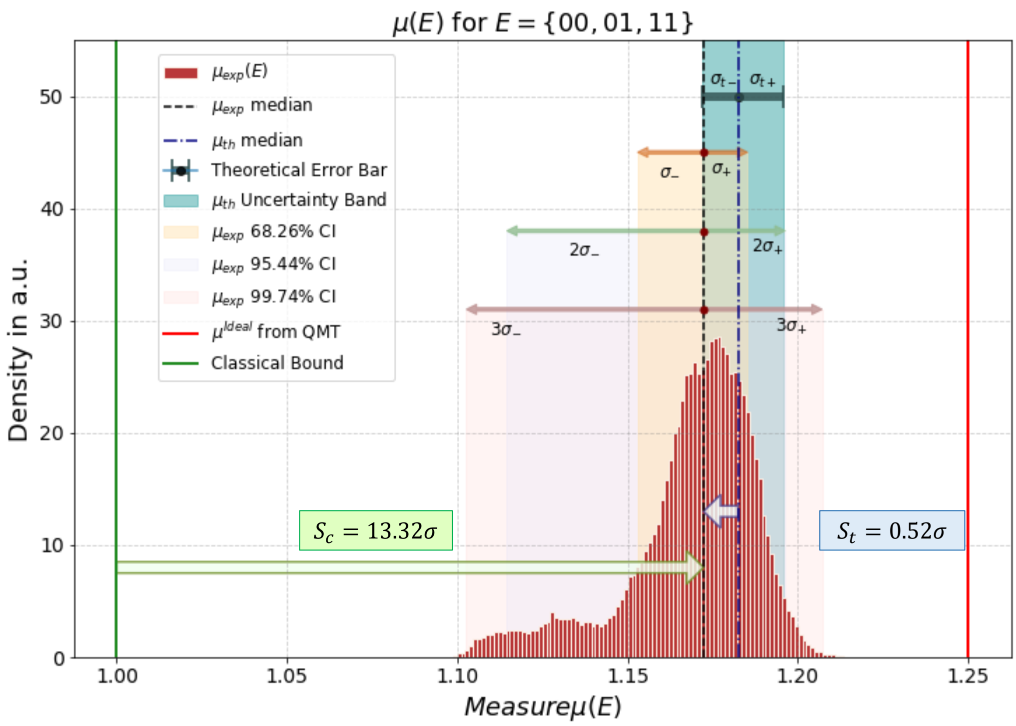

Figure 6.8: Quantum Measure associated with an event $E = \{00, 01, 11\}$ for a photonic system when it passes through a single device with two output ports twice.

The vertical “blue” line and the “blue” band in Fig. 6.8 respectively represent the *median* and the 1σ uncertainty, i.e., $\Delta\sigma_t = \sigma_{t+} + \sigma_{t-}$ of $\mu_{th}(E)$, which is the theoretical distribution of measure obtained for the event E considering the imperfections, limitations, losses and uncertainties associated with a real experiment. This “blue” band can be considered as the theoretical uncertainty band, within which the experimentally obtained quantity is expected to lie. Here, the *median* value of the experimental distribution $\mu_{exp}(E)$ is observed to be within 1σ of the theoretical estimation $\mu_{th}(E)$.

Results: For the event $E = \{00, 01, 11\}$ associated with a photonic system,

- Experimentally obtained measure, $\mu_{exp}(E):\ 1.1723^{+0.0129}_{-0.0194}$
- Theoretical expectation of measure $\mu_{th}(E):\ 1.1824^{+0.0134}_{-0.0106}$

The separation between the median values of $\mu_{exp}(E)$ and $\mu_{th}(E)$ is due to the systematic error introduced while determining the experimental quantity from the data sets (powers at different positions in the setup) recorded at different times, since the power data shows a slow periodic drift over time. In spite of the unavoidable systematic error, the median of $\mu_{exp}(E)$ falls within the theoretical uncertainty band. Further, the experimentally obtained quantity is shown to be $13.32\sigma_+$ away from $\mu_{C,max}$, which makes it significant enough to be considered as something non-classical. More about the significance of the experimental result will be discussed in the next section.

6.7 Statistical Significance Analysis and Hypothesis Testing

In statistical analysis, the inferential statistics allows us to make conclusions about a population based on the descriptive analysis of the sample data we possess. Any idea or mathematical model formulated based on one set of data (sample) is called an hypothesis and is applied for the entire population. Uncertainty of a distribution plays a key role in statistical inferences and in making any decisions about ideas or hypothesis corresponding to the population. Testing a hypothesis or a model, in the context of an experiment, involves determining how well the hypothesis can predict the obtained experimental result with appropriate evidence [28]. In an experimental study, identifying whether the results are meaningful or not is determined by examining their statistical significance, which serves as the evidence either to reject or failing to reject a hypothesis [29]. The statistical significance of a quantity of interest (say, t), which is a parameter related to the sample randomly drawn from the population, is determined as,

$$\mathcal{S} = \frac{t - m}{\sigma} \tag{6.31}$$

where, t is the sample mean, m is the population mean and σ is the standard deviation. Note that, the reference to the standard deviation in the above requires a normal or at least a Student-T distribution. However the statistical significance of a quantity can be applied to any distribution.

In this experiment, we aim to establish that the quantity "measure" (μ) associated with an event obtained for a quantum system is something non-classical. The classical measure space limits the maximum possible value of measure to be one, i.e., $\mu_{C(max)} = 1$. Thus any value of measure exceeding this limit is considered non-classical and is believed that it belongs to the quantum measure space where quantal interference allows the measure to take values above one. In order to establish the non-classical nature of the quantity μ for the event $E = \{00, 01, 11\}$, we need to ensure that the experimentally determined value of measure (μ_e) from the distribution $\mu_{exp}(E)$ is significantly away from the classical-quantum boundary (which is 1). The statistical significance of the experimentally obtained quantity with respect to the classical-quantum boundary is computed as the following,

$$\mathcal{S}_c = \frac{\mu_{e(m)} - \mu_{cq}}{\sigma_\mu} \tag{6.32}$$

Here, $\mu_{e(m)}$ is the mean of the experimentally determined distribution of the measure (i.e, μ_{exp}), μ_{cq} is the classical-quantum boundary, where $\mu_{cq} = \mu_{C(max)} = 1$, σ_μ is the standard deviation of the experimental distribution (μ_{exp}). If the significance is more than 3, it typically is agreed upon to be significant enough to be considered as evidence, the larger the better [30].

However, such statistical analysis involves assumptions like the distribution of the statistical values to be a normal distribution. This often is not the case in an experiment due to the non-idealness, imperfections and limitations associated with the real parameters that influence the experiment. Hence, we need to comment on the statistical significance of the quantity μ_e obtained experimentally, given the non-idealness of the distribution $\mu_{exp}(E)$. For a sample non-ideal distribution, the quantity whose statistical significance is to be established is considered as the median of the distribution instead of the mean and σ_μ is considered to be either σ_+ or σ_- depending on where the population median lies. Here σ_- to σ_+ gives the 68.26% confidence interval of the distribution about its median.

Next, assuming the quantity μ belong to the quantum measure space we have an expectation for the value to be $\mu_{th}^{ideal}(E) = 1.25$ under ideal lab-conditions as computed using the formula given in the quantum measure theory. After accounting for the possible phase fluctuations, the losses associated with different optics in different paths, the random and systematic drifts in the recorded powers and other influencing factors, we obtained a theoretical distribution of measure $\mu_{th}(E)$ within which the experimentally obtained quantity is expected to fall on. The statistical significance of our experimentally obtained quantity (μ_e) with respect to the theoretical expectations can be determined by computing,

$$\mathcal{S}_t = \frac{\mu_{e(m)} - \mu_{t(m)}}{\sigma_\mu} \tag{6.33}$$

Here, $\mu_{t(m)}$ is the median of the theoretical distribution $\mu_{th}(E)$. To establish that our experimental result is something that belongs to the quantum measure space, we need to show that $\mu_{e(m)}$ lies well within the range of the distribution ($\mu_{th}(E)$). A value of $\mathcal{S}_t$ being less than 1 (smaller the better) is in general, considered significant enough to serve as evidence which implies that $\mu_{e(m)}$ lies within 1σ uncertainty of the predicted distribution.

Experimentally, from the obtained distribution $\mu_{exp}(E)$ for the event $E = \{00, 01, 11\}$, we get the value of measure to be $\mu_e = 1.1723^{+0.013}_{-0.0194}$. For this distribution $\mu_{exp}(E)$, which is not Normal, we determine the statistical significance $\mathcal{S}_c = 13.32$ using the Eqn. 6.32. The value of $\mathcal{S}_c > 3$ is significant enough to be considered as an evidence that the experimentally obtained quantity is non-classical, i.e., lies beyond the classical measure space. Again using the theoretical distribution $\mu_{th}(E)$, computed from quantum measure theory, in Eqn. 6.33 we obtain the statistical significance $\mathcal{S}_t = 0.523$ which provides sufficient evidence that the idea of the experimentally obtained quantity μ_e belonging to quantum measure space can not be rejected.

The purpose of scientific methods in the context of hypothesis testing experiments is to be able to reject (or not reject) a potential hypothesis with appropriate statistical significance. In order to draw a conclusions about a population from the sample distribution, we first assume one or more hypothesis to be true and then determine how likely the observed value would occur just by random choice of samples alone, given the population distribution according to the hypothesis. Thus, testing of hypothesis involves analysis of probability of different outcomes given the random choice of the sample, which makes this hypothesis statistical in nature. Depending on the sufficient statistical evidence we either reject a hypothesis or fail to reject a hypothesis [31]. In the context of hypothesis testing, failing to reject a hypothesis does not imply acceptance of the hypothesis − it only means that there is not enough evidence to discard it [32]. It is important to note that absence of evidence is not the same as evidence of absence.

6.7.1 Null Hypothesis Testing

Null hypothesis testing tries to discredit an idea by first assuming the idea is true and then showing that something contradictory happens when this assumption is made. In the context of experimental observations and decision making about a hypothesis, we calculate a p-value to determine level of significance [33] of the observed result. p-value represents the probability of getting a data as extreme as the observed experimental outcome, considering the null hypothesis (given by $\mathcal{H}_0$) to be true i.e., it can take values between 0 to 1. The smaller the p-value is, the more rare it would be to get an extreme experimental result just by random chance alone even if the null hypothesis is true. Thus, we can reject the null-hypothesis when the obtained p-value is significantly low [34].

However, to decide whether the observed data is extreme or rare enough to lead us to believe that the sample probably does not belong to the null distribution and hence the null hypothesis can be rejected, we need to compare the obtained p-value with a pre-determined cutoff α. Here, α represents the threshold of statistical evidence, i.e., a p-value less than or equal to α is considered as sufficient evidence that the observed experimental result is unlikely due to random chance alone, allowing us to reject the null hypothesis. Conversely, for a p-value obtained to be more than the cutoff α, we fail to reject the null hypothesis. In the context of hypothesis testing, α gives the probability that we can commit a $Type - I$ error, i.e., mistakenly reject the hypothesis even if it is true due to the data obtained as a result of the uncertainty involved in the experiment (getting a false positive) [35].

Here, in this experiment where we determine the value of measure associated with an event E for a photonic system, the null hypothesis would presume that the measure μ as the ordinary classical probability measure and thus having an upper bound of $\mu_{C(max)} = 1$.

Null Hypothesis ($\mathcal{H}_0$) : The quantity μ is the same as the classical probability measure with an upper bound of 1.

$$\text{i.e.,} \qquad \mathcal{H}_0 : \ \mu_{\mathcal{N}} = 1 \tag{6.34}$$

$\mu_{\mathcal{N}}$ represents the median value of the measure considering the null distribution $\mathcal{N}$. In order to establish the significance of the experimental outcome μ_e given the null distribution $\mathcal{N}$, we would associate p-value to the experiment.

❑ **p-value:** Let, the distribution of data points (i.e., the measures) obtained in the experiment is given by the probability density function (PDF) $\rho(\mu)$. The cumulative density function (CDF) at μ_c is defined as the probability of obtaining $\mu \leq \mu_c$, i.e.,

$$\mathcal{C}(\mu_c) = \int_{-\infty}^{\mu_c} \rho(\mu) d\mu \tag{6.35}$$

$\mathcal{C}(\mu_c)$ represents the chance that we get the data μ_c or lower, given the distribution $\rho(\mu)$. If the null hypothesis $\mathcal{H}_0$ insists that the true value of measure is $\mu_{\mathcal{N}} = \mu_c$, then we get the null distribution $\mathcal{N}$ assuming the distribution $\rho(\mu)$ to be centered around μ_c. Considering $\rho(\mu)$ to be a symmetric distribution, we get the p-value to be the same as $\mathcal{C}(\mu_c)$ [24].

[24] This could be done since for a given symmetric distribution, the probability of getting an extreme value at a particular distance from the mean are the same regardless if it is higher or lower than the mean.

However, this relation is not applicable while computing the p-value for this experiment, as $\mu_{exp}(E)$ is not a symmetric distribution.

For the event $E = \{00, 01, 11\}$, we get our experimental result μ_e at the median of the experimentally obtained distribution $\mu_{exp}(E)$ since it is not a normal distribution. A p-value associated to the experiment, estimates how rare the experimental result μ_e can be, given the null distribution ($\mathcal{N}$) centered around $\mu_{\mathcal{N}}$. Considering $\rho_{\mathcal{N}}(\mu)$ to be the PDF of the null distribution ($\mathcal{N}$) for the obtained value μ_e in the experiment, the p-value can be computed as the probability of obtaining $\mu \geq \mu_e$.

$$p = \int_{\mu_e}^{\infty} \rho_{\mathcal{N}}(\mu) d\mu \tag{6.36}$$

If obtained p-value is very small, i.e., say $p = 10^{-3}$ or $p = 10^{-6}$, then chance that we obtain the value μ_e given $\mathcal{N}$, is one in a thousand or one in a million respectively. Hence, we can comment that the probability of obtaining μ_e just by random chance is very low and thus the hypothesis can be rejected. When ρ is a normal distribution, we can approximate the chance of one in a million or a thousand by 5σ or 3σ deviation from the mean[25]. According to the current scientific consensus, a deviation of more than 3σ provides evidence that the data might not be from the null distribution and hence the hypothesis can be rejected.

In this experiment, the outcome $\mu_e = 1.1723$ is found to be $13.32\sigma_+$[26] away from the true value $\mu_c = 1$ as claimed by the null hypothesis. Hence, if the null hypothesis is considered to be true, this experimental result is a very unlikely event. So, from the significance analysis, we can successfully reject the idea that the measure μ associated with a photonic system is the ordinary probability measure defined in the classical measure space. Rejecting the null hypothesis based on p-value or the level of significance implies that there is enough evidence that the observed data is improbable under the null distribution and must have come from some other distribution. However this, in no way, proves any alternate hypothesis to be true [36].

[25]For a normal distribution, 3σ and 5σ deviations from mean imply 0.27% and 0.00006% probability of occurrence.

[26]here, σ_+ as the distribution obtained in the experiment is not normal and the null distribution $\mathcal{N}$ is obtained assuming the PDF given by $\rho\mu$ to be centered around $\mu_{\mathcal{N}} = 1$.

6.7.2 Alternate Hypothesis Testing

In the case of experimentally determining the value of the measure for a photonic event $E = \{00, 01, 11\}$, we can form an alternate hypothesis assuming that the measure μ belongs to the quantum measure space, i.e., can be computed using the path-integral approach in quantum measure theory. Thus, for the given setup μ for the event E is predicted to be $\mu_t = 1.1824$ which is the median value of the estimated theoretical distribution $\mu_{th}(E)$.

Alternate Hypothesis ($\mathcal{H}_a$) : The quantity μ to have the value μ_t, which is the median of the theoretical distribution $\mu_{th}(E)$, given the experimental setup and non-ideal lab conditions.

$$\text{i.e.,} \qquad \mathcal{H}_a : \ \mu_{\mathcal{A}} = \mu_t \tag{6.37}$$

According to the alternate hypothesis, the theoretical value of the measure for a lossless system under ideal lab conditions would have been $\mu_t^{(ideal)} = 1.25$. However, for the setup as shown in Fig. 6.2, taking into account experimental non-idealness such as power fluctuations, phase-instability, losses and other parameters associated with the real components etc., we get the theoretical distribution $\mu_{th}(E)$ giving $\mu_{\mathcal{A}} = \mu_t$.

We may not reject this alternate hypothesis if the experimentally obtained result i.e., μ_e is within one standard deviation σ_μ of the prediction by alternate hypothesis, i.e.,

$$|\mu_e - \mu_{\mathcal{A}}| \leq \sigma_\mu. \tag{6.38}$$

If the above condition is satisfied, it is generally considered as a strong evidence that the experimentally observed quantity may have been chosen from alternate distribution $\mathcal{A}$ centered about $\mu_{\mathcal{A}}$. In this experiment, for the observed result $\mu_e = 1.1723$ and $\mu_{\mathcal{A}} = \mu_{t(m)} = 1.1824$, we get the value $|\mu_e - \mu_{\mathcal{A}}| = 0.526\sigma_-$[27].

[27] here, σ_- because the distribution is not normal and the alternate distribution $\mathcal{A}$ is obtained by assuming the PDF given by $\rho\mu$ centered about $\mu_{\mathcal{A}} = \mu_t$.

6.8 Conclusion

In this chapter, using a two-site hopper model in an optical setup, we have presented a table-top demonstration showing how the value of the 'generalized probability' or the 'quantum measure' of a set of histories associated with a photonic system can be inferred from an experiment. Further, we have established the non-classical nature of the experimentally obtained quantity μ_e from the evidence-based statistical significance analysis. The experiment involves devising a toy-model of the ancilla based 'event filter' setup that can extract the desired set of trajectories for the photon by manipulating the polarization degree of freedom, which serves as an effective ancilla. According to the original proposal, this could demonstrate a non-destructive procedure to infer the intermediate process that a micro-system undergoes during its evolution from preparation to detection. The experiment reports quantum measure μ_e for a photonic event E, which is found to be 13.32 standard deviation away from the maximum value ($\mu_{C(max)} = 1$) permissible for classical probability measure. This, based on sufficient evidence, implies that μ_e does not belong to the classical measure space and instead, is non-classical in nature. Moreover, the experimentally obtained quantity μ_e is observed to lie within 0.52 standard deviations of the theoretical estimation, computed within the framework of Quantum Measure Theory (QMT), which suggests that μ_e might belong to the quantum measure space. Unlike classical measure space, quantum measure space allows for interference that causes the measures to go beyond the classical-quantum boundary (μ_{cq}). Therefore, the non-classical nature of the experimentally obtained quantity captures the effect of quantum interference on the micro-system, which causes the quantum measure to differ from the standard Kolmogorov probability measure. Connecting the theoretical constructs like the concepts of events or quantum measure to more practical scenarios, through experiments like the one reported here, could pave the way for future exploration and comprehension of the micro-world.

References

[1] Álvaro Mozota Frauca and Rafael Dolnick Sorkin. "How to Measure the Quantum Measure". In: *International Journal of Theoretical Physics* 56.1 (2017), pp. 232–258. DOI: 10.1007/s10773-016-3181-x.

[2] Rafael D. Sorkin. "QUANTUM MECHANICS AS QUANTUM MEASURE THEORY". In: *Modern Physics Letters A* 09.33 (1994), pp. 3119–3127. DOI: 10.1142/S021773239400294X.

[3] Stanley P. Gudder and Rafael D. Sorkin. "Two-site quantum random walk". In: *General Relativity and Gravitation* 43.12 (2011), pp. 3451–3475. DOI: 10.1007/s10714-011-1245-z.

[4] Roy J. Glauber. "Coherent and Incoherent States of the Radiation Field". In: *Phys. Rev.* 131 (6 1963), pp. 2766–2788. DOI: 10.1103/PhysRev.131.2766.

[5] Jean-Pierre Gazeau. *Coherent States in Quantum Physics*. John Wiley & Sons, Ltd, 2009. DOI: 10.1002/9783527628285.

[6] E. C. G. Sudarshan. "Equivalence of Semiclassical and Quantum Mechanical Descriptions of Statistical Light Beams". In: *Phys. Rev. Lett.* 10 (7 1963), pp. 277–279. DOI: 10.1103/PhysRevLett.10.277.

[7] Dr. Rüdiger Paschotta. *Fiber Connectors*. https://www.rp-photonics.com/fiber_connectors.html.

[8] Chris Emslie. "Chapter 8 - Polarization Maintaining Fibers". In: *Specialty Optical Fibers Handbook*. Ed. by Alexis Méndez and T.F. Morse. Burlington: Academic Press, 2007, pp. 243–277. DOI: https://doi.org/10.1016/B978-012369406-5/50010-2.

[9] D. Marcuse. "Gaussian approximation of the fundamental modes of graded-index fibers". In: *J. Opt. Soc. Am.* 68.1 (1978), pp. 103–109. DOI: 10.1364/JOSA.68.000103.

[10] Ajoy Ghatak and K. Thyagarajan. *An Introduction to Fiber Optics*. Cambridge University Press, 1998. DOI: 10.1017/CBO9781139174770.

[11] *RefractiveIndex.INFO, Refractive index database*. https://refractiveindex.info/?shelf=glass&book=fused_silica&page=Malitsonl.

[12] Timothy C. Ralph Hans-A. Bachor. *A Guide to Experiments in Quantum Optics*. English. John Wiley & Sons, Ltd, 2019. DOI: 10.1002/9783527695805.

[13] H. Nyquist. "Certain Topics in Telegraph Transmission Theory". In: *Transactions of the American Institute of Electrical Engineers* 47 (1928), pp. 617–644.

[14] C.E. Shannon. "Communication in the Presence of Noise". In: *Proceedings of the IRE* 37.1 (1949), pp. 10–21. DOI: 10.1109/JRPROC.1949.232969.

[15] J.R. Taylor. *An Introduction to Error Analysis: The Study of Uncertainties in Physical Measurements*. University Science Books, 1997.

[16] Paul B. Ruffin. "Stress and temperature effects on the performance of polarization-maintaining fibers". In: *Polarimetry: Radar, Infrared, Visible, Ultraviolet, and X-Ray*. Ed. by Russell A. Chipman and John W. Morris. Vol. 1317. International Society for Optics and Photonics. SPIE, 1990, pp. 324–332. DOI: 10.1117/12.22068.

[17] M.P. Varnham et al. "Analytic solution for the birefringence produced by thermal stress in polarization-maintaining optical fibers". In: *IEEE Journal of Lightwave Technology* 1.2 (1983), pp. 332–9.

[18] John W. Leis. *Digital Signal Processing Using MATLAB for Students and Researchers*. English. Wiley, 2011.

[19] Thomas G. Mayerhöfer, Susanne Pahlow, and Jürgen Popp. "The Bouguer-Beer-Lambert Law: Shining Light on the Obscure". In: *ChemPhysChem* 21.18 (2020), pp. 2029–2046. DOI: 10.1002/cphc.202000464.

[20] J. H. Lambert. *Photometria sive de mensura et gradibus luminis, colorum et umbrae*. Latin. sumptibus vidvae E. Klett, typis C.P. Detleffsen, 1760.

[21] A. Beer. "Bestimmung der Absorption des rothen Lichts in farbigen Flüssigkeiten". In: *Annalen der Physik* 162.5 (1852), pp. 78–88. DOI: 10.1002/andp.18521620505.

[22] Ilze Oshina and Janis Spigulis. "Beer-Lambert law for optical tissue diagnostics: current state of the art and the main limitations". en. In: *J Biomed Opt* 26.10 (2021).

[23] Hemant Kumar Raut et al. "Anti-reflective coatings: A critical, in-depth review". In: *Energy Environ. Sci.* 4 (10 2011), pp. 3779–3804. DOI: 10.1039/C1EE01297E.

[24] *AR Coatings, Thorlabs.* https://www.thorlabs.com/newgrouppage9.cfm?objectgroup_id=5840.

[25] *UV Fused Silica High-Precision Windows, Thorlabs.* https://www.thorlabs.com/newgrouppage9.cfm?objectgroup_id=3983&pn=WG40530-B.

[26] *RefractiveIndex.INFO, Refractive index database.* https://refractiveindex.info/?shelf=glass&book=fused_silica&page=Malitsonl.

[27] *Measurement Uncertainty.* TECDOC Series 1585. Vienna: International Atomic Energy Agency, 2008.

[28] Jerzy Neyman, Egon Sharpe Pearson, and Karl Pearson. "IX. On the problem of the most efficient tests of statistical hypotheses". In: *Philosophical Transactions of the Royal Society of London. Series A, Containing Papers of a Mathematical or Physical Character* 231.694-706 (1933), pp. 289–337. DOI: 10.1098/rsta.1933.0009.

[29] R.A. Fisher. *Statistical Methods for Research Workers.* Biological monographs and manuals. Oliver and Boyd, 1925.

[30] Andrea Albert. *How special is "3 sigma"?* https://kipac.stanford.edu/highlights/how-special-3-sigma.

[31] Ronald Fisher. "Statistical Methods and Scientific Induction". In: *Journal of the Royal Statistical Society: Series B (Methodological)* 17.1 (1955), pp. 69–78. DOI: https://doi.org/10.1111/j.2517-6161.1955.tb00180.x.

[32] Tukur Dahiru. "P - value, a true test of statistical significance? A cautionary note". en. In: *Ann Ib Postgrad Med* 6.1 (2008), pp. 21–26.

[33] G. A. Brnard. "THE MEANING OF A SIGNIFICANCE LEVEL". In: *Biometrika* 34.1-2 (1947), pp. 179–182. DOI: 10.1093/biomet/34.1-2.179.

[34] S N Goodman. "p values, hypothesis tests, and likelihood: implications for epidemiology of a neglected historical debate". en. In: *Am J Epidemiol* 137.5 (1993), pp. 485–96.

[35] J A Sterne and G Davey Smith. "Sifting the evidence-what's wrong with significance tests?" en. In: *BMJ* 322.7280 (2001), pp. 226–231.

[36] S N Goodman. "Toward evidence-based medical statistics. 1: The P value fallacy". en. In: *Ann Intern Med* 130.12 (1999), pp. 995–1004.

Chapter 7

Summary and Outlook

This thesis presents the exploration of the phenomena of quantum interference in various aspects of quantum theory and investigates the potential applications of interferometric techniques in two distinct scenarios:

- As an experimental tool to characterize the unknown states of a quantum system, utilizing the information processed from a number of interference patterns.
- To illustrate the practical significance of the non-classical 'quantum measure' of an event related to a quantum system, within the context of a history-based framework.

The two distinct studies, outlined in the thesis, utilize the phenomena of quantum interference under various circumstances and include the examination of the interference patterns to elucidate the operational principles of the proposed schemes for determining quantum states and the non-classical quantum measure. Both works offer an experimental implementation of the suggested models in an optical setup, underscoring their practicality for photonic systems. The experimental results, in conjunction with the associated theories, are shown to have potential applications in the fields of quantum foundation, quantum computation, quantum communication and open up possibilities for future tests related to the fundamental aspects of quantum theory.

Given that the average statistical properties of light are equivalent for a coherent beam and an ensemble of photons, the interference pattern obtained using a coherent laser light source would be identical to the pattern produced with a stream of identical photons. As a result, the findings from the demonstration experiments presented in the thesis, which are performed using laser light sources, would also apply to the ensemble of identically prepared single photons. Here, we have preferably chosen laser lights for conducting the interferometric experiments since the interference patterns produced from single photons were expected to lack high contrast due to the low statistics of the available sources. Further, single photons generated from SPDC (spontaneous parametric down conversion) based sources are found to have significantly shorter longitudinal coherence lengths as compared to the continuous wave laser beams, which requires precise control over the alignment in a single photon interferometer to maintain the coherence between the interfering beams.

The discussions across different chapters of the thesis also highlight the challenges, limitations, and uncertainties associated with an experiment devised in a laboratory setting. These factors could lead to deviations in the experimental results as compared to the expectations derived from the theoretical models, thereby necessitating further correction techniques. As we continue to delve deeper into the quantum realm, it is anticipated that interferometric techniques will play an increasingly crucial role in shaping the future of quantum science and technology. The journey thus far has been fascinating, and the road ahead promises to be even more so.

In the next, we will summarize the significant points and the key findings related to the two applications of the quantum interferometry reported in this thesis and outline the prospective future research directions.

❑ Quantum State Estimation Using Interferometric Technique:

The knowledge of the quantum state is essential while dealing with a quantum system, as it enables effective and efficient manipulations of the system for experimental investigations on quantum foundations, for gauging the eventual fidelity of the quantum computation or communication-based protocols and for various applications of quantum mechanics towards the technological advancements. Only a thorough understanding and characterization of quantum states would enable us to harness the full potential of emerging quantum technologies. Here, the thesis introduces a novel method, known as Quantum State Interferography (QSI), for characterizing the quantum states. This scheme employs interferometry to reconstruct the indeterminate states of a quantum system by analyzing the information derived from interference patterns generated in a particular setup.

The fundamental principle of this interferometric state determination technique is based on the formation of a unique map between a set of interferometric quantities - phase shift, average intensity, visibility – derived from interference patterns and the set of parameters that describe the quantum state. The distinctive correlation between the two sets of quantities is established by evolving an ensemble of quantum systems in the unknown state through an interferometric arrangement with certain operators in the individual paths of the interferometer. The scheme lessens the amount of data collection and the number of experimental settings necessary for state reconstruction in comparison to the standard Quantum State Tomography (QST).

Quantum State Interferography (QSI) emerges as a “true single shot” state characterization technique for qubits, allowing the reconstruction of an arbitrary state in a two-dimensional Hilbert space from a single experimental setting unlike two (for pure state) or three (for mixed state) measurement settings required in QST. The state parameters of an unknown qubit, be it pure or mixed, can be inferred by analyzing a single interference pattern derived from a single setting of a two-path interferometer. The thesis reports a successful experimental implementation of the QSI protocol in an optical setup, achieving an average fidelity of 94%, for the reconstruction of polarization qubits of light. It also provides a comparative study of the results obtained from the QSI techniques implemented using two distinct interferometers - a Mach-Zehnder and a Sagnac interferometer, leading to a further discussion on the selection of one interferometric configuration over the other considering experimental imperfections and noises.

This thesis introduces a new parametric representation for pure qudit ($d > 2$) states, termed as ‘Episphere representation’, in which a pure state $|\psi\rangle^{(d)}$ in d-dimensions is visualized as an ordered sequence of $(d-1)$ Bloch vectors, each spanning a distinct two-dimensional subspace within the d-dimensional space. The thesis further extends the interferometric state determination scheme theoretically, proposing a method for single-shot characterization of an unknown pure qudit ($d > 2$) state utilizing the information derived from $(d-1)$ interference patterns. This involves inferring $(2d-2)$ state parameters associated with a qudit from a single setting of an interferometric setup, which could either consist of just two interferometers or $(d-1)$ two-path interferometers, each interferometer acting on a separate two-dimensional subspace. Consequently, QSI emerges as an efficient single-shot characterization method for qubits and pure qudits, opening up possibilities for future development of compact state estimating devices (could be a few *cm* long, using slit-based interferometers) where no changes in the internal settings would be required between the incidence of an unknown state at the input and extraction of the state information at the output. Additionally, the thesis presents a method to characterize a pure bipartite qubit state using a dual-interferometer setup and demonstrates it as a technique for the single-shot quantification of entanglement.

Future works could include:

(i) Discovering uses of this interferometric scheme for characterizing the mixed states in a d-dimensional ($d \geq 3$) Hilbert space, i.e., qudit mixed states.

(ii) Expanding this interferometric protocol in an efficient manner to characterize the mixed states of bipartite systems.

(iii) Exploring an interferometric scheme for determining a multi-partite ($N > 2$) quantum state, i.e., a state of a composite system comprising more than two subsystems.

❑ Determining the Non-classical Value of Quantum Measure:

In order to provide a comprehensive understanding of the micro-world and address the interpretational challenges present in standard quantum theory, it was felt necessary to introduce alternative approaches to quantum theory grounded on a realistic viewpoint avoiding abstract mathematical concepts such as wave functions, superposition, and measurement that presumes a division of the universe into 'observer' and 'observed'. Quantum Measure theory (QMT), drawing inspiration from the path integral approach, offers a history-based realistic formulation of quantum theory. It describes the kinematics of a micro-system using space-time histories akin to the classical theory and encodes the dynamics of the system in terms of 'generalized probability' or 'quantum measure'. This thesis presents an experimental protocol for determining the 'quantum measure' of realizing a specific set of space-time histories (referred to as an 'event') of a quantum system, as defined in the context of QMT, using an ancilla-based event filtering setup. Being able to assign an empirical significance to these (so far) theoretical concepts would shed light on the intermediate physical events occurring as a quantum system evolves from an initial state (at preparation) to a final state (at detection), which could lead to further developments in the foundational aspects of quantum theory.

The thesis investigates a two-site hopper model for a photonic system within the framework of Quantum Measure Theory (QMT) implemented in an optical setup employing amplitude division. It presents a discussion on the potential designs of an 'event filter' for a specific hopper event that would select the desired set of paths for a photon as it evolves through a two beam splitter setup and analyses their feasibility under conditions that could capture the 'generalized probability' beyond the classical limit, in contrast to the standard Kolmogorov probability. The thesis reports an experiment presenting a tabletop demonstration for identifying the 'quantum measure' of a particular photonic event involving interference and establishes the non-classical nature of the experimentally obtained quantity through hypothesis testing and statistical significance analysis. The observations that the result lies 13.32σ away from the classical-quantum boundary (which is 1) and within 0.52σ of the estimation made from theoretical analysis in QMT, provide strong evidence that the quantity is non-classical and lies within the quantum measure space. Since quantum measure theory expands the scope of measurement procedures by assigning generalized probabilities beyond the Born Rule probabilities to certain non-instrument events (specifically the non-serial events) that remain experimentally inaccessible in standard Quantum Mechanics, it could potentially lead to the design of new kinds of quantum circuits for the applications in quantum computation and quantum information protocols.

Future work could involve:

(i) Designing a Universal Event Filter in an optical setup for a photonic system that would be capable of determining the quantum measure of any event associated with the system, irrespective of its initial state, requiring modifications only in the measurement settings in the event filtration region depending on the choice of the event.

(ii) Determining the maximum achievable efficiency in designing an event filter for a given event of a photonic system while minimizing the losses owing to the design.